Transactions of the ASME®

Transactions of the ASME, Journal of Applied Mechanics (ISSN 0021-8936) is published quarterly (Mar., June, Sept., Dec.)
The American Society of Mechanical Engineers,
Three Park Avenue, New York, NY 10016.
Periodicals postage paid at New York, NY and additional mailing office. POSTMASTER: Send address changes to Transactions of the ASME, Journal of Applied Mechanics, c/o THE AMERICAN SOCIETY OF MECHANICAL ENGINEERS, 22 Law Drive, Box 2300, Fairfield, NJ 07007-2300.
CHANGES OF ADDRESS must be received at Society headquarters seven weeks before they are to be effective. Please send old label and new address.
STATEMENT from By-Laws. The Society shall not be responsible for statements or opinions advanced in papers or . . . printed in its publications (B7.1, Para. 3).

Journal of Applied Mechanics

Published Quarterly by The American Society of Mechanical Engineers

VOLUME 67 • NUMBER 1 • MARCH 2000

TECHNICAL PAPERS

(**Contents continued on inside back cover**)

This journal is printed on acid-free paper, which exceeds the ANSI Z39.48-1992 specification for permanence of paper and library materials. ♾™
♻ 85% recycled content, including 10% post-consumer fibers.

Journal of Applied Mechanics Volume 67, Number 1 MARCH 2000

BRIEF NOTES

ANNOUNCEMENTS AND SPECIAL NOTICES

Radiation of Body Waves Induced by the Sliding of an Elastic Half-Space Against a Rigid Surface

G. G. Adams
Professor,
Fellow ASME
Department of Mechanical Engineering,
Northeastern University,
Boston, MA 02115
e-mail: adams@neu.edu

The steady sliding of a flat half-space against a rigid surface with a constant interfacial coefficient of friction is investigated. It is shown here that steady sliding is compatible with the formation of a pair of body waves (a plane dilatational wave and a plane shear wave) radiated from the sliding interface. Each wave propagates at a different angle such that the trace velocities along the interface are equal and supersonic with respect to the elastic medium. The angles of wave propagation are determined by the Poisson's ratio and by the coefficient of friction. The amplitude of the waves are indeterminant, subject only to the restriction that the perturbations in interface contact pressure and tangential velocity satisfy the inequality constraints for unilateral sliding contact. It is also found that a rectangular wave train, or a rectangular pulse, can allow for motion of the two bodies with a ratio of remote shear to normal stress which is less than the coefficient of friction. Thus the apparent coefficient of friction is less than the interface coefficient of friction. Furthermore it is shown that the apparent friction coefficient decreases with increasing speed even if the interface friction coefficient is speed-independent. This result supports the interpretation of certain friction behavior as being a consequence of the dynamics of the system, rather than strictly as an interface property. In fact no distinction is made between the static and kinetic interface friction coefficients.
[S0021-8936(00)02101-2]

1 Introduction

The sliding of two surfaces upon each other is such a common occurrence. Yet this phenomenon remains one which is not well understood. The relative motion of two surfaces is resisted by a tangential force which is called the friction force. The ratio of this tangential force to the normal force is called the coefficient of kinetic friction (μ) and this coefficient can easily be determined experimentally. However, the mechanics of contact and friction is quite complex. Friction is a consequence of many interacting phenomena, e.g., adhesion, plastic deformation, roughness, and elastic waves. It is the interaction of elastic body waves with observed friction which is the subject of this investigation.

Rayleigh waves can propagate along the free surface of a semi-infinite elastic body and have amplitudes which decay exponentially with distance from the free surface. Similar waves can travel along the interface of two contacting elastic bodies. Such waves were investigated by Stoneley [1] for bonded contact and are known as Stoneley waves. Stoneley waves exist only if the shear wave speeds of the two materials do not differ greatly. Achenbach and Epstein [2] investigated interface waves in unbonded frictionless contacts in which separation does not occur. These ''smooth contact Stoneley waves'' (also known as slip waves) are qualitatively similiar to those for bonded contact and occur for a wider range of material combinations.

Slip waves with periodic regions of separation along a frictionless interface were found by Comninou and Dundurs [3]. Comninou and Dundurs [4] also investigated the possibility of two identical half-spaces sliding with friction due to the presence of separation waves and/or stick-slip waves. Both of their analyses showed that such waves could exist only with *square-root singularities* at the tips of the slip zones. Freund [5] pointed out that the singularities encountered by Comninou and Dundurs [3,4] would require energy sources and sinks.

Martins, Guimarães, and Faria [6] investigated the sliding of elastic and viscoelastic half-spaces against a rigid surface. Dynamic instabilities, in the form of subsonic surface waves, were found for cases in which the friction coefficient and the Poisson's ratio were sufficiently large. These instabilities were thought to play a role in Schallamach waves [7]. Adams [8] showed that the steady sliding of two elastic half-spaces is dynamically unstable. The instability mechanism is due to destabilization of interfacial slip waves and gives rise to a dynamic instability, in the form of self-excited motion, which is generally confined to a region near the sliding interface. It was speculated that the instability would eventually lead to either partial loss of contact or to regions of stick-slip motion. It is noted that the cases investigated by Comninou and Dundurs [3,4] were those of frictionless sliding of different materials and frictional sliding of identical materials. Neither of those cases would lead to the dynamic instabilities encountered by Adams [8].

Adams [9] investigated the sliding of two dissimiliar elastic bodies due to periodic regions of slip and stick propagating along the interface. It was found that such motion allows for the interface sliding conditions to differ from the observed sliding conditions. In particular the interface coefficient of friction can be constant or an increasing/decreasing function of slip velocity. However, the *apparent* coefficient of friction can be less than the *interface* friction coefficient. Furthermore the apparent coefficient of friction can decrease with sliding speed even though the interface friction coefficient is constant. Thus the measured coefficient of friction does not necessarily represent the behavior of the sliding interface. Also the presence of slip waves may make it pos-

Contributed by the Applied Mechanics Division of THE AMERICAN SOCIETY OF MECHANICAL ENGINEERS for publication in the ASME JOURNAL OF APPLIED MECHANICS. Manuscript received by the ASME Applied Mechanics Division, Jan. 12, 1999; final revision, Mar. 31, 1999. Associate Technical Editor: A. K. Mal. Discussion on the paper should be addressed to the Technical Editor, Professor Lewis T. Wheeler, Department of Mechanical Engineering, University of Houston, Houston, TX 77204-4792, and will be accepted until four months after final publication of the paper itself in the ASME JOURNAL OF APPLIED MECHANICS.

sible for two frictional bodies to slide without a resisting shear stress and without any interface separation. The notion that certain observed friction behavior is not a property of the interface, but rather a consequence of system dynamics, was suggested by Martins, Oden, and Simões [10]. In the limit as the slip region becomes very small compared to the stick region, the results of Adams [9] become that of a slip pulse travelling through a region which otherwise sticks. Rice [11] derived that result, in a simpler manner than the periodic solution of Adams, by using the moving dislocation formulation of Weertman [12]. Rice then extended the pulse solution to rate and state friction. Consequences to seismicity were also discussed. A numerical solution for a slip pulse was found by Andrews and Ben-Zion [13]. The amplitude of the slip-pulse increases and the pulse width decreases as the pulse continues to propagate. This self-sharpening effect is consistent with the Adams [8] solution for sliding.

This paper is motivated by the desire to better understand the nature of sliding interfaces. In particular it addresses the interaction of elastic body waves in the sliding of an elastic half-space against a rigid surface. It will be shown that steady sliding is compatible with the formation of a pair of body waves (a plane dilatational wave and a plane shear wave) radiated from the sliding interface. Each wave moves at a different angle with respect to the interface such that the trace velocities along the interface are equal and supersonic. It will further be shown that a rectangular wave train, or a rectangular pulse, can allow for motion of the two bodies with a ratio of remote shear to normal stress which is less than the coefficient of friction.

2 Formulation of the Sliding Problem

Consider a perfectly flat elastic half-space, moving to the left with constant speed V_0, in contact with an infinite rigid surface. The elastic body is subjected to a remotely applied compressive normal traction (p^*) and shearing traction (q^*) as shown in Fig. 1. The ratio q^*/p^* is, at this point of the analysis, the same as the coefficient of friction (μ), where no distinction is made between static and kinetic friction.

A well-known solution to the plane strain equations of motion is in the form of plane body waves in an infinite medium (e.g., Graff [14]). It is emphasized that solutions in the form of body waves, rather than surfaces waves, are sought here because, as was noted in the Introduction, surface waves for this configuration were shown to exist only for high values of the coefficient of friction ($\mu>1$) and of Poisson's ratio ([6]). Consider a plane dilatational and a plane shear wave which move away from the interface at angles θ_1 and θ_2, respectively. The displacement components in the $x-y$ coordinate system are

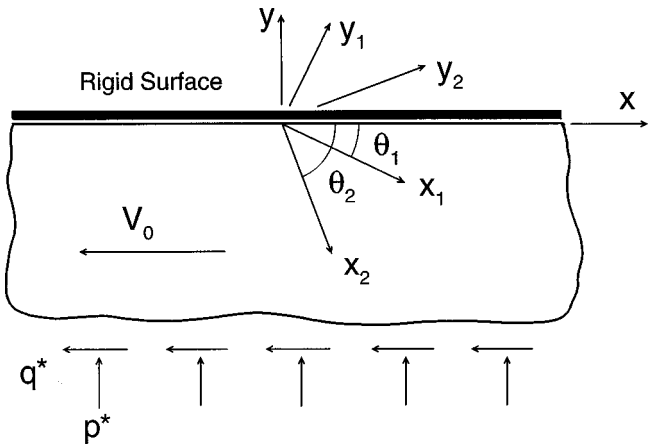

Fig. 1 An elastic half-space sliding against a rigid surface

$$
\begin{aligned}
u(x,y,t) &= A_1 \cos\theta_1 \exp[ik_1(x\cos\theta_1 - y\sin\theta_1 - c_1 t)] \\
&\quad + A_2 \sin\theta_2 \exp[ik_2(x\cos\theta_2 - y\sin\theta_2 - c_2 t)], \\
v(x,y,t) &= -A_1 \sin\theta_1 \exp[ik_1(x\cos\theta_1 - y\sin\theta_1 - c_1 t)] \\
&\quad + A_2 \cos\theta_2 \exp[ik_2(x\cos\theta_2 - y\sin\theta_2 - c_2 t)]
\end{aligned} \tag{1}
$$

which were determined by standard coordinate transformations. In (1), $u=u(x,y,t)$ and $v=v(x,y,t)$ are the components of displacement in the x and y-directions, respectively, A_1, A_2 are the wave amplitudes and k_1, k_2 are the wave numbers for dilatational and shear waves, respectively, and c_1 and c_2 are the dilatational and shear wave speeds, respectively.

In order for the boundary conditions at the sliding interface to be satisfied, it is necessary that the trace velocity (c) and the wave number along the interface (k) of both waves, be identical, i.e.,

$$
\begin{aligned}
c &\equiv c_1/\cos\theta_1 = c_2/\cos\theta_2, \\
k &\equiv k_1\cos\theta_1 = k_2\cos\theta_2, \ \Rightarrow \ k_2 = k_1 c_1/c_2.
\end{aligned} \tag{2}
$$

Thus it is observed from (2) that the dilatational and shear waves yield wave motion along the interface which is supersonic. Furthermore, $(2)_1$ provides a constraint between the angles of propagation of the dilatational and shear waves. Finally, the normal and shearing stresses are given by

$$
\begin{aligned}
\tau_{yy}(x,y,t) &= A_1 G i k_1 [(c_1/c_2)^2 - 1 - \cos 2\theta_1] \\
&\quad \times \exp[ik(x - y\tan\theta_1 - ct)] \\
&\quad - A_2 G i k_2 \sin 2\theta_2 \exp[ik(x - y\tan\theta_2 - ct)] \\
\tau_{xy}(x,y,t) &= -A_1 G i k_1 \sin 2\theta_1 \exp[ik(x - y\tan\theta_1 - ct)] \\
&\quad + A_2 G i k_2 \cos 2\theta_2 \exp[ik(x - y\tan\theta_2 - ct)]
\end{aligned} \tag{3}
$$

where G is the shear modulus.

3 Steady Sliding With Radiated Waves

For contact of the elastic body with a rigid surface

$$
v(x,0,t) = 0, \ \Rightarrow \ A_2 = A_1 \sin\theta_1/\cos\theta_2. \tag{4}
$$

Frictional contact obeying Coulomb's law requires

$$
q^* + \tau_{xy}(x,0,t) = \mu[p^* - \tau_{yy}(x,0,t)] \tag{5}
$$

which leads to

$$
\begin{aligned}
\frac{\sin\theta_1}{\cos\theta_2}\left(\frac{c_1}{c_2}\right)\cos 2\theta_2 - \sin 2\theta_1 = -\mu\Bigg[&\left(\frac{c_1}{c_2}\right)^2 - 1 - \cos 2\theta_1 \\
&- \left(\frac{\sin\theta_1}{\cos\theta_2}\right)\left(\frac{c_1}{c_2}\right)\sin 2\theta_2\Bigg]
\end{aligned} \tag{6}
$$

where

$$
\frac{c_1}{c_2} = \sqrt{\frac{2(1-\nu)}{1-2\nu}}, \quad \theta_2 = \cos^{-1}\left(\frac{\cos\theta_1}{c_1/c_2}\right). \tag{7}
$$

In $(7)_1$ ν is the Poisson's ratio and $(7)_2$ comes from $(2)_1$.

So in order to obtain solutions for sliding with a pair of body waves and for given Poisson's ratio and coefficient of friction, it is necessary to solve (6)–(7) for the dilatational wave angle (θ_1). It is, however, mathematically more convenient to vary θ_1, calculate θ_2 from $(7)_2$ and solve for μ from (6). Results have been obtained in this manner and are shown in Figs. 2–3. It is interesting to note that these waves result from the *boundary conditions* of frictional sliding of the elastic body against a rigid surface.

3.1 Results and Discussion. In Fig. 2 is shown the angles of propagation of dilatational waves (θ_1) and of shear waves (θ_2) versus friction coefficient (μ) for various values of Poisson's ratio (ν). Note that for small values of μ, the angle θ_1 is small and hence the dilatational wave travels in a direction nearly parallel to

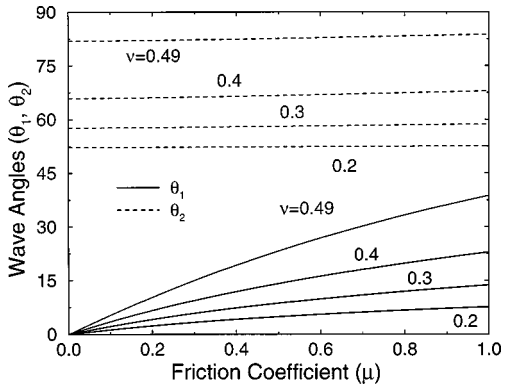

Fig. 2 The angles of propagation of dilatational waves (θ_1) and of shear waves (θ_2) versus friction coefficient (μ) for various values of Poisson's ratio (ν)

the interface. As μ increases so does θ_1. The angle of propagation of the shear wave θ_2 remains almost constant as μ varies. As Poisson's ratio (ν) increases, so do the values of θ_1 and θ_2. In fact as ν increases toward 0.5, the ratio c_1/c_2 becomes infinite requiring that the angle θ_2 approach 90 deg. In Fig. 3 is shown the ratio of amplitudes of the shear and dilatational waves (A_2/A_1) versus friction coefficient for various values of Poisson's ratio. Note that A_2/A_1 is always positive and its value increases with increasing friction. Thus small values of μ correspond to nearly pure dilatational waves, with the shear waves becoming more important as μ increases. This trend is especially true for a large value of Poisson's ratio in which case the shear component can be much greater than the dilatational part.

The question arises as to where the energy source is which generates these waves. The energy dissipated (due to friction) per unit surface area over one period of oscillation is given by

$$\varepsilon = \int_0^{2\pi/ck} \mu[p^* - \tau_{yy}(x,0,t)][V_0 - \dot{u}(x,0,t)]dt$$
$$= \frac{2\pi\mu p^* V_0}{ck} + \int_0^{2\pi/ck} \mu\tau_{yy}(x,0,t)\dot{u}(x,0,t)dt \tag{8}$$

where

$$\dot{u}(x,0,t) = -A_1 ikc \cos\theta_1(1+\tan\theta_1\tan\theta_2)\exp[ik(x-ct)]. \tag{9}$$

It can be shown that the phase of $\tau_{yy}(x,0,t)$ is opposite to the phase of $\dot{u}(x,0,t)$. Thus ε will be less than $(2\pi/ck)\mu p^* V_0$ and hence the energy dissipated at the interface will be less than the work done in moving the rigid body. This extra energy is the contributor to the energy of the radiated dilatational and shear waves.

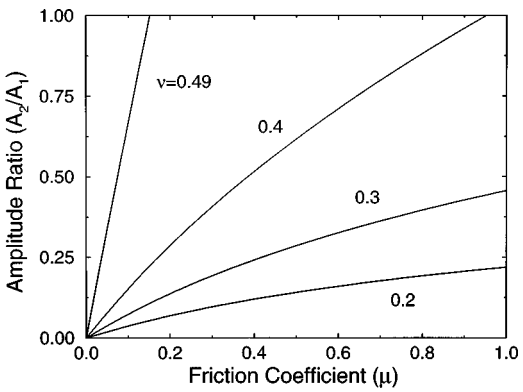

Fig. 3 The ratio of amplitudes of the shear and dilatational waves (A_2/A_1) versus friction coefficient for various values of Poisson's ratio (ν)

4 Propagating Stick-Slip Regions

In this section the possible relative motion of the two bodies due to the presence of propagating stick-slip regions is investigated. Due to the presence of stick regions, the ratio of the remotely applied shear-to-normal stress would not necessarily be the same as the ratio of the interface shear-to-normal stress. Thus

$$\mu^* \equiv q^*/p^*, \quad \mu^* \neq \mu \neq \bar{\mu},$$
$$\tau_{xy} + q^* = \bar{\mu}(p^* - \tau_{yy}) \quad \text{in slip regions} \tag{10}$$

where μ^* is the *apparent* friction coefficient, $\bar{\mu}$ is the *interface* coefficient of friction, and μ is the *ratio* of shear-to-normal tractions for the body waves. It will be shown that Coulomb's law of friction can be satisfied even though these three coefficients differ from each other.

Consider a superposition of the wave pairs obtained in the previous section, the form of which is a rectangular wave train in tangential velocity (Fig. 4) which is invariant in the moving coordinate "$k(x-ct)$." A typical stick region is defined by $k|x-ct|<a$, whereas slip occurs for $a<k|x-ct|<\pi$. For stick

$$\dot{u}(x,0,t) = V_0, \quad k|x-ct|<a \tag{11}$$

which states that the tangential velocity of the upper surface of the elastic body is equal to the sliding speed. The requirement that the average values of the velocity, shear stress, and normal stress are each zero for this superposition of harmonic waves leads to relationships between these quantities in the stick and slip regions, i.e.,

$$\dot{u}^{Slip} = -\frac{aV_0}{\pi - a}, \quad \tau_{xy}^{Slip} = -\frac{a\tau_{xy}^{Stick}}{\pi - a}, \quad \tau_{yy}^{Slip} = -\frac{a\tau_{yy}^{Stick}}{\pi - a}. \tag{12}$$

Now the parameter α is defined according to

$$\alpha \equiv [\tau_{xy}(x,0,t)/G]/[\dot{u}(x,0,t)/c_2], \tag{13}$$

where, from $(3)_2$ and (9), α depends only on μ and ν and is independent of x and t. From the plot in Fig. 5 of α versus the wave friction coefficient (μ) it can be seen that $\alpha>0$. Furthermore, (12)–(13) leads to

$$\frac{\tau_{xy}^{Stick}}{G} = \alpha\frac{V_0}{c_2}, \quad \frac{\tau_{xy}^{Slip}}{G} = -\frac{a\alpha}{(\pi - a)}\frac{V_0}{c_2}$$
$$\frac{\tau_{yy}^{Stick}}{G} = -\frac{\alpha}{\mu}\frac{V_0}{c_2}, \quad \frac{\tau_{yy}^{Slip}}{G} = \frac{a\alpha}{(\pi - a)\mu}\frac{V_0}{c_2}. \tag{14}$$

In the slip region, the shear stress is related to the normal stress through Coulomb's law, i.e.,

$$\tau_{xy}^{Slip} + q^* = \bar{\mu}(p^* - \tau_{yy}^{Slip}) \tag{15}$$

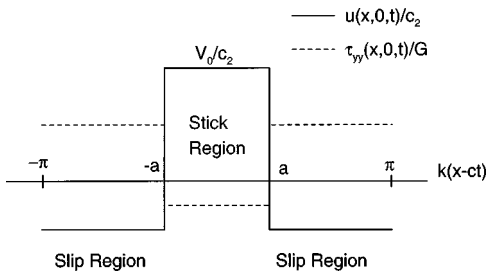

Fig. 4 A rectangular wave train of tangential velocity

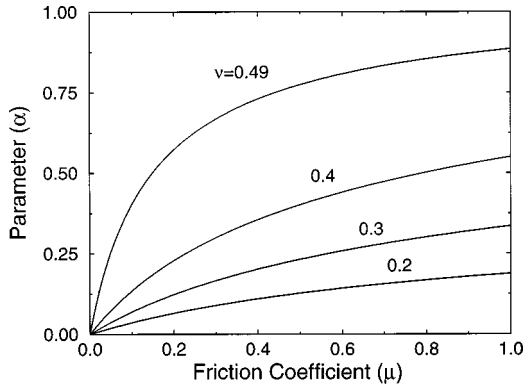

Fig. 5 The parameter α versus the wave friction coefficient (μ) for various values of Poisson's ratio (ν)

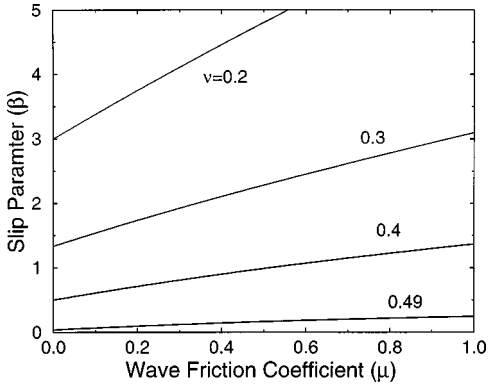

Fig. 6 The slip parameter β versus the wave friction coefficient (μ) for various values of Poisson's ratio

where the interface friction coefficient ($\bar{\mu}$) appears in (15). Substitution of $(10)_1$ and $(14)_{2,4}$ into (15) leads to

$$\mu^* = \bar{\mu} - \left(\frac{\bar{\mu}}{\mu} - 1\right)\frac{a\alpha(V_0/c_2)}{(\pi - a)(p^*/G)}. \tag{16}$$

The result (16) is significant only if sliding could occur with an apparent friction coefficient (μ^*) which is less that the interface friction coefficient ($\bar{\mu}$), i.e.,

$$\mu^* < \bar{\mu} \;\Rightarrow\; \bar{\mu} > \mu > 0. \tag{17}$$

The requirement that Coulomb's inequality be satisfied in the stick region, i.e.,

$$\tau_{xy}^{Stick} + q^* < \bar{\mu}(-\tau_{yy}^{Stick} + p^*) \tag{18}$$

is automatically satisfied due to (17).

The normal contact stress must remain compressive throughout the entire interface. This condition leads to a maximum value of the length of the stick zones ($2a/k$),

$$a_{Max} = \frac{\mu(p^*/G)}{\mu(p^*/G) + \alpha(V_0/c_2)}. \tag{19}$$

It is noted that the *shear stress is increased in the stick zone* and that this result may appear counterintuitive. However, the contact pressure also increases in the stick region. Since $\mu < \bar{\mu}$ Coulomb's inequality holds. Likewise, in the slip region, the shear stress and the contact pressure decrease. Thus Coulomb's law is satisfied in the slip region but with a different coefficient of friction that the ratio of the remote shear-to-normal traction (μ^*). The tangential velocity increases in the stick region such that it equals the sliding velocity.

4.1 Results and Discussion. It is observed that the nature of sliding friction is profoundly influenced by the length of the stick region, i.e.,

$$\begin{aligned} a = 0, \;&\Rightarrow\; \mu^* = \bar{\mu} \\ a = a_{Max}, \;&\Rightarrow\; \mu^* = \mu. \end{aligned} \tag{20}$$

Thus sliding with small stick zones is governed by the interface friction coefficient, whereas sliding with large stick regions is dominated by the behavior of radiated body waves. It is further noted that a vanishing value of μ causes a perturbation in the contact pressure without a change in the interface shear stress. This case corresponds to $c = c_1$, i.e., a dilatational wave parallel to the interface and no shear wave. Under these conditions consider an applied normal traction (p^*) without an applied shear traction (q^*), i.e., $\mu^* = 0$. In that case the results obtained here are qualitatively similar to the interface stick-slip problem of Adams [9]. However, the results of Adams were applicable for interface waves with material combinations for which slip waves exist. Such is not the case here in which there is a large mismatch in material properties.

It is also observed from (16) that the *apparent coefficient of friction* (μ^*) will decrease with increasing speed even though the interface friction coefficient ($\bar{\mu}$) is constant and speed-independent. This behavior is due to the existence of the stick-slip zones which propagate along the interface. Thus the use of a speed-independent interface friction coefficient is consistent with observations of friction decreasing with increasing sliding speed. The distinction between observed static and kinetic friction is greatly influenced by the time of repose [15]. Here the time of repose is equal to the wavelength divided by the speed of the interface wave. Hence the time of repose is short and the distinction between static and kinetic friction is not as great as it would otherwise be.

5 A Slip Pulse

In this section the propagation of an isolated slip pulse along an interface which otherwise sticks is investigated. Condition (4) still holds along the entire interface, along with (10) in the slip region ($k|x - ct| < b$), and

$$\dot{u}(x,0,t) = 0, \quad k|x - ct| > b, \tag{21}$$

in the stick region. The width of the stick region is $2b/k$ and the results for this case may be obtained by taking $b = \pi - a$ in the limit as b becomes very small. For this case $V_0 \to 0$ and from $(12)_1$ and $(14)_4$

$$\frac{\dot{u}^{Slip}}{c_2} = -\frac{\mu}{\alpha}\left(\frac{\tau_{yy}^{Slip}}{G}\right). \tag{22}$$

The magnitude of the slip distance is found by integrating the negative of the tangential velocity in the slip region. The result is

$$U^{Slip}/(b/k) = \beta(\tau_{yy}^{Slip}/p^*)(p^*/G), \quad \beta \equiv 2(\mu/\alpha)\cos\theta_2. \tag{23}$$

Thus the magnitude of the slip distance depends nonlinearly upon μ and linearly upon the magnitude and width of the pulse.[1] In Fig. 6 is shown the slip parameter β versus the wave friction coefficient μ for various values of Poisson's ratio. The slip increases with increasing μ and this trend is more pronounced with smaller values of Poisson's ratio.

The apparent friction coefficient for the slip pulse is found from $(14)_4$ and (16) and is given by

$$\mu^* = \bar{\mu} - (\bar{\mu} - \mu)(\tau_{yy}^{Slip}/p^*). \tag{24}$$

[1]Note that μ, α, and θ_2 are interrelated.

Thus the apparent friction (μ^*) decreases from $\overline{\mu}$ as the magnitude of the slip pulse increases, approaching μ as $\tau_{yy}^{Slip} \to p^*$. The coefficient μ is related to the wave angle θ_1 and to the Poisson's ratio through (6)–(7).

Finally it is noted that dynamic shear-dominated cracks, propagating at supersonic speeds along a bimaterial interface with a large mismatch in material properties, have recently been observed [16] using photoelasticity and high-speed photography. The [16] cracks exhibit large scale frictional contact between the crack faces at the leading edge of the crack-tip. That investigation, which includes stick, separation, and slip zones, differs from the slip pulse considered here.

6 Conclusions

The steady sliding of a flat half-space against a rigid surface with a constant interfacial coefficient of friction has been investigated. Steady sliding is compatible with the formation of a pair of body waves radiated from the sliding interface. Each wave moves at a different angle with respect to the interface such that the trace velocities along the interface are equal and supersonic with respect to the elastic medium. The angles of wave propagation are determined by the Poisson's ratio and by the coefficient of friction. The amplitude of the waves are indeterminant, subject only to the restriction that the perturbations in interface contact pressure and tangential velocity satisfy the inequality constraints of unilateral sliding contact. For identical materials, waves of this type appear not to exist. A complete study of material combinations has not been conducted and falls outside the scope of this paper.

It is found that a rectangular wave train or a rectangular pulse can allow for motion of the two bodies with a ratio of remote shear-to-normal stress which is less than the coefficient of friction. Sliding with small stick zones is dominated by the interface friction whereas sliding with large stick zones is governed by wave motion. Furthermore the *apparent* coefficient of friction is less than the *interface* coefficient of friction. It is also shown that the apparent friction coefficient decreases with increasing speed even if the interface friction coefficient is speed-independent. The *origin* of this wave motion is not addressed in this investigation. Furthermore this result supports the notion of certain frictional behavior as being a consequence of the dynamics of the sliding bodies, rather than as a property of the interface. No distinction is made between static and kinetic friction.

Acknowledgments

This material is based upon work supported by the National Science Foundation under Grant No. CMS-9622196 of the Surface Engineering and Tribology Program.

References

[1] Stoneley, R., 1924, ''Elastic Waves at the Surface of Separation of Two Solids,'' Proc. R. Soc. London, Ser. A, **106**, pp. 416–428.
[2] Achenbach, J. D., and Epstein, H. I., 1967, ''Dynamic Interaction of a Layer and a Half-Space,'' J. Eng. Mech. Div., Am. Soc. Civ. Eng., **EM5**, pp. 27–42.
[3] Comninou, M., and Dundurs, J., 1977, ''Elastic Interface Waves Involving Separation,'' ASME J. Appl. Mech., **44**, pp. 222–226.
[4] Comninou, M., and Dundurs, J., 1978, ''Elastic Interface Waves and Sliding Between Two Solids,'' ASME J. Appl. Mech., **45**, pp. 325–330.
[5] Freund, L. B., 1978, ''Elastic Waves Involving Separation,'' discussion ASME J. Appl. Mech., **45**, pp. 226–228.
[6] Martins, J. A. C., Guimarães, J., and Faria, L. O., 1995, ''Dynamic Surface Solutions in Linear Elasticity and Viscoelasticity With Frictional Boundary Conditions,'' ASME J. Vibr. Acoust., **117**, pp. 445–451.
[7] Schallamach, A., 1971, ''How Does Rubber Slide?,'' Wear, **17**, pp. 301–312.
[8] Adams, G. G., 1995, ''Self-Excited Oscillations of Two Elastic Half-Spaces Sliding With a Constant Coefficient of Friction,'' ASME J. Appl. Mech., **62**, pp. 867–872.
[9] Adams, G. G., 1998, ''Steady Sliding of Two Elastic Half-Spaces With Friction Reduction due to Interface Stick-Slip,'' ASME J. Appl. Mech., **65**, pp. 470–475.
[10] Martins, J. A. C., Oden, J. T., and Simões, F. M. F., 1990, ''A Study of Static and Kinetic Friction,'' Int. J. Eng. Sci., **28**, pp. 29–92.
[11] Rice, J. R., 1997, ''Slip Pulse at Low Driving Stress Along a Frictional Fault Between Dissimilar Media,'' EOS Trans. Am. Geophys. Union, **78**, No. 46, Fall Meeting Suppl., p. F464.
[12] Weertman, J., 1980, ''Unstable Slippage Across a Fault That Separates Elastic Media of Different Elastic Constants,'' J. Geophys. Res., **85**, pp. 1455–1461.
[13] Andrews, D. J., and Ben-Zion, Y., 1997, ''Wrinkle-Like Slip Pulse on a Fault Between Different Materials,'' J. Geophys. Res., **102**, pp. 553–571.
[14] Graff, K. F., 1975, *Wave Motion in Elastic Solids*, Ohio State University Press, Columbus, Ohio.
[15] Rabinowicz, E., 1995, *Friction and Wear of Materials*, 2nd Ed., John Wiley & Sons, New York.
[16] Rosakis, A., 1998, ''Dynamic Shear-Dominated Intersonic and Supersonic Crack Growth in Bimaterials and Layered Systems,'' Applied Mechanics Colloquium, Harvard University, Nov. 13.

A Mathematical Model for the Strained Shape of a Large Scientific Balloon at Float Altitude

F. Baginski
Associate Professor

W. Collier
Graduate Student

Department of Mathematics,
George Washington University,
Washington, DC 20052

A large scientific balloon is constructed from long flat tapered sheets of thin polyethylene film called gores which are sealed edge to edge to form a complete shape. The balloon is designed to carry a fixed payload to a predetermined altitude. Its design shape is based on an axisymmetric model that assumes that the balloon film is inextensible and that the circumferential stresses are zero. While suitable for design purposes, these assumptions are not valid for a real balloon. In this paper, we present a variational approach for computing strained balloon shapes at float altitude. Our model is used to estimate the stresses in the balloon film under various loads and for different sets of material constants. Numerical solutions are computed. [S0021-8936(00)02201-7]

1 Introduction

For design purposes, a large scientific balloon is usually modeled as a loaded axisymmetric inextensible membrane. Archimedes' principle states that the buoyant force acting on the balloon system is equal to the weight of the displaced air and lifting gas. The balloon system includes the weight of the film, load tapes, payload, ballast, venting ducts, end fittings, fins, etc. The design shape is based on conditions that the balloon will encounter at its float altitude. The standard model was developed by researchers at the University of Minnesota in the 1950s ([1]) and its solutions are often referred to as Σ-shapes (Σ is a parameter that appears in the model equations). When one assumes that the circumferential stresses are zero in the Σ-shape equations, its solutions are called ''natural-shape'' balloons. A common film used in the construction of large scientific balloons is 20.32 micron polyethylene. The balloon is constructed from flat tapered sheets of polyethylene called gores that are roughly 183 meters in length and about 2.5 meters at the widest point. The gores are heat sealed edge to edge to form a complete shape and load tapes are attached along each seam. As a material for the balloon structure, polyethylene is very forgiving and can adapt to flaws that may have been introduced during the manufacturing process. As evidenced by numerous successful balloon missions over many years, the natural-shape design has proven to be adequate for design purposes. Nevertheless, it would be desirable to estimate the stresses in the balloon film during the course of a normal balloon flight. Ignoring the variety of shapes that are observed shortly after launch, there are three types of configurations that warrant study: the in-spool configuration (prior to launch), ascent configurations, and the float configurations. In this paper, we will restrict our attention to strained float configurations. Our goal here is to present a mathematical model that can provide a reasonable estimate of the balloon film stresses while the balloon is in the fully deployed configuration.

Previous work on modeling balloon shapes focused on axisymmetric solutions based on the natural shape ([2–4]) or asymmetric models that consider large-scale geometric features ([5,6]). In these previously mentioned works, the straining in the film is ignored. In the model that is presented here, the total energy of the balloon system is modeled as the sum of the hydrostatic pressure potential due to the lifting gas, the gravitational potential energy due to the weight of the balloon system (film, caps, load tapes, end fittings, etc.), and the strain energy due to the balloon film and load tapes. The balloon surface is triangulated, using the gore structure as a fundamental building block. A flat reference configuration is associated with each gore in the balloon shape, and so it is possible to associate a triangle in the balloon surface with a unique triangle in the flat reference configuration. A constant strain model is used to compute the strain energy for the faceted balloon surface (including internal folds). An isotropic plane-stress constitutive model is used to estimate the stresses within each facet. The load tapes that run along the edges of the gores are modeled as linearly elastic strings. In the present work, we will assume that the zero-pressure level is at the base of the balloon. A strained zero-pressure balloon will always have some small internal folds, but we will refer to these as fully deployed configurations. These types of shapes are in contrast to those with deep internal folds such as those observed in partially inflated shapes ([5,6]).

The term fold has been used in membrane problems that involve wrinkling. For example, in Contri and Schrefler [7] the authors draw a distinction between a wrinkled region and what they term a ''fold'' (a large single wrinkle, but without self-contact); both features are included in their model. For the results presented here, the wrinkling in the balloon film is negligible in comparison to the magnitude of typical folds that are observed. We include a model for folds, and ignore wrinkling in the balloon fabric. In our work, a fold is a region of external contact forming in the center of a gore, where symmetric portions of a flat polyethylene film lie back to back against each other. This is different from the situation in ([7]), where a fold represents a large single wrinkle, but without self-contact.

Although large deformations of membrane-like structures have been studied theoretically and experimentally ([7,8]) the loading conditions and size of a typical large scientific balloon are nonstandard. For example, the axisymmetric elastic membrane in ([8]) is loaded under uniform pressure in the range 98.15 Pa to 981.5 Pa. However, the maximum differential pressure at the top of the balloon at float is only about 3.83 Pa when the tail of the balloon is at 39429 meters. Although the membrane considered in Fig. 18.20 of ([8]) had roughly the same thickness as polyethylene film, the structure is only about 20 cm in diameter. If one were to scale up this model to the size of a real balloon, one would find that the scaled-up version would have a thickness of nearly 1 cm, and so it would not be appropriate to extrapolate results to an actual balloon. A similar remark would apply to the results in

Contributed by the Applied Mechanics Division of THE AMERICAN SOCIETY OF MECHANICAL ENGINEERS for publication in the ASME JOURNAL OF APPLIED MECHANICS. Manuscript received by the ASME Applied Mechanics Division, Jan. 3, 1997; final revision, Oct. 12, 1999. Associate Technical Editor: M. M. Carroll. Discussion on the paper should be addressed to the Technical Editor, Professor Lewis T. Wheeler, Department of Mechanical Engineering, University of Houston, Houston, TX 77204-4792, and will be accepted until four months after final publication of the paper itself in the ASME JOURNAL OF APPLIED MECHANICS.

([7]), where experimental data is presented on an airbags (thickness: 50 to 150 microns, Young's modulus 85 to 177 MPa, Poisson's ratio 0.4); the pressure loadings for the experimental airbags were not reported, but the pressure in the corresponding numerical model was reported at 0.005 MPa (significantly higher than the hydrostatic pressure experienced by the balloon film). It would be virtually impossible to build a scaled-down version of a large scientific balloon, because the film thickness in the actual balloon is only 20.32 microns. These are reasons to develop an accurate mathematical model that is representative of how a real balloon behaves.

Material constants such as Young's modulus and Poisson's ratio are highly temperature-dependent and we will consider shapes for a variety of these parameter values. In reality, the balloon film is a nonlinear viscoelastic material, but we will model it as a linearly elastic material. We will ignore the stress response history of the ascent to float altitude and assume that the balloon is in quasi-static equilibrium for a fixed altitude. Since the balloon film is allowed to strain, internal folds of excess material (corresponding to regions of external contact) are possible at float. An internal fold is a region of external contact because the outside of the balloon comes into contact with itself. For balloons at or near float, the volume is sufficiently large to avoid internal contact and so we need not consider shapes with wing sections (wing sections are regions of internal contact; for further discussion, see ([5])). If one models a gore using standard membrane theory, one would find that the model would predict negative stresses. In reality, the balloon film does not undergo compression, but wrinkles and/or forms internal folds. One way to treat the negative compressions is to introduce a tension field model ([7,9,10]). A fully inflated balloon similar to those considered here is considered in ([10]). Tension field theory normally deals with finely wrinkled membranes ([11]), but has also been applied to larger scale structures such as ''folds'' in the sense of ([7]). While our definition of a fold is similar to what ([7]) term a single wrinkle, our definition of a fold refers to a region of external contact. In addition, the pressure loading in ([7]) is of significantly higher magnitude than that experienced by the balloon.

Our approach of modeling the behavior of the balloon film in the fully deployed configuration has several assumptions in common with the wrinkling of a thin membrane: (a) the use of plane stress theory (as applied to individual facets in our triangulation of the balloon), (b) the assumption that bending of the membrane does not introduce stresses, and (c) the assumption that the membrane is not able to support negative stress ([12–14]). Our approach in this paper is fundamentally different from that of a tension field. We do not impose the condition that the stresses are non-negative (as is done when the complementary approach is used [12]). Rather, we develop a geometric model that allows internal folds to form within each gore (just as in a real balloon). What we term a ''fold'' can be small when compared to the dimensions of a real balloon, but large in comparison to the wrinkles which are observed in the balloon film. Unlike ([9]) and ([15]), where a relaxed strain energy function is used, in our model, we use the usual energy for a constant strain triangle for folded and nonfolded facets (see Appendix A). This is appropriate as a first approximation, since we ignore the wrinkling. During the process of evolving an energy minimizing shape, it is possible that an intermediate state may possess regions of high negative stresses; similarly, the load tapes may also experience compressions. These transient states are not physically realistic. However, after we have solved the minimization problem and have computed a shape that minimizes the balloon's total energy, we find that the averaged principal stress resultants are non-negative to within the accuracy of our numerical model and the strains in the load tape segments are all strictly positive. In an approach like ([7]), the compressive stresses are eliminated through an iterative procedure at each stage of the incremental loading procedure in their algorithm.

In this paper, we present some results on strained float configurations of large scientific balloons that can be compared to published work using finite elements with a tension field ([10]). In the special case of float conditions, we find that the approach of ([10]) and our own approach lead to the same stress distribution and strained float shape. In this paper, we include numerical solutions for a variety of parameter values and estimate the maximum principal stresses for the corresponding shapes. We find that even in the extreme conditions, the maximum stresses fall well below stress tolerance levels for typical operating conditions. One advantage of our approach is that we will be able to apply our strain energy methods to ascent shape geometries with large regions of folded material ([16]).

In Section 2, we formulate our model for strained balloon shapes. In Section 3, we present a number of numerical results. We consider two types of designs. One is based on the natural-shape model as presented in ([2]). The second design is based on a variation of the natural shape, where the weight of the cap is incorporated as an added thickness in the Σ-shape model and the tail of the gore is tapered near the bottom of the balloon. We include computed equilibrium shapes for a variety of parameter values and a higher than nominal payload. In Section 4, we present some concluding remarks.

2 Problem Formulation

Before describing the variational principle that is used to model strained balloon shapes, we describe first how the unstrained flat reference configuration is obtained from the generating curve for the axisymmetric design shape. This construction is consistent with the way real balloons are manufactured. We will assume that the number of gores in a complete shape is n_g. Let

$$(R_d(s),0,Z_d(s)), \quad 0 \leqslant s \leqslant l_d, \tag{1}$$

be the generating curve for the design shape. We assume that the unstrained curved gore is a ruled cylindrical surface that is centered about the curve in Eq. (1). The unit vector normal to this surface is perpendicular to $\vec{j}=(0,1,0)$. The left edge of the gore lies in the plane $y=-\tan(\pi/n_g)x$ and the right edge of the gore lies in the plane $y=\tan(\pi/n_g)x$. If we flatten out this region, we obtain what we call the flat reference configuration. Load tapes are attached along the edges where the gores are sealed to one another. When evolving an equilibrium shape, the gore can undergo large rigid-body displacements and deformations that strain the film. We will assume that the deformed gore is symmetric about the $y=0$ plane, and so we only need to consider the right half. The load tape remains in the plane $y=\tan(\pi/n_g)x$. In Fig. 1(*a*), we present a flat reference configuration. In Fig. 1(*b*), we present the curved but unstrained design shape. Because the balloon film is so thin, it has negligible bending stiffness. Instead of compressing, a small fold of excess material will form along the center of each gore. This is based on observations of real balloons. In Fig. 1(*c*), we present a typical deformed half-gore with a small internal fold. The pre-image of the fold can be seen in Fig. 1(*a*). We will let $\mathcal{S}_f$ denote the right half of a deformed gore. The reflection of $\mathcal{S}_f$ in the $y=0$ plane is denoted by $\mathcal{S}_f'$. The complete balloon shape is made from n_g copies of $\mathcal{S}_f \cup \mathcal{S}_f'$. $\mathcal{C}_k$ will denote the class of balloon shapes generated in this fashion from a fundamental section $\mathcal{S}_f$. Corresponding to $\mathcal{S}_f$ and $\mathcal{S}_f'$ in the deformed configuration are the flat reference configurations, S_f and S_f', respectively.

A vertex $V_{i,j}$ in S_f is identified with a vertex $v_{i,j}$ in $\mathcal{S}_f$ where $j=0,\pm 1,\pm 2$ and $i=1,\ldots,n_c+2$ and n_c is the number of circumferential fibers. Perpendicular to the center axis of a flat reference configuration are the directed edges (see Fig. 2(*a*)) $C_i = V_{i,2}-V_{i,0}$, $i=1,\ldots,n_c+2$. Note, $C_1=C_{n_c+2}=\vec{0}$. Along the ''right'' boundary of a gore are the directed edges,

$$E_i = V_{i+1,2}-V_{i,2}. \tag{2}$$

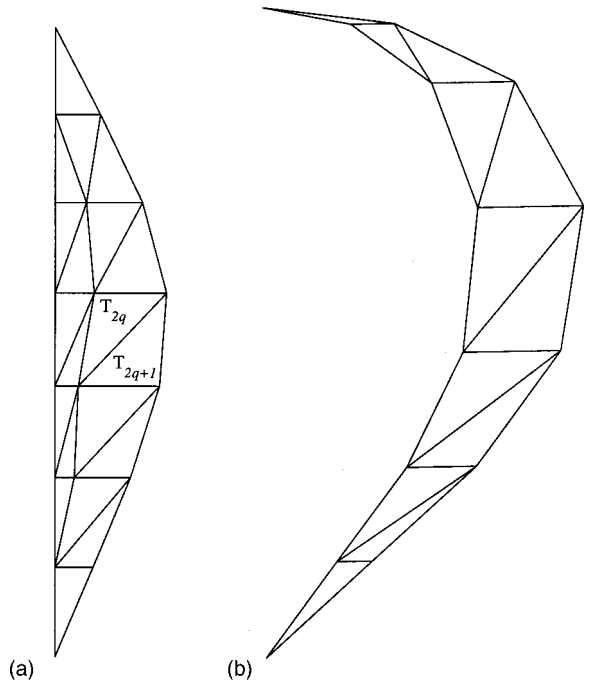

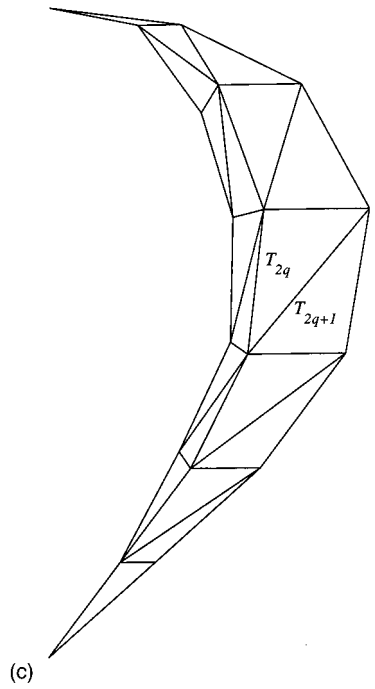

Fig. 1 (*a*) S_f–half-gore in the flat reference configuration; (*b*) unstrained curved configuration; (*c*) $\mathcal{S}_f$–deformed half-gore

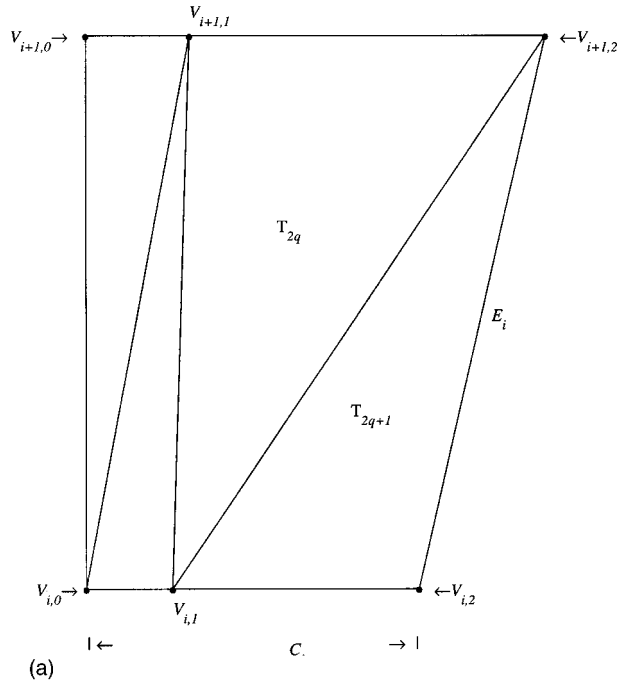

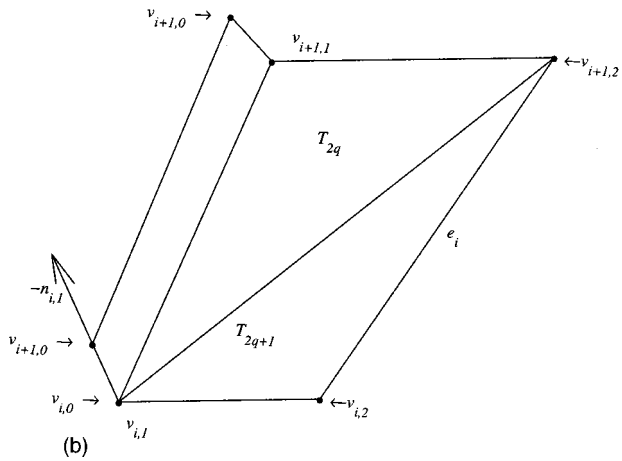

Fig. 2 (*a*) Typical quadrilateral in the reference configuration S_f defined by $V_{i,j}$; (*b*) distorted quadrilateral in the deformed configuration $\mathcal{S}_f$ defined by $v_{i,j}$

Vertices $v_{i,2}=(x_{i,2},y_{i,2},z_{i,2})$ lie in the plane $y=\tan(\pi/n_g)x$, and

$$e_i=v_{i+1,2}-v_{i,2}. \tag{3}$$

$\mathcal{M}_2$ will denote the edge of a deformed gore in R^3 formed by joining vertices $\{v_{i,2},i=1,\ldots,n_c+2\}$. A load tape will be located along $\mathcal{M}_2$. Since $y_{i,2}=\tan(\pi/n_g)x_{i,2}$, we say that $v_{i,2}$ has two degrees-of-freedom. Vertices $v_{i,1}$ are determined by projecting $v_{i,2}$ onto the xz-plane, i.e.,

$$\begin{aligned}(x_{i,1},y_{i,1},z_{i,1})&=\mathcal{P}_{xz}[(x_{i,2},y_{i,2},z_{i,2})]\\&=(x_{i,2},0,z_{i,2}).\end{aligned} \tag{4}$$

Vertex $v_{i,1}$ has zero degrees-of-freedom. $\mathcal{M}_1$ denotes the curve defined by $\{v_{i,1},i=1,\ldots,n_c+2\}$. The vertex at the top of the balloon has one degree-of-freedom, since only its z-component can vary. The vertex at the tail of the balloon is assumed to be fixed.

Vertices $v_{-2,i}$ and $V_{-2,i}$ are determined by symmetry, i.e., $v_{i,-2}=(x_{i,2},-y_{i,2},z_{i,2})$ and $V_{i,-2}=\mathcal{R}_Z[V_{i,2}]$, where $\mathcal{R}_Z[(Y,Z)]=(-Y,Z)$. The surface $\mathcal{S}_f$ is triangulated by facets formed from vertices $v_{i,j}$. Normal to each facet of this type is an outward pointing unit vector. We define an outward normal $n_{i,j}$ at the vertex $v_{i,j}$ that has the direction of the average of all normals of exterior facets that share the vertex $v_{i,j}$. Vertices

$$v_{i,0}=v_{i,1}-\alpha_i n_{i,1}$$

will form the crease of the internal fold. The parameter α_i measures the depth of the fold at the ith station and is computed as part of the solution process. In the flat reference configuration, we define

$$V_{i,1}=V_{i,0}+\frac{\alpha_i}{\alpha_i+y_{i,2}}C_i,$$
$$V_{i,-1}=\mathcal{R}_Z[V_{i,1}], \tag{5}$$

where $i=2,\ldots,n_c+1$. Note, both $V_{i,-1}$ and $V_{i,1}$ are identified with $v_{i,1}$ and the vertex $V_{i,0}$ is identified with $v_{i,0}$. When $\alpha_i=0$, then $V_{i,-1}=V_{i,1}=V_{i,0}$ and $v_{i,1}=v_{i,0}$.

The initial configuration of the balloon shape is triangulated. The superscript ''0'' of a vertex label indicates that it is in the (unstrained) initial configuration. By construction, $\alpha_i^0=0$ and $v_{i,1}^0=v_{i,0}^0=v_{i,-1}^0$ for all i and the $v_{i,1}^0$'s lie on the generating curve given by Eq. (1). Corresponding vertices in the flat reference configuration are given by $V_{i,2},V_{i,0}$. Note, material points $V_{i,2},V_{i,0}$ are fixed throughout the evolution, but $V_{i,\pm1}$ are determined by Eq. (5).

A typical fundamental section generated by the set of vertices $\{v_{i,j}\}$ will be denoted by $\mathcal{S}_f(v_{i,j})$ (see Fig. 1(*c*)). The initial unstrained configuration is denoted by $\mathcal{S}_f(v_{i,j}^0)$ (see Fig. 1(*b*)). As the balloon shape evolves to equilibrium, the vertices $v_{i,j}$ can move, subject to the degrees-of-freedom previously described.

Each triangle $\mathcal{T}_l$ in the deformed configuration is identified with a triangle $\mathcal{T}_l$ in the reference configuration. If we let $N_\mathcal{T}$ denote the total number of facets in a triangulation of a fundamental section, we have

$$\mathcal{S}_f=\bigcup_{l=1}^{N_\mathcal{T}}\mathcal{T}_l. \tag{6}$$

We can partition the set $\mathcal{T}_f=\{\mathcal{T}_l,l=1,\ldots,N_\mathcal{T}\}$ into two disjoint subsets $\mathcal{T}_f^o$ and $\mathcal{T}_f^i$, where $\mathcal{T}_f^o$ denotes the set of triangles that form the ''outside'' of the balloon and $\mathcal{T}_f^i$ denotes the set of triangles that form the internal folds. For the range of volumes considered here, the triangles $\mathcal{T}_f^o$ are those on which the atmospheric pressure acts. The triangles $\mathcal{T}_f^i$ are regions of external contact (the outside of the balloon contacts itself). Note, triangles in $\mathcal{T}_f^o$ are constructed from the sets $\{v_{i,1}\}$ and $\{v_{i,2}\}$, while triangles in $\mathcal{T}_f^i$ are constructed from $\{v_{i,0}\}$ and $\{v_{i,1}\}$. We let $N_\mathcal{T}^o$ denote the number of triangles in $\mathcal{T}_f^o$ and $N_\mathcal{T}^i$ denote the number of triangles in $\mathcal{T}_f^i$. Without loss of generality, we can assume that the triangles $\mathcal{T}_l$ are numbered so that

$$\mathcal{T}_l\in\mathcal{T}_f^o,\quad \text{for } l=1,\ldots,N_\mathcal{T}^o,$$
$$\mathcal{T}_l\in\mathcal{T}_f^i,\quad \text{for } l=N_\mathcal{T}^o+1,\ldots,N_\mathcal{T}, \tag{7}$$

where $N_\mathcal{T}=N_\mathcal{T}^i+N_\mathcal{T}^o$. The triangles are labeled from bottom to top as shown in Fig. 1(*c*). A similar convention will apply to triangles $\mathcal{T}_l$ and the reference configuration (see Fig. 1(*a*)). In particular, we let $\mathcal{S}_f=\cup_{l=1}^{N_\mathcal{T}}T_l$ denote the pre-image of $\mathcal{S}_f$. By construction, $N_\mathcal{T}^o=N_\mathcal{T}^i=2n_c$ and we say that T_{2q} and T_{2q+1} are adjacent in S_f.

The total energy of a balloon configuration E_{Total} is the sum of six terms,

$$E_{\text{Total}}=E_{\text{gas}}+E_{\text{film}}+E_{\text{tapes}}+S_{\text{tapes}}+S_{\text{film}}+E_{\text{top}}, \tag{8}$$

where E_{gas} is the gravitational potential energy due to the lifting gas (i.e., the hydrostatic pressure potential), E_{film} is the gravitational potential energy of the film, E_{tapes} is the gravitational potential energy of the load tapes, E_{top} is the gravitational potential energy of the top fitting, S_{tapes} is the strain energy of the load tapes, and S_{film} is the strain energy of the balloon film. In the following, we give a brief description of each of these quantities and indicate how they are computed numerically.

For a balloon at a fixed altitude, it is reasonable to assume that the densities of the lifting gas ρ_{gas} and ambient air ρ_{air} are constant over the height of the balloon. In this case, the pressure difference across the balloon film at level z is given by

$$P=-g(\rho_{\text{air}}-\rho_{\text{gas}})(z-z_0), \tag{9}$$

where z_0 indicates the location of the zero-pressure level ([3], Eq. (7), p. II.5). The specific buoyancy at float will be denoted by $b_d=g(\rho_{\text{air}}-\rho_{\text{gas}})$. In this work, as in previous works, we assume that the zero-pressure level is located at the base of the balloon, i.e., $z_0=0$. In this case, the potential energy of the lifting gas is given by

$$E_{\text{gas}}=-b_d\int\int\int_{\mathcal{V}}z\,dV, \tag{10}$$

where $\mathcal{V}$ is the region occupied by the gas bubble. Equation (10) is the potential for hydrostatic pressure ([17]). Using the divergence theorem and the symmetries of $\mathcal{S}$, Eq. (10) can be replaced by a sum of surface integrals (([6]))

$$E_{\text{gas}}=-2n_gb_d\sum_{l=1}^{N_\mathcal{T}^o}\int_{\mathcal{T}_l}\frac{1}{2}z^2\vec{k}\cdot d\vec{A}, \tag{11}$$

where $d\vec{A}=\vec{n}dA$, $\vec{n}$ is normal to $\mathcal{S}$, and dA is surface area measure on $\mathcal{S}$. Because triangles forming the internal fold will not contribute to E_{gas}, the summation in Eq. (11) is taken from $l=1$ to $l=N_\mathcal{T}^o$. For triangular facets, terms in Eq. (11) can be computed exactly (see Eq. (5), [18]).

Assuming a single balloon skin with uniform thickness e, the gravitational potential energy due to the weight of the balloon film is

$$E_{\text{film}}=\int\int_{\mathcal{S}}w_{\text{film}}z\,dS, \tag{12}$$

where the film weight density is w_{film}. A cap is a subset of S that covers the top portion of the balloon. If the balloon system includes several caps, their contribution to the gravitational potential in Eq. (12) can be incorporated by appropriately modifying the film weight density. For our purposes, we will assume there are two caps denoted by C^1 and C_2 where $C^2\subset C^1\subset S$. Each cap is assumed to have the same material properties as the single film layer of the complete balloon. We define a function $\omega(\cdot)$ on triangles in S_f as follows:

$$\omega(T_l)=\text{number of film layers covering } T_l.$$

E_{film} is given by

$$E_{\text{film}}=2n_gw_{\text{film}}\sum_{l=1}^{N_\mathcal{T}}\overline{z_l}\,\omega(T_l)\text{area}(T_l), \tag{13}$$

where $\overline{z_l}$ is the z-component of the centroid of triangle $\mathcal{T}_l$.

The gravitational potential energy due to the weight of the load tapes is

$$E_{\text{tapes}}=n_gw_{\text{tape}}\int_0^{L_m}\alpha_2(s)\cdot\vec{k}\,ds,$$

where w_{tape} is the weight density of the load tape, $\alpha_2(s)\in R^3$ for $0\leqslant s\leqslant L_d$ is a parametrization of the curve $\mathcal{M}_2$, s is arc length in the flat reference configuration, and $\vec{k}=(0,0,1)$. The z-component of the centroid corresponding to the edge e_i is $\overline{z_{i,2}}=\frac{1}{2}(z_{i+1,2}+z_{i,2})$. The contribution to the gravitational potential of this segment is $w_{\text{tape}}\overline{z_{i,2}}|E_i|$, where E_i is defined in Eq. (2). The energy of $\mathcal{M}_2$ is $w_{\text{tape}}\Sigma_{i=1}^{n_c+1}\overline{z_{i,2}}|E_i|$. The gravitational potential energy of the load tapes in a complete shape is

$$E_{\text{tapes}}=n_gw_{\text{tape}}\sum_{i=1}^{n_c+1}\overline{z_{i,2}}|E_i|. \tag{14}$$

We assume that the fibers making up a typical load tape behave like a linearly elastic string with stiffness constant K_{tape}. If s^* denotes arc length along a deformed meridional fiber, and s the

corresponding arc length in the undeformed state, the linearized strain is $\epsilon \approx (ds^* - ds)/ds$, and so the linearized strain of the ith segment in $\mathcal{M}_2$ is

$$\varepsilon_i = (|e_i| - |E_i|)/|E_i|, \quad i = 1, \ldots, n_c + 1, \tag{15}$$

where E_i and e_i are defined in (2) and (3), respectively. The corresponding strain energy for the ith segment of the load tape running along $\mathcal{M}_2$ with stiffness constant K_{tape} is $\frac{1}{2}K_{\text{tape}}(\varepsilon_i)^2|E_i|$. It follows that the strain energy of the load tapes in a complete shape is

$$S_{\text{tapes}} = \frac{1}{2} n_g K_{\text{tape}} \sum_{i=1}^{n_c+1} (\varepsilon_i)^2 |E_i|. \tag{16}$$

In what follows, we will assume that the balloon is made up of a single layer. Using the previously defined function ω, we will add the contribution of the caps. In our work, we will use a standard measure of shell strain energy (Eq. (1.2.20), [19]). However, since the balloon film has negligible bending stiffness, we drop terms related to the bending energy. Retaining only the first integral in Eq. (1.1.20) ([19])) and assuming a linearly elastic isotropic material, the film strain energy S_{film} is given by

$$S_{\text{film}} = \frac{Ee}{2(1-\nu^2)} \int \int_{\Omega} \{(1-\nu)\gamma_\beta^\alpha(\mathbf{u})\gamma_\alpha^\beta(\mathbf{u}) + \nu\gamma_\alpha^\alpha(\mathbf{u})\gamma_\beta^\beta(\mathbf{u})\} dA^0. \tag{17}$$

The mixed tensor γ_β^α corresponds to the Cauchy-Green strain. The set Ω denotes the parameter space for the flat reference configurations. The vector field $\mathbf{u}$ in Eq. (17) denotes the displacement field that maps a triangle in the reference configuration to one in the deformed configuration. We will not use $\mathbf{u}$ directly in our derivation of an expression for S_{film}, but we will compute the contribution to S_{film} for a typical facet, then sum the results to obtain an approximation of the total strain energy of $\mathcal{S}$.

There are alternative forms for S_{film} and in our computations, we use

$$S_{\text{film}} = \frac{1}{2} \int \int_{\Omega} \boldsymbol{n} : \boldsymbol{\gamma} dA^0, \tag{18}$$

where $\boldsymbol{n}$ represents the Second Piola-Kirkoff stress tensor, $\boldsymbol{\gamma}$ represents the strain tensor, and ":" is the tensor inner product. The contravariant components of $\boldsymbol{n}$ are denoted by $n^{\alpha\beta}$. Equation (18) is equivalent to Eq. (17) and follows after substituting $\boldsymbol{n} : \boldsymbol{\gamma} = n_\beta^\alpha \gamma_\alpha^\beta$ into Eq. (17), where

$$n^{\alpha\beta} = E^{\alpha\beta\lambda\mu}\gamma_{\lambda\mu}, \tag{19}$$

$E^{\alpha\beta\lambda\mu}$ is the tensor of elastic moduli, i.e.,

$$E^{\alpha\beta\lambda\mu} = \frac{eE}{2(1+\nu)} \left[a^{\alpha\lambda}a^{\beta\mu} + a^{\alpha\mu}a^{\beta\lambda} + \frac{2\nu}{1-\nu} a^{\alpha\beta}a^{\lambda\mu} \right], \tag{20}$$

E is Young's modulus, ν is Poisson's ratio, e is the shell thickness, and $a_{\alpha\beta}$ is the first fundamental form of the reference configuration. The Cauchy-Green strain $\gamma_{\alpha\beta}$ is defined in Appendix A. In our work, we use flat facets to approximate the balloon surface and so on each facet, we have $b_{\alpha\beta} = 0$, where $b_{\alpha\beta}$ denotes the second fundamental form of the reference configuration. Cartesian coordinates are used, so $a_{\alpha\beta} = \delta_\alpha^\beta$.

After triangulating $\mathcal{S}_f$, Eq. (18) can be written in the form

$$2n_g \sum_{l=1}^{N_\mathcal{T}} \frac{1}{2} \int_{T_l} \boldsymbol{n}(T_l) : \boldsymbol{\gamma}(T_l) dA^0. \tag{21}$$

For a constant strain model, terms of the form $\boldsymbol{n}(T_l)$ and $\boldsymbol{\gamma}(T_l)$ are constant on each triangle T_l, so $\int_{T_l} \boldsymbol{n}(T_l) : \boldsymbol{\gamma}(T_l) dA^0$ can be replaced by $\boldsymbol{n}(T_l) : \boldsymbol{\gamma}(T_l) \times \text{area}(T_l)$. If we add the contribution of the external caps, we have

$$S_{\text{film}} = 2n_g \sum_{l=1}^{N_\mathcal{T}} \frac{1}{2} \omega(T_l)(\boldsymbol{n}(T_l) : \boldsymbol{\gamma}(T_l)) \text{area}(T_l). \tag{22}$$

Let $\mathcal{S}_f(v_{i,j})$ denote the fundamental section of a faceted balloon defined by vertices $\{v_{i,j}\}$. The discrete form of the total energy of $\mathcal{S}$ will be denoted by $E(v_{i,j})$, and is obtained by substituting Eqs. (10), (13), (14), (16), (22) into Eq. (8). In particular, we have

$$E(v_{i,j}) = E_{\text{gas}} + E_{\text{film}} + E_{\text{tapes}} + S_{\text{tapes}} + S_{\text{film}} + z_{\text{top}} w_{\text{top}}. \tag{23}$$

The last term is the gravitational potential due to the top fitting of the balloon (w_{top} is the weight of the fitting and $z_{\text{top}} = z_{2,n_c+2}$ is its height of above the base).

A volume constraint,

$$\mathcal{V} - 2n_g \sum_{l=1}^{N_\mathcal{T}^o} \mathcal{V}_l = 0, \tag{24}$$

where $\mathcal{V}_l$ is the volume of the tetrahedron with base $\mathcal{T}_l$ in a partition of the gas bubble. Upper and lower bounds in the form

$$\begin{aligned} x_{i,2}^{\text{lb}} \le x_{i,2} \le x_{i,2}^{\text{ub}}, &\quad i = 2, \ldots, 2n_c + 1, \\ z_{i,2}^{\text{lb}} \le z_{i,2} \le z_{i,2}^{\text{ub}}, &\quad i = 2, \ldots, n_c + 2, \\ 0 \le \alpha_i \le \alpha_i^{\text{ub}}, &\quad i = 2, \ldots, n_c + 1, \end{aligned} \tag{25}$$

corresponding to vertices with nonzero degrees of freedom are applied. Because we are including strain energy in our problem formulation, we do not include the fiber constraints that were employed in previous work (Eqs. (13)–(14) of [5]). The Matlab software (constr) that is used to solve variational problems allows (25) to be specified. In practice, the upper and lower bounds are chosen sufficiently large so they do not affect the solution. The variational principle that is used to compute the numerical EM-shapes presented in Section 3 is given by the following:

Problem (*)

$$\text{For } \mathcal{S}(v_{i,j}) \in \mathcal{C}_k, \quad \begin{aligned} &\text{minimize:} && E(v_{i,j}), \\ &\text{subject to:} && G(v_{i,j}) = 0, \end{aligned}$$

satisfying (25), where G is defined by the left side of (24).

3 Numerical Solutions

Previous work on EM-shapes ([5,6]) rescaled the balloon dimensions to be in agreement with the scaling of the standard shapes based on the design parameters λ and Σ and the Σ-shape equations (see, e.g., [2,3]). In the present work, we use design shapes that are similar to those used for large scientific balloons flown by NASA. For our calculations, we will consider two types of designs. The first design is based on the standard natural-shape model as described in ([2]). This balloon has a volume of a 804,198 m^3 (28.4 million cubic feet), two caps, and uses a design value of $\Sigma = 0.29$. We will refer to this as the *natural-shape* design. The second design is a 835,347 m^3 (29.5 million cubic feet) balloon that is based on a variation of the natural shape, where the caps are modeled as added thickness and the gore is tapered more than usual near the bottom. For this particular design, the base of the balloon is nearly the shape of a cone (the source of the tapered design profile was a balloon manufacturer). We call this the *tapered* design. Because caps are included as an added thickness in the second model, the resulting design shapes are in general shorter in height and wider in diameter than the shapes produced by the natural-shape model, and we cannot assign a value of Σ to the shape. Material constants and additional parameters are presented in Table 1. Poisson's ratio ν and Young's modulus E for the balloon film are based on 20.32 micron polyethylene and are highly temperature-dependent. For example, under normal operating conditions, ν and E could lie within the respective intervals,

Table 1 Parameter values

Description (units)	Variable	
Young's modulus (MPa)	E	248.2, 124.1
Poisson's ratio	ν	0.82, 0.72
Film weight density (N/m^2)	w_{film}	0.18386
Load tape weight density (N/m)	w_{tape}	0.08785, 0.08002
Load tape stiffness parameter (N)	K_{tape}	25000, 26244
Film thickness (microns)	e	20.32
Specify buoyancy at float (N/m^3)	b_d	0.0354, 0.0542
Volume at float (m^3)	$\mathcal{V}_{\text{float}}$	804198, 835347
Number of gores	N_g	156, 159
Design gore length (m)	l_d	178.476, 181.905
Payload (N)		16035, 31751
Gross weight (N)		29531, 45247

$0.72 \leqslant \nu \leqslant 0.82$ and $124 \leqslant E \leqslant 248$ (MPa). For the purposes of this paper, we use nominal values $\nu = 0.82$, $E = 248$ MPA, but consider a number of different combinations of ν and E.

We use a specific buoyancy that corresponds to an altitude of 39,429 m ([20], p. 73) as the nominal altitude for Cases I. Case I(a) refers to the tapered design, while Case I(b) refers to the natural-shape design. For Cases II, the specific buoyancy corresponds to an altitude of 36,596 m. Case II uses the tapered gore and considers various combinations of Young's modulus and Poisson's ratio. In Cases I–II, the payload is adjusted appropriately so that the balloon is in equilibrium for the float conditions. The number of circumferential segments in the discretization is $n_c = 53$.

In the following, $\mu_{r,l}$ for $r = 1,2$ will denote the principal stress resultants of the lth triangle (see Appendix A). The averaged principal stress resultants are denoted by $\hat{\mu}_{r,q}$ where $\hat{\mu}_{r,1} = \mu_{r,1}$,

$$\hat{\mu}_{r,q} = \frac{1}{2}(\mu_{r,2q} + \mu_{r,2q+1}),$$

where $r = 1,2$, $q = 2, \ldots, n_c - 1$, and $\hat{\mu}_{r,n_c} = \mu_{r,2n_c}$. In S_f, the triangles T_{2q}, T_{2q+1} form a quadrilateral and we can interpret $\hat{\mu}_{r,q}$ as measured at the centroid of the qth quadrilateral (note, in S_f, T_{2q}, T_{2q+1} need not lie in the same plane).

In Table 2, we present data on the strained float shapes for the tapered and natural designs. In both cases, the strained shapes are roughly three meters taller than their respective designs. The diameter of the strained tapered shape is about 1.2 meters less in diameter than its design, while the strained natural shape is about 0.7 meters less than its design. Of the two design shapes considered here, the natural shape is curved more near its base (see Fig. 3(*a*)). This means that after straining, the natural shape will have slightly more excess material in this lower region. Consequently, its fold will extend all the way to the base of the balloon. On the other hand, the internal fold of the tapered design initiates much further up from the bottom of the balloon and nearer the top. Where the natural design forms a small internal fold near the base of the balloon to account for excess balloon material, because it is tapered near the base, the tapered design does not need to form a fold of excess material. In Fig. 3(*b*), we present the tension in each segment of the load tape.

For the tapered design, Fig. 4 suggests that the film is under biaxial tension near the base. Although the hoop stresses are positive, they are very small (less than 0.17 N/cm) and within the accuracy of our model, one could argue they are zero. In any case, this effect is due to the design shape, not our solution process (compare to Case I(b)). Near the base of the balloon, most of the load is carried by the load tapes. However, the tapering of the design in Case I(a) tends to transfer more of the load into the film near the bottom of the balloon (see Figs. 4). The corners in graphs near $s = 122$ m in Fig. 3(*b*) and Figs. 4 correspond to the boundary of the caps (when the caps are removed, we find that the corners are no longer present). The caps are not needed to support the balloon system at float altitude, but are needed to contain the gas bubble at launch and during the initial stages of ascent. In all figures, the locations of the fold initiation and termination points are indicated by a ''$\otimes$.'' The parameter s is measured along the edge of the gore in the undeformed configuration.

One major difference between the present work and our earlier work on energy minimizing shapes is that fiber constraints are not enforced here (compare to Eqs. (13)–(14) in [5]) where the lengths of certain fibers were required to be fixed). However, we find that our computed solutions at float that include strain energy have significantly less distortion when compared with those based on the variational principle in ([5]). If L_d is the unstrained length of a meridional fiber and l its strained length, $\delta_m = (l - L_d)/L_d$. The quantities $\delta_c^{\pm}$ are similarly defined, except δ_c^- is the minimum and δ_c^+ is the maximum over all circumferential fibers. In ([5]), the quantity δ_c was nonnegative by definition. However, in the present work, circumferential fibers are allowed to stretch or contract, so that δ_c could be negative. If $|E_{d,l}|$ represents the unstrained length of the ''diagonal'' edge in the lth triangle, and $|e_{d,l}|$ its corresponding strained length, then $\delta_d^+ = \max_l\{(|e_{d,l}| - |E_{d,l}|)/|E_{d,l}|, l = 1, \ldots, N_T^o\}$. Similarly, δ_d^- is the minimum diagonal strain and $\hat{\delta}_d$ is the average diagonal strain. One notable difference between the present results (that include strain energy)

Table 2 Strained EM-shapes with nominal load at float; units of energy are megajoules (MJ); units of strain are m/m

	Tapered Design		Natural Design	
Description	Initial	Strained	Initial	Strained
Young's modulus (MPa)	-	248.2	-	248.
Poisson's ratio	-	0.82	-	0.82
Strain energy of film	0	0.00425	0	0.00424
Strain energy of load tapes	0	0.00960	0	0.01007
Hydrostatic pressure potential	−1.83983	−1.89893	−1.68884	−1.74499
Gravitational potential of film	0.85422	0.89227	0.77447	0.79135
Gravitational potential of tapes	0.14013	0.14194	0.14013	0.14440
Gravitational potential of top fitting	0.01403	0.01451	0.01376	0.01418
Total energy of balloon system	−0.79567	−0.83634	−0.79567	−0.78073
Maximum depth of internal fold (cm)	0	1.05156	0	0.62484
Minimum contraction of circumferential fibers	0	−0.01891	0	−0.02027
Maximum elongation of circumferential fibers	0	0.00205	0	0.00188
Load tape strain	0	0.00485	0	0.00509
Maximum strain of diagonal fibers	0	0.00190	0	0.00188
Maximum strain of diagonal fibers	0	0.00655	0	0.00772
Average strain of diagonal fibers	0	0.00431	0	0.00455
Base angle (deg)	57.460	56.45	63	60.93
Height of top fitting (m)	105.156	108.784	103.176	106.301
Maximum radius in $y = \tan(\pi/n_g)x$-plane	64.5963	63.9269	63.0744	62.7787

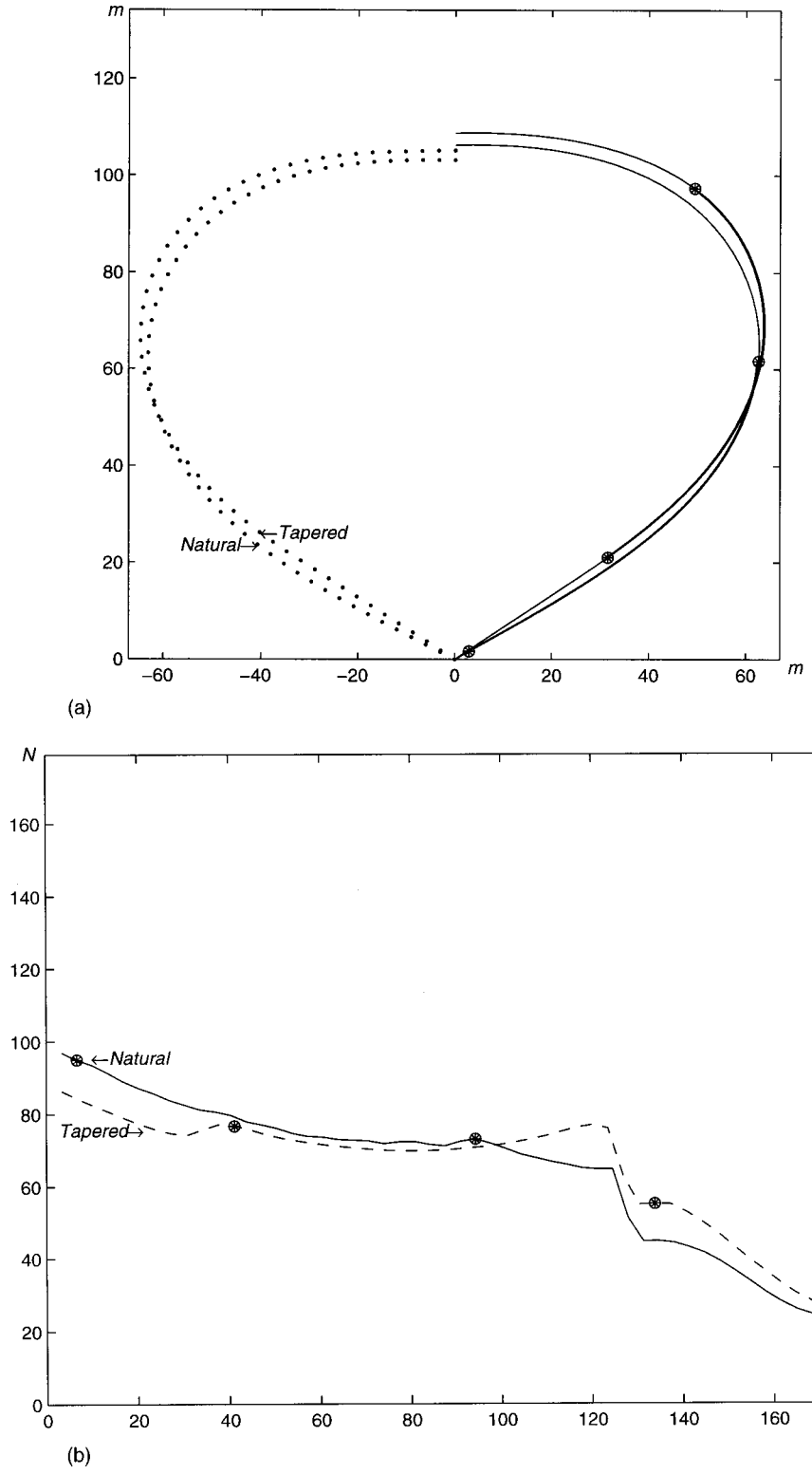

Fig. 3 (*a*) Profiles of natural-shape and tapered natural shape designs (···) and strained shapes (—); (*b*) one-half load tape tension at nominal conditions; ⊗ marks the range of the fold

and our previous work (where fiber constraints are included, e.g., [5]) is a reduction in the overall distortion of EM-shapes. Restricting our attention to the data on the float shapes in ([5]), we found distortions on the order of 0.2 percent for the maximum meridional stretch δ_m, 2.0 percent for the maximum circumferential stretch δ_c^+; there were a few triangles with a diagonal stretch δ_d^+ on the order of 4.0 percent and the average positive diagonal stretches $\hat{\delta}_d$ were on the order of 0.60 percent. In the present work on the natural design, we found that the meridional stretch was 0.50 percent and the maximum circumferential stretch was 0.20

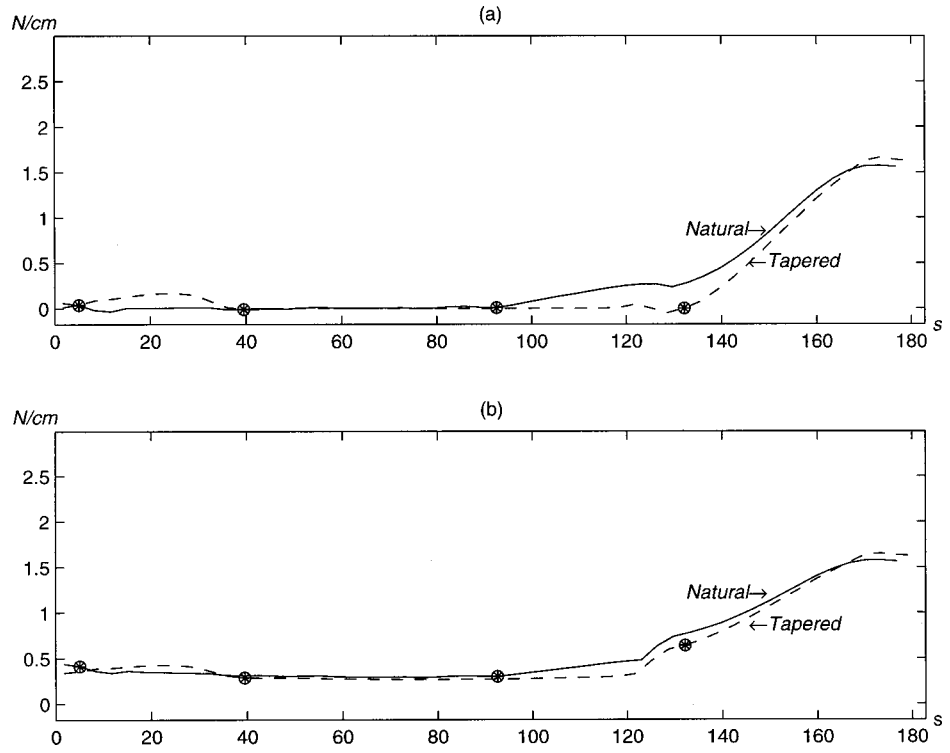

Fig. 4 Averaged principal stress resultants (N/cm) for nominal float conditions; (*a*) $\hat{\mu}_{1,q}$−circumferential stress resultants, (*b*) $\hat{\mu}_{2,q}$−meridional stress resultants; ⊗ marks the range of the fold

percent; a contraction of approximately 2.0 percent was observed in the strained float shape. For the EM-shape at float, we found that all triangles experienced a positive diagonal stretch that was at most 0.77 percent and on the average about 0.45 percent.

In order to compare our results with ([10]), we need to compute an estimate of the meridional and hoop stresses. By examining the eigenvectors corresponding to the principal stress resultants $\mu_{1,l}, \mu_{2,l}$, we observed that $\mu_{1,l}$ corresponds to the hoop direction and $\mu_{2,l}$ corresponds to the meridional direction. The zero load tape slackness case presented in ([10]) that were obtained using the commercial finite element code ABACUS is the most appropriate set of results that are available in the literature for comparisons with our results on float shapes. The tapered balloon design used here is very similar to the one in ([10]), where shapes have a volume of around 826,852 m^3 (29.2 mcf), the specific buoyancy is 0.0344 N/m^3, and $\nu=0.82$, $E=248$ Pa. The volume is not included as a constraint, and is computed after a solution is found; quadrilateral elements and a finer mesh are used in ([10]). The author in ([10]) uses an artificial bending stiffness to aid convergence, but indicates that this does not affect the membrane solution. Since the directions of our principal stresses for the float shape align with the circumferential and meridional directions, we can directly compare our results with the meridional and circumferential stress resultants presented in ([10]). We find that our estimated meridional stress resultants are relatively constant (approximately 0.28 N/cm) over the bottom two-thirds of the gore,

Table 3 Strained EM-shapes with heavy load at float, tapered design; units of energy are megajoules (MJ); strains are measured in m/m

Description	Initial	Case II(a)	Case II(b)	Case II(c)	Case II(d)
Young's modulus (MPa)	-	248.2	124.1	248.2	124.1
Poisson's ratio	-	0.82	0.82	0.72	0.72
Strain energy of film	0	0.01428	0.01107	0.01481	0.01550
Strain energy of load tapes	0	0.03404	0.04347	0.03458	0.04446
Hydrostatic pressure potential	−1.83851	−2.98221	−3.00368	−2.98545	−3.00769
Gravitational potential of film	0.81339	0.91330	0.91878	0.91401	0.91959
Gravitational potential of tapes	0.13782	0.14542	0.14632	0.14552	0.14643
Gravitational potential of top fitting	0.01403	0.01490	0.01499	0.01491	0.01499
Total energy of balloon system	−0.88728	−1.86025	−1.86903	−1.86159	−1.87069
Maximum depth of internal fold (cm)	0	1.93548	2.28905	2.26162	2.54203
Minimum contraction of circumferential fibers	0	−0.03485	−0.04074	−0.03058	−0.03591
Maximum elongation of circumferential fibers	0	0.00339	0.00514	0.00459	0.00662
Load tape strain	0	0.00899	0.01032	0.00917	0.01055
Minimum strain of diagonal fibers	0	0.00328	0.00504	0.00450	0.00647
Maximum strain of diagonal fibers	0	0.01279	0.01288	0.01283	0.01292
Average strain of diagonal fibers	0	0.00804	0.00924	0.00828	0.00954
Base angle (deg)	57.460	55.28	55.55	55.66	55.68
Height of top fitting (m)	105.156	111.726	112.392	111.735	112.375
Maximum radius in $y=0$ plane (m)	64.622	63.139	63.020	63.121	63.002

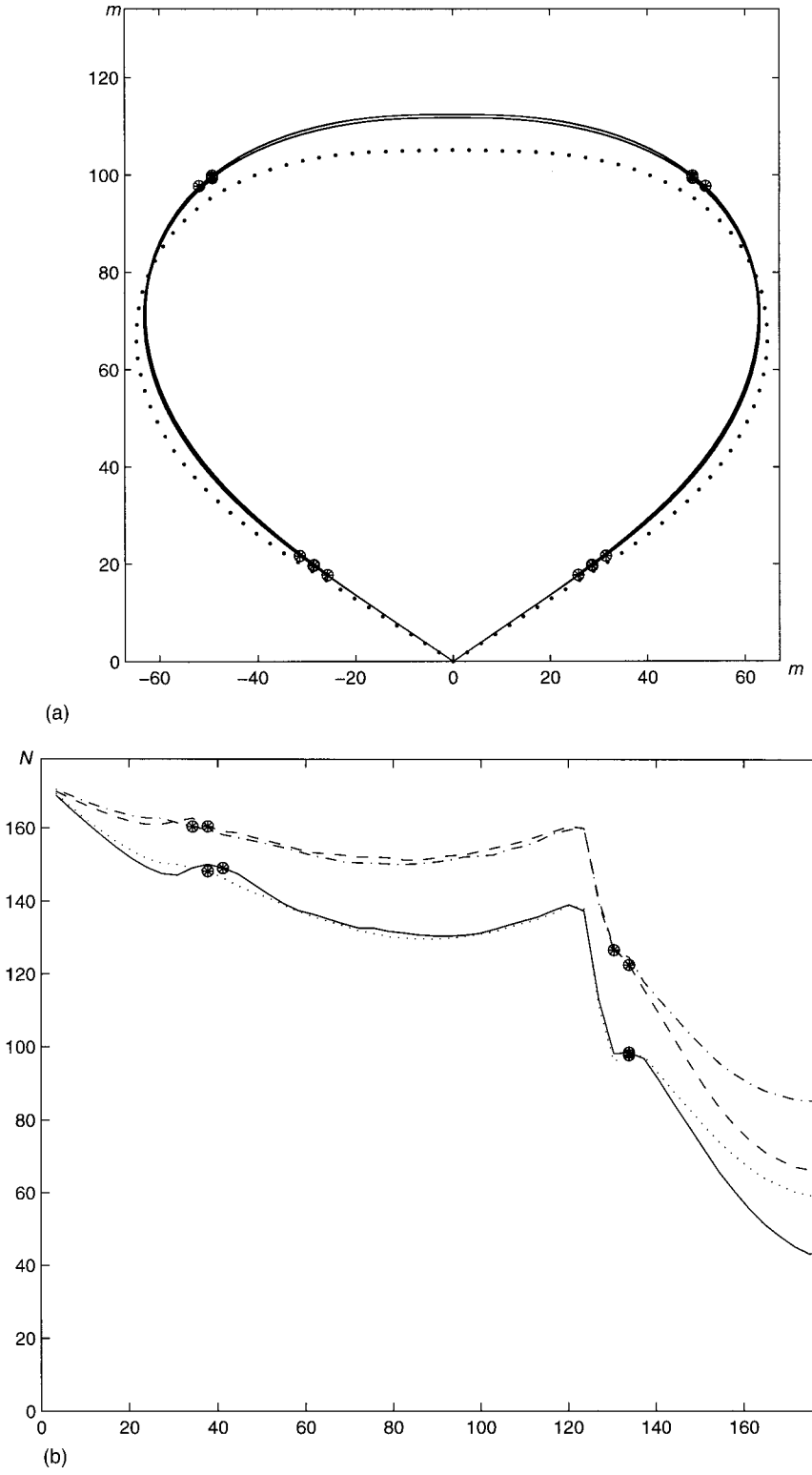

Fig. 5 ***(a)*** **Profiles of tapered shape design (⋯) and strained shapes (—) for Cases II(a)–(d);** (***b***) **one-half load tape tensions; ⊗ marks the range of the fold**

rising sharply in the top one-third of the gore to a maximum value of 1.68 N/cm. In ([10]), the maximum meridional stress resultant is roughly 1.75 N/cm and the minimum meridional stress resultant is approximately 0.49 N/cm. The results from ([10]) were obtained from graphs and so an error on the order of 0.2 N/cm should be taken into account. In addition to the good agreement on the maximum and minimum principle stress resultants, we find that our plots of the meridional and circumferential stress resultants in Figs. 4 and the corresponding figure in ([10]) are in good qualitative agreement (i.e., stresses are relatively constant over the bottom two-thirds of the gore, and begin rising at about the same station along the gore to roughly the same maximum values. In summary, we find good agreement.

Based on the results presented in Case I, we see that the

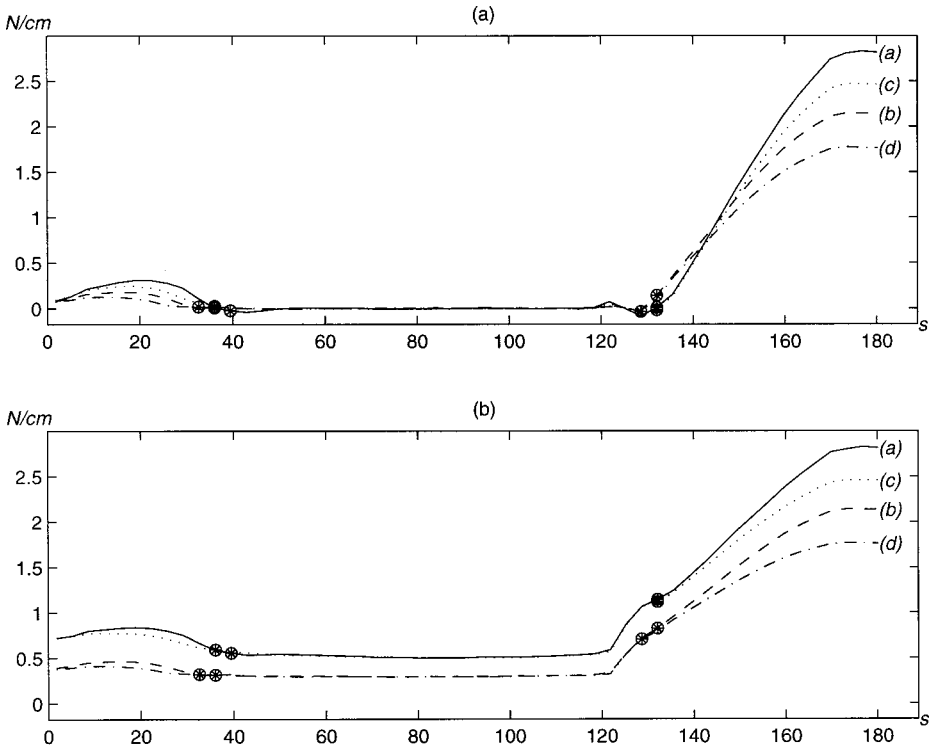

Fig. 6 Averaged principal stress resultants (N/cm) ($\hat{\mu}_{1,q}, \hat{\mu}_{2,q}$) for Cases II(a)–(d); (*a*)–circumferential stress resultants; (*b*)–meridional stress resultants; ⊗ marks the range of the fold

natural-shape design and tapered design behaved roughly the same, so we carried out the parameter studies only for the tapered design. In Table 3, we present results for strained float shapes that support a heavy payload (almost double that used in Case I). As one might expect, we see upon comparing Table 2 (column 3) with Table 3 (column 3), a doubling of the payload results in a doubling of the load tape strain and the corresponding maximum principal stresses. From Table 3, we see that varying Poisson's ratio over the range $0.72 \leqslant \nu \leqslant 0.82$ has little effect on the corresponding solutions where the fold is present. Near the top of the balloon, the solution with the higher Poisson ratio (and same Young's modulus) has the larger principal stress resultants. A reduction in Young's modulus by a factor of two, is accompanied by an increase in strain of about ten percent (as indicated by the load tape strain and average strain of diagonal fibers in Table 3). For comparison purposes, the launch specification for maximum film stress is roughly 3.85 N/cm (2.2 lbf/in), so the maximum stresses that are considered here are within the range that a real balloon film might experience. Plots of the design shapes and strained equilibrium shapes are presented in Fig. 5(a). Plots of the load tape tensions are presented in Fig. 5(b). Plots of the stress resultants are presented in Fig. 6.

4 Concluding Remarks

A mathematical model for estimating the stresses in a strained large scientific balloon is proposed. Though in some ways less sophisticated than many standard finite element method packages, our model can accurately describe the geometry of the gore structure with internal folds of excess material as observed in real balloons. For float conditions, a balloon should behave like a standard membrane under biaxial tension near the top of the balloon, but somewhere below its shoulder, the balloon should behave more like a degenerate membrane where tension is predominantly in the meridional direction. Our model predicts similar behavior and can handle strained balloon shapes with internal folds, providing reasonable estimates of the film stresses. Our solutions are in good qualitative and quantitative agreement when compared with similar results obtained using a commercial finite element package that is combined with a tension field model. Our results on strained float shapes give us confidence that when we apply our model to ascent shapes (i.e., partially inflated configurations) with significant regions of folded material, we should be able to obtain useful estimates for the principal stresses. Our EM-approach is tailored to handle configurations with excess folded material.

Appendix A

Computation of Principal Stresses. In the following, let T and $\mathcal{T}$ denote triangles in the reference and deformed configuration, respectively. We temporarily drop the subscript l for triangles. In the following, Ω^e represents the ''standard triangle'' for a typical T in the reference configuration,

$$\Omega^e = \{(\xi_1, \xi_2) | 0 \leqslant \xi_1 + \xi_2 \leqslant 1, 0 \leqslant \xi_1, \xi_2 \leqslant 1\}.$$

Let **n** and **j** denote the edges of the standard triangle. Let M_R be the linear map that takes **i**,**j** to the respective edges $\mathbf{c}_1, \mathbf{c}_2 \in R^2$ of a typical triangle T in the reference configuration. Similarly, let M_D be the linear map that takes **i**,**j** to the edges of a typical triangle $\mathcal{T}$ in the deformed configuration $\mathbf{f}_1, \mathbf{f}_2 \in R^3$, respectively. The deformation mapping is linear and is given by $p \in T \rightarrow q \in \mathcal{T}$ where $q = M_D \circ M_R^{-1}(p)$. The displacement mapping u is defined by the equation $q = p + u$.

Because the mapping $p \rightarrow q$ is linear, the deformation gradient **F** is the map itself, i.e.,

$$\mathbf{F} = \frac{\partial q}{\partial p} = M_D \circ M_R^{-1}.$$

In matrix form, the Cauchy strain tensor is given by

$$\mathbf{C}=\mathbf{F}^T\mathbf{F}.$$

Because $\mathbf{C}$ is symmetric, by the spectral representation theorem, there exist orthonormal vectors $\mathbf{e}_1, \mathbf{e}_2$ such that

$$\mathbf{C}=\lambda_1\mathbf{e}_1\mathbf{e}_1^T+\lambda_2\mathbf{e}_2\mathbf{e}_2^T.$$

The Cauchy-Green strain $\boldsymbol{\gamma}$ in matrix form is given by

$$\mathbf{E}=\tfrac{1}{2}(\mathbf{C}-\mathbf{I}).$$

The eigenvectors of $\mathbf{E}$ and $\mathbf{C}$ are the same, and so $\mathbf{E}$ has the representation

$$\mathbf{E}=\tfrac{1}{2}(\lambda_1-1)\mathbf{e}_1\mathbf{e}_1^T+\tfrac{1}{2}(\lambda_2-1)\mathbf{e}_2\mathbf{e}_2^T.$$

In matrix form, the second Piola-Kirkoff stress is given by

$$\mathbf{N}=\frac{eE}{1-\nu^2}[(1-\nu)\mathbf{E}+\nu\mathrm{Trace}(\mathbf{E})\mathbf{I}],$$

and follows from Eqs. (11.1.22)–(11.1.23) in ([21]) for the special case of a formulation with respect to Cartesian coordinates (i.e., $a^{\alpha\beta}=\delta^{\alpha}_{\beta}$), where E is Young's modulus and ν is Poisson's ratio. Since $\mathbf{E}=\mathbf{E}^T$,we see that $\mathbf{N}=\mathbf{N}^T$, and by the spectral representation theorem we have

$$\mathbf{N}=\mu_1\mathbf{n}_1\mathbf{n}_1^T+\mu_2\mathbf{n}_2\mathbf{n}_2^T,$$

where $\mathbf{n}_1$ and $\mathbf{n}_2$ are orthonormal vectors. The eigenvectors of $\mathbf{C}$ determine the principal axis of strain, $\sqrt{\lambda_1}$ and $\sqrt{\lambda_2}$ are the principal stretches, and μ_1 and μ_2 are the principal stress resultants (see, e.g., [22]).

Each of the above quantities are defined for a typical triangle, T_l, and so we will use a subscript l to indicate that a quantity is related to the lth triangle. For triangle T_l, we have the following representations:

$$\mathbf{C}(T_l)=\lambda_{1,l}\mathbf{e}_{1,l}\mathbf{e}_{1,l}^T+\lambda_{2,l}\mathbf{e}_{2,l}\mathbf{e}_{2,l}^T,$$

$$\mathbf{E}(T_l)=\tfrac{1}{2}(\lambda_{1,l}-1)\mathbf{e}_{1,l}\mathbf{e}_{1,l}^T+\tfrac{1}{2}(\lambda_{2,l}-1)\mathbf{e}_{2,l}e_{2,l}^T,$$

$$\mathbf{N}(T_l)=\mu_{1,l}\mathbf{n}_{1,l}\mathbf{n}_{1,l}^T+\mu_{2,l}\mathbf{n}_{2,l}\mathbf{n}_{2,l}^T.$$

For a constant strain model, the strain energy corresponding to T_l can be written as

$$\int_{T_l}\boldsymbol{n}(T_l):\boldsymbol{\gamma}(T_l)dA^0=\mathbf{N}(T_l):\mathbf{E}(T_l)\times\mathrm{area}(T_l).$$

Note, the above descriptions assumed a single shell thickness for all triangles. The values for the principle stresses for triangle T_l would need to be modified based on the number of caps.

Acknowledgment

The research presented in this paper was supported by NASA Award NAG5-697. The authors would like to thank the referees for a number of helpful suggestions.

References

[1] Anon., 1951–1956, ''Research Development in the Field of High Altitude Plastic Balloons,'' NONR-710(01a) Reports, Department of Physics, University of Minnesota, Minneapolis, MN.

[2] Baginski, F., Collier, W., and Williams, T., 1998, ''A Parallel Shooting Method for Determining the Natural-Shape of a Large Scientific Balloon,'' SIAM (Soc. Ind. Appl. Math.) J. Appl. Math., **58**, No. 3, pp. 961–974.

[3] Morris, A. L., ed., 1975, ''Scientific Ballooning Handbook,'' NCAR Technical Note, NCAR-TN-99, National Center for Atmospheric Research, Boulder, CO, Section V, pp. 1–45.

[4] Smalley, J. H., 1964, ''Determination of the Shape of a Free Balloon,'' AFCRL-65-68, Nov.

[5] Baginski, F., 1996, ''Modeling Nonaxisymmetric Off-Design Shapes of Large Scientific Balloons,'' AIAA J., **34**, No. 2, pp. 400–407.

[6] Baginski, F., and Ramamurti, S., 1995, ''Variational Principles for the Ascent Shapes of Large Scientific Balloons,'' AIAA J., **33**, No. 4, pp. 764–768.

[7] Contri, P., and Schrefler, B. A., 1988, ''A Geometrically Nonlinear Finite Element Analysis of Wrinkled Membrane Surfaces by a No-Compression Material Model,'' Commun. Appl. Numer. Methods, **4**, No. 1, pp. 5–15.

[8] Oden, J. T., 1972, *Finite Elements of Nonlinear Continua*, McGraw-Hill, New York.

[9] Haseganu, E. M., and Steigmann, D. J., 1994, ''Analysis of Partly Wrinkled Membranes by the Method of Dynamic Relaxation,'' Comput. Mech., **14**, No. 6, pp. 596–614.

[10] Schur, W., 1992, ''Recent Advances in the Structural Analysis of Scientific Balloons,'' A Compendium of NASA Balloon Research and Development Activities for Fiscal Year 1992, NASA Balloon Projects, Wallops Flight Facility, Wallops Island, VA.

[11] Steigmann, D. J., 1991, ''Tension-Field Theories of Elastic Membranes and Networks,'' *Recent Developments in Elasticity*, ASME, New York, pp. 41–49.

[12] Jeong, D. G., and Kwak, B. M., 1992, ''Complementary Problem Formulation for the Wrinkled Membrane and Numerical Implementation,'' Finite Elem. Anal. Design, **12**, pp. 91–104.

[13] Roddeman, D. G., Drukker, J., Oomens, C. W. J., and Janssen, J. D., 1987, ''The Wrinkling of Thin Membranes: Part I–Theory,'' ASME J. Appl. Mech., **54**, pp. 884–887.

[14] Roddeman, D. G., Drukker, J., Oomens, C. W. J., and Janssen, J. D., 1987, ''The Wrinkling of Thin Membranes: Part II–Numerical Analysis,'' ASME J. Appl. Mech., **54**, pp. 888–897.

[15] Pipkin, A. C., 1994, ''Relaxed Energy Densities for Large Deformations of Membranes,'' IMA J. Appl. Math., **52**, pp. 297–308.

[16] Baginski, F., and Collier, W., 1998, ''Energy Minimizing Shapes of Partially Inflated Large Scientific Balloons,'' Adv. Space Res., **21**, No. 7, pp. 975–978.

[17] Fisher, D., 1988, ''Configuration Dependent Pressure Potentials,'' J. Elast., **19**, pp. 77–84.

[18] Brakke, K., 1993, *The Surface Evolver Manual*, Version 1.91, The Geometry Center, Minneapolis, MN, May.

[19] Oden, J. T., and Carey, G. F., 1984, *Finite Elements. Special Problems in Solid Mechanics*, Vol. V, Prentice-Hall, Englewood Cliffs, NJ.

[20] Warren, J. C., Smalley, J. H., and Morris, A. L., 1971, ''Aerostatic Lift of Helium and Hydrogen in the Atmosphere,'' NCAR Technical Notes, National Center for Atmospheric Research, NCAR-TN/IA-69, Dec.

[21] Green, A. E., and Zerna, W., 1992, *Theoretical Elasticity*, Dover, New York.

[22] Antman, S. S., 1995, *Nonlinear Problems of Elasticity*, Springer-Verlag, New York.

On the Development of Volumetric Strain Energy Functions

S. Doll

K. Schweizerhof

Institute for Mechanics,
University of Karlsruhe,
76128 Karlsruhe, Germany
e-mail: mechanik@bau-verm.uni-karlsruhe.de

To describe elastic material behavior the starting point is the isochoric-volumetric decoupling of the strain energy function. The volumetric part is the central subject of this contribution. First, some volumetric functions given in the literature are discussed with respect to physical conditions, then three new volumetric functions are developed which fulfill all imposed conditions. One proposed function which contains two material parameters in addition to the compressibility parameter is treated in detail. Some parameter fits are carried out on the basis of well-known volumetric strain energy functions and experimental data. A generalization of the proposed function permits an unlimited number of additional material parameters. Dedicated to Professor Franz Ziegler on the occasion of his 60th birthday. [S0021-8936(00)00901-6]

1 Introduction

The success achieved in the application of finite element techniques during the recent years has the consequence that nowadays nonlinear material laws at finite strains are frequently applied in structural analysis. In the case of finite elasticity, strain energy functions for compressible (or nearly compressible) materials are preferable because displacement-based finite elements can be used. As a special assumption the isochoric-volumetric decoupling of the energy function is frequently applied in this context. An advantage appears that the isochoric and the volumetric material behavior can be treated as completely independent, which permits their decoupled treatment in the development of finite elements, e.g., using different integration schemes to avoid locking phenomena. A disadvantage of the split is the increase of computational effort due to the product formula that must be taken into account, deriving the stresses and the elasticity tangent from the strain energy function.

The outline of this contribution is as follows: After reviewing the isochoric-volumetric decoupling of the strain energy function, the conditions imposed on the decoupled energy function are motivated and a complete representation is given. Then the focus is on the volumetric part, first discussing known functions and then developing new functions.

2 Decoupling of the Strain Energy Function

As is well known (e.g., [1]) under the assumption of isotropy the strain energy function depends only on the left (or right) Cauchy-Green tensor $\mathbf{b}$ through the invariants $I_{\mathbf{b}}$, $II_{\mathbf{b}}$, $III_{\mathbf{b}}$ or the related principal stretches λ_1, λ_2, λ_3:

$$W = W(\mathbf{b}) = W(I_{\mathbf{b}}, II_{\mathbf{b}}, III_{\mathbf{b}}) = W(\lambda_1, \lambda_2, \lambda_3).$$

In the compressible case all invariants and principal stretches are independent and no constraint exists. The determinant of the deformation gradient, which allows for the measurement of the local change of volume during the deformation, is given by $J = \sqrt{III_{\mathbf{b}}} = \lambda_1\lambda_2\lambda_3$ with $0 < J < \infty$.

Contributed by the Applied Mechanics Division of THE AMERICAN SOCIETY OF MECHANICAL ENGINEERS for publication in the ASME JOURNAL OF APPLIED MECHANICS. Manuscript received by the ASME Applied Mechanics Division, July 27, 1997; final revision, Oct. 12, 1999. Associate Technical Editor: M. M. Carroll. Discussion on the paper should be addressed to the Technical Editor, Professor Lewis T. Wheeler, Department of Mechanical Engineering, University of Houston, Houston, TX 77204-4792, and will be accepted until four months after final publication of the paper itself in the ASME JOURNAL OF APPLIED MECHANICS.

For compressible materials a totally decoupled isochoric and volumetric material behavior is commonly assumed (see citations in Section 4). This leads to the definition of the isochoric left Cauchy-Green tensor $\hat{\mathbf{b}}$ with the invariants

$$I_{\hat{\mathbf{b}}} = J^{-2/3} I_{\mathbf{b}}, \quad II_{\hat{\mathbf{b}}} = J^{-4/3} II_{\mathbf{b}}, \quad III_{\hat{\mathbf{b}}} = 1 \tag{1}$$

and the isochoric principal stretches

$$\hat{\lambda}_i = J^{-1/3} \lambda_i, \tag{2}$$

which date back to Flory [2]. Because of the isochoric incompressibility the classical constraint $(1)_3$ holds, thus $\hat{\lambda}_1\hat{\lambda}_2\hat{\lambda}_3 = 1$. Now only two of three isochoric principal stretches are independent. Including the isochoric-volumetric decoupling into the strain energy function leads to

$$\begin{aligned} W &= \hat{W}(I_{\hat{\mathbf{b}}}, II_{\hat{\mathbf{b}}}) + U(J), \\ W &= \hat{W}(\hat{\lambda}_1, \hat{\lambda}_2, \hat{\lambda}_3 = \hat{\lambda}_1^{-1}\hat{\lambda}_2^{-1}) + U(J) \end{aligned} \tag{3}$$

where $\hat{W}$ is the isochoric part and $U(J)$ is the volumetric part.

The question for which materials or in which range such a decoupled strain energy function holds is not discussed here (see, e.g., Penn [3]) for some criticism of the additive split or van den Bogert and de Borst [4] for the investigation of coupling terms). In the following we assume that the additive split (3) is valid for the materials considered.

3 Requirements for the Strain Energy Function

The strain energy function has to satisfy some physical conditions. For completeness the conditions are listed for the isochoric part as well as for the volumetric part separately. In each case a short motivation is given. For simplicity the considerations are based on the representation $(3)_2$. Some typical references are Ogden [5,1] or Ciarlet [6]. It should be noted that all of the conditions imposed on the isochoric strain energy $\hat{W}$ in this contribution coincide exactly with those imposed on the strain energy function for incompressible materials. The only difference is that the isochoric principal stretches $\hat{\lambda}_i$ replace the principal stretches of the incompressible case.

Isotropy requires that the principal stretches can be arbitrarily ordered in the strain energy function

$$\hat{W}(\hat{\lambda}_i, \hat{\lambda}_j, \hat{\lambda}_k) = \hat{W}(\hat{\lambda}_l, \hat{\lambda}_m, \hat{\lambda}_n)$$
$$\text{for } i \neq j \neq k \neq i \quad \text{and} \quad l \neq m \neq n \neq l.$$

The determinant J and therefore the volumetric part fulfill this requirement automatically. For isotropic materials the derivatives must fulfill the following conditions:

$$\begin{aligned}
&\partial_{\hat{\lambda}_i}\hat{W}(\hat{\lambda}_1,\hat{\lambda}_2,\hat{\lambda}_3)|_{\hat{\lambda}_m=1}=\partial_{\hat{\lambda}_k}\hat{W}(\hat{\lambda}_1,\hat{\lambda}_2,\hat{\lambda}_3)|_{\hat{\lambda}_m=1},\\
&\partial^2_{\hat{\lambda}_i\hat{\lambda}_i}\hat{W}(\hat{\lambda}_1,\hat{\lambda}_2,\hat{\lambda}_3)|_{\hat{\lambda}_m=1}=\partial^2_{\hat{\lambda}_j\hat{\lambda}_j}\hat{W}(\hat{\lambda}_1,\hat{\lambda}_2,\hat{\lambda}_3)|_{\hat{\lambda}_m=1},\\
&\partial^2_{\hat{\lambda}_i\hat{\lambda}_j}\hat{W}(\hat{\lambda}_1,\hat{\lambda}_2,\hat{\lambda}_3)|_{\hat{\lambda}_m=1}=\partial^2_{\hat{\lambda}_k\hat{\lambda}_l}\hat{W}(\hat{\lambda}_1,\hat{\lambda}_2,\hat{\lambda}_3)|_{\hat{\lambda}_m=1}\\
&\qquad\qquad\text{for } i\neq j,\ k\neq l.
\end{aligned}\tag{4}$$

Herein ∂ denotes the first partial derivative with respect to the indicated variable and ∂^2 denotes the second partial derivative. These conditions hold only in the case of identical principal stretches. Because of definition (2), identical principal stretches always lead to $\hat{\lambda}_m=1$. The corresponding conditions on the derivatives of the volumetric part are then automatically fulfilled.

In the strainless initial state no strain energy

$$\hat{W}(\hat{\lambda}_1=1,\hat{\lambda}_2=1,\hat{\lambda}_3=1)=0 \quad\text{and}\quad U(J=1)=0 \tag{5}$$

is stored. If the strainless state is assumed to be stressfree the condition

$$\partial_J U|_{J=1}=0 \tag{6}$$

must hold, where $p(J)=\partial_J U$ represents the volumetric stress (=hydrostatic pressure). Due to $(4)_1$, no similar statement for $\partial_{\hat{\lambda}_i}\hat{W}$ can be obtained. If strains are present, i.e., $\hat{\lambda}_i\neq 1$, the stored energy

$$\hat{W}(\hat{\lambda}_1\neq 1,\hat{\lambda}_2\neq 1,\hat{\lambda}_3=\hat{\lambda}_1^{-1}\hat{\lambda}_2^{-1})>0,\quad U(J\neq 1)>0 \tag{7}$$

must be always positive.

In the case of infinitesimal strains the strain energy function leads in the limit to the classical Saint-Venant-Kirchhoff (SVK) material law

$$\hat{W}(\hat{\lambda}_1\to 1,\hat{\lambda}_2\to 1,\hat{\lambda}_3=\hat{\lambda}_1^{-1}\hat{\lambda}_2^{-1})+U(J\to 1)\to W_{\mathrm{SVK}}.$$

Considering the tangent of the stress-strain relation in the initial state the conditions

$$[\partial_{\hat{\lambda}_i}\hat{W}+\partial^2_{\hat{\lambda}_i\hat{\lambda}_i}\hat{W}-\partial^2_{\hat{\lambda}_i\hat{\lambda}_j}\hat{W}]_{\hat{\lambda}_1\to 1,\hat{\lambda}_2\to 1,\hat{\lambda}_3=\hat{\lambda}_1^{-1}\hat{\lambda}_2^{-1}}\to 2\mu \quad\text{for } i\neq j \tag{8}$$

and

$$\partial^2_{JJ}U|_{J\to 1}\to K$$

occur, where μ is the shear modulus and K is the bulk modulus of the infinitesimal theory.

In the limit case when the continuum degenerates to a single point, the strain energy tends to positive infinity and the volumetric stress to negative infinity:

$$U(J\to+0)\to+\infty \quad\text{and}\quad \partial_J U|_{J\to+0}\to-\infty. \tag{9}$$

Accordingly, a infinitely stretched continuum results in a positive infinite strain energy and a positive infinite volumetric stress

$$U(J\to+\infty)\to+\infty \quad\text{and}\quad \partial_J U|_{J\to+\infty}\to+\infty. \tag{10}$$

These two limit cases lead to undeterminable isochoric stretches (2) due to a product zero times infinity. Therefore no conditions for $\hat{W}$ and $\partial_{\hat{\lambda}_i}\hat{W}$ are available.

With respect to the requirement of polyconvexity of the strain energy function the volumetric part has to satisfy the convexity condition

$$\partial^2_{JJ}U\geqslant 0 \tag{11}$$

which appears in conjunction with the existence of solutions (see, e.g., [6]).

In the following the attention is focused on the volumetric strain energy function U exclusively.

4 Discussion of Volumetric Strain Energy Functions

The first part of this section extends the considerations of Liu and Mang [7] and sets the motivation for the second part which deals with the design of alternative volumetric strain energy functions.

4.1 Functions Suggested in the Literature. In Table 1 some volumetric strain energy functions suggested in the literature are summarized. Some characteristic references are: for U_1 Sussman and Bathe [8], Simo [9], van den Bogert and de Borst [10], Chang et al. [11], van den Bogert et al. [4]; for U_2 Hencky [12], Valanis and Landel [13], Simo et al. [14], Simo [15], Roehl and Ramm [16]; for U_3 Simo and Taylor [17], van den Bogert and de Borst [10], Liu and Mang [7]; for U_4 Ogden [18], Simo and Taylor [19], Miehe [20], Kaliske and Rothert [21] and for U_5 Liu et al. [22–23]. The cited references show that the isochoric-volumetric decoupling of the strain energy function is very common, especially in the treatment of nonlinear elasticity using the finite element method. In some references the extension of incompressible materials to nearly incompressible materials is dis-

Table 1 $U(J)$ suggested in the literature (see references)

$U_1(J)=K(J-1)^2/2$
$U_2(J)=K(\ln J)^2/2$
$U_3(J)=K[(J-1)^2+(\ln J)^2]/4$
$U_4(J)=K\theta^{-2}(\theta\ln J+J^{-\theta}-1)$ for $\theta<-1$
$U_5(J)=K(J\ln J-J+1)$

Table 2 Fulfillment of the volumetric conditions for the given and proposed $U(J)$

	Literature					Proposed		
Condition	U_1	U_2	U_3	U_4	U_5	U_6	U_7	U_8
$(5)_2$	√	√	√	√	√	√	√	√
(6)	√	√	√	√	√	√	√	√
$(7)_2$	√	√	√	√	√	√	√	√
$(8)_2$	√	√	√	√	√	√	√	√
$(9)_1$	$\to K/2$	√	√	√	$\to K$	√	√	√
$(9)_2$	$\to -K$	√	√	√	√	√	√	√
$(10)_1$	√	√	√	√	√	√	√	√
$(10)_2$	√	$\to 0$	√	√	√	√	√	√
(11)	√	$1\gtrsim \ln J$	√	√	√	√	√	√

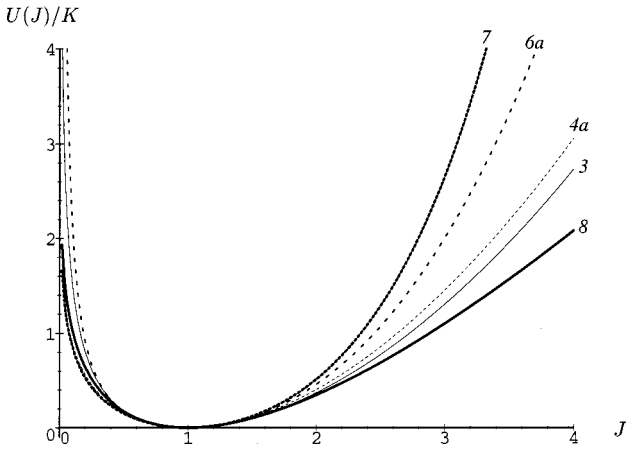

Fig. 1 Curves $U(J)/K$

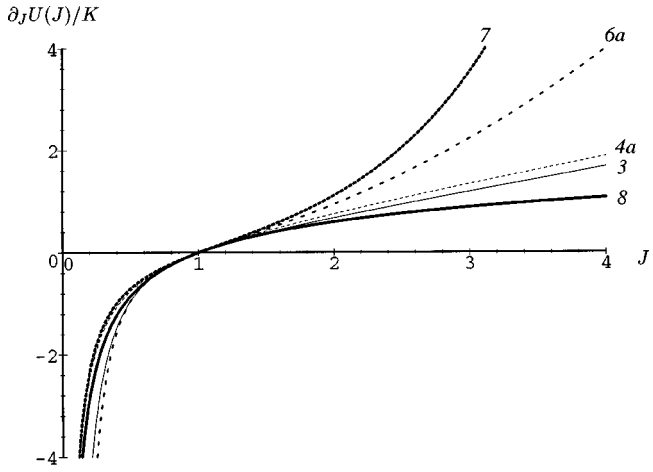

Fig. 2 Curves of the first derivative $\partial_J U(J)/K$

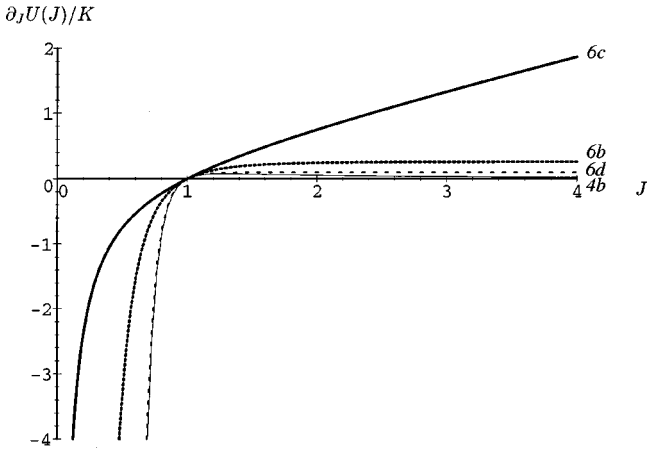

Fig. 4 Fitted curves of the first derivative $\partial_J U(J)/K$

cussed. These proposed extensions are closely related to the volumetric strain energy function and can be interpreted in a similar fashion.

For the given volumetric strain energy functions, the fulfillment of the conditions (5)–(11) in Section 3 is given in Table 2. A $\surd$ denotes the fulfillment of the corresponding condition. In the case of violation the limit value is listed instead. It is obvious that only the behavior of the functions U_3 and U_4 is correct. The functions U_1, U_2, and U_5 show some deficiencies. In particular, U_1 and U_5 should not be used in applications with large compression while U_2 does not make sense in cases where large volumetric expansions occur. In Figs. 1, 2, and 3 the functions U_3, U_{4a} (index a stands for $\theta=-2$) and their derivatives $\partial_J U$, $\partial^2_{JJ} U$ are given (the newly proposed functions U_{6-8} are discussed later). All curves are plotted using K to scale. The fulfillment of the conditions (5)–(11) can be checked now very easily. It appears also that the functions U_3 and U_{4a} lead to very similar shapes.

The compressibility parameter K only scales the functions but does not change their shapes. In this context K can be interpreted as a penalty parameter that enforces incompressibility if large values are chosen. The function U_4 seems to be superior compared to the other functions given in Table 1 because it contains one additional parameter θ which permits to fit the shape of the function to experimental data. However, only values of $\theta<-1$ guarantee the fulfillment of all conditions. In the literature the choice $\theta=-2$ is very popular. As found by Ogden [18] the value $\theta=9\lessgtr-1$ fits experimental data for nearly incompressible rubber rather well. In this respect the violation of the conditions $(10)_2$ and (11) seems to be acceptable because for nearly incompressible materials a large K has to be taken and J remains close to 1. Applications with $J>1$ should be handled with care due to the small volumetric stress obtained in this range (see also Fig. 4).

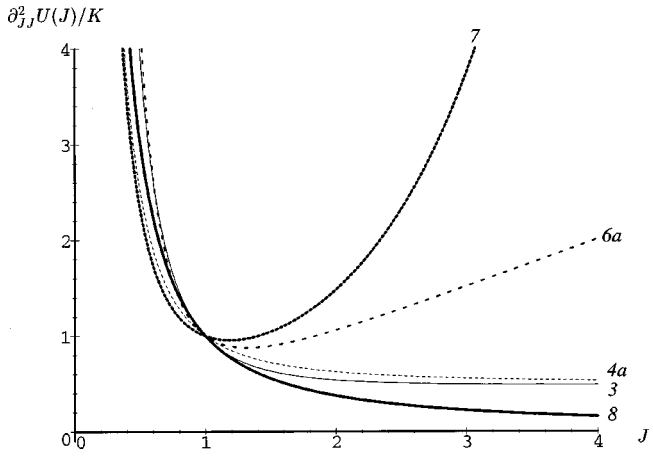

Fig. 3 Curves of the second derivative $\partial^2_{JJ} U(J)/K$

4.2 Alternatively Proposed Functions. Before developing alternative volumetric functions their desirable properties must be defined: First, the functions must be conform with the physical conditions (5)–(11) and, second, the functions should be as general as possible. The fulfillment of the second requirement has the advantage that a wide range of experimental data can be fitted with only one general function. Then a wide range of elastic volumetric material behavior can be described with little effort—which can be seen as an advantage in conjunction with finite element codes. This means not each special material should have its special volumetric function but its special parameters within a general function. Generality of a volumetric strain energy function is only achieved, if some additional material parameters are incorporated. In the following a class of volumetric functions with two additional parameters is proposed. The design process of such functions is described in detail with respect to the fulfillment of the physical conditions.

4.2.1 Function With Two Additional Parameters. The proposed starting point of the development is the following equation

$$p_6(J)=\partial_J U_6(J) = K(J^{\alpha}-J^{-\beta})(\alpha+\beta)^{-1} \quad \text{with} \quad \boxed{\alpha>0 \ \text{ and } \ \beta>1} \tag{12}$$

for the volumetric stress. The index 6 indicates a new volumetric strain energy function. Condition (6) is obviously fulfilled. The first term with the positive exponent ($\alpha>0$) vanishes as $J\rightarrow+0$. The second term with the negative exponent ($\beta>1$) vanishes as $J\rightarrow+\infty$. Consequently the conditions $(9)_2$ and $(10)_2$ hold. The differentiation of Eq. (12) with regard to J shows that conditions $(8)_2$ and (11) are fulfilled. It has to be noted, that starting with an undetermined constant in (12) the constant $K(\alpha+\beta)^{-1}$ follows directly from condition $(8)_2$. The integration of Eq. (12) with regard to J results in the following according volumetric strain energy function:

$$U_6(J)=K[(\alpha+1)^{-1}J^{\alpha+1}+(\beta-1)^{-1}J^{-(\beta-1)}](\alpha+\beta)^1-K(\alpha+1)^{-1}(\beta-1)^{-1} \tag{13}$$

The integration constant is chosen such that condition $(5)_2$ is satisfied. Conditions $(7)_2$, $(9)_1$, and $(10)_1$ are directly fulfilled. Differentiating or integrating (12) the negative exponent of the second term is preserved whereas the sign changes. This property holds as $\beta>1$ and ensures that the volumetric strain energy function as well as the second derivative remain always positive. Thus in the limit U_6 tends to infinity as $J\to+0$ or $J\to+\infty$, as it should.

In Eqs. (12) and (13) two special cases are contained. Setting $\beta=\alpha$ the relation $p_6(J)=-p_6(J^{-1})$ holds. That means in a homogeneously compressed brick with the stretch factor $\gamma^{-1}(\gamma>1)$ and in a homogeneously expanded brick with the stretch factor γ volumetric stresses act with identical absolute values but different signs—once as compressive and once as tensile stress. Using $\beta=\alpha+2$ the relation $U_6(J)=U_6(J^{-1})$ holds, i.e., two identical bricks, the first compressed homogeneously by γ^{-1} and the second expanded homogeneously by γ, store the same volumetric strain energy.

Figures 1, 2, and 3 contain the curves for function U_{6a} (index a means $\alpha=\beta=2$) and its derivatives. The identical constants refer to the first one of the special cases considered above. The fulfillment of the conditions (5)–(11) is obvious.

The major task now is to assess the new volumetric function U_6.

1 Assessment: The limit process $\alpha\to0$ in Eq. (12) leads directly to the pressure formula

$$p(J)=K(1-J^{-\beta})\beta^{-1} \tag{14}$$

given in Murnaghan ([24], pg. 73). Note, that in this contribution the compressive volumetric stress has a negative sign in contrast to the positive pressure in the cited papers. The advantage of the pressure formula (14) is its excellent adjustment to experimental data for sodium (see references in Murnaghan [24] for information concerning the experiments). Setting $\beta=3.79$ the experimental values $p(J)$ are approximated at pressures up to 10GPa within the accuracy of measurement (three percent). Therefore the practical applicability of U_6 is proofed. On the other hand the volumetric strain energy function based on Murnaghan's pressure formula (14) is a limit case ($\alpha\to0$) of the well-behaved more general function (13) which fulfills all conditions (5)–(11). In Fig. 4 the volumetric stress curve derived from U_{6b} (index b means $\alpha=0.001$, $\beta=3.79$) is given. The curve for $\alpha=0$ is omitted here, because no difference compared to $\partial_J U_{6b}$ is visible. Due to experimental considerations the fit of the volumetric stress (=pressure) seems to be superior over the fit of the energy function itself or the second derivative. Therefore the plots of the U-curves and $\partial^2_{JJ}U$-curves are omitted.

2 Assessment: The task now is to fit the constants α and β in U_6 to obtain similar curves as given by the two frequently used and well-behaved functions U_3 and U_{4a} (index a means $\theta=-2$). Because both functions are similar, the attention is restricted here to function U_{4a}. Looking at the first derivative of U_{4a} the comparison with Eq. (12) would lead directly to the constants $\alpha=\beta=1$, which in turn would violate the second restriction in relation (12). But the choice $\alpha=1$, $\beta\to1$ (especially $\beta=1.001$ referenced as U_{6c}) satisfies the second restriction and a perfect parameter fit with respect to U_{4a} can be observed. In Fig. 4 the volumetric stress curve $\partial_J U_{6c}$ is plotted. The curve for $\partial_J U_{4a}$ (see Fig. 2) is omitted here because it is indistinguishable from $\partial_J U_{6c}$. Because for $\alpha=1$, $\beta\to1$ the function U_6 becomes identical to the well-known function U_{4a}, the applicability of U_6 is confirmed once more.

3 Assessment: As mentioned previously, the volumetric function U_{4b} (index b means $\theta=9$) was found to fit experimental data rather well in the compression range for nearly incompressible rubber. But for this choice of θ, the violation of two physical conditions must be accepted. The first derivative of U_{4b} in comparison with Eq. (12) would suggest to use the values $\alpha=-1$ and $\beta=10$, which would violate the restriction for parameter α in (12). Choosing $\alpha=0.001$ and $\beta=10$ (referenced as U_{6d}) the restrictions for α, β and all physical conditions (5)–(11) are fulfilled. The two volumetric stress graphs derived from U_{4b}, U_{6d} are given in Fig. 4. In the compression range ($J<1$) both graphs are nearly indistinguishable. Thus once more a good parameter fit to experimental data (see Ogden [18] and references) is obtained, and the general stability and versatility of U_6 is confirmed. As a drawback the physically nonreasonable small stresses for $J>1$ should be mentioned. Due to the fulfillment of all conditions the performance of U_{6d} appears to be somewhat more reasonable in this range.

4.2.2 Generalization of the Two-Parameter Function. A further generalization of the volumetric strain energy function U_6 is possible by the additive composition of single functions of the proposed type (12). The volumetric stress of the generalized function is then given by

$$p_{6\mathrm{gen}}(J)=\partial_J U_{6\mathrm{gen}}(J)=K\left[\sum_{i=1}^{n}(J^{\alpha_i}-J^{-\beta_i})\right]\left[\sum_{i=1}^{n}(\alpha_i+\beta_i)\right]^{-1}$$
$$\text{with}\quad \alpha_i>0\quad\text{and}\quad \beta_i>1. \tag{15}$$

Integration of Eq. (15) results in the generalized function $U_{6\mathrm{gen}}(J)$. The integration constant has to be determined from $(5)_2$. It is straightforward to verify that $U_{6\mathrm{gen}}(J)$ fulfills all conditions (5)–(11). Now more general strain energy functions with an unlimited number of additional material parameters α_i, β_i can be derived.

It should be mentioned that every additive composition of the single volumetric strain functions U_{1-6} which fulfills the physical conditions is an admissible ''generalization'' of the single functions; e.g., the function $(U_1+U_4)/2$ leads to an admissible new function which overcomes the deficiencies of the single function U_1.

4.2.3 Further Functions. In addition to function U_6, two further functions

$$U_7(J)=K(\exp(J-1)-\ln J-1)/2$$
$$U_8(J)=K(J-1)\ln J/2 \tag{16}$$

are newly proposed here in the context of volumetric strain energy functions. As reported in Table 2 these two functions fulfill all conditions (5)–(11) as well. However, they do not contain some constants to influence their shapes, which reduces the possibilities to fit experimental data in general. But both functions (16) seem to be superior over U_1, U_2, and U_5 because they do not violate any condition. For further comparison the functions U_7 and U_8, respectively, their derivatives are also plotted in Figs. 1, 2, and 3.

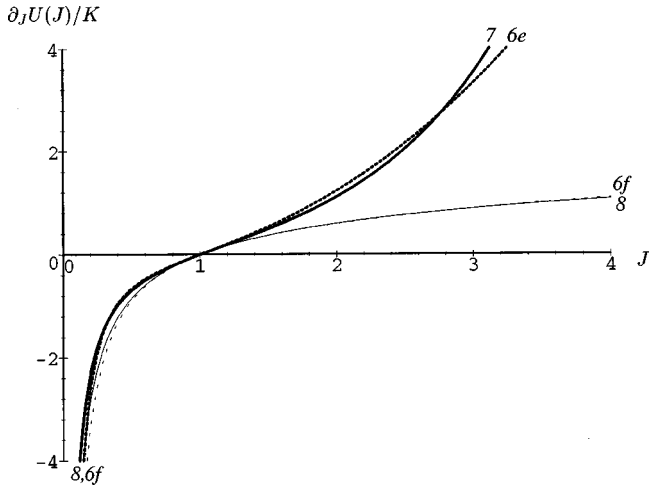

Fig. 5 Fitted curves of the first derivative $\partial_J U(J)/K$

Two additional parameter fits of the single function U_6 are performed now with respect to the functions U_7 and U_8. This should give an idea of the possibilities and limits in the approximation of volumetric stress data using U_6. With $\alpha=2.3$, $\beta=1.4$ referenced as U_{6e} the function U_7 is fitted and with $\alpha=0.45$, $\beta=1.05$ referenced as U_{6f} the function U_8 is approximated. The derived volumetric stress curves are plotted in Fig. 5. The comparison shows that both U_7 and U_8 can be nearly approximated by U_6. To expect a perfect approximation in the whole range of J would require more parameters, e.g., using the generalized function $U_{6\text{gen}}$. But the really good parameter fit over most important ranges has to be noted.

5 Concluding Remarks

Well-known and newly proposed volumetric strain energy functions have been discussed. The newly proposed functions are closely related to frequently used functions. The advantage of these new functions is the fulfillment of all known physical conditions. The more general function U_6 contains two material constants in addition to the compressibility parameter. Therefore a good fit to given data is possible. The good adaptability of the proposed volumetric strain energy function U_6 to well-known functions and experimental data is proofed.

It must be noted that applications with small volumetric deformations do not require general volumetric strain energy functions. Because of the physical conditions all admissible functions are close together in this range of deformation. The proposed function U_6 with two additional constants and its generalization $U_{6\text{gen}}$ with an arbitrary number of additional constants must be seen in the context of large volumetric deformations. A good adjustment of the volumetric function to given data in a wide range of volumetric deformation can only be expected if sufficient material parameters are available, as in U_6, $U_{6\text{gen}}$. However, it has to be noted that the determination of the constants is difficult, because in the volumetric stress formula the constants appear simultaneously in the exponent and in the denominator. Furthermore, considering real materials, the modeling failure due to the assumed isochoric-volumetric split of the strain energy function should be taken into account to prevent an overprecise volumetric part.

References

[1] Ogden, R. W., 1984, *Non-Linear Elastic Deformations*, Ellis Horwood, Chichester, UK.

[2] Flory, P. J., 1961, ''Thermodynamic Relations for High Elastic Materials,'' Trans. Faraday Soc., **57**, pp. 829–838.

[3] Penn, R. W., 1970, ''Volume Changes Accompanying the Extension of Rubber,'' Trans. Soc. Rheol., **14**, No. 4, pp. 509–517.

[4] van den Bogert, P. A. J., de Borst, R., Luiten, G. T., and Zeilmaker, J., 1991, ''Robust Finite Elements for 3D—Analysis of Rubber-Like Materials,'' Eng. Comput., **8**, pp. 3–17.

[5] Ogden, R. W., 1982, ''Elastic Deformations of Rubberlike Solids,'' *Mechanics of Solids, The Rodney Hill 60th Anniversary Volume* H. G. Hopkins and M. J. Sewell eds., Pergamon Press, Tarrytown, NY, pp. 499–537.

[6] Ciarlet, P. G., 1988, *Mathematical Elasticity. Volume 1: Three Dimensional Elasticity*, Elsevier, Amsterdam.

[7] Liu, C. H., and Mang, H. A., 1996, ''A Critical Assessment of Volumetric Strain Energy Functions for Hyperelasticity at Large Strains,'' Z. Angew. Math. Mech., **76**, No. S5, pp. 305–306.

[8] Sussman, T., and Bathe, K. J., 1987, ''A Finite Element Formulation for Nonlinear Incompressible Elastic and Inelastic Analysis,'' Comput. Struct., **26**, No. 1–2, pp. 357–409.

[9] Simo, J. C., 1988, ''A Framework for Finite Strain Elastoplasticity Based on Maximum Plastic Dissipation and the Multiplicative Decomposition: Part I. Continuum Formulation,'' Comput. Methods Appl. Mech. Eng., **66**, pp. 199–219.

[10] van den Bogert, P. A. J., and de Borst, R., 1990, ''Constitutive Aspects and Finite Element Analysis of 3D Rubber Specimens in Compression and Shear,'' *NUMETA 90: Numerical Methods in Engineering: Theory and Applications*, G. N. Pande and J. Middleton, eds., Elsevier Applied Science, Swansea, pp. 870–877.

[11] Chang, T. Y., Saleeb, A. F., and Li, G., 1991, ''Large Strain Analysis of Rubber-Like Materials Based on a Perturbed Lagrangian Variational Principle,'' Comput. Mech., **8**, pp. 221–233.

[12] Hencky, H., 1933, ''The Elastic Behavior of Vulcanized Rubber,'' ASME J. Appl. Mech., **1**, pp. 45–53.

[13] Valanis, K. C., and Landel, R. F., 1967, ''The Strain-Energy Function of a Hyperplastic Material in Terms of the Extension Ratios,'' J. Appl. Phys., **38**, No. 7, pp. 2997–3002.

[14] Simo, J. C., Taylor, R. L., and Pfister, K. S., 1985, ''Variational and Projection Methods for Volume Constraint in Finite Deformation Elasto-Plasticity,'' Comput. Methods Appl. Mech. Eng., **51**, pp. 177–208.

[15] Simo, J. C., 1992, ''Algorithms for Static and Dynamic Multiplicative Plasticity That Preserve the Classical Return Mapping Schemes of the Infinitesimal Theory,'' Comput. Methods Appl. Mech. Eng., **99**, pp. 61–112.

[16] Roehl, D., and Ramm, E., 1996, ''Large Elasto-Plastic Finite Element Analysis of Solids and Shells With the Enhanced Assumed Strain Concept,'' Int. J. Solids Struct., **33**, No. 20–22, pp. 3215–3237.

[17] Simo, J. C., and Taylor, R. L., 1982, ''Penalty Function Formulations for Incompressible Nonlinear Elastostatics,'' Comput. Methods Appl. Mech. Eng., **35**, pp. 107–118.

[18] Ogden, R. W., 1972, ''Large Deformation Isotropic Elasticity: on the Correlation of Theory and Experiment for Compressible Rubberlike Solids,'' Proc. R. Soc. London, Ser. A, **328**, pp. 567–583.

[19] Simo, J. C., and Taylor, R. L., 1991, ''Quasi-Incompressible Finite Elasticity in Principal Stretches. Continuum Basis and Numerical Algorithms,'' Comput. Methods Appl. Mech. Eng., **85**, pp. 273–310.

[20] Miehe, C., 1994, ''Aspects of the Formulation and Finite Element Implementation of Large Strain Isotropic Elasticity,'' Int. J. Numer. Methods Eng., **37**, pp. 1981–2004.

[21] Kaliske, M., and Rothert, H., 1997, ''On the Finite Element Implementation of Rubber-Like Materials at Finite Strains,'' Eng. Comput., **14**, pp. 216–232.

[22] Liu, C. H., Hofstetter, G., Mang, H. A., 1992, ''Evaluation of 3D FE-Formulations for Incompressible Hyperplastic Materials at Finite Strains,'' *Proceedings of the First European Conference on Numerical Methods in Engineering* C. Hirsch, O. C. Zienkiewicz, and E. Oñate, eds., Sept. 7–11, Brussels, Belgium, Elsevier Science, Ltd., pp. 757–764.

[23] Liu, C. H., Hofstetter, G., and Mang, H. A., 1994, ''3D Finite Element Analysis of Rubber-Like Materials at Finite Strains,'' Eng. Comput., **11**, pp. 111–128.

[24] Murnaghan, F. D., 1951, *Finite Deformation of an Elastic Solid*, John Wiley and Sons, New York.

Melan's Problems With Weak Interface

S. Lenci
Instituto di Scienza e Tecnica delle Costruzioni,
Universita di Ancona via Brecce Bianche,
Monte d'Ago,
60100 Ancona, Italy

The problem of a fiber attached to an infinite sheet (Melan's problem) has been reconsidered under the hypothesis that the adherence between the two bodies is not perfect. We have assumed that the link is guaranteed by the so-called ''weak interface,'' i.e., we have supposed that the jump of the displacement is linearly proportional to the interface stress. The solutions of (i) the case with a concentrated force acting on the fiber and (ii) the case of the redistribution of stresses as a consequence of the rupture of the fiber have been obtained in closed form. We have discussed how the interface stiffness k influences the solutions and, in particular, the interfacial stress. Emphasis is placed on determining how the zone of influence of the applied load is modified by k. Approximate (though accurate) simple expressions for the length of the zone of influence are given and discussed. [S0021-8936(00)01001-1]

1 Introduction

In 1932, Melan [1] studied the problem of transmission of stress between an infinite stiffener and an infinite, linear elastic, sheet. By supposing perfect adherence between the bodies and by treating the fiber as a uniaxial bar, he was able to obtain the closed-form solution of the problem when the exterior load consists of a single force directly applied to the fiber (Fig. 1). He determined the interface tangential stress and he found that it becomes unbounded in the neighborhood of the force application point. The singularity is of the logarithmic type, contrary to that of power type observed in the case of force directly applied to the plate ([2]) (Article 148). This fact emphasizes one of the practical advantages obtained by introducing a stiffener to transmit a concentrate force to a plate. Melan further considers the case of an infinite edge-stiffener glued to the boundary of a semi-infinite sheet, but this problem gives rise to the same mathematical formulation as the former.

The pioneering work of Melan was successively reconsidered and extended by different authors, especially as a consequence of its importance in the field of reinforcing aircraft structures and, later, in the field of fibro-reinforced composites. Koiter [3] obtained a very involved solution for the case of a semi-infinite fiber attached to an infinite and to a semi-infinite sheet, a problem previously treated by Buell [4]. Benscoter [5] and Erdogan and Gupta [6] studied the case of finite-length fiber, the first when it is glued to an infinite shell and the second when it adheres to the boundary of a semi-infinite sheet. Lee and Klang [7] extend the work of Erdogan and Gupta, considering the presence of a circular hole within the plate.

The hypothesis of one-dimensional behavior for the string was removed by Muki and Sternberg [8] (infinite stiffener) and by Shield and Kim [9] (finite-length fiber), who consider the flexural stiffness of the fiber, and by Bufler [10] and by Muki and Sternberg [8], who, in the framework of two-dimensional elasticity, model the stiffener as an infinite strip attached to the boundary of a semi-infinite plate.

A geometrically different problem was analyzed by Reissner [11] and by Goodier and Hsu [12], who consider the case of the stiffener perpendicular, rather than parallel, to the boundary of the semi-infinite plate. Their works are based on the hypothesis of line contact between the bodies, a hypothesis removed initially by LeFevre et al. [13] and successively by Muki and Sternberg [14] by considering an area contact model.

The numerous contributions of the Russian school, sometimes overlapping with the previously cited works, are summarized in Grigolyuk and Tolkachev [15] (Section 3.2).

So far, all the authors have considered perfect adherence between the plate and the string. Budiansky and Wu [16] and Rybakov and Cherepanov [17] remove this hypothesis by considering the case where the stiffener is riveted to the plate at discrete points with a constant spacing, while Rybakov [18] studied the same case but with a broken stringer.

Another different interface is that with friction. This case has been analyzed, for example, by Antipov and Arutyunyan [19], who consider the simultaneous presence of Coulomb friction and perfect adherence.

By experience, apart from perfect bonding, riveted contact, and friction, another transmission condition is suggested. In fact, when the stiffener is glued to the sheet by an adhesive (a third material), a jump in displacement proportional to the transmission stress is observed, although the continuity of the tensions is maintained for equilibrium. In the framework of linearized elasticity, a natural way to model such a situation consists by assuming that the transmission stress linearly depends on the jump of displacement

$$\tau = k(u_{\text{fiber}} - u_{\text{sheet}}). \tag{1}$$

Equation (1) is a particular case of a more general theory aimed at describing the mechanical properties of interphases, which was initially developed by Goland and Reissner [20] and by Gilibert and Rigolot [21] and which was successively studied by Klarbring [22] and by Geymonat et al. [23]. In (1), the parameter k summarizes the mechanical characteristics of the interface, and it can be computed from the elastic moduli of the interphase on the basis of the formulas reported in [23]. Equation (1) is called a *weak interface* transmission condition, and it describes also the behavior of adhesives and of many kinds of nonperfect bonding (fractured, damaged etc.).

The interface which allows jump in the displacement is sometimes appositely designed. In fact, it has at least two advantages, which may be very useful in applications. The first is that it avoids the singularity of the stresses in the presence of a concentrate force. Secondly, it relaxes the peaks of the interface stress, giving a better redistribution of the applied load. These facts, in general, considerably reduce the probability of failure of the assemblage and increase its ductility.

Contributed by the Applied Mechanics Division of THE AMERICAN SOCIETY OF MECHANICAL ENGINEERS for publication in the ASME JOURNAL OF APPLIED MECHANICS. Manuscript received by the ASME Applied Mechanics Division, Nov. 18, 1997; final revision, Oct. 12, 1999. Associate Technical Editor: M. M. Carroll. Discussion on the paper should be addressed to the Technical Editor, Professor Lewis T. Wheeler, Department of Mechanical Engineering, University of Houston, Houston, TX 77204-4792, and will be accepted until four months after final publication of the paper itself in the ASME JOURNAL OF APPLIED MECHANICS.

In this paper Melan's problem is reconsidered (Section 3) by supposing that the interaction between the fiber and the sheet is governed by Eq. (1) and by the continuity of stresses. The plate is supposed to be in a generalized plane-stress state and the fiber is a uniform uniaxial bar. We further assume that the fiber is so narrow the hypothesis of line contact holds.

In the second part (Section 4), we study the case of a broken fiber embedded in the matrix, a problem which is common in fibro-reinforced materials and which is a nonclassical Melan's problem. First we study the case of a single broken fiber, and then we analyze the reinforcing effects of the nearby fibers. We show how the interface stiffness can be used as a design parameter to optimize the response of the composite with respect to the damage due to the rupture of a fiber.

The previous solutions are particular cases of a more general elastic solution, admitting force as well as distortion loads on the fiber, which has been obtained in Section 2 and which can also be used to solve other situations.

2 The General Solution

Let us consider an infinite sheet of a constant width $h=1$, supposing that it is homogeneous, isotropic linearly elastic with Lamé constants λ and μ, and that it is subject to a state of generalized plane stress (Fig. 1). If a (averaged) distribution of tangential stresses $\tau_x(x)=\tau(x)$ is applied to the matrix on the x-axis, then the (averaged) displacement on the same axis is given by [2] (Article 148),

$$u(x)=-\frac{1}{16\pi\mu}\frac{5\lambda+6\mu}{\lambda+\mu}\int_{-\infty}^{\infty}\tau(t)\ln|t-x|dt. \tag{2}$$

In (2) $\tau(x)$ is positive if directed as the x axis. Considering the Fourier transforms $\hat{f}(s)=\int_{-\infty}^{\infty}f(x)e^{isx}dx$ of the displacement and of the $\tau(x)$, Eq. (2) can be rewritten as [15] (Section 3.4)

$$\hat{u}(s)=\frac{1}{16\mu}\frac{5\lambda+6\mu}{\lambda+\mu}\frac{\hat{\tau}(s)}{|s|}. \tag{3}$$

We suppose that, along the x-axis, a uniform string is attached to the sheet and we suppose that the interface is governed by (1). Denoting by $U(x)$ the axial displacement of the fiber, and assuming that the interface stiffness k is constant, Eq. (1) can be expressed in terms of Fourier transforms as

$$\hat{\tau}(s)=k[\hat{U}(s)-\hat{u}(s)]. \tag{4}$$

Apart from the reaction $\tau(x)$ of the sheet, the string is subjected to an external normal force per unit length $p(x)$ (positive if directed as the x-axis) and to an axial distortion per unit length $\varepsilon^*(x)$ (positive if it produces compression on the fiber). Assuming its axial stiffness is EA, the equilibrium equation is

$$\frac{d^2U(x)}{dx^2}-\frac{d\varepsilon^*(x)}{dx}+\frac{p(x)}{EA}-\frac{\tau(x)}{EA}=0, \tag{5}$$

namely,

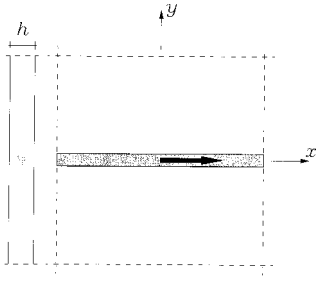

Fig. 1 The infinite sheet with a stiffener loaded by a single force

$$-s^2\hat{U}(s)+is\hat{\varepsilon}^*(s)+\frac{\hat{p}(s)}{EA}-\frac{\hat{\tau}(s)}{EA}=0. \tag{6}$$

Equations (3), (4), and (6) constitute an algebraic system of three equations in the three unknowns $\hat{\tau}(s)$, $\hat{u}(s)$, and $\hat{U}(s)$. We therefore obtain

$$\hat{\tau}(s)=\frac{is\hat{\varepsilon}^*(s)+\dfrac{\hat{p}(s)}{EA}}{\dfrac{1}{k}s^2+\dfrac{1}{16\mu}\dfrac{5\lambda+6\mu}{\lambda+\mu}|s|+\dfrac{1}{EA}},$$

$$\hat{u}(s)=\frac{1}{16\mu}\frac{5\lambda+6\mu}{\lambda+\mu}\frac{1}{|s|}\frac{is\hat{\varepsilon}^*(s)+\dfrac{\hat{p}(s)}{EA}}{\dfrac{1}{k}s^2+\dfrac{1}{16\mu}\dfrac{5\lambda+6\mu}{\lambda+\mu}|s|+\dfrac{1}{EA}}, \tag{7}$$

$$\hat{U}(s)=\left(\frac{1}{k}+\frac{1}{16\mu}\frac{5\lambda+6\mu}{\lambda+\mu}\frac{1}{|s|}\right)\frac{is\hat{\varepsilon}^*(s)+\dfrac{\hat{p}(s)}{EA}}{\dfrac{1}{k}s^2+\dfrac{1}{16\mu}\dfrac{5\lambda+6\mu}{\lambda+\mu}|s|+\dfrac{1}{EA}}.$$

Given the external ''loads'' $p(x)$ and $\varepsilon^*(x)$, the general solution of Melan's problem with weak interface can be obtained from (7) by using the inverse Fourier transform $f(x)=(1/2\pi)\int_{-\infty}^{\infty}\hat{f}(s)e^{-isx}ds$.

Remark 1. The case of a stiffener glued to the boundary of a semi-infinite sheet can be solved in the same manner. In fact, (4) and (6) are still valid, while (3) is replaced by [15] (Section 3.4)

$$\hat{u}(s)=\frac{1}{\mu_1}\frac{2\lambda_1+2\mu_1}{3\lambda_1+2\mu_1}\frac{\hat{\tau}(s)}{|s|}, \tag{8}$$

which is equal to (3), assuming

$$\mu=\mu_1,\quad \lambda=-\mu_1\frac{14\lambda_1+20\mu_1}{17\lambda_1+22\mu_1} \tag{9}$$

in (3). Therefore, the solution of this problem is (7) with μ and λ given by (9).

Remark 2. We consider only problems symmetric with respect to the x-axis and with in-plane loads. Thus, the bending stiffness of the fiber and of the sheet are not involved in the analysis. This does not mean that we disregard them. We suppose that they are as large as required to avoid instability phenomena in the compressed zones.

Remark 3. All solutions obtained in the following sections are odd or even functions of x. Therefore, in order to simplify the exposition, we will report only the formulas valid for $x>0$. The extension to the negative part of the x-axis can be easily obtained by symmetry.

3 The Single Force on the Fiber

When a concentrated force acts on the fiber at, say, $x=0$, we have $p(x)=P\,\delta(x)$ ($\delta(x)$ is the Dirac delta) and $\varepsilon^*(x)=0$. In this case $\hat{p}(s)=P$, $\hat{\varepsilon}^*(s)=0$, and the solution can be expressed in terms of known functions. In fact, (7) furnishes

$$\hat{\tau}(s)=\frac{P}{EA}\frac{1}{\dfrac{1}{k}s^2+\dfrac{1}{16\mu}\dfrac{5\lambda+6\mu}{\lambda+\mu}|s|+\dfrac{1}{EA}} \tag{10}$$

and therefore

$$\tau(x)=\frac{1}{\pi}\frac{Pk}{EA}\int_0^\infty \frac{\cos(sx)}{s^2+2as+b}\,ds, \tag{11}$$

where we have assumed $a=(k/32\mu)\ (5\lambda+6\mu)/(\lambda+\mu)$, $b=k/EA$. Let us further define $\alpha_1=a-\sqrt{a^2-b}$ and $\alpha_2=a+\sqrt{a^2-b}$. These relations assure that

$$\tau(x)=\frac{1}{\pi}\frac{Pk}{EA}\frac{1}{2\sqrt{a^2-b}}\left(\int_0^\infty \frac{\cos(sx)}{s+\alpha_1}\,ds-\int_0^\infty \frac{\cos(sx)}{s+\alpha_2}\,ds\right). \tag{12}$$

The integrals which appear in (12) can be computed explicitly [24] (formula 3.722.3):

$$\int_0^\infty \frac{\cos(sx)}{s+\alpha}\,ds=g(x\alpha),\quad \alpha>0, \tag{13}$$

where [25] (Section 5.2)

$$\begin{gathered} g(z)=-\sin(z)si(z)-\cos(z)ci(z),\\ si(z)=-\int_z^\infty \frac{\sin(t)}{t}\,dt,\quad ci(z)=-\int_z^\infty \frac{\cos(t)}{t}\,dt. \end{gathered} \tag{14}$$

Therefore,

$$\tau(x)=\frac{P}{\pi}\frac{b}{2\sqrt{a^2-b}}[g(x\alpha_1)-g(x\alpha_2)]. \tag{15}$$

Before discussing Eq. (15), we wish to show the behavior of the previous solution when the interface becomes rigid. From

$$\begin{gathered} \lim_{k\to\infty}\alpha_1=16\mu\frac{\lambda+\mu}{5\lambda+6\mu}\frac{1}{EA}=\overline{\alpha}_1,\\ \lim_{k\to\infty}\alpha_2=\infty,\quad \lim_{k\to\infty}\frac{b}{2\sqrt{a^2-b}}=\overline{\alpha}_1,\quad \lim_{z\to\infty}g(z)=0, \end{gathered} \tag{16}$$

we obtain

$$\lim_{k\to\infty}\tau(x)=\frac{P\overline{\alpha}_1}{\pi}g(x\overline{\alpha}_1), \tag{17}$$

which, in different notation, is Melan's solution, valid in the case of perfect bonding.

In the positive part of the x-axis, the transmission stress $\tau(x)$ is a decreasing function vanishing for $x\to\infty$. Its maximum value is therefore $\tau_{\max}=\tau(0)$. To calculate this stress, let us observe that, for $x\to 0$, $ci(x)\cong\gamma+\ln(x)+\ldots$, where $\gamma=0.577\ldots$ is the Euler constant. Using this relation, we obtain

$$\tau_{\max}=\frac{P}{\pi}\frac{b}{\sqrt{a^2-b}}\operatorname{arccosh}\left(\frac{a}{\sqrt{b}}\right), \tag{18}$$

where we have used the identity $\ln[(a+\sqrt{a^2-b})/(a-\sqrt{a^2-b})]=2\ \operatorname{arccosh}(a/\sqrt{b})$, $a,b>0$. Equation (18) shows that, contrary to the case of perfect bonding, the maximum interface shear is bounded everywhere. This is one of the practical advantages of having weak bonding between the fiber and the sheet.

The axial force in the stiffener can be computed integrating the $\tau(x)$. To compute this integral, we observe that

$$g(z)=-\frac{df(z)}{dz},\quad f(z)=\sin(z)ci(z)-\cos(z)si(z). \tag{19}$$

Equation (19) permits us to conclude

$$N(x)=\frac{Pb}{2\sqrt{a^2-b}}\left[-\frac{f(x\alpha_1)}{\alpha_1}+\frac{f(x\alpha_2)}{\alpha_2}\right]. \tag{20}$$

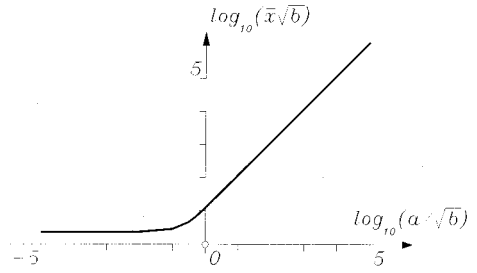

Fig. 2 The semi-length of the zone of influence

To measure the region where the effects of the applied load vanish, we define the ''zone of influence'' as the part of the fiber which satisfies

$$\frac{N(x)}{N(0^+)}\geqslant 0.10. \tag{21}$$

Thus, because in this case $N(0^+)=P/2$, we assume that the effect of the concentrated force can be neglected when the axial force in the fiber is less than five percent of P. Considering the equality in (21), we obtain an equation in the semi-length $\overline{x}$ of the zone of influence, and the results of the numerical solution are depicted in Fig. 2.

Figure 2 shows that a fairly good approximation of the true curve is the bilinear function.

$$\begin{gathered} \log_{10}(\overline{x}\sqrt{b})\cong 0.362,\quad \text{if } \log_{10}(a/\sqrt{b})<-0.724,\\ \log_{10}(\overline{x}\sqrt{b})\cong 1.086+\log_{10}(a/\sqrt{b}),\\ \text{if } \log_{10}(a/\sqrt{b})>-0.724. \end{gathered} \tag{22}$$

In terms of the original variables, (22) can be expressed in the form

$$\begin{gathered} \overline{x}\cong 2.301\sqrt{\frac{EA}{k}},\quad \text{if } k<k_{cr},\\ \overline{x}\cong 0.381\frac{5\lambda+6\mu}{\lambda+\mu}\frac{EA}{\mu},\quad \text{if } k>k_{cr}, \end{gathered} \tag{23}$$

where $k_{cr}=36.5(\mu^2/EA)((\lambda+\mu)/(5\lambda+6\mu))^2$. If k is greater than k_{cr}, the zone of influence no longer depends on the stiffness of the interface and it is the same as in the perfect bonding case. Thus, from a practical point of view and in the case of a single force applied to the fiber, we may consider condition $k>k_{cr}$ as the definition of rigid interfaces.

The Fourier transform of the displacement $u(x)$ is

$$\hat{u}(s)=P\frac{2a}{EA}\frac{1}{|s|^3+2as^2+b|s|}, \tag{24}$$

which gives

$$u(x)-u(0)=\frac{P}{\pi}\frac{2a}{EA}\int_0^\infty \frac{\cos(sx)-1}{s^3+2as^2+bs}\,ds. \tag{25}$$

Using the relations

$$\begin{gathered} \frac{1}{s^3+2as^2+bs}=\frac{1}{2b\sqrt{a^2-b}}\left(\frac{\alpha_2}{s}-\frac{\alpha_1}{s}-\frac{\alpha_2}{s+\alpha_1}+\frac{\alpha_1}{s+\alpha_2}\right),\\ \int_0^\infty \frac{\cos(sx)-1}{s}\,ds-\int_0^\infty \frac{\cos(sx)-1}{s+\alpha}\,ds\\ =-\gamma-\ln(x\alpha)-g(x\alpha),\quad \alpha>0, \end{gathered} \tag{26}$$

permits us to obtain

$$u(x)-u(0)=\frac{P}{\pi EA}\frac{a}{b\sqrt{a^2-b}}\{\alpha_1[\gamma+\ln(x\alpha_2)+g(x\alpha_2)]$$
$$-\alpha_2[\gamma+\ln(x\alpha_1)+g(x\alpha_1)]\}. \quad (27)$$

The displacement is unbounded for $x\to\infty$. In particular, it assumes the form

$$u(x)-u(0)\cong P\ \text{const.}\ln(x)+\cdots. \quad (28)$$

This is due to the fact that the sum of the forces applied to the sheet is not zero. Equation (28) agrees with the general prediction of Muskhelishvili [26] (Section 36).

3.1 A String Loaded by Two Forces. The property expressed by (28) is unsatisfactory from a practical point of view, though it is exact within the framework of two-dimensional elasticity. To overcome this difficulty, we consider the case of a fiber loaded by two aligned, equal, and opposite concentrate forces. In fact, in a neighborhood of the force application point, the following solution has all the features of the one in Section 3, but it has a more suitable—and realistic—behavior at infinity.

The problem analyzed in this section may also deserve an independent interest. In fact, when a load must be transferred from a point A to a point B on a sheet, it is convenient to reinforce the plate by inserting a string along the line AB. The solution of this problem is required to design the strengthening, because it is necessary to know the part of the load carried by the string and the part of the load carried by the sheet. We will show that this interaction strongly depends on the properties of the interface, and on the distance between the forces as well.

The Fourier transform of two equal and opposite forces P acting on the x-axis at the points $x=-d$ and $x=+d$ is $\hat{p}(s)=2iP\sin(sd)$. Inserting this expression and $\hat{\varepsilon}^*(s)=0$ in (7) yields

$$\hat{\tau}(s)=\frac{2iPk}{EA}\frac{\sin(sd)}{s^2+2a|s|+b}. \quad (29)$$

Inverting (29) with the same procedure used in the previous sections, we obtain

$$\tau(x)=\frac{P}{\pi}\frac{b}{2\sqrt{a^2-b}}\{g(|x-d|\alpha_1)-g(|x-d|\alpha_2)-g[(x+d)\alpha_1]$$
$$+g[(x+d)\alpha_2]\}, \quad (30)$$

which is an odd function, vanishing for $x\to\infty$ and with (absolute) maximum value

$$\tau_{\max}=\frac{P}{\pi}\frac{b}{\sqrt{a^2-b}}\left[\operatorname{arccosh}\left(\frac{a}{\sqrt{b}}\right)+\frac{g(2d\alpha_2)-g(2d\alpha_1)}{2}\right]. \quad (31)$$

Comparing (31) with (18) it is possible to see how the presence of the second force reduces $\tau_{\max}$. In fact, the difference is given by the second term in the square brackets of (31). However, when d is sufficiently large, this term is negligible and we have the same maximum interface shear.

To obtain the expression of the axial load $N(x)$, we integrate (30) obtaining

$$N(x)=\frac{-bP}{2\pi\sqrt{a^2-b}}\left\{\frac{f[(x-d)\alpha_2]}{\alpha_2}-\frac{f[(x-d)\alpha_1]}{\alpha_1}-\frac{f[(x+d)\alpha_2]}{\alpha_2}\right.$$
$$\left.+\frac{f[(x+d)\alpha_1]}{\alpha_1}\right\},\quad x>d,$$

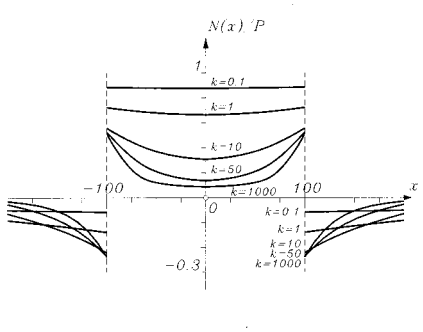

Fig. 3 The axial load in the fiber

$$N(x)=\frac{-bP}{2\pi\sqrt{a^2-b}}\left\{\frac{f[(d-x)\alpha_2]}{\alpha_2}-\frac{f[(d-x)\alpha_1]}{\alpha_1}+\frac{f[(x+d)\alpha_2]}{\alpha_2}\right.$$
$$\left.-\frac{f[(x+d)\alpha_1]}{\alpha_1}\right\},\quad x<d, \quad (32)$$

For $a=1.25k\times10^{-4}$, $b=1.76k\times10^{-5}$, and $d=100$, we have the curves depicted in Fig. 3. When the interface is ''soft'' ($k=0.1$) the load is carried almost entirely by the fiber, while, on the contrary, for ''strong'' interface ($k=1000$) is the sheet that assures the transmission of force between the two points. A quantitative measure of the reciprocal participation in carrying P can be obtained by considering the axial load in the fiber in the point of symmetry $x=0$, given by

$$N(0)=\frac{bP}{\pi\sqrt{a^2-b}}\left\{\frac{f(d\alpha_1)}{\alpha_1}-\frac{f(d\alpha_2)}{\alpha_2}\right\}. \quad (33)$$

$N(0)$ varies from P, when $d=0$, to 0, when $d\to\infty$. On the other hand, $\lim_{k\to0}N(0)=P$ while $\lim_{k\to\infty}N(0)=(2P/\pi)f(d\overline{\alpha_1})$.

Finally, the expression of the displacement of the sheet is obtained by inverting

$$\hat{u}(s)=P\frac{4ia}{EA}\frac{\sin(sd)}{|s|^3+2as^2+b|s|}, \quad (34)$$

and it is

$$u(x)=\frac{P}{16\pi\mu}\frac{5\lambda+6\mu}{\lambda+\mu}\ln\left|\frac{x+d}{x-d}\right|$$
$$+\frac{P}{\pi k}\frac{a}{\sqrt{a^2-b}}\{\alpha_1[g(x-d|\alpha_2)-g(|x+d|\alpha_2)]$$
$$-\alpha_2[g(|x-d|\alpha_1)-g(|x+d|\alpha_1])]\}. \quad (35)$$

The displacement is everywhere bounded and tends to zero for $x\to\infty$. It is worth remarking that in Eq. (35), the first term is the displacement without the reinforcement, while the second is due to the presence of the fiber. Thus, the effect of the strengthening is immediately recognized.

4 The Broken Fiber

One common failure of composites, in particular fibro-reinforced with polymeric matrix, is related to the breaking of the fibers. In fact, when one fiber breaks, its axial force is transferred to the matrix, which increases its prebreaking maximum stress. If the sheet has no extra strength, it fails, with the consequence that rupture of a single fiber causes the failure of the whole body. Therefore, it is necessary to calculate the effects of the broken fiber in the surrounding matrix and, if possible, it is useful to design the composite which minimizes the stress increment. This problem is addressed in this section.

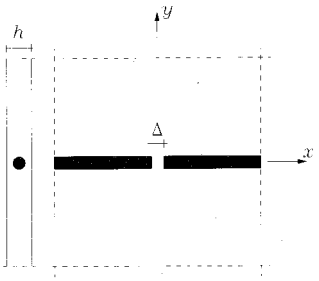

Fig. 4 The sheet with a broken fiber

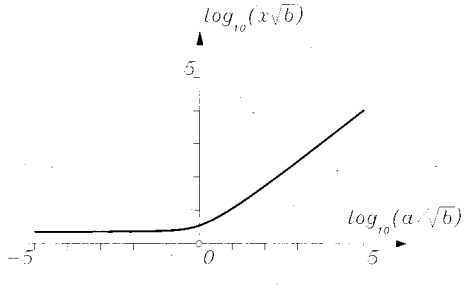

Fig. 5 The semi-length of the zone of influence

Initially we study the rupture of a single fiber embedded in the sheet. The reinforcing effects of nearby fibers (if any) will be analyzed in the next section. Furthermore, we suppose that the load is applied far from the breaking point. Thus, the simplified problem of an infinite sheet with a single broken fiber weakly attached to the plate can be considered.

The plate is supposed to be loaded by $\varepsilon_{xx}=\tilde{\varepsilon}$, $\sigma_{yy}=\sigma_{xy}=0$ at infinity. However, by the superposition principle, we can directly consider the case of a fiber open by a concentrated distortion such that $U(0^+)-U(0^-)=\Delta$ and the strain (and the stress) vanishes at infinity (Fig. 4). This action furnishes a nonzero compressive force $N(0^+)=N(0^-)=-N(\Delta)$. Equating $N(\Delta)$ with $\tilde{\varepsilon}EA$ (the axial force in the uniform case) we obtain $\Delta=\Delta(\tilde{\varepsilon})$, which, added to the constant strain solution, gives the solution in terms of the applied strain $\tilde{\varepsilon}$.

The situation of Fig. 4 is a nonclassical Melan's problem, which can be solved on the basis of (7). In fact, in this case $\hat{p}(s)=0$ and $\hat{\varepsilon}^*(s)=\Delta$ and we have

$$\hat{\tau}(s)=\frac{isk\Delta}{s^2+2a|s|+b}. \tag{36}$$

Inverting and rearranging as in Section 3, gives

$$\tau(x)=\frac{\Delta k}{2\pi\sqrt{a^2-b}}\left(-\alpha_1\int_0^\infty\frac{\sin(sx)}{s+\alpha_1}ds+\alpha_2\int_0^\infty\frac{\sin(sx)}{s+\alpha_2}ds\right). \tag{37}$$

Computing the integrals of (37) by means of formula 3.722.1 of [24] (see (19) for the definition of $f(z)$), we obtain

$$\tau(x)=\frac{\Delta k}{2\pi\sqrt{a^2-b}}[-\alpha_1 f(x\alpha_1)+\alpha_2 f(x\alpha_2)]. \tag{38}$$

On $x>0$, the interface shear stress is a decreasing function vanishing for $x\to\infty$ and $\tau_{\max}=\tau(0)=\Delta k/2$. Therefore, the maximum transmission stress is again proportional to k and using soft adhesives permits relaxing the peak of the extra stress due to the breaking of the fiber.

Integrating the equilibrium equation gives the expression of the axial load

$$N(x)=\frac{\Delta k}{2\pi\sqrt{a^2-b}}[-g(x\alpha_1)+g(x\alpha_2)]. \tag{39}$$

Therefore,

$$N(0^+)=-\frac{\Delta k}{2\pi\sqrt{a^2-b}}\operatorname{arccosh}\left(\frac{a}{\sqrt{b}}\right) \tag{40}$$

and

$$\Delta(\tilde{\varepsilon})=\tilde{\varepsilon}\frac{\pi\sqrt{a^2-b}}{b\operatorname{arccosh}(a/\sqrt{b})}. \tag{41}$$

Adopting the same definition (21) for the zone of influence, we obtain the curve plotted in Fig. 5. Qualitatively, this curve is similar to that of Fig. 2, and can be approximated by the bilinear function

$$\begin{aligned}&\log_{10}(\bar{x}\sqrt{b})\cong 0.362, \quad \text{if } \log_{10}(a/\sqrt{b})<0.347,\\ &\log_{10}(\bar{x}\sqrt{b})\cong 0.089+0.787\log_{10}(a/\sqrt{b}),\\ &\qquad\qquad \text{if } \log_{10}(a/\sqrt{b})>0.347,\end{aligned} \tag{42}$$

or, in terms of the original variables,

$$\begin{aligned}&\bar{x}\cong 2.301\sqrt{\frac{EA}{k}}, \quad \text{if } k<\tilde{k},\\ &\bar{x}\cong\frac{0.080}{k^{0.106}}\left(\frac{5\lambda+6\mu}{\lambda+\mu}\frac{1}{\mu}\right)^{0.787}EA^{0.893}, \quad \text{if } k>\tilde{k},\end{aligned} \tag{43}$$

where $\tilde{k}=5059(\mu^2/EA)((\lambda+\mu)/(5\lambda+6\mu))^2$. In this case $\bar{x}$ is no longer constant for $k>\tilde{k}$, and it is not possible to give a practical definition of perfect bonding.

From (7*b*) and $\hat{p}(s)=0$, $\hat{\varepsilon}^*(s)=\Delta$, it follows

$$\hat{u}(s)=\frac{i\Delta 2a\,\operatorname{sign}(s)}{s^2+2a|s|+b} \tag{44}$$

and, inverting,

$$u(x)=\frac{\Delta a}{\pi\sqrt{a^2-b}}[f(x\alpha_1)-f(x\alpha_2)]. \tag{45}$$

4.1 The Effect of Nearby Fibers. The successive step consists in analyzing the reinforcing effects of the nearby fibers. In fact, unidirectional fibro-reinforced materials have an array of parallel, equally spaced, and identical fibers embedded in the sheet. When one of these breaks, not all the extra load is transferred to the plate, but only a part which depends on the properties of the composite. If the fibro-reinforced material is correctly designed, this extra load is modest and does not induce rupture in the sheet or in the adjacent fiber as well.

The reinforcing effects of the fibers decrease by increasing the distance from the broken fiber, so that, in the first approximation, it is reasonable to consider only the case of the sheet with three fibers, two reinforcing and the broken one. Therefore, let us consider the sheet of Section 2 and let us suppose that on the line $y=+d$ is applied a line load $\tau_1(x)$, on the line $y=0$ is applied a line load $\tau_2(x)$, and on the line $y=-d$ is applied a line load $\tau_3(x)=\tau_1(x)$ (for symmetry with respect to the line $y=0$). Both $\tau_1(x)$ and $\tau_2(x)$ are parallel to the x-axis and positive if directed accordingly. Then

$$
\begin{aligned}
u(x,+d)=u_1(x)=&-\frac{1}{16\pi\mu}\frac{5\lambda+6\mu}{\lambda+\mu}\int_{-\infty}^{\infty}\tau_1(t)\ln|t-x|dt\\
&-\frac{1}{16\pi\mu}\frac{5\lambda+6\mu}{\lambda+\mu}\int_{-\infty}^{\infty}\tau_2(t)\ln\sqrt{(t-x)^2+d^2}\,dt\\
&-\frac{1}{16\pi\mu}\frac{3\lambda+2\mu}{\lambda+\mu}\int_{-\infty}^{\infty}\frac{\tau_2(t)d^2}{(t-x)^2+d^2}dt\\
&-\frac{1}{16\pi\mu}\frac{5\lambda+6\mu}{\lambda+\mu}\int_{-\infty}^{\infty}\tau_1(t)\ln\sqrt{(t-x)^2+4d^2}dt\\
&-\frac{1}{16\pi\mu}\frac{3\lambda+2\mu}{\lambda+\mu}\int_{-\infty}^{\infty}\frac{\tau_1(t)4d^2}{(t-x)^2+4d^2}dt,\\
u(x,0)=u_2(x)=&-\frac{1}{16\pi\mu}\frac{5\lambda+6\mu}{\lambda+\mu}\int_{-\infty}^{\infty}\tau_2(t)\ln|t-x|dt\\
&-\frac{2}{16\pi\mu}\frac{5\lambda+6\mu}{\lambda+\mu}\int_{-\infty}^{\infty}\tau_1(t)\ln\sqrt{(t-x)^2+d^2}dt\\
&-\frac{2}{16\pi\mu}\frac{3\lambda+2\mu}{\lambda+\mu}\int_{-\infty}^{\infty}\frac{\tau_1(t)d^2}{(t-x)^2+d^2}dt.
\end{aligned}
\tag{46}
$$

The Fourier transforms of (46) are

$$
\begin{aligned}
\hat{u}_1(s)=&\frac{1+e^{-2d|s|}}{16\mu}\frac{5\lambda+6\mu}{\lambda+\mu}\frac{\hat{\tau}_1(s)}{|s|}-\frac{2de^{-2d|s|}}{16\mu}\frac{3\lambda+2\mu}{\lambda+\mu}\hat{\tau}_1(s)\\
&+\frac{e^{-d|s|}}{16\mu}\frac{5\lambda+6\mu}{\lambda+\mu}\frac{\hat{\tau}_2(s)}{|s|}-\frac{de^{-d|s|}}{16\mu}\frac{3\lambda+2\mu}{\lambda+\mu}\hat{\tau}_2(s),\\
\hat{u}_2(s)=&\frac{1}{16\mu}\frac{5\lambda+6\mu}{\lambda+\mu}\frac{\hat{\tau}_2(s)}{|s|}+\frac{2e^{-d|s|}}{16\mu}\frac{5\lambda+6\mu}{\lambda+\mu}\frac{\hat{\tau}_1(s)}{|s|}\\
&-\frac{de^{-d|s|}}{16\mu}\frac{3\lambda+2\mu}{\lambda+\mu}\hat{\tau}_1(s).
\end{aligned}
\tag{47}
$$

Associated with (47) there are the interface equations (see (4))

$$
\hat{\tau}_1(s)=k[\hat{U}_1(s)-\hat{u}_1(s)],\quad \hat{\tau}_2(s)=k[\hat{U}_2(s)-\hat{u}_2(s)],
\tag{48}
$$

and the equilibrium equations of the fibers (see (6))

$$
\begin{aligned}
-s^2\hat{U}_1(s)-\frac{\hat{\tau}_1(s)}{EA}=0,\\
-s^2\hat{U}_2(s)+is\hat{\varepsilon}^*(s)+\frac{\hat{p}(s)}{EA}-\frac{\hat{\tau}_2(s)}{EA}=0.
\end{aligned}
\tag{49}
$$

Note that we have supposed that all the fibers are uniform and identical and that the reinforcing fibers are not loaded. Also the three interfaces are uniform and identical.

Eliminating $\hat{U}_1(s)$ and $\hat{U}_2(s)$ from (48) and (49) we have

$$
\begin{aligned}
\hat{u}_1(s)=&-\hat{\tau}_1(s)\left(\frac{1}{k}+\frac{1}{EAs^2}\right),\\
\hat{u}_2(s)=&-\hat{\tau}_2(s)\left(\frac{1}{k}+\frac{1}{EAs^2}\right)+\frac{i\hat{\varepsilon}^*(s)}{s}+\frac{\hat{p}(s)}{EAs^2}.
\end{aligned}
\tag{50}
$$

Inserting these expressions in (47) we obtain a system of two equations in the two unknowns $\hat{\tau}_1(s)$ and $\hat{\tau}_2(s)$, the solution of which is

$$
\begin{aligned}
\hat{\tau}_1(s)=&-\hat{\tau}_2(s)\frac{B(s)}{A(s)},\\
\hat{\tau}_2(s)=&\left(\frac{i\hat{\varepsilon}^*(s)}{s}+\frac{\hat{p}(s)}{EAs^2}\right)\frac{A(s)}{A(s)C(s)-2B(s)^2},
\end{aligned}
\tag{51}
$$

where

$$
\begin{aligned}
A(s)=&\frac{1+e^{-2d|s|}}{16\mu|s|}\frac{5\lambda+6\mu}{\lambda+\mu}-\frac{2de^{-2d|s|}}{16\mu}\frac{3\lambda+2\mu}{\lambda+\mu}+\frac{1}{k}+\frac{1}{EAs^2},\\
B(s)=&\frac{e^{-d|s|}}{16\mu|s|}\frac{5\lambda+6\mu}{\lambda+\mu}-\frac{de^{-d|s|}}{16\mu}\frac{3\lambda+2\mu}{\lambda+\mu},\\
C(s)=&\frac{1}{16\mu|s|}\frac{5\lambda+6\mu}{\lambda+\mu}+\frac{1}{k}+\frac{1}{EAs^2}.
\end{aligned}
\tag{52}
$$

The general solution of the problem can be obtained inverting (50) and (51) with $\hat{p}(s)=0$ and $\hat{\varepsilon}^*(s)=\Delta$. It is given in terms of definite integrals, which cannot be expressed in terms of known functions, but which can be easily computed numerically.

Usually, in fibro-reinforced composites the space between the fibers is very narrow (it is the same order of the fibers diameter) and d is a very small number. Therefore, it makes sense to study the limit case $d=0$ and to suppose that it represents a good approximation of the actual configuration. Assuming $d=0$ ($\hat{p}(s)=0$ and $\hat{\varepsilon}^*(s)=\Delta$) we have, after some simplifications,

$$
\hat{\tau}_2(s)=i\Delta k\frac{s^3+4as|s|+bs}{s^4+6a|s|^3+2bs^2+6ab|s|+b^2},
\tag{53}
$$

and therefore

$$
\tau_2(x)=\frac{\Delta k}{\pi}\int_0^{\infty}\frac{(s^3+4as^2+bs)\sin(sx)}{s^4+6as^3+2bs^2+6abs+b^2}ds.
\tag{54}
$$

Expressing the integrand in the sum

$$
\frac{s^3+4as^2+bs}{s^4+6as^3+2bs^2+6abs+b^2}=\frac{2s}{3(s^2+b)}+\frac{s}{3(s^2+6as+b)},
\tag{55}
$$

recalling the formula [24] (formula 3.723.3) $\int_0^{\infty}(\sin(sx)s)/(s^2+b)ds=(\pi/2)e^{-x\sqrt{b}}$, and calculating the second integral as in Section 3, we obtain the final expression for the interfacial shear

$$
\tau_2(x)=\frac{\Delta k}{2}\left[\frac{2}{3}e^{-x\sqrt{b}}+\frac{-\beta_1 f(x\beta_1)+\beta_2 f(x\beta_2)}{3\pi\sqrt{9a^2-b}}\right],
\tag{56}
$$

where $\beta_1=3a-\sqrt{9a^2-b}$ and $\beta_2=3a+\sqrt{9a^2-b}$. There are no qualitative differences between (56) and (38), corresponding to the case of only one fiber: on the positive part of the x-axis, $\tau_2(x)$ is a decreasing function of x, vanishing for $x\to\infty$ and with maximum value $\tau_{\max}=\tau_2(0^+)=\Delta k/2$.

Integrating $\tau_2(x)$ we obtain the axial load in the broken fiber:

$$
N_2(x)=-\frac{\Delta k}{2}\left[\frac{2}{3}\frac{e^{-x\sqrt{b}}}{\sqrt{b}}+\frac{g(x\beta_1)-g(x\beta_2)}{3\pi\sqrt{9a^2-b}}\right].
\tag{57}
$$

From (57) we can compute

$$
N_2(0)=-\Delta k\left[\frac{1}{3\sqrt{b}}+\frac{\operatorname{arccosh}(3a/\sqrt{b})}{3\pi\sqrt{9a^2-b}}\right]
\tag{58}
$$

that with the equation $-N_2(0)=\tilde{\varepsilon}EA$, furnishes the fiber gap Δ as a function of the applied load $\tilde{\varepsilon}$:

$$
\Delta(\tilde{\varepsilon})=\tilde{\varepsilon}\frac{3}{\sqrt{b}+\dfrac{b}{\pi\sqrt{9a^2-b}}\operatorname{arccosh}(3a/\sqrt{b})}.
\tag{59}
$$

On the reinforcing fibers we have (see (51))

$$
\hat{\tau}_1(s)=-i\Delta k\frac{2as|s|}{s^4+6a|s|^3+2bs^2+6ab|s|+b^2},
\tag{60}
$$

so that

$$\tau_1(x) = -\frac{\Delta k}{\pi}\int_0^\infty \frac{2as^2\sin(sx)}{s^4+6as^3+2bs^2+6abs+b^2}\,ds. \quad (61)$$

By the same integral used for computing $\tau_2(x)$, (61) can be rearranged as

$$\tau_1(x) = -\frac{\Delta k}{2}\left[\frac{1}{3}e^{-x\sqrt{b}} - \frac{-\beta_1 f(x\beta_1)+\beta_2 f(x\beta_2)}{3\pi\sqrt{9a^2-b}}\right]. \quad (62)$$

It remains to compute the axial load in the reinforcing fibers, which is obtained integrating (62), and is given by

$$N_1(x) = \frac{\Delta k}{2}\left[\frac{1}{3}\frac{e^{-x\sqrt{b}}}{\sqrt{b}} - \frac{g(x\beta_1)-g(x\beta_2)}{3\pi\sqrt{9a^2-b}}\right]. \quad (63)$$

The maximum value is attained in correspondence of the symmetry axis $x=0$ and it has the following expression:

$$N_1(0) = \Delta k\left[\frac{1}{6\sqrt{b}} - \frac{\operatorname{arccosh}(3a/\sqrt{b})}{3\pi\sqrt{9a^2-b}}\right]. \quad (64)$$

Using (59), we have the axial force as a function of the applied load $\tilde{\varepsilon}$. To obtain the actual axial force $\tilde{N}_1(0)$ of the reinforcing fibers, by the superposition we must add to (64) the term $\tilde{\varepsilon}EA$, the axial force corresponding to the constant strain solution.

To have a quantitative measure of the increasing of the axial force in the reinforcing fibers as a consequence of the breaking of the middle one, let us compare $\tilde{N}_1(0)$ with its prebreaking values, obviously given by $\tilde{N}_1(0)_{\text{p.b.}} = \tilde{\varepsilon}EA$. We have

$$\frac{\tilde{N}_1(0)}{\tilde{N}_1(0)_{\text{p.b.}}} = \frac{3}{2}\frac{1}{1+\dfrac{\operatorname{arccosh}(3a/\sqrt{b})}{3\sqrt{9a^2/b-1}}}. \quad (65)$$

In the limit case of strong interface $\lim_{k\to\infty}\tilde{N}_1(0)/\tilde{N}_1(0)_{\text{p.b.}} = 1.5$, which shows that each reinforcing fiber carries one half of the force previously carried by the broken fiber. In this case, there is no extra load on the sheet. In the other limit case of very soft interface, on the other hand, $\lim_{k\to 0}\tilde{N}_1(0)/\tilde{N}_1(0)_{\text{p.b.}} = 1$ and therefore the extra load is carried entirely by the plate.

Based on the previous observations, we can solve the following design problem: How does one choose the stiffness of the interface in order to have a given redistribution of the load previously carried by the broken fiber? In fact, it is sufficient to fix the percents which must be carried by the reinforcing fibers and, by inverting (65), the optimal value of k is obtained. For example, if we want the extra load carried in equal parts by the sheet and by the reinforcing fibers, we solve $\tilde{N}_1(0)/\tilde{N}_1(0)_{\text{p.b.}} = 1.25$ and we obtain $a/\sqrt{b} = 0.9845$, or $k = 992.5(\mu^2/EA)((\lambda+\mu)/(5\lambda+6\mu))^2$. Note how, in this way, the interface stiffness can be used as a design parameter to optimize the behavior of the composite subjected to the rupture of a fiber.

References

[1] Melan, E., 1932, ''Ein Beitrag zur Theori geschweisster Verbindungen,'' Ing.-Arch., **3**, pp. 123–129.

[2] Love, A. E. H., 1926, *A Treatise on the Mathematical Theory of Elasticity*, Oxford Univ. Press, Oxford (reprinted by Dover, New York, 1944).

[3] Koiter, W. T., 1955, ''On the Diffusion of Load From a Stiffener into a Sheet,'' Q. J. Mech. Appl. Math., **VIII**, pp. 164–178.

[4] Buell, E. L., 1948, ''On the Distribution of Plane Stress in a Semi-infinite Plate With Partially Stiffened Edge,'' J. Math. Phys., **26**, pp. 223–233.

[5] Benscoter, S., 1949, ''Analysis of a Single Stiffener on an Infinite Sheet,'' ASME J. Appl. Mech., **16**, pp. 242–246.

[6] Erdogan, and F., Gupta, G. D., 1971, ''The Problem of an Elastic Stiffener Bonded to a Half Plane,'' ASME J. Appl. Mech., **38**, pp. 937–941.

[7] Lee, E. J., and Klang, E. C., 1992, ''Stress Distribution in an Edge-Stiffened Semi-Infinite Elastic Plate Containing a Circular Hole,'' ASME J. Appl. Mech., **59**, pp. 789–795.

[8] Muki, R., and Sternberg, E., 1967, ''Transfer of Load From an Edge Stiffener to a Sheet—A Reconsideration of Melan's Problem,'' ASME J. Appl. Mech., **34**, pp. 679–686.

[9] Shield, T. W., and Kim, K. S., 1992, ''Beam Theory Models for Thin Film Segments Cohesively Bonded to an Elastic Half Space,'' Int. J. Solids Struct., **29**, pp. 1085–1103.

[10] Bufler, H., 1964, ''Zur Krafteinleitung in Scheiben Uber Geschweisste Oder Geklebte Verbindungen,'' Ing.-Arch., **18**, p. 284.

[11] Reissner, E., 1940, ''Note on the Problem of Distribution of Stress in a Thin Stiffened Elastic Sheet,'' Proc. Natl. Acad. Sci. USA **26**, pp. 300–305.

[12] Goodier, J. N., and Hsu, C. S., 1954, ''Transmission of Tension From a Bar to a Plate,'' ASME J. Appl. Mech., **21**, pp. 147–150.

[13] LeFevre, E. J., Mudge, D. R. J., and Dickie, J. F., 1966, ''An Analysis of the Distribution of Tension in a Bar Attached to a Plate,'' J. Strain Anal., **1**, pp. 389–393.

[14] Muki, R., and Sternberg, E., 1968, ''On the Diffusion of Load From a Transverse Tension Bar Into a Semi-Infinite Elastic Sheet,'' ASME J. Appl. Mech., **35**, pp. 737–746.

[15] Grigolyuk, E. I., and Tolkachev, V. M., 1987, *Contact Problems in the Theory of Plates and Shells*, Mir, Moscow.

[16] Budiansky, B., and Wu, T. T., 1961, ''Transfer of a Load to a Sheet From a Rivet-Attached Stiffener,'' J. Math. Phys., **40**, pp. 142–162.

[17] Rybakov, L. S., and Cherepanov, G. P., 1977, ''Discrete Interaction of a Plate With a Semi-infinite Stiffener,'' Prikl. Mat. Mekh., **41**, pp. 322–328.

[18] Rybakov, L. S., 1982, ''On Discrete Interaction of a Plate and a Damaged Stringer,'' J. Appl. Math. Mech., (transl. of Prik. Mat. Mek.) **45**, pp. 127–133

[19] Antipov, Y. A., and Arutyunyan, N. K., 1993, ''A Contact Problem With Friction and Adhesion for an Elastic Layer With Stiffeners,'' J. Appl. Math. Mech., **57**, pp. 159–170 (transl. of Prik. Mat. Mek.).

[20] Goland, M., and Reissner, E., 1944, ''The Stresses in Cemented Joints,'' ASME J. Appl. Mech., **11**, pp. A17–A27.

[21] Gilibert, Y., and Rigolot, A., 1979, ''Analyze Asymptotique des Assemblage Collés a Double Recouvrement Sollicités au Cisaillement en Traction,'' J. Mec. Appl., **3**, No. 3, pp. 341–372.

[22] Klarbring, A., 1991, ''Derivation of a Model of Adhesively Bonded Joints by the Asymptotic Expansion Method,'' Int. J. Eng. Sci., **29**, pp. 493–512.

[23] Geymonat, G., Krasucki, F., and Lenci, S., 1999, ''Mathematical Analysis of a Bonded Joint With Soft Thin Adhesive,'' Math. Mech. Sol., **4**, pp. 201–225.

[24] Gradshteyn, I. S., and Ryzhik, I. M., 1965, *Tables of Integrals, Series, and Products*, Academic Press, New York.

[25] Abramowitz, M., and Stegun, I. A., 1965, *Handbook of Mathematical Functions*, Dover Publications, New York.

[26] Muskhelishvili, N. I., 1953, *Some Basic Problems of the Mathematical Theory of Elasticity*, Noordhoff, Leyden.

Ill-Posedness in a Thermomechanically Consistent Constrained Theory for Materials With Prescribed Temperature-Dependent Density

Q. Wang
Department of Mathematical Sciences,
Indiana University-Purdue University
Indianapolis,
Indianapolis, IN 46202

We examine the local dynamics of nonisothermal viscous flows in the neighborhood of the constant equilibria using the thermomechanically consistent constrained theory for materials with prescribed temperature-dependent density developed by Cao et al.. We discover that the linearized growth rate of small length scale, infinitesimal disturbances near the equilibria is proportional to the reciprocal of their wave length, a classical phenomenon known as the Hadamard instability, indicating the local ill-posedness of the constrained theory. Therefore, the use of the theory to model transient flow phenomenon is not advised. [S0021-8936(00)01901-2]

1 Introduction

Cao et al. [1] developed a thermomechanically consistent constrained theory for materials with prescribed temperature-dependent density. This theory successfully captures the expansion cooling phenomenon observed in nonisothermal steady-state Poiseuille flows of viscous fluids ([1,2]) while the ad hoc theories ([3–5]) where a temperature-dependent density is a posteriori inserted into the classical theory for incompressible materials ([6]), fail. In this regard, the constrained theory of Cao et al.'s marks a notable theoretical advance in modeling steady-state nonisothermal flows.

When applied to transient flow problems, however, the theory is found to be pathological in that not only the constant equilibria are unstable at any experimentally attainable temperature, but also infinitesimal disturbances of small length scales near the equilibrium grow proportionally to the reciprocal of their wave length. This catastrophic phenomenon has been referred to as the classical Hadamard instability ([7]).

Examples of mathematical models exhibiting Hadamard instabilities include the ''transient'' Laplace equation, in which one of the independent variables is treated as time-like, incompressible fluid models for inviscid interfacial flows (Kelvin-Helmholtz, Rayleigh-Taylor instability, etc.) ([8]) and some models (interpolated Maxwell model, etc.) for non-Newtonian fluids ([7,9]). The emergence of the instability in the models is often an indication of their failure to model the underlying physics ([7,9]) or onset of catastrophies. Regularization of the models is thus necessary; sometimes, the regularization is done numerically. In most evolutionary equations, where Hadamard instabilities are observed at any constant equilibrium, the corresponding initial or initial boundary value problem does not have a solution except that the initial data are analytical. Evolutionary equations exhibiting this behavior are often said to be locally ill-posed ([7]). The constrained theory of Cao et al. ([1]) is thus locally ill-posed.

The ''unconstrained'' (compressible) theory for nonisothermal viscous fluids is known to be well-posed, i.e., all the constant equilibria are stable. A general proof can be found in [10] for thermomechanical processes satisfying the Gibbs conditions ([11,12]). The local ill-posedness of the constrained theory ([1]) found in this study certainly contradicts both the unconstrained theory and the common experience with nonisothermal viscous fluids. Consequently, its direct use in transient flow phenomenon is not advised.

In the remaining parts of the paper, we detail our near-equilibrium dynamical analysis for nonisothermal viscous flows using the thermomechanically consistent constrained theory, which leads to our discovery of the catastrophic instability in the theory and so its ill-posedness, following a brief review of the constrained theory.

2 Near Equilibrium Dynamics in the Thermomechanically Consistent Constrained Theory

First, we briefly review the thermomechanically consistent constrained theory for materials with prescribed temperature-dependent density developed by Cao et al. [1]. Then, we study the dynamical behavior of the theory near constant equilibria followed by a brief discussion about a more general constraint.

2.1 Thermomechanically Consistent Constrained Theory for Materials With Temperature-Dependent Density. In the constrained theory of Cao et al. [1], the density of the material ρ is assumed a given function of the absolute temperature θ:

$$\rho = \rho(\theta). \tag{1}$$

With the prescribed density, the conservation of mass acts effectively as a thermomechanical constraint:

$$\operatorname{div}\mathbf{v} + \frac{\rho'(\theta)}{\rho(\theta)}\dot{\theta} = \mathbf{I}\cdot\mathbf{D} + \frac{\rho'(\theta)}{\rho(\theta)}\dot{\theta} = 0, \tag{2}$$

where $\mathbf{D} = \frac{1}{2}(\nabla\mathbf{v} + \nabla\mathbf{v}^{\mathbf{T}})$ is the rate-of-strain tensor, $\mathbf{v}$ is the velocity vector, $\mathbf{I}$ is the second-order isotropic tensor. The constrained responses for the stress, free energy, entropy, and heat flux are derived subject to constraint (2) in [1]. It is shown that the constraint response in the entropy is given by $p(\rho'/\rho^2)$ and that the stress is given by $-p\mathbf{I}$, where p is a Lagrange multiplier corresponding to the constraint recognized as the pressure, whereas the

Contributed by the Applied Mechanics Division of THE AMERICAN SOCIETY OF MECHANICAL ENGINEERS for publication in the ASME JOURNAL OF APPLIED MECHANICS. Manuscript received by the ASME Applied Mechanics Division, July 7, 1998; final revision, June 25, 1999. Associate Technical Editor: D. A. Siginer. Discussion on the paper should be addressed to the Technical Editor, Professor Lewis T. Wheeler, Department of Mechanical Engineering, University of Houston, Houston, TX 77204-4792, and will be accepted until four months after final publication of the paper itself in the ASME JOURNAL OF APPLIED MECHANICS.

free energy and heat flux are not affected by the constraint at all. With the constraint responses, the total stress, free energy, entropy, and heat flux are expressed as

$$\mathbf{T}=\hat{\mathbf{T}}-p\mathbf{I}, \quad \psi=\hat{\psi}, \quad \eta=\hat{\eta}+p\frac{\rho'(\theta)}{\rho(\theta)^2}, \quad \mathbf{q}=\hat{\mathbf{q}}, \tag{3}$$

where $\hat{\mathbf{T}}$, $\hat{\psi}$, $\hat{\eta}$, $\hat{\mathbf{q}}$ represent the constitutive part of the physical variables to be determined by the material properties. Accordingly, the total internal energy is given by

$$\epsilon=\hat{\epsilon}+\theta\hat{\eta}+\theta p\frac{\rho'(\theta)}{\rho(\theta)}. \tag{4}$$

Substituting (3) and (4) into the energy balance

$$\rho\dot{\epsilon}=\mathbf{T}\cdot\mathbf{D}+\rho\gamma-\operatorname{div}\mathbf{q}, \tag{5}$$

where γ is the internal heat per unit mass, Cao et al. arrived at

$$\left[\rho c(\theta)+\frac{p\theta}{\rho}\left(\rho''-2\frac{\rho'^2}{\rho}\right)\right]\dot{\theta}+\frac{\rho'}{\rho}\theta\dot{p}=\hat{\mathbf{T}}\cdot\mathbf{D}+\rho\gamma-\operatorname{div}\hat{\mathbf{q}}. \tag{6}$$

In the derivation, an increase in the constitutive part of the internal energy is assumed due exclusively to the increase of temperature:

$$d\hat{\epsilon}=c(\theta)d\theta, \tag{7}$$

where $c(\theta)$ is the specific heat (a prescribed function of θ) corresponding to the constitutive part of the internal energy.

Equations (2), (6), and the conservation of linear momentum

$$\rho\dot{\mathbf{v}}=\operatorname{div}\hat{\mathbf{T}}-\operatorname{grad}p+\mathbf{g}, \tag{8}$$

where $\mathbf{g}$ is the external force per unit volume, along with the constitutive equations for the extra stress $\hat{\mathbf{T}}$ and heat flux $\hat{\mathbf{q}}$ constitute the thermomechanically consistent constrained theory for materials with prescribed temperature-dependent density ([1]).

2.2 Linearized Stability Around Constant Flow Equilibria of Nonisothermal Viscous Fluids Using the Constrained Theory. For a nonisothermal viscous fluid, the constitutive part of the extra stress, satisfying the Clausius-Duhem inequality, is given by

$$\hat{\mathbf{T}}=\lambda(\theta)tr(\mathbf{D})+2\mu(\theta)\mathbf{D}, \tag{9}$$

where $\lambda(\theta)$, $\mu(\theta)$ are prescribed temperature-dependent bulk viscosity and viscosity, respectively, with $\lambda+\frac{2}{3}\mu\geqslant 0$ and $\mu\geqslant 0$ and $tr(\mathbf{D})$ is the trace of $\mathbf{D}$. We note that the first term was not included in the original derivation of Cao et al. [1].

In consistence with the second law of thermodynamics, we adopt the Fourier law for the heat flux,

$$\hat{\mathbf{q}}=-K(\theta)\nabla\theta, \tag{10}$$

where $K(\theta)$ is the heat conductivity, a prescribed function of temperature.

When the external force and the specific heat effect are neglected, the governing system of equations for nonisothermal viscous flows, consisting of Eqs. (2), (6), (8), (9), and (10), admits a constant solution (flow equilibrium)

$$\mathbf{v}=\mathbf{v}_0, \quad p=p_0, \quad \theta=\theta_0, \tag{11}$$

where $\mathbf{v}_0$ is an arbitrary constant vector, p_0 an arbitrary constant, and θ_0 an arbitrary positive constant.

We are interested in the local dynamics of the governing system of equations near the equilibrium. So, we linearize the governing Eqs. (2), (6), (8)–(10) about the equilibrium (11), yielding a constant coefficient partial differential equation system. We then seek solutions of the linearized equations in forms of plane waves:

$$(\bullet)(\mathbf{x},t)=e^{\alpha t-i\mathbf{n}\cdot\mathbf{x}}\delta(\bullet), \tag{12}$$

where $(\bullet)$ represents the perturbations of the physical variables $\mathbf{v}=(v_1,v_2,v_3)$, p, θ, $\mathbf{x}=(x_1,x_2,x_3)$ is the position vector in the Cartesian coordinate (x_1,x_2,x_3), $\mathbf{n}=(n_1,n_2,n_3)$ is the wave vector, and the real part of α gives the growth rate.

Without loss of generality, we proceed with $\mathbf{v}_0=\mathbf{0}$ and $\mathbf{n}=(n,0,0)$. After some algebraic manipulations, we transform the linearized partial differential equation system into the following algebraic equation system for α and the perturbations

$$\begin{cases} -in\delta v_1+\alpha\dfrac{\rho(\theta_0)}{\rho(\theta_0)}\delta\theta=0, \\ \alpha\rho(\theta_0)\delta v_1=in\delta p-n^2(2\mu(\theta_0)+\lambda(\theta_0))\delta v_1, \\ \alpha\left\{\left[\rho(\theta_0)c(\theta_0)+\dfrac{p_0\theta_0}{\rho(\theta_0)}\left(\rho''(\theta_0)-2\dfrac{\rho'^2(\theta_0)}{\rho(\theta_0)}\right)\right]\delta\theta+\dfrac{\rho'(\theta_0)}{\rho(\theta_0)}\theta_0\delta p\right\}=-n^2K(\theta_0)\delta\theta. \end{cases} \tag{13}$$

The dispersion equation of the linearized equation system is then obtained as follows:

$$n^2\left[\alpha\left(\rho(\theta_0)c(\theta_0)+\frac{p_0\theta_0}{\rho(\theta_0)}\left(\rho''(\theta_0)-\frac{2(\rho'(\theta_0))^2}{\rho(\theta_0)}\right)\right)+K(\theta_0)n^2\right] -\left(\frac{\rho'(\theta_0)}{\rho(\theta_0)}\right)^2\theta_0\alpha^2[\rho(\theta_0)\alpha+(2\mu+\lambda)n^2]=0. \tag{14}$$

This is a cubic equation for α. Although its roots can be expressed explicitly in algebraic formulas, their expressions are tedious and not illuminating. Instead, we seek their asymptotic representations in the range of large $|n|\gg 1$. The leading terms in the three roots of the cubic dispersion equation are found either linear or quadratic in wave number n, provided $2\mu(\theta_0)+\lambda(\theta_0)>0$,

$$\begin{cases} \alpha_1\sim-\dfrac{2\mu(\theta_0)+\lambda(\theta_0)}{\rho(\theta_0)}n^2, \\ \alpha_\pm\sim\pm\sqrt{\dfrac{K(\theta_0)}{(2\mu(\theta_0)+\lambda(\theta_0))\theta_0}}\left|\dfrac{\rho(\theta_0)}{\rho'(\theta_0)}n\right|. \end{cases} \tag{15}$$

The expression for α_+ indicates that there is a positive growth rate proportional to the magnitude of the wave vector in the short wave limit ($|n|\gg 1$). Namely, the disturbance grows in proportion to the reciprocal of its wave length. The indication of this is that the smaller the spatial length scale is in the disturbance, the faster it grows. This phenomenon is known as the classical Hadamard instability ([7]). Its existence at any constant equilibrium implies that the governing system in the theory is locally ill-posed as an evolutionary equation system so that it cannot be applied directly

to transient problems. In fact, its usefulness in steady states is also questionable since all steady states are achieved through transient processes.

If $2\mu(\theta_0)+\lambda(\theta_0)=0$, the leading terms of the three roots of the dispersion equation are

$$\alpha^-_{j+1}\sim\left[\frac{\rho(\theta_0)K(\theta_0)n^4}{\rho'(\theta_0)^2\theta_0}\right]^{1/3}e^{(2\pi ij/3)},\quad j=0,1,2. \tag{16}$$

The real part of α_2^-, α_3^- are negative corresponding to decays, but the real part of α_1^- is positive yielding a growth rate proportional to $n^{4/3}$. Therefore, Hadamard instability persists and so does the local ill-posedness in the theory.

The ''eigenfunctions'' of the linearized system (13) give the directions of growth corresponding to the three growth rates (15). Their leading order terms for large $|n|\gg 1$ are given by

$$\begin{cases}\alpha_1\Leftrightarrow \delta v_1=1, \quad \delta p=0, \quad \delta\theta=0,\\ \alpha_\pm\Leftrightarrow \delta v_1=1, \quad \delta p=-in(\lambda(\theta_0)+2\mu(\theta_0)), \quad \delta\theta=in\dfrac{\rho(\theta_0)}{\rho'(\theta_0)\alpha_\pm}.\end{cases} \tag{17}$$

So the disturbance in the direction dominated by δp grows the most for large $|n|\gg 1$ in time corresponding to α_+.

Now that the constrained theory is locally ill-posed at any constant equilibrium, we must regularize the theory before it is applied to nonisothermal viscous fluids. Next, we report our attempts to regularize the constrained theory.

2.3 Thermomechanically Consistent Constrained Theory With a More General Constraint. Here, we adopt a more general constraint of Green et al. [13] and Trapp [14]

$$\mathbf{I}\cdot\mathbf{D}+\mathbf{b}\cdot\nabla\theta+a\dot{\theta}=0, \tag{18}$$

in place of the constraint imposed by the conservation of mass (2), where the vector $\mathbf{b}$ and scalar a are independent of $(\theta,\nabla\theta,\mathbf{D})$ and the constraint is invariant under the superposed rigid-body motions. We note that constraint (2) corresponds to $\mathbf{b}=0$, $a=\rho'(\theta)/\rho(\theta)$ here. Following the same argument outlined in Cao et al. [1], we obtain the total stress, entropy, free energy, and heat flux, including both the constrained response and constitutive part, as follows:

$$\mathbf{T}=\hat{\mathbf{T}}-p\mathbf{I},\quad \eta=\hat{\eta}+\frac{pa}{\rho},\quad \psi=\hat{\psi},\quad q=\hat{\mathbf{q}}+p\theta\mathbf{b}. \tag{19}$$

The new constraint (18) yields a nonzero constrained response in the heat flux, entropy, and stress, respectively. The additional term $(\mathbf{b}\cdot\nabla\theta)$ in constraint (18) is responsible for the constrained response in the heat flux. Using (7) and (5), we arrive at the energy balance for the material subject to constraint (18):

$$\left[\rho c(\theta)+\left(\frac{a}{\rho}\right)'p\right]\dot{\theta}+a\theta\dot{p}=\hat{\mathbf{T}}\cdot\mathbf{D}+\rho\gamma-\nabla\cdot\hat{\mathbf{q}}-\nabla\cdot(p\theta\mathbf{b}). \tag{20}$$

The other governing equations in the constrained theory are (8) and (18) along with the constitutive equations for the stress and heat flux.

For nonisothermal viscous flows, we repeat the linearized stability analysis around constant equilibrium (11) and obtain three growth rates in the range of $(|n|\gg 1)$, provided $a\neq 0$ and $2\mu(\theta_0)+\lambda(\theta_0)>0$, given asymptotically by

$$\begin{cases}\alpha_1^*\sim-\dfrac{(2\mu(\theta_0)+\lambda(\theta_0))}{\rho}n^2,\\ \alpha_\pm^*\sim\dfrac{b_1}{a}i\pm\sqrt{\dfrac{K(\theta_0)}{(2\mu(\theta_0)+\lambda(\theta_0))a^2\theta_0}}|n|,\end{cases} \tag{21}$$

where $b_1=\mathbf{b}\cdot\mathbf{e}_1$ and $\mathbf{e}_1$ is the unit base vector in the x_1-direction in the Cartesian coordinate (x_1,x_2,x_3). Analogous to (15), there is an unstable growth rate proportional to the magnitude of the wave vector and independent of the new term $\mathbf{b}\cdot\nabla\theta$ in the constraint. When $2\mu(\theta_0)+\lambda(\theta_0)=0$, we have analogous growth rate formulas like (16), which are omitted here. Hadamard instability thus persists unless $a=0$. If $a=0$, the dispersion equation of the linearized system has only one nonzero root α, yielding a negative growth rate (decay rate) proportional to n^2 so that the equilibrium is stable.

This analysis reveals that the additional term $\mathbf{b}\cdot\nabla\theta$ in the constraint is not enough to regularize the thermomechanically consistent constrained theory of Cao et al. [1]. It hints that the catastrophic instability may be intrinsic to the essential relation between the density and temperature implied by the constraints (2) and (18). We have also derived a thermomechanically consistent constraint theory with the density modified to the following form:

$$\rho=\rho(\theta)+\rho_1(\theta,\nabla\theta)\cdot\nabla\theta, \tag{22}$$

where the second term is assumed invariant under the superimposed rigid-body motions. The modified theory again fails to avoid the Hadamard instability at the constant equilibria. Furthermore, we also looked into the possibility of density as a function of temperature and the rate-of-strain, which is invariant under the superimposed rigid-body motions. We were unable to derive the constrained responses then. This approach therefore seems infeasible. Fortunately, by taking a different approach, we have been able to formulate a well-posed constrained theory for nonisothermal viscous flows.

2.4 Constrained Theory for Materials With Entropy-Dependent Density. Recently, Rooney et al. [10], reformulated a constrained theory for nonisothermal viscous flows assuming density a function of entropy. The constant equilibria are shown to be stable to infinitesimal disturbances, indicating local well-posedness of the new theory near the constant equilibria. They noticed an analogous approach had been taken by Scott [15,16] for thermoelastic materials. Details about the new constrained theory and local dynamical analysis are reported in [10].

3 Conclusion

We have demonstrated analytically that the thermomechanically consistent constrained theory for materials with prescribed temperature dependent density derived by Cao et al. [1] is locally ill-posed for transient problems due to the existence of the catastrophic Hadamard instability, despite its promising predictions of expansion cooling in steady-state Poiseuille flows of nonisothermal viscous fluids. This illustrates that a thermomechanically consistent constrained theory cannot be derived by simply assuming the material density a prescribed function of temperature. A satisfactory regularization of the theory within the same framework by allowing explicit dependence between the density and temperature as well as other additional thermodynamic variables remains

elusive. However, a well-posed thermomechanically consistent constrained theory for nonisothermal viscous fluids has been formulated lately by allowing the density a prescribed function of entropy. Details about the derivation and analysis of the new theory are given in [10].

Acknowledgment and Disclaimer

The author thanks Prof. S. E. Bechtel and M. G. Forest for helpful discussions on Cao et al.'s constrained theory. Effort sponsored by the Air Force Office of Scientific Research, Air Force Materials Command, USAF, under grant number F49620-96-1-0131 and F49620-99-1-0003 is gratefully acknowledged. The U.S. Government is authorized to reproduce and distribute reprints for governmental purposes notwithstanding any copyright notation thereon. The views and conclusions contained herein are those of the authors and should not be interpreted as necessarily representing the official policies or endorsements, either expressed or implied, of the Air Force Office of Scientific Research or the U.S. Government.

References

[1] Cao, D., Bechtel, S. E., and Forest, M. G., 1996, ''Thermomechanical Equations Governing a Material with Prescribed Temperature-Dependent Density with Application to Nonisothermal Plane Poiseuille Flow,'' ASME J. Appl. Mech., **63**, pp. 1011–1018.

[2] Winter, H. H., 1977, ''Viscous Dissipation in Shear Flows of Molten Polymers,'' Adv. Heat Transfer, **13**, pp. 205–267.

[3] Kase, S. and Matsuo, T., 1965, ''Studies on Melt Spinning, I. Fundamental Equations on the Dynamics of Melt Spinning,'' J. Polym. Sci., Part A: Gen. Pap., **3**, pp. 2541–2554.

[4] Sabhapathy, P. and Cheng, K. C., 1986, ''The Effects of Temperature-Dependent Viscosity and Coefficient of Thermal Expansion on the Stability of Laminar, Natural Convective Flow Along an Isothermal, Vertical Surface,'' Int. J. Heat Mass Transf., **29**, No. 10, pp. 1521–1529.

[5] Hayashi, S., Tani, K., Ishihara, H., and Yasuda, H., 1992, ''Fundamental Analysis of Hot Drawing in Spinline and Introduction of Basic Equations for Simulation,'' Sen-I Gakkaishi, **48**, No. 10, pp. 541–549.

[6] Bird, R. B., Armstrong, R. C., and Hassager, O., 1987, *Dynamics of Polymer Liquids*, Vol. V1, John Wiley and Sons, New York.

[7] Joseph, D. D., 1990, *Fluid Dynamics of Viscoelastic Liquids*, Springer-Verlag, New York.

[8] Drazin, P. G., and Reid, W. H., 1981, *Hydrodynamic Stability*, Cambridge University Press, Cambridge, U.K.

[9] Wang, Q., Bechtel, S. E., and Forest, M. G., 1995, ''Modeling and Computational of the Onset of Failure in Polymeric Liquid Filaments,'' J. Non-Newtonian Fluid Mech., **58**, pp. 97–129.

[10] Rooney, F. J., Wang, Q., Bechtel, S. E., and Forest, M. G., 1999, ''On the Stability of the Rest State of Thermomechanically Constrained Newtonian Fluids,'' submitted for publication.

[11] Gibbs, J. W., 1873, ''A Method of Geometrical Representation of the Thermodynamic Properties of Substances by Means of Surface,'' Trans. Connecticut Acad. II, 1873, Collected Works, pp. 33–54.

[12] Gibbs, J. W., 1878, ''On the Equilibrium of Heterogeneous Substances,'' Trans. Connecticut Acad. III, 1875–1878, Collected Works, pp. 55–354.

[13] Green, A. E., Naghdi, P. M., and Trapp, J. A., 1970, ''Thermodynamics of a Continuum with Internal Constraints,'' Int. J. Eng. Sci., **8**, pp. 891–908.

[14] Trapp, J. A., 1971, ''Reinforced Materials With Thermo-mechanical Constraints,'' Int. J. Eng. Sci., **9**, pp. 757–773.

[15] Scott, N. H., 1992, ''Linear Dynamical Stability in Constrained Thermoelasticity, II. Deformation-Entropy Constraints,'' Q. J. Mech. Appl. Math., **45**, pp. 651–662.

[16] Scott, N. H., 1996, ''Connections Between Deformation-Temperature and Deformation-Entropy Constraints and Near Constraints in Thermoelasticity,'' Int. J. Eng. Sci., **34**, pp. 1689–1704.

Combined Torsion, Circular and Axial Shearing of a Compressible Hyperelastic and Prestressed Tube

M. Zidi
Laboratoire de Mécanique Physique,
UPRESA CNRS 7052,
Université Paris 12,
61, avenue du Général De Gaulle,
94010 Cretéil Cédex, France
e-mail: zidi@univ-paris12.fr

In this paper, we study the combined torsion, circular and axial shearing of a compressible hyperelastic and prestressed tube. The analysis is carried out for a class of Ogden elastic material and the governing nonlinear equations are solved numerically using the Runge-Kutta method. The results reported present the effects of the torsion for different shearing loads on the local volume change and the circumferential stretch ratio. The effect of the second invariant-dependent behavior of polynomial materials is also investigated. [S0021-8936(00)01301-5]

1 Introduction

The combined axial and torsional shearing of a circular cylindrical tube for homogeneous isotropic incompressible nonlinearly elastic material was first considered by Ogden et al. [1]. The assumption that the material is incompressible was made in order to simplify the mathematical analysis. After, the same problem for compressible materials was solved numerically by Mioduchowski and Haddow [2]. They have considered the case in which the outer boundary does displace radially, and the results have been obtained for two strain energy functions (those proposed by Levinson and Burgess [3] and by Blatz and Ko [4]). Furthermore, Mioduchowski and Haddow [2] have discussed an approximate numerical solution in which the cylinder is divided into a number of co-axial thin-walled tubes of equal undeformed wall thickness. Distributions on the stresses and the radial stretch ratio of the current thickness to the undeformed wall thickness have been obtained. Ogden and Isherwood [5] have also presented the solution of some finite plane-strain problems for compressible, isotropic elastic solids by using the direct method. Carroll and Horgan [6] have also proposed several closed-form finite strain equilibrium solution for the Blatz–Ko constitutive law. These solutions have been obtained by the semi-inverse method, and each of the deformations is a nonisochoric generalization of a deformation which is controllable for homogeneous, isotropic, incompressible elastic solids. It must be emphasized that these previous studies [5,6] did not include the combined torsion with axial or circular shearing for a thick tube. Soon after, Tao et al. [7] studied circular shearing and torsion in generalized power-law neo-Hookean materials in the incompressible case. For certain values of the power-law exponent, an explicit exact solution has been given and in general cases the equations have been solved numerically. What is more, they have shown that the equations lose ellipticity for a certain range value of the power-law exponent. This problem of loss ellipticity has also been investigated for the generalized Blatz–Ko materials and for a complete discussion, we refer the reader to Knowles and Sternberg [8], Abeyaratne and Knowles [9], and Horgan [10]. Clearly, the problem of a circular tube composed of compressible elastic material and subjected to combined kinematics is rather tricky. Indeed, recent papers have explored the difficulties taken into account the torsion when the circular cylinder is subjected to shearing. Hence, the combined problems of the torsion with axial shearing ([11]) or with circular shearing ([12]) have recently been solved. However, the exact solutions have not been obtained when a class of Blatz–Ko material is considered and the highly nonlinear coupled differential equations have been integrated numerically. This paper is a sequel to these previous studies and our approach is to give a solution to the combined torsion, circular, and axial shearing problem. The cylindrical tube is considered prestressed ([13]) and made of a polynomial compressible material in its most general form, taking into account the effect of the second strain invariant. The hollow's cylinder inner and outer surfaces are fixed radially and are allowed to rotate by the torsion and the circular shear. Furthermore, the outer surface is allowed to displace in the longitudinal direction by the axial shear. The study is carried out using a particular Ogden constitutive equation which was used by Le Tallec and Vidrascu [14] to apply the augmented Lagrangian techniques for the numerical solution of equilibrium problems of compressible hyperelastic bodies subjected to large deformations. Based on a recent approach ([11,12,15]) the coupled nonlinear differential equations governing this new problem are solved by the Runge-Kutta method completed with an iterative process to obtain the local volume change and the circumferential stretch ratio. We show the effects of the torsion when the tube is subjected to axial and circular shearing. The effect of the second invariant ([16]) is also investigated.

2 Formulation and Analysis of the Combined Torsion, Circular and Axial Shearing Problem

Consider a nonlinearly elastic sector of a circular cylinder defined by the angle Θ_0 (Fig. 1). Let us suppose that the tube undergoes two successive deformations. First, the cylinder is closed, which induces residual strains ([13]) and then it is subjected to torsion, circular and axial shearing. The mapping is described by

$$r=r(R), \quad \theta=\left(\frac{\pi}{\Theta_0}\right)\Theta+\psi Z+\phi(r), \quad z=Z+\omega(r), \qquad (1)$$

where (R,Θ,Z) and (r,θ,z) are, respectively, the reference and the deformed positions of a material particle in a cylindrical system. Here, ψ is a twist angle per unloaded length, ϕ is an angle which defines the circular shear, and $\omega(r)$ is an axial displacement which defines the axial shear. Let R_i and r_i denote, respectively, the inner surfaces of the cylinder in the reference state and in the deformed state (R_e and r_e are the outer surfaces).

Contributed by the Applied Mechanics Division of THE AMERICAN SOCIETY OF MECHANICAL ENGINEERS for publication in the ASME JOURNAL OF APPLIED MECHANICS. Manuscript received by the ASME Applied Mechanics Division, Jan. 6, 1999; final revision, Oct. 12, 1999. Associate Technical Editor: M. M. Carroll. Discussion on the paper should be addressed to the Technical Editor, Professor Lewis T. Wheeler, Department of Mechanical Engineering, University of Houston, Houston, TX 77204-4792, and will be accepted until four months after final publication of the paper itself in the ASME JOURNAL OF APPLIED MECHANICS.

It follows from Eq. (1) that the physical components of the deformation gradient **F**, the left Cauchy-Green tensor **B**, and its inverse have the following representation in a cylindrical system:

$$\mathbf{F}=\begin{bmatrix} \dot{r} & 0 & 0 \\ r\dot{r}\dot{\phi} & \dfrac{r}{R}\dfrac{\pi}{\Theta_0} & r\psi \\ \dot{r}\dot{\omega} & 0 & 1 \end{bmatrix}=\begin{bmatrix} \lambda_r & 0 & 0 \\ K_1\lambda_r & \dfrac{\lambda_\theta \pi}{\Theta_0} & r\psi \\ K_2\lambda_r & 0 & 1 \end{bmatrix}, \tag{2}$$

$$\mathbf{B}=\begin{bmatrix} \lambda_r^2 & K_1\lambda_r^2 & K_2\lambda_r^2 \\ K_1\lambda_r^2 & (K_1\lambda_r)^2+\left(\lambda_\theta\dfrac{\pi}{\Theta_0}\right)^2+(r\psi)^2 & K_1K_2\lambda_r^2+r\psi \\ K_2\lambda_r^2 & K_1K_2\lambda_r^2+r\psi & (K_2\lambda_r)^2+1 \end{bmatrix}, \tag{3}$$

$$\mathbf{B}^{-1}=\left(\frac{\Theta_0}{\lambda_\theta\pi}\right)^2\begin{bmatrix} \dfrac{1}{\lambda_r^2}\left(\dfrac{\lambda_\theta\pi}{\Theta_0}\right)^2+(-K_1+K_2r\psi)^2+\left(K_2\dfrac{\lambda_\theta\pi}{\Theta_0}\right)^2 & -K_1+K_2r\psi & K_1r\psi-K_2\left[(r\psi)^2+\left(\dfrac{\lambda_\theta\pi}{\Theta_0}\right)^2\right] \\ -K_1+K_2r\psi & 1 & -r\psi \\ K_1r\psi-K_2\left[(r\psi)^2+\left(\dfrac{\lambda_\theta\pi}{\Theta_0}\right)^2\right] & -r\psi & (r\psi)^2+\left(\dfrac{\lambda_\theta\pi}{\Theta_0}\right)^2 \end{bmatrix}, \tag{4}$$

where the dot denotes the differentiation with respect to the argument, K_1, K_2, λ_r, and λ_θ are, respectively, the local shear measures, the radial, and the circumferential stretch ratio.

The principal invariants of **B** are

$$J_1=\mathrm{Tr}\,\mathbf{B}=\lambda_r^2(1+K_1^2+K_2^2)+\left(\frac{\lambda_\theta\pi}{\Theta_0}\right)^2+(r\psi)^2+1,$$

$$J_2=\mathrm{Tr}\,\mathbf{B}^{-1}=\frac{1}{\lambda_r^2}+\left(\frac{\Theta_0}{\lambda_\theta\pi}\right)^2[1+(-K_1+K_2r\psi)^2+(r\psi)^2]+1+K_2^2,$$

$$J_3=\mathrm{Det}\,\mathbf{F}=\lambda_r\lambda_\theta\frac{\pi}{\Theta_0}. \tag{5}$$

The deformation equation (1) is inhomogeneous and thus is not possible in all compressible isotropic elastic material. For that reason, the material of the tube is assumed to be polynomial compressible material [14] whose strain energy density function is expressed as

$$W(J_1,J_2,J_3)=\frac{C_1}{2}(J_1-3)+\frac{C_2}{2}(J_2J_3^2-3)+a(J_3^2-1)-(C_1+2C_2+2a)\mathrm{Log}\,J_3, \tag{6}$$

where C_1, C_2, and a are constant material parameters.

The constitutive equation has the form [17]

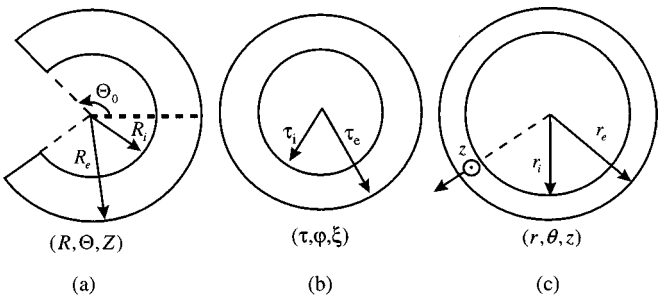

Fig. 1 Cross section of the tube in the stress-free (*a*), unloaded (*b*), and loaded configuration (*c*)

$$\bar{\sigma}=\frac{\sigma}{C_1}=\bar{\beta}_0\mathbf{1}+\bar{\beta}_1\mathbf{B}+\bar{\beta}_{-1}\mathbf{B}^{-1}, \tag{7}$$

where σ is the Cauchy stress tensor and **1** is the identity tensor. The elastic response functions $\bar{\beta}_k$ in the constitutive equation (7) for the strain energy equation (6) are given by

$$\bar{\beta}_0=\frac{1}{C_1}\frac{\partial W}{\partial J_3}=\alpha J_2J_3+\gamma J_3+\frac{\delta}{J_3},\quad \bar{\beta}_1=\frac{2}{C_1J_3}\frac{\partial W}{\partial J_1}=\frac{1}{J_3},$$

$$\bar{\beta}_{-1}=-\frac{2}{C_1J_3}\frac{\partial W}{\partial J_2}=-\alpha J_3, \tag{8}$$

where

$$\alpha=\frac{C_2}{C_1},\quad \gamma=\frac{2a}{C_1}$$

and

$$\delta=-(1+2\alpha+\gamma).$$

Using Eqs. (3) and (4), the nondimensional stress components from the constitutive Eq. (7) with respect to cylindrical coordinates are found to be

$$\bar{\sigma}_{rr}=\bar{\beta}_0(J_2,J_3)+J_3\left(\frac{\Theta_0}{\lambda_\theta\pi}\right)^2[1-\alpha(-K_1+K_2r\psi)^2]-\frac{\alpha}{J_3}\left(\frac{\lambda_\theta\pi}{\Theta_0}\right)^2-\alpha J_3K_2^2,$$

$$\bar{\sigma}_{\theta\theta}=\bar{\beta}_0(J_2,J_3)+J_3\left(\frac{\Theta_0}{\lambda_\theta\pi}\right)^2(K_1^2-\alpha)+\frac{1}{J_3}\left[\left(\frac{\lambda_\theta\pi}{\Theta_0}\right)^2+(r\psi)^2\right],$$

$$\bar{\sigma}_{zz}=\bar{\beta}_0(J_2,J_3)+J_3\left(\frac{\Theta_0}{\lambda_\theta\pi}\right)^2\left[K_2^2-\alpha(r\psi)^2-\alpha\left(\frac{\lambda_\theta\pi}{\Theta_0}\right)^2\right]+\frac{1}{J_3}$$

$$\bar{\sigma}_{r\theta}=J_3\left(\frac{\Theta_0}{\lambda_\theta\pi}\right)^2[(1+\alpha)K_1-\alpha K_2r\psi)],$$

$$\bar{\sigma}_{z\theta}=J_3\left(\frac{\Theta_0}{\lambda_\theta\pi}\right)^2(K_1K_2+\alpha r\psi)+\frac{r\psi}{J_3},$$

$$\bar{\sigma}_{rz}=J_3\left(\frac{\Theta_0}{\lambda_\theta\pi}\right)^2[K_2-\alpha r\psi(K_1-K_2r\psi)]+\alpha J_3K_2. \tag{9}$$

We use $\bar{r}=r/R_i$, $\bar{R}=R/R_i$, and $\bar{z}=z/R_i$ as nondimensional variables. From Eq. (9), the equilibrium equations in the absence of body forces are

$$\frac{d\bar{\sigma}_{rr}}{d\bar{r}}+\frac{\bar{\sigma}_{rr}-\bar{\sigma}_{\theta\theta}}{\bar{r}}=0 \tag{10}$$

$$\frac{d\bar{\sigma}_{r\theta}}{d\bar{r}}+\frac{2\bar{\sigma}_{r\theta}}{\bar{r}}=0 \tag{11}$$

$$\frac{d\bar{\sigma}_{rz}}{d\bar{r}}+\frac{\bar{\sigma}_{rz}}{\bar{r}}=0. \tag{12}$$

Equations (11) and (12) can be solved for the circumferential shear stress and for the axial shear stress distributions as follows:

$$\bar{\sigma}_{r\theta}=\frac{\bar{M}_1}{\bar{r}^2}, \tag{13}$$

$$\bar{\sigma}_{rz}=\frac{\bar{M}_2}{\bar{r}}, \tag{14}$$

where $\bar{M}_1$ and $\bar{M}_2$ are the nondimensional moments per unit length. Then, from Eqs. (7), (13), and (14), the expressions for the local shear measures K_1 and K_2 are

$$K_1=\frac{1}{\Delta}\left[A\frac{\bar{M}_1}{\bar{r}^2}-B\frac{\bar{M}_2}{\bar{r}}\right],\quad K_2=\frac{1}{\Delta}\left[C\frac{\bar{M}_2}{\bar{r}}-B\frac{\bar{M}_1}{\bar{r}^2}\right] \tag{15}$$

with $\Delta=AC-B^2$, where A, B, and C are expressed in terms of the material element volume ratio J_3, stretch ratio λ_θ as follows:

$$\begin{aligned} A&=J_3\left(\frac{\Theta_0}{\lambda_\theta\pi}\right)^2\left\{1+\alpha\left[(\bar{r}\bar{R}_i\psi)^2+\left(\frac{\lambda_\theta\pi}{\Theta_0}\right)^2\right]\right\},\\ B&=-\alpha J_3\left(\frac{\Theta_0}{\lambda_\theta\pi}\right)^2\bar{r}\bar{R}_i\psi,\quad C=J_3\left(\frac{\Theta_0}{\lambda_\theta\pi}\right)^2(1+\alpha). \end{aligned} \tag{16}$$

Then, using Eqs. (7) and (15), (11) and (12) are automatically satisfied because the form of the constitutive equation.

On the other hand, using equation $\lambda_r=(J_3/\lambda_\theta)(\Theta_0/\pi)$ and on substitution from Eq. (15), the normalized Cauchy stress tensor can be written from $\bar{r}$, J_3, and λ_θ, and the result is noted $\bar{\bar{\sigma}}$. Then, it easily follows that from Eq. (10), we have a system of nonlinear ordinary differential equations for $\lambda_\theta(\bar{r})$ and $J_3(\bar{r})$ which can be written as

$$\frac{d\lambda_\theta}{d\bar{r}}=\frac{\lambda_\theta}{\bar{r}}\left(1-\frac{\lambda_\theta^2}{J_3}\frac{\pi}{\Theta_0}\right) \tag{17}$$

$$\frac{dJ_3}{d\bar{r}}=\left(\frac{d\bar{\bar{\sigma}}_{rr}}{d\bar{r}}-\frac{\partial\bar{\bar{\sigma}}_{rr}}{\partial\bar{r}}-\frac{\partial\bar{\bar{\sigma}}_{rr}}{\partial\lambda_\theta}\frac{d\lambda_\theta}{d\bar{r}}\right)\left(\frac{\partial\bar{\bar{\sigma}}_{rr}}{\partial J_3}\right)^{-1} \tag{18}$$

where

$$\begin{aligned} \frac{d\bar{\bar{\sigma}}_{rr}}{d\bar{r}}=&-\frac{J_3}{\bar{r}}\left(\frac{\Theta_0}{\lambda_\theta\pi}\right)^2\left\{1-\alpha(-K_1+K_2\bar{r}\bar{R}_i\psi)^2-\alpha\left(\frac{K_2\lambda_\theta\pi}{\Theta_0}\right)^2\right.\\ &\left.-K_1^2+\alpha\right\}+\frac{1}{\bar{r}J_3}\left(\frac{\lambda_\theta\pi}{\Theta_0}\right)^2\left\{1+\alpha+\left(\frac{\bar{r}\bar{R}_i\psi\Theta_0}{\lambda_\theta\pi}\right)^2\right\}, \end{aligned} \tag{19}$$

$$\frac{\partial\bar{\bar{\sigma}}_{rr}}{\partial\bar{r}}=2\alpha J_3\left(\frac{\Theta_0}{\lambda_\theta\pi}\right)^2\bar{r}(R_i\psi)^2, \tag{20}$$

$$\frac{\partial\bar{\bar{\sigma}}_{rr}}{\partial\lambda_\theta}=\frac{-2J_3}{\lambda_\theta^3}\left(\frac{\Theta_0}{\pi}\right)^2\{1+\alpha[1+(\bar{r}\bar{R}_i\psi)^2]\}, \tag{21}$$

$$\frac{\partial\bar{\bar{\sigma}}_{rr}}{\partial J_3}=\frac{\delta}{J_3^2}+\left(\frac{\Theta_0}{\lambda_\theta\pi}\right)^2[1+\alpha(1+(\bar{r}\bar{R}_i\psi)^2]+\alpha+\gamma. \tag{22}$$

To complete the boundary value problem, we consider the boundary conditions such as $r(R_i)=R_i$ and $r(R_e)=R_e$, which imply

$$\lambda_\theta(\bar{r}_i)=\lambda_\theta(\bar{r}_e)=1, \tag{23}$$

where $\bar{r}_i=1$ and $\bar{r}_e=R_e/R_i$.

Equations (17) and (18) subject to the conditions of Eq. (23) form a boundary value problem for $\lambda_\theta(\bar{r})$ and $J_3(\bar{r})$ where $\bar{M}_1$ and $\bar{M}_2$ are fixed. The reader should consult Wineman's paper [15] where a similar formulation of a related boundary value problem is carried out in complete detail.

Furthermore, it is instructive to obtain the necessary and sufficient conditions on the strain energy function equation (6) for pure kinematics without radial displacement or local volume change ([15,18–21]). In these cases we have $\lambda_r=\lambda_\theta=J_3=1$.

For pure torsion ($\bar{M}_1=\bar{M}_2=0$), it follows from Eqs. (15), (16), (5), and (8),

$$K_1=K_2=0,\quad J_2=3+(\bar{r}\bar{R}_i\psi)^2,\quad \bar{\beta}_0=3\alpha+\gamma+\delta+\alpha(\bar{r}\bar{R}_i\psi)^2. \tag{24}$$

Then, from Eq. (9) we obtain

$$\begin{aligned} \bar{\bar{\sigma}}_{rr}&=2\alpha+\gamma+\delta+1+\alpha(\bar{r}\bar{R}_i\psi)^2,\\ \bar{\bar{\sigma}}_{\theta\theta}&=2\alpha+\gamma+\delta+1+(\alpha+1)(\bar{r}\bar{R}_i\psi)^2. \end{aligned} \tag{25}$$

Substituting (25) in equilibrium Eq. (10), yields

$$(2\alpha-1)\bar{r}(R_i\psi)^2=0. \tag{26}$$

This is verified if $\alpha=\frac{1}{2}$ for any twist angle ψ.

For pure circular shear ($\bar{M}_2=\psi=0$), it follows from Eqs. (15), (16), (5), and (8),

$$\begin{aligned} K_1&=\frac{\bar{M}_1}{(1+\alpha)\bar{r}^2},\quad J_2=3+\left[\frac{\bar{M}_1}{(1+\alpha)\bar{r}^2}\right]^2,\\ \bar{\beta}_0&=3\alpha+\gamma+\delta+\alpha\left[\frac{\bar{M}_1}{(1+\alpha)\bar{r}^2}\right]^2. \end{aligned} \tag{27}$$

Then, from Eq. (9) we obtain

$$\begin{aligned} \bar{\bar{\sigma}}_{rr}&=2\alpha+\gamma+\delta+1,\\ \bar{\bar{\sigma}}_{\theta\theta}&=2\alpha+\gamma+\delta+1+(1+\alpha)\left[\frac{\bar{M}_1}{(1+\alpha)\bar{r}^2}\right]^2. \end{aligned} \tag{28}$$

Substituting Eq. (28) in equilibrium Eq. (10), yields

$$-\frac{1}{(1+\alpha)}\frac{\bar{M}_1^2}{\bar{r}^5}=0. \tag{29}$$

This is not satisfied for any nonzero applied moment $\bar{M}_1$.

For pure axial shear ($\bar{M}_1=\psi=0$), it follows from Eqs. (15), (16), (5), and (8),

$$\begin{aligned} K_2&=\frac{\bar{M}_2}{(1+\alpha)\bar{r}},\quad J_2=3+\left[\frac{\bar{M}_2}{(1+\alpha)\bar{r}}\right]^2,\\ \bar{\beta}_0&=3\alpha+\gamma+\delta+\alpha\left[\frac{\bar{M}_2}{(1+\alpha)\bar{r}}\right]^2. \end{aligned} \tag{30}$$

Then, from Eq. (9) we obtain

$$\bar{\bar{\sigma}}_{rr}=2\alpha+\gamma+\delta+1,\quad \bar{\bar{\sigma}}_{\theta\theta}=2\alpha+\gamma+\delta+1+\alpha\left[\frac{\bar{M}_2}{(1+\alpha)\bar{r}}\right]^2. \tag{31}$$

Substituting Eq. (31) in equilibrium Eq. (10), yield

$$-\frac{\alpha}{(1+\alpha)^2}\frac{\bar{M}_2^2}{\bar{r}^3}=0 \tag{32}$$

This is verified if $\alpha=0$ for any applied moment $\bar{M}_2$.

3 Results and Discussion

Equations (17) and (18) are integrated numerically using the fourth-order Runge-Kutta method, complete with an iterative process ([15]). Fifty-one points along the radial coordinate are used in the numerical integration of the governing equations. First, for given values of $\bar{M}_1$ and $\bar{M}_2$, $J(\bar{r}_i)$ is estimated. Using these values and the boundary condition $\lambda_\theta(\bar{r}_i)=1$, Eqs. (17) and (18) are integrated for $\bar{r}=[\bar{r}_i,\bar{r}_e]$. The value of the circumferential stretch ratio is checked against the boundary condition $\lambda_\theta(\bar{r}_e)=1$. Then, iterations are used to adjust the estimate for $J(\bar{r}_i)$ until the boundary condition $\lambda_\theta(\bar{r}_e)=1$ is satisfied. As an illustrative example, we take $\bar{r}_e=2$, $\Theta_0=180$ deg, $\gamma=0$, and three loading conditions $(\bar{M}_1,\bar{M}_2)=\{(1,0),(0,1),(1,1)\}$. We focus our attention when the cylinder is subjected to different twisting moments $\psi=\{0\text{ deg},15\text{ deg},30\text{ deg},45\text{ deg}\}$. Furthermore, we examine the influence of the second invariant defined by the value of the parameter α.

To begin with, we give the results for $\alpha=0.25$. Figures 2 and 3 show the distribution of circumferential stretch ratio and the volume ratio when $(\bar{M}_1,\bar{M}_2)=(0,1)$. As is made clear by the figures, an increase of ψ modifies the results. For each angle of twist ψ, the material element volume is decreased ($J<1$) at the inner support and increases with increasing $\bar{r}$ (Fig. 3). Near the outer shell, material element volume is increased ($J>1$). At approximately $\bar{r}=155$, the material element volume is unchanged. Since $\lambda_\theta<1$, the cylindrical surfaces move inward which is consistent with the volume change as shown in Fig. 2. It follows from Fig. 2 that the circumferential stretch ratio passes through a minimum. This minimum is smaller as ψ is greater. Furthermore, the complex nature of the system of Eqs. (17) and (18) governing the equilibrium problem of coupled deformations does not seem to permit one to study the existence and the uniqueness of the solution by an analytical method. However, it is worthy of note that the examination of Figs. 2 and 3 shows that these distributions are not perfectly smooth. This can be attributed to a loss of ellipticity of the governing partial differential equations as suggested by Simmonds and Warne [22]. Analogous examples for this loss of ellipticity can be found in different papers ([12,15]) and a comprehensive treatment of this problem may be found in the paper of Horgan [10]. On the other hand, when the loading conditions become $(\bar{M}_1,\bar{M}_2)=(1,1)$, the results do not change qualitatively. Indeed, as is shown in Figs. 4 and 5, only the intensities of distributions are modified and become smaller. In that case, it appears that the loss of ellipticity is less pronounced than in the above case when $(\bar{M}_1,\bar{M}_2)=(0,1)$. Plots for $(\bar{M}_1,\bar{M}_2)=(1,0)$ are omitted for the purpose of brevity. As we have observed, the results do not change qualitatively compared to the case $(\bar{M}_1,\bar{M}_2)=(0,1)$ and the distributions lie between the above plots ($(\bar{M}_1,\bar{M}_2)=(0,1)$ and $(\bar{M}_1,\bar{M}_2)=(1,1)$).

For the purposes of comparison, we have also studied the case $\alpha=0$ which corresponds to neglect the second invariant in Eq. (6). Figures 6 and 7 show the distribution of the circumferential stretch ratio and the volume ratio when $(\bar{M}_1,\bar{M}_2)=(0,1)$. As illustrated by the figures, it may be seen that varying ψ leads to a variation of results. As a result, the above remarks when $\alpha=0.25$ may also be claimed here. Note that relative to the above case $\alpha=0.25$, we have found the same results when $(\bar{M}_1,\bar{M}_2)=(1,0)$ and $(\bar{M}_1,\bar{M}_2)=(1,1)$. This is plotted in Figs. 8 and 9. Moreover, in contrast to the case $\alpha=0.25$, when $\alpha=0$, the loss of ellipticity does not occur and the distributions are always smooth. It is comparable with the results of Wineman and Waldron, Jr. [15] when they have omitted the second invariant in the Blatz-Ko strain energy function. Without going into further detail of the parametric study, it is important to point out that the results reported here do not change significantly when varying the intensity of the moments $\bar{M}_1$ and $\bar{M}_2$.

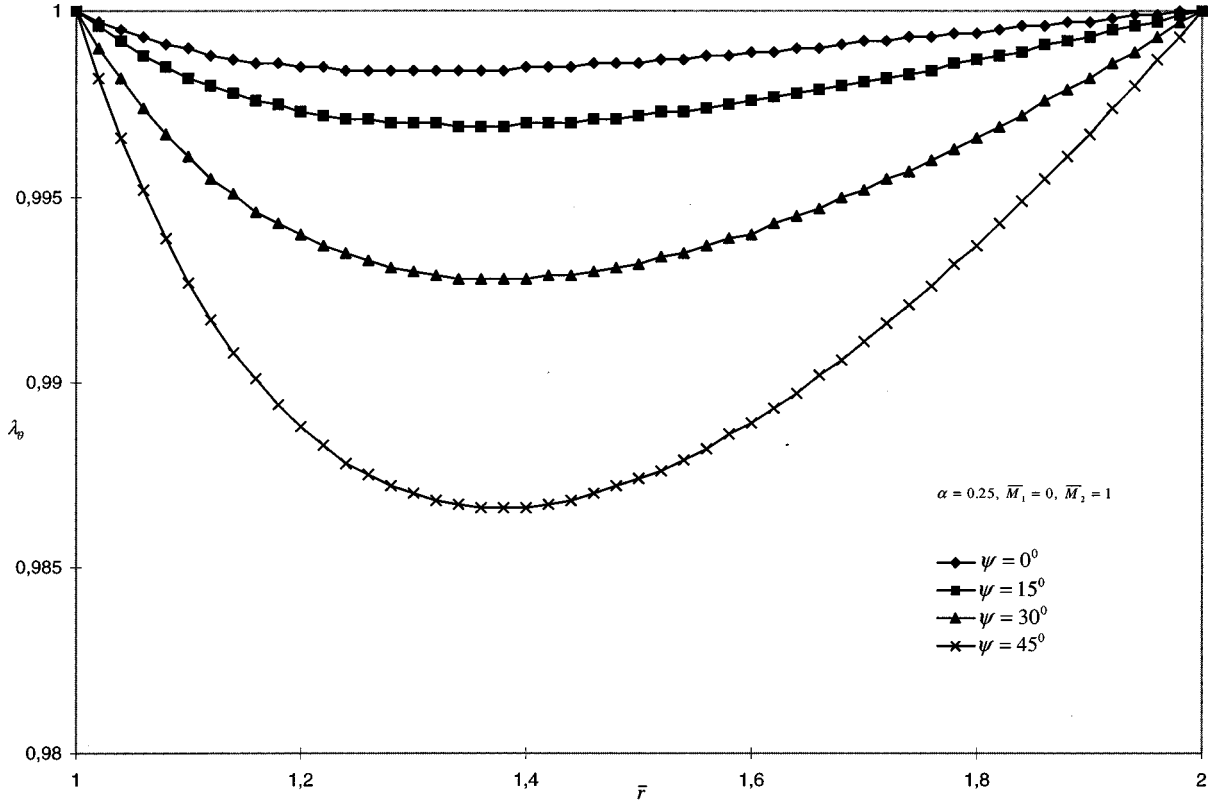

Fig. 2 Circumferential stretch ratio versus radius for different angles of twist when $\alpha=0.25$, $\bar{M}_1=0$, $\bar{M}_2=1$

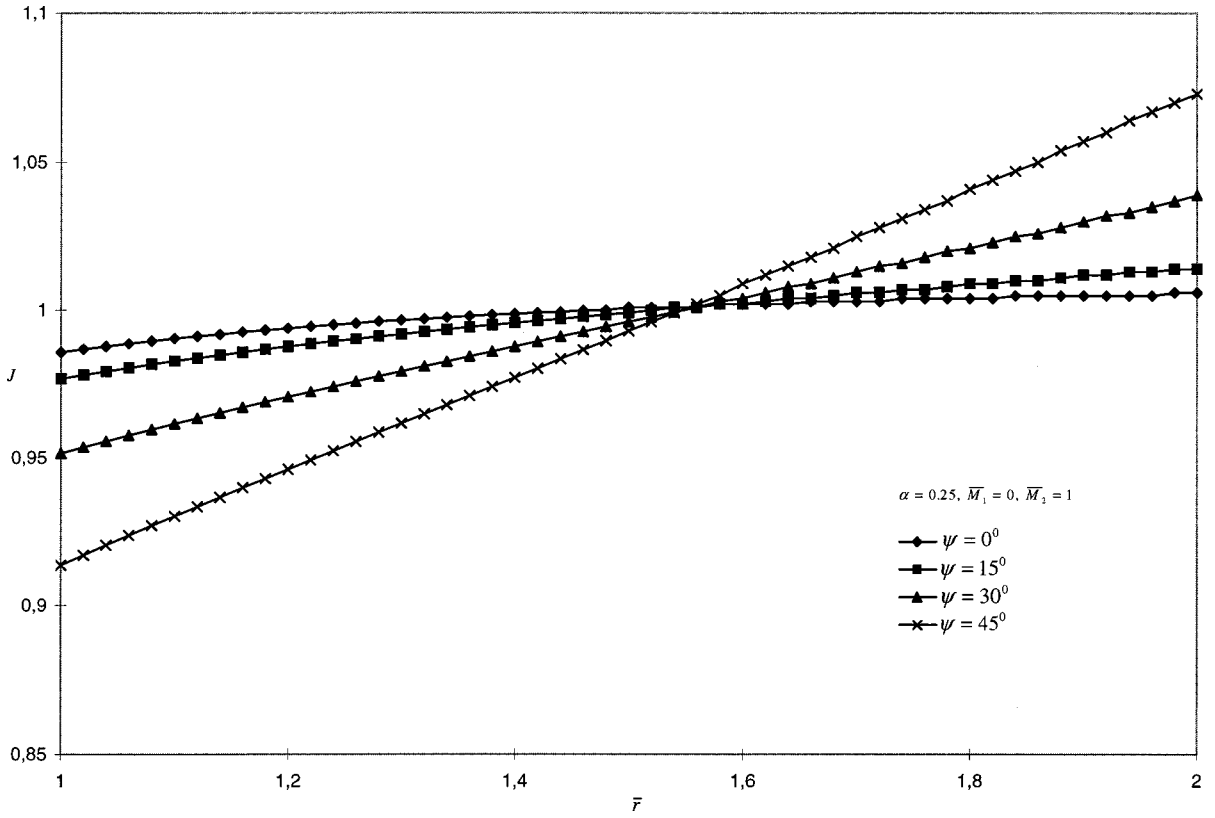

Fig. 3 Volume ratio versus radius for different angles of twist when $\alpha=0.25$, $\bar{M}_1=0$, $\bar{M}_2=1$

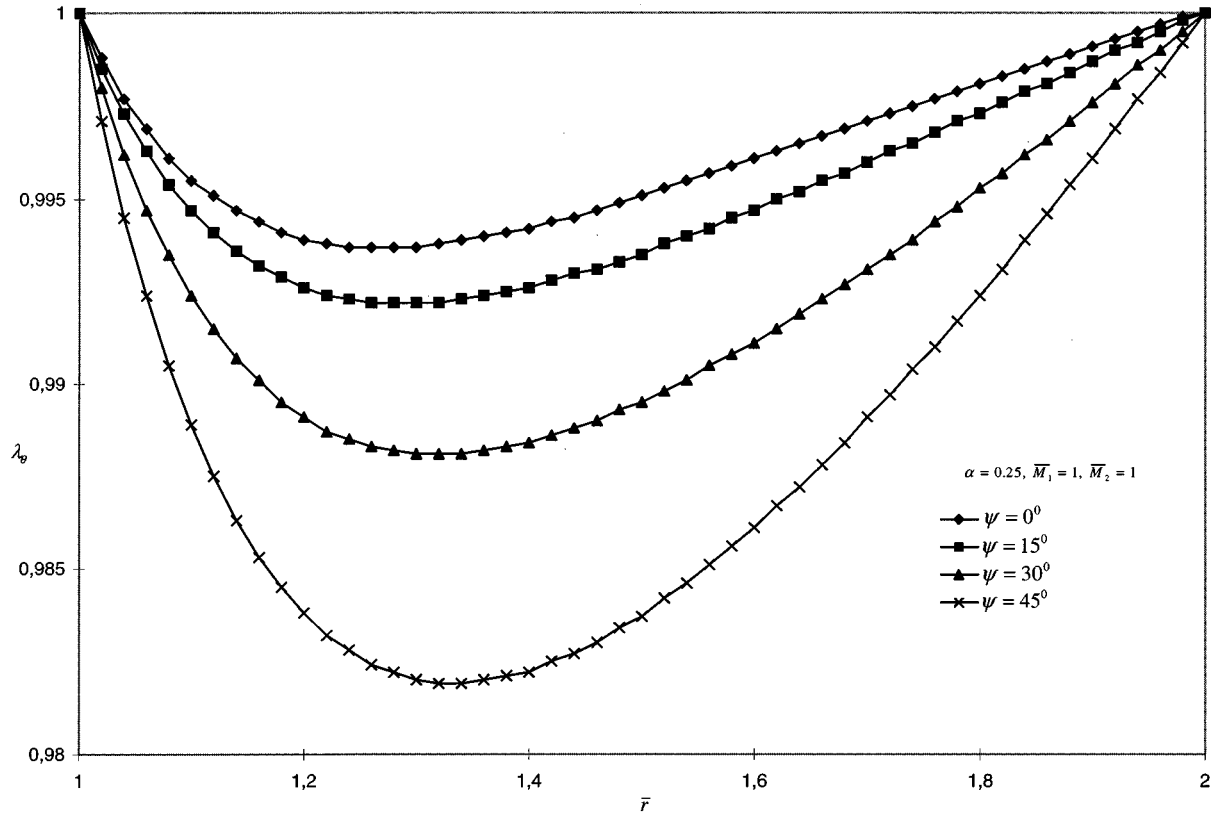

Fig. 4 Circumferential stretch ratio versus radius for different angles of twist when $\alpha=0.25$, $\bar{M}_1=1$, $\bar{M}_2=1$

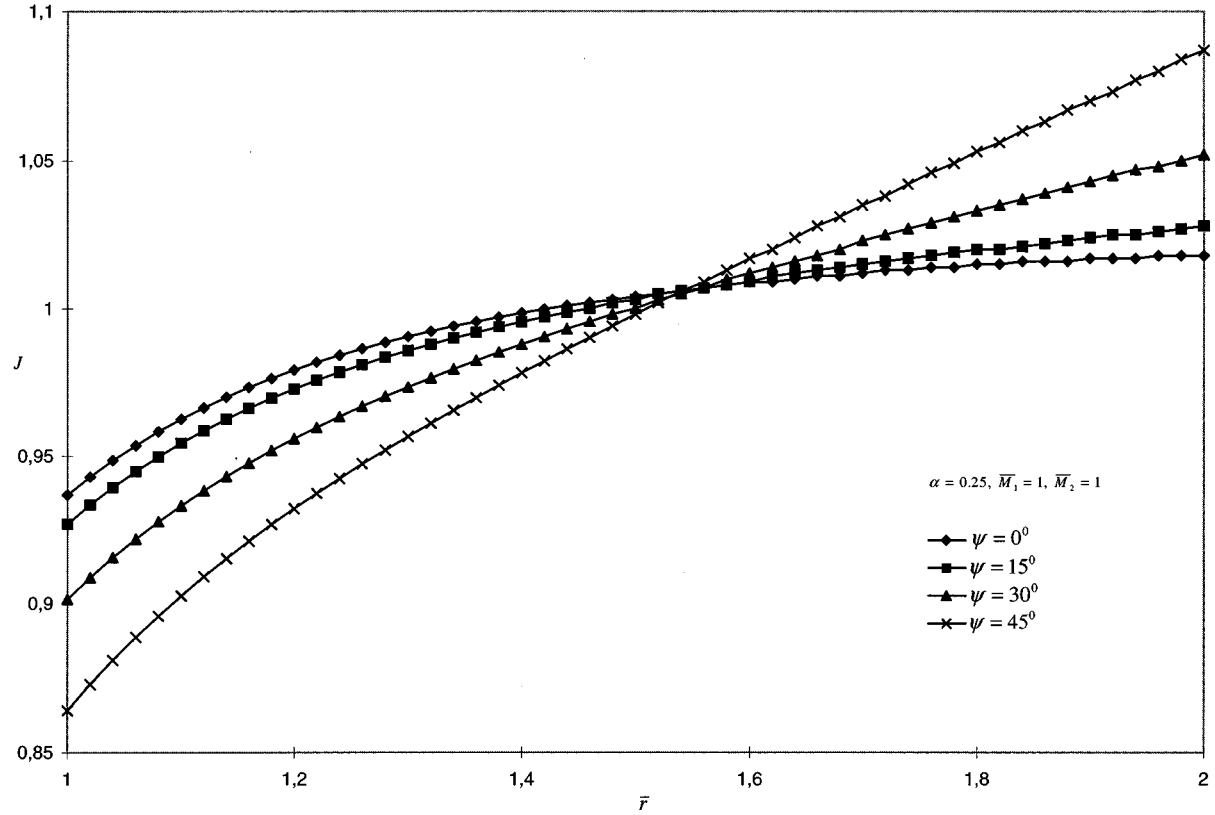

Fig. 5 Volume ratio versus radius for different angles of twist when $\alpha=0.25$, $\bar{M}_1=1$, $\bar{M}_2=1$

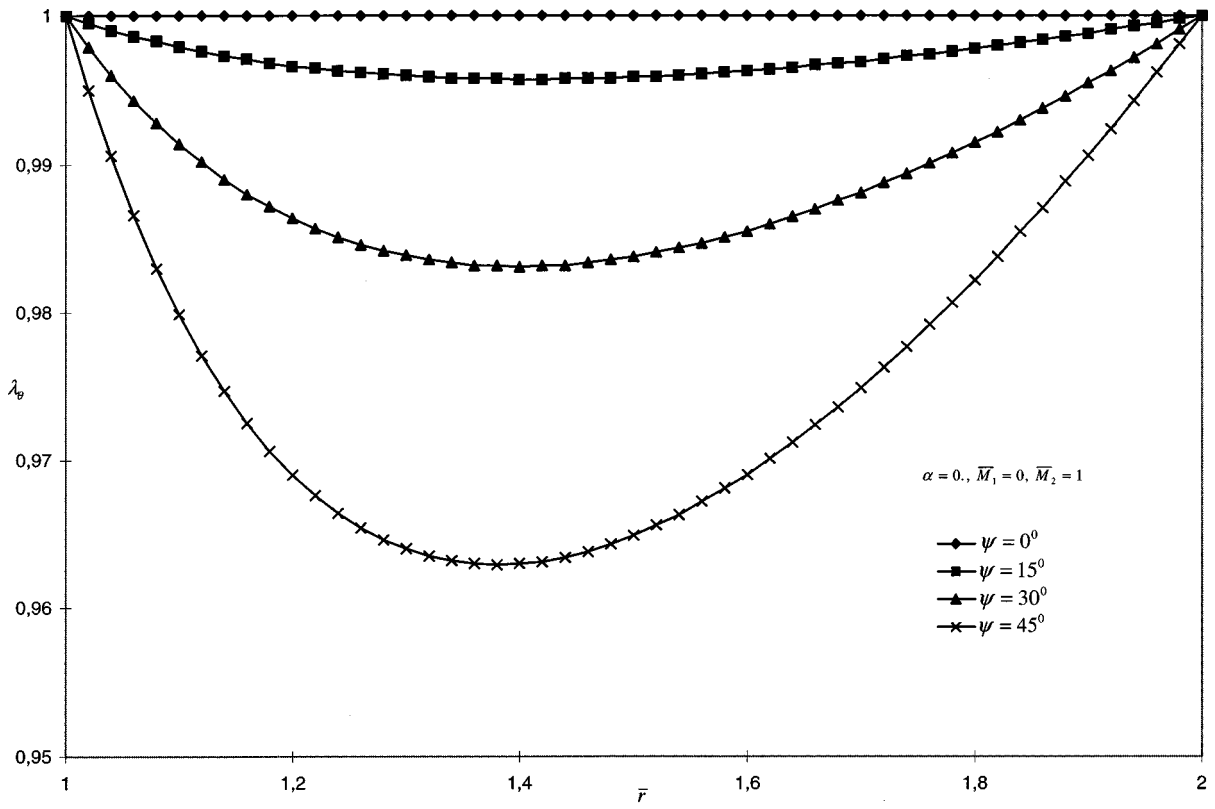

Fig. 6 Circumferential stretch ratio versus radius for different angles of twist when $\alpha=0$, $\bar{M}_1=0$, $\bar{M}_2=1$

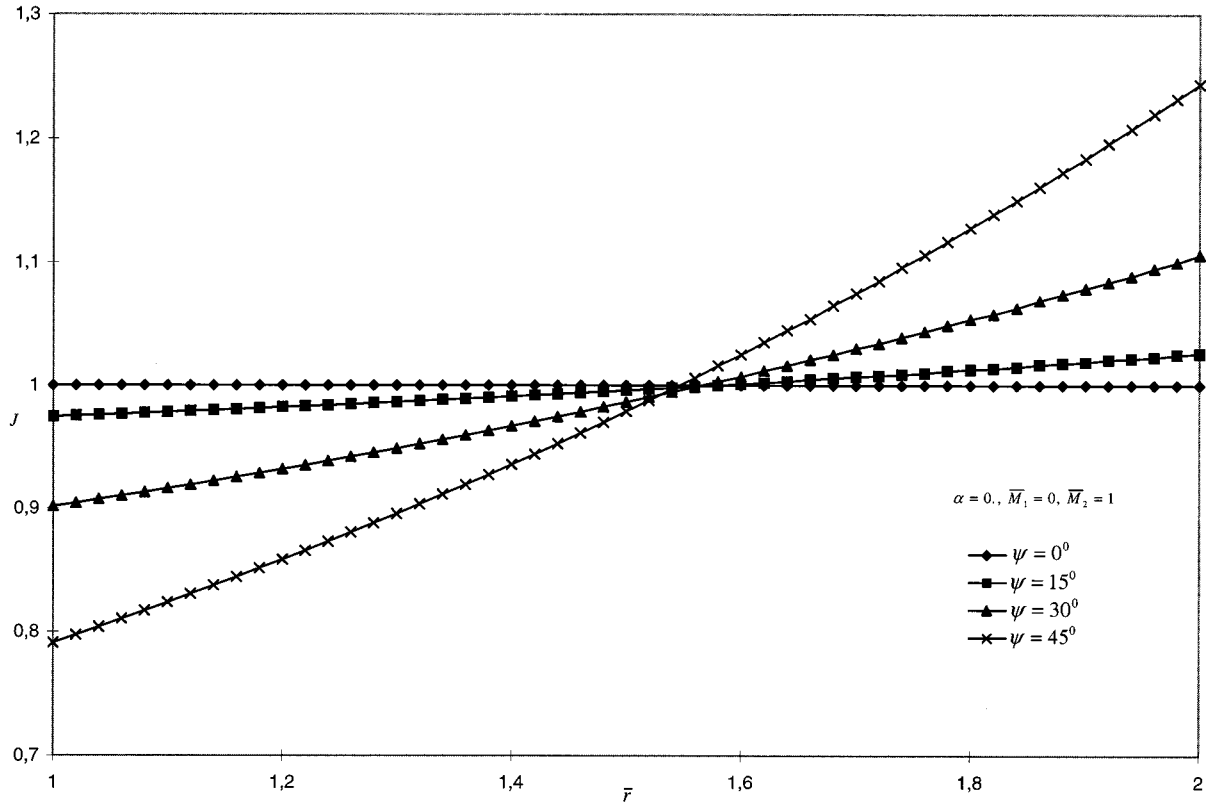

Fig. 7 Volume ratio versus radius for different angles of twist when $\alpha=0$, $\bar{M}_1=0$, $\bar{M}_2=1$

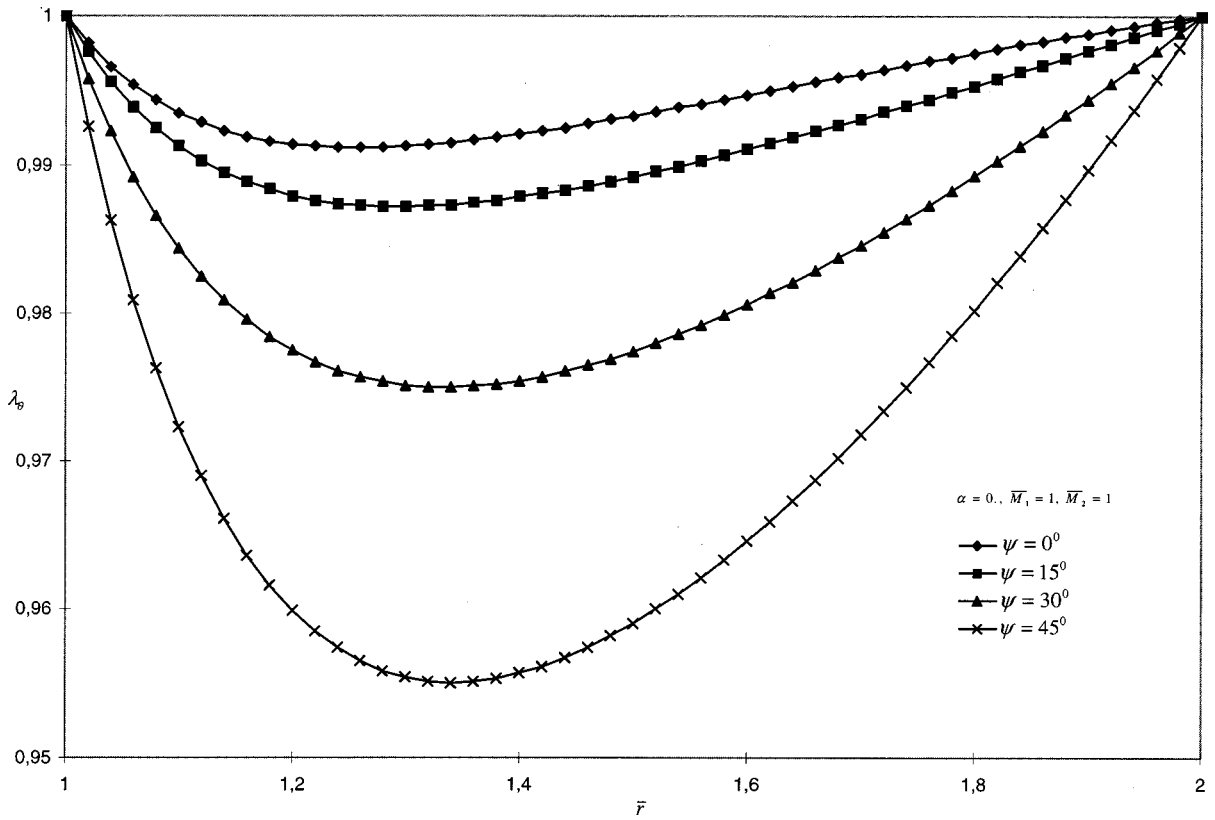

Fig. 8 Circumferential stretch ratio versus radius for different angles of twist when $\alpha=0$, $\bar{M}_1=1$, $\bar{M}_2=1$

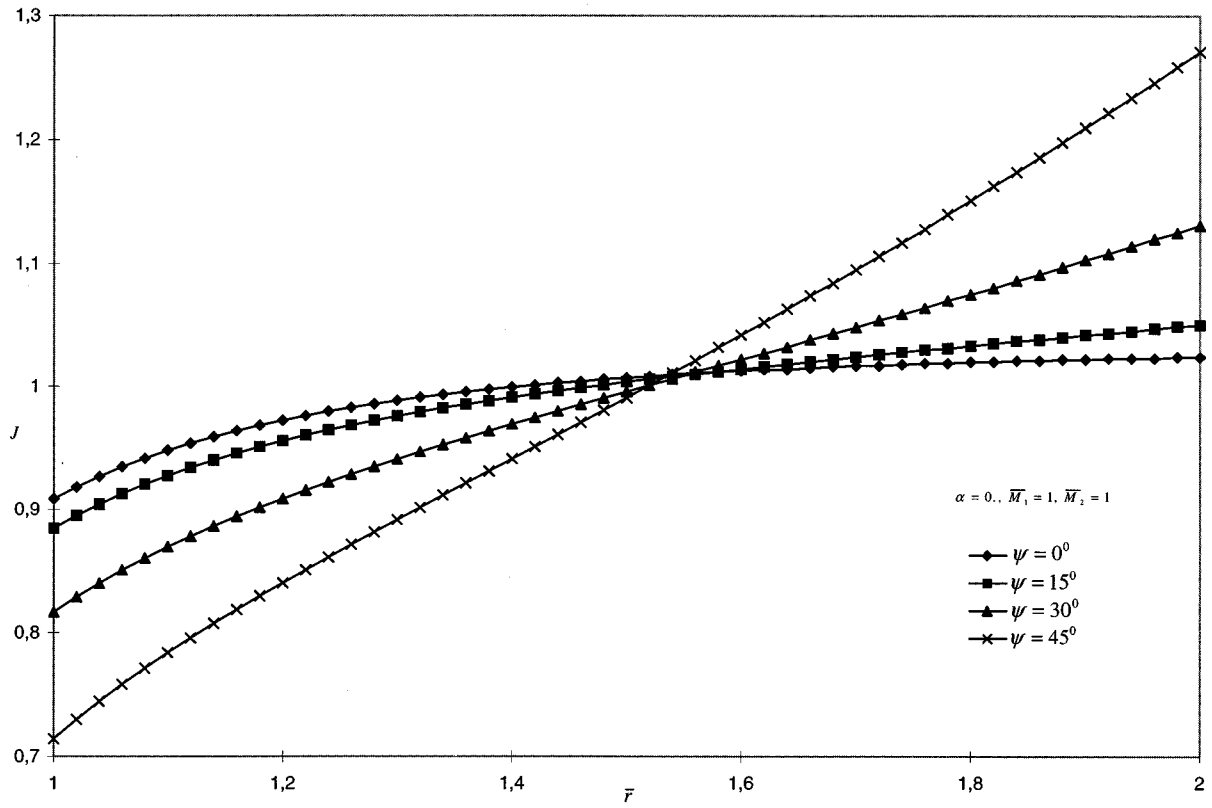

Fig. 9 Volume ratio versus radius for different angles of twist when $\alpha=0$, $\bar{M}_1=1$, $\bar{M}_2=1$

References

[1] Ogden, R. W., Chadwick, P., and Haddon, E. W., 1973, ''Combined Axial and Torsional Shear of Tube of Incompressible Isotropic Elastic Material,'' Q. J. Mech. Appl. Math., **26**, pp. 23–41.

[2] Mioduchowski, A., and Haddow, J. B., 1979, ''Combined Torsional and Axial Shear of a Compressible Hyperelastic Tube,'' ASME J. Appl. Mech., **46**, pp. 223–226.

[3] Levinson, M., and Burgess, I. W., 1971, ''A Comparison of Some Simple Constitutive Relations for Slightly Compressible Rubber-Like Materials,'' Int. J. Mech. Sci., **13**, pp. 563–572.

[4] Blatz, P. J., and Ko, W. L., 1962, ''Application of Finite Elastic Theory to the Deformation of Rubbery Materials,'' Trans. Soc. Rheol., **6**, pp. 223–251.

[5] Ogden, R. W., and Isherwood, D. A., 1978, ''Solution of Some Finite Plane-Strain Problems for Compressible Elastic Solids,'' Q. J. Mech. Appl. Math., **31**, pp. 219–249.

[6] Carroll, M. M., and Horgan, C. O., 1990, ''Finite Strain Solutions for a Compressible Elastic Solid,'' Q. Appl. Math., **48**, No. 4, pp. 767–780.

[7] Tao, L., Rajagopal, K. R., and Wineman, A. S., 1992, ''Circular Shearing and Torsion of Generalized Neo-Hookean Materials,'' IMA J. Appl. Math., **48**, pp. 23–37.

[8] Knowles, J. K., and Sternberg, E., 1975, ''On the Ellipticity of the Equations of Nonlinear Elastostatics for a Special Material,'' J. Elast., **5**, pp. 341–361.

[9] Abeyaratne, R., and Knowles, J. K., 1987, ''Non-elliptic Elastic Materials and the Modeling of Dissipative Mechanical Behavior: An Example,'' J. Elast., **18**, pp. 227–278.

[10] Horgan, C. O., 1996, ''Remarks on Ellipticity for the Generalized Blatz-Ko Constitutive Model for Compressible Nonlinearly Elastic Solid,'' J. Elast., **42**, pp. 165–176.

[11] Zidi, M., 1999, ''Torsion and Axial Shearing of a Compressible Hyperelastic Tube,'' Mech. Res. Commun., **26**, No. 2, pp. 245–252.

[12] Zidi, M., 2000, ''Circular Shearing and Torsion of a Compressible Hyperelastic and Prestressed Tube,'' Int. J. Non-Linear Mech., **35**, pp. 201–209.

[13] Sensening, C. B., 1965, ''Non Linear Theory for the Deformation of Prestressed Circular Plates and Rings,'' Commun. Pure Appl. Math., **18**, pp. 147–161.

[14] Le Tallec, P., and Vidrascu, M., 1984, ''A Numerical Method for Solving Equilibrium Problems of Compressible Hyperelastic Bodies in Large Deformations,'' Numer. Math., **43**, pp. 199–224.

[15] Wineman, A. S., and Waldron, Jr., W. K., 1995, ''Normal Stress Effects Induced During Circular Shear of a Compressible Non-linear Elastic Cylinder,'' Int. J. Non-Linear Mech., **30**, No. 3, pp. 323–339.

[16] Ertepinar, A., 1990, ''On the Finite Circumferential Shearing of Compressible Hyperelastic Tubes,'' Int. J. Eng. Sci., **18**, No. 9, pp. 889–896.

[17] Beatty, M. F., 1987, ''Topics in Finite Elasticity: Hyperelasticity of Rubber, Elastomers and Biological Tissues—With Examples,'' Appl. Mech. Rev., **40**, pp. 1699–1734.

[18] Polignone, D. A., and Horgan, C. O., 1991, ''Pure Torsion of Compressible Nonlinearly Elastic Circular Cylinders,'' Q. Appl. Math., **49**, No. 3, pp. 591–607.

[19] Polignone, D. A., and Horgan, C. O., 1992, ''Axisymmetric Finite Anti-plane Shear of Compressible Nonlinearly Elastic Circular Tubes,'' Q. Appl. Math., **50**, pp. 323–341.

[20] Haughton, D. M., 1993, ''Shearing of Compressible Elastic Cylinders,'' Q. J. Mech. Appl. Math., **46**, pp. 471–486.

[21] Polignone, D. A., and Horgan, C. O., 1994, ''Pure Circular Shear of Compressible Non-linearly Elastic Tubes,'' Q. Appl. Math., **50**, pp. 113–131.

[22] Simmonds, J. G., and Warne, P., 1992, ''Azimuthal Shear of Compressible or Incompressible, Non-linearly Elastic Polar Orthotropic Tubes of Infinite Extent,'' Int. J. Non-Linear Mech., **27**, No. 3, pp. 447–464.

Modeling of Interphases in Fiber-Reinforced Composites Under Transverse Loading Using the Boundary Element Method

Y. J. Liu[1]
Assistant Professor,
e-mail: Yijun.Liu@uc.edu
Mem. ASME

N. Xu
Graduate Student
Department of Mechanical, Industrial,
and Nuclear Engineering,
P.O. Box 210072,
University of Cincinnati,
Cincinnati, OH 45221-0072

J. F. Luo
Graduate Student,
Department of Mechanical Engineering,
University of California,
Berkeley, CA 94720-1740

In this paper, interphases in unidirectional fiber-reinforced composites under transverse loading are modeled by an advanced boundary element method based on the elasticity theory. The interphases are regarded as elastic layers between the fiber and matrix, as opposed to the spring-like models in the boundary element method literature. Both cylinder and square unit cell models of the fiber-interphase-matrix systems are considered. The effects of varying the modulus and thickness (including nonuniform thickness) of the interphases with different fiber volume fractions are investigated. Numerical results demonstrate that the developed boundary element method is very accurate and efficient in determining interface stresses and effective elastic moduli of fiber-reinforced composites with the presence of interphases of arbitrarily small thickness. Results also show that the interphase properties have significant effect on the micromechanical behaviors of the fiber-reinforced composites when the fiber volume fractions are large.
[S0021-8936(00)02501-0]

1 Introduction

Interphases, or interfacial zones, in fiber-reinforced composite materials are the thin layers between the fiber and matrix (Fig. 1). These interphases are formed due to, for example, chemical reactions between the fiber and matrix materials, or the use of protective coatings on the fiber during manufacturing. The fiber, which is employed to reinforce the matrix material in the fiber direction, is usually much stiffer than the matrix material. Different levels of stresses and deformations can develop in the fiber and matrix materials, because of this mismatch in the material properties. It is the interphases that bond the fiber and matrix together to ensure the desired functionality of the composite material under external loads. Although small in thickness, interphases can significantly affect the overall mechanical properties of the fiber-reinforced composites, as observed in many studies ([1–9]). It is the weakest link in the load path, and consequently most failures in fiber-reinforced composites, such as debonding, fiber pullout, and matrix cracking, occur in or near this region. Thus, it is crucial to fully understand the mechanism and effects of the interphases in fiber-reinforced composites. Numerical techniques such as the finite element method and the boundary element method are indispensable tools in serving this purpose.

Numerical modeling of fiber-reinforced composite materials presents great challenges to both the finite element method and boundary element method especially for the analysis at the microstructural level. The main issue in the micromechanics analysis of fiber-reinforced composites is to predict the interface stresses for durability assessment, and to determine the engineering properties, such as the effective Young's moduli, Poisson's ratios, and thermal expansion coefficients needed for structural analysis. Idealized models using the unit cell (or representative volume element) concept are usually employed in micromechanics analysis, in which the fibers are assumed to be infinitely long and packed in a square or hexagonal pattern (see, e.g., [10,11,12]). Although only one fiber and the surrounding matrix are modeled in the unit cell approach, the presence of the interphase between the fiber and matrix still makes the finite element method and boundary element method modeling difficult, simply because of the thinness of the interphases which are at the micrometer level or below.

Many finite element models based on the two-dimensional elasticity theory have been developed to study the micromechanical properties of fiber-reinforced composites under transverse loading and with the presence of an interphase, for example, in [13,6,14], and [8], and most recently in [9]. In all these finite element method models, a layer of very fine finite elements was used between the fiber and matrix to model the interphase. Because of the thinness of the interphase, a large number of small finite elements are needed in these models, in order to avoid elements with large aspect ratios which can deteriorate the finite element method solutions. This, in turn, causes a large number of elements in the fiber and matrix regions because of the connectivity requirement in the finite element method. For instance, in [9], more than 3500 finite elements were used to model only *one quarter* of the chosen unit cell. With further smaller thickness of the interphase as compared with the diameter of the fiber, or nonuniform thickness, even more elements will be needed in the finite element method model. Thus, using finite elements based on the elasticity theory for the modeling of interphases can be costly and inefficient.

The boundary element method has been demonstrated to be a viable alternative to the finite element method due to its features of boundary-only discretization and high accuracy in stress analysis, especially in fracture analysis (see, e.g., [15–18]). For the analysis of micromechanical behaviors of fiber-reinforced composites using the boundary element method, there are very few publications in the literature, and all of the boundary element method models developed so far are two-dimensional ones based on perfect-bonding or spring-like interface conditions. No boundary element method models have been attempted earlier to model the interphases directly as an elastic region between the fiber and matrix.

Achenbach and Zhu [2] developed a two-dimensional model of

[1]To whom correspondence should be addressed.

Contributed by the Applied Mechanics Division of THE AMERICAN SOCIETY OF MECHANICAL ENGINEERS for publication in the ASME JOURNAL OF APPLIED MECHANICS. Manuscript received by the ASME Applied Mechanics Division, Sept. 23, 1998; final revision, Sept. 23, 1999. Associate Technical Editor: W. K. Liu. Discussion on the paper should be addressed to the Technical Editor, Professor Lewis T. Wheeler, Department of Mechanical Engineering, University of Houston, Houston, TX 77204-4792, and will be accepted until four months after final publication of the paper itself in the ASME JOURNAL OF APPLIED MECHANICS.

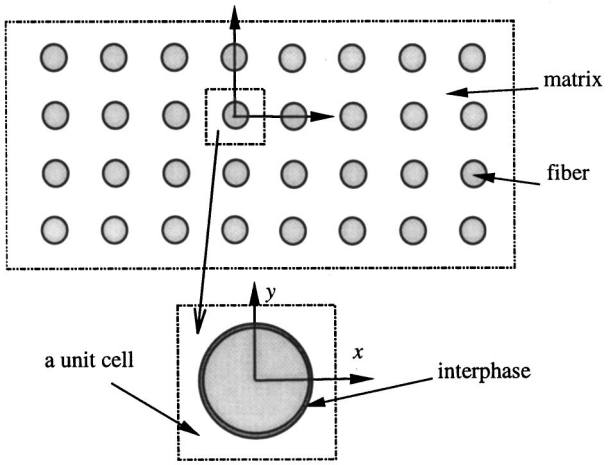

Fig. 1 The interphase in a fiber-reinforced composite

a square unit cell using the boundary element method. To study the effect of the interphase, the continuity of the tractions across the interface of fiber and matrix is maintained, while a linear relation between the displacement differences and the tractions across the interface is introduced. This simple relation represents a spring-like model of the interphase. The proportionality constants used in this model characterize the stiffness of the interphase. Based on this model, it was shown that the variations of the interphase parameters can cause pronounced changes in the stress distributions in the fiber and matrix. The initiation, propagation and arrest of the interface cracks were also analyzed. The same approach to the interphase modeling was extended in [3] to study hexagonal-array fiber composites, and in [4] to study the micromechanical behaviors of a cluster of fibers. Oshima and Watari [19] calculated the transverse effective Young's modulus using a two-dimensional boundary element method for a square unit cell model. No interphase was modeled and perfect bonding between the fiber and the matrix was assumed. Nevertheless, the boundary element method results using constant elements were shown to be in very good agreement with the experimental data. Gulrajani and Mukherjee [20] studied the sensitivities and optimal design of composites with a hexagonal array of fibers. A two-dimensional boundary element method model with the same spring-like interphase model as in [2] was used. The sensitivities of stresses at the interphase were calculated and employed to optimize the value of the stiffness of an interphase in order to minimize the possibility of failure of a composite. Most recently, Pan, Adams, and Rizzo [21] developed a similar two-dimensional boundary element method model using the same interphase relation as in [2] to study the perfectly bonded as well as imperfectly bonded fiber-reinforced composites. A main component in this research was the development of a library of Green's functions (or matrices of boundary element method equations) for analyzing fiber-reinforced composite materials, which can be used by engineers in the design of such composites. Although successful to some extent, all the above boundary element method models of the unit cells for fiber-reinforced composites with the spring-like interphase relations are incapable of providing other important information about the properties of composites, such as effects of changes of the thickness and nonuniform distribution of the interphases. Furthermore, in order to avoid overlapping of the fiber and matrix in the spring-like model, an iteration approach is needed. A trial calculation needs to be done first to check the sign of the normal traction at the interface. If the spring is in compression, continuity of the normal displacement is resumed and the boundary element method is applied again. This procedure is inefficient and can be costly. An improved boundary element method model of the interphases based on elasticity theory is desirable.

Interphases, as in fiber-reinforced composites, are thin shell-like structures. For this class of structures, there have been two major concerns in applying the boundary element method. The first concern is whether or not the conventional boundary integral equation for elasticity can be applied successfully to thin structures. It is well known in the boundary integral equation/boundary element method literature that the conventional boundary integral equation will degenerate when it is applied to cracks or thin voids in structures because of the closeness of the two crack surfaces (see, e.g., [16] and [22]). One of the remedies to such degeneracy in the conventional boundary integral equation for crack-like problems (*exterior-like* problems), is to employ the hypersingular boundary integral equation (see, e.g., [18,23–25]). Does this degeneracy occur when the conventional boundary integral equation is applied to thin structures (*interior-like* problems), such as thin shells? It was not clear in the boundary element method literature and the boundary element method based on elasticity had been avoided in analyzing thin shell-like structures for a long time due to this concern. Recently, it was shown in [26] and [27], both analytically and numerically, that the conventional boundary integral equation will not degenerate, contrary to the case of crack-like problems, when it is applied to thin shell-like structures if the displacement boundary conditions are not imposed at all the boundaries. Further discussions on this nondegeneracy issue for the boundary element method applied to shell-like structures can be found in [26] and [28]. Based on these new results, the degeneracy issue should no longer be a concern when the conventional boundary integral equation is applied to thin structures, once the second concern, that is, the numerical difficulty is addressed.

The numerical difficulty in the boundary integral equation is the nearly singular integrals which arise in thin structures when two parts of the boundary become close to each other. Detailed studies on the behaviors of the nearly singular integrals and comprehensive reviews of the earlier work in this regard can be found in [29] and [30]. One of the most efficient and accurate approaches to deal with the nearly singular integrals in the boundary element method for three-dimensional problems is to transform these (surface) integrals to line integrals analytically before the numerical integration ([22,26,31]). A similar approach can be established for two-dimensional elasticity problems ([27]). It has been demonstrated in [27] that very accurate numerical solutions can be obtained for thin structures with the thickness-to-length ratio in the micro and even nanoscales, using the newly developed boundary element method approach, without seeking refinement of the meshes as the thickness decreases.

Once the degeneracy issue for the conventional boundary integral equation in thin structure problems has been clarified and the nearly singular integrals can be dealt with accurately and efficiently, it is believed that the boundary element method can now be applied to a wide range of engineering problems, including simulations of thin shell-like structures ([26]) thin-film, and coatings in the micro or nanoscales ([27]) and in particular, the interphases in fiber-reinforced composite materials.

In this paper, detailed two-dimensional models for the interphases in fiber-reinforced composite materials have been developed based on the elasticity theory to study their micromechanical behaviors under transverse loading. All the regions—the fiber, matrix, and interfacial zone contained in a unit cell, are modeled using the advanced two-dimensional boundary element method with thin-body capabilities ([27]) and extended to multidomain cases. The interphases can have uniform thickness of any arbitrarily small values or nonuniform thickness. Interface stresses in the interphases and effective elastic moduli in the transverse directions are computed using this approach. This two-dimensional model of the interphases can provide more accurate interface stresses and therefore a more accurate account on the micromechanical behaviors of fiber-reinforced composites than the current spring-like models in the boundary element method literature.

2 The Boundary Element Method Formulation

For the unit cell models under transverse loading (Fig. 2), the following boundary integral equation for two-dimensional elasticity problems can be applied in each material domain (index notation is used in this section, where repeated subscripts imply summation):

$$C_{ij}(P_0)u_j^{(\beta)}(P_0)=\int_S [U_{ij}^{(\beta)}(P,P_0)t_j^{(\beta)}(P)-T_{ij}^{(\beta)}(P,P_0) \times u_j^{(\beta)}(P)]dS(P), \quad (1)$$

in which $u_i^{(\beta)}$ and $t_i^{(\beta)}$ are the displacement and traction fields, respectively; $U_{ij}^{(\beta)}(P,P_0)$ and $T_{ij}^{(\beta)}(P,P_0)$ the displacement and traction kernels (Kelvin's solution or the fundamental solution), respectively; P the field point and P_0 the source point; and S the boundary of the single material domain, (Fig. 2). $C_{ij}(P_0)$ is a constant coefficient matrix depending on the smoothness of the curve S at the source point P_0 (e.g., $C_{ij}(P_0)=1/2\delta_{ij}$ if S is smooth at point P_0, where δ_{ij} is the Kronecker delta). The superscript β on the variables in Eq. (1) signifies the dependence of these variables on the material domains, as specified below:

$$\beta=f: \quad \text{fiber domain} \quad (S=S_1);$$

$$\beta=i: \quad \text{interphase domain} \quad (S=S_1\cup S_2);$$

$$\beta=m: \quad \text{matrix domain} \quad (S=S_2\cup S_3).$$

The two kernel functions $U_{ij}^{(\beta)}(P,P_0)$ and $T_{ij}^{(\beta)}(P,P_0)$ in boundary integral equation (1) are given as follows for plane-strain problems:

$$U_{ij}^{(\beta)}(P,P_0)=\frac{1}{8\pi\mu^{(\beta)}(1-\nu^{(\beta)})}\left[(3-4\nu)\delta_{ij}\ln\left(\frac{1}{r}\right)+r_{,i}r_{,j}\right],$$

$$T_{ij}^{(\beta)}(P,P_0)=-\frac{1}{4\pi(1-\nu^{(\beta)})}\frac{1}{r}\{r_{,n}[(1-2\nu^{(\beta)})\delta_{ij}+2r_{,i}r_{,j}] +(1-2\nu^{(\beta)})(r_{,j}n_i-r_{,i}n_j)\}, \quad (2)$$

where $\mu^{(\beta)}$ is the shear modulus and $\nu^{(\beta)}$ the Poisson's ratio for the three different domains, respectively; r the distance from the source point P_0 to the field point P; n_i the directional cosines of the outward normal n; and $(),_i=\partial()/\partial x_i$ with x_i being the coordinates of the field point P.

In Eq. (1) the integral containing the $U_{ij}^{(\beta)}(P,P_0)$ kernel is weakly singular, while the one containing $T_{ij}^{(\beta)}(P,P_0)$ is strongly singular and must be interpreted in the Cauchy principal value sense. There is a vast body of literature on how to deal with the Cauchy principle value integrals in the boundary element method formulations for bulky-shaped structures, either analytically for some special cases or numerically for other cases. An alternative approach is to transform the boundary integral equation in the form of Eq. (1) into a weakly singular form by using some simple solutions or integral identities for the fundamental solution ([32,33]), before doing any numerical work. However, when the structure becomes thin in shape, such as the interphase shown in Fig. 2, both integrals in Eq. (1) are difficult to deal with when the source point is on one side and the integration is carried out on the other side of the thin structure. These types of integrals are called nearly singular integrals since the distance r is very small in this case but is still not zero. Most techniques for dealing with the singular integrals do not work for nearly singular integrals and special attention is needed. Recently, several techniques, including singularity subtractions, analytical integration, and nonlinear coordinate transformations have been developed for the two-dimensional elasticity boundary integral equation to calculate the nearly singular integrals arising in thin structures ([27]). The combination of these techniques is found to be extremely effective and efficient in computing the nearly singular integrals in the two-dimensional boundary integral equation, no matter how close the source point is to the element of integration. Very accurate boundary element method results have been obtained using this approach for thin structures, such as coatings on macroscale structures, with the coating thickness-to-length ratios in the micro to nanoscales and with a small number of boundary elements. The same approach in [27] is applied in this paper to compute the nearly singular integrals arising in the modeling of the interphases.

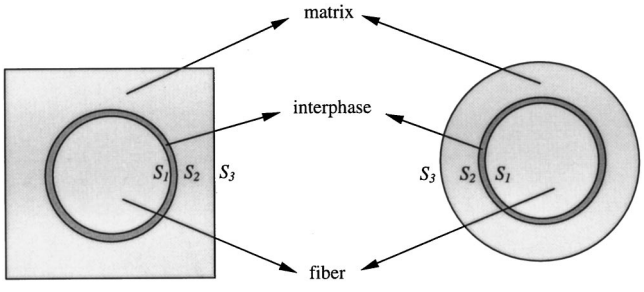

Fig. 2 Two unit cell models of the fiber-interphase-matrix system

Employing the boundary elements (line elements in two-dimensional) on the boundary and interfaces S_1, S_2, and S_3, the discretized equations of the three boundary integral equations as given in (1) for the fiber, interphase, and matrix can be written as follows (cf., e.g., [17]):

$$\mathbf{T}_1^{(f)}\mathbf{u}_1^{(f)}=\mathbf{U}_1^{(f)}\mathbf{t}_1^{(f)}, \quad \text{(in fiber domain)} \quad (3)$$

$$\mathbf{T}_1^{(i)}\mathbf{u}_1^{(i)}+\mathbf{T}_2^{(i)}\mathbf{u}_2^{(i)}=\mathbf{U}_1^{(i)}\mathbf{t}_1^{(i)}+\mathbf{U}_2^{(i)}\mathbf{t}_2^{(i)}, \quad \text{(in interphase domain)} \quad (4)$$

$$\mathbf{T}_2^{(m)}\mathbf{u}_2^{(m)}+\mathbf{T}_3^{(m)}\mathbf{u}_3^{(m)}=\mathbf{U}_2^{(m)}\mathbf{t}_2^{(m)}+\mathbf{U}_3^{(m)}\mathbf{t}_3^{(m)}, \quad \text{(in matrix domain)} \quad (5)$$

in which $\mathbf{U}$ and $\mathbf{T}$ are matrices generated from the $U_{ij}^{(\beta)}(P,P_0)$ and $T_{ij}^{(\beta)}(P,P_0)$ kernels, respectively; $\mathbf{u}$ and $\mathbf{t}$ the displacement and traction vectors, respectively. The superscripts indicate the material domain, while the subscripts indicate the interface or boundary (S_1, S_2, or S_3) on which the integration is performed.

Assuming perfect bonding at the fiber/interphase (S_1) and interphase/matrix (S_2) interfaces, one can write the following interface conditions:

$$\text{On } S_1: \quad \mathbf{u}_1^{(f)}=\mathbf{u}_1^{(i)}\equiv\mathbf{u}_1, \quad \text{(continuity)} \quad (6)$$

$$\mathbf{t}_1^{(f)}=-\mathbf{t}_1^{(i)}\equiv\mathbf{t}_1, \quad \text{(equilibrium)} \quad (7)$$

$$\text{On } S_2: \quad \mathbf{u}_2^{(i)}=\mathbf{u}_2^{(m)}\equiv\mathbf{u}_2, \quad \text{(continuity)} \quad (8)$$

$$\mathbf{t}_2^{(i)}=-\mathbf{t}_2^{(m)}\equiv\mathbf{t}_2, \quad \text{(equilibrium)} \quad (9)$$

where $\mathbf{u}_1$, $\mathbf{t}_1$, $\mathbf{u}_2$, and $\mathbf{t}_2$ are defined as the interface displacement or traction vectors.

Applying the interface conditions (6)–(9) in Eqs. (3)–(5), one obtains the following system:

$$\begin{bmatrix} \mathbf{T}_1^{(f)} & \mathbf{0} & \mathbf{0} \\ \mathbf{T}_1^{(i)} & \mathbf{T}_2^{(i)} & \mathbf{0} \\ \mathbf{0} & \mathbf{T}_2^{(m)} & \mathbf{T}_3^{(m)} \end{bmatrix} \begin{Bmatrix} \mathbf{u}_1 \\ \mathbf{u}_2 \\ \mathbf{u}_3 \end{Bmatrix} = \begin{bmatrix} \mathbf{U}_1^{(f)} & \mathbf{0} & \mathbf{0} \\ -\mathbf{U}_1^{(i)} & \mathbf{U}_2^{(i)} & \mathbf{0} \\ \mathbf{0} & -\mathbf{U}_2^{(m)} & \mathbf{U}_3^{(m)} \end{bmatrix} \begin{Bmatrix} \mathbf{t}_1 \\ \mathbf{t}_2 \\ \mathbf{t}_3 \end{Bmatrix},$$

where $\mathbf{u}_3\equiv\mathbf{u}_3^{(m)}$ and $\mathbf{t}_3\equiv\mathbf{t}_3^{(m)}$ have been used for simplicity. Rearranging the columns and moving all the (unknown) interface variables to the left-hand side, one finally arrives at

$$\begin{bmatrix} \mathbf{T}_1^{(f)} & -\mathbf{U}_1^{(f)} & \mathbf{0} & \mathbf{0} & \mathbf{0} \\ \mathbf{T}_1^{(i)} & \mathbf{U}_1^{(i)} & \mathbf{T}_2^{(i)} & -\mathbf{U}_2^{(i)} & \mathbf{0} \\ \mathbf{0} & \mathbf{0} & \mathbf{T}_2^{(m)} & \mathbf{U}_2^{(m)} & \mathbf{T}_3^{(m)} \end{bmatrix} \begin{Bmatrix} \mathbf{u}_1 \\ \mathbf{t}_1 \\ \mathbf{u}_2 \\ \mathbf{t}_2 \\ \mathbf{u}_3 \end{Bmatrix} = \begin{bmatrix} \mathbf{0} \\ \mathbf{0} \\ \mathbf{U}_3^{(m)} \end{bmatrix} \{\mathbf{t}_3\}. \tag{10}$$

The last column in the matrix on the left-hand side and the matrix on the right-hand side may need to be rearranged again according to the boundary conditions specified on S_3.

Equation (10) is the global system of equations for the fiber-interphase-matrix model. The system has a banded matrix due to the multidomain nature of the problem. This system of equations satisfies both the continuity and equilibrium conditions at the interfaces explicitly, which is an advantage of the boundary element method approach over the finite element method in which only the continuity of displacement fields can be satisfied explicitly. By solving Eq. (10), one can obtain the displacements and tractions at the two interfaces and the boundary, and then calculate the interface stresses based on the traction and displacement fields.

3 Two Unit Cell Models With the Interphase

Two unit cell models are used in this paper, namely, the concentric cylinder model and the square model (see, e.g., [12]) both of which include the interphase (Fig. 2). For the cylinder model, analytical solutions are obtained for the displacement and stress fields, which can be employed to validate the boundary element method results. For the square model, many finite element and boundary element solutions are available in the literature for the effective elastic moduli which will be compared with the data from the present boundary element method approach.

3.1 Concentric Cylinder Model. For the concentric cylinder model, Fig. 3, the response of the composite in the x-y plane is axisymmetric if the applied load or displacement on the boundary S_3 is also axisymmetric. Here it is assumed that a radial displacement δ is given on S_3 (at $r=c$, Fig. 3). Applying the theory of elasticity for plane strain case in the polar coordinate system (r,θ), one can derive the following expressions for the radial displacement and stress fields in the fiber, interphase, and matrix, respectively (see the Appendix for details):

$$\begin{aligned} u^{(f)}(r) &= A^{(f)} r, \quad (0 \leqslant r \leqslant a) \\ u^{(i)}(r) &= A^{(i)} r + \frac{B^{(i)}}{r}, \quad (a \leqslant r \leqslant b) \\ u^{(m)}(r) &= A^{(m)} r + \frac{B^{(m)}}{r}, \quad (b \leqslant r \leqslant c) \end{aligned} \tag{11}$$

and

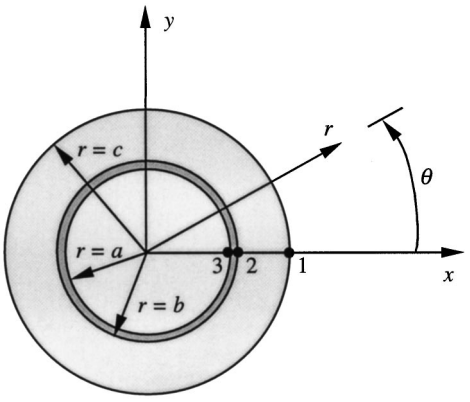

Fig. 3 Concentric cylindrical model

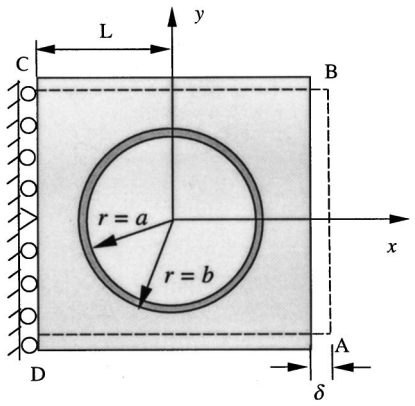

Fig. 4 Square model under tension

$$\begin{aligned} \sigma_r^{(f)} &= \sigma_\theta^{(f)} = k^{(f)} A^{(f)}, \quad (0 \leqslant r \leqslant a) \\ \sigma_r^{(i)} &= k^{(i)} \left[A^{(i)} - (1-2\nu^{(i)}) \frac{B^{(i)}}{r^2} \right], \\ \sigma_\theta^{(i)} &= k^{(i)} \left[A^{(i)} + (1-2\nu^{(i)}) \frac{B^{(i)}}{r^2} \right], \quad (a \leqslant r \leqslant b) \\ \sigma_r^{(m)} &= k^{(m)} \left[A^{(m)} - (1-2\nu^{(m)}) \frac{B^{(m)}}{r^2} \right], \\ \sigma_\theta^{(m)} &= k^{(m)} \left[A^{(m)} + (1-2\nu^{(m)}) \frac{B^{(m)}}{r^2} \right], \quad (b \leqslant r \leqslant c) \end{aligned} \tag{12}$$

where the constants $A^{(\beta)}$, $B^{(\beta)}$, and $k^{(\beta)}$ ($\beta = f$, i and m) are given in the Appendix.

From the above expressions, one can compute the radial displacement and stress components at any point in the three domains within the cylinder model for any small values of the interphase thickness.

3.2 Square Model. As shown in Fig. 4, the boundary conditions for the square model under *tension* are

$$\begin{aligned} &\text{along } AB: \quad u_x = \delta, \quad t_y = 0; \\ &\text{along } BC: \quad u_y = -C_0, \quad t_x = 0; \\ &\text{along } CD: \quad u_x = 0, \quad t_y = 0, \\ &\text{except at } y = 0 \text{ where } u_x = u_y = 0; \\ &\text{along } DA: \quad u_y = C_0, \quad t_x = 0; \end{aligned} \tag{13}$$

where u_x, u_y, t_x, and t_y are the displacement and traction components, respectively; δ the given displacement (Fig. 4); and C_0 an unknown constant. This unknown constant is meant to keep the edges BC and DA straight after the deformation. This represents the constraint of the neighboring cells to the one under study. In the literature, there are several ways in dealing with these subtle boundary conditions along the top and bottom edges. For example, in [9] C_0 is chosen as zero in one case and nonzero in another case. This is equivalent to another given displacement condition besides the one imposed along the two vertical edges. In [2] and recently in [21], C_0 is regarded as an unknown and the condition $\int_{-L}^{L} \sigma_y dx = 0$ along the top or bottom edges is used to provide the additional equation needed for solving this unknown together with other unknown boundary variables. Discretization of this simple equation using shape functions is needed. In [19], however, this straight-line constraint is totally ignored, and $t_x = t_y = 0$ (traction-free conditions) are assumed. It is found that results for the unit cell model is not very sensitive to all the different techniques mentioned above. In this paper, C_0 is as-

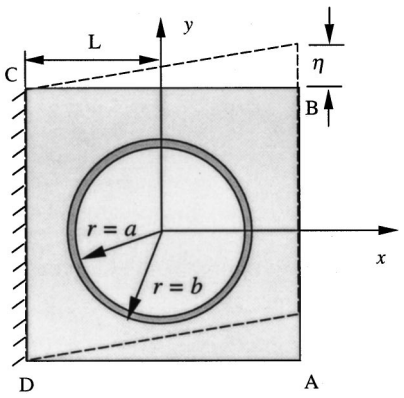

Fig. 5 Square model under shear deformation

sumed to be unknown, but a different approach is employed to enforce the straight-line condition, instead of solving for this unknown constant with additional equations. Here the penalty method used in the finite element method for multipoint constraints (see, e.g., [34]) is introduced in the boundary element method equations to enforce that all the nodes along edges BC and DA remain along straight lines after deformation. To implement this penalty method in the boundary element method equations a very large number (penalty) with a proper sign is placed in the locations in the matrix corresponding to the related displacement components. Then these displacement components will have the same value after the system of equations is solved. It is very easy to implement this penalty method in the boundary element method equations and no additional equation is needed.

Once stresses on the boundary are determined, the average tensile stress along the edge AB is evaluated by

$$\overline{\sigma_x}=\frac{1}{2L}\int_{-L}^{L}\sigma_x(L,y)dy. \tag{14}$$

The effective Young's modulus in the transverse direction and under the *plane-strain* condition is thus determined by

$$E_x'=\frac{\overline{\sigma_x}}{\overline{\varepsilon_x}}=\frac{\int_{-L}^{L}\sigma_x(L,y)dy}{\delta}, \tag{15}$$

where $\overline{\epsilon_x}=\delta/2L$ is the average tensile strain. The effective Poisson's ratio under the *plane-strain* condition can be determined by

$$v_{xy}'=-\frac{\overline{\varepsilon_y}}{\overline{\varepsilon_x}}, \tag{16}$$

in which $\overline{\varepsilon_y}$ is the average strain in the *y*-direction.

For the square model under *shear* deformation, Fig. 5, the boundary conditions are

$$\begin{aligned}&\text{along } AB: \quad u_x=0,\ u_y=\eta;\\ &\text{along } BC: \quad u_x=0,\ t_y=0;\\ &\text{along } CD: \quad u_x=0,\ u_y=0;\\ &\text{along } DA: \quad u_x=0,\ t_y=0.\end{aligned} \tag{17}$$

The average shear stress along edge AB can be evaluated by

$$\overline{\tau_{xy}}=\frac{1}{2L}\int_{-L}^{L}\tau_{xy}(L,y)dy, \tag{18}$$

and the effective shear modulus in the transverse plane and under the *plane-strain* condition is

$$G_{xy}'=\frac{\overline{\tau_{xy}}}{\overline{\gamma_{xy}}}=\frac{\int_{-L}^{L}\tau_{xy}(L,y)dy}{\eta}, \tag{19}$$

where $\overline{\gamma_{xy}}=\eta/2L$ is the average shear strain.

Finally, one recognizes that the material constants E_x', ν_{xy}', and G_{xy}' given in Eqs. (15), (16), and (19), respectively, are determined under the *plane-strain* condition which accounts for the constraint in the *z*-direction ($\varepsilon_z=0$). These constants are related to the intrinsic material properties by the following relations (cf., e.g., [35] and [21]):

$$E_x=\frac{1+2\nu_{xy}'}{(1+\nu_{xy}')^2}E_x',\quad \nu_{xy}=\frac{\nu_{xy}'}{1+\nu_{xy}'},\quad G_{xy}=G_{xy}', \tag{20}$$

which are the effective Young's modulus, Poisson's ratio, and shear modulus, respectively, in the transverse direction for the composite.

4 Numerical Examples

4.1 Cylinder Model. The cylinder model (Fig. 3) is studied first to validate the developed boundary element method formulation and the solution strategy, since for this idealized geometry the analytical solutions are available (see Eqs. (11)–(12) and the Appendix). The specified radial displacement on the boundary (at $r=c$) is δ. The following material constants for a glass/epoxy composite are used:

$$\begin{aligned}&\text{for fiber:} \quad E^{(f)}=72.4 \text{ GPa } (10.5\times10^6 \text{ psi}),\ \nu^{(f)}=0.22;\\ &\text{for interphase:} \quad E^{(i)}=36.2 \text{ GPa } (5.25\times10^6 \text{ psi}),\ \nu^{(i)}=0.30;\\ &\text{for matrix:} \quad E^{(m)}=3.45 \text{ GPa } (0.5\times10^6 \text{ psi}),\ \nu^{(m)}=0.35;\end{aligned}$$

where the Young's modulus of the interphase has been taken as half of that of the fiber; and the dimensions used are

$$a=c/2,\quad b=a+h,$$

with *h* being the thickness of the interphase, which is varying.

Quadratic line elements are employed in the discretization and two meshes are tested, one with 24 elements (eight on each circle) and another one with 48 elements (16 on each circle). Differences

Table 1 Results of the radial displacement $u(\times10^{-2}\delta)$ for the cylinder model

	$h=0.1a$		$h=0.01a$		$h=0.001a$	
	Point 2	Point 3	Point 2	Point 3	Point 2	Point 3
BEM	8.2961	7.0833	6.7379	6.6225	6.5909	6.5794
Analytical	8.2958	7.0830	6.7378	6.6224	6.5925	6.5810
Error (%)	0.0036	0.0042	0.0015	0.0015	0.0243	0.0243

Table 2 Results of the radial stress $\sigma_r(\times E^{(m)}\delta/c)$ for the cylinder model

	$h=0.1a$			$h=0.01a$			$h=0.001a$		
	Point 1	Point 2	Point 3	Point 1	Point 2	Point 3	Point 1	Point 2	Point 3
BEM	3.6515	4.2806	4.3550	3.4215	4.0636	4.0714	3.4009	4.0442	4.0449
Analytical	3.6513	4.2803	4.3544	3.4214	4.0633	4.0711	3.4006	4.0461	4.0458
Error (%)	0.0055	0.0070	0.0138	0.0029	0.0074	0.0074	0.0088	0.0470	0.0222

in the results from the two meshes are less than five percent and the results from the refined mesh (48 elements) are reported. The radial displacements and stresses at selected points (Fig. 3) are given in Table 1 and Table 2, respectively. It is observed that the maximum errors of the displacement and stress using the developed boundary element method are less than 0.05 percent in all the cases with different thickness of the interphase. These results demonstrate that the developed boundary element method approach is extremely accurate and effective in modeling the interphases with any small thickness, as has been confirmed in the context of single material problems ([27]).

4.2 Square Model

(a) Calculation of Effective Young's Modulus With Varying Interphase Property. First, the square model under a stretch in the *x*-direction is considered (Fig. 4). The properties of the constituent materials considered are

$$\text{for fiber:} \quad E^{(f)}=84.0 \text{ GPa}, \quad \nu^{(f)}=0.22;$$

$$\text{for interphase:} \quad E^{(i)}=4.0\sim 12.0 \text{ GPa}, \quad \nu^{(i)}=0.34;$$

$$\text{for matrix:} \quad E^{(m)}=4.0 \text{ GPa}, \quad \nu^{(m)}=0.34;$$

and, $a=8.5\ \mu$m, $b=a+h$, $2L=21.31\ \mu$m (fiber volume fraction $V_f=50$ percent). Young's modulus for the interphase is changing in the range between 4.0 and 12.0 GPa. The effect of the variations in the interphase material on the effective Young's modulus of the composite is of the primary interest here. A total of 64 quadratic boundary elements are used, with 16 elements on each of the two circular interfaces and 32 elements on the outer boundary. Table 3 shows the effective Young's moduli obtained from the boundary element method stress data using Eq. (15) and then Eq. (20), and compared with those from the finite element method quarter model with 3518 linear triangular elements in [9] for the thickness $h=1.0\ \mu$m. The boundary element method results are slightly lower than those from the finite element method data. This may be caused by the use of linear triangular element in the finite element method which tends to overestimate the stiffness of the structure. It is noticed that the different boundary conditions along the top and bottom edges of the square model (free-traction or straight-line conditions) have very little influences on the final effective Young's modulus. It should also be pointed out that for the finite element results in [9], the only thickness considered is $h=1.0\ \mu$m which is relatively large compared with the fiber radius ($a=8.5\ \mu$m). If a smaller thickness were used in the finite element model, a much larger number of elements would have been needed in order to avoid large aspect ratios in the finite element mesh, as demonstrated in a similar study (see [27]). However, for the boundary element method employed here, the same number of elements can be used no matter how small the thickness of the interphase is.

(b) Effect of the Interphase Thickness. Figure 6 shows the effect of different interphase thicknesses to the effective Young's modulus. In order to compare with the data in [21] and [19], the same material constants as listed in Section 4.1 (for the cylinder model) are used. It is found that the effect of the thickness is not significant on the effective Young's moduli when the fiber volume fraction V_f is small (50 percent and less), while significant effect is observed when V_f is large (70 percent). This may be due to the fact that the effective elastic moduli are obtained by evaluating the average stress on the outer boundary of the matrix (edge AB, Fig. 4). When the fiber volume fraction is small, the interphase is away from the matrix outer boundary and thus changing the interphase thickness does not considerably affect the stresses on the edge AB. This will change if the fiber volume fraction is large (e.g., 70 percent) when the interphase becomes closer to the outer boundary of the matrix. It should also be pointed out that when the fiber volume fraction is large, it will present additional difficulty in the modeling using the finite element method and earlier boundary element method formulation, because of the thinness of the matrix region. However, for the current boundary element method formulation, this additional thinness of the matrix domain does not present any problem.

(c) Effect of Nonuniform Thickness. Next, the effect of nonuniform thickness of the interphase on the interface stresses and effective elastic moduli is investigated. The starting model (Fig. 4) is the same as the one used for Table 3 with the material constants listed at the beginning of this subsection (with $E^{(i)}=42.0$ GPa). To form the nonuniform distribution of the interphase, the outer boundary of the interphase is shifted to the left

Table 3 Effective transverse elastic modulus (GPa) using the square unit cell model

Interphase property $E^{(i)}$ (GPa)	*Current BEM with traction-free conditions on BC and DA*	*Current BEM with straight-line conditions on BC and DA*	*FEM* ([9])
4.0	11.61	11.61	12.25
6.0	13.18	13.02	13.71
8.0	13.97	13.89	14.68
12.0	15.04	14.93	15.91

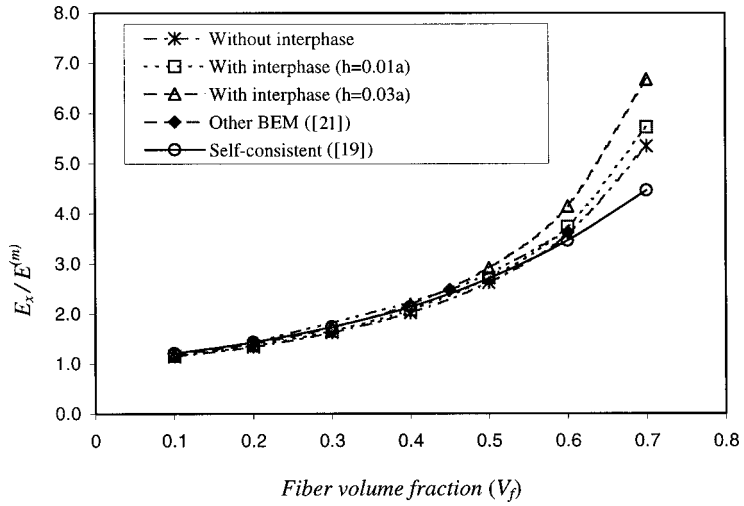

Fig. 6 Influence of the thickness on the effective Young's modulus

slightly (see Fig. 7). When the offset Δ is close to h (the initial, uniform thickness), the change of the interphase thickness in the x-direction is the largest ($\Delta = 0$ corresponds to the uniform interphase). The interface normal stresses at points 1 and 2 (Fig. 7), normalized by those in the uniform case, are plotted in Fig. 8. Due to the misalignment of the fiber and interphase centers, the interface stress at point 1 (which is the maximum interface normal stress) increases for about 50 percent while the stress at point 2 (the second largest interface stress) increases for about 30 percent. However, the effect of the nonuniform thickness of the interphase on the effective Young's modulus is found to be less than three percent. This, again, is largely due to the averaging process on the edge AB which is away from the interphase.

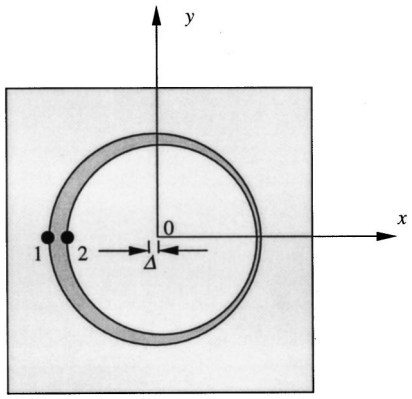

Fig. 7 The interphase with nonuniform thickness

(d) Calculation of Shear Modulus With Varying Interphase Thickness. Finally, the effective shear modulus in the transverse direction is calculated using the square unit cell model shown in Fig. 5. The boundary conditions applied are listed in (17) and Eqs. (19)–(20) are used to compute the shear modulus. In order to compare the results with those in the literature, the following materials properties for a Kevlar/epoxy composite are used in the current boundary element method calculation:

$$\text{for fiber:} \quad E^{(f)} = 7.0 \text{ GPa}, \quad \nu^{(f)} = 0.30;$$

$$\text{for interphase:} \quad E^{(i)} = 5.0 \text{ GPa}, \quad \nu^{(i)} = 0.35;$$

$$\text{for matrix:} \quad E^{(m)} = 3.0 \text{ GPa}, \quad \nu^{(m)} = 0.35.$$

Table 4 shows the results of the effective shear modulus by the current boundary element method with and without the presence of the interphase. The data without the interphase ($h = 0$) agrees very well with the results from the finite element method ([6]) and

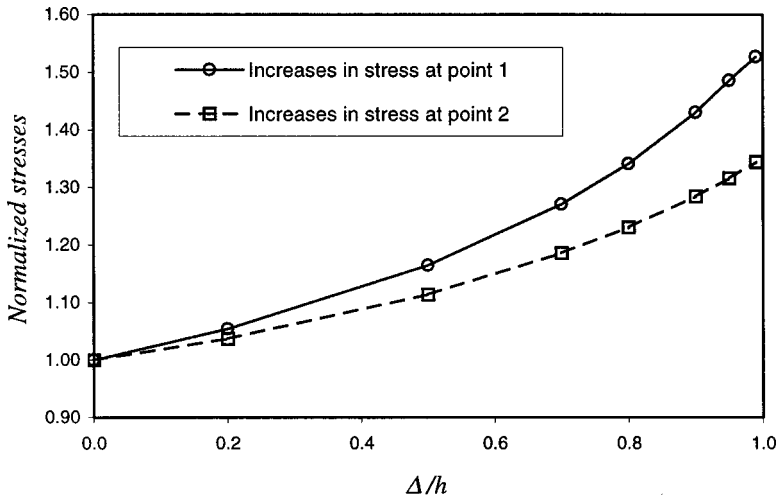

Fig. 8 Effect of nonuniform thickness on the interface stress

Table 4 Effective transverse shear modulus (GPA)

	Fiber volume fraction (V_f)			
	0.2	0.4	0.6	0.7
FEM ([6])	1.297	1.529	1.826	---
Other BEM ([21])	1.294	1.513	1.798	---
Current BEM ($h = 0.0$)	1.2939	1.5133	1.7981	1.9866
Current BEM ($h = 0.001a$)	1.2941	1.5139	1.7994	1.9885
Current BEM ($h = 0.01a$)	1.2964	1.5196	1.8111	2.0059
Current BEM ($h = 0.1a$)	1.3205	1.5807	1.9446	---

the other boundary element method ([21]) both of which used the perfect bonding condition and did not model the interphase. With the increase of the thickness of the interphase, the shear modulus deviates from the perfect bonding case slightly, with the largest change (about eight percent) occurring at the fiber volume fraction $V_f = 0.6$, for the interphase property considered. When $V_f = 0.7$ and $h = 0.1a$, the interphase will be outside the boundary of the unit cell. This is not permissible and thus no boundary element method data are generated.

5 Conclusion

The advanced boundary element method formulation with thin-body capabilities for elastostatic problems has been extended to multidomain problems and applied to model the interphases in fiber-reinforced composites under transverse loading. Compared with the current spring-like models for the interphases in the boundary element method literature, this new interphase model is based on the elasticity theory and thus provides a more accurate account of the interphases in fiber-reinforced composites within the linear theory. The developed boundary element code using the object-oriented programming language (C++) can be utilized in analyzing the micromechanical properties of fiber-reinforced composites with the presence of interphases of any arbitrarily small thickness (uniform or nonuniform). The approach is very accurate as is validated using the concentric cylinder model for which the analytical solution has been derived. It is also very efficient as only a small number (less than one hundred) of boundary elements are needed to model a *whole* unit cell for the boundary element analysis, compared with the large number (more than a few thousands) of finite elements often needed for a *quarter* model in the finite element method analysis. The approach provides a greater flexibility in parametric study of the interphases as well, since the geometry, size, or material property of the interphases can be changed very easily to investigate their effect on the micromechanical behaviors of the fiber-reinforced composites.

Numerical studies in this paper show that the thickness, nonuniform distribution, and material property of the interphase can have significant influences on the micromechanical behaviors of the composites, such as effective elastic moduli and interface stresses, especially when the fiber volume fractions are large. These observations are consistent with the findings in both the finite element method and boundary element method literatures on this subject.

Considerations of interface cracks in the present boundary element model and extension of the boundary element code to three dimensions to study the fiber-pullout failure modes will be interesting and challenging next steps, both of which will further demonstrate the robustness of the developed boundary element method approach as compared with the finite element method or previous boundary element method approaches to the micromechanical analysis of fiber-reinforced composites.

Acknowledgment

Support of this research by the National Science Foundation under the grant CMS 9734949 is gratefully acknowledged. The first author would like to thank Prof. Frank Rizzo at Iowa State University and Dr. Lingyun Pan at Caterpillar, Inc. for many discussions and help on this project.

Appendix

Analytical Solution for the Concentric Cylinder Model. Here the analytical solution for the concentric cylinder model used to validate the boundary element method results is derived. For the concentric cylinders, the response of the composite is axisymmetric. Thus the equilibrium equation for two-dimensional elasticity in the polar coordinate system reduces to

$$\frac{d\sigma_r}{dr} + \frac{1}{r}(\sigma_r - \sigma_\theta) = 0, \tag{A1}$$

where the stress components $(\sigma_r, \sigma_\theta)$ are functions of r only, and the shearing stress $\tau_{r\theta}$ is zero. The stress-strain relations for the plane-strain case are

$$\sigma_r = \frac{E}{(1+\nu)(1-2\nu)}[(1-\nu)\varepsilon_r + \nu\varepsilon_\theta],$$

$$\sigma_\theta = \frac{E}{(1+\nu)(1-2\nu)}[(1-\nu)\varepsilon_\theta + \nu\varepsilon_r]. \tag{A2}$$

The strain-displacement relations are

$$\varepsilon_\theta = \frac{u}{r}, \quad \varepsilon_r = \frac{du}{dr}. \tag{A3}$$

Equations (*A*1), (*A*2), and (*A*3) lead to the following equation for the radial displacement:

$$\frac{d^2u}{dr^2} + \frac{1}{r}\frac{du}{dr} - \frac{u}{r^2} = 0, \tag{A4}$$

where u is the displacement in the radial direction.

The solution of the above equation has the following form:

$$u(r) = Ar + \frac{B}{r}, \tag{A5}$$

in which A and B are determined by the applied boundary conditions. The above form of the solution is the general form which valid for the fiber, interphase, and matrix. Thus for the three domains, one has

$$u^{(f)}(r) = A^{(f)}r, \quad (\text{assume } B^{(f)} = 0) \quad (0 \leqslant r \leqslant a)$$

$$u^{(i)}(r) = A^{(i)}r + \frac{B^{(i)}}{r}, \quad (a \leqslant r \leqslant b)$$

$$u^{(m)}(r) = A^{(m)}r + \frac{B^{(m)}}{r}, \quad (b \leqslant r \leqslant c). \tag{A6}$$

If $B^{(f)} \neq 0$, then at $r = 0$, the displacement $u^{(f)}(0)$ will approach infinity, which is not warranted.

Boundary and interface conditions are

$$\begin{aligned} &\text{at } r = c, \quad u^{(m)}(c) = \delta, \\ &\text{at } r = b, \quad u^{(i)}(b) = u^{(m)}(b), \\ &\qquad\qquad \sigma_r^{(i)}(b) = \sigma_r^{(m)}(b), \\ &\text{at } r = a, \quad u^{(i)}(a) = u^{(f)}(a), \\ &\qquad\qquad \sigma_r^{(i)}(a) = \sigma_r^{(f)}(a), \end{aligned} \tag{A7}$$

where δ is the displacement applied on the outer boundary of the matrix.

Applying the relations (*A*2), (*A*3), and (*A*6) in the above five equations in (*A*7) from the boundary and interface conditions, one can find the five constants to be

$$A^{(m)}=\frac{c\,\delta\left[(1-2\nu^{(m)})-\dfrac{k^{(i)}}{k^{(m)}}M\right]}{b^2+(1-2\nu^{(m)})c^2+\dfrac{k^{(i)}}{k^{(m)}}(b^2-c^2)M},$$

$$B^{(m)}=c\,\delta-A^{(m)}c^2,$$

$$\text{and}\quad k^{(f)}=\frac{E^{(f)}}{(1+\nu^{(f)})(1-2\nu^{(f)})},\qquad k^{(i)}=\frac{E^{(i)}}{(1+\nu^{(i)})(1-2\nu^{(i)})},$$

$$k^{(m)}=\frac{E^{(m)}}{(1+\nu^{(m)})(1-2\nu^{(m)})},$$

$$M=\frac{a^2(1-2\nu^{(i)})(k^{(f)}-k^{(i)})+b^2[k^{(f)}+(1-2\nu^{(i)})k^{(i)}]}{a^2(k^{(f)}-k^{(i)})-b^2[k^{(f)}+(1-2\nu^{(i)})k^{(i)}]},$$

$$B^{(i)}=\frac{(b^2-c^2)A^{(m)}+c\,\delta}{1-\dfrac{b^2}{a^2}\dfrac{k^{(f)}+k^{(i)}(1-2\nu^{(i)})}{k^{(f)}-k^{(i)}}},$$

$$A^{(i)}=-\frac{B^{(i)}}{a^2}\frac{k^{(f)}+(1-2\nu^{(i)})k^{(i)}}{k^{(f)}-k^{(i)}},$$

$$A^{(f)}=A^{(i)}+\frac{B^{(i)}}{a^2}. \tag{A8}$$

These results, together with Eqs. (11)–(12), provide the analytical solutions of the displacement and stress for the cylinder model. Note that the solution is valid for any arbitrarily small thickness of the interphase and thus is very useful in validating the boundary element solutions. This solution can also be applied to other layered structures of cylindrical shapes, such as cables.

References

[1] Chawla, K. K., 1987, *Composite Materials: Science and Engineering*, Springer-Verlag, New York.

[2] Achenbach, J. D., and Zhu, H., 1989, ''Effect of Interfacial Zone on Mechanical Behavior and Failure of Fiber-Reinforced Composites,'' J. Mech. Phys. Solids, **37**, No. 3, pp. 381–393.

[3] Achenbach, J. D., and Zhu, H., 1990, ''Effect of Interphases on Micro and Macromechanical Behavior of Hexagonal-Array Fiber Composites,'' ASME J. Appl. Mech., **57**, pp. 956–963.

[4] Zhu, H., and Achenbach, J. D., 1991, ''Effect of Fiber-Matrix Interphase Defects on Microlevel Stress States at Neighboring Fibers,'' J. Compos. Mater., **25**, pp. 224–238.

[5] Hashin, Z., 1991, ''Composite Materials With Interphase: Thermoelastic and Inelastic Effects,'' *Inelastic Deformation of Composite Materials*, G. J. Dvorak, ed., Springer, New York, pp. 3–34.

[6] Yeh, J. R., 1992, ''The Effect of Interface on the Transverse Properties of Composites,'' Int. J. Solids Struct., **29**, pp. 2493–2505.

[7] Jasiuk, I., and Kouider, M. W., 1993, ''The Effect of an Inhomogeneous Interphase on the Elastic Constants of Transversely Isotropic Composites,'' Mech. Mater., **15**, pp. 53–63.

[8] Lagache, M., Agbossou, A., Pastor, J., and Muller, D., 1994, ''Role of Interphase on the Elastic Behavior of Composite Materials: Theoretical and Experimental Analysis,'' J. Compos. Mater., **28**, No. 12, pp. 1140–1157.

[9] Wacker, G., Bledzki, A. K., and Chate, A., 1998, ''Effect of Interphase on the Transverse Young's Modulus of Glass/Epoxy Composites,'' Composites, **29A**, pp. 619–626.

[10] Aboudi, J., 1989, ''Micromechanical Analysis of Composites by the Method of Cells,'' Appl. Mech. Rev., **42**, No. 7, pp. 193–221.

[11] Sun, C. T., and Vaidya, R. S., 1996, ''Prediction of Composite Properties From a Representative Volume Element,'' Compos. Sci. Technol., **56**, pp. 171–179.

[12] Hyer, M. W., 1998, *Stress Analysis of Fiber-Reinforced Composite Materials*, McGraw-Hill, New York.

[13] Adams, D. F., 1987, ''A Micromechanics Analysis of the Influence of the Interface on the Performance of Polymer-Matrix Composites,'' J. Reinforced Plastics Compos., **6**, pp. 66–88.

[14] Nassehi, V., Dhillon, J., and Mascia, L., 1993, ''Finite Element Simulation of the Micromechanics of Interlayered Polymer/Fibre Composites: A Study of the Interactions Between the Reinforcing Phases,'' Compos. Sci. Technol., **47**, pp. 349–358.

[15] Mukherjee, S., 1982, *Boundary Element Methods in Creep and Fracture*, Applied Science Publishers, New York.

[16] Cruse, T. A., 1988, *Boundary Element Analysis in Computational Fracture Mechanics*, Kluwer, Dordrecht, The Netherlands.

[17] Banerjee, P. K., 1994, *The Boundary Element Methods in Engineering*, McGraw-Hill, New York.

[18] Cruse, T. A., 1996, ''BIE Fracture Mechanics Analysis: 25 Years of Developments,'' Computational Mech., **18**, pp. 1–11.

[19] Oshima, N., and Watari, N., 1992, ''Calculation of Effective Elastic Moduli of Composite Materials With Dispersed Parallel Fibers,'' *Theoretical and Applied Mechanics*, M. Hori and G. Yagawa, eds., Japan National Committee for Theoretical and Applied Mechanics, Science Council of Japan, **41**, pp. 181–188.

[20] Gulrajani, S. N., and Mukherjee, S., 1993, ''Sensitivities and Optimal Design of Hexagonal Array Fiber Composites With Respect to Interphase Properties,'' Int. J. Solids Struct., **30**, No. 15, pp. 2009–2026.

[21] Pan, L., Adams, D. O., and Rizzo, F. J., 1998, ''Boundary Element Analysis for Composite Materials and a Library of Green's Functions,'' Comput. Struct., **66**, No. 5, pp. 685–693.

[22] Krishnasamy, G., Rizzo, F. J., and Liu, Y. J., 1994, ''Boundary Integral Equations for Thin Bodies,'' Int. J. Numer. Methods Eng., **37**, pp. 107–121.

[23] Gray, L. J., Martha, L. F., and Ingraffea, A. R., 1990, ''Hypersingular Integrals in Boundary Element Fracture Analysis,'' Int. J. Numer. Methods Eng., **29**, pp. 1135–1158.

[24] Krishnasamy, G., Rizzo, F. J., and Rudolphi, T. J., 1991, ''Hypersingular Boundary Integral Equations: Their Occurrence, Interpretation, Regularization, and Computation,'' *Developments in Boundary Element Methods*, Vol. VII, P. K. Banerjee et al., eds., Elsevier Applied Science Publishers, London, Chapter 7.

[25] Liu, Y. J., and Rizzo, F. J., 1997, ''Scattering of Elastic Waves From Thin Shapes in Three Dimensions Using the Composite Boundary Integral Equation Formulation,'' J. Acoust. Soc. Am., **102**, No. 2, Pt. 1, Aug., pp. 926–932.

[26] Liu, Y. J., 1998, ''Analysis of Shell-Like Structures by the Boundary Element Method Based on 3-D Elasticity: Formulation and Verification,'' Int. J. Numer. Methods Eng., **41**, pp. 541–558.

[27] Luo, J. F., Liu, Y. J., and Berger, E. J., 1998, ''Analysis of Two-Dimensional Thin Structures (From Micro-to Nano-scales) Using the Boundary Element Method,'' Computational Mech., **22**, pp. 404–412.

[28] Mukherjee, S., 1999, ''On Boundary Integral Equations for Cracked and for Thin Bodies,'' Math. Mech. Solids, in press.

[29] Cruse, T. A., and Aithal, R., 1993, ''Non-singular Boundary Integral Equation Implementation,'' Int. J. Numer. Methods Eng., **36**, pp. 237–254.

[30] Huang, Q., and Cruse, T. A., 1993, ''Some Notes on Singular Integral Techniques in Boundary Element Analysis,'' Int. J. Numer. Methods Eng., **36**, pp. 2643–2659.

[31] Liu, Y. J., Zhang, D., and Rizzo, F. J., 1993, ''Nearly Singular and Hypersingular Integrals in the Boundary Element Method,'' *Boundary Elements XV*, C. A. Brebbia and J. J. Rencis, eds., Computational Mechanics Publications, Southampton, UK, pp. 453–468.

[32] Rudolphi, T. J., 1991, ''The Use of Simple Solutions in the Regularization of Hypersingular Boundary Integral Equations,'' Mathl. Comput. Modelling, **15**, pp. 269–278.

[33] Liu, Y. J., and Rudolphi, T. J., 1991, ''Some Identities for Fundamental Solutions and Their Applications to Weakly-Singular Boundary Element Formulations,'' Eng. Anal. Boundary Elem., **8**, No. 6, pp. 301–311.

[34] Chandrupatla, T. R., and Belegundu, A. D., 1997, *Introduction to Finite Elements in Engineering*, 2nd Ed., Prentice-Hall, Englewood Cliffs, NJ.

[35] Timoshenko, S. P., and Goodier, J. N., 1987, *Theory of Elasticity*, 3rd Ed., McGraw-Hill, New York.

Analysis of a Sector Crack in a Three-Dimensional Voronoi Polycrystal With Microstructural Stresses

M. S. Wu
Mem. ASME

J. Guo
Graduate Student

Department of Engineering Mechanics,
University of Nebraska-Lincoln,
W317.4 Nebraska Hall,
Lincoln, NE 68588-0526

The Mode I stress intensity factor of a sector crack in a three-dimensional Voronoi polycrystal is computed by the body force technique. Microstructural stresses arising from the elastic anisotropy of grains (cubic and hexagonal) and the random grain orientations are estimated using the Eshelby procedure and incorporated in the stress intensity factor calculations. For metallic polycrystals, it is shown that the stress intensity factor depends significantly on the elastic anisotropy ratio, the grain orientations, the remote stress state, and the microstructural stresses. [S0021-8936(00)03401-2]

1 Introduction

Microstructural stress distributions can be generated in a polycrystalline aggregate due to the elastic anisotropy or thermal expansion anisotropy mismatch between the constituent grains. For instance, cooling from the processing temperature gives rise to residual microstructural stresses in ceramic materials due to thermal expansion anisotropy and can result in spontaneous grain boundary cracks ([1,2]). Grain boundary misorientation, which gives rise to stress concentrations due to the different orientations of elastically anisotropic grain neighbors, is also known to have an influence on corrosion ([3]) and intergranular stress corrosion cracking of metallic alloys ([4,5]).

There exists a large body of literature on estimating microstructural stresses due to thermal expansion and elastic anisotropy. Evans [2] computed the thermal stresses in a two-dimensional polycrystal of regular hexagonal grains by the procedure of cutting, straining, and welding ([6]). Assuming that the grains are elastically isotropic and thermally anisotropic, the complete stress distribution was shown to be logarithmically singular at the triple junctions. Evans [7] simplified these calculations by extracting from the complete stress distribution the constant component which is dominant over the major portion of the grain boundary. In this latter work, the stress singularity was neglected in the calculations of the stress intensity factors of the triple junction cracks. Subsequently, Laws and Lee [8] obtained the microstructural stress field in a polycrystal of regular hexagons using the complex potentials of elasticity and on the same assumption of thermally anisotropic but elastically isotropic grains. They showed that about 200 grains surrounding a point of interest are necessary for accurate estimation of the stress at that point. They also showed that the stress intensity factors of grain boundary cracks are sensitive to the orientations of the surrounding grains.

Investigations of microcracking in ceramics using a polycrystal of regular hexagons while taking into account elastic and thermal expansion anisotropy were pursued by Tvergaard and Hutchinson [9] using the finite element method. Planar orthotropic and cubic crystals were considered. The order of the stress singularity at the triple junctions, taken to be of the power-law type, was computed as a function of grain orientation and the degree of elastic anisotropy. For cubic crystals, the degree of elastic anisotropy is measured by $R=(C_{12}+2C_{44})/C_{11}$ and $Q=2C_{44}/C_{12}$, where C_{ij} $(i,j=1,2,\ldots,6)$ are the elastic constants of a cubic crystal. For $Q=1$, the J-integral associated with a triple junction crack in a material under uniaxial plane strain was shown to be less than the value for the isotropic case if $R>1$ and more than it if $R<1$. Subsequently, the probability density functions of the residual stresses in ceramic materials due to elastic anisotropy, thermal anisotropy, and microcracking were shown to be Gaussian ([10]). The computations were carried out by the finite element method on planar hexagonal grains. It was also shown that the Gaussian nature of the distributions and the magnitude of the residual stresses were not affected by random distortions of the hexagonal grains.

A two-dimensional polycrystal modeled by the Poisson-Voronoi (or simply Voronoi) tessellation was used by Wu and Niu [11] to investigate microstructural stresses in polycrystalline S2 ice with hexagonal structure (S2 refers to a type of ice with *c*-axes randomly distributed and confined within planes perpendicular to the growth direction). Using the Eshelby procedure, they showed that the microstructural stresses due to elastic or thermal anisotropy are Gaussian with zero means. Also, the standard deviations are dependent on the components of the microstructural stress and on positions on the grain boundary. Furthermore, stable cracks nucleated under multiple dislocation pileups have a positively skewed length probability density function, i.e., the mode is less than the mean. Subsequently, Wu and He [12] studied crack statistics under the same mechanism in polycrystalline aluminum using a two-dimensional Voronoi polycrystal, but without considering the microstructural stresses. The focus in that paper is the interaction between the pile ups of grain boundary dislocations on intersecting grain boundaries and the nucleating crack. This work accounts for redistribution of stress acting on the site of the crack prior to its formation. It was found that the probability density functions of the stable and unstable crack lengths are positively and negatively skewed, respectively.

In several recent works, microstructural stresses due to elastic anisotropy in three-dimensional Voronoi polycrystals were computed by the finite element method. For instance, Kozaczek et al. [13] analyzed the distributions of microstructural stress measures, i.e., the von Mises stress and the hydrostatic stress, as a function of grain orientations, microstructure, and loading conditions. Up to 500 three-dimensional grains were analyzed. The grain shape, size, and orientation were found to have a more pronounced effect on the distributions than the loading conditions. The hydrostatic

Contributed by the Applied Mechanics Division of THE AMERICAN SOCIETY OF MECHANICAL ENGINEERS for publication in the ASME JOURNAL OF APPLIED MECHANICS. Manuscript received by the ASME Applied Mechanics Division, Apr. 21, 1999; final revision, Sept. 15, 1999. Associate Technical Editor: M. Ortiz. Discussion on the paper should be addressed to the Technical Editor, Professor Lewis T. Wheeler, Department of Mechanical Engineering, University of Houston, Houston, TX 77204-4792, and will be accepted until four months after final publication of the paper itself in the ASME JOURNAL OF APPLIED MECHANICS.

stress showed greater dependence on the disorientation angle than the von Mises stress. Also, Kumar et al. [14] studied the dependence of several micrcstructural stress measures on the elastic anisotropy of fourteen cubic materials, as characterized by the Zener anisotropy parameter $A=2C_{44}/(C_{11}-C_{12})$. Their calculations were based on the use of the finite element method on a three-dimensional polycrystal with 200 grains. For $0.25<A<9$, stress measures such as the average principal stress and the average von Mises stress were shown to be dependent on A with a minimum just beyond $A=1$. The largest values of the average maximum principal stress and the average maximum von Mises stress occur at the largest value of A considered, and are about 1.05 and 1.30 times the applied stress, respectively.

Investigations of a crack within a three-dimensional polycrystal with microstructural stresses due to elastic or thermal expansion anisotropy are limited. Ghahremani and Hutchinson [15] investigated the exponent of the stress singularity at conical wedge vertices with consideration of elastic as well as thermal expansion anisotropy. Super singularities with exponents greater than the classical crack singularity of 1/2 were found. They also studied the energy release rate of an axisymmetric conical crack, and concluded that the nucleated crack is highly stable and its size is typically a small fraction of the grain diameter. In this paper, the effects of elastic anisotropy and random grain orientation on a planar crack in a random and topologically accurate polycrystal model are analyzed. A three-dimensional Voronoi polycrystal of 1139 grains is constructed, out of which the central 300 grains are used to determine the microstructural stress distribution at the site of an interface crack. The microstructural stresses are estimated by the Eshelby procedure and used in the calculation of the Mode I stress intensity factor of the crack. The crack is assumed to be a sector of a penny-shaped crack, i.e., a crack bounded by two edges of a grain face and a circular front. The body force method is used to compute the stress intensity factor. The dependence of the stress intensity factor on the elastic anisotropy, the grain orientations, the remote stress state, and the microstructural stresses is investigated for metallic materials with cubic and hexagonal structures.

The paper is organized as follows. In Section 2, the algorithm for generating a three-dimensional Voronoi polycrystal is outlined. In Section 3, the method of estimating the microstructural stress is described. In Section 4, the fundamental equations for a three-dimensional sector crack modeled by body force densities are summarized. The numerical results are presented in Section 5, and the conclusions are given in Section 6.

2 Generation of Three-Dimensional Voronoi Polycrystal

The three-dimensional Voronoi tessellation is topologically equivalent to the microstructure of real metals and ceramics. It has the following main characteristics: All grain nuclei appear at the same instant of time at random spatial positions which remain fixed in time, and the growth rate of each grain is the same in all directions. Voronoi grains satisfy the following basic property: All points closer to a given nucleus belong to the grain with that nucleus. Points on grain faces, edges, and vertices are shared by two, three, and four grains, respectively. The grains are convex polyhedral cells with planar faces. Kumar et al. [16] have developed an algorithm for generating a three-dimensional Voronoi polycrystal containing several hundred thousand grains. In this paper, a simple algorithm based on the basic property is developed. It can be used to produce several thousand grains with ease. The algorithm is based on finding the vertices of a grain associated with a nucleus, from which the faces and then the edges are determined by post-processing. The algorithm is outlined in the following:

1 Define a unit cube containing M randomly distributed nuclei. The nuclei positions are assigned by a random number generator.

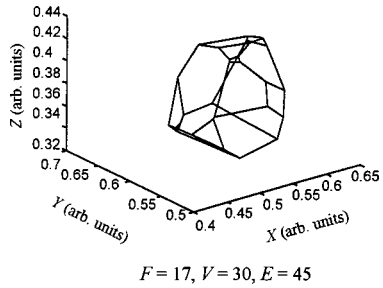

Fig. 1 A typical Voronoi grain generated by the algorithm described in Section 2

2 Select the ith nucleus N_i, $i=1,2,\ldots,M$.

3 Select a spherical region S of radius r around N_i. Denote by M_i the number of nuclei within S.

4 Within S, draw a straight line between N_i and N_j, $j=1,2,\ldots,M_i$; $j\neq i$. This yields a set of M_i-1 lines.

5 Construct the M_i-1 planes perpendicular to and which bisect the above lines.

6 Determine the coordinates of the ${}^{M_i-1}C_3$ intersection points I_k, $k=1,2,\ldots,{}^{M_i-1}C_3$ of groups of three planes generated from Step 5.

7 Compare the distance d_{ik} between N_i and I_k with all other distances d_{jk} between N_j and I_k in S. If $d_{ik}\leqslant d_{jk}\ \forall j\neq i$, I_k is a vertex associated with the ith nucleus and the three associated grain planes are infinite planes containing the grain faces. All vertices and grain planes for the ith grain are determined in this manner. Let V and F be the number of vertices and distinct faces of the ith grain, respectively.

8 Repeat Steps 3–7 for different N_i's so that vertices and planes of all M grains are determined.

9 An infinite grain plane becomes a finite grain face when delimited by the vertices lying on it. It is a simple matter to determine which of those previously found vertices of the ith grain satisfy the equation of a specific grain plane. In this manner, all F grain faces are exactly determined.

10 To determine if two vertices of a grain face should be connected to from a grain edge, check if these two vertices belong to another face of the same grain. If they do, they must connect to form an edge and these two faces must share this edge. In this manner, all edges of a particular grain face are exactly determined. Avoiding repeat counting, the total number of edges for a given grain can then be determined and denoted by E.

For each grain, the topological constraints given by Euler's relation $V+F-E=2$ and the relation $V=2F-4$ ([17]) are verified. Grains that do not satisfy these relations are typically those lying at the edges of the cube. Occasionally, one or two grains in the central region of the cube may not satisfy these relations due to inaccuracies in comparing distances. This is resolved by repositioning the associated nuclei randomly within a small radius around their original locations. Also, the purpose of the sphere S with radius r is to limit the number of searches around any ith nucleus to within reasonable computation times. A value of $r=0.2$ is found to be sufficient for generating 1139 complete grains from a total of 1500 nuclei.

Figure 1 shows a typical grain generated by the algorithm. The number of faces, vertices and edges is given by $F=17$, $V=30$, and $E=45$. Based on the sample of 1139 grains, the probability of the number of faces of a grain is shown in Fig. 2(a). The mean is 14.9043, compared to the value of 15.5355 obtained by a simulation study of 358,000 grains ([16]). The maximum number of faces is 27 and the minimum is 7. By the topological constraints, the mean number of vertices and mean number of edges of a grain are 25.8086 and 38.7129, respectively, compared to the values of 27.0710 and 40.6065 (based on $F=15.5355$). Furthermore, the

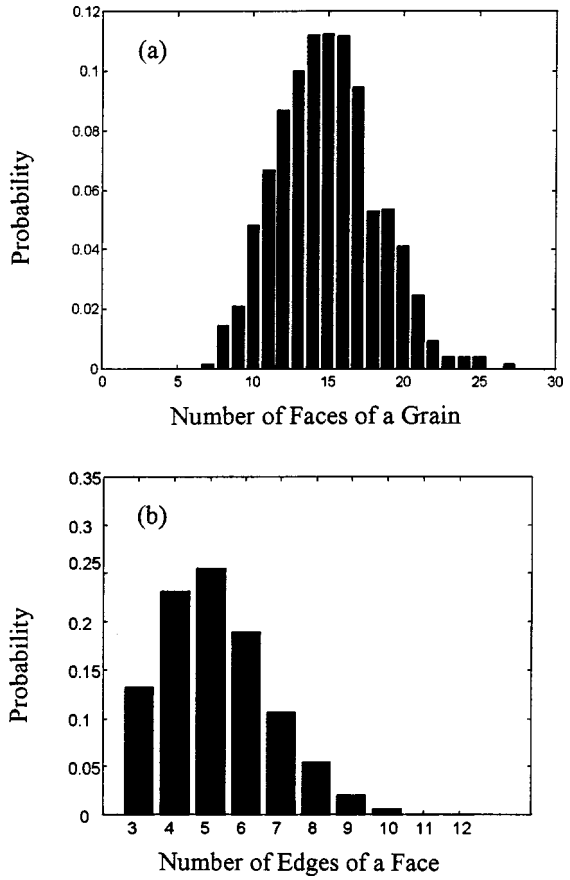

Fig. 2 The probability distributions of (*a*) the number of faces of a grain and (*b*) the number of edges of a grain face in a three-dimensional Voronoi tessellation

probability of the number of edges of a grain face is shown in Fig. 2(*b*). The mean is 5.195, compared to the value of 5.226 ([16]). The maximum number of edges of a grain face is 12 and the minimum is three. These comparisons show that for the limited sample size simulated in this study, the major statistical characteristics of a theoretical three-dimensional Voronoi tessellation are essentially reproduced.

3 Microstructural Stress Estimation

The microstructural stress is estimated on the assumption that the elastically anisotropic grains are randomly oriented, i.e., the polycrystal has no texture. Thus, the polycrystal is globally isotropic and all equations for the polycrystal are written using linear isotropic elasticity. Anisotropy elasticity is only used for individual grains.

The Eshelby procedure of cutting, straining and welding ([6]) is used to estimate the microstructural stress, as was also used by Evans [2] and Wu and Niu [11]. Assume that a remote stress $\boldsymbol{\sigma}^{\infty}$ is applied to a polycrystal and the stress state at an interior point is of interest. Figure 3(*a*) shows a group of grains (generated by the algorithm) surrounding the point. A certain number (m_t) of these grains are removed from the polycrystal (cutting) and strained freely under the remote stress (straining), see Fig. 3(*b*). The deformation $\boldsymbol{\varepsilon}^m$ in the grains $m=1,2,3,\ldots,m_t$ is therefore

$$\boldsymbol{\varepsilon}^m=\mathbf{S}^m\boldsymbol{\sigma}^{\infty}, \tag{1}$$

where $\mathbf{S}^m$ is the six-by-six compliance matrix for the mth grain in the global coordinate system $X-Y-Z$. The deformation in the mth grain differs from the average deformation in the polycrystal of compliance $\tilde{\mathbf{S}}$ by

$$\Delta\boldsymbol{\varepsilon}^m=(\tilde{\mathbf{S}}-\mathbf{S}^m)\boldsymbol{\sigma}^{\infty}. \tag{2}$$

The corresponding misfit stress $\boldsymbol{\sigma}^{om}$ is

$$\boldsymbol{\sigma}^{om}=\mathbf{C}^m\Delta\boldsymbol{\varepsilon}^m=(\mathbf{C}^m\tilde{\mathbf{S}}-\mathbf{I})\boldsymbol{\sigma}^{\infty}, \tag{3}$$

where $\mathbf{I}$ is the six-by-six identity matrix and $\mathbf{C}^m$ is the six-by-six stiffness matrix of the mth grain. Each separated grain is then subjected to the additional strain $\Delta\boldsymbol{\varepsilon}^m$ so that it has the same average strain of the polycrystal. This is done by applying tractions $\mathbf{T}^{mn}$ on the grain faces $n=1,2,3,\ldots,n_t$ of the mth grain:

$$\mathbf{T}^{mn}=\boldsymbol{\sigma}^{om}\cdot\mathbf{n}^{mn}, \tag{4}$$

where $\mathbf{n}^{mn}$ is the unit normal to the nth face of the mth grain. In the last step, all grains are placed back in the polycrystal and the surface tractions are removed by the application of body forces equal in magnitude but opposite in direction to $\mathbf{T}^{mn}$, see Fig. 3(*c*). The body forces $-\mathbf{T}^{mn}$ induce additional stresses $\boldsymbol{\sigma}^r$ in the polycrystal. The total stress at the point is thus given by

$$\boldsymbol{\sigma}^t=\boldsymbol{\sigma}^{\infty}+\tilde{\boldsymbol{\sigma}}=\boldsymbol{\sigma}^{\infty}+\left(\boldsymbol{\sigma}^{om}+\sum_{m=1}^{m_t}\sum_{n=1}^{n_t}\boldsymbol{\sigma}^r\right). \tag{5}$$

The term within the parentheses is the microstructural stress $\tilde{\boldsymbol{\sigma}}$ due to elastic anisotropy.

The microstructural stress averaged over space yields a zero mean so that $\langle\boldsymbol{\sigma}^t\rangle=\langle\boldsymbol{\sigma}^{\infty}\rangle$. This has been shown numerically by Wu and Niu [11] for a two-dimensional polycrystal, in which $\tilde{\boldsymbol{\sigma}}$ at all positions of the same type is found to be normally distributed with zero mean. The positions of the same type refer to, for instance, midpoints of all grain boundaries in the sample, or points at distances equal to a thousandth of the grain boundary lengths from the triple junctions. This latter result also suggests that the stress singularities at triple junctions can be tensile or compressive, or that they do not exist.

To compute $\boldsymbol{\sigma}^r$, it is noted that the stress components in the cylindrical frame $r-\theta-z$ due to a point load P along the z-direction in an infinite isotropic medium are ([18])

$$\sigma_r=\frac{P}{8\pi(1-\nu)}[(1-2\nu)z(r^2+z^2)^{-3/2}-3r^2z(r^2+z^2)^{-5/2}], \tag{6}$$

$$\sigma_\theta=\frac{P}{8\pi(1-\nu)}(1-2\nu)z(r^2+z^2)^{-3/2}, \tag{7}$$

$$\sigma_z=-\frac{P}{8\pi(1-\nu)}[(1-2\nu)z(r^2+z^2)^{-3/2}+3z^3(r^2+z^2)^{-5/2}], \tag{8}$$

$$\sigma_{rz}=-\frac{P}{8\pi(1-\nu)}[(1-2\nu)z(r^2+z^2)^{-3/2}+3rz^2(r^2+z^2)^{-5/2}], \tag{9}$$

where ν is the Poisson's ratio. Because of axisymmetric loading about the z-axis, the above are the nonvanishing stress components. To perform integration associated with body forces acting over the entire grain face, it is expedient to work with a local Cartesian frame $x'-y'-z'$ with z' normal to the grain face (Fig. 4). First, consider the case where P is normal to the grain face. In the local frame, let $P=\sigma^N dA$ act at the position $(p,q,0)$ parallel to z', where dA is the elemental area over which σ^N (defined later) acts. Suppose the stress components at another point $M(x',y',z')$ are desired (see Fig. 4(*a*)). Then, it is straightforward to show that the stress components in the local frame are

$$\sigma_{x'}=\sigma_r\cos^2\theta+\sigma_\theta\sin^2\theta, \tag{10}$$

$$\sigma_{y'}=\sigma_r\sin^2\theta+\sigma_\theta\cos^2\theta, \tag{11}$$

$$\sigma_{z'}=\sigma_z \tag{12}$$

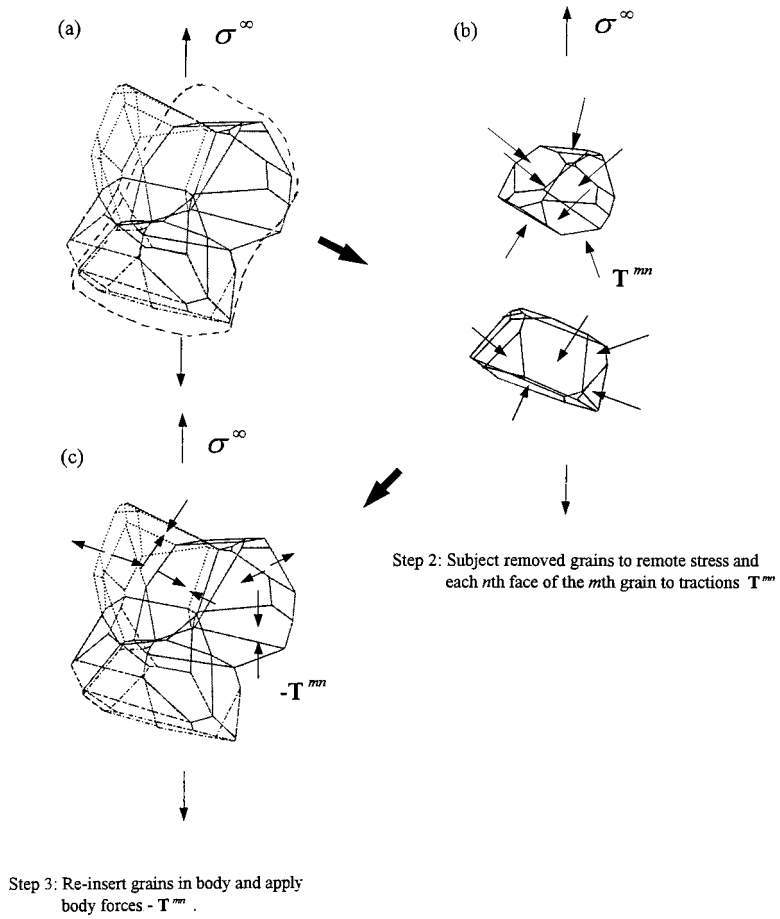

Fig. 3 The Eshelby procedure of (*a*) cutting, (*b*) straining, and (*c*) welding for estimating microstructural stresses in a polycrystal

$$\sigma_{x'y'}=(\sigma_r-\sigma_\theta)\sin\theta\cos\theta, \tag{13}$$

$$\sigma_{x'z'}=\sigma_{rz}\cos\theta, \tag{14}$$

$$\sigma_{y'z'}=\sigma_{rz}\sin\theta, \tag{15}$$

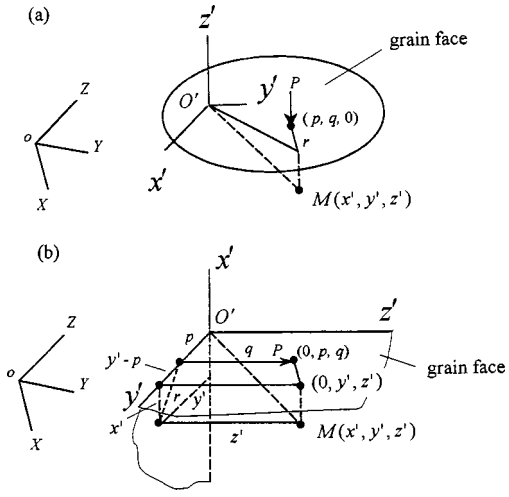

Fig. 4 Point forces *P* acting on a grain face: (*a*) *P* is normal to the grain face, (*b*) *P* is tangential to the grain face

where the cylindrical components are given in Eqs. (6)–(9). Also,

$$z=z',r^2=(x'-p)^2+(y'-q)^2, \tag{16}$$

$$\sin\theta=\frac{y'-q}{\sqrt{(x'-p)^2+(y'-q)^2}},\quad \cos\theta=\frac{x'-p}{\sqrt{(x'-p)^2+(y'-q)^2}}. \tag{17}$$

Next, consider the case where the body force $P=\sigma^T dA$ is tangential to the grain face, see Fig. 4(*b*). The stress σ^T is defined later. In this case, let x' be perpendicular to the grain face and P be along z'. Also, the r-axis is now in the $x'-y'$ plane. In the local cylindrical frame, the stress components at $M(x',y',z')$ due to P is still given by Eqs. (6)–(9) but with $z'-q$ replacing z and r^2 given by

$$r^2=x'^2+(y'-p)^2. \tag{18}$$

In the $x'-y'-z'$ system, the stress components take the same form as Eqs. (10)–(15), except that $\sin\theta$ and $\cos\theta$ are now given by

$$\sin\theta=\frac{y'-p}{\sqrt{x'^2+(y'-p)^2}},\quad \cos\theta=\frac{x'}{\sqrt{x'^2+(y'-p)^2}}. \tag{19}$$

In the global frame $X-Y-Z$, which is fixed in position and orientation in the polycrystal, the stress components can be obtained

from the components in the local frames $x'-y'-z'$ by transformation using the direction cosines between the local axes of Figs. 4(*a*) and 4(*b*) and the global axes.

In the above equations, σ^N and σ^T are the magnitudes of the normal and traction vectors $\boldsymbol{\sigma}^N$ and $\boldsymbol{\sigma}^T$ determined from the negative of the traction $\mathbf{T}^{mn}$ of Eq. (4), i.e.,

$$\boldsymbol{\sigma}^N=-(\mathbf{n}^{mn}\otimes\mathbf{n}^{mn})\mathbf{T}^{mn},\quad \boldsymbol{\sigma}^T=-(\mathbf{I}-\mathbf{n}^{mn}\otimes\mathbf{n}^{mn})\mathbf{T}^{mn}. \quad (20)$$

The direction of $\boldsymbol{\sigma}^T$ determines the direction of the local z'-axis in Fig. 4(*b*). To obtain the stress $\boldsymbol{\sigma}^{r\prime}=\{\sigma^r_{x'},\sigma^r_{y'},\sigma^r_{z'},\sigma^r_{y'z'},\sigma^r_{z'x'},\sigma^r_{x'y'}\}^T$ (T is the transpose) in the polycrystal due to σ^N and σ^T over a grain face, the stress components must be integrated over the polygonal face Δ_f, i.e.,

$$\boldsymbol{\sigma}^{r\prime}(x',y',z')=\int_{\Delta_f}\boldsymbol{\sigma}'(x',y',z',p,q)dA, \quad (21)$$

where the integrand $\boldsymbol{\sigma}'=\{\sigma_{x'},\sigma_{y'},\sigma_{z'},\sigma_{y'z'},\sigma_{z'x'},\sigma_{x'y'}\}^T$ is the stress due to either σ^N or σ^T (see Eqs. (10)–(15)). The above area integral is computed numerically by Gauss quadrature.

4 Mode I Stress Intensity Factor of a Sector Crack

It is assumed that the crack has the shape of a sector of a penny-shaped crack and is embedded between two grains on the interface. Only the Mode I stress intensity factor is considered. It is calculated by the body force technique ([19,20]), which is outlined in the following. The crack is interfacial, and although the stress intensity factor of an interfacial penny-shaped crack can be calculated by using a bimaterial model ([21]), theoretical techniques for treating a sector crack in a multigrain ensemble are not presently available. Consequently, it is assumed that the sector crack exists in an isotropic polycrystal and the anisotropy effects are incorporated through microstructural stresses superimposed on the remote loading.

Define a Cartesian coordinate system $x-y-z$ having the x and y-axes in the plane of the crack. The crack problem is then treated as the problem of an uncracked solid subjected to remote and microstructural stresses in addition to certain body force distributions over the site where the crack is to form. The body forces consist of the force doublet with density $f_{zz}(\xi,\eta)$ and in-plane forces with densities $f_x(\xi,\eta)$ and $f_y(\xi,\eta)$ such that

$$f_x(\xi,\eta)=-\frac{\nu}{1-\nu}\frac{\partial f_{zz}(\xi,\eta)}{\partial\xi},\quad f_y(\xi,\eta)=-\frac{\nu}{1-\nu}\frac{\partial f_{zz}(\xi,\eta)}{\partial\eta}, \quad (22)$$

where ξ and η are the coordinates of the location of the body forces (see Fig. 5(*a*)). It can be shown that the normal stress σ^B_z on the crack face due to the body forces is given by the area integral

$$\sigma^B_z(x,y,0)=\frac{H}{2\pi}\left[\int_{\Delta_c}\left(\frac{1}{r_1^3}+\frac{6z^2}{r_1^5}-\frac{15z^4}{r_1^7}\right)f_{zz}(\xi,\eta)dA\right]_{z\to 0}, \quad (23)$$

where

$$r_1=[(x-\xi)^2+(y-\eta)^2+z^2]^{1/2},\quad H=\frac{1-2\nu}{4(1-\nu)^2}, \quad (24)$$

and Δ_c is the region of the crack. The crack region is divided into triangular elements, and the density of the body force doublet over the elements is assumed to be

$$f_{zz}(\xi,\eta)=\frac{W(\xi,\eta)}{H}\sqrt{2c\varepsilon-\varepsilon^2}, \quad (25)$$

where $W(\xi,\eta)$ is a weight function, c is a specific length of the crack, and ε is the shortest distance from the point (ξ,η) to the crack front. The weights W_{jk} at the kth vertex (nodal point) of the jth triangle are taken as unknown. The value of the weight at a point inside each element is assumed to be a linear function of the coordinates of the three vertices of the element

$$W(\xi,\eta)=c_j\xi+d_j\eta+e_j, \quad (26)$$

where c_j, d_j, and e_j can be expressed in terms of W_{jk} and the coordinates of the three vertices.

On the crack surface, it is required that the resultant force associated with $\sigma^B_z(x,y,0)$ in each subregion should compensate that due to the remote and microstructural stresses. If the original triangular elements are taken as the subregions for these resultant force conditions, the number of equations differs from the number of unknowns. Consequently, polygonal subregions Δ_p are formed by connecting the centroids of the triangular elements and where necessary, the midpoints of the crack front (see Fig. 5(*b*)). Assuming that the crack is traction-free, the resultant force condition over Δ_p is then given by

$$P_z+\int_{\Delta_p}\sigma^t_z(x,y)dA=0, \quad (27)$$

where the integral represents the z-component of the total stress (remote and microstructural, see Eq. (5)) acting over Δ_p, and P_z is the resultant force over Δ_p due to the body forces

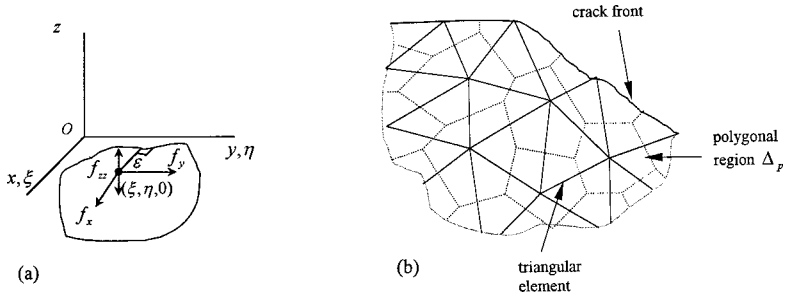

Fig. 5 (*a*) Body force doublet of density f_{zz} and body forces of densities f_x and f_y acting at the point $(\xi,\eta,0)$ within the crack plane. (*b*) Triangular finite elements and polygonal regions within crack used to obtain the resultant force boundary conditions.

$$P_z = \int_{\Delta_p} \sigma_z^B(x,y,0)\,dA$$
$$= \frac{1}{2\pi}\int_{\Delta_p}\left[\int_{\Delta_c}\left(\frac{1}{r_1^3}+\frac{6z^2}{r_1^5}-\frac{15z^4}{r_1^7}\right)\right.$$
$$\left.\times W(\xi,\eta)\sqrt{2c\varepsilon-\varepsilon^2}\,d\varepsilon\right]_{z\to 0} dA. \quad (28)$$

Equation (28) is a quadruple integral containing the unknowns W_{jk} in the expression for $W(\xi,\eta)$. Substituting Eqs. (5) and (28) into Eq. (27), a system of algebraic equations is obtained corresponding to all the polygonal subregions Δ_p. For details, refer to Isida et al. [20]. The Mode I stress intensity factor along an arbitrary point (ξ,η) can be computed from the expression

$$K_I = W(\xi,\eta)\sqrt{\pi c}, \quad (29)$$

where $W(\xi,\eta)$ is the weight at this point. In this investigation, c is chosen to be the radius a of the sector crack.

By the superposition in Eq. (27), the redistribution of the remote and microstructural stress due to the formation of the crack is taken into account. The stress intensity factor computed should be more accurate than that obtained by integrating the Green's functions due to concentrated loads over the crack surface, since the latter method assumes that the total stress acting on the site of the crack is unperturbed by the nucleating crack.

5 Numerical Results

A polycrystal containing 300 cubic or hexagonal grains is analyzed. A remote stress σ_Z^∞ is applied in the global Z-direction. The grain orientation is defined by the three Euler angles θ, ϕ, and κ, which are assigned to each of the 300 grains by using a random number generator. Using standard notation, the three independent elastic constants of a cubic grain are C_{11}, C_{12}, and C_{44}, while the five independent constants of a hexagonal grain are C_{11}, C_{12}, C_{13}, C_{33}, and C_{44}. Assuming random grain orientations, the Lamé constants μ and λ for the polycrystal are given by

$$\mu = C_{44} - \frac{2C_{44}+C_{12}-C_{11}}{5},$$
$$\lambda = C_{12} - \frac{2C_{44}+C_{12}-C_{11}}{5}, \quad (30)$$

for cubic materials and

$$\mu = \frac{1}{30}(7C_{11}-5C_{12}+2C_{33}+12C_{44}-4C_{13}),$$
$$\lambda = \frac{1}{15}(C_{11}+C_{33}+5C_{12}+8C_{13}-4C_{44}), \quad (31)$$

Table 1 (*a*) Cubic materials (C_{11}, C_{12}, C_{44}, μ, and E are given in GPa)

	C_{11}	C_{12}	C_{44}	ν	μ	E	A
Cr	350	57.8	101	0.13	121	273.46	0.69
W	521	201	160	0.278	160	408.96	1
Al	108.2	61.3	28.5	0.347	26.5	71.39	1.21
Cu	168.4	121.4	75.4	0.324	54.6	144.58	3.21

(*b*) Hexagonal materials (C_{11}, C_{12}, C_{13}, C_{33}, C_{44}, μ, and E are given in GPa)

	C_{11}	C_{12}	C_{13}	C_{33}	C_{44}	ν	μ	E	A_h
Co	307	165	103	358.5	75.3	0.307	84.42	220.67	0.86
Cd	121	48.1	44.2	51.3	18.5	0.368	25.14	68.78	2.36
Zn	161	34.2	50.1	61.0	38.3	0.245	44.57	110.98	2.64

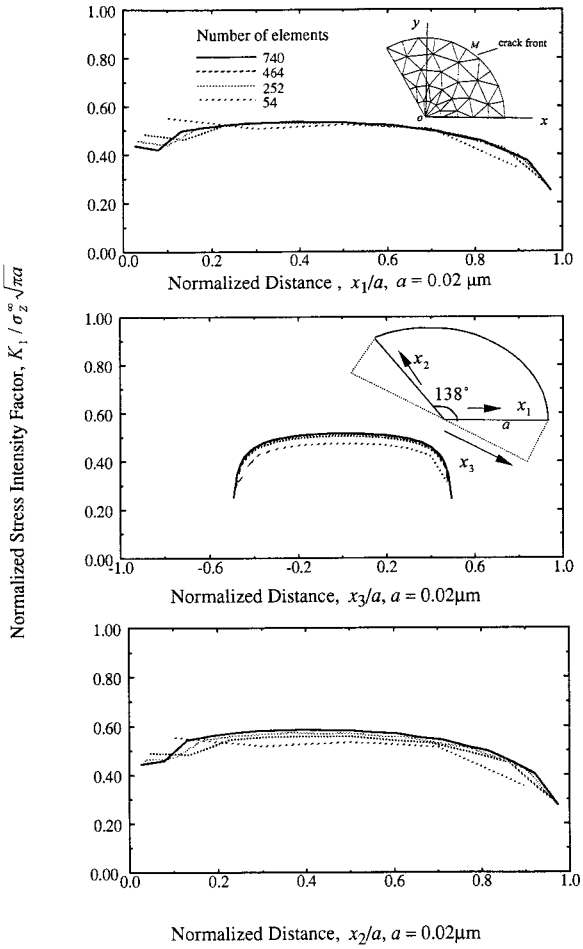

Fig. 6 Convergence of the normalized Mode I stress intensity factor along the crack edge with increase in the number of triangular elements

for hexagonal materials. The Young's modulus is given by $E = \mu(3\lambda+2\mu)/(\mu+\lambda)$. For the cubic grains, the Zener ratio $A = 2C_{44}/(C_{11}-C_{12})$ is used as a measure of the degree of elastic anisotropy. The value of $A=1$ corresponds to isotropy. For the hexagonal grains, the simple ratio $A_h = C_{11}/C_{33}$ is used instead. Four cubic (Al, Cr, Cu, and W) and three hexagonal (Cd, Co, and Zn) materials are considered in this paper. The values of the material parameters are listed in Table 1.

To determine the number of elements necessary for convergence of the numerical stress intensity factor, simulations were carried out for a sector crack using 54, 252, 464, and 740 elements. The crack is located in an infinite homogeneous body and has a radius of $a = 0.02\,\mu$m and an angle of 138 deg. The crack plane is normal to the Z-axis. Figure 6 shows an example of the mesh pattern. Microstructural stresses are omitted in these calculations. A uniform stress of 1 unit is applied in the Z-direction. In the figure, the normalized Mode I stress intensity factor $K_I/\sigma_Z^\infty\sqrt{\pi a}$ is plotted against the normalized coordinates x_1/a and x_2/a along the straight edges, and against x_3/a, the projected position of a point of the circular edge onto an imaginary diameter parallel to the tangent at the midpoint of the circular edge. It can be seen that numerical convergence is attained on both the circular and straight edges, except near the point $x_1/a = x_2/a = 0$ where the straight edges meet. Also, the results for the circular edge are symmetric about $x_3/a = 0$, while the results for the straight edges are approximately symmetric with respect to each other. Based on these results, a total of 252 elements are used in all subsequent calculations. Other than convergence, these results also show that

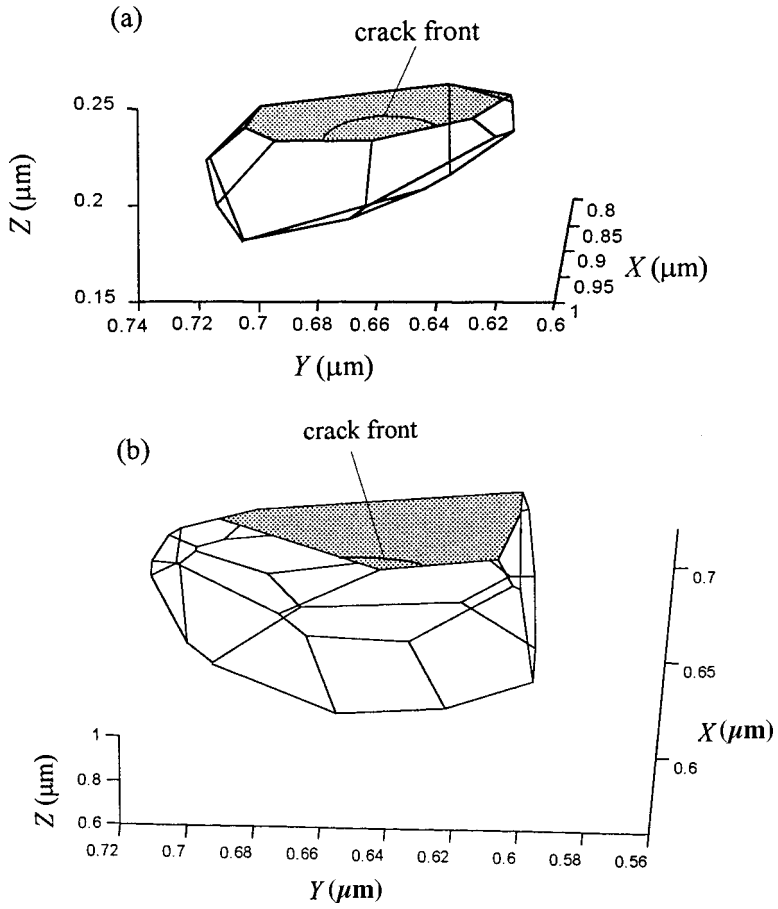

Fig. 7 Two grains used to investigate the dependence of the stress intensity factor of a sector crack on crack length, elastic anisotropy, crack angle, and remote stress state; (*a*) the crack plane is almost normal to the *Z*-direction, (*b*) the crack plane is about 45 deg to the *X*-axis and *Z*-axis

the normalized stress intensity factor has a maximum in the middle of the circular edge and decreases sharply near the ends. The maximum normalized stress intensity factor is ~0.51, which is less than the value of 0.64 calculated by the same program for a circular penny-shaped crack (exact value is 0.6366 to four decimal places).

Figure 7(*a*) shows a Voronoi grain with the orientation $\theta=74.67$ deg, $\phi=82.51$ deg, and $\kappa=99.37$ deg. The sector crack is located on a face with normal almost parallel to the *Z*-direction; the direction cosines of the unit normal being $n_X=0.04$, $n_Y=0.06886$, and $n_Z=0.9968$. The crack on this grain face is used in most of the following investigations (Figs. 8–10). To study the

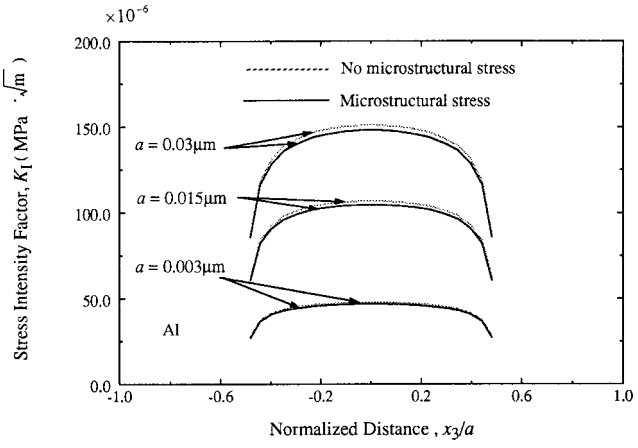

Fig. 8 Variation of the Mode I stress intensity factor along the circular edge with the projected position x_3/a, and dependence of the stress intensity factor on the crack length

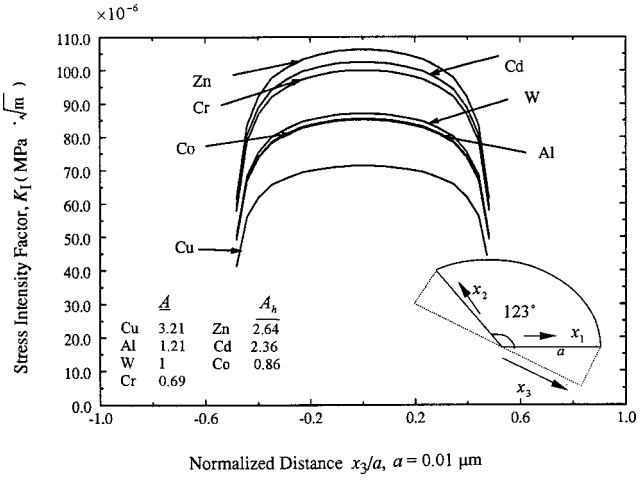

Fig. 9 Dependence of the Mode I stress intensity factor on the elastic anisotropy ratio (*A* for cubic materials and A_h for hexagonal materials)

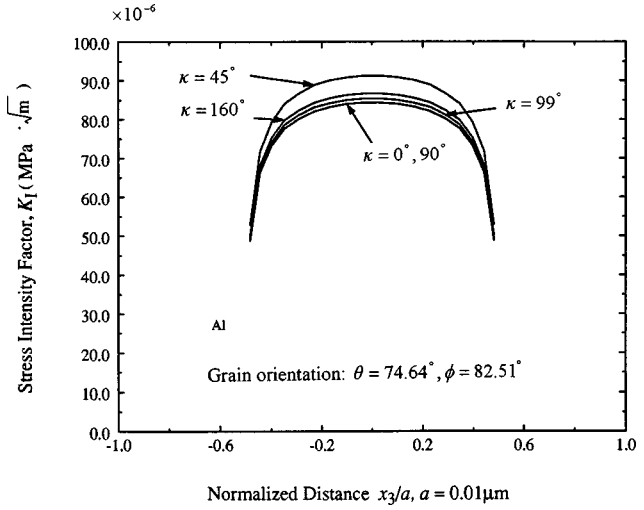

Fig. 10 Variation of the Mode I stress intensity factor with the orientation κ of one grain

effects of remote biaxial tension (Fig. 11), the second grain shown in Fig. 7(*b*) is used, for which $\theta=72.46$ deg, $\phi=79.32$ deg, and $\kappa=102.36$ deg. The unit normal to the grain face on which the sector crack is assumed to exist has the direction cosines $n_X=0.7036$, $n_Y=0.02546$, and $n_Z=0.7102$. The grain face makes an angle of about 45 deg with both the *X* and *Z*-axis. Also, both grains are located close to the center of the sample of 300 grains. The sample lies within a cube (containing 1139 complete grains) with edge lengths of 1 μm. The average grain size, calculated as the edge length of an equivalent grain of cubic shape in a sample of 1139 cubes, is therefore $\sim$0.1 μm.

The microstructural stress distribution on a grain face is found to have the following characteristics. It does not vary greatly over the grain face, and its average magnitude depends on *A*. For $A=1.21$ (aluminum), current calculations show that the microstructural stress is about 2.5 percent of the applied load, but for $A=0.69$ (chromium), it is about 20 percent of the applied load. Near the corners of the grain face, it is conjectured that the stress components may or may not be singular. As shown by Wu and Niu [11] for two-dimensional grains, the stress distributions at points very close to the triple junctions (one-thousandth of the

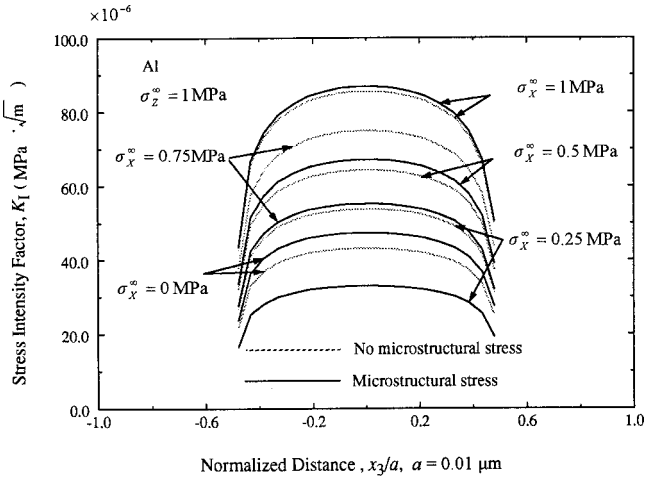

Fig. 11 Dependence of the Mode I stress intensity factor on the remote biaxial tension stress state. Discrepancies between results computed with and without microstructural stresses can be very significant.

grain boundary length) are normal with zero means, and have standard deviations two to three times larger than those of the stress distributions at the midpoints of grain boundaries. Unlike this previous investigation, however, the stresses induced by the negative of the body forces of Eq. (4) are not obtained in closed form, but their accuracy is consistent with the approximation associated with the Eshelby procedure as applied here to a globally isotropic polycrystal without detailed considerations of the stress singularities between contiguous grains isolated from the surrounding polycrystal. A further point of interest is that although 300 surrounding grains are used to determine the microstructural stress, the results have converged when the sample reaches a size as small as about 50 grains. The larger sample of $\sim$200 necessary for convergence in the case of a two-dimensional polycrystal can be attributed to the decay of elastic stresses with inverse distance in two-dimensional bodies but with inverse square distance in three-dimensional bodies.

In Figs. 8–10, the sector crack is located on the grain face shown in Fig. 7(*a*). The sector angle is $\sim$123 deg. The remote stress $\sigma_Z^\infty=1$ MPa. The polycrystal is assumed to be aluminum with $A=1.21$, unless otherwise specified (Fig. 9).

Figure 8 plots K_I in MPa$\sqrt{\mathrm{m}}$ versus the projected coordinate x_3/a for $a=0.003$, 0.015, and 0.03 μm. The stress intensity factors computed with and without microstructural stresses are both shown in the figure. It can be observed that K_I along the circular edge increases with *a*. The effect of microstructural stress on K_I is small for aluminum, but its effect increases for larger crack lengths. Furthermore, K_I is smaller if the microstructural stress is incorporated in the computations. This can be rationalized since the corresponding microstructural stress is compressive for the particular site under consideration. In general, however, K_I can be either underestimated or overestimated. Also, K_I is approximately symmetric about $x_3/a=0$. This is likely due to the fact that any microstructural stress asymmetry over the very small crack regions is not very significant.

Figure 9 shows the variation of K_I with x_3/a for four cubic and three hexagonal materials. The crack length is 0.01 μm. For the cubic materials Cu, Al, W, and Cr with $A=3.21$, 1.21, 1, and 0.69, respectively, K_I is shown to be a strong function of *A*. As *A* increases from 0.69 to 3.21, the maximum K_I decreases by $\sim$30 percent. For the present case, the greater (smaller) *A* is compared to 1 (isotropic case), the more compressive (tensile) the microstructural stress and the smaller (larger) K_I becomes. Whether *A* is greater or smaller than 1 depends on whether C_{44} is larger or smaller than $(C_{11}-C_{12})/2$. Hence, whether K_I computed without microstructural stress is an overestimate or underestimate depends on whether the shear resistance (C_{44}) on a (1 0 0) plane is larger or smaller than the shear resistance ($(C_{11}-C_{12})/2$) on a (1 1 0) plane. For the hexagonal materials, K_I for Zn ($A_h=2.64$) or Cd ($A_h=2.36$) is greater than the value for the isotropic case while K_I for Co ($A_h=0.86$) is less than it. As A_h increases from 0.86 to 2.36, the maximum K_I increases by $\sim$25 percent. For Zn and Cd, $C_{11}=C_{22}>C_{33}$, but for Co, $C_{11}=C_{22}<C_{33}$. Hence, whether K_I is an overestimate or an underestimate depends on whether the stiffness in the basal plane is larger or smaller than that in the perpendicular direction. It should be emphasized that these results are obtained for a specific crack on a specific grain face for uniaxial loading. For different orientations and shapes of grains around the crack, completely different results may be obtained. It is clear, however, that the elastic anisotropy of the grains has a strong effect on the stress intensity factor of a crack. Also, Fig. 9 shows that negligence of microstructural stresses in the calculation of K_I leads to serious errors. The results for W correspond to the case of isotropy and hence no microstructural stresses. If microstructural stresses in the other six materials were not taken into account, their stress intensity factor would have the same values as those calculated for W. Figure 9, however, shows that the maximum K_I value for Zn is $\sim$150 percent of the value for Cu when microstructural stresses are taken into consideration.

Figure 10 shows the influence of grain orientation. In this study, the orientations of all grains in the sample are held fixed, except for the orientation of the grain containing the crack on one of its faces. For this grain, $\theta=74.64$ deg, $\phi=82.51$ deg, but κ assumes five different values: 0 deg, 45 deg, 90 deg, 99 deg, and 160 deg. The case of weak anisotropy $A=1.21$ is considered. The crack length is again 0.01 μm. It can be seen that the maximum K_I depends quite significantly on the grain orientation, although the difference diminishes near the outer ends of the circular edge front. The results for $\kappa=0$ deg and 90 deg are identical because of cubic symmetry. The largest difference in results, which is about 10×10^{-6} MPa$\sqrt{\text{m}}$, occurs between $\kappa=45$ deg and 0 deg or 90 deg.

Figure 11 shows the dependence of K_I on the remote stress state (biaxial tension). The crack analyzed is that shown in Fig. 7(*b*). The radius is $a=0.01$ μm and the sector angle is $\sim$125 deg. Also, $A=1.21$ and $\sigma_Z^\infty=1$ MPa. The lateral stress assumes five values $\sigma_X^\infty=0$, 0.25, 0.5, 0.75, 1 MPa. The results computed with and without microstructural stresses are included in the figure. It can be seen that K_I does not increase monotonically with σ_X^∞ if microstructural stresses are included in the calculations. Specifically, the maximum K_I decreases substantially from $\sim47.5\times10^{-6}$ to $\sim32\times10^{-6}$ MPa$\sqrt{\text{m}}$ as σ_X^∞ increases from 0 to 0.25 MPa. If σ_X^∞ increases further until a state of equibiaxial tension is reached, the maximum K_I reaches a value of $\sim87.5\times10^{-6}$ MPa$\sqrt{\text{m}}$. In contrast, K_I increases monotonically with σ_X^∞ if microstructural stresses are neglected in the calculations. Furthermore, the difference in results between computations with and without microstructural stresses is a complicated function of σ_X^∞. For $\sigma_X^\infty=0$, 0.5, and 1 MPa, the maximum K_I computed without microstructural stresses underestimates the value determined with microstructural stresses by the factors of $\sim$1.1, 1.05, and 1.02, respectively. For $\sigma_X^\infty=0.25$ and 0.75 MPa, it overestimates the value computed with microstructural stresses by the factors of $\sim$1.6 and 1.35, respectively. It is also noteworthy that unlike the previous case of $\sigma_X^\infty=0$ in Fig. 8, K_I computed without microstructural stresses is an underestimate. Comparison of Figs. 8 and 11 also shows the importance of the morphological and crystallographic details surrounding the crack: For the same uniaxial tension and approximately the same sector angle and crack length, the maximum K_I in Fig. 8 is $\sim105\times10^{-6}$ MPa$\sqrt{\text{m}}$, while in Fig. 11 it is only $\sim47.5\times10^{-6}$ MPa$\sqrt{\text{m}}$.

6 Conclusions

An approximate theoretical analysis of the Mode I stress intensity factor of a sector crack in a three-dimensional polycrystal is presented. The analysis consists of three parts: (1) development of an algorithm for the Voronoi tessellation, (2) estimation of the microstructural stresses in the polycrystal by the Eshelby procedure of cutting, straining, and welding, and (3) computation of the stress intensity factor using the method of body forces. The results of the analysis for isolated sector cracks in a sample of 300 grains can be summarized as follows.

1 The stress intensity factor depends strongly on the elastic anisotropy of the grains. For cubic grains and the particular crack investigated, variation of A from 0.69 to 3.21 causes the maximum stress intensity factor on the circular crack front to change by $\sim$30 percent. For hexagonal grains and the same crack, variation of A_h from 0.86 to 2.64 causes the maximum stress intensity factor to change by $\sim$25 percent.

2 The SIF also depends significantly on the orientations and shapes of the grains around the crack.

3 In general, the stress intensity factor depends strongly on the remote biaxial stress state $(\sigma_X^\infty,\sigma_Z^\infty)$. The dependence on σ_X^∞ for a fixed σ_Z^∞ is nonmonotonous.

4 Computing the stress intensity factor without microstructural stresses may lead to serious errors. The error magnitude and sign depend on the morphological and crystallographic details of the grains around the crack as well as the remote loading.

Acknowledgments

The authors would like to express deep gratitude for the financial support of the National Science Foundation (Grant No: CMS-9523028), and the Department of Engineering Mechanics and the Center for Materials Research and Analysis, both of the University of Nebraska-Lincoln.

References

[1] Clarke, F. J. P., 1964, ''Residual Strain and the Fracture Stress-Grain Size Relationship in Brittle Solids,'' Acta Metall., **12**, pp. 139–143.
[2] Evans, A. G., 1978, ''Microfracture from Thermal Expansion Anisotropy—I. Single Phase Systems,'' Acta Metall., **26**, pp. 1845–1853.
[3] Palumbo, G., and Aust, K. R., 1990, ''Structure-Dependence of Intergranular Corrosion in High Purity Nickel,'' Acta Metall. Mater., **38**, pp. 2343–2352.
[4] Yamashita, M., and Mimaki, T., 1991, ''Intergranular Corrosion of Copper and α-Cu-Al Alloy Bicrystals,'' Philos. Mag. A, **63**, pp. 695–705.
[5] Crawford, D. C., and Was, G. S., 1992, ''The Role of Grain Boundary Misorientation in Intergranular Cracking of Ni-16Cr-9Fe in 360°C Argon and High-Purity Water,'' Metall. Trans. A, **23**, pp. 1195–1205.
[6] Eshelby, J. D., 1957, ''The Determination of the Elastic Field of an Ellipsoidal Inclusion, and Related Problems,'' Proc. R. Soc. London, Ser. A, **241**, pp. 376–396.
[7] Evans, A. G., 1984, *Fracture in Ceramic Materials: Toughening Mechanisms, Machining Damage, Shock*, Noyes Publications, Park Ridge, NJ.
[8] Laws, N., and Lee, J. C., 1989, ''Microcracking in Polycrystalline Ceramics: Elastic Isotropy and Thermal Anisotropy,'' J. Mech. Phys. Solids, **37**, pp. 603–618.
[9] Tvergaard, V., and Hutchinson, J., 1988, ''Microcracking in Ceramics Induced by Thermal Expansion or Elastic Anisotropy,'' J. Am. Ceram. Soc., **71**, pp. 157–166.
[10] Ortiz, M., and Suresh, S., 1993, ''Statistical Properties of Residual Stresses and Intergranular Fracture in Ceramic Materials,'' ASME J. Appl. Mech. **60**, pp. 77–84.
[11] Wu, M. S., and Niu, J., 1995, ''A Theoretical Analysis of Crack Nucleation due to Grain Boundary Dislocation Pile-ups in a Random Ice Microstructure,'' Philos. Mag. A, **71**, pp. 831–854.
[12] Wu, M. S., and He, M. D., 1999, ''Prediction of Crack Statistics in a Random Polycrystal Damaged by the Pile-ups of Extrinsic Grain-Boundary Dislocations,'' Philos. Mag. A, **79**, pp. 271–292.
[13] Kozaczek, K. J., Petrovic, B. G., Ruud, C. O., Kurtz, S. K., and McIlree, A. R., 1995, ''Microstructural Modelling of Grain-Boundary Stresses in Alloy 600,'' J. Mater. Sci., **30**, pp. 2390–2400.
[14] Kumar, S., Kurtz, S. K., and Agarwala, V. K., 1996, ''Micro-stress Distribution Within Polycrystalline Aggregate,'' Acta Mech., **114**, pp. 203–216.
[15] Ghahremani, F., and Hutchinson, J. W., 1990, ''Three-Dimensional Effects in Microcrack Nucleation in Brittle Polycrystals,'' J. Am. Ceram. Soc., **73**, pp. 1548–1554.
[16] Kumar, S., Kurtz, S. K., Banavar, J. R., and Sharma, M. G., 1992, ''Properties of a Three-Dimensional Voronoi Tessellation: A Monte-Carlo Study,'' J. Stat. Phys., **67**, pp. 523–551.
[17] Williams, W. M., and Smith, S. C., 1952, ''A Study of Grain Shape in an Aluminum Alloy and other Applications of Stereoscopic Microradiography,'' Trans. Am. Inst. Min. Metall. Eng., **194**, pp. 755–765.
[18] Timoshenko, S. P., and Goodier, J. N., 1970, *Theory of Elasticity*, 3rd Ed., McGraw-Hill, New York.
[19] Isida, M., Yoshida, T., and Noguchi, H., 1990, ''Tension of a Finite-Thickness Plate With a Pair of Semi-Elliptical Surface Cracks,'' Eng. Fract. Mech., **35**, pp. 961–965.
[20] Isida, M., Tsuru, H., and Noguchi, H., 1994, ''An Analysis for Three Dimensional Cracks,'' Fatigue Fract. Eng. Mater. Struct., **17**, pp. 737–749.
[21] Qu, J., and Xue, Y., 1998, ''Three-Dimensional Interface Cracks in Anisotropic Bimaterials: The Non-Oscillatory Case,'' ASME J. Appl. Mech., **65**, pp. 1048–1055.

Effects of Mixed-Mode and Crack Surface Convection in Rapid Crack Growth in Coupled Thermoelastic Solids

L. M. Brock
Fellow ASME
Department of Mechanical Engineering,
University of Kentucky,
Lexington, KY 40506

Two Green's function problems for rapid two-dimensional steady-state crack growth governed by fully coupled (dynamic) linear thermoelasticity are analyzed. In Problem A, normal and in-plane shear line loads move on the insulated surfaces of a semi-infinite crack growing at a subcritical speed. Problem B involves only normal line loads, but crack surface convection is allowed. Problem A involves, therefore, mixed traction/displacement boundary conditions, while Problem B also exhibits mixed thermal boundary conditions. Robust asymptotic forms based on exact solutions for related problems reduce Problems A and B to coupled sets of integral equations. Both sets exhibit both Cauchy and Abel operators, but are solved exactly. The solutions show that Mode II loading couples the tangential crack face separation and discontinuity in crack-face temperature changes, while crack surface convection enhances thermal response, especially at large distances. [S0021-8936(00)03101-9]

Introduction

The fracture of linearly thermoelastic solids is generally ([1]) viewed as a quasi-static process, thereby allowing the governing equations for temperature to be uncoupled from those for linear momentum. If, however, loading is time-dependent and crack growth is rapid, then fracture is a dynamic process ([2]) and linear thermoelasticity ([3,4]) fully couples the temperature and linear momentum equations. Recent studies ([5]) have found that steady-state crack growth is sensitive to coupling effects, especially at high crack speeds.

However, these studies are complicated by the inclusion of crack-edge inelasticity, yet they also treat only Mode I loading, and assume a negligible crack surface heat flux, i.e., the crack faces are insulated. This article, therefore, extends and combines preliminary efforts ([6–9]) and considers two Green's function problems of two-dimensional steady-state crack growth which, variously, are mixed mode and allow crack surface convection. As in the work of Brock [5] the cracks are semi-infinite, are driven by mechanical line loads, and grow at subcritical speeds in unbounded solids that obey the fully coupled (dynamic) equations of thermoelasticity. To focus attention on the effects of mixed-mode loading and convection, crack edge inelasticity is neglected.

Problem A depicts mixed-mode crack growth by treating loads which are constant normal and in-plane shear tractions (line loads in the out-of-plane direction) applied to opposite faces of the crack. These loads move at the same (constant) speed as the crack, thereby justifying a steady-state analysis. Problem B treats only normal (Mode I) line loads, but incorporates the idea that crack surfaces ([10]) may have an effective layer of fracture-altered material. While perhaps negligible in modeling elastic response, such layers can cause heat flux by convection. Problem B includes, therefore, a standard ([3]) convection law that enforces proportionality between crack surface heat flux and temperature change.

Both problems are formulated in the next section, where Problem A is seen to involve mixed traction/displacement boundary conditions, while Problem B exhibits mixed thermal boundary conditions in addition. Related problems that involve unmixed conditions are addressed, therefore, and exact integral transforms obtained. Robust asymptotic forms are then extracted and used to reduce both problems A and B to coupled sets of integral equations. Each set displays both Cauchy and Abel operators, yet tractable exact solutions are possible. These solutions show that crack-face separation and thermal behavior are coupled in Mode II, and that crack-surface convection allows crack-surface temperature changes where none are seen for an insulated surface and, in general, results in steady-state crack-plane temperature changes which are more prominent at large distances than those for an insulated surface. Both solutions also exhibit characteristic lengths which are proportional to the characteristic length of coupled thermoelasticity, but which also depend on material properties and crack/load speed.

Formulations for Problems A and B

Consider an unbounded linear isotropic homogeneous thermoelastic solid, initially at rest under a uniform (absolute) temperature T_o, and containing a crack of infinite width and semi-infinite length. The crack then opens and grows in its original plane under the action of normal and in-plane shear line loads of magnitudes (P_n, P_s), respectively, which are applied to opposite faces of the crack and then moved toward the crack edge at a constant subcritical speed v. This wedging action eventually produces a steady-state situation in which the crack also grows with speed v, and the line loads remain a fixed distance L behind its edge. This two-dimensional process is represented schematically in Fig. 1, where it is seen that only Cartesian planar coordinates (x,y) are needed, and can be fixed to the moving crack edge so that $(y=0,\ x<0)$ always defines the crack.

In the two-dimensional steady state, only the change θ in temperature from T_o, displacement components (u_x, u_y) and traction components $(\sigma_x, \sigma_y, \sigma_{xy})$ are required. Because time derivatives in the moving coordinate system can be neglected, these fields depend only on (x,y), and time derivatives in the inertial frame can be written as $-v\,\partial(..)/\partial x$. Then, the results of Chadwick [4] can be adapted to give the governing field equations of coupled thermoelasticity

Contributed by the Applied Mechanics Division of THE AMERICAN SOCIETY OF MECHANICAL ENGINEERS for publication in the ASME JOURNAL OF APPLIED MECHANICS. Manuscript received by the ASME Applied Mechanics Division, Mar. 2, 1999; final revision, Oct. 12, 1999. Associate Technical Editor: J. W. Ju. Discussion on the paper should be addressed to the Technical Editor, Professor Lewis T. Wheeler, Department of Mechanical Engineering, University of Houston, Houston, TX 77204-4792, and will be accepted until four months after final publication of the paper itself in the ASME JOURNAL OF APPLIED MECHANICS.

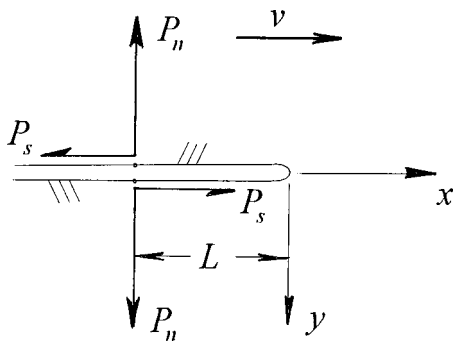

Fig. 1 Schematic of crack growth driven by moving line loads

$$\left(\nabla^2 - m^2c^2\frac{\partial^2}{\partial x^2}\right)(u_x,u_y) + \left(\frac{\partial}{\partial x},\frac{\partial}{\partial y}\right)[(m^2-1)\Delta + \chi\theta] = 0 \tag{1a}$$

$$h\nabla^2\theta + c\,\frac{\partial}{\partial x}\left(\theta - \frac{m^2\varepsilon}{\chi}\Delta\right) = 0 \tag{1b}$$

$$\frac{1}{\mu}\sigma_{xy} = \frac{\partial u_x}{\partial y} + \frac{\partial u_y}{\partial x}, \qquad \frac{1}{\mu}(\sigma_x,\sigma_y) = 2\left(\frac{\partial u_x}{\partial x},\frac{\partial u_y}{\partial y}\right) + (m^2-2)\Delta + \chi\theta. \tag{1c}$$

In (1), (∇^2,Δ) are the 2D Laplacian and dilatation, and

$$\chi = \chi_o(4-3m^2), \quad \varepsilon = \frac{T_o}{c_v}\left(\frac{\chi v_r}{m}\right)^2, \quad h = \frac{kv_r}{\mu m c_v}, \qquad m = \frac{v_d}{v_r}, \quad c = \frac{v}{v_d} \tag{2}$$

where (χ_o, c_v, k, μ) are, respectively, the thermal expansion coefficient, specific heat, thermal conductivity, and shear modulus. The parameters (v_r, v_d) are the rotational and isothermal dilatational wave speeds, while (h,ε) are the thermoelastic characteristic length and dimensionless coupling constant. It can be shown ([4,11]) that for many materials

$$\varepsilon \approx O(10^{-2}), \quad h \approx O(10^{-4})\ \ \mu\text{m}, \quad m > \sqrt{2}. \tag{3}$$

In light of (3), we will assume that $L/h \gg 1$. We expect $(\sigma_x,\sigma_y,\sigma_{xy},\theta)$ to vanish as $\sqrt{x^2+y^2}\to\infty$ and to be nonsingular everywhere except perhaps at $y=0$, $x=0$ and $y=0$, $x=-L$. The fields (u_x,u_y,θ) should also be continuous everywhere except perhaps the region $y=0$, $x<0$. At this juncture, critical crack/load speed is taken to be v_r; that is, $0<c<1/m$.

In Problem A of this scenario, the insulated crack surface conditions are

$$y = 0\pm, \quad x<0: \ \ \sigma_{xy} = -P_s\delta(x+L), \qquad \sigma_y = -P_n\delta(x+L), \quad \frac{\partial\theta}{\partial y} = 0 \tag{4}$$

where $\delta(..)$ is the Dirac function. In Problem B, only the normal loads are imposed $(P_s=0)$, and crack surface convection occurs, so that the crack surface conditions are

$$y = 0\pm, \ \ x<0: \ \ \sigma_{xy} = 0, \ \ \sigma_y = -P_n\delta(x+L), \ \ \mp\frac{\partial\theta}{\partial y} + \frac{\theta}{h_c} = 0. \tag{5}$$

In (5), h_c is a length which characterizes convection; if the convection represents a layer of effective thickness l on the crack surface, then the Biot number ([3]) for the crack is

$$B_l = \frac{l}{h_c}. \tag{6}$$

Related Problem Formulations

Problem A, in effect, involves the two half-planes $y>0$ and $y<0$ whose boundary conditions arise from (4) and continuity of $(u_x,u_y,\theta,\sigma_{xy},\sigma_y,\partial\theta/\partial y)$ for $y=0$, $x>0$. That is, it exhibits mixed traction/displacement boundary conditions. In keeping with a standard procedure ([12]), it is convenient to first treat the related problem with the unmixed conditions

$$u_x]_-^+ = U(x), \quad u_y]_-^+ = V(x), \quad \theta]_-^+ = \Theta(x), \qquad \sigma_{xy}]_-^+ = [\sigma_y]_-^+ = \left[\frac{\partial\theta}{\partial y}\right]_-^+ = 0 \tag{7}$$

for all $y=0$. Here $[\ ]_-^+$ denotes a discontinuity as the x-axis is crossed from $y=0-$ to $y=0+$, and the discontinuities $(U,V,\Theta)\to 0$ continuously as $x\to-(0,\infty)$, are no worse than integrally singular for $x<0$, and vanish identically for $x>0$. Problem A is reduced, therefore, to solving this related problem and using the results for either $y>0$ or $y<0$ in (4) to find (U,V,Θ). In this light, these quantities are, respectively, the tangential and normal crack face separation and the jump in temperature from one crack face to the other.

For Problem B, crack-plane $(y=0)$ symmetry exists, so that only the half-plane $y>0$ need be considered by requiring from (5) that

$$\sigma_y = -P_n\delta(x+L), \quad \frac{\partial\theta}{\partial y} - \frac{\theta}{h_c} = 0 \tag{8}$$

for $y=0+$, $x<0$ while $\sigma_{xy}=0$ and $(u_y,\partial\theta/\partial y=0)$ for, respectively, $y=0$ and $y=0$, $x>0$. Here, the thermal boundary conditions are also mixed, so that a related problem imposes for all $y=0$ the unmixed conditions

$$\sigma_{xy} = 0, \quad u_y = \frac{1}{2}V(x), \quad \frac{\partial\theta}{\partial y} = G(x) \tag{9}$$

where (V,G) vanish identically for $x>0$, are no worse than integrally singular for $x<0$ and remain finite as $x\to-\infty$. Problem B is reduced, therefore, to solving this related problem and using the results in (8) to find (V,G). In this light, (V,h_cG) are the normal crack-face separation and the crack-surface temperature change. Thus, V should vanish continuously as $x\to 0-$.

For both related problems, the boundedness/continuity conditions imposed on the original problems are retained.

Transform Solutions for Related Problems

To treat the related problems, the bilateral Laplace transform/inversion operations ([13])

$$g^* = \int_{-\infty}^{\infty} g(x)e^{-px}\,dx, \tag{10a}$$

$$g(x) = \frac{1}{2\pi i}\int g^* e^{px}\,dp \tag{10b}$$

are introduced, where p is generally complex and integration in (10*b*) is along the Bromwich contour. Application of (10*a*) to (1) gives a set of three coupled ordinary differential equations in y that can be solved for the relevant transforms

$$\begin{bmatrix} u_x^* \\ \frac{1}{p^2}\theta^* \\ \frac{1}{\mu p}\sigma_y^* \end{bmatrix} = \begin{bmatrix} -p & -p & 1 \\ \omega_+ & \omega_- & 0 \\ -Kp & -Kp & -2 \end{bmatrix} \begin{bmatrix} A_+e^{\alpha_+ y}+A_-e^{-\alpha_+ y} \\ B_+e^{\alpha_- y}+B_-e^{-\alpha_- y} \\ C_+e^{\beta y}+C_-e^{-\beta y} \end{bmatrix} \tag{11a}$$

$$\begin{bmatrix} u_y^* \\ \frac{1}{p^2}\frac{\partial\theta^*}{\partial y} \\ \frac{1}{\mu p}\sigma_{xy}^* \end{bmatrix} = \begin{bmatrix} -1 & -1 & -p \\ \omega_+ & \omega_- & 0 \\ -2 & -2 & Kp \end{bmatrix} \begin{bmatrix} \alpha_+(A_+e^{\alpha_+ y}-A_-e^{-\alpha_+ y}) \\ \alpha_-(B_+e^{\alpha_- y}-B_-e^{-\alpha_- y}) \\ \frac{1}{\beta}(C_+e^{\beta y}-C_-e^{-\beta y}) \end{bmatrix} \tag{11b}$$

for each half-plane, where the coefficients $(A_\pm, B_\pm, C_\pm)$ are arbitrary functions of p, and

$$\alpha_\pm = a_\pm\sqrt{p}\sqrt{-p}, \quad \beta = b\sqrt{p}\sqrt{-p}, \quad \omega_\pm = \frac{m^2}{\chi}(1-c^2-a_\pm^2) \tag{12a}$$

$$a_\pm = \sqrt{1+\frac{c}{p}(\tau_+\pm\tau_-)^2}, \quad b=\sqrt{1-m^2c^2}, \quad K=m^2c^2-2 \tag{12b}$$

$$2\tau_\pm = \sqrt{\left(\sqrt{-cp}\pm\frac{1}{\sqrt{h}}\right)^2+\frac{\varepsilon}{h}}, \quad \omega_+\omega_- = \frac{m^4c^3\varepsilon}{\chi^2 hp}. \tag{12c}$$

Here $\mathrm{Re}(\alpha_\pm,\beta)\geqslant 0$ in the cut p-plane, so that boundedness requires

$$A_+^{(+)}=B_+^{(+)}=C_+^{(+)}=0 (y>0), \quad A_-^{(-)}=B_-^{(-)}=C_-^{(-)}=0 (y<0) \tag{13}$$

where the superscripts signify a coefficient associated with half-plane $y>0(+)$ or $y<0(-)$.

For the problem related to Problem A, application of (10*a*) and (11) to (7) gives the six equations needed to determine the remaining coefficients as

$$2(\omega_+-\omega_-)A_-^{(+)} = \frac{\omega_-}{m^2c^2}\left(\frac{2}{p}U^*-\frac{K}{\alpha_+}V^*\right)+\frac{\Theta^*}{p^2} \tag{14a}$$

$$2(\omega_--\omega_+)B_-^{(+)} = \frac{\omega_+}{m^2c^2}\left(\frac{2}{p}U^*-\frac{K}{\alpha_-}V^*\right)+\frac{\Theta^*}{p^2} \tag{14b}$$

$$2m^2c^2C_-^{(+)} = \frac{K}{p}U^*+\frac{2}{\beta}V^* \tag{14c}$$

for $y>0$ and

$$2(\omega_--\omega_+)A_+^{(-)} = \frac{\omega_-}{m^2c^2}\left(\frac{2}{p}U^*+\frac{K}{\alpha_+}V^*\right)+\frac{\Theta^*}{p^2} \tag{15a}$$

$$2(\omega_+-\omega_-)B_+^{(-)} = \frac{\omega_+}{m^2c^2}\left(\frac{2}{p}U^*+\frac{K}{\alpha_-}V^*\right)+\frac{\Theta^*}{p^2} \tag{15b}$$

$$2m^2c^2C_+^{(-)} = -\frac{K}{p}U^*+\frac{2}{\beta}V^* \tag{15c}$$

for $y<0$. For the problem related to Problem *B*, only the half-plane $y>0$ is of interest, so that $(A_+^{(-)}, B_+^{(-)}, C_+^{(-)})$ can be discarded. Application of (10*a*) and (11) to (9) then gives three equations that can be solved to yield

$$2\alpha_+(\omega_--\omega_+)A_-^{(+)} = \frac{K\omega_-}{m^2c^2}V^*+\frac{2}{p^2}G^* \tag{16a}$$

$$2\alpha_-(\omega_+-\omega_-)B_-^{(+)} = \frac{K\omega_+}{m^2c^2}V^*+\frac{2}{p^2}G^* \tag{16b}$$

$$m^2c^2C_-^{(+)} = \frac{\beta}{p}V^*. \tag{16c}$$

Asymptotic Inversions for Related Problems

With (11)–(16) available, the two related problems are essentially solved. Solution of Problem A requires in view of (4) and (7) that expressions for $(\sigma_{xy}^*, \sigma_y^*, \partial\theta^*/\partial y)$ for either $y>0$ or $y<0$ be inverted for $y=0$, $x<0$ by means of (10*b*). Similarly, solution of Problem B requires in view of (8) and (9) that expressions for (σ_y^*, θ^*) be inverted for $y=0$, $x<0$. The inversions, however, give expressions that lead to semi-numerical determinations of the unknown functions (U,V,Θ) and (V,G). We make use, therefore, of asymptotic results: Bilateral Laplace transforms valid for $|hp|\ll 1$ give inversions that are valid for $|x/h|\gg 1$ ([13]); because (2) and (3) show that h is of micron order, such inversions are robust.

For the problem related to Problem A, (14) and (15) are substituted into (11) and, in view of (12), the results are expanded in Taylor series for $|hp|\ll 1$. Keeping the lowest-order terms then gives the asymptotic form. For example, it can be shown that the relation

$$\theta^* = \frac{-\varepsilon}{\chi(1+\varepsilon)}\left(pU^*+\frac{K}{2a}pV^*\frac{\sqrt{p}}{\sqrt{-p}}\right)e^{ay\sqrt{p}\sqrt{-p}} + \left[\frac{\varepsilon}{\chi(1+\varepsilon)}pU^*-\frac{\Theta^*}{2}\right]e^{y\sqrt{c/h(1+\varepsilon)}\sqrt{-p}} \tag{17}$$

holds for $y<0$. In view of (10*a*) and the restrictions on (U,V,Θ) noted earlier, one can write

$$(pU^*, pV^*) = \int_{-\infty}^{0}(U',V')e^{-pt}\,dt, \quad \Theta^* = \int_{-\infty}^{0}\Theta e^{-pt}\,dt \tag{18}$$

in (17), where $(\,)'$ denotes x-differentiation. The appearance of the crack-face separation gradients (U',V') as the functions to be determined presents no difficulty since a unique solution to the steady-state Problem A can be obtained only to within an arbitrary rigid-body motion. In (17) the positive real quantity

$$a = \sqrt{1-\frac{c^2}{1+\varepsilon}} \tag{19}$$

is a manifestation of the asymptotic dilatational wave speed $v_d\sqrt{1+\varepsilon}$.

If it is assumed that the orders of inversion and t-integration can be interchanged, then inversion of (17) is reduced to finding the inversions of the four functions

$$I_1^* = e^{-pt+ay\sqrt{p}\sqrt{-p}}, \tag{20a}$$

$$I_2^* = \frac{\sqrt{p}}{\sqrt{-p}}I_1^*, \tag{20b}$$

$$I_3^* = \frac{e^{-pt+y\sqrt{c/h(1+\varepsilon)}\sqrt{-p}}}{\sqrt{-p}}, \tag{20c}$$

$$I_4^* = \frac{\sqrt{h}}{\sqrt{c(1+\varepsilon)}}\frac{dI_3^*}{dy} \tag{20d}$$

where $(t,y)<0$. In view of the requirements that $\mathrm{Re}(\alpha_\pm,\beta)\geqslant 0$ in the cut p-plane, we must have $\mathrm{Re}(\sqrt{p},\sqrt{-p})\geqslant 0$ in the plane with branch cuts $\mathrm{Im}(p)=0$, $\mathrm{Re}(p)<0$ and $\mathrm{Im}(p)=0$, $\mathrm{Re}(p)>0$, respectively. Therefore the Bromwich contour in (10*b*) for the forms

(20) can be taken as the entire Im(p)-axis. The results are real integrals that can be carried out with standard tables ([14]) to give

$$I_1=\frac{1}{\pi}\frac{-ay}{(t-x)^2+a^2y^2},\quad I_2=\frac{1}{\pi}\frac{t-x}{(t-x)^2+a^2y^2}. \tag{21}$$

Substitution of (20c) into (10b) produces the integrand branch cut Im(p)=0, Re(p)>0, so that use of Cauchy theory to change the contour gives $I_3=0$ for $x>t$, but a real integral for $x<t$ which yields ([14])

$$I_3=\frac{1}{\sqrt{\pi(t-x)}}e^{-(c(1+\varepsilon)y^2)/(4h(t-x))}(t>x). \tag{22}$$

The function I_4 follows by differentiation. Use of these results gives

$$\theta=\frac{-\varepsilon}{\chi(1+\varepsilon)}\frac{1}{\pi}\int_{-\infty}^{0}\left[ayU'+\frac{K}{2a}(t-x)V'\right]\frac{dt}{(t-x)^2+a^2y^2}$$
$$+\frac{1}{\sqrt{\pi}}\frac{\partial}{\partial y}\int_x^0\left[\frac{\varepsilon U'}{\chi(1+\varepsilon)}-\frac{\Theta}{2}\right]e^{-(c(1+\varepsilon)y^2)/(4h(t-x))}$$
$$\times\frac{dt}{\sqrt{t-x}}(y<0). \tag{23}$$

By the same procedure, the fields of more immediate interest are obtained as

$$\frac{1}{\mu}\sigma_{xy}=\frac{a}{m^2c^2}\frac{1}{\pi}\int_{-\infty}^{0}[2(t-x)U'+KyV']\frac{dt}{(t-x)^2+a^2y^2}$$
$$-\frac{K}{m^2c^2}\frac{1}{\pi}\int_{-\infty}^{0}\left[\frac{K}{2b}(t-x)U'+byV'\right]\frac{dt}{(t-x)^2+b^2y^2}$$
$$-\frac{\chi}{m^2}\frac{\sqrt{h}}{\sqrt{\pi c(1+\varepsilon)}}\frac{\partial}{\partial x}\int_x^0\frac{\Theta}{\sqrt{t-x}}e^{-c(1+\varepsilon)y^2/4h(t-x)}\,dt \tag{24a}$$

$$\frac{1}{\mu}\sigma_y=\frac{K}{m^2c^2}\frac{1}{\pi}\int_{-\infty}^{0}\left[ayU'-\frac{K}{2a}(t-x)V'\right]\frac{dt}{(t-x)^2+a^2y^2}$$
$$+\frac{b}{m^2c^2}\frac{1}{\pi}\int_{-\infty}^{0}[2(t-x)V'-KyU']\frac{dt}{(t-x)^2+b^2y^2}$$
$$+\frac{h\chi}{2m^2c(1+\varepsilon)}\frac{\partial}{\partial x}\left[\frac{ay}{\pi}\int_{-\infty}^{0}\frac{\Theta dt}{(t-x)^2+a^2y^2}\right.$$
$$\left.+\frac{\sqrt{h}}{\sqrt{\pi c(1+\varepsilon)}}\frac{\partial}{\partial y}\int_x^0\Theta e^{-c(1+\varepsilon)y^2/4h(t-x)}\frac{dt}{\sqrt{t-x}}\right] \tag{24b}$$

$$\frac{\partial\theta}{\partial y}=\sqrt{\frac{c(1+\varepsilon)}{\pi h}}\frac{\partial}{\partial x}\int_x^0\left[\frac{\Theta}{2}-\frac{\varepsilon U'}{\chi(1+\varepsilon)}\right]e^{-c(1+\varepsilon)y^2/4h(t-x)}\frac{dt}{\sqrt{t-x}} \tag{24c}$$

for $y<0$. Comparison of (23) and (24c) illustrates the asymptotic nature of the expressions.

For the problem related to Problem B, (16) is substituted into (11) and, in view of (12), the results are also expanded in a Taylor series for $|hp|\ll 1$. Based on keeping the lowest-order terms, inversion of the expressions for (σ_y^*,θ^*) by means of (10b) gives for $y>0$

$$\frac{1}{\mu}\sigma_y=\frac{1}{2m^2c^2a}\frac{1}{\pi}\int_{-\infty}^{0}V'\left[\frac{4ab}{(t-x)^2+b^2y^2}-\frac{K^2}{(t-x)^2+a^2y^2}\right]$$
$$\times(t-x)dt+\frac{Kh\chi}{m^2c^2a(1+\varepsilon)}\frac{1}{\pi}\int_{-\infty}^{0}\frac{G(t-x)dt}{(t-x)^2+a^2y^2} \tag{25a}$$

$$\theta=\frac{-K\varepsilon}{2\chi(1+\varepsilon)a}\frac{1}{\pi}\int_{-\infty}^{0}\frac{V'(t-x)dt}{(t-x)^2+a^2y^2}$$
$$-\frac{\sqrt{h}}{\sqrt{\pi c(1+\varepsilon)}}\int_x^0 Ge^{-c(1+\varepsilon)y^2/4h(t-x)}\frac{dt}{\sqrt{t-x}}. \tag{25b}$$

Solution for Problem A

With (4) and (24) available, Problem A reduces to the equations

$$\frac{\mu R}{2m^2c^2a}\frac{1}{\pi}\fint_{-\infty}^{0}\frac{V'dt}{t-x}=-P_n\delta(x+L) \tag{26a}$$

$$\frac{\mu R}{2m^2c^2b}\frac{1}{\pi}\fint_{-\infty}^{0}\frac{U'dt}{t-x}-\frac{\mu\chi}{m^2}\frac{\sqrt{h}}{\sqrt{\pi c(1+\varepsilon)}}\frac{d}{dx}\int_x^0\frac{\Theta dt}{\sqrt{t-x}}$$
$$=-P_s\delta(x+L) \tag{26b}$$

$$\frac{\varepsilon}{\chi(1+\varepsilon)}\frac{d}{dx}\int_x^0\frac{U'dt}{\sqrt{t-x}}-\frac{1}{2}\frac{d}{dx}\int_x^0\frac{\Theta dt}{\sqrt{t-x}}=0 \tag{26c}$$

for x in $(-\infty,0-)$, where f denotes Cauchy principal value integration. In (26)

$$R=4ab-K^2 \tag{27}$$

is the asymptotic thermoelastic Rayleigh function which exhibits the roots $c=\pm(0,c_R)$ in the cut c-plane. The constant c_R lies in the range $(0,1/m)$ and is the asymptotic thermoelastic Rayleigh speed, nondimensionalized with respect to v_d, and can be written ([15]) as

$$c_R=\sqrt{2\left(m^2-\frac{1}{1+\varepsilon}\right)}\frac{1}{m^2F_o},\quad \ln F_o=\frac{1}{\pi}\int_{1/m}^{\sqrt{1+\varepsilon}}\frac{\Phi dt}{t} \tag{28a}$$

$$\Phi=\tan^{-1}\frac{4\sqrt{1+\varepsilon-t^2}\sqrt{m^2t^2-1}}{\sqrt{1+\varepsilon}(m^2t^2-2)^2}. \tag{28b}$$

Because the nature of (26a,b) changes when R vanishes, we now restrict the range of subcritical crack speeds to

$$0<c<c_R. \tag{29}$$

Equation (26a) defines V', is uncoupled from (26b,c) and is of the Fredholm type with a Cauchy operator. Its solution is found by standard methods ([16]) to be

$$\frac{V'}{m^2c^2}=\frac{C_1}{\sqrt{-\pi x}}-\frac{2a}{\pi R}\frac{P_n}{\mu}\frac{\sqrt{L}}{\sqrt{-x}(x+L)}(x<0) \tag{30}$$

where C_1 is a real constant. The integral Eq. (26c) is of the Abel type for a linear combination of the functions (U',Θ), and can be solved for the relation

$$\frac{2\varepsilon U'}{\chi(1+\varepsilon)}-\Theta=\frac{C_2}{\sqrt{-\pi x}} \tag{31}$$

where C_2 is a real constant. Finally, linearly combining (26b,c) and introducing the variables $(\xi=-x,\ \tau=-t)$ yields the equation

$$\frac{1}{\pi}\int_0^\infty \frac{U'd\tau}{\xi-\tau}+\sqrt{\frac{d}{\pi}}\frac{d}{d\xi}\int_0^\xi \frac{U'd\tau}{\sqrt{\xi-\tau}}=C_o\delta(\xi-L) \tag{32}$$

on U' for ξ in $(0,\infty)$. In (32) d is a characteristic length and C_o is a constant defined as

$$\frac{d}{h}=\left(\frac{4b\varepsilon}{R}\right)^2\left(\frac{c}{1+\varepsilon}\right)^3,\quad C_o=-\frac{2m^2c^2b}{R}\frac{P_s}{\mu}. \tag{33}$$

The integral Eq. (32) exhibits both Cauchy and Abel operators, and the magnitudes of (h,ε) in (3) suggest that the latter is a perturbation. However, (27) and (33) show that

$$\begin{aligned} c\to 0:\ \frac{d}{h}&\approx\left[\frac{2\varepsilon}{m^2(1+\varepsilon)-1}\right]^2\frac{1}{(1+\varepsilon)c},\\ c\to c_R-:\ \frac{d}{h}&\approx\left[\frac{b_R\varepsilon}{m^4F_R(c_R-c)}\right]^2\frac{1}{c_R^3(1+\varepsilon)^3}. \end{aligned} \tag{34}$$

where

$$b_R=\sqrt{1-m^2c_R^2},\quad \ln F_R=\frac{2}{\pi}\int_{1/m}^{\sqrt{1+\varepsilon}}\frac{t\Phi dt}{t^2-c_R^2} \tag{35}$$

and (c_R,Φ) are given in (28). That is, for low and near-critical crack/load speeds, it is the Cauchy operator that can be seen as the perturbation. Therefore, (32) is treated directly by introducing the unilateral Laplace transform/inversion operations ([17])

$$\hat{g}=\int_0^\infty g(\xi)e^{-s\xi}\,d\xi, \tag{36a}$$

$$g(\xi)=\frac{1}{2\pi i}\int \hat{g}e^{s\xi}\,ds. \tag{36b}$$

Here $\mathrm{Re}(s)>0$ and is large enough to ensure existence of (36*a*), and integration in (36*b*) is along a Bromwich contour. Application of (36*a*) to (32) and the use of standard tables ([18]) gives the integral equation

$$\frac{1}{\pi}\int_0^\infty \frac{\hat{U}'du}{u-s}+\sqrt{s}\hat{U}'=C_oe^{-sL}(\mathrm{Re}(s)>0) \tag{37}$$

for the transform $\hat{U}'$. This equation is of the Fredholm type with a Cauchy operator and, by following standard methods [16] its solution can be written as

$$\hat{U}'=\frac{C_3}{(sd)^{3/2}}+C_o\frac{\sqrt{sd}}{1+sd}\left(e^{-sL}+\frac{1}{\pi}\int_0^\infty\frac{e^{-uL}}{u-s}\frac{du}{\sqrt{ud}}\right). \tag{38}$$

In (38) $\sqrt{s}$ has the branch cut $\mathrm{Im}(s)=0$, $\mathrm{Re}(s)<0$ in order that its real part be positive indefinite in the cut plane, and C_3 is a constant. Boundedness of U as $\xi\to\infty(x\to-\infty)$ requires that $\hat{U}'/s$ have a nonsingular integral as $s\to 0$. In this light, behavior of (38) demonstrates that

$$C_3=0. \tag{39}$$

Use of (33), standard tables ([18]) and re-introduction of the variable x gives the inversion

$$\begin{aligned} U'=&\frac{2m^2c^2b}{R\sqrt{\pi}}\frac{P_s}{\mu d}\left[e^{1/d(x+L)}\int_0^{-1/d(x+L)}\frac{e^u}{\sqrt{u}}du-\frac{\sqrt{d}}{\sqrt{-x-L}}\right]\\ &\times H(-x-L)+\frac{2m^2c^2b}{R}\frac{P_s}{\mu d}\frac{e^{x/d}}{\pi}\sqrt{\frac{L}{d}}\int_0^{-x/d}\frac{e^u}{\sqrt{u}}\frac{du}{\frac{L}{d}-u} \end{aligned} \tag{40}$$

for $x<0,|x/h|\gg 1$. For $-L<x<0$ the second term in (40) is taken in the Cauchy principal value sense. Because (V,Θ) should also be bounded as $x\to-\infty$, one can conclude from (30), (31), and (40) that

$$C_1=C_2=0. \tag{42}$$

Equations (30), (31), (40), and (41) illustrate the coupling inherent in (26): That is, for mixed-mode loading, the normal crack face separation V is, as in the isothermal case, dependent only on Mode I loading (P_n) and is independent of the thermal response of the crack surface. The tangential crack face separation U depends only on Mode II loading (P_s), but it and the discontinuity Θ in temperature between the crack faces are coupled.

Solution for Problem B

With (8) and (25) at hand, Problem B reduces to the equations

$$\begin{aligned} &\frac{\mu R}{2m^2c^2a}\frac{1}{\pi}\int_{-\infty}^0\frac{V'dt}{t-x}+\frac{\mu Kh\chi}{m^2ca(1+\varepsilon)}\frac{1}{\pi}\int_{-\infty}^0\frac{Gdt}{t-x}\\ &\quad=-P_n\delta(x+L) \end{aligned} \tag{42a}$$

$$\frac{K\varepsilon}{2\chi(1+\varepsilon)a}\frac{1}{\pi}\int_{-\infty}^0\frac{V'dt}{t-x}+\frac{\sqrt{h}}{\sqrt{\pi c(1+\varepsilon)}}\int_x^0\frac{Gdt}{\sqrt{t-x}}+h_cG=0 \tag{42b}$$

for x in $(-\infty,0-)$. Equation (42*a*) is of the Fredholm type for a linear combination of the functions (V',G), and its solution is readily found by standard methods ([16]) to be

$$\frac{1}{2}V'+\frac{Kh\chi c}{(1+\varepsilon)R}G=\frac{C_1}{\sqrt{-\pi x}}-\frac{m^2c^2a}{\pi R}\frac{P_n}{\mu}\frac{\sqrt{L}}{\sqrt{-x}(x+L)}(x<0) \tag{43}$$

where C_1 is a constant. Linearly combining (42*a*,*b*) and introducing the variables $(\xi=-x,\ \tau=-t)$ gives the integral equation

$$\frac{1}{\pi}\int_0^\infty\frac{Gd\tau}{\tau-\xi}+\frac{1}{\sqrt{\pi d}}\int_0^\xi\frac{Gd\tau}{\sqrt{\xi-\tau}}+AG=C_o\delta(\xi-L) \tag{44}$$

on G for ξ in $(0,\infty)$, where now

$$\begin{aligned} A=\frac{aR}{cK^2}\frac{(1+\varepsilon)^2}{\lambda\varepsilon},\quad \lambda=\frac{h}{h_c},\quad \frac{d}{h}=\left(\frac{cK^2}{aR}\right)^2\frac{\varepsilon^2c}{(1+\varepsilon)^3},\\ C_o=\frac{m^2ca(1+\varepsilon)}{Kh\chi}\frac{P_n}{\mu}. \end{aligned} \tag{45}$$

In (45) the positive real parameters (A,d) are, respectively, a dimensionless constant and a characteristic length, c.f. (33), while λ is a dimensionless convection parameter.

Equation (44) exhibits both Cauchy and Abel operators, but the transform (36*a*) reduces it to an integral equation

$$\frac{1}{\pi}\int_0^\infty\frac{\hat{G}du}{u-s}+\left(\frac{1}{\sqrt{sd}}+A\right)\hat{G}=C_oe^{-sL}(\mathrm{Re}(s)>0) \tag{46}$$

of the Fredholm type. By again using standard methods [16], its solution is found to be

$$\hat{G}=\frac{C_3}{sd}\frac{(sd)^{\alpha}e^{-\Omega}}{\sqrt{sd+(1+A\sqrt{sd})^2}}+\frac{C_o\sqrt{sd}}{\sqrt{sd+(1+A\sqrt{sd})^2}}$$
$$\times\frac{(1+A\sqrt{sd})e^{-sL}}{\sqrt{sd+(1+A\sqrt{sd})^2}}$$
$$+(sd)^{\alpha}\frac{e^{\Omega}}{\pi}\int\!\!\!\!\!\!\diagup_0^{\infty}\frac{\sqrt{ud}e^{-uL-\Omega}}{(ud)^{\alpha}(u-s)}\frac{du}{\sqrt{ud+(1+A\sqrt{ud})^2}} \quad (47)$$

where the parameters (α,Ω) are defined by

$$\alpha=\frac{1}{\pi}\tan^{-1}A(0<\alpha<1/2;A\geqslant 0),$$
$$\Omega=\frac{1}{\pi}\int\!\!\!\!\!\!\diagup_0^{\infty}\frac{dt}{t-sd}\tan^{-1}\frac{1}{A+(1+A^2)\sqrt{t}}. \quad (48)$$

In this instance boundedness of V as $\xi\to\infty(x\to-\infty)$ requires that

$$C_1=C_3=0. \quad (49)$$

Unlike (40), the transform (47) is best inverted by direct use of (36*b*): The entire Im(*s*)-axis is suitable as the Bromwich contour but, despite their forms, the terms in (47) have no roots in the plane cut along Im(*s*)=0, Re(*s*)<0 in order that $\mathrm{Re}(\sqrt{s})\geqslant 0$, nor any branch cuts save that for $\sqrt{s}$ itself. Thus, Cauchy theory can be used to change the integration path to one collapsing onto the branch cut. The result is, upon use of (45), introduction of the robust approximation

$$\Omega=\left(\alpha-\frac{1}{2}\right)\ln sd+\Omega_0,\Omega_0=\frac{2}{\pi}\int_0^{\infty}\frac{\ln t\,dt}{t^2+(1+At)^2} \quad (50)$$

valid for $|hs|\ll 1(\xi/h\gg 1)$, and re-introduction of the variable *x*,

$$h_cG=\frac{m^2ca(1+\varepsilon)}{K\chi\lambda}\frac{P_n}{\mu d}\frac{H(-x-L)}{\pi\sqrt{-x-L}}$$
$$\times\int_0^{\infty}\frac{[x+L+(1-A^2)t]\sqrt{t}e^{-t/d}\,dt}{[x+L+(1-A^2)t]^2+4A^2t^2}$$
$$+\frac{m^2ca(1+\varepsilon)}{K\chi\lambda}\frac{P_n}{\mu d}\frac{H(-x)}{\pi^2}\int_0^{\infty}\frac{\sqrt{t}e^{-t/d}\,dt}{\sqrt{\rho(-x,t)}}$$
$$\times\int_0^{t/d}\frac{\sqrt{u}e^{u/d}}{\sqrt{\rho(L,u)}}\frac{du}{xu+Lt}\sin[\Psi(-x,t)+\Psi(L,u)] \quad (51a)$$

$$\rho(\alpha,\beta)=\sqrt{[\alpha-(1+A^2)\beta]^2+4A^2\alpha\beta},$$
$$2\Psi(\alpha,\beta)=\tan^{-1}\frac{2A\sqrt{\alpha\beta}}{\alpha-(1+A^2)\beta} \quad (51b)$$

for $x<0,|x/h|\gg 1$. For $|x/L|\gg 1$ (51*a*) behaves as

$$h_cG\approx-\frac{m^2ca(1+\varepsilon)}{K\chi\lambda}\frac{P_n}{2\mu}\sqrt{\frac{d}{\pi}}\frac{1}{(-x-L)^{3/2}}$$
$$-\frac{m^2ca(1+\varepsilon)}{K\chi\lambda}\frac{P_n}{\mu}\frac{1}{\pi^2(-x)^{3/2}}$$
$$\times\int_0^{\infty}\left[1+\frac{1}{2}\sqrt{\frac{\pi d}{t}}e^{t/d}erfc(\sqrt{t/d})\right]$$
$$\times\frac{dt}{\sqrt{\rho(L,t)}}\sin\Psi(L,t). \quad (52)$$

Equations (51*a*) and (52) give in view of (8) and (9), of course, the temperature change on the crack surface. The temperature change ahead of the crack follows from (25*a*) as

$$\theta=\frac{-K\varepsilon}{2\chi(1+\varepsilon)}\frac{1}{\pi}\int_{-\infty}^{0}\frac{V'dt}{t-x}\quad(y=0,x/h\gg 1). \quad (53)$$

Substitution of (43), (49), and (51*a*) into (53) and use of Cauchy residue theory produces a result whose dominant terms are

$$\theta=-\frac{Km^2c^2\varepsilon a}{\chi(1+\varepsilon)R}\frac{P_n}{\mu}\frac{\sqrt{L}}{\sqrt{x}(x+L)}$$
$$+\frac{Km^2c^2\varepsilon a}{\chi(1+\varepsilon)R}\frac{P_n}{\mu}\frac{A}{2\pi(1+A^2)}\frac{1}{x+L}+\frac{Km^2c^2\varepsilon a}{\chi(1+\varepsilon)R}\frac{P_n}{\mu}\frac{1}{\pi^2x}$$
$$\times\int_0^{\infty}\frac{\sqrt{t}dt}{\sqrt{\rho(L,t)}}\cos\Psi(L,t)\int_0^{\infty}\frac{du}{(ut+Ld)\sqrt{1+(A+\sqrt{u})^2}} \quad (54)$$

for $y=0,x/h\gg 1$.

Comparison of Problem B With Insulated Limit

In view of (5) and (8) the limit case of an insulated crack surface occurs when $h_c\to\infty(\lambda\to 0)$. In this limit it can be shown that the function *G* itself vanishes, but that the product h_cG given in (51*a*) behaves as

$$h_cG\to\frac{Km^2c^2\varepsilon}{\chi(1+\varepsilon)R}\frac{P_n}{\mu}\delta(x+L)\quad(y=0,x<0,|x/h|\gg 1) \quad (55)$$

and that only the first term in (54) remains, i.e.,

$$\theta=-\frac{Km^2c^2\varepsilon}{\chi(1+\varepsilon)R}\frac{P_n}{\mu}\frac{1}{\pi}\frac{\sqrt{L}}{\sqrt{x}(x+L)}\quad(y=0,x/h\gg 1). \quad (56)$$

Comparison of (55) with (51*a*) shows that crack surface convection creates a temperature change over the full extent of the crack surfaces, while for an insulated surface, the change is asymptotically negligible except at the moving line loads. Equation (55) is also identical to the steady-state temperature change generated on an insulated thermoelastic half-space by a moving normal line load ([8]). This implies that the asymptotic steady-state crack-surface temperature change is independent of the fracture process itself.

Comparison of (56) with (54) shows that convection allows a more extensive temperature change field to arise ahead of the moving crack edge and, in particular, that the convection-induced field is more prominent at large distances from the crack edge. That is, (56) behaves as $O(x^{-3/2})$ for $x/L\gg 1$ while (54) behaves only as $O(1/x)$. A similar weakening in decay with distance has been noted ([9]) for a line load moving on a thermoelastic half-space with surface convection. Indeed, comparison of (54) with (52) indicates that the temperature change on the crack surface with convection decays more rapidly with distance than does that on the plane ahead of the crack. In this sense, crack surface convection does not alter the fact, demonstrated by (55) and (56) for the insulated case, that steady-state temperature changes generated ahead of the crack are, asymptotically at least, more prominent at large distances than those generated on the crack surface itself.

Some Observations

This article considered two Green's function problems for subcritical two-dimensional steady-state crack growth in an unbounded solid governed by the fully coupled (dynamic) equations of thermoelasticity. In Problem A, mixed-mode loading was achieved by moving normal and in-plane shear line loads along insulated crack surfaces at a fixed distance from the edge. In Problem B, only Mode I loading was considered by dropping the mov-

ing shear loads, but crack-surface convection was allowed. Thus, Problem A involved mixed traction/displacement boundary conditions, while Problem B exhibited mixed thermal boundary conditions in addition. Exact integral transform solutions for two related unmixed boundary value problems were obtained, and robust asymptotic forms inverted and used to reduce both Problems A and B to sets of coupled integral equations. Despite the presence of both Cauchy and Abel operators, exact solutions were derived.

The solution for Problem A demonstrated that the normal crack-face separation depends only on the Mode I loading, and is unaffected by the thermal response of the crack surface. That is, it behaves as if the solid were isothermal. The tangential crack-face separation depends, analogously, only on the Mode II loading, but it and the discontinuity in temperature change between the crack faces are coupled.

The solution for Problem B showed that crack surface convection creates a more extensive temperature change field in the crack plane than that generated for an insulated crack surface. Moreover, the field generated ahead of the crack decays less with distance from the crack edge than does its insulated crack surface counterpart.

The solutions for both problems depended, of course, on the thermoelastic characteristic length h, defined in (2), which arises from the fully coupled equations of thermoelasticity. However, this length was manifest in each solution as a characteristic length d. The expressions (33) and (46) for d for the solutions to Problems *A* and *B*, respectively, were similar in form, and both depended on material properties (m,h,ε) and crack/load speed (c). In particular, the speed dependence involved the asymptotic thermoelastic Rayleigh function R, whose nonzero root c_R was the nondimensionalized thermoelastic Rayleigh speed. An exact formula for the root was provided, and it served as the limiting crack/load speed for both problems.

Clearly, the analysis involved Green's function problems, which are *de facto* brittle fracture studies, and two-dimensional steady-state situations were treated with asymptotic solutions. Nevertheless, the results provided do indicate that some thermal effects in rapid crack growth in a fully coupled thermoelastic solid may be more sensitive to Mode II loading, and that crack surface convection enhances thermal response. That convection is justified followed from the idea that crack surfaces may exhibit layers of fracture-altered material ([10]) while perhaps negligible in elastic modeling, such layers can give rise to heat flux by convection ([3]).

In closing, several other observations are in order: First, the convection law employed did not explicitly feature the layer thickness l, which does appear in the crack surface Biot number (6). However, one should assume that l is both small and uniform. The former assumption, of course, justifies neglect of the layer in modeling elastic response, but the latter assumption is also important; transient studies ([11]) of insulated thermoelastic half-spaces indicate that even small-scale nonplanarity of the surface can affect its thermal response.

Then, comparison of (23)–(25) with the corresponding exact transforms (11)–(16) indicate that thermoelastic coupling is diminished through use of asymptotic forms. Indeed, the Cauchy operators in the integral Eqs. (26) and (43) suggest similarities with classical equilibrium ([19]) treatments of thermoelasticity. However, besides the advantage of tractability, the present analysis does preserve elements of coupling, and illustrates, in fact, through the coefficients of the operators in (26) and (43), its sensitivity to crack/load speed. Moreover, the development of exact steady-state transform expressions (11)–(16) provide the basis for a more exact treatment in the future.

While the study of Problem B made use of symmetry arguments to reduce the analysis to a single half-plane, the study of Problem *A* did not. This approach was adopted to avoid the need for considering the two separate (symmetric and antisymmetric) problems that would arise, and because the additional difficulties of dealing with the full unbounded solid were minor. Indeed, the analysis allows insight into the interface crack problem.

Finally, it is noted that key mathematical operations in both Problems A and B reduced, *via* unilateral Laplace transforms, integral equations with both Cauchy and Abel operators to those of a standard Cauchy type. The original equations followed from the inversions of bilateral Laplace transforms, which suggests that corresponding equations in that transform space could have been formulated, and addressed by standard ([20]) Wiener-Hopf techniques. However, it is noted ([7]) that such an approach requires product-splitting operations and resultant transforms whose inversions would require some effort to produce expressions as tractable as those developed here.

References

[1] Noda, N., Matsunaga, Y., Tsuji, T., and Nyuko, H., 1989, ''Thermal Shock Problems of Elastic Bodies With a Crack,'' J. Therm. Stresses, **12**, pp. 369–384.

[2] Freund, L. B., 1993, *Dynamic Fracture Mechanics*, Cambridge University Press, New York.

[3] Boley, B. A., and Weiner, J. H., 1985, *Theory of Thermal Stresses*, Krieger, Malabar, FL.

[4] Chadwick, P., 1960, ''Thermoelasticity: The Dynamical Theory,'' *Progress in Solid Mechanics*, Vol. 1, I. N. Sneddon and R. Hill, eds., North-Holland, Amsterdam.

[5] Brock, L. M., 1996, ''Effects of Thermoelasticity and a von Mises Criterion in Rapid Steady-State Quasi-Brittle Fracture,'' Int. J. Solids Struct., **33**, pp. 4131–4142.

[6] Brock, L. M., 1999, ''Rapid Crack Growth in a Thermoelastic Solid Under Mixed-Mode Thermomechanical Loading,'' IMA J. Appl. Math., **62**, pp. 31–44.

[7] Brock, L. M., 1999, ''Effects of Crack Surface Convection for Rapid Crack Growth in a Thermoelastic Solid,'' Int. J. Solids Struct., to appear.

[8] Brock, L. M., and Georgiadis, H. G., 1997, ''Steady-State Motion of a Line Mechanical/Heat Source Over a Half-Space: A Thermoelasodynamic Solution,'' ASME J. Appl. Mech., **64**, pp. 562–567.

[9] Brock, L. M., and Georgiadis, H. G., 1999, ''Convection Effects for Rapidly-Moving Mechanical Sources on a Half-Space Governed by Fully Coupled Thermoelasticity,'' ASME J. Appl. Mech., **66**, pp. 347–351.

[10] Ewalds, H. L., and Wanhill, R. J. H., 1985, *Fracture Mechanics*, Edward Arnold, London.

[11] Brock, L. M., Rodgers, M., and Georgiadis, H. G., 1996, ''Dynamic Thermoelastic Effects for Half-Planes and Half-Spaces With Nearly-Planar Surfaces,'' J. Elast., **44**, pp. 229–254.

[12] Erdogan, F., 1976, ''Mixed Boundary Value Problems in Mechanics,'' *Mechanics Today*, Vol. 4, S. Nemat-Nasser, ed., Pergamon Press, New York.

[13] van der Pol, B., and Bremmer, H., 1950, *Operational Calculus Based on the Two-Sided Laplace Integral*, Cambridge University Press, Cambridge, UK.

[14] Gradshteyn, I. S., and Ryzhik, I. M., 1980, *Table of Integrals, Series and Products*, Academic Press, New York.

[15] Brock, L. M., 1996, ''Some Analytical Results for Heating due to Irregular Sliding Contact of Thermoelastic Solids,'' Indian J. Pure Appl. Math., **27**, pp. 1257–1278.

[16] Carrier, G. F., Krook, M., and Pearson, C. E., 1966, *Functions of a Complex Variable*, McGraw-Hill, New York.

[17] Sneddon, I. N., 1972, *The Use of Integral Transforms*, McGraw-Hill, New York.

[18] Abramowitz, M., and Stegun, I. A., 1970, *Handbook of Mathematical Functions*, Dover, New York.

[19] Muskhelishvili, N. I., 1975, *Some Basic Problems in the Mathematical Theory of Elasticity*, Noordhoff, Leyden.

[20] Stakgold, I., 1971, *Boundary Value Problems of Mathematical Physics*, Vol. 2, MacMillan, New York.

Critical Wavelengths for Gap Nucleation in Solidification—Part I: Theoretical Methodology

F. Yigit
Department of Mechanical Engineering,
King Saud University,
P.O. Box 800
Riyadh 11421, Saudi Arabia

L. G. Hector, Jr.
Surface Science Division,
Alcoa Technical Center,
Alcoa Center, PA 15069

A theoretical model of the gap nucleation process during pure metal solidification on a deformable mold of finite thickness is presented. Both surfaces of the mold follow a sinusoidal lay for which the ratio of the amplitude to the wavelength, or aspect ratio, is much less than one. This makes the aspect ratio a convenient perturbation parameter for the thermal and mechanical problems since it is indicative of the spatial variation in the surfaces. The thermal and mechanical fields are coupled along the upper surface of the mold through a pressure-dependent thermal contact resistance. The main goal of the model is to develop a means for examining the contact pressure along the mold-shell interface and how variation of the mold surface wavelength affects the time and location of gap nucleation. Gaps, which result from irregular distortion of the shell due to the modest variation of the mold surface geometry, are assumed to nucleate when the contact pressure locally falls to zero. The model leads to two coupled differential equations for the shell thickness and contact pressure perturbations which are solved with a numerical scheme. Using a series solution methodology, it is shown that the contact pressure perturbation predicted by the present model reduces to that for a rigid, perfectly conducting mold (which was considered in another work) in the limit of zero mold thickness. In the companion paper, we specifically examine various combinations of pure materials acting either as the shell or the mold material. The concept of a critical wavelength, which separates those wavelengths that lead to gap nucleation at the crests, from those that lead to gap nucleation at the troughs, is introduced. The potential for development of design criteria for mold surface topographies using the present theoretical model as a limiting solution for finite element models of more complex casting processes is discussed. [S0021-8936(00)03201-3]

1 Introduction

One of the most challenging problems associated with any metal casting process is the control of heat extraction through the mold-shell interface during the early stages of solidification. If heat extraction is, on the average, too rapid along the metal-shell interface, then gross contraction of the ingot from the mold occurs leading to macro-gaps which can span much of the contact length. If heat extraction is locally nonuniform due, for example, to stochastic variations from parting agents, surface topography, oxides, or lubricants, then micro-gaps, which have a lateral span less than the nominal wavelength of the mold surface topography, nucleate. In both cases, the thermal conductivity in the gap region is less than adjacent solid-solid contacts thereby constricting heat flow through these contacts. This leads to locally elevated temperatures and ultimately remelting of portions of the ingot surface adjacent to the gap region or regions. The ingot surface can become rich in alloying agents and related geometrical defects, which subsequently have to be removed through such process-intensive techniques as surface milling or ''scalping.''

Irregular contraction and associated gap nucleation are also thought to adversely impact the growth of the shell. For example, it has been observed in decanted steel and aluminum castings that the shell can grow with a nonuniform thickness ([1–2]). This phenomenon, which has previously been referred to as cellular undulation ([3]), is indicative of a macroscale growth instability since the internal surface of the shell contains ''humps'' which are of the order of several centimeters in span and exceed the surrounding ingot thickness by at least an order-of-magnitude. Cellular undulation is observed both in static and continuous casting processes ([4]). Cracks develop in the shell which can greatly reduce the integrity of a product formed from the cast ingot in a subsequent forming operation (such as rolling or extrusion) ([5]). Nonuniform casting thickness and crack nucleation and growth are thought to be prime contributing factors to breakout, in which the shell is unable to retain the residual molten metal upon extraction from the molds in continuous casting processes. Surface remelting and exudation (or bleeding out of molten metal into the interface) have been found beneath the thinnest regions of the shell along the mold-shell contact ([6]).

A thermomechanical mechanism for the onset of cellular undulation was proposed by Halliday [7] and further developed by Richmond and Huang [8]. They proposed that stochastic variations in metal-shell heat extraction led to locally nonuniform temperature gradients within the shell. Irregular distortion of the shell resulted in local variations in the metal-shell contact pressure. Microscale air gap nucleation was assumed to occur when the pressure fell to zero. Shell growth rates in regions adjacent to the gaps were greatly diminished. If shell distortion acted to increase the contact pressure above the hydrostatic stress from the residual fluid, then the growth rate was enhanced. Lateral growth of the gaps across the metal-shell interface, and hence continued variation of shell growth rates led to cellular undulation.

There is a small body of theoretical work on the cellular undulation phenomenon that follows the spirit of the proposed mechanism. For example, Richmond et al. [9] developed a beam theory model to explore the onset of growth instability assuming that thickness nonuniformity of a pure metal shell was due to a periodic heat extraction profile. It was proposed that gap nucleation

Contributed by the Applied Mechanics Division of THE AMERICAN SOCIETY OF MECHANICAL ENGINEERS for publication in the ASME JOURNAL OF APPLIED MECHANICS. Manuscript received by the ASME Applied Mechanics Division, Mar. 9, 1999; final revision, Sept. 30, 1999. Associate Technical Editor: J. R. Barber. Discussion on the paper should be addressed to the Technical Editor, Professor Lewis T. Wheeler, Department of Mechanical Engineering, University of Houston, Houston, TX 77204-4792, and will be accepted until four months after final publication of the paper itself in the ASME JOURNAL OF APPLIED MECHANICS.

occurred when the contact pressure along the mold-shell interface fell to zero. They found that gap nucleation occurred beneath the thinnest regions of the shell, which presumably diminished further growth of these regions, with a corresponding increase in contact pressure beneath the thickest regions of the shell, the thicker regions subsequently growing at a faster rate. Li and Barber [10] extended this work using a stress function approach and found that the Richmond model was appropriate for the earliest stages of casting when the shell is very thin. Their model assumed that the temperature and stress fields in the growing shell were coupled along the mold-shell interface through a pressure-dependent thermal contact resistance. Additional models, which address such added complexities as strain rate relaxation due to viscous creep ([11]) and Stefan number ([12]) have been developed.

Experimentalists have addressed the issue of gap nucleation and shell thickness nonuniformity with a number process-related enhancements. One of the most common enhancements involves the application of a specific mold surface topography (see [13–21]). For example, periodic ''groove'' topographies that mimic the extended surface of a radiator, and hence allow for multidirectional heat flow at the mold-shell interface, have been routinely investigated with empirical methodologies. Unfortunately, there are no process models of the mold-shell interface that point to topography design criteria for the selection of important parameters such as amplitude and wavelength.

In light of existing experimental work on the mold surface topography effect on shell growth uniformity, Hector et al. [22] reformulated the Li and Barber [10] model so that nonuniform heat extraction at the mold-shell interface was due to a sinusoidal mold surface that was held at a uniform temperature. Their model assumed that the mold was a rigid, perfect conductor of heat. Clearly, this was a very restrictive assumption since most casting processes involve a mold of finite thickness which undergoes thermoelastic distortion. A methodology was presented for the calculation of the total contact pressure. It was found that gaps always nucleate at the lowest points of the surface troughs, while the evolving distortion of the shell increased the contact pressure beyond the hydrostatic pressure at the highest points of the crests. They also found that gap nucleation time and the mean shell thickness were influenced by the topography wavelength such that gap nucleation was delayed or even prevented over the time frame of interest with increasing wavelength. Gap nucleation was faster for a pure iron shell than for a pure aluminum shell, given the same process conditions.

Based upon the work of Comninou and Dundurs [23], Zhang and Barber [24], and others on steady-state thermoelastic contact problems, it is expected that mold distortion will play an important role in the gap nucleation process. For example, Comninou and Dundurs [23] found that the interface between two dissimilar thermoelastic half-planes can involve periodic contact and separation zones in addition to a state of uniform contact pressure. Zhang and Barber [24] found that growth of a sinusoidal perturbation in the contact pressure between two dissimilar materials depends upon the direction of heat flow, and, specifically, the distortivity of the materials, which relates the distortion to the local heat flux. They also found that when the system becomes unstable, the growth of the instability depends upon the spatial wavelength of the perturbation. The work of these authors suggests that the location of gap nucleation along the mold-shell interface may be controlled by the wavelength of the perturbation in the thermal field. In casting, the thermal field at the interface, and hence distortion of both the mold and shell, can be affected by the surface roughness of the mold (in addition to the other effects, such as ingot extraction rates, surface oxides, fluid flow, meniscus behavior and surface tension (see [25])). In practice, this is typically a ground finish which consists of a spectrum of roughness wavelengths. Hence, in some situations gap nucleation may occur at the peaks or crest regions, which suggests planar growth of the shell thickness, while in others, gap nucleation might occur in the trough or valley regions, which suggests the onset of undulatory growth and ultimately, cellular undulation.

The only prior work on the mold distortion problem is due to Yigit [26] who extended the Li and Barber [10] formulation for a mold of finite thickness with planar surfaces. Yigit [26] examined only the perturbation quantities resulting from a spatially nonuniform cooling profile along a planar mold surface, and hence he did not examine the evolution of the total contact pressure at the mold-shell interface. It is therefore not possible to draw any definitive conclusions from his work about gap nucleation at the mold-shell interface and how the topography wavelength affects gap nucleation time and location.

The present work is divided into two parts. In this first part, we use the Hector et al. [22] methodology to reformulate Yigit's [26] model of mold distortion. We consider solidification of a pure metal on a thin, deformable mold having sinusoidal surfaces with the same wavelength or center-to-center spacing between adjacent crests. Both surfaces are of low aspect ratio and hence the ratio of the amplitude to the wavelength is much less than one. This ratio is used as a perturbation parameter in the analysis since it is indicative of the extent to which lateral heat flow occurs along the interface due to the modest spatial variation of the topography. Following Li and Barber [10], the heat conduction and thermal stress problems in the mold and the shell are coupled along their interface through a pressure-dependent thermal contact resistance. The analysis leads to two coupled differential equations for the shell thickness perturbation and a function that represents residual stress. The solutions of these equations are used to calculated the contact pressure perturbation at the mold surface crests. This solution is valid for all times. A method for calculating series solutions of these differential equations is presented: These solutions are valid for short times after the start of solidification. It is shown that the resulting expressions for the shell thickness and contact pressure perturbations reduce to the result developed by Hector et al. [22] for the limit of zero mold thickness. In the second part, we use the theory developed in Part I to examine the gap nucleation process when the mold and shell materials are combinations of either pure aluminum, copper, iron, or lead. The effect of mold surface wavelength on gap nucleation time and position is explored for a given material combination. The concept of a critical wavelength, which separates those wavelengths that lead to gap nucleation at the crests from those that lead to gap nucleation at the troughs, is introduced. Future development of design criteria for mold surface topographies using the present theoretical model as a limiting solution for finite element models of more complex casting processes is discussed.

2 The Thermal Problem

The system to be modeled is shown in Fig. 1. Heat is withdrawn from the bottom of a thermoelastic mold of mean thickness h_0. Both the upper surface of the mold, which is contact with the shell along $y=0$, and the lower surface at $y=-h_0$, have sinusoidal surface topographies of wavelength λ. Molten metal, which is initially at its fusion temperature, T_f, perfectly wets the upper surface of the mold at $t=0$. The modest spatial variation in the upper mold surface leads to a corresponding spatial perturbation of the temperature fields in the shell, the mold, and the freezing front once solidification begins. The location of the freezing front is denoted by $s(x,t)$. All material properties are assumed to be constant and independent of temperature.

The temperature field in the solidified shell, $T^c(x,y,t)$, and that in the mold, $T^d(x,y,t)$, are governed by the heat conduction equation

$$\nabla^2 T^c = \frac{1}{k^c}\frac{\partial T^c}{\partial t} \quad ; \quad \nabla^2 T^d = \frac{1}{k^d}\frac{\partial T^d}{\partial t} \tag{1}$$

which are subject to the following initial and boundary conditions:

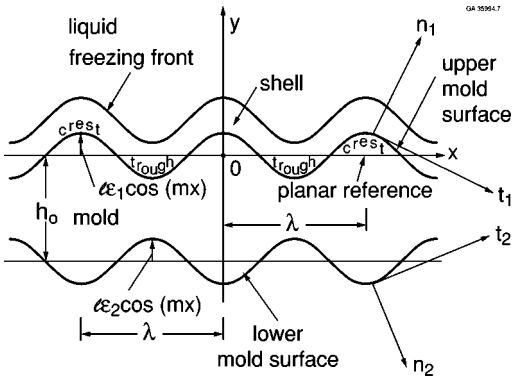

Fig. 1 Pure metal shell solidifying on a deformable mold with nominal thickness h_0 and sinusoidal surface topographies with wavelength λ

$$T^c(x,s,t)=T_f \tag{2}$$

$$K^c\frac{\partial T^c}{\partial y}(x,s,t)=L^c\rho^c\frac{\partial s}{\partial t}(x,t) \tag{3}$$

$$s(x,0)=l\epsilon_1\cos(mx) \tag{4}$$

$$K^c\frac{\partial T^c}{\partial y}(x,y_1,t)=K^d\frac{\partial T^d}{\partial y}(x,y_1,t) \quad ; \quad y_1=l\epsilon_1\cos(mx) \tag{5}$$

$$T^d(x,y_2,t)=0 \quad ; \quad y_2=-(h_0+l\epsilon_2\cos(mx)) \tag{6}$$

$$K^d\frac{\partial T^d}{\partial y}(x,y_2,t)=Q(x,t) \quad ; \quad y_2=-(h_0+l\epsilon_2\cos(mx)) \tag{7}$$

where

$$RQ(x,t)=T^c(x,y_1,t)-T^d(x,y_1,t) \quad ; \quad y_1=l\epsilon_1\cos(mx) \tag{8}$$

and $Q(x,t)$ is an unknown heat flux that is to be determined from the analysis. Equation (3) defines the energy balance between heat conducted away from the moving interface into the shell and the latent heat released during solidification. Note that L^c is the latent heat of fusion of the material, and

$$R(x,t)=R(P(x,t)) \tag{9}$$

is the pressure-dependent thermal contact resistance, where $P(x,t)$ is the contact pressure along the mold-shell interface. The reader is referred to Yigit [26] for additional background on Eqs. (2)–(9). We define

$$\epsilon_1=a_1/l \quad ; \quad \epsilon_2=a_2/l \tag{10}$$

as the upper and the lower mold surface aspect ratios, respectively, where $l=\lambda/2\pi=1/m$ and a_1,a_2 are, respectively, the amplitudes of the upper and lower sinusoidal mold surfaces. Finally, to simplify the analysis, we assume that the Stefan number for the casting material is small, and the heat diffusivity of the mold is infinitely large, i.e., the heat capacity of the mold is zero, in which case Eqs. (1) become steady-state heat conduction equations. It is also assumed that there is no transversal heat transfer in the solidified shell and in the mold.

2.1 Perturbation of the Thermal Problem. Due to the modest spatial variation of the upper mold surface, we may express the temperature fields, $T(x,y,t)$, shell thickness, $s(x,t)$, thermal contact resistance, $R(P(x,t))$, and mold-shell interfacial heat flux, $Q(x,t)$, as follows:

$$T(x,y,t)=T_0(y,t)+T_1(y,t)\cos(mx) \tag{11}$$

$$s(x,t)=s_0(t)+s_1(t)\cos(mx) \tag{12}$$

$$R(P(x,t))=R_0+R_1(P(x,t))\cos(mx) \tag{13}$$

$$Q(x,t)=Q_0(t)+Q_1(t)\cos(mx). \tag{14}$$

We insert Eq. (11) into Eq. (1) and separate the zeroth-order and first-order governing thermal equations. We next proceed to expand each of the temperature fields $T^c(x,y,t),T^d(x,y,t)$ in a Taylor series about $y=s=s_0(t)+s_1(t)\cos(mx)$, $y=y_1=l\epsilon_1\cos(mx)$, and $y=y_2=-(h_0+l\epsilon_2\cos(mx))$, respectively, to $O(\epsilon)$. This gives

$$T^c(x,s,t)=T_0^c(s_0(t),t)+s_1(t)\frac{\partial T_0^c(s_0(t),t)}{\partial y}\cos(mx)+T_1^c(s_0(t),t)\cos(mx) \tag{15}$$

$$T^c(x,y_1,t)=T_0^c(0,t)+l\epsilon_1\frac{\partial T_0^c(0,t)}{\partial y}\cos(mx)+T_1^c(0,t)\cos(mx) \tag{16}$$

$$T^d(x,y_1,t)=T_0^d(0,t)+l\epsilon_1\frac{\partial T_0^d(0,t)}{\partial y}\cos(mx)+T_1^d(0,t)\cos(mx) \tag{17}$$

$$T^d(x,y_2,t)=T_0^d(-h_0,t)-l\epsilon_2\frac{\partial T_0^d(-h_0,t)}{\partial y}\cos(mx)+T_1^d(-h_0,t)\cos(mx). \tag{18}$$

Equation (8) gives

$$\{Q_0(t)+Q_1(t)\cos(mx)\}\{R_0+R_1(P(x,t))\cos(mx)\}=\left\{T_0^c(0,t)+l\epsilon_1\frac{\partial T_0^c(0,t)}{\partial y}\cos(mx)+T_1^c(0,t)\cos(mx)\right\}-\left\{T_0^d(0,t)+l\epsilon_1\frac{\partial T_0^d(0,t)}{\partial y}\cos(mx)+T_1^d(0,t)\cos(mx)\right\} \tag{19}$$

where we have neglected terms higher than $O(\epsilon)$. After substituting these equations into the boundary conditions given above, we separate expressions corresponding to the zeroth-order and the first-order thermal problems: These are listed in the following sections.

2.2 The Zeroth-Order Problem.

$$\frac{\partial^2 T_0^c}{\partial y^2}(y,t)=0 \quad ; \quad \frac{\partial^2 T_0^d}{\partial y^2}(y,t)=0 \tag{20}$$

$$T_0^c(s_0,t)=T_f \tag{21}$$

$$L^c\rho^c\frac{ds_0(t)}{dt}=K^c\frac{\partial T_0^c}{\partial y}(s_0,t) \tag{22}$$

$$K^c\frac{\partial T_0^c}{\partial y}(0,t)=K^d\frac{\partial T_0^d}{\partial y}(0,t) \tag{23}$$

$$T_0^d(-h_0,t)=0 \tag{24}$$

$$K^d\frac{\partial T_0^d}{\partial y}(-h_0,t)=Q_0(t) \tag{25}$$

where

$$Q_0(t)=\frac{T_0^c(0,t)-T_0^d(0,t)}{R_0}. \tag{26}$$

2.3 The First-Order Problem.

$$\frac{\partial^2 T_1^c}{\partial y^2}(y,t)-m^2T_1^c(y,t)=0 \quad ; \quad \frac{\partial^2 T_1^d}{\partial y^2}(y,t)-m^2T_1^d(y,t)=0 \tag{27}$$

$$s_1(t)\frac{\partial T_0^c}{\partial y}(s_0,t)+T_1^c(s_0,t)=0 \tag{28}$$

$$L^c\rho^c\frac{ds_1(t)}{dt}=K^c\left[\frac{\partial T_1^c(s_0,t)}{\partial y}+s_1(t)\frac{\partial^2 T_0^c(s_0,t)}{\partial y^2}\right] \tag{29}$$

$$K^c\left[l\epsilon_1\frac{\partial^2 T_0^c}{\partial y^2}(0,t)+\frac{\partial T_1^c}{\partial y}(0,t)\right]=K^d\left[l\epsilon_1\frac{\partial^2 T_0^d}{\partial y^2}(0,t)+\frac{\partial T_1^d}{\partial y}(0,t)\right] \tag{30}$$

$$T_1^d(-h_0,t)-l\epsilon_2\frac{\partial T_0^d}{\partial y}(-h_0,t)=0 \tag{31}$$

$$K^d\left[\frac{\partial T_1^d}{\partial y}(-h_0,t)-l\epsilon_2\frac{\partial^2 T_0^d}{\partial y^2}(-h_0,t)\right]=Q_1(t) \tag{32}$$

where

$$Q_1(t)=\frac{1}{R_0(t)}\left\{l\epsilon_1\left[\frac{\partial T_0^c}{\partial y}(0,t)-\frac{\partial T_0^d}{\partial y}(0,t)\right]+T_1^c(0,t)-T_1^d(0,t)-Q_0(t)R_1\right\}. \tag{33}$$

Notice that the zeroth-order boundary conditions are identical to that for the unperturbed problem, whereas those for the first-order problem include terms from the zeroth-order solution. This permits the two problems to be solved sequentially.

2.4 The Zeroth-Order Solution. The procedure for solving the zeroth-order problem may be found in Yigit [26]. We therefore summarize the solution without proof.

$$T_0^c(y,t)=T_f+\frac{Q_0(t)}{K^c}[y-s_0(t)] \tag{34}$$

$$T_0^d(y,t)=\frac{Q_0(t)}{K^d}[y+h_0] \tag{35}$$

where

$$Q_0(t)=\frac{T_fK^cK^d}{R_0K^cK^d+K^ds_0(t)+K^ch_0} \tag{36}$$

$$s_0(t)=-(\zeta h_0+R_0K^c)+\sqrt{(\zeta h_0)^2+2R_0K^c\zeta h_0+(R_0K^c)^2+\frac{2T_fK^c}{L^c\rho^c}t} \tag{37}$$

and

$$\zeta=\frac{K^c}{K^d}. \tag{38}$$

2.5 The First-Order Solution. The solution to the first-order thermal problem may be written as

$$T_1^c(y,t)=a_1(t)\sinh(my)+a_2(t)\cosh(my) \tag{39}$$

$$T_1^d(y,t)=a_3(t)\sinh(my)+a_4(t)\cosh(my) \tag{40}$$

where

$$a_1(t)=\frac{Q_0(t)}{mK^c}\left[\frac{Q_1(t)}{Q_0(t)}\cosh(mh_0)+\epsilon_2\sinh(mh_0)\right] \tag{41}$$

$$a_2(t)=-\frac{Q_0(t)}{mK^c\cosh(ms_0)}\left[\frac{Q_1(t)}{Q_0(t)}\cosh(mh_0)\sinh(ms_0(t))+ms_1(t)+\epsilon_2\sinh(mh_0)\sinh(ms_0(t))\right] \tag{42}$$

$$a_3(t)=\frac{Q_0(t)}{mK^d}\left[\frac{Q_1(t)}{Q_0(t)}\cosh(mh_0)+\epsilon_2\sinh(mh_0)\right] \tag{43}$$

$$a_4(t)=\frac{Q_0(t)}{mK^d}\left[\frac{Q_1(t)}{Q_0(t)}\sinh(mh_0)+\epsilon_2\cosh(mh_0)\right]. \tag{44}$$

Substituting Eqs. (34) and (39) into (29) we obtain

$$Q_1(t)=\frac{1}{\cosh(mh_0)}\left\{\rho^cL^c\frac{ds_1(t)}{dt}\cosh(ms_0(t))+Q_0(t)\times[ms_1(t)\sinh(ms_0(t))-\epsilon_2\sinh(mh_0)]\right\} \tag{45}$$

where we have used Eqs. (41) and (42) for $a_1(t)$ and $a_2(t)$, respectively. Finally, substituting Eqs. (34), (35), (36), (39), (40), (45) into Eq. (33), and rearranging terms, we obtain

$$[K^cR_0+s_0(t)+\zeta h_0]\left[\frac{1}{\cosh(mh_0)}(mK^cR_0+\zeta\sinh(mh_0))\times\cosh(ms_0(t))+\sinh(ms_0(t))\right]\frac{\rho^cL^c}{K^cT_f}\frac{ds_1(t)}{dt}+\left\{\left[\frac{mK^cR_0}{\cosh(mh_0)}+\zeta\tanh(mh_0)\right]\sinh(ms_0(t))+\cosh(ms_0(t))\right\}ms_1(t)+[mK^cR_0\sinh(mh_0)+\zeta]\times\frac{\epsilon_2}{\cosh(mh_0)}+\epsilon_1(\zeta-1)+mK^cR'P_1(t)=0 \tag{46}$$

where we have used the following equation for R_1:

$$R_1(P(x,t))=R'P_1(t) \tag{47}$$

which comes from the Taylor series expansion

$$R(P(x,t))=R(P_0(t)+P_1(t)\cos(mx))=R(P_0)+R'(P_0)P_1(t)\cos(mx) \tag{48}$$

and

$$R'=\frac{dR(P_0)}{dP}. \tag{49}$$

Notice that the differential equation for $s_1(t)$ is a function of the first-order contact pressure, $P_1(t)$. In other words, the first-order thermal problems are coupled with their mechanical counterparts. In the next section, we will develop the stress field within the casting and the mold in order to determine $P_1(t)$.

3 The Thermal Stress Problem

Since the spatial variation of the upper mold surface leads to corresponding perturbations in the thermal fields and interface heat flux, we assume the thermal stress distributions in the mold and shell, and the contact pressure, adopt the following forms:

$$\sigma_{jk}(x,y,t)=\sigma_{jk0}(y,t)+\sigma_{jk}(x,y,t)=\sigma_{jk0}(y,t)+\sigma_{jk1}(x,y,t) \tag{50}$$

$$P(x,t)=P_0(t)+P_1(t)\cos(mx) \tag{51}$$

$$P_0(t)=-\sigma_{yy0}(y_1,t) \quad ; \quad P_1(t)\cos(mx)=-\sigma_{yy1}(x,y_1,t) \quad ; \quad y_1=l\epsilon_1\cos(mx). \tag{52}$$

As discussed by Li and Barber [10], the total stress distribution in the solid shell and in the mold can be expressed as a linear combination of a particular solution, σ^p_{jk}, that corresponds to the thermal field, an isothermal solution, σ^h_{jk}, which is allowed to vary in time so as to satisfy time-varying terms in the boundary conditions, and a residual stress, σ^r_{jk}, which is the stress that remains in the solid shell after it is cooled to a uniform temperature and relieved of all boundary tractions. In general, σ^r_{jk} may be subsumed under σ^h_{jk}. Once the stress field is determined, then $P_1(t)$ is obtained from the second of Eqs. (52). A condition that may lead to unstable growth of the shell once micro-air gaps nucleate along the mold surface results when $P_1(t)$ increases at a mold surface crest while simultaneously decreasing in a trough. The present theory assumes that the shell retains contact with the mold surface and hence goes only so far as to monitor $P_1(t)$ up to air gap nucleation.

The mechanical boundary conditions for frictionless contact at the upper surface of the mold are

$$\sigma^c_{n_1t_1}=0 \quad ; \quad \sigma^d_{n_1t_1}=0 \quad ; \quad y=y_1=l\epsilon_1\cos(mx) \tag{53}$$

$$\dot{u}^c_{n_1}=\dot{u}^d_{n_1} \quad ; \quad y=y_1=l\epsilon_1\cos(mx) \tag{54}$$

where $\sigma^c_{n_1t_1}, \sigma^d_{n_1t_1}$ are the shear stresses in the (n_1,t_1) coordinate system that rides along the upper surface of the mold (see Fig. 1), and $\dot{u}^c_{n_1}, \dot{u}^d_{n_1}$ are the normal velocities of the shell and the mold, respectively. Note that Eq. (54) can only be stated in terms of a time derivative since there is no reference state for displacement of the solid. Solidification at the freezing front is assumed to occur in a state of hydrostatic stress

$$\sigma^c_{xx}=-P_0 \quad ; \quad \sigma^c_{yy}=-P_0 \quad ; \quad \sigma^c_{xy}=0 \quad ; \quad y=s(x,t) \tag{55}$$

where P_0 is the molten metal pressure.

Also, frictionless contact is assumed on the lower surface of the mold, and the normal stresses between the solidified shell and the mold are continuous. So

$$\sigma^d_{n_2t_2}=0 \quad ; \quad y=y_2=-(h_0+l\epsilon_2\cos(mx)) \tag{56}$$

$$\sigma^c_{n_1}=\sigma^d_{n_1} \quad ; \quad y=y_1=l\epsilon_1\cos(mx) \tag{57}$$

where $\sigma^d_{n_2t_2}$ is the shear stress in the (n_2,t_2) coordinate system that rides along the lower surface of the mold. To preserve the equilibrium of the mold as a whole, we must have

$$\sigma^d_{yy}(x,y_1,t)=\sigma^d_{yy}(x,y_2,t). \tag{58}$$

3.1 The Particular Solution. The stress field corresponding to the particular solution can be constructed from the thermoelastic displacement potential, φ^i, through ([27])

$$2\mu^i\mathbf{u}^i=\nabla\varphi^i \quad , \quad (i=c,d) \tag{59}$$

where $\varphi^i(x,y,t)$ satisfies

$$\nabla^2\varphi^i=\frac{2\mu^i\alpha^i(1+\nu^i)}{1-\nu^i}T^i \quad ; \quad \mu^i=\frac{E^i}{2(1+\nu^i)} \quad , \quad (i=c,d) \tag{60}$$

and T^i is given by the sum of Eqs. (34), (39) and (35), (40). The superscript i refers to either the shell or mold materials. The stress and displacement fields corresponding to the particular solution are then derived from ([27])

$$(\sigma^i_{xx})^p=-\frac{\partial^2\varphi^i}{\partial y^2} \quad ; \quad (\sigma^i_{yy})^p=-\frac{\partial^2\varphi^i}{\partial x^2} \quad ; \quad (\sigma^i_{xy})^p=\frac{\partial^2\varphi^i}{\partial x\partial y} \tag{61}$$

$$(\dot{u}^i)^p_{y_1}=\frac{1}{2\mu^i}\frac{\partial}{\partial t}\left[\frac{\partial\varphi^i}{\partial y}\right] \quad , \quad (i=c,d)$$

where the rate-dependent form of Eq. (59) has been used (as previously discussed) and the subscript ''1'' denotes a first-order component. Particular integrals of Eq. (60) are

$$\varphi^c=\frac{\mu^c\alpha^c(1+\nu^c)}{m(1-\nu^c)}\left\{\frac{my^2T_f}{3}\left[\frac{y+3(K^cR_0+\zeta h_0)}{s_0(t)+K^cR_0+\zeta h_0}\right]+y[a_2(t)\sinh(my)+a_1(t)\cosh(my)]\cos(mx)\right\} \tag{62}$$

$$\varphi^d=\frac{\mu^d\alpha^d(1+\nu^d)}{m(1-\nu^d)}\left\{\frac{my^2T_f\zeta}{3}\left[\frac{y+3h_0}{\zeta(h_0+K^dR_0)+s_0(t)}\right]+y[a_4(t)\sinh(my)+a_3(t)\cosh(my)]\cos(mx)\right\}. \tag{63}$$

We can simplify the problem somewhat by adjusting Eqs. (62) and (63) so that the components of Eq. (54) corresponding to the particular solution, $(\dot{u}^c)^p_{n_1}$ and $(\dot{u}^d)^p_{n_1}$, are automatically satisfied. We first express the displacement normal to the mold surface in the planar reference via the following transformation equations:

$$(\dot{u}^i)^p_{n_1}=(\dot{u}^i)^p_{y_1}\cos(\phi_1)-(\dot{u}^i)^p_{x_1}\sin(\phi_1) \quad ; \quad (i=c,d) \tag{64}$$

where

$$\phi_1=\frac{dy}{dx}=-\epsilon_1\sin(mx). \tag{65}$$

Since $\phi_1\ll 1$, Eqs. (64) can be written as

$$(\dot{u}^i)^p_{n_1}=(\dot{u}^i)^p_{y_1}+\epsilon_1(\dot{u}^i)^p_{x_1}\sin(mx) \quad ; \quad (i=c,d). \tag{66}$$

Since the zeroth-order solution requires that $(\dot{u}^i)^p_{n_1}=(\dot{u}^i)^p_{y_1}$, it is true that $(\dot{u}^i)^p_{x_1}$ is at least of $O(\epsilon)$ and hence the second term in Eq. (66) is at least of $O(\epsilon^2)$. We may therefore write

$$(\dot{u}^i)^p_{n_1}\approx(\dot{u}^i)^p_{y_1} \quad ; \quad y=y_1=l\epsilon_1\cos(mx) \quad ; \quad (i=c,d) \tag{67}$$

since we are only interested in terms to $O(\epsilon)$. The expression for $(\dot{u}^i)^p_{y_1}$ in Eqs. (61), along with Eqs. (52), (63), and (64) give

$$(\dot{u}^c)^p_{y_1}|_{l\epsilon_1\cos(mx)}=\frac{\alpha^c(1+\nu^c)}{2m(1-\nu^c)}\frac{d}{dt}\times\left\{\frac{2\epsilon_1T_f(K^cR_0+\zeta h_0)}{s_0(t)+K^cR_0+\zeta h_0}+a_1(t)\right\}\cos(mx) \tag{68}$$

$$(\dot{u}^d)^p_{y_1}|_{l\epsilon_1\cos(mx)}=\frac{\alpha^d(1+\nu^d)}{2m(1-\nu^d)}\frac{d}{dt}\times\left\{\frac{2\zeta\epsilon_1T_fh_0}{\zeta(h_0+K^dR_0)+s_0(t)}+a_3(t)\right\}\cos(mx) \tag{69}$$

which result after we expand the hyperbolic functions in a Taylor series about $y=y_1=l\epsilon_1\cos(mx)$ and retain terms to $O(\epsilon)$. We can eliminate this unwanted velocity by superposing a suitable harmonic function onto φ^i in Eqs. (62) and (63). Let

$$(\varphi^i)_k=D_i(t)\sinh(my)\cos(mx) \quad , \quad (i=c,d) \tag{70}$$

where $D_i(t)$ are unknown functions of time. The expression for $(\dot{u}^i)^p_{y_1}$ in Eqs. (61) gives

$$(\dot{u}^i)^p_{yk}=\frac{d}{dt}\left[\frac{mD_i(t)}{2\mu^i}\cosh(my)\cos(mx)\right] \quad , \quad (i=c,d). \tag{71}$$

In order to eliminate the term on the right-hand sides of Eqs. (68) and (69), we write

$$D_c(t)=-\frac{\mu^c\alpha^c(1+\nu^c)}{m(1-\nu^c)}\left\{\frac{2l\epsilon_1T_f(K^cR_0+\zeta h_0)}{s_0(t)+K^cR_0+\zeta h_0}+\frac{a_1(t)}{m}\right\}\cos(mx) \tag{72}$$

$$D_d(t)=-\frac{\mu^d\alpha^d(1+\nu^d)}{m(1-\nu^d)}\left\{\frac{2l\zeta\epsilon_1T_fh_0}{\zeta(h_0+K^dR_0)+s_0(t)}+\frac{a_3(t)}{m}\right\}\cos(mx) \tag{73}$$

and hence

$$(\dot{u}^c)^p_{yk}|_{l\epsilon_1\cos(mx)}=-\frac{\alpha^c(1+\nu^c)}{2m(1-\nu^c)}\frac{d}{dt}\times\left\{\frac{2\epsilon_1T_f(K^cR_0+\zeta h_0)}{s_0(t)+K^cR_0+\zeta h_0}+a_1(t)\right\}\cos(mx) \tag{74}$$

$$(\dot{u}^d)^p_{yk}|_{l\epsilon_1\cos(mx)}=-\frac{\alpha^d(1+\nu^d)}{2m(1-\nu^d)}\frac{d}{dt}\times\left\{\frac{2\zeta\epsilon_1T_fh_0}{\zeta(h_0+K^dR_0)+s_0(t)}+a_3(t)\right\}\cos(mx) \tag{75}$$

since $\cosh(\epsilon_1\cos(mx))\approx 1$. When Eq. (70) is superposed onto Eqs. (62) and (63), we obtain

$$\varphi^c=\frac{\mu^c\alpha^c(1+\nu^c)}{m(1-\nu^c)}\left\{\frac{my^2T_f}{3}\left[\frac{y+3(K^cR_0+\zeta h_0)}{s_0(t)+K^cR_0+\zeta h_0}\right]-\frac{2l\epsilon_1T_f(K^cR_0+\zeta h_0)}{s_0(t)+K^cR_0+\zeta h_0}\sinh(my)\cos(mx)+\left[a_2(t)y\sinh(my)+a_1(t)\left(y\cosh(my)-\frac{1}{m}\sinh(my)\right)\right]\cos(mx)\right\} \tag{76}$$

$$\varphi^d=\frac{\mu^d\alpha^d(1+\nu^d)}{m(1-\nu^d)}\left\{\frac{my^2T_f\zeta}{3}\left[\frac{y+3h_0}{\zeta(h_0+K^dR_0)+s_0(t)}\right]-\frac{2l\zeta\epsilon_1T_fh_0}{\zeta(h_0+K^dR_0)+s_0(t)}\sinh(my)\cos(mx)+\left[a_4(t)y\sinh(my)+a_3(t)\left(y\cosh(my)-\frac{1}{m}\sinh(my)\right)\right]\cos(mx)\right\} \tag{77}$$

which provide the velocity fields (corresponding to the particular solution) that automatically satisfy Eqs. (54). The stress field corresponding to the particular solution can now be derived via Eqs. (61), (76), and (77).

3.2 The Homogeneous Solution. We pose the following form of the zeroth-order homogeneous solution

$$(\sigma^i_{yy0})^h=-P_0\quad;\quad(\sigma^i_{xx0})^h=F_i(y)\quad;\quad(\sigma^i_{xy0})^h=0\quad;\quad(i=c,d) \tag{78}$$

where $F_i(y)$ are unknown functions of position. The lateral stresses, $(\sigma^i_{xx0})^h$, are constructed by adding the zeroth-order term from $(\sigma^i_{xx})^p$ (determined from Eqs. (61), (76), and (77)) to $F_i(y)$ as follows:

$$(\sigma^c_{xx0})^h=-\frac{2\mu^c\alpha^cT_f(1+\nu^c)}{(1-\nu^c)}\left[\frac{y+K^cR_0+\zeta h_0}{s_0(t)+K^cR_0+\zeta h_0}\right]+F_c(y) \tag{79}$$

$$(\sigma^d_{xx0})^h=-\frac{\mu^d\alpha^d(1+\nu^d)}{(1-\nu^d)}\left[\frac{2T_f\zeta(y+h_0)}{\zeta(h_0+K^dR_0)+s_0(t)}\right]+F_d(y). \tag{80}$$

From Eqs. (55), we have $(\sigma^c_{xx0})^h(s_0,t)=-P_0$. Hence,

$$F_c(y)=-P_0+\frac{2\mu^c\alpha^cT_f(1+\nu^c)}{(1-\nu^c)} \tag{81}$$

and the zeroth-order lateral stress in the shell corresponding to the homogeneous solution is

$$(\sigma^c_{xx0})^h=-P_0+\frac{2\mu^c\alpha^cT_f(1+\nu^c)}{(1-\nu^c)}\left[\frac{s_0(t)-y}{s_0(t)+K^cR_0+\zeta h_0}\right]. \tag{82}$$

Also

$$(\sigma^c_{xy0})^h=0\quad;\quad(\sigma^c_{yy0})^h=-P_0. \tag{83}$$

In similar manner,

$$F_d(y)=-P_0 \tag{84}$$

and the zeroth-order lateral stress in the mold corresponding to the homogeneous solution is

$$(\sigma^d_{xx0})^h=-P_0-\frac{\mu^d\alpha^d(1+\nu^c)}{(1-\nu^c)}\left[\frac{2T_f\zeta(y+h_0)}{\zeta(h_0+K^dR_0)+s_0(t)}\right]. \tag{85}$$

Also

$$(\sigma^d_{xy0})^h=0\quad;\quad(\sigma^d_{yy0})^h=-P_0. \tag{86}$$

The first-order stress field corresponding to the homogeneous solution is derived from ([28])

$$(\sigma^i_{xx})^h=\frac{\partial^2\Phi^i}{\partial y^2}\quad;\quad(\sigma^i_{yy})^h=\frac{\partial^2\Phi^i}{\partial x^2}\quad;\quad(\sigma^i_{xy})^h=-\frac{\partial^2\Phi^i}{\partial x\partial y}\quad,\quad(i=c,d) \tag{87}$$

where Φ^i is the Airy stress function which satisfies the following compatibility relation:

$$\frac{\partial}{\partial t}\nabla^4\Phi^i=0\quad,\quad(i=c,d). \tag{88}$$

In view of Eqs. (88), the time derivative of Φ^i must be biharmonic. It can be verified by substitution that the appropriate forms are

$$\Phi^c=\{[b_1(t)y+b_2(t)]\cosh(my)+[b_3(t)y+b_4(t)]\sinh(my)+g(y)\}\cos(mx) \tag{89}$$

$$\Phi^d=\{[B_1(t)y+B_2(t)]\cosh(my)+[B_3(t)y+B_4(t)]\sinh(my)\}\cos(mx). \tag{90}$$

Note that $b_1(t)-b_4(t)$, and $B_1(t)-B_4(t)$ are unknown functions of time and $g(y)$ is a time-independent function that represents residual stress (or the stress in the shell when it is cooled to a uniform temperature and relieved of all boundary tractions). Using Eqs. (87), (89), and (90), the homogeneous solution of the first-order problem becomes

$$(\sigma^c_{xx1})^h=\{[2mb_3(t)+m^2(b_1(t)y+b_2(t))]\cosh(my)+[2mb_1(t)+m^2(b_3(t)y+b_4(t))]\sinh(my)+g''(y)\}\cos(mx) \tag{91}$$

$$(\sigma^c_{xy1})^h=m\{[b_1(t)+m(b_3(t)y+b_4(t))]\cosh(my)+[b_3(t)+m(b_1(t)y+b_2(t))]\sinh(my)+g'(y)\}\sin(mx) \tag{92}$$

$$(\sigma^c_{yy1})^h = -m^2\{[b_1(t)y + b_2(t)]\cosh(my) + [b_3(t)y + b_4(t)]\sinh(my) - g(y)\}\cos(mx) \quad (93)$$

$$(\sigma^d_{xx1})^h = \{[2mB_3(t) + m^2(B_1(t)y + B_2(t))]\cosh(my) + [2mB_1(t) + m^2(B_3(t)y + B_4(t))]\sinh(my)\}\cos(mx) \quad (94)$$

$$(\sigma^d_{xy1})^h = m\{[B_1(t) + m(B_3(t)y + B_4(t))]\cosh(my) + [B_3(t) + m(B_1(t)y + B_2(t))]\sinh(my)\}\sin(mx) \quad (95)$$

$$(\sigma^d_{yy1})^h = -m^2\{[B_1(t)y + B_2(t)]\cosh(my) + [B_3(t)y + B_4(t)]\sinh(my)\}\cos(mx) \quad (96)$$

where the prime denotes differentiation with respect to y. The components of the total stress field are obtained through superposition of the particular and homogeneous stress fields via Eq. (50).

3.3 Determination of the b_i and B_i. The b_i and B_i in Eqs. (89) and (96) are determined by requiring the total stress field to satisfy Eqs. (53) and (55)–(58), and the homogeneous stress field to satisfy Eq. (54). The total shear stress in the mold surface system may be written in terms of the planar reference via

$$\begin{aligned}\sigma^c_{n_1t_1}(x,y_1,t) &= \sigma^c_{xy}(\cos^2(\phi_1) - \sin^2(\phi_1)) + (\sigma^c_{yy} - \sigma^c_{xx})\sin(\phi_1)\cos(\phi_1)\\ &\approx \sigma^c_{xy} - (\sigma^c_{yy} - \sigma^c_{xx})\epsilon_1 \sin(mx). \end{aligned} \quad (97)$$

Similarly,

$$\begin{aligned}\sigma^d_{n_1t_1}(x,y_1,t) &= \sigma^d_{xy}(\cos^2(\phi_1) - \sin^2(\phi_1)) + (\sigma^d_{yy} - \sigma^d_{xx})\sin(\phi_1)\cos(\phi_1)\\ &\approx \sigma^d_{xy} - (\sigma^d_{yy} - \sigma^d_{xx})\epsilon_1 \sin(mx). \end{aligned} \quad (98)$$

The total shear stress at the bottom surface of the mold may be written in terms of the planar reference via

$$\begin{aligned}\sigma^d_{n_2t_2}(x,y_2,t) &= \sigma^d_{xy}(\cos^2(\phi_2) - \sin^2(\phi_2)) + (\sigma^d_{yy} - \sigma^d_{xx})\sin(\phi_2)\cos(\phi_2)\\ &\approx \sigma^d_{xy} + (\sigma^d_{yy} - \sigma^d_{xx})\epsilon_2 \sin(mx) \end{aligned} \quad (99)$$

where we have used

$$\phi_2 = \frac{dy}{dx} = \epsilon_2 \sin(mx). \quad (100)$$

The total normal stresses relative to the planar reference of the upper surface of the mold become

$$\begin{aligned}\sigma^c_{n_1}(x,y_1,t) &= \sigma^c_{xx}\sin^2(\phi_1) + \sigma^c_{yy}\cos^2(\phi_1) - 2\sigma^c_{xy}\sin(\phi_1)\cos(\phi_1)\\ &\approx \sigma^c_{yy} + 2\epsilon_1\sigma^c_{xy}\sin(mx) \end{aligned} \quad (101)$$

$$\begin{aligned}\sigma^d_{n_1}(x,y_1,t) &= \sigma^d_{xx}\sin^2(\phi_1) + \sigma^d_{yy}\cos^2(\phi_1) - 2\sigma^d_{xy}\sin(\phi_1)\cos(\phi_1)\\ &\approx \sigma^d_{yy} + 2\epsilon_1\sigma^d_{xy}\sin(mx) \end{aligned} \quad (102)$$

$$\begin{aligned}\sigma^d_{n_2}(x,y_2,t) &= \sigma^d_{xx}\sin^2(\phi_2) + \sigma^d_{yy}\cos^2(\phi_2) - 2\sigma^d_{xy}\sin(\phi_2)\cos(\phi_2)\\ &\approx \sigma^d_{yy} - 2\epsilon_2\sigma^d_{xy}\sin(mx). \end{aligned} \quad (103)$$

Equations (53), (61), (76), (92), and (97) give

$$b_1(t) + mb_4(t) + g'(0) = \frac{2\mu^c\alpha^c\epsilon_1 T_f(1+\nu^c)}{m(1-\nu^c)} \quad (104)$$

where we have retained terms to $O(\epsilon)$. The elastic constitutive law for plane strain (where the associated rigid-body displacements have been neglected) is

$$(\dot{u}^i)^h_{n_1} \approx (\dot{u}^i)^h_{y_1} = \frac{1+\nu^i}{E^i}\left\{(1-\nu^i)\int (\dot{\sigma}^i_{yy1})^h dy - \nu^i\int (\dot{\sigma}^i_{xx1})^h dy\right\} \quad , \quad (i=c,d). \quad (105)$$

Application of Eq. (54), using Eqs. (91), (92), and (94), (96) gives

$$\frac{(1+\nu^c)E^d}{(1+\nu^d)E^c}\left[b_4(t) - (1-2\nu^c)\frac{b_1(t)}{m}\right] = B_4(t) - (1-2\nu^d)\frac{B_1(t)}{m}. \quad (106)$$

Application of the expression for $\sigma^d_{n_1t_1}$ in Eqs. (53), using Eq. (98) gives

$$B_1(t) = -mB_4(t) \quad (107)$$

We expand each of Eqs. (55) in a Taylor series about the mean position of the freezing front, s_0, beginning with σ^c_{xx}. Hence

$$\sigma^c_{xx}(x,s,t) = \sigma^c_{xx}(x,s_0,t) + (s-s_0)\frac{\partial\sigma^c_{xx}(x,s_0,t)}{\partial y} + \ldots = -P_0. \quad (108)$$

We have

$$\frac{\partial\sigma^c_{xx}(x,s_0,t)}{\partial y} = -\frac{2\mu^c\alpha^c T_f(1+\nu^c)}{(1-\nu^c)[s_0(t) + K^cR_0 + \zeta h_0]} + 0(\epsilon) \quad (109)$$

where $\sigma^c_{xx} = (\sigma^c)^p_{xx} + (\sigma^c)^h_{xx}$ is derived from Eqs. (61), (76), and (91). Equation (108) may therefore be written as

$$\begin{aligned}\sigma^c_{xx}(x,s,t) &= \sigma^c_{xx}(x,s_0,t) - \frac{2\mu^c\alpha^c s_1(t)T_f(1+\nu^c)}{(1-\nu^c)[s_0(t) + K^cR_0 + \zeta h_0]}\cos(mx)\\ &= -P_0. \end{aligned} \quad (110)$$

Substitution of the sum of $(\sigma^c)^p_{xx}$ and Eq. (91) into Eq. (110) gives

$$\begin{aligned}&\left[\frac{2b_1(t)}{m} + b_3(t)s_0(t) + b_4(t)\right]\sinh(ms_0(t)) + \left[b_1(t)s_0(t) + b_2(t) + \frac{2b_3(t)}{m}\right]\cosh(ms_0(t)) + \frac{g''(s_0)}{m^2}\\ &= \frac{\mu^c\alpha^c(1+\nu^c)}{m^2(1-\nu^c)}\left\{2T_f\left[\frac{s_1(t) - \epsilon_1(K^cR_0 + \zeta h_0)\sinh(ms_0(t))}{s_0(t) + K^cR_0 + \zeta h_0}\right] + (2\cosh(ms_0(t)) + ms_0\sinh(ms_0(t)))a_2(t)\right.\\ &\left. + (\sinh(ms_0(t)) + ms_0\cosh(ms_0(t)))a_1(t)\right\}. \end{aligned} \quad (111)$$

Following the same procedure for σ^c_{xy} and σ^c_{yy} gives, respectively,

$$\begin{aligned}&[m\cosh(ms_0(t)) + m^2s_0(t)\sinh(ms_0(t))]b_1(t) + m^2\sinh(ms_0(t))b_2(t)\\ &+ [m\sinh(ms_0(t)) + m^2s_0(t)\cosh(ms_0(t))]b_3(t) + m^2\cosh(ms_0(t))b_4(t) + mg'(s_0)\\ &= \frac{\mu^c\alpha^c(1+\nu^c)}{(1-\nu^c)}\left\{(\sinh(ms_0(t)) + ms_0(t)\cosh(ms_0(t)))a_2(t) + ms_0(t)\sinh(ms_0(t))a_1(t)\right. \end{aligned}$$

$$-\frac{2\epsilon_1 T_f(K^c R_0+\zeta h_0)\cosh(ms_0(t))}{s_0(t)+K^c R_0+\zeta h_0}\Bigg\} \tag{112}$$

$$[b_1(t)s_0(t)+b_2(t)]\cosh(ms_0(t))$$
$$+[b_3(t)s_0(t)+b_4(t)]\sinh(ms_0(t))+g(s_0)$$
$$=-\frac{\mu^c\alpha^c(1+\nu^c)}{m^2(1-\nu^c)}\Bigg\{\Bigg[\frac{2\epsilon_1 T_f(K^c R_0+\zeta h_0)}{s_0(t)+K^c R_0+\zeta h_0}-ms_0(t)a_2(t)\Bigg]$$
$$\times\sinh(ms_0(t))-[ms_0(t)\cosh(ms_0(t))$$
$$-\sinh(ms_0(t))]a_1(t)\Bigg\}. \tag{113}$$

Application of Eq. (57), using Eqs. (101), (102) gives

$$B_2(t)=b_2(t)+g(0). \tag{114}$$

Application of Eq. (56), using Eqs. (99) gives

$$[m\cosh(mh_0)+m^2h_0\sinh(mh_0)]B_1(t)-m^2\sinh(mh_0)B_2(t)$$
$$-[m^2h_0\cosh(mh_0)+m\sinh(mh_0)]B_3(t)$$
$$+m^2\cosh(mh_0)B_4(t)$$
$$=-\frac{\mu^d\alpha^d(1+\nu^d)}{(1-\nu^d)}\Bigg\{(\sinh(mh_0)+mh_0\cosh(mh_0))a_4(t)$$
$$-mh_0\sinh(mh_0)a_3(t)$$
$$+\frac{2\zeta\epsilon_1 T_f h_0}{\zeta(h_0+K^d R_0)+s_0(t)}\cosh(mh_0)\Bigg\} \tag{115}$$

Finally, application of boundary condition Eq. (58) gives

$$-B_2(t)+[B_2(t)-B_1(t)h_0]\cosh(mh_0)$$
$$-[B_4(t)-B_3(t)h_0]\sinh(mh_0)$$
$$=-\frac{\mu^d\alpha^d(1+\nu^d)}{m^2(1-\nu^d)}\Bigg\{-\frac{2\zeta\epsilon_1 T_f h_0\sinh(mh_0)}{\zeta(h_0+K^d R_0)+s_0(t)}$$
$$-mh_0\sinh(mh_0)a_4(t)$$
$$-[\sinh(mh_0)-mh_0\cosh(mh_0)]a_3(t)\Bigg\} \tag{116}$$

where we expanded Eqs. (56) and (58) in a Taylor series about the mean thickness of the mold, $-h_0$, and have retained terms to $O(\epsilon)$.

Equations (104), (106), (107), (111)–(116) determine the unknown residual stress function $g(s_0)$ and eight unknown time-dependent coefficients. These nine equations can be reduced to a single differential equation through elimination of the unknown functions $b_1(t)-b_4(t)$, $B_1(t)-B_4(t)$. As a result of this procedure, we obtain a second-order ordinary differential equation for the unknown residual stress function, $g(s_0)$, as follows:

$$g''(s_0)+\theta_1 g'(s_0)+\theta_2 g(s_0)=\theta_3\frac{ds_1(t)}{dt}+\theta_4 s_1(t)+\theta_5. \tag{117}$$

Note that we have imposed the arbitrary conditions $g(0)=g'(0)=0$ since the arbitrary constants implied by the general solution of Eq. (117) simply determine the partition of an arbitrary, time-independent biharmonic function between the two functions Φ_1 and Φ_2 and have no effect on the physical quantities predicted by the solution. Once $g(s_0)$ is known, we can recover $b_2(t)$ and the remaining $b_i(t)$ and $B_i(t)$ through back substitution. Finally, we determine the contact pressure perturbation at the crests of the upper surface of the mold (using the expression for $P_1(t)$ in Eqs. (52)) via

$$P_1(t)=m^2 b_2(t) \tag{118}$$

where

$$b_2(t)=\theta_6\frac{s_1(t)}{dt}+\theta_7 s_1(t)+\theta_8 g(s_0)+\theta_9 g'(s_0)+\theta_{10}. \tag{119}$$

Note that the coefficients θ_i $(i=1,\ldots,10)$ are functions of $s_0(t)$ and the material and casting process parameters. Dimensionless forms of these coefficients are listed in the Appendix.

4 Dimensionless Formulation for Perturbation Quantities

To facilitate the numerical calculations associated with the results presented in the companion paper, we found it convenient to rewrite Eqs. (46) and (117) in terms of the following dimensionless quantities:

$$\beta=\frac{m^2K^cT_f}{\rho^cL^c}t \quad ; \quad \eta=ms_0(t)=my \quad ;$$

$$H_0=mh_0 \quad ; \quad \overline{s_1}(\beta_0(\eta))=\frac{ms_1(t_0(y))}{\epsilon_1}$$

$$\overline{g}(\eta)=\frac{m^2(1-\nu^c)}{E^c\alpha^c\epsilon_1 T_f}g(y) \quad ; \quad \overline{R}_0=mK^cR_0 \quad ;$$

$$\overline{R}'=\frac{E^c\alpha^cT_fR'}{(1-\nu^c)R_0} \quad ; \quad \overline{T}_1(0,\eta)=\frac{T_1(0,t)}{\epsilon_1T_f}$$

$$\overline{b}_2(\eta)=\frac{m^2(1-\nu^c)}{E^c\alpha^c\epsilon_1T_f}b_2(t) \quad ; \quad \overline{P}(\eta)=\frac{(1-\nu^c)}{E^c\alpha^c\epsilon_1T_f}P_1(t) \quad ;$$

$$\overline{Q}_0(\eta)=\frac{Q_0(t)}{mK^cT_f}$$

$$\overline{Q}_1(\eta)=\frac{R_0Q_1(t)}{\epsilon_1T_f} \quad ; \quad \kappa=\frac{\epsilon_2}{\epsilon_1} \quad ; \quad \xi=\frac{E^d\alpha^d(1-\nu^c)}{E^c\alpha^c(1-\nu^d)} \quad ;$$

$$\gamma=\frac{E^d(1+\nu^c)}{E^c(1+\nu^d)}. \tag{120}$$

Note that we define $\beta_0(\eta)$ as the dimensionless time when the mean melt line reaches the position $Y=my$. The ratio of the amplitudes of the mold surfaces is denoted by κ.

5 Numerical Solution Procedure for the Contact Pressure Perturbation

The dimensionless forms of Eqs. (46) and (117) are as follows:

$$\omega_1\overline{s_1}'(\eta)+\omega_2\overline{s_1}(\eta)+\omega_3\overline{g}(\eta)+\omega_4\overline{g}'(\eta)+\omega_5=0 \tag{121}$$

$$\overline{g}''(\eta)+\omega_6\overline{g}'(\eta)+\omega_7\overline{g}(\eta)=\omega_8\overline{s_1}'(\eta)+\omega_9\overline{s_1}(\eta)+\omega_{10} \tag{122}$$

The dimensionless contact pressure is

$$\overline{P}_1(\eta)=\overline{b}_2(\eta) \tag{123}$$

where

$$\overline{b}_2(\eta)=\tau_1\overline{s_1}'(\eta)+\tau_2\overline{s_1}(\eta)+\tau_3\overline{g}(\eta)+\tau_4\overline{g}'(\eta)+\tau_5. \tag{124}$$

The coefficients ω_i $(i=1,\ldots,10)$ and τ_j $(j=1,\ldots,5)$ are listed in the Appendix. Note that in Eqs. (121), (122), and (124) $(')$ denotes differentiation with respect to η, and we have used

$$\frac{d\overline{s_1}}{d\eta}=[\eta+\overline{R}_0+\zeta H_0]\frac{d\overline{s_1}}{d\beta} \tag{125}$$

in order to write the equations as a function of η only.

The second-order differential equations with variable coefficients, Eqs. (121) and (122), which must be solved prior to deter-

mining $\overline{P}_1(\eta)$, can be reduced to a single higher-order differential equation and solved by numerical methods described in Li and Barber [10]. An alternative approach is to first write these equations in the state-space form, and then solve them simultaneously ([28]). Defining the state variables as

$$x_1=\overline{s}_1 \quad ; \quad x_2=\overline{g}(\eta) \quad ; \quad x_3=\overline{g}'(\eta). \tag{126}$$

We can then write Eqs. (121) and (122) in the following form

$$x_1'=e_1x_1+e_2x_2+e_3x_3+e_4 \tag{127}$$

$$x_2'=x_3 \tag{128}$$

$$x_3'=e_5x_1+e_6x_2+e_7x_3+e_8 \tag{129}$$

where the coefficients e_i $(i=1,\ldots,8)$ are functions of η and the material and casting process parameters. Note that in Eqs. (127)–(129), $(')$ denotes differentiation with respect to η.

The governing first-order differential equations are linear and have three initial conditions. In order to be able to compare the predictions of this work to the limiting case of a rigid mold (see [22]) we adopt the same initial conditions used by these authors. In the present formulation, this requires $x_1=1$, $x_2=0$, and $x_3=0$ when η is very small but finite.

The solution is obtained by integrating Eqs. (127)–(129) with the given initial conditions. A variable step, variable order predictor-corrector algorithm suitable for stiff problems is used for this purpose ([29]).

6 Solution for $\eta, H_0 \ll 1$ and the Rigid Mold Limit

It is important to check that Eq. (123) reduces to the result previously obtained by ([22]) for solidification on a rigid mold (or rigid, perfectly conducting foundation) with a sinusoidal surface. In addition, we wish to examine the relative importance of the coupling process at short times after the start of solidification. For this purpose, we evaluate Eqs. (121) and (122) using the following series solutions:

$$\overline{s}_1(\eta)=1+\sum_{i=1}^{N}\hat{A}_i\eta^i \tag{130}$$

$$\overline{g}(\eta)=\sum_{i=1}^{N}\hat{B}_{i+1}\eta^{i+1} \tag{131}$$

where $\eta \ll 1$. Note that the time-independent term in Eq. (130) accounts for the fact that the thin shell is compliant to the mold surface at initial time. Solutions for the unknown constant coefficients, $\hat{A}_i$ and $\hat{B}_i$, are obtained by first inserting Eqs. (130) and (131) into Eqs. (121) and (122), then replacing each transcendental function with its series form, and finally by writing

$$\frac{1}{\eta+\overline{R}_0}=\frac{1}{\overline{R}_0}\left(1-\frac{\eta}{\overline{R}_0}+\frac{\eta^2}{\overline{R}_0^2}-\cdots\right). \tag{132}$$

Equation (123) is then evaluated using the series expressions for $\overline{s}_1(\eta)$ and $\overline{g}_1(\eta)$. Although the resulting expression for $\overline{P}_1(\eta)$ for arbitrarily large H_0 is too lengthy to report here, we consider the limiting case of $H_0 \ll 1$, for which we retain terms to order H_0 after replacing hyperbolic functions of argument H_0 with their Taylor series expansions. For $N=4$, the contact pressure perturbation at the highest point of a crest is

$$\begin{aligned}\overline{P}_1(\eta)=&\frac{\eta^2}{2(\overline{R}_0+\zeta H_0)}-\frac{1}{60(1-\nu^c)}\left[\begin{array}{l}10\overline{R}_0\{6(1-\nu^d)\xi\zeta^2+\gamma(1-\nu^c)(3+\zeta+\kappa\zeta)\}\\ -H_0\left\{\begin{array}{l}\xi\zeta(1-\nu^d)[(6-5\kappa)\overline{R}_0^2-10(14-\kappa)\zeta^2]\\ +5\gamma(1-\nu^c)[(\overline{R}_0^2-8\zeta^2)\kappa-2\zeta(3+4\zeta)]\end{array}\right\}\end{array}\right]\frac{\eta^3}{(\overline{R}_0+3\zeta H_0)\gamma\overline{R}_0^2}\\ &+\frac{1}{48(1-\nu^c)}\left[H_0\left\{\begin{array}{l}\gamma(1-\nu^c)[3(8+3\zeta+3\kappa\zeta)-4\overline{R}_0^2]\\ -3\xi\zeta^2(7-\kappa)(1-\nu^d)\end{array}\right\}-6(1-\nu^d)\xi\zeta\overline{R}_0\right]\frac{\eta^4}{\gamma H_0\overline{R}_0^3}\\ &-\frac{1}{60(1-\nu^c)}\left[\begin{array}{l}H_0\left\{\begin{array}{l}\xi\zeta[24\overline{R}_0+6(17+2\kappa)\zeta-\overline{R}_0^2(2-\overline{R}'-81\zeta)]\\ -2\gamma(1-\nu^c)[2\overline{R}_0^2(1+\zeta+\kappa\zeta)-3(5+\zeta+\kappa\zeta)]\end{array}\right\}\\ -12\xi\zeta\overline{R}_0\end{array}\right]\frac{\eta^5}{\gamma H_0\overline{R}_0^4}.\end{aligned} \tag{133}$$

The first (quadratic) term in Eq. (133) does not change in the course of imposing the limit of very small H_0. Note that the denominator in this term consists of the sum of the mean resistance of the mold-shell interface, $\overline{R}_0$, and the thermal resistance of the mold, viz., ζH_0.

In the limit $H_0 \to 0$, or, equivalently $\zeta \to 0$, Eq. (133) reduces to the rigid mold result previously determined by Hector et al. [22]. For $N=5$, $\overline{P}_1(\eta)$ at the highest point of a crest in a rigid mold surface is

$$\begin{aligned}\overline{P}_1(\eta)=&\frac{\eta^2}{2\overline{R}_0}-\frac{\eta^3}{2\overline{R}_0^2}+\frac{(6-\overline{R}_0^2)\eta^4}{12\overline{R}_0^3}-\frac{(15-2\overline{R}_0^2)\eta^5}{30\overline{R}_0^4}\\ &+\frac{(720-5(4+9\overline{R}')\overline{R}_0^2+32\overline{R}_0^4)\eta^6}{1440\overline{R}_0^5}+\ldots.\end{aligned} \tag{134}$$

The limiting form of $\overline{s}_1(\eta)$ was also obtained from Eqs. (122) and (123). Series expressions similar to Eq. (134) can be derived for $\overline{Q}_1(\eta)$ and $\overline{T}_1(0,\eta)$ following the procedure outlined above. Note that Eqs. (133) and (134) were derived with a symbolic processor.

We observe that the contact resistance sensitivity, $\overline{R}'$, first appears in the coefficient of η^5 of Eq. (133) for the deformable mold. In the case of Eq. (134) (i.e., for the rigid mold), $\overline{R}'$ first appears in the coefficient of η^6. Hence, for sufficiently short times after the start of solidification, the evolution of the contact pressure perturbation for both the rigid mold and the deformable mold is essentially controlled through uncoupled physics since the sensitivity is more of a longer time effect. We shall address this issue more extensively in the companion paper.

7 Gap Nucleation Criterion

Determination of the conditions for gap nucleation can be achieved through examination of P^{tr}, which is the ratio of the total contact pressure at the lowest points of the troughs, P, to the

mean pressure, P_0. Since we shall be interested in specific mold-shell material combinations in Part II, we consider the dimensional forms of these quantities. Hence

$$P^{tr}=\frac{P}{P_0}=1-\frac{P_1}{P_0}. \tag{135}$$

Note that for $P_1/P_0\rightarrow 1$, the following condition, which is derived in Hector et al. [22], must be met:

$$-\frac{R'P_0}{R_0}\ll 1. \tag{136}$$

This limits the proposed gap nucleation analysis to either weakly coupled systems, or the extreme case of a fully uncoupled system. All other perturbation quantities are required to be much less than one.

Gap nucleation occurs when

$$P^{tr}=0. \tag{137}$$

Gap nucleation at the troughs will indicate the possibility of irregular growth of the shell since contact will simultaneously increase at the crests (the sign in front of P_1 will positive, rather than negative, due to the cos(mx) term in Eq. (51)). Beyond gap nucleation time, the present model is no longer valid since it cannot account for continued growth of the gaps and the shell.

8 Conclusions

A theoretical methodology has been developed for the purpose of examining the effect of mold surface wavelength and mold-shell material properties on gap nucleation in pure metal solidification processes. A metal shell is assumed to solidify on a thin mold having sinusoidal surfaces of equivalent wavelengths. The thermal and mechanical fields in the shell are coupled through a pressure-dependent thermal contact resistance. This leads to a pair of coupled differential equations for the shell thickness perturbation and a function that represents residual stress. The contact pressure along the mold-shell interface is determined both through numerical solution of these equations and through appropriate series solutions. For the numerical solution, there is no restriction on time, whereas the series solution is limited to small times after the start of solidification. The series solution was used to demonstrate that the contact pressure for the deformable mold problem reduces to that for a rigid, perfectly conducting foundation in the limit of zero mold thickness. It was also found through examination of each of the series terms that the coupling effect is more appropriate at longer solidification times for both the rigid foundation and deformable mold problems: If gap nucleation occurs during this time frame, it is primarily controlled through uncoupled physics.

In the companion paper (Part II), we shall use the results of the theoretical methodology developed herein to examine the evolution of the contact pressure in systems where the mold-shell materials are combinations of pure aluminum, copper, iron, or lead. Based upon experimental evidence that periodic mold topographies can have a positive influence on the growth of the shell, we shall examine the gap nucleation process as a function of mold surface wavelength. We shall specifically focus on the effect that the wavelength has on the time and location of gap nucleation as controlled through variation of the contact pressure at the mold-shell interface. Additional material parameters such as the distortivity shall also be examined. The overall motivation for this work is to provide not only theoretical evidence for a wavelength effect on shell growth (within the restrictions placed upon the theoretical model), but also to stimulate effort into the development of quantitative design criteria for casting mold surfaces through further theoretical and experimental work.

Acknowledgments

The authors are indebted to Prof. J. A. Howarth of the University of Hull for carefully checking all of the algebraic details up to Eq. (129), and for directing the authors' attention to several errors in an earlier version of the manuscript which have subsequently been corrected. In addition, Professor Howarth patiently answered the authors' queries about the series solution methodology. The authors wish to express their gratitude to Dr. Owen Richmond of Alcoa Technical Center for suggesting this problem and to Prof. J. R. Barber of the University of Michigan for his continuous guidance and support during all phases of the work. Faruk Yigit is pleased to acknowledge support from the King Saud University, College of Engineering Research Center under project number 13/419.

Appendix

Coefficients of Eqs. (121)–(124). The coefficients ω_i ($i=1,\ldots 10$) and τ_j ($j=1,\ldots,5$) in Eqs. (121)–(124) are

$$\eta=-(\zeta H_0+\overline{R}_0)+\sqrt{\zeta^2H_0^2+2\overline{R}_0\zeta H_0+\overline{R}_0^2+2\beta}\quad ;$$

$$\overline{Q}_0=\frac{1}{\overline{R}_0+\eta+\zeta H_0} \tag{A1}$$

$$Z_1=\cosh(\eta)\quad ;\quad Z_2=\sinh(\eta)\quad ;\quad Z_3=\cosh(H_0)\quad ;$$

$$Z_4=\sinh(H_0) \tag{A2}$$

$$Z_5=\eta Z_1+2Z_2\quad ;\quad Z_6=2Z_1+\eta Z_2\quad ;\quad Z_7=\eta Z_2+Z_1\quad ;$$

$$Z_8=Z_2+\eta Z_1 \tag{A3}$$

$$Z_9=-1\quad ;\quad Z_{10}=-(Z_4+H_0Z_3)\quad ;\quad Z_{11}=-(1-2\nu^c)\quad ;$$

$$Z_{12}=\frac{1}{\gamma} \tag{A4}$$

$$Z_{13}=-(1-2\nu^d)Z_{12}\quad ;\quad Z_{14}=1-\frac{Z_3Z_4+H_0}{Z_4+H_0Z_3}\quad ;$$

$$Z_{15}=\frac{Z_{11}(H_0^2-Z_4^2)}{(Z_{12}-Z_{13})Z_{10}} \tag{A5}$$

$$Z_{16}=\frac{Z_{15}}{Z_{11}}\quad ;\quad Z_{17}=\frac{1}{2}(\eta-Z_1Z_2)\quad ;$$

$$Z_{18}=\overline{Q}_0\left(1-Z_1^2+\frac{Z_2^2}{2}\right)\quad ;\quad Z_{19}=-\overline{Q}_0(\overline{R}_0+\zeta H_0) \tag{A6}$$

$$Z_{20}=-\frac{1}{2}Z_2^2\quad ;\quad Z_{21}=-\frac{1}{2}\overline{Q}_0(Z_1Z_2+\eta)\quad ;$$

$$Z_{22}=\frac{1}{2}(\eta-Z_1Z_2)\quad ;\quad Z_{23}=-\frac{Z_2^2\overline{Q}_0}{2} \tag{A7}$$

$$Z_{24}=-\frac{1}{2}\zeta\xi Z_1\frac{Z_4^2}{Z_3}\quad ;\quad Z_{25}=-\frac{1}{2}\zeta\xi\overline{Q}_0Z_2\frac{Z_4^2}{Z_3} \tag{A8}$$

$$Z_{26}=-\frac{\kappa\zeta\xi}{2Z_3}\overline{Q}_0(Z_4+H_0Z_3)-\zeta\xi H_0Z_3\overline{Q}_0\quad ;$$

$$Z_{27}=-\frac{1}{2}\zeta\xi Z_1\left(\frac{H_0Z_4Z_4}{Z_3}+Z_4-H_0Z_3\right) \tag{A9}$$

$$Z_{28}=-\frac{1}{2}\zeta\xi Z_2\overline{Q}_0\left(\frac{H_0Z_4^2}{Z_3}+Z_4-H_0Z_3\right)\quad ;$$

$$Z_{29}=-\zeta\xi H_0\overline{Q}_0Z_4-\frac{\kappa\zeta\xi}{2Z_3}H_0Z_4\overline{Q}_0 \tag{A10}$$

$$Z_{30}=Z_{27}+\frac{H_0Z_4Z_{24}}{Z_{10}}\quad ;\quad Z_{31}=Z_{28}+\frac{H_0Z_4Z_{25}}{Z_{10}}\quad ;$$

$$Z_{32}=Z_{29}+\frac{H_0Z_4Z_{26}}{Z_{10}} \tag{A11}$$

$$Z_{33}=\frac{Z_{30}}{Z_{15}-Z_{16}} \quad ; \quad Z_{34}=\frac{Z_{31}}{Z_{15}-Z_{16}} \quad ; \quad Z_{35}=\frac{Z_{32}-Z_{16}Z_9}{Z_{15}-Z_{16}} \tag{A12}$$

$$Z_{36}=Z_{17}-(Z_5-Z_2)Z_{33} \quad ; \quad Z_{37}=Z_{18}-(Z_5-Z_2)Z_{34} \tag{A13}$$

$$Z_{38}=Z_{19}Z_2-Z_2Z_9-(Z_5-Z_2)Z_{35} \quad ; \quad Z_{39}=Z_{20}-(Z_7-Z_1)Z_{33} \tag{A14}$$

$$Z_{40}=Z_{21}-(Z_7-Z_1)Z_{34} \quad ; \quad Z_{41}=Z_{19}Z_1-Z_1Z_9-(Z_7-Z_1)Z_{35} \tag{A15}$$

$$Z_{42}=Z_{22}-(\eta Z_1-Z_2)Z_{33} \quad ; \quad Z_{43}=Z_{23}-(\eta Z_1-Z_2)Z_{34} \tag{A16}$$

$$Z_{44}=Z_{19}Z_2-Z_2Z_9-(\eta Z_1-Z_2)Z_{35} \quad ;$$

$$Z_{45}=Z_{36}-\frac{Z_6Z_{42}}{\eta Z_2} \quad ; \quad Z_{46}=Z_{37}-\frac{Z_6Z_{43}}{\eta Z_2} \tag{A17}$$

$$Z_{47}=Z_{38}-\frac{Z_6Z_{44}}{\eta Z_2} \quad ; \quad Z_{48}=Z_{39}-\frac{Z_8Z_{42}}{\eta Z_2} \quad ;$$

$$Z_{49}=Z_{40}-\frac{Z_8Z_{43}}{\eta Z_2} \quad ; \quad Z_{50}=Z_{41}-\frac{Z_8Z_{44}}{\eta Z_2} \tag{A18}$$

$$Z_{51}=\frac{Z_{14}}{Z_{15}-Z_{16}} \quad ; \quad Z_{52}=Z_1-(Z_5-Z_2)Z_{51} \quad ;$$

$$Z_{53}=Z_2-(Z_7-Z_1)Z_{51} \tag{A19}$$

$$Z_{54}=Z_1-(\eta Z_1-Z_2)Z_{51} \quad ; \quad Z_{55}=Z_{52}-\frac{Z_6Z_{54}}{\eta Z_2} \quad ;$$

$$Z_{56}=Z_{53}-\frac{Z_8Z_{54}}{\eta Z_2} \tag{A20}$$

$$Z_{57}=(\overline{R}_0+\eta+\zeta H_0)\left[\frac{1}{Z_3}(\overline{R}_0+\zeta Z_4)Z_1+Z_2\right] \quad ;$$

$$Z_{58}=\left(\frac{\overline{R}_0}{Z_3}+\frac{\zeta Z_4}{Z_3}\right)Z_2+Z_1 \tag{A21}$$

$$Z_{59}=\frac{\kappa}{Z_3}(\overline{R}_0Z_4+\zeta)+\zeta-1 \quad ; \quad \omega_1=\frac{1}{\overline{Q}_0}\left(Z_{57}+\frac{\overline{R}_0\overline{R}'Z_{48}}{Z_{56}}\right) \quad ;$$

$$\omega_2=Z_{58}+\frac{\overline{R}_0\overline{R}'Z_{49}}{Z_{56}} \tag{A22}$$

$$\omega_3=\frac{\overline{R}_0\overline{R}'Z_8}{Z_{37}\eta Z_2} \quad ; \quad \omega_4=-\frac{\overline{R}_0\overline{R}'}{Z_{56}} \quad ; \quad \omega_5=\frac{\overline{R}_0\overline{R}'Z_{50}}{Z_{56}}+Z_{59} \quad ;$$

$$\omega_6=-\frac{Z_{55}}{Z_{56}} \quad ; \quad \omega_7=\frac{Z_{55}Z_8}{\eta Z_{56}Z_2}-\frac{Z_6}{\eta Z_2} \tag{A23}$$

$$\omega_8=\frac{1}{\overline{Q}_0}\left(Z_{45}-\frac{Z_{55}Z_{48}}{Z_{56}}\right) \quad ; \quad \omega_9=Z_{46}-\frac{Z_{55}Z_{49}}{Z_{56}} \quad ;$$

$$\omega_{10}=Z_{47}-\frac{Z_{55}Z_{50}}{Z_{56}} \tag{A24}$$

$$\tau_1=\frac{Z_{48}}{\overline{Q}_0Z_{56}} \quad ; \quad \tau_2=\frac{Z_{49}}{Z_{56}} \quad ; \quad \tau_3=\frac{Z_8}{\eta Z_2Z_{56}} \quad ;$$

$$\tau_4=-\frac{1}{Z_{56}} \quad ; \quad \tau_5=\frac{Z_{50}}{Z_{56}} \tag{A25}$$

References

[1] Singh, S., and Blazek, K., 1974, ''Heat Transfer and Skin Formation in a Continuous Casting Mold as a Function of Steel Carbon Content,'' J. Metals, pp. 17–27.

[2] Cisse, J., Cole, G., and Bolling, G., 1971, ''Freezing Front Asymmetry During Ingot Solidification of Aluminum and Its Alloys,'' AFS Cast Metals. Res. J., **7**, pp. 158–161.

[3] Wray, P. J., 1977, ''Nonuniform Growth of a Plate Solidifying on a Chilled Surface,'' Presentation Notes, *Proceedings of the AIME Conference*, Atlanta, GA.

[4] Wray, P. J., 1981, ''Geometric Features of Chill-Cast Surfaces,'' Metall. Trans. B, **12B**, pp. 167–176.

[5] Sugitani, Y., Nakamura, M., Okuda, M., Kawasaki, M., and Miyahara, S., 1992, ''Control of Uneven Solidified Shell Formation of Hypo-peritectic Carbon Steels in Continuous Casting Mold,'' Trans. Iron Steel Inst. Jpn., **25**, pp. B–91.

[6] Collins, D. W. L., 1967, ''A New Explanation of the Surface Structure of DC Ingots,'' Metallurgica, **76**, pp. 137–144.

[7] Halliday, J. M. D., 1965, discussion one, *Iron and Steel Institute Special Report*, No. 89, p. 98.

[8] Richmond, O., and Huang, N. C., 1979, ''Interface Instability During Unidirectional Solidification of a Pure Metal,'' *Proc. Sixth Canadian Congress of Applied Mechanics*, National Research Council of Canada, Vancouver, pp. 453–454.

[9] Richmond, O., Hector, Jr., L. G., and Fridy, J. M., 1990, ''Growth Instability During Nonuniform Directional Solidification of Pure Metals'' ASME J. Appl. Mech., **57**, pp. 529–536.

[10] Li, N.-Y., and Barber, J. R., 1991, ''Thermoelastic Instability in Planar Solidification,'' Int. J. Mech. Sci., **33**, pp. 945–959.

[11] Hector, Jr., L. G., Li, N.-Y., and Barber, J. R., 1994, ''Strain Rate Relaxation Effect on Freezing Front Growth Instability During Planar Solidification of Pure Metals, Part 1: Uncoupled Theory,'' J. Thermal Stresses, **17**, pp. 619–646.

[12] Yigit, F., and Barber, J. R., 1992, ''Effect of Thermal Capacity on the Development of Sinusoidal Perturbation During the Unidirectional Solidification of Pure Metals,'' *Micro/Macro Scale Phenomena in Solidification*, ASME, New York, pp. 141–150.

[13] Mizikar, E. A., Wojcik, W. M., and Li, K., 1967, ''Method of Producing Steel Strip of Uniform Thickness by Direct Casting,'' U.S. letters patent #3,345,738.

[14] Morales, A., Glicksman, M. E., and Biloni, H., 1977, ''Influence of Mould Wall Microgeometry on Casting Structure,'' *Proc. Int. Conf. on Solidification*, Sheffield Metallurgical Eng. Assn., Univ. Sheffield, and The Metals Society, Sheffield, U.K. pp. 184–192.

[15] Buxmann, K., Boliger, M., and Gyongyos, I., 1981, ''Mould With Roughened Surface for Casting Metals,'' U.S. letters patent #4,250,950.

[16] Laki, R. S., Beech, J., and Davies, G. J., 1985, ''Surface Structures of Chill and Continuously Cast Stainless Steels,'' Ironmaking Steelmaking, **12**, pp. 233–241.

[17] Gaspar, T. A., 1987, ''Textured Substrate and Method for the Direct, Continuous Casting of Metal Sheet Exhibiting Improved Uniformity,'' U.S. letters patent #4,705,095.

[18] Ostlund, A., and West, R., 1988, ''Influence of Wheel Surface Roughness on Microstructure and Heat Transfer in Meltspun $Fe_{0.79}Si_{0.03}C_{0.04}B_{0.14}$,'' Int. J. Rapid Solidif., **3**, pp. 177–188.

[19] Bartlett, E., Maringer, R., and Rayment, J., 1989, ''Direct Strip Casting on Grooved Wheels,'' U.S. letters patent #4,865,117.

[20] Murakami, H., Suzuki, M., Kitagawa, T., and Miyahara, S., 1992, ''Control of Uneven Solidified Shell Formation of Hypo-peritectic Carbon Steels in Continuous Casting Mold,'' Trans. Iron Steel Inst. Jpn., **78**, pp. 105–112.

[21] Haga, T., and Motomura, M., 1994, ''Effect of Polishing Condition on the Roll of the Surface of Foils of Pure Aluminum and Al-Si Alloy Manufactured by Single Roll Rapid Solidification,'' J. Jpn. Inst. Light Metals, **44**, pp. 22–27.

[22] Hector, Jr., L. G., Howarth, J. A., Richmond, O., and Kim, W.-S., 2000, ''Mold Surface Wavelength Effect on Gap Nucleation in Solidification,'' ASME J. Appl. Mech., **67**, pp. 155–164.

[23] Comninou, M., and Dundurs, J., 1980, ''On the Lack of Uniqueness in Heat Conduction Through a Solid to Solid Contact,'' ASME J. Heat Transfer, **102**, pp. 319–323.

[24] Zhang, R. G., and Barber, J. R., 1990, ''Effect of Material Properties on the Stability of Static Thermoelastic Contact,'' ASME J. Appl. Mech., **57**, pp. 365–369.

[25] Weirauch, Jr., D. A., and Giron, A., 1998, ''The Early Stages of Aluminum Solidification in the Presence of a Moving Meniscus,'' *Proceedings on the Integration of Material, Process and Product Design—A Conference dedicated to the 70th birthday of Owen Richmond*, A. A. Balkema, Rotterdam, Netherlands, pp. 183–191.

[26] Yigit, F., 1998, ''Effect of Mold Properties on Thermoelastic Instability in Unidirectional Planar Solidification,'' J. Thermal Stresses, **21**, pp. 55–81.

[27] Westegraard, H. M., 1964, *Theory of Elasticity and Plasticity*, Dover, New York.

[28] Timoshenko, S. P., and Goodier, J. N., 1970, *Theory of Elasticity*, 3rd Ed., McGraw-Hill, New York.

[29] Byrne, G. D., and Hindmarsh, A. C., 1975, ''A Polyalgorithm for the Numerical Solution of Ordinary Differential Equations,'' ACM Trans. Math. Softw., **1**, pp. 71–96.

Critical Wavelengths for Gap Nucleation in Solidification—Part II: Results for Selected Mold-Shell Material Combinations

F. Yigit
Department of Mechanical Engineering,
King Saud University,
P.O. Box 800,
Riyadh 11421, Saudi Arabia

L. G. Hector, Jr.
Surface Science Division,
Alcoa Technical Center,
Alcoa Center, PA 15069

In this second part, we examine the contact pressure ratio, P^{tr}, at the lowest points of the upper mold surface troughs in a directional solidification process using the theoretical methodology developed in Part I. Since there is ample experimental evidence that the mold surface topography affects gap nucleation at the mold-shell interface and the uniformity of the shell, we explore how the wavelength of the upper mold surface impacts the evolution of P^{tr} for specific material combinations and process parameters. For this purpose, the mold-shell materials are assumed to be combinations of four pure materials, viz., aluminum, copper, iron and lead: these materials offer a wide range of thermal and mechanical properties. Critical wavelengths, for which P^{tr} and its time derivative simultaneously equal zero, are predicted for all mold-shell material combinations. The theoretical model also predicts the existence of wavelength bands which are delimited by upper and lower critical wavelengths. All wavelengths that lie within the bands lead to gap nucleation, whereas all wavelengths that lie outside of the bands do not. The effects of distortivity ratio, which is a measure of the extent to which the mold-shell interface deforms under a given thermal loading, and selected process parameters (such as the mean mold thickness, contact resistance, and pressure) on bandwidth size, are considered in detail. Extensions of the present work to more sophisticated models that might lead to rudimentary mold topography design criteria are considered. [S0021-8936(00)03301-8]

1 Introduction

In the companion paper, a theoretical methodology was developed for an idealized solidification process in which a quiescent bath of a pure molten metal solidifies on a deformable mold of finite thickness. The mold was assumed to be fabricated from a pure metal. In order to examine a possible wavelength effect on the gap nucleation process at the mold-shell interface, the mold surfaces were assumed to follow a sinusoidal lay of the same wavelength, but with differing amplitudes. This assumption, although idealized, follows the spirit of ground surface finishes used in practice and unidirectional groove topographies tested in the experimental literature. Two coupled differential equations were derived for the thickness perturbation in the shell and a function that represents residual stress. A numerical solution procedure was developed from which the time variation of the contact pressure perturbation at the crests of the mold surface could be obtained. A method for solving the coupled differential equations via a series solution was also developed, and a solution for short times and very thin molds was derived. It was shown that this solution reduced to the rigid mold solution: This provided the confidence needed to proceed with the numerical solution of the considerably more complicated deformable mold problem. The series solution also implied that thermomechanical coupling along the mold-shell interface becomes more significant at later stages of solidification (and hence does not play a prominent role in the process during the earliest stages of solidification). A criterion for gap nucleation at the lowest points of the troughs in the mold surface was presented in anticipation of our examination of selected mold-shell material combinations in this second part.

Motivation for the theoretical methodology presented in Part I, and the associated predictions we shall examine in the present paper, was largely provided by the experimental literature cited in Part I. With respect to the present paper, the most important work on the mold topography wavelength effect in solidification is that of Murakami et al. [1], and their results deserve further commentary. Following Singh and Blazek [2], who noticed uneven shell formation during continuous casting of iron-carbon alloys, Murakami et al. [1] conducted a series of immersion (or dip) tests in which water-cooled copper plates, with a (presumably) smooth surface finish, were immersed in a bath of molten steel with a specified carbon concentration over a controlled time period. They found that a 0.10–0.18wt percent C alloy, or hypoperitectic steel, exhibited prominent thickness nonuniformities on the molten steel side of the ingots: The authors coined the term ''tortoise shell patterns,'' since they resembled the shell of a tortoise. These patterns, which are the ''humps'' discussed in Part I of the present work ([3]), formed during the initial stages of solidification. Irregular distortion of the shell occurred during the δ/γ transformation that is characteristic of hypoperitectic steels. The distortion occurred at regular intervals due to the hydrostatic pressure of the residual molten steel. Gap nucleation resulted leading to continued growth of the tortoise shells during the early stages of solidification. It was found that the wavelength of the tortoise shells exhibited a linear deviation from the gap wavelength at the mold-shell interface (about 10 mm) since the tortoise shells increased in size with solidification time.

Contributed by the Applied Mechanics Division of THE AMERICAN SOCIETY OF MECHANICAL ENGINEERS for publication in the JOURNAL OF APPLIED MECHANICS. Manuscript received by the ASME Applied Mechanics Division, Mar. 9, 1999; final revision, Sept. 30, 1999. Associate Technical Editor: J. R. Barber. Discussion on the paper should be addressed to the Technical Editor, Professor Lewis T. Wheeler, Department of Mechanical Engineering, University of Houston, Houston, TX 77204-4792, and will be accepted until four months after final publication of the paper itself in the JOURNAL OF APPLIED MECHANICS.

Murakami et al. [1] proposed that periodic grooves in the mold surface, which led to gaps of a controlled size along the mold-shell interface due to imperfect wetting of the molten metal, resulted in a number of important improvements. Perhaps the most significant improvements were more uniform contact along the mold-shell interface, and a reduction in crack nucleation in the ingot due to slower, but more uniform heat extraction. To test this hypothesis, the immersion tests were repeated for hypopertictic steels using casting molds with machined grooves. A key parameter that was investigated was the groove pitch or wavelength. In all tests, the depth or amplitude of the topographies was held fixed at 0.5 mm. Both longitudinal and lattice-type grooves were found to reduce the size of the tortoise shell patterns, with the lattice pattern generating a more uniform shell thickness than the longitudinal pattern. By conducting a series of experiments wherein the mold wavelength was varied up to 30 mm (holding all other process parameters constant for each experiment), Murakami et al. found that a 5 mm wavelength led to the most uniform growth of the shell, with a near order-of-magnitude improvement in the shell thickness uniformity compared with corresponding results using wavelengths of 0.1 mm and 30 mm. The authors observed that this corresponded to one-half the wavelength of the tortoise shells associated with the most extreme case of irregular shell growth over the same time interval. This behavior suggested the possibility of a wavelength selection process wherein the system ''picked-off'' a mold surface wavelength or band of wavelengths such that the shell grew with greater uniformity. Experiments similar to those of Murakami et al., which revealed analogous behavior for aluminum alloys, were reported by Weirauch and Giron [4].

Wavelength selection processes are often associated with instabilities commonly observed in fluids and solids: A disturbance in the boundary conditions leads to a specific size or extent of a feature that is characteristic of the affected system. For example, the familiar Bénard convection cells that result from buoyancy-driven instabilities exhibit a periodicity due to a selection process ([5]). Displaced ridge waviness during single asperity plowing of metal alloys ([6]), chatter in mechanical contacts ([7]), bubble nucleation in gummed wine labels ([8]), and buckling of structural members, such as plates and shells ([9]), all involve a wavelength selection process. Based upon the existence of wavelength selection processes in these and other physical systems, Richmond [10] proposed the existence of critical mold topography wavelengths for gap nucleation in solidification processes. According to Richmond's definition, the wavelength of a heat extraction profile is ''critical'' if it leads to zero values of the mold-shell contact pressure and its time derivative at those regions of the mold-shell interface where heat extraction is least. For a smooth mold surface (or at least one with no prominent periodicity), the perturbations in heat extraction result from stochastic variations in the mold-shell interface heat flux due to a variety of process-related conditions and material properties/metallurgical transformations. An equally random arrangement of thickness irregularities in the shell results during the early stages of solidification. As the shell thickens, however, the boundary conditions at the mold-shell interface have a diminishing impact on the growth of irregularities at the freezing front. In the idealized case of a mold surface with a purely sinusoidal topography (for example), the controlling factor is the topography geometry, since this creates a spatial perturbation in the heat extraction profile. A critical wavelength leads to the simultaneous occurrence of zero values of the mold-shell contact pressure and its time derivative at the lowest points of the mold surface troughs. Hence, a wavelength is critical if

$$P^{tr} = \frac{dP^{tr}}{dt} = 0 \tag{1}$$

where P^{tr} is the contact pressure at the lowest points of the troughs. At the same time, the contact pressure increases at the highest points of the surface crests. The mismatch in contact pressure can establish the right conditions for the onset of irregular growth, since heat extraction is diminished at the thinnest sections of the shell (i.e., directly above the lowest points of the troughs), while heat extraction beneath the thickest sections of the shell (i.e., directly above the highest points of the crests) is improved due to improved contact. Richmond [10] further proposed that quantitative criteria are needed for the selection of wavelengths that minimize irregular shell growth by avoiding those wavelengths deemed critical, according to his definition. Such criteria will allow casting process engineers to design mold surfaces in much the same way that optical engineers design antireflection coatings (for example). At the present time, no criteria of this type are available for even the most rudimentary casting process.

It is the purpose of the present paper to examine the mold-shell contact pressure (as predicted by the theoretical framework in Part I) and what it infers about gap nucleation along the mold-shell interface. We shall avoid the complicated phenomena associated with mold movement relative to the mold metal, imperfect wetting of the molten metal, and shell deformation due to metallurgical transformation (all of which were part of the Murakami et al. [1] experiments): These and related phenomena will ultimately have to be incorporated into future models in order to obtain a better grasp on the reality of those solidification systems where they are important. We wish to specifically focus on the mold-shell material combination influence on the gap nucleation process at the mold-shell interface. For this purpose, the mold and shell materials are assumed to be one of four pure metals. We calculate the contact pressure ratio, P^{tr}, at the lowest points of the troughs in the mold surface and examine the impact of the mold conductivity and upper mold surface wavelength on P^{tr} for an aluminum shell solidifying on a mold consisting of one of the remaining three materials. We also examine the role that distortivity plays in the gap nucleation process since this parameter is responsible for much of the rich behavior of thermoelastic contact mechanics ([11]). Critical wavelengths are sought following the definition proposed by Richmond [10]. Conditions for the existence of wavelength bands that are bounded by two critical wavelengths (one being larger than the other) are identified for a given mold-shell material combination. The bands are shown to consist of a continuous spectrum of wavelengths that promote gap nucleation. Wavelengths that lie outside of the bands do not lead to gap nucleation.

The impact of selected process parameters on the width of the bands is explored through variation of the mean pressure of the molten metal, the mean mold thickness, the mean contact resistance, the amplitude of the upper surface of the mold (in contact with the shell), and the ratio of the amplitudes of the mold surfaces for a fixed wavelength. Finally, extensions to the present theoretical model that will be necessary in the course of developing quantitative design criteria for casting mold surface topographies are discussed.

2 Material Properties and Process Parameters

We wish to examine the evolution of P^{tr} (defined by Eq. (135) of Part I) for systems where the mold and shell materials are combinations pure aluminum, iron, copper, and lead. The materials properties used in the calculations are listed in Table 1 along with pertinent references to those properties. Note that the properties for pure aluminum are taken from Richmond et al. [12]. The symbols T_f, K, ρ, L, E, by α, and ν denote the fusion temperature, thermal conductivity, density, latent heat, Young's modulus, thermal expansion coefficient, and Poisson's ratio, respectively. Although it is assumed that each property is a temperature-independent constant, most of the reported values were measured close to the melting temperature of each material. For more information on the temperature-dependence of these materials, the reader is referred to Heinlein et al. [13].

The quantities represented in each of the following figures were obtained through conversion to dimensional forms via the dimensionless quantities defined in Eq. (120) of Part I. As discussed in

Table 1 Material properties for pure aluminum, iron, copper, and lead at the fusion temperature

	Material						
	Al	Fe		Cu		Pb	
Property	Value	Value	Fe Reference	Value	Cu Reference	Value	Pb Reference
T_f (°C)	660	1536	[14]	1084	Same as Fe	327.5	Same as Fe
$K\left(\frac{\mathrm{W}}{\mathrm{m}\cdot°\mathrm{C}}\right)$	229.4	36.2	[15]	345.4	Same as Fe	32.7	Same as Fe
$\rho\left(\frac{\mathrm{kg}}{\mathrm{m}^3}\right)$	2650	7265	[16]	7938	[17]	10665	[18]
$L\left(10^5\frac{\mathrm{J}}{\mathrm{kg}}\right)$	3.9	2.7	[19]	2.0	Same as Fe	0.23	Same as Fe
E (10^{10} Pa)	6.0	14.4	[20]	6.4	[21]	0.852	[22]
$\alpha(10^{-6}\,°\mathrm{C}^{-1})$	37.8	23.4	[23]	26	Same as Fe	37.1	Same as Fe
ν	0.33	0.33	[20]	0.37	[24]	0.35	Assumed

Part I, the coupling effect is likely to play a more prominent role at longer times in solidification processes wherein gap nucleation occurs at much longer times (due, for example, to high values of the mean contact pressure from the molten metal). Hence, in all cases, we chose $R' = -10^{-12}\,\mathrm{m}^2\,\mathrm{sec°C/J\cdot Pa}$. Although this implies that the thermal and mechanical problems are very weakly coupled along the mold-shell interface, it allowed us to satisfy the restriction imposed on the contact pressure via Eq. (136) of Part I provided that we limited the sizes of P_0 and R_0. Unless otherwise specified, $a_1 = 1.0\,\mu$m, $\kappa = 0.1$, and $R_0 = 10^{-5}\,\mathrm{m}^2\,\mathrm{sec°C/J}$. Justification behind fixing the amplitude while varying the wavelength is discussed in Hector et al. [25]. All wavelength selections satisfied the small aspect ratio restriction from the perturbation analysis, i.e., $\epsilon \ll 1$.

Each of the following figures was generated through numerical solution of the coupled differential equations (Eqs. (121) and (122)) in Part I. The results from these calculations were used to generate P^{tr} for a variety of process conditions and mold-shell material combinations.

3 The Mold Material Conductivity Effect

Figure 1 examines the evolution of P^{tr} during solidification of a pure aluminum shell. The four curves correspond to the case of a rigid mold, a copper mold, an iron mold, and a lead mold. Note that the thickness of each deformable mold was $h_0 = 0.5$ mm. The normal pressure, P_0, was held at 10,000 Pa, the wavelength of each mold surface was $\lambda = 2.0$ mm and the ratio of mold surface amplitudes was $\kappa = 0.1$.

The contact pressure ratio drops to zero at the fastest rate for the rigid mold case, with gap nucleation occurring at 0.73×10^{-3} sec. Note that this curve is exactly that predicted by the rigid mold theory of Hector et al. [25]. Gap nucleation on the copper mold occurs at 0.90×10^{-3} sec; gap nucleation on the iron mold occurs at about 2.74×10^{-3} sec; gap nucleation on the lead mold occurs at about 3.00×10^{-3} sec. The contact pressure perturbation, P_1, at the highest points of the crests increases where heat extraction is the greatest. An increase in P_1 at the crests implies a corresponding decrease in P^{tr} at the lowest points of the troughs (due to a change in sign associated with $P_1 \cos(mx)$ in Eq. (51) of Part I). The behavior predicted by these curves is consistent with that first observed by Richmond et al. [12] who used a beam theory model to calculate the contact pressure evolution of a pure metal shell solidifying on a planar, rigid mold surface with a spatially periodic cooling profile. The contact pressure derived in this earlier work was limited to a two term series expansion, and hence did not capture all of the physics incorporated in the present model.

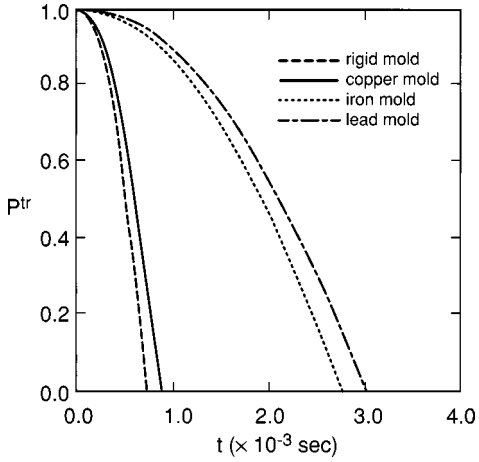

Fig. 1 The mold conductivity effect as shown through P^{tr} versus t ($\times 10^{-3}$ sec) for an aluminum shell solidifying on a mold with $h_0 = 0.5$ mm and $\lambda = 2.0$ mm

The ordering of the four curves in Fig. 1 is dictated by the mold thermal conductivity. Gap nucleation is fastest for the rigid mold since it is perfectly conducting (i.e., has an infinite thermal conductivity). Of the three pure mold materials considered in Fig. 1, gap nucleation is fastest for the copper mold since it has the highest thermal conductivity (i.e., it is nearest to a thermomechanically ''rigid'' material). Gaps take a longer time to nucleate on the iron and lead molds. Note that gap nucleation times are closer for these latter two mold materials since their conductivities are very similar (see Table 1). Hence, the higher the mold thermal conductivity, the higher the heat extraction, and the quicker gaps will nucleate along the mold-shell interface (for a given set of process parameters).

4 The Mold Surface Wavelength Effect

Solidification process conditions are not always conducive to gap nucleation. For example, Fig. 2 shows the evolution of P^{tr} for solidification of a pure aluminum shell with the same process/mold materials considered in Fig. 1, except that the wavelength of both mold surfaces has been increased to $\lambda = 40.0$ mm. Consider first the P^{tr} versus t curves corresponding to the iron and lead molds. These achieve minimum values of 0.9 and 0.85, respectively (i.e., without falling to zero) and then turn around and in-

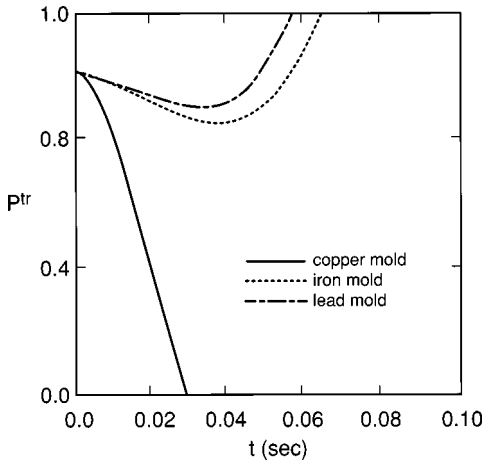

Fig. 2 The mold conductivity effect as shown through P^{tr} versus t (sec) for an aluminum shell solidifying on a mold with $h_0 = 0.5$ mm and $\lambda = 40.0$ mm

crease. Hence, gaps do not nucleate for these mold-shell material combinations. Beyond a certain time, the evolving distortion of the shell acts to increase P^{tr} at the lowest points of the troughs, thereby improving heat extraction in those regions. On the other hand, the contact pressure ratio at the highest points of the crests tends to decrease to zero resulting in gap nucleation. The shell freezing front is more likely to grow with a planar, rather than undulatory geometry. The obvious catalyst for this behavior is the change in wavelength from $\lambda = 2.0$ mm to $\lambda = 40.0$ mm between Figs. 1 and 2 (since we have fixed all other process parameters).

The reason why the contact pressure at the troughs turns around for these mold materials is that the larger wavelength causes less heat to flow through interface. We see an indication of this effect in the leading order term in the series expression for the heat flux perturbation, Q_1, at the mold-shell interface (which is valid only for very short times, but not subject to any limitation on the size of h_0):

$$Q_1 = \frac{4\pi^2 a_1 K^c T_f}{\lambda^2 \left(R_0 + \dfrac{h_0}{K^d} \right)^4} \left(\frac{T_f t}{\rho^c L^c} \right)^2 . \tag{2}$$

Equation (2) reveals that a larger wavelength acts to diminish the heat flux right from the start of solidification. The size of this effect is also controlled by the sum of the mean mold-shell interface resistance, R_0, and the resistance due to the mold itself, h_0/K^d. However, it is not until later in the process that this effect predominates to the point where the relaxation of the contact surface (due to diminished cooling) under the influence of the contact pressure acts to counter the trend that is promoted by the rigid mold effect, which is always toward gap nucleation.

The P^{tr} curves corresponding to the iron and lead molds in Fig. 2 therefore depict two competing effects for different mold materials, those being the conductivity effect and the wavelength effect. When the conductivities of the shell and mold materials are substantially different, an increase in λ causes a more rapid turnaround in P^{tr}. On the other hand, the behavior of a system in which the conductivities of the shell and the mold materials are similar in magnitude is quite different. In these situations, the conductivity effect predominates to longer solidification times, beyond which the trend toward gap nucleation can be arrested with a longer wavelength through a reduction in heat extraction.

Unlike that for the iron or lead molds, a gap nucleates at 2.9×10^{-2} sec for the aluminum-copper combination (solid curve in Fig. 2). As previously discussed, the copper mold is nearest to being thermomechanically rigid and an increase in the mold surface wavelength merely serves to delay, rather than prevent gap nucleation.

Note that the ordering of the curves in Fig. 2 follows that in Fig. 1: This is dictated primarily by the mold conductivity effect.

5 The Distortivity Effect

A more physically meaningful way to understand the shapes of the three P^{tr} curves in Fig. 2 is with the distortivity, δ ([26]). This is defined as

$$\delta = \frac{\alpha(1+\nu)}{K} . \tag{3}$$

The distortivity of a boundary through which heat flows is a measure of the extent to which that boundary deforms when a heat flux q_n pass through it. When heat flows through the interface between two different materials, then the ratio of the distortivities of the two materials is important for determining the extent to which the two materials comprising the interface deform relative to one another under the imposed thermal load. For the aluminum-lead and aluminum-iron shell-mold combinations, $\delta^d/\delta^c = 6.989$ and 3.923, respectively, and these mold materials tend to be more compliant to the evolving distortion of the aluminum shell. The tendency toward gap nucleation is thus dramatically reduced at much earlier stages in solidification. In the case of the aluminum-copper system, $\delta^d/\delta^c = 0.471$. Hence, the copper mold tends to be less compliant to the evolving distortion in the aluminum shell. The evolution of P^{tr} for this case reflects behavior that is similar to that exhibited by a rigid mold.

6 Critical Wavelengths for Gap Nucleation

Figures 3–5 show the evolution of P^{tr} for an aluminum shell solidifying on an iron mold for selected process parameters. In Fig. 3, the mean thickness of the mold is $h_0 = 0.5$ mm and the mean pressure is $P_0 = 10{,}000$ Pa. Six curves, corresponding to wavelengths of 10.0 mm, 15.0 mm, 16.6 mm, 17.0 mm, 20.0 mm, and 30.0 mm, are shown. Over the 0.04 sec time frame considered in Fig. 3, P^{tr} due to the 30.0 mm wavelength exhibits the smallest deviation from $P^{tr} = 1$. As the wavelengths are decreased, P^{tr} decreases more rapidly at the earlier stages of solidification. This is evident from a comparison of the curves corresponding to $\lambda = 20.0$ mm and $\lambda = 30.0$ mm (for example). Some insight into the wavelength effect at these very short times can be obtained

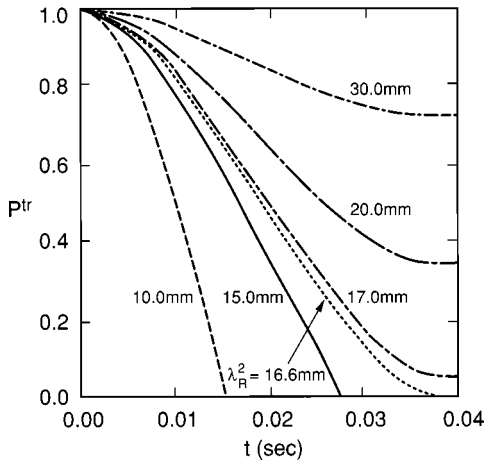

Fig. 3 P^{tr} versus t (sec) variation for an aluminum shell solidifying on an iron mold showing a critical wavelength at $\lambda_R^2 = 16.6$ mm. $h_0 = 0.5$ mm, $P_0 = 10{,}000$ Pa.

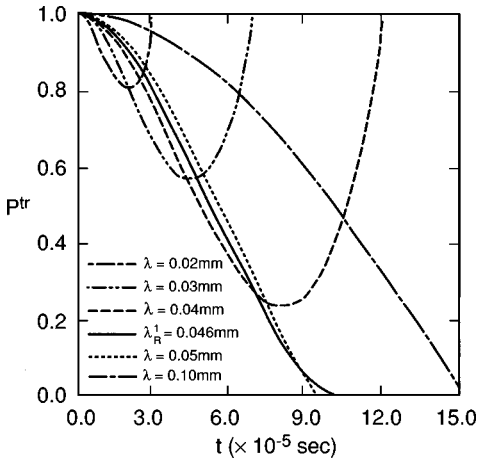

Fig. 4 P^{tr} versus t ($\times 10^{-5}$ sec) variation for an aluminum shell solidifying on an iron mold showing a critical wavelength at $\lambda_R^1 = 0.046$ mm. $h_0 = 0.5$ mm, $P_0 = 10{,}000$ Pa.

through examination of P^{tr} described with only the first term in the series solution, Eq. (133), of Part 1 (since this is not restricted by the size of h_0). In dimensional form, this is

$$P^{tr} = 1 - \frac{E^c \alpha^c K^c T_f \pi a_1}{\lambda^2 P_0 (1-\nu^c)\left(R_0 + \dfrac{h_0}{K^d}\right)^3}\left(\frac{T_f t}{\rho^c L^c}\right)^2. \tag{4}$$

Equation (4) is only valid for $t \ll 1$. Since λ appears in the denominator, a larger value of λ leads to a smaller value of the contact pressure perturbation, P_1 (which is the second term in Eq. (4)), over the earliest solidification times, and this causes the apparent ordering of the P^{tr} curves shown in Fig. 3 (assuming all other parameters are held constant). Note that this trend is enhanced through an increase in h_0/K^d, which represents the mean resistance of the mold, and/or R_0, which is the mean resistance of the mold-shell interface. The time-varying term is proportional to the resistance of the growing shell. For fixed λ, R_0, and h_0, the total contact pressure decreases, since P_1 increases, as the shell thickens. Figure 3 shows that there is at least one wavelength, this being at 16.6 mm, and which we denote as λ_R^2, that meets the

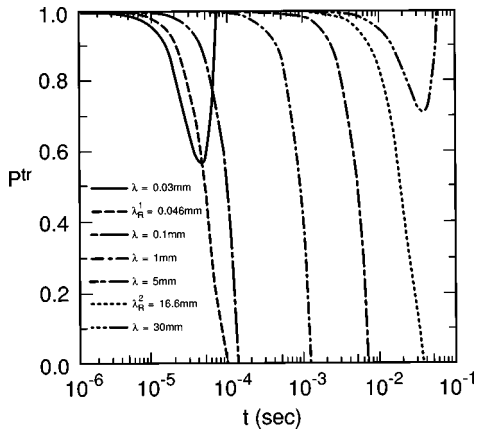

Fig. 5 P^{tr} versus t (sec) variation for an aluminum shell solidifying on an iron mold showing critical wavelengths at $\lambda_R^1 = 0.046$ mm and $\lambda_R^2 = 16.6$ mm with gap nucleation times of $t_R^1 = 1.1\times 10^{-3}$ sec and $t_R^2 = 38.5\times 10^{-3}$ sec, respectively. $h_0 = 0.5$ mm, $P_0 = 10{,}000$ Pa.

critical wavelength criteria in Eq. (1). Gap nucleation occurs at $t_R^2 = 3.80\times 10^{-2}$ sec. Wavelengths less than λ_R^2 lead to gap nucleation. For the 10.0 mm and 15.0 mm wavelengths, gap nucleation occurs at 1.56×10^{-2} sec and 2.78×10^{-2} sec, respectively. However, wavelengths that are larger than λ_R^2 never lead to gap nucleation over the time range in Fig. 3, since P^{tr} never touches the time axis. For these larger wavelengths, P^{tr} increases at the lowest points of the upper mold surface troughs, while simultaneously decreasing at the highest points of the upper surface crests.

Figure 4 examines the evolution of P^{tr} for the system considered in Fig. 3 due to wavelengths that are two to three orders-of-magnitude less than those in Fig. 3. Note that the time scale in Fig. 4 has been decreased by three orders-of-magnitude. The trend established over the short times and described by Eq. (4) changes such that the curves corresponding to the shortest three wavelengths (i.e., 0.02 mm, 0.03 mm, and 0.04 mm) achieve a minimum value (without reaching zero) at which point they turn around toward increasing values of P^{tr}. The curves corresponding to the longer wavelengths, i.e., 0.05 mm, 0.10 mm, however, fall to zero at $t = 0.95\times 10^{-4}$ sec and $t = 1.50\times 10^{-4}$ sec, respectively, and hence gaps nucleate at the lowest points of the troughs. More importantly, there is at least one more wavelength (in addition to the 16.6 mm wavelength in Fig. 3), which meets the critical wavelength criteria in Eq. (1). This wavelength is $\lambda_R^1 = 0.046$ mm, and the corresponding gap nucleation time is $t_R^1 = 1.1\times 10^{-4}$ sec. Wavelengths in excess of λ_R^1 (at least up to 0.10 mm) lead to gap nucleation: However, wavelengths that are less that λ_R^1 never lead to gap nucleation.

Figure 5 combines the P^{tr} curves separately considered in Figs. 3 and 4. In order to show all curves in one plot, the time axis has been converted to a logarithmic scale. Two critical wavelengths appear over the time range of interest, and we refer to these as λ_R^1 (the smaller critical wavelength) and λ_R^2 (the larger critical wavelength). The three wavelengths that lie between $\lambda_R^1 = 0.046$ mm and $\lambda_R^2 = 16.6$ mm, i.e., $\lambda = 0.1$ mm, 1.0 mm, and 5.0 mm, each lead to gap nucleation since they satisfy Eq. (2). Gap nucleation for the 1.0 mm and 5.0 mm wavelengths (which have been added in Fig. 5 for the sake of illustration) occurs at 1.4×10^{-3} sec and 8.0×10^{-3} sec, respectively. Hence, the two critical wavelengths delimit a band or continuous spectrum of wavelengths that lead to gap nucleation. We define the bandwidth, $\Delta\lambda_R$, thus

$$\Delta\lambda_R = \lambda_R^2 - \lambda_R^1. \tag{5}$$

For the situation considered in Fig. 5, $\Delta\lambda_R = 16.55$ mm. Gap nucleation does not occur at the lowest points of the upper mold surface troughs for all wavelengths that lie outside of this band. For these situations, shell growth is likely to be planar, rather than undulatory. The bands are indicative of the interacting distortions of the mold and shell materials along the mold-shell interface: This interaction is mitigated by the mold surface wavelength. Note that process conditions and mold-shell material combinations should be chosen so as to minimize or even eliminate $\Delta\lambda_R$.

The behavior of P^{tr} depicted for $\lambda_R^1 \leqslant \lambda \leqslant \lambda_R^2$ and $\lambda > \lambda_R^2$ has been discussed relative to Figs. 3 and 5, respectively. At this point, some additional comments for situations where $\lambda < \lambda_R^1$ (considered, for example, in Fig. 4) are warranted. For these shortest wavelengths, the stabilizing effect of mold-shell interface relaxation overcomes the destabilizing effect of a rapid cooling rate after an initial period of time. The shell quickly deforms to conform to the mold. Therefore, P^{tr} decreases quickly, due to higher cooling, only to achieve a minimum value at the point where the effect of interface relaxation starts to be pronounced. These effects become less balanced as $\lambda \to \lambda_R^1$, since shell distortion is not as quick due to lower heat extraction.

Figure 6 considers the evolution of P^{tr} due to a copper shell solidifying on an aluminum mold under the same process condi-

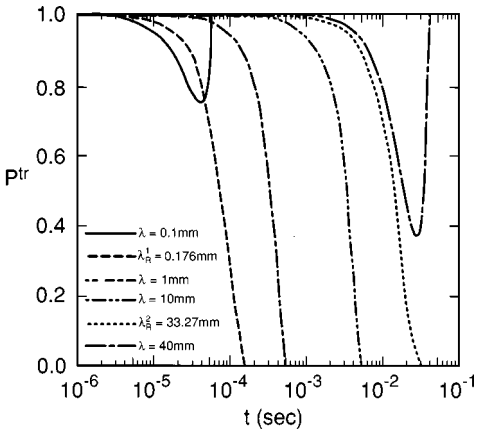

Fig. 6 P^{tr} versus t (sec) variation for a copper shell solidifying on an aluminum mold showing critical wavelengths at $\lambda_R^1 = 0.176$ mm and $\lambda_R^2 = 33.27$ mm with gap nucleation times of $t_R^1 = 0.165 \times 10^{-3}$ sec and $t_R^2 = 31.50 \times 10^{-3}$ sec, respectively. $h_0 = 0.5$ mm, $P_0 = 10{,}000$ Pa.

tions considered in Figs. 3–5. Two critical wavelengths are shown at $\lambda_R^1 = 0.18$ mm and $\lambda_R^2 = 33.3$ mm, with gaps nucleating at $t_R^1 = 1.65 \times 10^{-4}$ sec and $t_R^2 = 3.15 \times 10^{-2}$ sec, respectively. The bandwidth for the copper-aluminum system is $\Delta\lambda_R = 33.12$ mm which is twice as large as the 16.55 mm bandwidth predicted for an aluminum shell solidifying on an iron mold in Fig. 5. Hence, this system is more restrictive as to which wavelengths can be chosen to avoid gap nucleation. However, the initial gap nucleation time (i.e., t_R^1) for the copper-aluminum and aluminum-iron systems is essentially the same. The two wavelengths within $\lambda_R^1 \leqslant \lambda \leqslant \lambda_R^2$, viz., 1.0 mm and 10.0 mm lead to gap nucleation at 5.0×10^{-4} sec and 5.52×10^{-3} sec, respectively. For the cases where heat extraction is either very rapid or very slow, the evolving distortion of the mold-shell interface prevents gap nucleation. For intermediate heat extraction levels, gaps nucleate since the distortion of the interface cannot keep pace with the deformation of the shell.

With respect to Figs. 5 and 6, it is worth noting that the smaller critical wavelength approaches zero and the larger critical wavelength approaches infinity as $1/K^d$, κ and h_0 simultaneously go to zero. This observation enables us to conclude that the critical wavelengths corresponding to the limiting case of a rigid mold are $\lambda_R^1 = 0$ and $\lambda_R^2 = \infty$. Hence, gap nucleation *always* occurs on a rigid mold: This was one of the major conclusions in the work of Hector et al. [25] for solidification on a rigid, perfectly conducting mold.

Figure 7 summarizes the critical wavelength concept introduced in Figs. 3–6. Figure 7(*a*) shows the mold-shell system prior to gap nucleation after the formation of a thin metal shell but prior to gap nucleation. Figures 7(*b*) and 7(*c*) show the two locations where gap nucleation can occur along the upper mold surface at later times in the process. Note that we represent each gap with a slight separation between the shell and the mold in each of these figures. This is for the purpose of illustration only, since the present theory is valid only to the point where the contact pressure falls to zero. Figure 7(*b*) shows the case where gaps nucleate at the highest points of the upper mold surface crests. The wavelengths that lead to this situation are restricted to $\lambda < \lambda_R^1$ and $\lambda > \lambda_R^2$. The anticipated growth of the shell freezing front (barring competing material and process-related factors) in Fig. 7(*c*) is planar. This is the more desirable situation from a metallurgical standpoint. Figure 7(*c*) shows the case where gaps nucleate at the lowest points of the troughs in the upper mold surface. The wavelengths that lead to this situation are restricted to $\lambda_R^1 \leqslant \lambda \leqslant \lambda_R^2$, and hence lie in a band denoted by $\Delta\lambda_R$. The shell freezing front is likely to exhibit an undulatory morphology which is greatly in excess of the dendritic morphology (again, barring competing material and process-related factors). This situation should be avoided by careful choice of the process parameters and mold-shell material combinations. As a final observation about Fig. 7, we note that the present theory always predicts that gaps will nucleate at points corresponding to extrema in the curvature of a sinusoidal mold surface: We have been referring to these points as the highest and lowest points of the crests and troughs, respectively. While this may be true for a purely sinusoidal surface, it may not apply to nonperiodic surfaces.

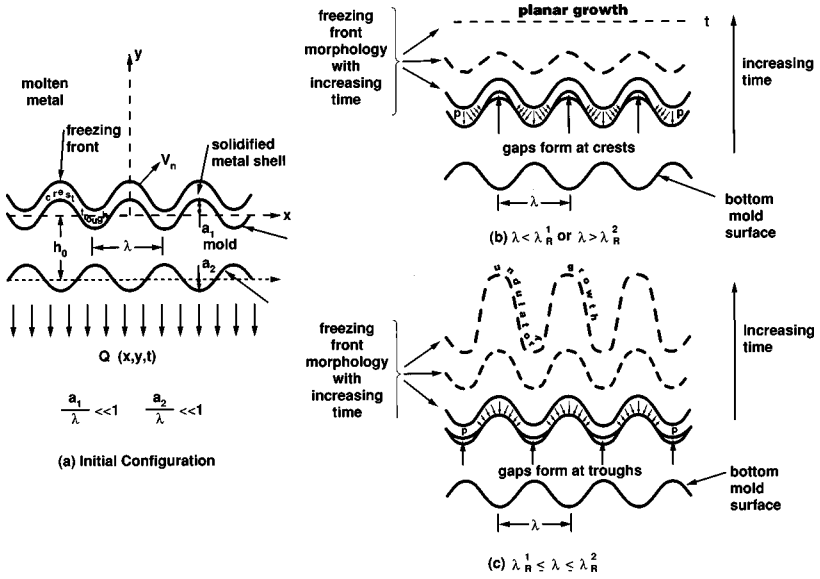

Fig. 7 Critical wavelength effect on position of gap nucleation along the mold-shell interface

7 Distortivity Ratio Effect on Bandwidth

Zhang and Barber [27] showed that quantitatively distinct kinds of thermoelastic behavior are obtained for the contact of two half-planes, depending on the relative values of the distortivity ratios. The finite thickness of the mold and moving solid/liquid interface of the solidification problem can be expected to modify this behavior, but the results they found enable us to characterize the behavior of this more complex system on the basis of distortivity ratios. When $\delta^d/\delta^c<1$ (note that δ^d is the mold distortivity, and δ^c is the shell distortivity), the mold material has a smaller distortivity than the shell material: heat flow is directed into the less distortive material due to cooling of the lower surface of the mold. Alternatively, when $\delta^d/\delta^c>1$, then the mold material distortivity is larger than that of the shell material: Heat flow is directed into the more distortive material. A comparison of the distortivities predicted with the material properties listed in Table 1 shows that copper is the least distortive material, and lead is the most distortive material, since $\delta_{\mathrm{Cu}}<\delta_{\mathrm{Al}}<\delta_{\mathrm{Fe}}<\delta_{\mathrm{Pb}}$.

Figures 5 and 6 examined the case where heat flows from less distortive shell materials (i.e., aluminum and copper) into more distortive mold materials (i.e., iron and aluminum). The question remains, therefore, as to what impact the distortivity effect will have in situations where a more distortive shell material solidifies on a less distortive mold. To address this question, we considered each of the four materials as shell materials solidifying on molds consisting of the remaining three materials. We first searched for critical wavelengths, and then if any were found, calculated the bandwidth, $\Delta\lambda_R$, associated gap nucleation times corresponding to the critical wavelengths, $t_R^{1,2}$, and the time range of the band delimited by the smaller and larger critical wavelengths, defined as Δt_R. The following process parameters were used for each case: $h_0=0.5$ mm, $a_1=1.0\ \mu$m, $\kappa=0.1$, $R_0=10^{-5}$ m^2 sec°C/J, $R'=-10^{-12}$ m^2 sec°C/J·Pa, $P_0=10{,}000$ Pa. Results for each case are tabulated in Tables 2–5 that follow. The corresponding distortivity ratio is listed for each material combination.

Table 2 shows results for pure lead solidifying on copper, aluminum, and iron molds. Lead is the most distortive of the four materials, and hence for each material combination in Table 2, $\delta^d/\delta^c<1$. When solidifying on copper and aluminum molds, a lead shell immediately nucleates gaps (i.e., according to the present theory). This implies that at the earliest stages of lead solidification, these mold materials may be considered to be thermomechanically rigid. When solidifying on an iron mold, which is a more distortive material than either of the aluminum or copper molds (but which is closer to lead in its thermomechanical behavior), gap nucleation occurs at 1.04×10^{-4} sec. Note, however, that $\Delta\lambda_R$ decreases in going from the copper to the aluminum to the iron molds. Hence, the range of wavelengths that lead to gap nucleation is decreased when a mold-shell combination is chosen such that δ^d/δ^c approaches or exceeds unity. A similar comment applies to Δt_R.

Table 3 shows theoretical predictions for pure iron solidifying on copper, aluminum, and lead molds. An iron shell is slightly less distortive than a lead shell. It is therefore not surprising to

Table 2 Distortivity ratio effect on critical wavelengths and gap nucleation times for a pure lead shell

		Shell Material=Lead					
Mold Material	δ^d/δ^c	λ_R^1 (mm)	λ_R^2 (mm)	$\Delta\lambda_R$ (mm)	t_R^1 (sec)	t_R^2 (sec)	Δt_R (sec)
Copper	0.067	0.000000	32.45	32.45000	0.000000	0.7000	0.700000
Aluminum	0.143	0.000000	22.92	22.92000	0.000000	0.2200	0.220000
Iron	0.561	0.049319	9.71	9.660681	0.000104	0.0372	0.037096

Table 3 Distortivity ratio effect on critical wavelengths and gap nucleation times for a pure iron shell

		Shell Material=Iron					
Mold Material	δ^d/δ^c	λ_R^1 (mm)	λ_R^2 (mm)	$\Delta\lambda_R$ (mm)	t_R^1 (sec)	t_R^2 (sec)	Δt_R (sec)
Copper	0.120	0.0458495	194.3500	194.3041505	7.10×10^{-6}	0.600	0.5999929
Aluminum	0.255	0.0344424	132.3000	132.2655576	5.50×10^{-6}	0.170	0.1699945
Lead	1.782	0.0083640	47.2841	47.2841000	3.66×10^{-6}	0.033	0.0329963

Table 4 Distortivity ratio effect on critical wavelengths and gap nucleation times for a pure aluminum shell

		Shell Material=Aluminum					
Mold Material	δ^d/δ^c	λ_R^1 (mm)	λ_R^2 (mm)	$\Delta\lambda_R$ (mm)	t_R^1 (sec)	t_R^2 (sec)	Δt_R (sec)
Copper	0.471	0.221305	60.0000	59.778695	0.002200	0.1000	0.09978
Iron	3.923	0.045550	16.5994	16.553850	0.000110	0.0385	0.03839
Lead	6.989	0.040800	14.0360	13.995200	0.000105	0.0330	0.03289

Table 5 Distortivity ratio effect on critical wavelengths and gap nucleation times for a pure copper shell

		Shell Material=Copper					
Mold Material	δ^d/δ^c	λ_R^1 (mm)	λ_R^2 (mm)	$\Delta\lambda_R$ (mm)	t_R^1 (sec)	t_R^2 (sec)	Δt_R (sec)
Aluminum	2.125	0.176205	33.270	33.093795	0.000165	0.0315	0.031335
Iron	8.337	0.047060	14.970	14.922940	0.000110	0.0300	0.029890
Lead	14.852	0.040255	12.964	12.923745	0.000100	0.0258	0.025700

find that an iron shell very quickly nucleates gaps (i.e., of the order of a 10^{-6} sec) following the formation of a thin shell. The iron-copper system has a very wide range of wavelengths ($\Delta\lambda_R = 194.30$ mm) that lead to the situation shown in Fig. 7(*c*). Each $\Delta\lambda_R$ in Table 2 greatly exceeds its counterpart in Table 2. This means that an increase in the mold surface wavelength has much less of an influence on gap nucleation during iron solidification than a corresponding increase for a lead solidification. The iron-aluminum combination is certainly not much better with $\Delta\lambda_R = 132.26$ mm. Again, the bandwidth decreases with increasing δ^d/δ^c, which implies that a more distortive mold material is more desirable than a less distortive mold material from the standpoint of limiting the number of wavelengths that promote gap nucleation at the lowest points of the troughs.

Table 4 shows results for pure aluminum solidifying on copper, iron and lead molds. The bandwidths associated with copper, iron and lead molds are considerably smaller than those associated with the iron shell of Table 3. The times to initial gap nucleation are three to four orders-of-magnitude longer than those for the iron shell.

Table 5 shows results for pure copper solidifying on aluminum, iron and lead molds. Copper is the most thermomechanically rigid of the four materials, and hence for each material combination in Table 5, $\delta^d/\delta^c > 1$. Initial gap nucleation for each of the three mold materials occurs two orders-of-magnitude later than that corresponding to the iron shell of Table 3. The smallest bandwidth occurs for the copper-lead combination for which $\delta^d/\delta^c > 1$ is greatest since λ_R^2 decreases at a faster rate than λ_R^1 with increasing δ^d/δ^c. A comparison of Tables 4 and 5 shows that the copper and aluminum shells exhibit similar thermomechanical behavior for each of the three mold materials considered in those tables.

8 Process Parameter Effect on Bandwidth

The data presented in Tables 2–5 was generated for a single set of process parameters and hence it is not possible to infer how the bandwidth will change as the individual process parameters vary for a given mold-shell material combination. It would be desirable, however, to select combinations based upon a given set of process parameters, such that the bandwidth is minimal, or even nonexistent. Figures 8–12 explore the process parameter effect on the bandwidth, $\Delta\lambda_R$. Each figure considers a pure aluminum shell solidifying on the mold materials designated in that figure. Note that lead was not considered as a mold material since iron and copper adequately represent, respectively, the cases in which a less distortive material solidifies on a more distortive mold and a more distortive shell material solidifies on a less distortive mold. In all cases, $R' = -10^{-12}\,\mathrm{m^2\,sec°C/J\cdot Pa}$.

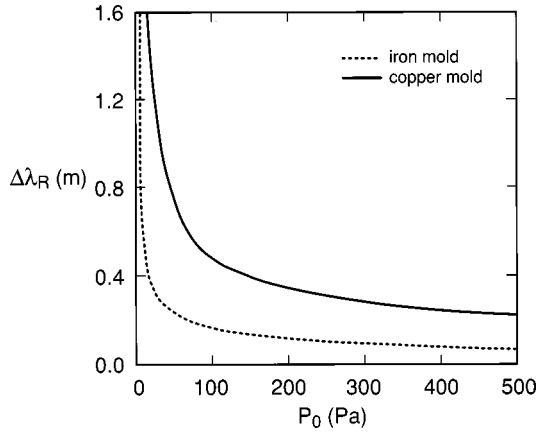

Fig. 8 $\Delta\lambda_R$ variation with P_0 for an aluminum shell

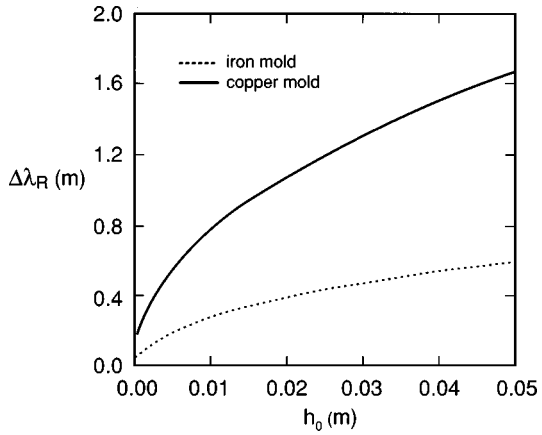

Fig. 9 $\Delta\lambda_R$ variation with h_0 for an aluminum shell

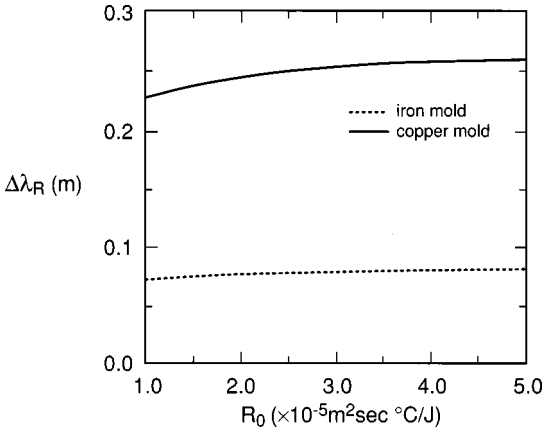

Fig. 10 $\Delta\lambda_R$ variation with R_0 for an aluminum shell

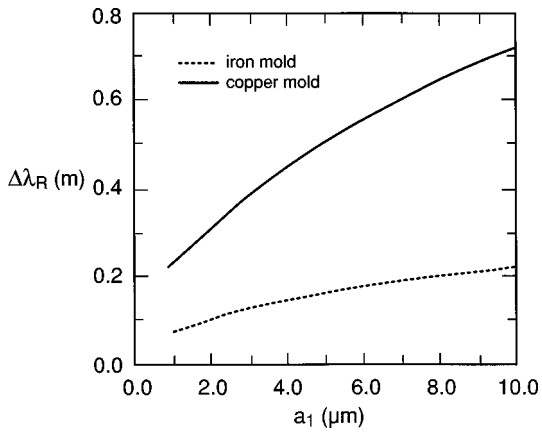

Fig. 11 $\Delta\lambda_R$ variation with a_1 for an aluminum shell

Figure 8 shows the variation of $\Delta\lambda_R$ with mean pressure, P_0. The remaining process parameters were fixed at $h_0 = 0.5$ mm, $a_1 = 1.0\,\mu$m, $\kappa = 0.1$, and $R_0 = 10^{-5}\,\mathrm{m^2\,sec°C/J}$. The smallest mean pressure evaluated in Fig. 8 is $P_0 = 1.0$ Pa. The $\Delta\lambda_R$ values for both mold materials are greatest at the smallest pressures. Also, the difference between these values is the least at the smallest pressures. As P_0 is increased, $\Delta\lambda_R$ decreases nonlinearly in both cases. Both systems give nearly constant values of $\Delta\lambda_R$ as further increase in P_0 has a diminishing effect. For all values of P_0 con-

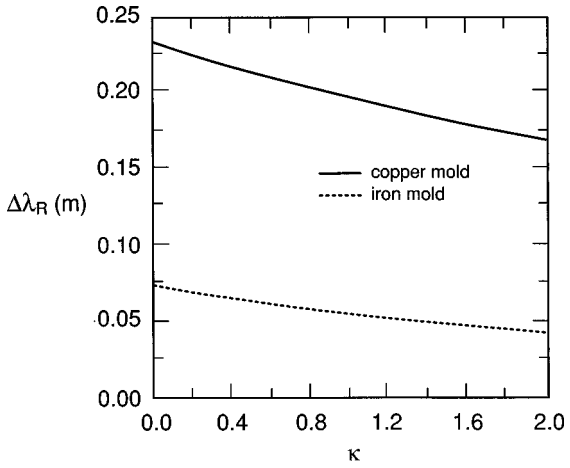

Fig. 12 $\Delta\lambda_R$ variation with κ for an aluminum shell

sidered in Fig. 8, $\Delta\lambda_R$ for the aluminum-iron system is less than that for the aluminum-copper system. Hence, the range of wavelengths that lead to gap nucleation can be decreased by solidifying a less distortive casting material on a more distortive mold material at increased mean pressures.

Figure 9 shows the bandwidth variation with mean mold thickness, h_0, for $0.5\,\text{mm} \leqslant h_0 \leqslant 50.0\,\text{mm}$. The remaining process parameters were fixed at $a_1 = 1.0\,\mu\text{m}$, $P_0 = 500\,\text{Pa}$, $\kappa = 0.1$, and $R_0 = 10^{-5}\,\text{m}^2\,\text{sec°C/J}$. Since the corresponding mold materials have finite thermal conductivities (and small $\Delta\lambda_R$ values), the rigid mold limit is not included in Fig. 9. Note that both curves imply that $\Delta\lambda_R$ varies as $\sqrt{h_0}$. Over the range of h_0 values considered in the figure, $\Delta\lambda_R$ is always larger for the aluminum-copper shell-mold system than for the aluminum-iron shell-mold system. Hence variation of h_0 has a much greater effect on $\Delta\lambda_R$ in a system where a more distortive shell material solidifies on a less distortive mold material (e.g., the aluminum-copper system). When a less distortive shell material solidifies on a more mold distortive material (e.g., the aluminum-iron combination), increasing h_0 has a relatively small effect on $\Delta\lambda_R$.

Figure 10 shows the bandwidth variation with mean contact resistance, R_0. The remaining process parameters were fixed at $h_0 = 0.5\,\text{mm}$, $a_1 = 1.0\,\mu\text{m}$, $\kappa = 0.1$, and $P_0 = 500\,\text{Pa}$. For both material combinations, variation of the mean resistance over the $1.0 \times 10^{-5}\,\text{m}^2\,\text{sec°C/J} < R_0 < 5.0 \times 10^{-5}\,\text{m}^2\,\text{sec°C/J}$ range gives little variation in $\Delta\lambda_R$ since both curves are nearly horizontal.

Figure 11 shows the bandwidth variation with the amplitude, a_1, of the upper surface of the mold (i.e., in contact with the aluminum shell) over the $1.0\,\mu\text{m} < a_1 < 10.0\,\mu\text{m}$ range. The remaining process parameters were fixed at $h_0 = 0.5\,\text{mm}$, $\kappa = 0.1$, $P_0 = 500\,\text{Pa}$, and $R_0 = 10^{-5}\,\text{m}^2\,\text{sec°C/J}$. Variation of a_1 in the aluminum-copper shell-mold system leads to a rapid increase in the bandwidth, whereas a similar variation in the aluminum-iron shell-mold system leads to much smaller bandwidths. Hence, $\Delta\lambda_R$ for a system in which a more distortive shell material solidifies on a less distortive mold material is more sensitive to changes in the mold surface amplitude than a corresponding system in which a less distortive shell material solidifies on a more distortive mold material.

Figure 12 shows the bandwidth variation with the mold surface amplitude ratio, κ, over the $0.001 < \kappa < 2.0$ range. The remaining process parameters were fixed at $h_0 = 0.5\,\text{mm}$, $P_0 = 500\,\text{Pa}$, and $R_0 = 10^{-5}\,\text{m}^2\,\text{sec°C/J}$. Note that increasing κ implies an increased roughness of the lower mold surface.

For the range of κ values considered in Fig. 12, $\Delta\lambda_R$ for the aluminum-copper shell-mold system is always greater than that for the aluminum-iron shell-mold system. Hence, $\Delta\lambda_R$ for a system in which a more distortive shell material solidifies on less distortive mold material is more sensitive to changes in κ. It is interesting to note that for both material combinations, $\Delta\lambda_R$ tends to decrease as κ is increased. This implies that the tendency to gap nucleation can be diminished by roughening the lower mold surface relative to the upper mold surface.

9 Conclusions

The evolution of the contact pressure at the lowest points of the upper mold surface troughs for the idealized solidification system modeled in Part I has been examined for different mold-shell material combinations. Gap nucleation along the mold-shell interface was assumed to occur when the contact pressure fell to zero within a certain time after the start of solidification. This implied the possibility of nonuniform or undulatory growth of the shell at later stages of the process since the contact pressure simultaneously increases at the highest points of the upper mold surface crests. The shell thickness above these points increases, whereas the shell thickness above the lowest points of the troughs diminishes. Since the theoretical model was only valid up to gap nucleation time, continued growth of the gaps and the shell could not be monitored. Gap nucleation is quickest in those situations where the distortivity of the shell material greatly exceeds that of the mold material (e.g., lead solidifying on a copper mold). The critical wavelength concept was introduced and critical wavelengths were predicted for all mold-shell material combinations. Those wavelengths which led to gap nucleation were found to fall within a region delimited by smaller and larger critical wavelengths: The difference between the critical wavelengths was defined as the wavelength bandwidth for gap nucleation. The bandwidth was largest for the iron-copper shell-mold combination. Much greater care would therefore have to be exercised in the selection of a mold wavelength for this combination. On the other hand, the bandwidths were smallest in those cases where a less distortive shell material (such as copper) solidified on a more distortive mold material (such as lead), or if the distortivity ratio of the two materials is near unity.

Effects of important casting processes parameters, such as mean mold thickness, contact resistance, and pressure, on the size of the wavelength bands were also examined. A general conclusion from these results is that the bandwidths predicted for solidification of a more distortive shell on a less distortive mold generally exceed those for a less distortive shell solidifying on a more distortive mold irrespective of the size of a selected process parameter.

The spirit behind the present work has three important components: (a) to theoretically demonstrate (within the constraints of the theoretical assumptions) that mold surface topography may play a significant role in casting processes; (b) to provide a limiting solution against which more sophisticated models that require a full numerical implementation (e.g., the finite element method) of the governing equations can be checked; (c) to suggest new solidification experiments that are directed toward development of mold surface topography design criteria.

Clearly, the present methodology lacks many of the complicated phenomena considered in the work of Murakami et al. [1] and others. Future models will have to take the present methodology beyond the point of gap nucleation and into the time range where the shell thickness becomes substantially undulatory (i.e., when the tortoise shells first appear at the freezing front) due to lateral growth of the gaps. Future models will also have to account for mold movement due to the increasing importance of continuous casting processes. Surface wetting of the molten metal, which is certainly imperfect for the majority of mold topographies considered in the experimental literature, must be adequately simulated. Nonsinusoidal topographies (such as trapezoidal gaps and rectified cosine waves) should also be modeled. These may lead to new conclusions about the relationship between the local curvature of the topography and the location of gap nucleation. The shell constitutive model should be extended to include strain rate relaxation due to viscous creep. It is likely that this will alter the

extent of the bandwidths for most, if not all material and process parameter combinations considered in the present work. Finally, the evolution of cast shell microstructure during solidification should also be interwoven with the present thermomechanical model.

Acknowledgments

The authors wish to express their gratitude to Dr. Owen Richmond of Alcoa Technical Center for suggesting this problem and to Prof. J. R. Barber of the University of Michigan for his continuous guidance and support during all phases of the work. Faruk Yigit is pleased to acknowledge support from the King Saud University, College of Engineering Research Center under project number 13/419.

References

[1] Murakami, H., Suzuki, M., Kitagawa, T., and Miyahara, S., 1992, ''Control of Uneven Solidified Shell Formation of Hypo-peritectic Carbon Steels in Continuous Casting Mold,'' J. Iron Steel Inst. Jpn., **78**, pp. 105–112.

[2] Singh, S., and Blazek, K., 1974, ''Heat Transfer and Skin Formation in a Continuous Casting Mold as a Function of Steel Carbon Content,'' J. Metals, pp. 17–27.

[3] Yigit, F., and Hector, Jr., L. G., 2000, ''Critical Wavelengths for Gap Nucleation in Solidification. Part 1: Theoretical Methodology,'' ASME J. Appl. Mech., **67**, pp. 66–76.

[4] Weirauch, Jr., D. A., and Giron, A., 1998, ''The Early Stages of Aluminum Solidification in the Presence of a Moving Meniscus,'' *Proceedings on the Integration of Material, Process and Product Design—A Conference dedicated to the 70th birthday of Owen Richmond*, A. A. Balkema Publishers, Rotterdam, Netherlands, pp. 183–191.

[5] Schneck, P., and Veronis, G., 1967, ''Comparison of Some Recent Experimental and Numerical Results in Bénard Convection,'' Phys. Fluids, **10**, pp. 927–930.

[6] Hector, Jr., L. G., and Schmid, S. R., 1997, ''Simulation of Asperity Plowing in an Atomic Force Microscope. Part I: Experimental and Theoretical Methods,'' Wear, **215**, pp. 247–256.

[7] Yun, I.-S., Wilson, W. R. D., and Ehmann, K. F., 1998, ''Chatter in the Strip Rolling Process,'' ASME J. Manuf. Sci. Eng., **120**, pp. 330–336.

[8] Broadbridge, P., Fulford, G. R., Fowkes, N. D., Chan, D. Y. C., and Lassig, C., 1999, ''Bubbles in Wet, Gummed Wine Labels,'' SIAM Rev., **41**, pp. 363–372.

[9] Brush, D. O., and Almroth, B. O., 1975, *Buckling of Bars, Plates, and Shells*, McGraw-Hill, New York.

[10] Richmond, O., 1987, personal communication with L. G. Hector, Jr., Alcoa Laboratories, Alcoa Technical Center, PA.

[11] Yeo, T., and Barber, J. R., 1994, ''Finite Element Analysis of Thermoelastic Contact Stability,'' ASME J. Appl. Mech., **61**, pp. 919–922.

[12] Richmond, O., Hector, Jr., L. G., and Fridy, J. M., 1990, ''Growth Instability During Nonuniform Directional Solidification of Pure Metals,'' ASME J. Appl. Mech., **57**, pp. 529–536.

[13] Heinlein, M., Mukherjee, S., and Richmond, O., 1986, ''A Boundary Element Method of Analysis of Temperature Fields and Stresses During Solidification,'' Acta Mech., **59**, pp. 59–81.

[14] Boltz, R. E., and Tuve, G. L., 1984, *CRC Handbook of Tables for Applied Engineering and Science*, CRC Press, Boca Raton, FL.

[15] Touloukian, Y. S., Powell, R. W., Ho, C. Y., and Klemens, P. G., 1970, *Thermophysical Properties of Matter: Thermal Conductivity*, Vol. 1, IFI/Plenum, New York.

[16] Lucas, L. D., 1972, ''Density of Metals at High Temperatures in the Solid and Molten States, Part 2,'' Mem. Sci. Rev. Met., **69**, No. 6, pp. 479–492.

[17] Lucas, L. D., 1972, ''Density of Metals at High Temperatures in the Solid and Molten States, Part 1,'' Mem. Sci. Rev. Met., **69**, No. 5, pp. 395–409.

[18] Mathiak, E., Nistler, E., Waschkowski, W., and Koester, L., 1983, ''Precision Density Measurements of Liquid Gallium, Tin, Cadmium, Thallium, Lead and Bismuth,'' Z. Metallkd., **74**, pp. 793–796.

[19] Baumeister, T., Avallone, E. A., and Baumeister, III, T., 1978, *Marks' Standard Handbook for Mechanical Engineers*, 8th ed., McGraw-Hill, New York.

[20] Wawra, H. H., 1974, ''The Elastomechanical Properties of Pure Iron and FeS_2 in Different Crystallographic Directions as a Function of Temperature and Pressure,'' Arch. Eisenhuettenwes., **45**, No. 5, pp. 317–320.

[21] Ledbetter, H. M., and Naimon, E. R., 1974, ''Elastic Properties of Metals and Alloys, II. Coper,'' J. Phys. Chem. Ref. Data, **3**, pp. 897–935.

[22] Drapkin, B. M., Birfel'd, A. A., Kononenko, V. K., and Kalyukin, H. P., 1980, ''Study of the Young's Modulus and Internal Friction in the Range 20°C to T_m Inclusive,'' Phys. Met. Metallogr., **49**, pp. 150–155.

[23] Touloukian, Y. S., Kirby, R. K., Taylor, R. E., and Desai, P. D., 1978, *Thermophysical Properties of Matter: Thermal Expansion*, Vol. 12, IFI/Plenum, New York.

[24] Wawra, H. H., 1978, ''Accurate Elastomechanical Values of Copper Materials,'' Metall., **32**, pp. 346–348.

[25] Hector, Jr., L. G., Howarth, J. A., Richmond, O., and Kim, W.-S., 2000, ''Mold Surface Wavelength Effect on Gap Nucleation in Solidification,'' ASME J. Appl. Mech., **67**, pp. 155–164.

[26] Dundurs, J., 1974, ''Distortion of a Body Caused by Free Thermal Expansion,'' Mech. Res. Commun., **1**, pp. 121–124.

[27] Zhang, R. G., and Barber, J. R., 1990, ''Effect of Material Properties on the Stability of Static Thermoelastic Contact,'' ASME J. Appl. Mech., **57**, pp. 365–369.

Thermoelastic Fracture Mechanics for Nonhomogeneous Material Subjected to Unsteady Thermal Load

B. L. Wang[1]
e-mail: wangbl@public.hr.hl.cn

J. C. Han
Professor

S. Y. Du
Professor

Center for Composite Materials,
Harbin Institute of Technology,
Harbin 150001, P. R. China

This article provides a comprehensive treatment of cracks in nonhomogeneous structural materials such as functionally graded materials. It is assumed that the material properties depend only on the coordinate perpendicular to the crack surfaces and vary continuously along the crack faces. By using a laminated composite plate model to simulate the material nonhomogeneity, we present an algorithm for solving the system based on the Laplace transform and Fourier transform techniques. Unlike earlier studies that considered certain assumed property distributions and a single crack problem, the current investigation studies multiple crack problems in the functionally graded materials with arbitrarily varying material properties. The algorithm can be applied to steady state or transient thermoelastic fracture problem with the inertial terms taken into account. As a numerical illustration, transient thermal stress intensity factors for a metal-ceramic joint specimen with a functionally graded interlayer subjected to sudden heating on its boundary are presented. The results obtained demonstrate that the present model is an efficient tool in the fracture analysis of nonhomogeneous material with properties varying in the thickness direction. [S0021-8936(00)01601-9]

1 Introduction

In recent years, the structures subjected to severe thermal loading that gives rise to intense thermal stresses in components. These components and systems are subjected to ultra-high temperature, ultra-high gradient temperature, and cyclical changes of ultra-high temperature. At such operating temperatures the new materials design can be accomplished by suitably varying composition and/or microstructure of the medium. The greater part of the work in the field has been on the introduction of functionally graded materials. Functionally graded materials usually consist of two distinct material phases, such as ceramic and metal alloy phases, and the composition would vary continuously. The development of functionally graded materials has demonstrated that they have the potential to reduce the magnitude of residual and thermal stresses, reduce the stress concentration near the ends and increase the fracture toughness, and provide the composite medium with a natural *R*-curve behavior (see Saito and Takahashi [1]).

An important aspect that needs to be addressed in various engineering applications of functionally graded materials is the question of reliability and durability, in general, and fracture related failure, in particular. Jin and Noda [2,3] and Noda and Jin [4,5] investigated the steady thermal stress intensity factors of the functionally gradient semi-infinite space with an internal crack parallel to the boundary surface. Noda and Jin [6] and Jin and Noda [7] studied the transient thermal stress intensity factors of a functionally gradient finite space with an internal crack parallel to the boundary surface. They assumed an exponential variation of material properties. All of these authors conclude that the appropriate selection of the nonhomogeneous parameters of the material can reduces the thermal stress intensity factors.

When functionally graded materials are subjected to an ultra-high temperature on the boundary surface, the crack may occur on the boundary surface of the material that is exposed to the ultra-high temperature. Erdogan and Wu [8] investigated steady-state thermal stress intensity factors in a functionally gradient layer with a vertical crack normal to the boundary surface. Jin and Noda [9] investigated steady-state thermal stress intensity factors in a functionally gradient semi-infinite space with an edge crack subjected to thermal load. Nemat-Alla and Noda [10] considered the crack problem in semi-infinite functionally graded materials under thermal load. Jin and Batra [11] studied transient thermal stress intensity factors in a functionally gradient plate with an edge crack subjected to a sudden cooling at the cracked surfaces. The shear modulus and the thermal conductivity of the material are selected to vary hyperbolically and exponentially, respectively. Transient thermal stress intensity factors in a functionally graded plate with an edge crack at the ceramic boundary subjected to a thermal load, such as a cycle of heating and cooling, were considered by Noda [12].

The crack problems are very often not amenable to comprehensive analytical treatments, apart from a few idealized cases, mainly due to the complexities and difficulties involved. This is especially true if the interest is focused on examining the transient response of a cracked media with arbitrarily varying material properties. Most of the previous studies appear to have apparently been limited to such configurations as having an infinite extent, single crack problem, and certain assumed property distributions. But certain assumed property distributions presented in the literature must be used with care, as they are not physically realizable for certain material combinations ([13]).

When functionally graded materials are subjected to ultra-high temperature the materials properties are dependent upon the temperature, however, this is beyond the scope of the present study. The purpose of this paper is to investigate the time behavior of a multiple crack problems for nonhomogeneous materials with ar-

[1]Present address: Department of Mechanical Engineering, Shizuoka University, Hamamatsu 432-8561, Japan. e-mail: tbwong@ipc.shizuoka.ac.jp or wangbl@public.hr.hl.cn

Contributed by the Applied Mechanics Division of THE AMERICAN SOCIETY OF MECHANICAL ENGINEERS for publication in the ASME JOURNAL OF APPLIED MECHANICS. Manuscript received by the ASME Applied Mechanics Division, Apr. 21, 1999; final revision, Sept. 8, 1999. Associate Technical Editor: W. J. Drugan. Discussion on the paper should be addressed to the Technical Editor, Professor Lewis T. Wheeler, Department of Mechanical Engineering, University of Houston, Houston, TX 77204-4792, and will be accepted until four months after final publication of the paper itself in the ASME JOURNAL OF APPLIED MECHANICS.

bitrarily varying material properties. By utilizing laminated composite plate model to simulate material nonhomogeneity, we present an algorithm for solving the system based on Laplace transform and Fourier transform techniques. Singular integral equations are derived and solved to investigate the multiple crack problems in the functionally graded materials with arbitrarily varying material properties. Numerical examples are provided for a metal-ceramic joint specimen with a functionally graded interlayer under non-uniform heating condition. Transient and steady-state thermal stress intensity factors are calculated, and the variation in the thermal stress intensity factors due to the change in material gradient is studied. The results obtained show that the present model is an efficient tool in the fracture analysis of composite material with properties varying in the thickness direction.

2 Formulation of the Problem

Consider a cracked nonhomogeneous material plate of thickness h with properties that vary as a function of coordinate y (Fig. 1), in which C_{mn} denote the stiffness coefficients of the medium $(m, n=1,2,6)$, α_x and α_y are the linear thermal expansion coefficients, k stands for the thermal conductivity, c_v represents specific heat, and ρ is mass density. The medium is infinite in the x-direction. (x, y) is the global coordinate system. In order to simulate the material nonhomogeneity in the y-direction, divide the elastic plate into many layers of infinite length (say N layers). Assume that cracks are normal to the thickness of the plate, and a crack lies on the interface between two layers. The material properties are taken to be constants for each layer. The analytical model is shown in Fig. 2. The principal axes of elasticity are parallel to the x-axis and the y-axis. For the Jth layer, the thickness is h_J, throughout the paper the subscript J stands for the Jth layer, counting from the lower surface, whereas the subscript j denotes the interface number between the Jth layer and the $(J+1)$th layer. The local coordinate y_J is measured from the bottom of the Jth layer.

Denote the interlaminar stress $(\sigma_y)_j$ as $\sigma_j(x,t)$, $(\tau_{xy})_j$ as $\tau_j(x,t)$ and interlaminar thermal flux $(q_y)_j$ as $q_j(x,t)$. The adjacent two layers are perfectly bonded or have a crack. The crack length is $2a_j$, and the crack center is located at $x_j=c_j$. The initial displacement, velocity, and temperature are zero. The stress, displacement, thermal flux, and temperature vanish at infinity. The boundary conditions are

1 applied normal stress and shear stress on crack faces are σ_{0j} and τ_{0j}, respectively.

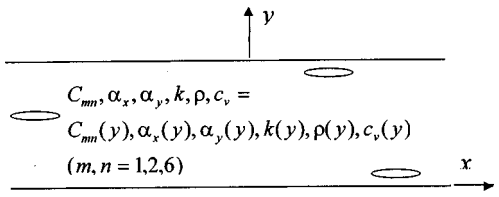

Fig. 1 Geometry and coordinates of a nonhomogeneous material plate

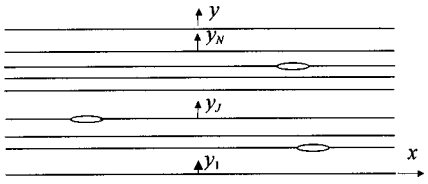

Fig. 2 Analytical model of the nonhomogeneous material plate

2 applied normal stresses and shear stress are, respectively, σ_{00} and τ_{00} for the lower surface, and σ_{0N} and τ_{0N} for the upper surface of the plate.
3 crack faces remain completely insulated, i.e., $q_j=0$.
4 the applied thermal flux on the lower surface and the upper surface of the medium are q_{00} and q_{0N}, respectively. The applied temperature on the lower surface and the upper surface of the medium are T_{00} and T_{0N}, respectively.

For an orthotropic material, the thermal flux for each layer is

$$(q_x)_J=-(k_x)_J\partial T_J/\partial x \quad (q_y)_J=-(k_y)_J\partial T_J/\partial y. \tag{1}$$

Assume that the temperature is independent of deformations. Combining the balance of energy with the Fourier's law, the heat equation can be written for each layer as follows:

$$(k_x)_J\partial^2 T_J/\partial x^2+(k_y)_J\partial^2 T_J/\partial y_J^2=\rho_J(c_v)_J\partial T_J/\partial t. \tag{2}$$

Under plane stress and small deformation conditions, the displacements and stresses are

$$(U_x)_J=u_J(x,y_J,t) \quad (U_y)_J=v_J(x,y_J,t) \tag{3}$$

$$\left.\begin{aligned}\sigma_{xJ}&=(C_{11})_J\partial u_J/\partial x+(C_{12})_J\partial v_J/\partial y_J-(\beta_x)_J T_J\\ \sigma_{yJ}&=(C_{12})_J\partial u_J/\partial x+(C_{22})_J\partial v_J/\partial y_J-(\beta_y)_J T_J\\ \tau_{xyJ}&=(C_{66})_J(\partial u_J/\partial y_J+\partial \nu_J/\partial x)\end{aligned}\right\} \tag{4}$$

The equations of motion are

$$\left.\begin{aligned}(C_{11})_J\frac{\partial^2 u_J}{\partial x^2}+(C_{66})_J\frac{\partial^2 u_J}{\partial y_J^2}+(C_{12}+C_{66})_J\frac{\partial^2 v_J}{\partial x\partial y_J}&\\ =\rho_J\frac{\partial^2 u_J}{\partial t^2}+(\beta_x)_J\frac{\partial T_J}{\partial x}&\\ (C_{66})_J\frac{\partial^2 v_J}{\partial x^2}+(C_{22})_J\frac{\partial^2 v_J}{\partial y_J^2}+(C_{12}+C_{66})_J\frac{\partial^2 u_J}{\partial x\partial y_J}&\\ =\rho_J\frac{\partial^2 v_J}{\partial t^2}+(\beta_y)_J\frac{\partial T_J}{\partial y_J}&\end{aligned}\right\}. \tag{5}$$

3 The Temperature Field

Referring to nondimensional variables $\overline{x}=x/h$, $\overline{y_J}=y_J/h$, $\overline{h_J}=h_J/h$, $\overline{a_j}=a_j/h$, $\overline{c_j}=c_j/h$, $k_j=2/(1/\sqrt{(k_xk_y)_J}+1/\sqrt{(k_xk_y)_{J+1}})$ and $t_{0J}=h^2\rho_J(c_v)_J/(k_y)_J$. Applying Laplace transform over the time variable t and Fourier transform over the space variable x, Eq. (2) may be solved to give the temperature in each layer of the plate

$$T_J^*(\overline{x},\overline{y_J},p)=\frac{1}{2\pi}\int_{-\infty}^{+\infty}[A_{0J}e^{-|s|\lambda_{0J}\overline{y_J}}+B_{0J}e^{|s|\lambda_{0J}\overline{y_J}}]e^{-is\overline{x}}ds \tag{6}$$

where the superscript * denotes the Laplace transform, $A_{0J}(s,p)$ and $B_{0J}(s,p)$ are unknowns to be determined, and

$$\lambda_{0J}=\sqrt{(k_x)_J/(k_y)_J+pt_{0J}/s^2}. \tag{7}$$

Substituting Eq. (6) into (1) gives thermal flux q_j^* at $\overline{y_J}=\overline{h_J}$ and q_{j-1}^* at $\overline{y_J}=0$. By applying the inverse Fourier transform one gets A_{0J} and B_{0J} in terms of q_j^* and q_{j-1}^*. The temperature in each layer can thus be determined in terms of q_j^* and q_{j-1}^* by substituting A_{0J} and B_{0J} back into (6),

$$\begin{aligned}T_J^*(\overline{x},\overline{y_J},p)=-\frac{h}{2\pi}\int_{-\infty}^{+\infty}e^{-is\overline{x}}\frac{R_J(s,p)}{s}ds\int_{-\infty}^{+\infty}[(e^{-|s|\lambda_{0J}\overline{y_J}}&\\ +e^{|s|\lambda_{0J}\overline{y_J}})q_j^*(\overline{r},p)-(e^{-|s|\lambda_{0J}(\overline{h_J}-\overline{y_J})}&\\ +e^{|s|\lambda_{0J}(\overline{h_J}-\overline{y_J})})q_{j-1}^*(\overline{r},p)]e^{is\overline{r}}d\overline{r},&\end{aligned} \tag{8}$$

where

$$R_J(s,p)=\frac{\mathrm{sgn}(s)}{(k_y)_J\lambda_{0J}(e^{|s|\lambda_{0J}\bar{h}_J}-e^{-|s|\lambda_{0J}\bar{h}_J})}. \tag{9}$$

If the temperature on the lower surface of the medium is prescribed, the temperature field for the first layer can also be expressed in terms of $T_{00}^*(\bar{x},p)$ and $q_1^*(\bar{x},p)$ as

$$\begin{aligned}T_1^*(\bar{x},\bar{y}_1,p)=&-\frac{h}{2\pi}\int_{-\infty}^{+\infty}e^{-is\bar{x}}\frac{R_1(s,p)}{s}ds\\&\times\int_{-\infty}^{+\infty}\Big[(e^{|s|\lambda_{01}\bar{y}_1}-e^{-|s|\lambda_{01}\bar{y}_1})q_1^*(\bar{r},p)\\&-\frac{\mathrm{sgn}(s)(k_y)_1s\lambda_{01}}{h}(e^{-|s|\lambda_{01}(\bar{h}_1-\bar{y}_1)}\\&+e^{|s|\lambda_{01}(\bar{h}_1-\bar{y}_1)})T_{00}^*(\bar{r},p)\Big]e^{is\bar{r}}d\bar{r}\end{aligned} \tag{10}$$

where

$$R_1(s,p)=\frac{\mathrm{sgn}(s)}{(k_y)_1\lambda_{01}(e^{|s|\lambda_{01}\bar{h}_1}+e^{-|s|\lambda_{01}\bar{h}_1})} \tag{11}$$

If the temperature on the upper surface of the medium is prescribed, the temperature for the Nth layer may be expressed in terms of $q_{N-1}^*(\bar{x},p)$ and $T_{0N}^*(\bar{x},p)$ as

$$\begin{aligned}T_N^*(\bar{x},\bar{y}_N,p)=&-\frac{h}{2\pi}\int_{-\infty}^{+\infty}e^{-is\bar{x}}\frac{R_N(s,p)}{s}ds\\&\times\int_{-\infty}^{+\infty}\Big[-\frac{\mathrm{sgn}(s)(k_y)_Ns\lambda_{0N}}{h}(e^{-|s|\lambda_{0N}\bar{y}_N}\\&+e^{|s|\lambda_{0N}\bar{y}_N})T_{0N}^*(\bar{r},p)+(e^{-|s|\lambda_{0N}(\bar{h}_N-\bar{y}_N)}\\&-e^{|s|\lambda_{0N}(\bar{h}_N-\bar{y}_N)})q_{N-1}^*(\bar{r},p)\Big]e^{is\bar{r}}d\bar{r}\end{aligned} \tag{12}$$

where

$$R_N(s,p)=\frac{\mathrm{sgn}(s)}{(k_y)_N\lambda_{0N}(e^{|s|\lambda_{0N}\bar{h}_N}+e^{-|s|\lambda_{0N}\bar{h}_N})}. \tag{13}$$

Define now the following auxiliary function:

$$\phi_{0j}(\bar{x},p)=\partial T_{J+1}^*(\bar{x},\bar{y}_{J+1}=0,p)/\partial x-\partial T_J^*(\bar{x},\bar{y}_J=\bar{h}_J,p)/\partial x. \tag{14}$$

Substituting (8) into (14) we find

$$\begin{aligned}\phi_{0j}(\bar{r},p)=&-\frac{i}{2\pi}\int_{-\infty}^{+\infty}e^{-is\bar{r}}ds\int_{-\infty}^{+\infty}[L_jq_{j-1}^*(\bar{x},p)+M_jq_j^*(\bar{x},p)\\&+N_jq_{j+1}^*(\bar{x},p)]e^{is\bar{x}}d\bar{x}\end{aligned} \tag{15}$$

where

$$L_j(s,p)=-2R_J(s,p) \tag{16}$$

$$N_j(s,p)=-2R_{J+1}(s,p) \tag{17}$$

$$\begin{aligned}M_j(s,p)=&(e^{|s|\lambda_{0(J+1)}\bar{h}_{J+1}}+e^{-|s|\lambda_{0(J+1)}\bar{h}_{J+1}})R_{J+1}(s,p)\\&+(e^{|s|\lambda_{0J}\bar{h}_J}+e^{-|s|\lambda_{0J}\bar{h}_1})R_J(s,p).\end{aligned} \tag{18}$$

If $T_1^*(\bar{x},\bar{y}_N,p)$ is expressed by Eq. (10), $\phi_{01}(\bar{r},p)$ will be given by

$$\begin{aligned}\phi_{01}(\bar{r},p)=&-\frac{i}{2\pi}\int_{-\infty}^{\infty}e^{-is\bar{r}}ds\\&\times\int_{-\infty}^{+\infty}\Big[L_1\frac{\mathrm{sgn}(s)(k_y)_1s\lambda_{01}}{h}T_{00}^*(\bar{x},p)\\&+M_1q_1^*(\bar{x},p)+N_1q_2^*(\bar{x},p)\Big]e^{is\bar{x}}d\bar{x}\end{aligned} \tag{19}$$

where

$$L_1(s,p)=-2R_1(s,p) \tag{20}$$

$$N_1(s,p)=-2R_2(s,p) \tag{21}$$

$$\begin{aligned}M_1(s,p)=&(e^{|s|\lambda_{02}\bar{h}_2}+e^{-|s|\lambda_{02}\bar{h}_2})R_2(s,p)\\&+(e^{|s|\lambda_{01}\bar{h}_1}-e^{-|s|\lambda_{01}\bar{h}_1})R_1(s,p).\end{aligned} \tag{22}$$

If $T_N^*(\bar{x},\bar{y}_N,p)$ is expressed by Eq. (12), $\phi_{0(N-1)}(\bar{r},p)$ will be given by

$$\begin{aligned}\phi_{0(N-1)}(\bar{r},p)=&-\frac{i}{2\pi}\int_{-\infty}^{+\infty}e^{-is\bar{r}}ds\\&\times\int_{-\infty}^{\infty}\Big[L_{N-1}q_{N-2}^*(\bar{x},p)+M_{N-1}q_{N-1}^*(\bar{x},p)\\&+N_{N-1}\frac{\mathrm{sgn}(s)(k_y)_Ns\lambda_{0N}}{h}T_{0N}^*(\bar{x},p)\Big]e^{is\bar{x}}d\bar{x}\end{aligned} \tag{23}$$

where

$$L_{N-1}(s,p)=-2R_{N-1}(s,p) \tag{24}$$

$$N_{N-1}(s,p)=2R_N(s,p) \tag{25}$$

$$\begin{aligned}M_{N-1}(s,p)=&(e^{|s|\lambda_{0N}\bar{h}_N}-e^{-|s|\lambda_{0N}\bar{h}_N})R_N(s,p)+(e^{|s|\lambda_{0(N-1)}\bar{h}_{N-1}}\\&+e^{-|s|\lambda_{0(N-1)}\bar{h}_{N-1}})R_{N-1}(s,p).\end{aligned} \tag{26}$$

By defining the following two vectors of $(N-1)$ rows, each

$$\{Q^*(\bar{x},p)\}=\{q_1^*(\bar{x},p),\ldots,q_{N-1}^*(\bar{x},p)\}^T \tag{27}$$

$$\begin{aligned}&\{\Phi_0(s,p)\}\\&=\Big\{\int_{\bar{c}_1-\bar{a}_1}^{\bar{c}_1+\bar{a}_1}\phi_{01}e^{is\bar{r}}d\bar{r},\ldots,\int_{\bar{c}_{N-1}-\bar{a}_{N-1}}^{\bar{c}_{N-1}+\bar{a}_{N-1}}\phi_{0(N-1)}e^{is\bar{r}}d\bar{r}\Big\}^T\end{aligned} \tag{28}$$

and using inverse Fourier transform to (15), (19), and (23) gives

$$[-D]\int_{-\infty}^{+\infty}\{Q^*\}e^{is\bar{x}}d\bar{x}=\frac{1}{i}\{\Phi_0\}+\{\Phi_{0a}\} \tag{29}$$

where $[D(s,p)]$ has the form

$$[D(s,p)]=\begin{bmatrix}M_1&N_1&&&\\L_2&M_2&N_2&&\\&&\ddots&&\\&&L_{N-2}&M_{N-2}&N_{N-2}\\&&&L_{N-1}&M_{N-1}\end{bmatrix} \tag{30}$$

and $\{\Phi_{0a}(s,p)\}$ is a vector of $(N-1)$ rows, with the first and the last elements the only nonzero elements, these elements are related to the boundary conditions by

$$\Phi_{0a1}(s,p)=L_1(s,p)\int_{-\infty}^{+\infty}q_{00}^*(\bar{r},p)e^{is\bar{r}}d\bar{r} \tag{31}$$

$$\Phi_{0a(N-1)}(s,p)=N_{N-1}(s,p)\int_{-\infty}^{+\infty}q_{0N}^{*}(\bar{r},p)e^{is\bar{r}}d\bar{r} \quad (32)$$

if surface heat flows are prescribed; and by

$$\Phi_{0a1}(s,p)=L_1(s,p)\,\frac{\mathrm{sgn}(s)(k_y)_1 s\lambda_{01}}{h}\int_{-\infty}^{+\infty}T_{00}^{*}(\bar{r},p)e^{is\bar{r}}d\bar{r} \quad (33)$$

$$\Phi_{0a(N-1)}(s,p)=N_{N-1}(s,p)\,\frac{\mathrm{sgn}(s)(k_y)_N s\lambda_{0N}}{h}\times\int_{-\infty}^{+\infty}T_{0N}^{*}(\bar{r},p)e^{is\bar{r}}d\bar{r} \quad (34)$$

if surface temperatures are prescribed.

Referring to the variables K_{mn}, which denotes the mth row and the nth column element in matrix $[D(s,p)]^{-1}$, one can see from the expressions $[D(s,p)]$ that $|s|\to\infty$, the only nonzero elements in $[K(s,p)]$ are $K_{jj}(s\to\pm\infty,p)=\mathrm{sgn}(s)\kappa_j/2$. Defining $K'_{jk}(s,p)=K_{jk}(s,p)-K_{jk}(\infty,p)$. Applying inverse Fourier transform to (29) yields

$$-q_j^{*}(\bar{x},p)-q_{aj}^{*}(\bar{x},p)=\frac{1}{\pi}\sum_{k=1}^{N-1}\int_{\bar{c}_k-\bar{a}_k}^{\bar{c}_k+\bar{a}_k}\phi_{0k}(\bar{r},p)d\bar{r}\times\int_0^{\infty}K'_{jk}\sin s(\bar{r}-\bar{x})ds+\frac{\kappa_j}{2\pi}\int_{\bar{c}_j-\bar{a}_j}^{\bar{c}_j+\bar{a}_j}\frac{\phi_{0j}(\bar{r},p)}{\bar{r}-\bar{x}}d\bar{r} \quad (35)$$

where

$$q_{aj}^{*}(\bar{x},p)=\frac{1}{2\pi}\int_{-\infty}^{+\infty}(K_{j1}\ \ K_{j(N-1)})\{\Phi_{0a1}\ \ \Phi_{0a(N-1)}\}^{T}e^{-is\bar{x}}ds \quad (36)$$

Equation (35) is the relationship between interfacial heat flows and interfacial auxiliary functions, and there are $N-1$ equations in (35). For those interfaces with no cracks, the auxiliary function is zero, so the number of equations needed to be solved is the same as the crack number.

Equation (35) provides the expression for $q_j^{*}(\bar{x},p)$ outside as well as inside the crack. In the case of inside the crack it is an ordinary singular integral equation having a simple Cauchy-type kernel as the dominant singular part. The crack-tip behavior can be characterized by a standard square-root singular. The integral equation can be solved numerically by noting that its fundamental function corresponds to the weight function of the Chebyshev polynomial of the first kind $T_m(\bar{r}_j)$.

$$\phi_{0j}(\bar{a}_j\bar{r}_j+\bar{c}_j,p)=\sum_{m=1}^{\infty}C_{jm}(p)T_m(\bar{r}_j)/\sqrt{1-\bar{r}_j^{2}} \quad (37)$$

where $\bar{r}_j=(\bar{r}-\bar{c}_j)/\bar{a}_j$, C_{jm} are the unknowns to be evaluated. After substituting (37), truncated with the first M terms into (14), the temperature difference between the upper surface and the lower surface of the jth crack can be evaluated as

$$T_{J+1}^{J*}(\bar{x},p)=-a_j\sum_{n=1}^{M}C_{jn}(p)\sin(n\arccos\bar{x}_j)/n \quad |\bar{x}_j|<1 \quad (38)$$

in which $\bar{x}_j=(\bar{x}-\bar{c}_j)/\bar{a}_j$. The crack face thermal flux boundary condition requires $q_j^{*}(x,p)=0$, this can be satisfied by using the following weighted residuals method:

$$\int_{-1}^{1}[q_j^{*}(\bar{a}_j\bar{x}_j+\bar{c}_j,p)]\,\frac{\sin(n\cos^{-1}\bar{x}_j)}{n}d\bar{x}_j=0. \quad (39)$$

Thus the integral Eq. (35) is reduced to a finite algebraic system to evaluate the unknown C_{jm}. Once the coefficient C_{jm} is obtained, the numerical solution of the integral Eq. (35) can be calculated from (37). The temperature in the Laplace transform domain can be obtained from (35) and (8).

As crack-tip thermal flow has standard square-root singular, it can be seen from (35) and (37) that the thermal flow intensity factor can be calculated as

$$(K_q^{*})_j=(\sqrt{2[(c_j-a_j)-x]})_{x\to(c_j-a_j)^{-}}q_j^{*}(\bar{x},p)=-\frac{\kappa_j\sqrt{a_j}}{2}\sum_{m=1}^{M}(-1)^m C_{jm}(p) \quad (40)$$

for left-hand side crack tip and

$$(K_q^{*})_j=(\sqrt{2[x-(c_j+a_j)]})_{x\to(c_j+a_j)^{+}}q_j^{*}(\bar{x},p)=\frac{\kappa_j\sqrt{a_j}}{2}\sum_{m=1}^{M}C_{jm}(p) \quad (41)$$

for right-hand side crack tip.

After the solutions in the Laplace transform plane are obtained, inverse Laplace transform can be performed numerically using the method given by Miller and Guy [14]. This method has also been used by Jin and Noda [7] in thermoelastic fracture dynamics.

4 Thermal Stress Field

Solving the governing Eq. (5) by means of the Laplace transform technique, the displacements in each layer are given by

$$\begin{Bmatrix}u_J^{*}(\bar{x},\bar{y}_J,p)/i\\ \nu_J^{*}(\bar{x},\bar{y}_J,p)\end{Bmatrix}=\frac{h}{2\pi}\int_{-\infty}^{+\infty}[e_J]\begin{Bmatrix}A_{1J}\\B_{1J}\\A_{2J}\\B_{2J}\end{Bmatrix}e^{-is\bar{x}}ds+\frac{h}{2\pi}\int_{-\infty}^{+\infty}\frac{1}{s}[e_{0J}]\begin{Bmatrix}A_{0J}\\B_{0J}\end{Bmatrix}e^{-is\bar{x}}ds \quad (42)$$

The first and the second term on the right-hand side of Eq. (42) represent the homogeneous solution and the particular solution of Eq. (5), respectively; $A_{mJ}(s,p)$ and $B_{mJ}(s,p)$ are unknowns to be determined ($m=1,2$). $[e_J]$ is a 2×4 matrix of $\bar{y}_J$, while $[e_{0J}]$ is a 2×2 matrix of $\bar{y}_J$.

$$[e_J(\bar{y}_J,p,s)]=\begin{bmatrix}e^{-|s|\lambda_{1J}\bar{y}_J} & e^{|s|\lambda_{1J}\bar{y}_J} & e^{-|s|\lambda_{2J}\bar{y}_J} & e^{|s|\lambda_{2J}\bar{y}_J}\\ \zeta_{1J}e^{-|s|\lambda_{1J}\bar{y}_J} & -\zeta_{1J}e^{|s|\lambda_{1J}\bar{y}_J} & \zeta_{2J}e^{-|s|\lambda_{2J}\bar{y}_J} & -\zeta_{2J}e^{|s|\lambda_{2J}\bar{y}_J}\end{bmatrix} \quad (43)$$

$$[e_{0J}(\bar{y}_J,p,s)]=\begin{bmatrix}\zeta_{xJ}e^{-|s|\lambda_{0J}\bar{y}_J} & \zeta_{xJ}e^{|s|\lambda_{0J}\bar{y}_J}\\ -\mathrm{sgn}(s)\zeta_{yJ}e^{-|s|\lambda_{0J}\bar{y}_J} & \mathrm{sgn}(s)\zeta_{yJ}e^{|s|\lambda_{0J}\bar{y}_J}\end{bmatrix} \quad (44)$$

and λ_{iJ} ($i=1,2$) are the roots of the following characteristic equation:

$$\lambda_{iJ}^{4}-\left[\left(\frac{C_{11}C_{22}-2C_{12}C_{66}-C_{12}^{2}}{C_{22}C_{66}}\right)_J+\left(\frac{ph}{sC_{aJ}}\right)^{2}+\left(\frac{ph}{sC_{bJ}}\right)^{2}\right]\lambda_{iJ}^{2}+\left[\left(\frac{C_{11}}{C_{22}}\right)_J+\left(\frac{ph}{sC_{aJ}}\right)^{2}\right]\left[1+\left(\frac{ph}{sC_{bJ}}\right)^{2}\right]=0 \quad (45)$$

while $\zeta_{iJ}=\mathrm{sgn}(s)\eta_{iJ}$ ($i=1,2$), and

$$\eta_{iJ}=\frac{(C_{11})_J/(C_{66})_J+(ph/sC_{bJ})^2-\lambda_{iJ}^2}{\lambda_{iJ}(1+(C_{12})_J/(C_{66})_J)}. \tag{46}$$

In (44), ζ_{xJ} and ζ_{yJ} are the solutions of the following equations:

$$\left[\left(\frac{C_{11}}{C_{66}}\right)_J-\lambda_{0J}^2+\left(\frac{ph}{sC_{bJ}}\right)^2\right]\zeta_{xJ}+\left[\left(\frac{C_{12}}{C_{66}}\right)_J+1\right]\lambda_{0J}\zeta_{yJ}=\frac{\beta_{xJ}}{(C_{66})_J}$$

$$\left(\frac{C_{12}+C_{66}}{C_{22}}\right)_J\lambda_{0J}\zeta_{xJ}+\left[\lambda_{0J}^2-\left(\frac{C_{66}}{C_{22}}\right)_J+\left(\frac{ph}{sC_{aJ}}\right)^2\right]\zeta_{yJ}=\frac{\lambda_{0J}\beta_{yJ}}{(C_{22})_J}. \tag{47}$$

Substitution of Eq. (42) into constitutive Eqs. (4) gives the stress (σ_j^*,τ_j^*) at $(\bar{y}_J=\bar{h}_J)$ and $(\sigma_{j-1}^*,\tau_{j-1}^*)$ at $(\bar{y}_J=0)$,

$$\begin{Bmatrix}\sigma_j^*(\bar{x},p)\\ \tau_j^*(\bar{x},p)/i\\ \sigma_{j-1}^*(\bar{x},p)\\ \tau_{j-1}^*(\bar{x},p)/i\end{Bmatrix}=\frac{1}{2\pi}\int_{-\infty}^{+\infty}[K_{0J}]\begin{Bmatrix}A_{0J}\\ B_{0J}\end{Bmatrix}e^{-is\bar{x}}ds+\frac{1}{2\pi}\int_{-\infty}^{+\infty}s[K_J]\begin{Bmatrix}A_{1J}\\ B_{1J}\\ A_{2J}\\ B_{2J}\end{Bmatrix}e^{-is\bar{x}}ds, \tag{48}$$

where $[K_{0J}(s,p)]$ is a 4×2 matrix and $[K_J(s,p)]$ is a 4×4 matrix.

Defining matrices $\lfloor D_J^a(s,p)\rfloor$ and $\lfloor D_J^b(s,p)\rfloor$ of four rows and two columns each,

$$[D_J^a(s,p),D_J^b(s,p)]=[K_J(s,p)]^{-1}. \tag{49}$$

Applying the Fourier transform to (48) yields A_{1J}, B_{1J}, A_{2J}, and B_{2J} in terms of σ_j^*, τ_j^*, σ_{j-1}^*, and τ_{j-1}^*. By substituting A_{1J}, B_{1J}, A_{2J}, and B_{2J} back into (42), the displacements in each layer can be determined in terms of σ_j^*, τ_j^*, σ_{j-1}^*, and τ_{j-1}^*, namely,

$$\begin{Bmatrix}u_J^*(\bar{r},\bar{y}_J,p)/i\\ \nu_J^*(\bar{r},\bar{y}_J,p)\end{Bmatrix}=\frac{h}{2\pi}\int_{-\infty}^{+\infty}\frac{1}{s}([e_{1J}])\begin{Bmatrix}A_{0J}\\ B_{0J}\end{Bmatrix}e^{-is\bar{r}}ds+\frac{h}{2\pi}\int_{-\infty}^{+\infty}\frac{1}{s}[e_J]([D_J^a]\ \ [D_J^b])$$

$$\left\{\int_{-\infty}^{+\infty}\sigma_j^*e^{is\bar{x}}d\bar{x}\int_{-\infty}^{+\infty}\frac{\tau_j^*}{i}e^{is\bar{x}}d\bar{x}\times\int_{-\infty}^{+\infty}\sigma_{j-1}^*e^{is\bar{x}}d\bar{x}\int_{-\infty}^{+\infty}\frac{\tau_{j-1}^*}{i}e^{is\bar{x}}d\bar{x}\right\}^Te^{-is\bar{r}}ds \tag{50}$$

where

$$\lfloor e_{1J}(\bar{y}_J,s,p)\rfloor=[e_{0J}]-[e_J]([D_J^a]\ \ [D_J^b])[K_{0J}]. \tag{51}$$

Introducing the following dislocation density functions,

$$\phi_{xj}(\bar{x},p)=\partial u_{J+1}^*(\bar{x},\bar{y}_{J+1}=0,p)/\partial x-\partial u_J^*(\bar{x},\bar{y}_J=\bar{h}_J,p)/\partial x \tag{52}$$

$$\phi_{yj}(\bar{x},p)=\partial \nu_{J+1}^*(\bar{x},\bar{y}_{J+1}=0,p)/\partial x-\partial \nu_J^*(\bar{x},\bar{y}_J=\bar{h}_J,p)/\partial x. \tag{53}$$

Substituting (50) into the above equations gives

$$\begin{Bmatrix}\phi_{xj}(\bar{r},p)/i\\ \phi_{yj}(\bar{r},p)\end{Bmatrix}=\frac{1}{2\pi}\int_{-\infty}^{+\infty}([L]_j\ [M]_j\ [N]_j)e^{-is\bar{r}}ds\times\int_{-\infty}^{+\infty}\{i\sigma_{j-1}^*\ \ \tau_{j-1}^*\ \ i\sigma_j^*\ \ \tau_j^*\ \ i\sigma_{j+1}^*\ \ \tau_{j+1}^*\}^Te^{is\bar{x}}d\bar{x}-\frac{i}{2\pi}\int_{-\infty}^{+\infty}\begin{Bmatrix}\phi_{Tx}\\ \phi_{Ty}\end{Bmatrix}_j e^{-is\bar{r}}ds \tag{54}$$

where $[L(s,p)]_j$, $[M(s,p)]_j$, $[N(s,p)]_j$ are 2×2 matrices

$$[L]_j=[e_J(\bar{h}_J,p)][D_J^b(s,p)], \tag{55}$$

$$[N]_j=-[e_{J+1}(0,p)]\lfloor D_{J+1}^a(s,p)\rfloor, \tag{56}$$

$$[M]_j=[e_J(\bar{h}_J,p)][D_J^a(s,p)]-[e_{J+1}(0,p)][D_{J+1}^b(s,p)], \tag{57}$$

and

$$\begin{Bmatrix}\phi_{Tx}(s,p)\\ \phi_{Ty}(s,p)\end{Bmatrix}_j=[e_{1(J+1)}(0,s,p)]\begin{Bmatrix}A_{0(J+1)}(s,p)\\ B_{0(J+1)}(s,p)\end{Bmatrix}-[e_{1J}(\bar{h}_J,s,p)]\times\begin{Bmatrix}A_{0J}(s,p)\\ B_{0J}(s,p)\end{Bmatrix}. \tag{58}$$

Defining the following three vectors of $2(N-1)$ rows,

$$\{\Phi(s,p)\}=\left\{\int_{\bar{c}_1-\bar{a}_1}^{\bar{c}_1+\bar{a}_1}\frac{\phi_{x1}}{i}e^{is\bar{r}}d\bar{r},\ \int_{\bar{c}_1-\bar{a}_1}^{\bar{c}_1+\bar{a}_1}\phi_{y1}e^{is\bar{r}}d\bar{r}\cdots\int_{\bar{c}_{N-1}-\bar{a}_{N-1}}^{\bar{c}_{N-1}+\bar{a}_{N-1}}\frac{\phi_{x(N-1)}}{i}e^{is\bar{r}}d\bar{r},\ \int_{\bar{c}_{N-1}-\bar{a}_{N-1}}^{\bar{c}_{N-1}+\bar{a}_{N-1}}\phi_{y(N-1)}e^{is\bar{r}}d\bar{r}\right\}^T, \tag{59}$$

$$\{\Sigma(\bar{x},p)\}=\{i\sigma_1^*\ \ \tau_1^*\cdots i\sigma_{N-1}^*\ \ \tau_{N-1}^*\}^T, \tag{60}$$

$$\{\Phi_r(s,p)\}=\{(\phi_{Tx})_1\ \ (\phi_{Ty})_1\cdots(\phi_{Tx})_{N-1}\ \ (\phi_{Ty})_{N-1}\}^T, \tag{61}$$

and utilizing Fourier transform to (54) yields

$$[D]\int_{-\infty}^{+\infty}\{\Sigma\}e^{is\bar{x}}d\bar{x}=\{\Phi\}+i\{\Phi_T\}-\{\Phi_a\}, \tag{62}$$

where matrix $[D(s,p)]$ has the same form as (30), and $\{\Phi_a(s,p)\}$ is a vector of $2(N-1)$ rows, with the first two elements and the last two elements the only nonzero elements. These elements are related to the boundary conditions by

$$\begin{Bmatrix}\Phi_{a1}(s,p)\\ \Phi_{a2}(s,p)\end{Bmatrix}=L_1(s,p)\int_{-\infty}^{+\infty}\begin{Bmatrix}i\sigma_{00}^*(\bar{r},p)\\ \tau_{00}^*(\bar{r},p)\end{Bmatrix}e^{is\bar{r}}d\bar{r} \tag{63}$$

$$\begin{Bmatrix}\Phi_{a(2N-3)}(s,p)\\ \Phi_{a(2N-2)}(s,p)\end{Bmatrix}=N_{N-1}(s,p)\int_{-\infty}^{+\infty}\begin{Bmatrix}i\sigma_{0N}^*(\bar{r},p)\\ \tau_{0N}^*(\bar{r},p)\end{Bmatrix}e^{is\bar{r}}d\bar{r}. \tag{64}$$

Defining the inverse of matrix $[D(s,p)]$ by $[K(s,p)]$, referring to $K_m^n(s,p)$, which denotes the mth row and the nth column element in matrix $[K(s,p)]$, and applying the inverse Fourier transform to (62) yields

$$\begin{Bmatrix} i\sigma_j^*(\bar{x},p) \\ \tau_j^*(\bar{x},p) \end{Bmatrix}$$

$$= \frac{1}{2\pi}\sum_{k=1}^{N-1}\int_{\bar{c}_k-\bar{a}_k}^{\bar{c}_k+\bar{a}_k}\left(\int_{-\infty}^{+\infty}\begin{bmatrix} K_{(2j-1)}^{(2k-1)} & K_{(2j-1)}^{(2k)} \\ K_{(2j)}^{(2k-1)} & K_{(2j)}^{(2k)} \end{bmatrix} e^{is(\bar{r}-\bar{x})}ds\right)$$

$$\times\begin{Bmatrix} \phi_{xk}/i \\ \phi_{yk} \end{Bmatrix} d\bar{r} + \frac{i}{2\pi}\sum_{k=1}^{N-1}\int_{-\infty}^{+\infty}\begin{bmatrix} K_{(2j-1)}^{(2k-1)} & K_{(2j-1)}^{(2k)} \\ K_{(2j)}^{(2k-1)} & K_{(2j)}^{(2k)} \end{bmatrix}$$

$$\times\begin{Bmatrix} \phi_{Tx} \\ \phi_{Ty} \end{Bmatrix}_k e^{-is\bar{x}}ds - \begin{Bmatrix} i\sigma_j^*(\bar{x},p) \\ \tau_j^*(\bar{x},p) \end{Bmatrix}_a \tag{65}$$

where

$$\begin{Bmatrix} i\sigma_j^*(\bar{x},p) \\ \tau_j^*(\bar{x},p) \end{Bmatrix}_a = \frac{1}{2\pi}\int_{-\infty}^{+\infty}\left(\begin{bmatrix} K_{2j-1}^1 & K_{2j-1}^2 \\ K_{2j}^1 & K_{2j}^2 \end{bmatrix}\begin{Bmatrix} \Phi_{a1} \\ \Phi_{a2} \end{Bmatrix}\right.$$

$$\left. + \begin{bmatrix} K_{2j-1}^{2N-3} & K_{2j-1}^{2N-2} \\ K_{2j}^{2N-3} & K_{2j}^{2N-2} \end{bmatrix}\begin{Bmatrix} \Phi_{a(2N-3)} \\ \Phi_{a(2N-2)} \end{Bmatrix}^T\right) e^{-is\bar{x}}ds. \tag{66}$$

Equation (65) is the relationship between interfacial stresses and dislocation density functions, and there are $2(N-1)$ equations in it. For those interfaces with no crack, the dislocation density function is zero, so (65) is independent of the layers number N. The number of singular integral equations in (65) needed to be solved is twice the crack number.

We now analyze the asymptotic behavior of matrix $K(s,p)$. Since the dislocation density function for the interface with no crack is zero, only the elements related to the cracked interfaces need to be analyzed. If material properties are not continuous along the crack interface, the local stress behavior would be of an oscillatory nature. This would yield interpenetrating of material points of the crack surface ([15]). Such a condition cannot be realized physically. Hence, consider only the special case of continuously varying material properties along the cracked interface. As $|s|\to\infty$, the only nonzero elements in $[K(s,p)]$ are

$$K_{(2j-1)}^{(2j)}(\infty,p) = \lim_{s\to\pm\infty} K_{(2j-1)}^{(2j)}(s,p) = \mathrm{sgn}(s)(G_y)_j/2 \tag{67}$$

$$K_{(2j)}^{(2j-1)}(\infty,p) = \lim_{s\to\pm\infty} K_{(2j)}^{(2j-1)}(s,p) = \mathrm{sgn}(s)(G_x)_j/2 \tag{68}$$

where $(G_x)_j$ and $(G_y)_j$ are functions of material elastic constants.

By defining $\bar{k}_m^n(s,p) = k_m^n(s,p) - k_m^n(\infty,p)$, Eq. (65) may now be written as follows:

$$\begin{Bmatrix} i\sigma_j^*(\bar{x},p) \\ \tau_j^*(\bar{x},p) \end{Bmatrix} + \begin{Bmatrix} i\sigma_j^*(\bar{x},p) \\ \tau_j^*(\bar{x},p) \end{Bmatrix}_a$$

$$= \frac{i}{2\pi}\sum_{k=1}^{N-1}\int_{-\infty}^{+\infty}\begin{bmatrix} K_{(2j-1)}^{(2k-1)} & K_{(2j-1)}^{(2k)} \\ K_{(2j)}^{(2k-1)} & K_{(2j)}^{(2k)} \end{bmatrix}\begin{Bmatrix} \phi_{Tx} \\ \phi_{Ty} \end{Bmatrix}_k e^{-is\bar{x}}ds$$

$$+ \frac{1}{2\pi}\sum_{k=1}^{N-1}\int_{\bar{c}_k-\bar{a}_k}^{\bar{c}_k+\bar{a}_k}\left(\int_{-\infty}^{+\infty}\begin{bmatrix} \bar{k}_{(2j-1)}^{(2k-1)} & \bar{k}_{(2j-1)}^{(2k)} \\ \bar{k}_{(2j)}^{(2k-1)} & \bar{k}_{(2j)}^{(2k)} \end{bmatrix} e^{is(\bar{r}-\bar{x})}ds\right)$$

$$\times\begin{Bmatrix} \phi_{xk}/i \\ \phi_{yk} \end{Bmatrix} d\bar{r} + \begin{Bmatrix} \dfrac{i(G_y)_j}{2\pi}\displaystyle\int_{\bar{c}_j-\bar{a}_j}^{\bar{c}_j+\bar{a}_j}\frac{\phi_{yj}}{\bar{r}-\bar{x}}d\bar{r} \\ \dfrac{(G_x)_j}{2\pi}\displaystyle\int_{\bar{c}_j-\bar{a}_j}^{\bar{c}_j+\bar{a}_j}\frac{\phi_{xj}}{\bar{r}-\bar{x}}d\bar{r} \end{Bmatrix} \tag{69}$$

The solution of Eq. (69) can be expressed by the following formulas:

$$\phi_{xj}(\overline{a_j r_j}+\bar{c}_j,p) = \sum_{m=1}^{\infty} C_{jm}^x(p)T_m(\bar{r}_j)/\sqrt{1-\bar{r}_j^2} \tag{70}$$

$$\phi_{yj}(\overline{a_j r_j}+\bar{c}_j,p) = \sum_{m=1}^{\infty} C_{jm}^y(p)T_m(\bar{r}_j)/\sqrt{1-\bar{r}_j^2} \tag{71}$$

where C_{jm}^x and C_{jm}^y are the unknowns to be evaluated. The displacement difference between the upper surface and the lower surface of the jth crack can be evaluated as

$$(u_{J+1}^{J*}(\bar{x})\,v_{J+1}^{J*}(\bar{x})) = -a_j\sum_{m=1}^{M}(C_{jm}^x C_{jm}^y)\frac{\sin(m\,ar\cos\bar{x}_j)}{m}. \tag{72}$$

Weighted residuals methods can be used to evaluate (C_{jm}^x, C_{jm}^y) from the singular integral Eq. (69). The mode I and mode II stress intensity factors can be calculated as

$$(K_1^*, K_{\mathrm{II}}^*)_j = \frac{\sqrt{a_j}}{2}\sum_{m=1}^{M}(-1)^m((G_y)_j C_{jm}^y,\quad (G_x)_j C_{jm}^x) \tag{73}$$

for a left-hand side crack-tip and

$$(K_1^*, K_{\mathrm{II}}^*)_j = -\frac{\sqrt{a_j}}{2}\sum_{m=1}^{M}((G_y)_j C_{jm}^y,\quad (G_x)_j C_{jm}^x) \tag{74}$$

for a right-hand side crack-tip.

5 Numerical Example

For the purpose of numerical illustration, a metal/ceramic joint specimen with a functionally graded material interlayer is taken into account. The geometrical configuration and the coordinate system are shown in Fig. 3. Assume that cracks are normal to the thickness of the plate, and the two cracks lie on the interfaces. The temperature in the lower surface of the joint is kept zero and a sudden uniform temperature change T_0 is applied on the upper boundary of the joint. The functionally graded material is made of Ni and TiC. The material properties, elastic modulus E, Poisson's ratio v, coefficient of thermal expansion α, density ρ, thermal conductivity κ, and specific heat c, are, respectively, $E_m = 200$ Gpa, $\nu_m = 0.31$, $\alpha_m = 18\times10^{-6}/°\mathrm{C}$, $\rho_m = 6825\ \mathrm{Kg/m^3}$, $k_m = 54\ \mathrm{W/m°C}$, $c_m = 595\ \mathrm{J/Kg°C}$, $E_c = 460$ Gpa, $\nu_c = 0.34$, $\alpha_c = 7.4\times10^{-6}/°\mathrm{C}$, $\rho_c = 4127\ \mathrm{Kg/m^3}$, $k_c = 27\ \mathrm{W/m°C}$, $c_c = 682\ \mathrm{J/Kg°C}$, in which the subscript m and c signify metal and ceramic, respectively. The functionally graded material interlayer is pure metal at the bottom and pure ceramic at the top. At any position y in the functionally graded material interlayer, the local volume fraction of metal is assumed to be $V_m(y)$ which obeys a power-law type relation $(y/h_g)^g$, where g is known as the gradient exponent. To relate local volume fraction to the effect properties of the functionally graded material, the micromechanical models must be used. According to the criteria given by Zuiker [13] the three-phase model or the so-called generalized self-consistent model ([16,17]) is better than other models. Bao and Wang [18] used the three-phase model to determine approximately the effective properties of a functionally graded material coating. The three-phase model was also used by Jin and Batra [11,19] to determine the volume fraction of constituents in the functionally graded material. Assuming that the functionally graded material is obtained by dispersing ceramic particulates in metal matrix, we use three-phase models to determine effective shear modulus and thermal conductivity. Composite spheres model ([16]) is utilized to determine effective bulk modulus and coefficient of thermal

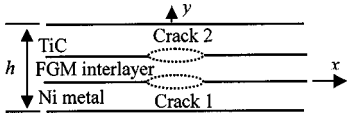

Fig. 3 A metal-ceramic joint with functionally graded interlayer

expansion, while the effective density and the specific heat of the functionally graded material is evaluated by rule-of-mixture.

We treat the graded regions as a series of perfectly bonded composite layers (say, N layers), each layer being assigned slightly different material properties. The related integrals are evaluated by using the Gauss-Chebyshev formulas. The number of integral points is selected to be large enough for obtaining the solutions to the defined problem with a required degree of accuracy. Assume that the thickness of the ceramic base, metal base, functionally graded material interlayer, and half-crack length are taken to be equal. For a fixed gradient exponent $g=1$, the influences of N on thermal flux intensity factor and thermal stress intensity factors are depicted in Figs. 4–6, respectively. It is found that at any time t thermal flux intensity factors and thermal stress intensity factors tend to converge to steady values as N becomes sufficiently large, this indicates that we can use a laminated composite plate model to simulate material nonhomogeneity in the thickness direction. The result implies that we can divide the functionally graded material into a large number of layers to simulate material gradient and the present model is an efficient tool for the fracture analysis of composite materials with properties varying in the thickness direction.

For a fixed crack length $2a=0.5h$ and $g=1$, the thermal stress intensity factors for different graded layer thickness hg are drawn in Fig. 7 and 8. Due to the interaction among different cracks, influences of graded layer thickness on stress intensity factors are very complicated. It appears that as the thickness of a functionally graded interlayer decreases, the mode II stress intensity factors will decrease. It also seems that there exists an optimized interlayer thickness which relates to the minimum mode I stress intensity factors. Furthermore, it is found that the influence of interlayer thickness is more significant for peak stress intensity factors than for steady stress intensity factors. In all cases, stress intensity factors for crack 2 are larger than for crack 1. The results indicate that the ceramic side is more likely cracking under thermal load.

In the foregoing analysis, we have treated the functionally graded interlayer as a number of thin layers. By making use of this laminate model, almost all the analytical models containing cracks perpendicular to the thickness direction in which material properties varying, can be analyzed theoretically for the case of transient state or a steady state, either under mechanical loading or under thermal loading. The existing analytical models in which the material properties were specifically selected, such as a nonhomogeneous half-plane ([20]) two dissimilar homogeneous half-planes bonded by a thin layer of nonhomogeneous material ([21]) two bonded half-planes with one plane being homogeneous and the other nonhomogeneous ([22]) a nonhomogeneous medium bonded to a rigid subspace ([23]), a nonhomogeneous half-plane under steady thermal loading ([2]) a strip of a functionally graded material under steady thermal loading ([4]), and a semi-infinite plate of a functionally graded material under transient thermal loading ([7]) can also be treated by utilizing the present method. For a comparison, a pure metal medium shown in Fig. 9 was analyzed. The dimension a is kept fixed and the normalized thermal stress intensity factors $(\overline{K}_{\mathrm{I}},\overline{K}_{\mathrm{II}})=(K_{\mathrm{I}},K_{\mathrm{II}})/(E_s\alpha_s T_0\sqrt{a})$ are depicted in Fig. 10 for different d values. It should be noted that

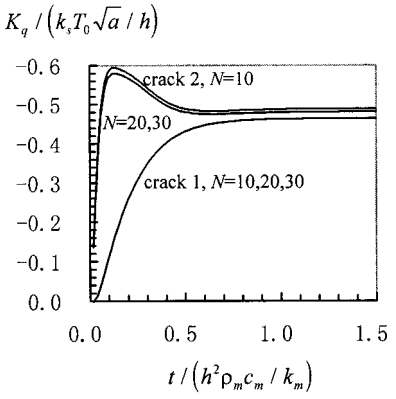

Fig. 4 Influences of divided layers number N on thermal flux intensity factors (the subscript m signify metal)

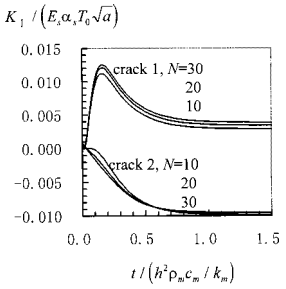

Fig. 5 Influences of divided layers number N on mode I thermal stress intensity factors

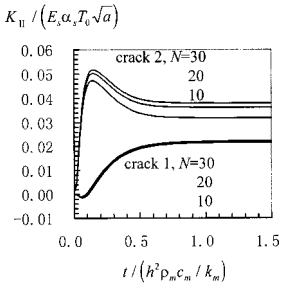

Fig. 6 Influences of divided layers number N on mode II thermal stress intensity factors

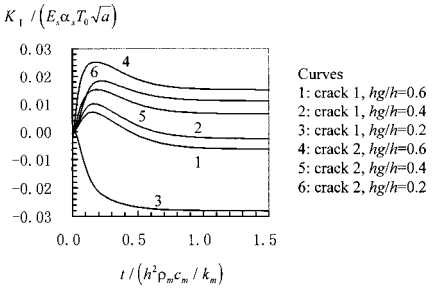

Fig. 7 Influences of functionally graded material interlayer thickness on mode I thermal stress intensity factors

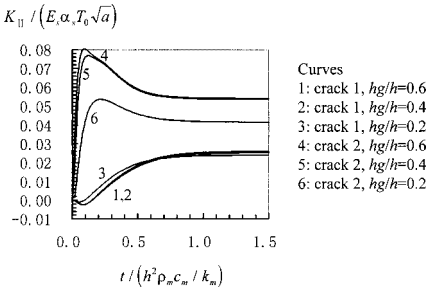

Fig. 8 Influences of functionally graded material interlayer thickness on mode II thermal stress intensity factors

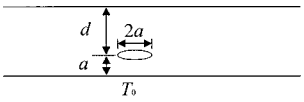

Fig. 9 A cracked homogeneous medium

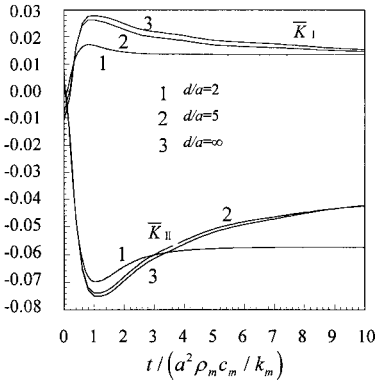

Fig. 10 Variation of thermal stress intensity factors with time for different crack position

Table 1 The convergence of results with respect to *M*

	peak $\overline{K_I}$	steady $\overline{K_I}$	peak $\overline{K_{II}}$	steady $\overline{K_{II}}$
$M=4$	0.0327	0.0270	−0.0761	−0.0522
$M=6$	0.0325	0.0192	−0.0760	−0.0439
$M=8$	0.0324	0.0144	−0.0759	−0.0361
$M=10$	0.0322	0.0125	−0.0758	−0.0332
$M\geqslant 12$	0.0322	0.0122	−0.0758	−0.0328

Noda and Jin [4] have investigated this crack configuration for steady thermal loading. Matsunaga and Noda [24] have studied the penny-shaped crack problem in an infinite plate under transient thermal loading. When *d* trends to be infinite, the present solutions agree with those by Jin and Noda [7] and Tsuji et al. [25]. In the numerical procedure, we have truncated the infinite series in (37) to *M* terms in (38). To validate the numerical procedure, the peak stress intensity factor and the steady stress intensity factor for the infinite *d* value are tabulated in Table 1. It is clear that as *M* increases the result converges to some steady values that have been reported by Jin and Noda [7] and Tsuji [25].

6 Conclusions

In this paper we proposed an algorithm to investigate a dynamic fracture mechanics problem for nonhomogeneous materials under nonuniform heating. Transient and steady-state thermal flux intensity factors and thermal stress intensity factors are calculated. Numerical examples are provided to examine the feasibility of the proposed method by analyzing the response of a joint to the nonuniform transient temperature distribution over the system.

For a nonhomogeneous medium, the governing equations for the temperature field and the associated thermoelastic field become varying coefficients because of the nonuniform materials constants. For these equations, it is very difficult to obtain the analytical solutions in general cases. The laminated composite model has been proved to be efficiency adapted to almost all the analytical models composed of nonhomogeneous materials in the absence of a crack (see, for examples, [26–32]). The results given in this paper suggest that the laminated composite model can also be used in the analysis of functionally graded materials composites with cracks perpendicular to the gradient direction.

The algorithm given above can be applied to steady-state or transient mechanical loading with the inertia terms taken into account. Differing from the existing works reported in the literature, the present method can be used for arbitrarily varying material properties through the thickness direction and the number of cracks can be larger than one.

Acknowledgment

The authors would like to give their grateful acknowledgment to the anonymous reviewers and Professor W. J. Drugan for their valuable comments on this paper. The work of Dr. B. L. Wang was partially supported by the Post-doctor Research Fund of China and the Failure Mechanics Lab Fund of the State Education Commission of China.

References

[1] Saito, M., and Takahashi, H., 1990, ''Development of Small Punch Test Procedure for FGM Fabrication,'' *FGM-90: Proc. First Int. Symposium on Functionally Gradient Materials*, M. Yamanouchi et al., eds., FGM Forum, Tokyo, Japan, pp. 297–305.
[2] Jin, Z. H., and Noda, N., 1993, ''Minimization of Thermal Stress Intensity Factors for a Crack in a Metal-Ceramic Mixture,'' *Ceramics Transactions, Functionally Gradient Materials*, Vol. 34, J. B. Holt et al., eds., The American Ceramic Society, OH.
[3] Jin, Z. H., and Noda, N., 1993, ''An Internal Crack Parallel to the Boundary of a Nonhomogeneous Half Plane Under Thermal Loading,'' Int. J. Eng. Sci., **31**, pp. 793–806.
[4] Noda, N., and Jin, Z. H., 1993, ''Thermal Stress Intensity Factors for a Crack in a Functionally Gradient Material,'' Int. J. Solids Struct., **30**, pp. 1039–1056.
[5] Noda, N., and Jin, Z. H., 1993, ''Steady Thermal Stresses in an Infinite Non-Homogeneous Elastic Solid Containing a Crack,'' J. Thermal Stresses, **16**, pp. 181–197.
[6] Noda, N., and Jin, Z. H., 1994, ''A Crack in a Functionally Gradient Material Under Thermal Shock,'' Arch. Appl. Mech, **64**, pp. 99–110.
[7] Jin, Z. H., and Noda, N., 1994, ''Transient Thermal Stress Intensity Factors for a Crack in a Semi-Infinite Plate of a Functionally Gradient Material,'' Int. J. Solids Struct., **31**, pp. 203–218.
[8] Erdogan, F., and Wu, B. H., 1996, ''Crack Problem in FGM Layers Under Thermal Stresses,'' J. Thermal Stresses, **19**, pp. 237–265.
[9] Jin, Z. H., and Noda, N., 1994, ''Edge Crack in a Nonhomogeneous Half Plane Under Thermal Loading,'' J. Thermal Stresses, **17**, pp. 591–599.
[10] Nemat-Alla, M., and Noda, N., 1996, ''Study of an Edge Crack Problem in a Semi-Infinite Functionally Graded Medium with Two Dimensionally Non-Homogeneous Coefficients of Thermal Expansion Under Thermal Loading,'' J. Thermal Stresses, **19**, pp. 863–888.
[11] Jin, Z. H., and Batra, R. C., 1996, ''Stress Intensity Relaxation at the Tip of an Edge Crack in a Functionally Graded Material Subjected to a Thermal Shock,'' J. Thermal Stresses, **19**, pp. 317–339.
[12] Noda, N., 1997, ''Thermal Stress Intensity Factor for Functionally Gradient Plate With an Edge Crack,'' J. Thermal Stresses, **20**, pp. 373–387.
[13] Zuiker, J. R., 1995, ''Functionally Graded Materials: Choice of Micromechanics Model and Limitations in Property Variation,'' Composites Eng., **5**, pp. 807–819.
[14] Miller, M. K., and Guy, W. T., 1966, ''Numerical Inversion of the Laplace Transform by Use of Jacobi Polynomials,'' SIAM (Soc. Ind. Appl. Math.) J. Numer. Anal., **3**, pp. 624–635.
[15] Williams, M. L., 1959, ''The Stress Around a Fault of Crack in Dissimilar Media,'' Bull. Seismol. Soc. Am., **49**, pp. 199–204.
[16] Christensen, R. M., 1979, *Mechanics of Composite Materials*, John Wiley and Sons, New York.
[17] Christensen, R. M., and Lo, K. H., 1979, ''Solutions for Effective Shear Properties in Three Phase Sphere and Cylinder Models,'' J. Mech. Phys. Solids, **27**, pp. 315–330.
[18] Bao, G., and Wang, L., 1995, ''Multiple Cracking in Functionally Graded Ceramic/Metal Coatings,'' Int. J. Solids Struct., **32**, pp. 2853–2871.
[19] Jin, Z. H., and Batra, R. C., 1996, ''Some Basic Fracture Mechanics Concepts in Functionally Graded Materials,'' J. Mech. Phys. Solids, **44**, pp. 1221–1235.
[20] Delale, F., and Erdogan, F., 1983, ''The Crack Problem for a Nonhomogeneous Plane,'' ASME J. Appl. Mech., **50**, pp. 609–613.
[21] Delale, F., and Erdogan, F., 1988, ''On the Mechanical Modeling of the Interfacial Region in Bonded Half-Planes,'' ASME J. Appl. Mech., **55**, pp. 317–324.
[22] Delale, F., and Erdogan, F., 1988, ''Interface Crack in a Nonhomogeneous Elastic Medium,'' Int. J. Eng. Sci., **26**, pp. 559–568.
[23] Erdogan, F., and Ozturk, M., 1992, ''Diffusion Problems in Bonded Nonhomogeneous Materials With an Interface Cut,'' Int. J. Eng. Sci., **30**, pp. 1507–1523.
[24] Matsunaga, Y., and Noda, N., 1996, ''Transient Thermoelastic Problem for a Infinite Plate Containing a Penny-Shaped Crack at an Arbitrary Position,'' J. Thermal Stresses, **19**, pp. 379–394.
[25] Tsuji, T., et al., 1986, ''Transient Thermal Stresses in a Half Plane With a

Crack Parallel to the Surface,'' Bull. JSME, **29**, pp. 343–347.
[26] Kawamura, R., and Tanigawa, Y., 1995, ''Nonlinear Thermal Bending Problem of Nonhomogeneous Beam Due to Unsteady Thermal Supply,'' Trans. Jpn. Soc. Mech. Eng., Ser. A, **61**, pp. 777–783.
[27] Ootao, Y., Akai, T., and Tanigawa, Y., 1993, ''Three-Dimensional Transient Thermal Stress Analysis of Nonhomogeneous Hollow Circular Cylinder,'' Trans. Jpn. Soc. Mech. Eng., Ser. A, **59**, pp. 1684–1690.
[28] Ootao, Y., and Tanigawa, Y., 1994, ''Three-Dimensional Transient Thermal Stress Analysis of a Nonhomogeneous Hollow Sphere with Respect to Rotating Heating Source,'' Trans. Jpn. Soc. Mech. Eng., Ser. A, **60**, pp. 2273–2279.
[29] Ootao, Y., Tanigawa, Y., Kasai, T., and Nakanishi, N., 1992, ''Inverse Problem Analysis of Transient Thermal Stresses in a Nonhomogeneous Solid Circular Cylinder Due to Asymmetric Heating,'' Trans. Jpn. Soc. Mech. Eng., Ser. A, **58**, pp. 567–573.
[30] Tanigawa, Y., Akai, T., Kawamura, R., and Oka, N., 1996, ''Transient Heat Conduction and Thermal Stresses Problems of a Nonhomogeneous Plate with Temperature Dependent Material Properties,'' J. Thermal Stresses, **19**, pp. 77–102.
[31] Tanigawa, Y., Matsumoto, M., and Akai, T., 1996, ''Optimization Problem of Material Composition for Nonhomogeneous Plate to Minimize Thermal Stresses When Subjected to Unsteady Heat Supply,'' Trans. Jpn. Soc. Mech. Eng., Ser. A, **62**, pp. 115–122.
[32] Tanigawa, Y., Oka, N., Akai, T., and Kawamura, R., 1996, ''One-Dimensional Transient Thermal Stress Problem for Nonhomogeneous Hollow Circular Cylinder and Its Optimization,'' Trans. Jpn. Soc. Mech. Eng., Ser. A, **62**, pp. 128–136.

An Iterative Method for Solving Elasticity Problems for Composite Laminates

A. Makeev
Post Doctoral Fellow

E. A. Armanios
Professor

School of Aerospace Engineering,
Georgia Institute of Technology,
Atlanta, GA 30332-0150

An iterative method for approximate analytical solution of elasticity problems in composite laminates is presented. The stress analysis is performed for laminates in the three-dimensional strain state independent of the longitudinal direction. Predictions of the method are compared with results from existing analytical and numerical models. Simple and accurate approximations for stresses are obtained. [S0021-8936(00)02001-8]

Introduction

Analysis of practical laminated composite structures often requires three-dimensional elasticity modeling. Since analytical solutions are available for few boundary value problems, numerical modeling is generally the only option. In some cases, the cost of large numerical simulations results in a need for developing approximate analytical elasticity solutions. One example is the design of laminated composite flexbeams in helicopter rotor systems. These symmetric laminates with a thick rectangular cross section entail a large number of candidate stacking sequences. Interlaminar stresses must be accurately determined to gain an understanding of the influence of the primary design variables such as ply orientation and stacking sequence on failure under tension, torsion, and bending loading.

The distribution of the interlaminar stresses in flexbeams is needed for selecting candidate configurations at the preliminary design stage. To this end, a cross-sectional finite element stress analysis was applied by Sen and Fish [1,2] to determine the stresses in glass-epoxy 32-ply flexbeam laminates under torsion and combined tension-torsion loads. The largest mesh in the finite element analysis consisted of 7144 elements with 21,945 degrees-of-freedom. The cost associated with such a finite element modeling makes it highly inefficient for analyzing every candidate lay-up at the preliminary design stage. On the other hand, existing engineering laminated plate or beam theories, which would allow for a closed-form solution, are based on assumptions restricting the strain or stress state and, therefore, are not appropriate for a reliable prediction of all stress components such as the peel stress.

The need for a simple and accurate analytical modeling of the three-dimensional stress state independent of the longitudinal direction is addressed in this work. An approximate elasticity solution, which provides rigorous trend information for all stress components in laminated composites, is developed.

The interlaminar stresses in symmetric laminates with off-axis plies were first evaluated by Pipes and Pagano [3] for the case of uniform axial extension by applying a finite difference technique to solve the Navier equations of elasticity for off-axis plies. A number of finite element models were subsequently developed. Brief reviews are provided in Wang and Choi [4,5] and Sen and Fish [1]. Wang and Choi [4,5] assumed the form of the stress functions in order to analytically solve the compatibility equations for two adjacent off-axis plies. A singular stress field at the free edge was obtained. While this solution provides a rigorous prediction of the free-edge interlaminar stresses, its mathematical complexity makes it unsuitable for practical multilayer laminates. Other existing analytical approaches are based on *ad hoc* assumptions regarding the stress or strain fields in addition to the classical two-dimensional formulation of the three-dimensional strain state.

An iterative method for one-term approximate solution of partial differential equations was developed by Makeev [6]. The method was applied to several boundary value problems and its predictions were in good agreement with exact solutions. The method was also used for predicting interlaminar stresses in symmetric laminates under axial extension and torsion in Makeev and Armanios [7]. One and two-term approximations for the stress functions were obtained. A close agreement was established with the numerical results of Pipes and Pagano [3], Sen and Fish [2], and the analytical predictions of Wang and Choi [4,5]. The method is simple and, therefore, ideally suited for parametric design studies where a large number of candidate configurations need to be evaluated quickly and economically.

In this work, the approximate model for the classical elasticity formulation [8] for laminated composites in the three-dimensional state of strain dependent on two coordinates is developed. A detailed solution of Poisson's equation for the case of pure torsion of an orthotropic beam with a rectangular cross section is presented first in order to illustrate the iterative procedure. This is followed by a general formulation of the method for composite laminates. Finally, the method is applied to laminates subjected to uniform extension and torsion.

Analysis

Solution of Poisson's Equation. In this section, details of the iterative procedure are illustrated for the case of pure torsion of an orthotropic beam with a rectangular cross section shown in Fig. 1. The stress function for this problem is governed by Poisson's equation

$$\frac{1}{G_{23}}\Psi_{,xx}+\frac{1}{G_{13}}\Psi_{,yy}=-2 \tag{1}$$

where G_{23} and G_{13} are the shear moduli in the (y,z) and (x,z)-planes, respectively, and the partial derivatives are denoted by subscript commas. The function Ψ is zero at the edges, $x=\pm b$ and $y=\pm h$. Construct a weak form of Eq. (1) as follows:

$$\int_{-h}^{h} dy \int_{-b}^{b}\left(\frac{1}{G_{23}}\Psi_{,xx}+\frac{1}{G_{13}}\Psi_{,yy}+2\right)\delta\Psi\, dx=0. \tag{2}$$

Select the following first approximation for Ψ:

$$\Psi^{(1)}=\sum_{i=1}^{N} f_i^{(1)}(x)\varphi_i^{(1)}(y)=\sum_{i=1}^{N}\cos\left([2i-1]\frac{\pi}{2}\frac{x}{b}\right)\varphi_i^{(1)}(y). \tag{3}$$

Contributed by the Applied Mechanics Division of THE AMERICAN SOCIETY OF MECHANICAL ENGINEERS for publication in the JOURNAL OF APPLIED MECHANICS. Manuscript received by teh ASME Applied Mechanics Division, July 15, 1998; final revision, May 18, 1999. Associate Technical Editor: J. W. Ju. Discussion on the paper should be addressed to the Technical Editor, Professor Lewis T. Wheeler, Department of Mechanical Engineering, University of Houston, Houston, TX 77204-4792, and will be accepted until four months after final publication of the paper itself in the JOURNAL OF APPLIED MECHANICS.

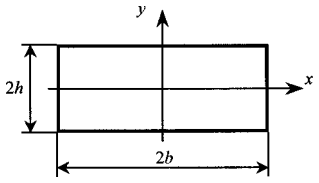

Fig. 1 Coordinate system and dimensions

The functions $f_i^{(1)}(x)$ satisfy the boundary conditions at $x=\pm b$. Substitute Eq. (3) into the weak form (2) and integrate with respect to x to obtain the system of ordinary differential equations for $\varphi_i^{(1)}(y)$

$$[a_{ij}^{(1)}]\left\{\frac{d^2\varphi_j^{(1)}}{dy^2}\right\}+[b_{ij}^{(1)}]\{\varphi_j^{(1)}\}=-2\{c_i^{(1)}\} \tag{4}$$

where

$$a_{ij}^{(1)}=\frac{1}{G_{13}}\int_{-b}^{b} f_i^{(1)}f_j^{(1)}dx=\frac{1}{G_{13}}b\,\delta_{ij}$$

$$b_{ij}^{(1)}=\frac{1}{G_{23}}\int_{-b}^{b} f_i^{(1)}\frac{d^2f_j^{(1)}}{dx^2}dx=-\frac{1}{G_{23}}\left([2i-1]\frac{\pi}{2}\frac{1}{b}\right)^2 b\,\delta_{ij} \tag{5}$$

$$c_i^{(1)}=\int_{-b}^{b} f_i^{(1)}dx=\frac{4(-1)^{i-1}}{\pi(2i-1)}b$$

and δ_{ij} is the Kronecker delta. Solve system (4) using the free-edge boundary conditions $\varphi_i^{(1)}(\pm h)=0$. The result is

$$\varphi_i^{(1)}=\frac{32}{\pi^3}b^2G_{23}\frac{(-1)^{i-1}}{(2i-1)^3}\left[1-\frac{\cosh\left(\sqrt{\frac{G_{13}}{G_{23}}}\frac{h}{b}[2i-1]\frac{\pi}{2}\frac{y}{h}\right)}{\cosh\left(\sqrt{\frac{G_{13}}{G_{23}}}\frac{h}{b}[2i-1]\frac{\pi}{2}\right)}\right]. \tag{6}$$

This completes the first approximation which is due to Kantorovich and is referred to as a Combined Method in Timoshenko [9]. It is worth noting that the particular choice of functions $f_i^{(1)}(x)$ in Eq. (3) results in the exact solution of Eq. (1) as N tends to infinity

$$\Psi=\frac{32}{\pi^3}b^2G_{23}\sum_{i=1}^{\infty}\frac{(-1)^{i-1}}{(2i-1)^3}\cos\left([2i-1]\frac{\pi}{2}\frac{x}{b}\right)$$

$$\times\left[1-\frac{\cosh\left(\sqrt{\frac{G_{13}}{G_{23}}}\frac{h}{b}[2i-1]\frac{\pi}{2}\frac{y}{h}\right)}{\cosh\left(\sqrt{\frac{G_{13}}{G_{23}}}\frac{h}{b}[2i-1]\frac{\pi}{2}\right)}\right]. \tag{7}$$

The second and higher approximations of the stress function Ψ have the same form as the first approximation (3) with the same number of terms N in the series. The second approximation $\Psi^{(2)}$ uses the functions $\varphi_i^{(1)}(y)$ obtained from the first iteration

$$\Psi^{(2)}=\sum_{i=1}^{N} f_i^{(2)}(x)\varphi_i^{(1)}(y). \tag{8}$$

Substitute Eq. (8) into Eq. (2) and integrate with respect to y to obtain the following system of ordinary differential equations for $f_i^{(2)}(x)$:

$$[a_{ij}^{(2)}]\left\{\frac{d^2f_i^{(2)}}{dx^2}\right\}+[b_{ij}^{(2)}]\{f_j^{(2)}\}=-2\{c_i^{(2)}\} \tag{9}$$

where

Table 1 Properties of S2/F584 glass-epoxy material system [2]

$E_{33}=44.13$ GPa
$E_{11}=E_{22}=12.41$ GPa
$G_{13}=G_{23}=4.46$ GPa
$G_{12}=4.14$ GPa
$\nu_{31}=\nu_{32}=0.29$
$\nu_{12}=0.5$

$$a_{ij}^{(2)}=\frac{1}{G_{23}}\int_{-h}^{h}\varphi_i^{(1)}\varphi_j^{(1)}dy$$

$$b_{ij}^{(2)}=\frac{1}{G_{13}}\int_{-h}^{h}\varphi_i^{(1)}\frac{d^2\varphi_j^{(1)}}{dy^2}dy \tag{10}$$

$$c_i^{(2)}=\int_{-h}^{h}\varphi_i^{(1)}dy.$$

Solve system (9) with the free-edge boundary conditions $f_i^{(2)}(\pm b)=0$ to complete the second approximation. The iteration process can be continued till a desired level of convergence is met.

Consider through-the-thickness distribution of the transverse shear stress at the edge $x=b$ for a beam, 40 mm wide and 10 mm thick, made of S2/F584 unidirectional glass-epoxy material system with properties provided in Table 1. The transverse shear stress σ_{yz} normalized by the cross section width $2b$ and the twist rate θ is defined as follows:

$$\frac{\sigma_{yz}}{2b\theta}=-\frac{1}{2b}\Psi_{,x}. \tag{11}$$

One-term approximation ($N=1$) is compared with the exact solution in Fig. 2. The expressions for the first, second, and third iterations are

$$\Psi^{(1)}=1841.18\cos(0.0785398x)$$
$$\times[1-0.927556\cosh(0.0785398y)]$$
$$\Psi^{(2)}=1841.18[0.83373-0.0029737\cosh(0.316465x)]$$
$$\times[1-0.927556\cosh(0.0785398y)] \tag{12}$$
$$\Psi^{(3)}=1841.18[0.83373-0.0029737\cosh(0.316465x)]$$
$$\times[0.618456-0.546135\cosh(0.101823y)]$$

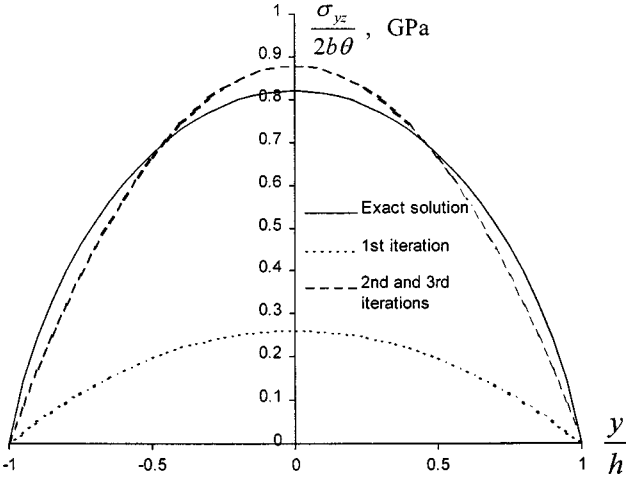

Fig. 2 Shear stress distribution at the free edge $x=b$ for orthotropic beam torsion. Comparison of one-term approximation with exact solution.

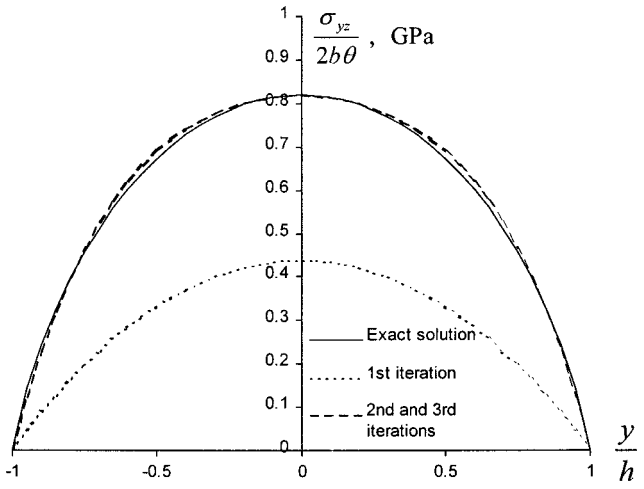

Fig. 3 Shear stress distribution at the free edge $x=b$ for orthotropic beam torsion. Comparison of two-term approximation with exact solution.

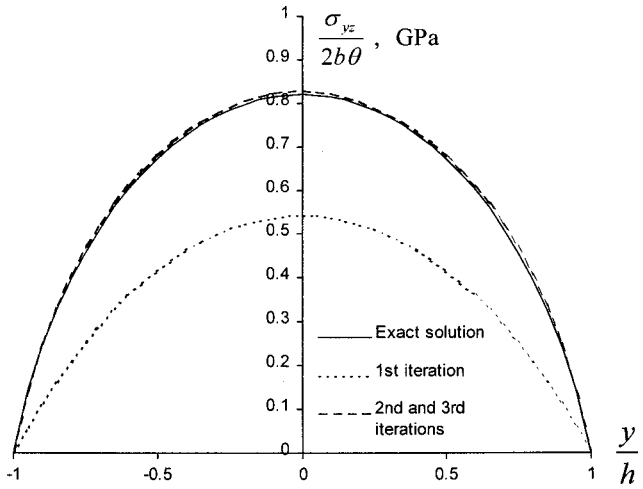

Fig. 4 Shear stress distribution at the free edge $x=b$ for orthotropic beam torsion. Comparison of three-term approximation with exact solution.

and the exact solution is given by series (7) where 120 terms were kept. Predictions of the second and third iterations are within 0.7 percent difference from each other.

Comparison for a two-term approximation is presented in Fig. 3. The first, second, and third iterations are expressed by

$$\Psi^{(1)}=\sum_{i=1}^{2} f_i^{(1)}(x)\varphi_i^{(1)}(y), \quad \Psi^{(2)}=\sum_{i=1}^{2} f_i^{(2)}(x)\varphi_i^{(1)}(y), \quad \Psi^{(3)}=\sum_{i=1}^{2} f_i^{(2)}(x)\varphi_i^{(2)}(y) \tag{13}$$

where

$$f_1^{(1)}=\cos(0.0785398x), \quad f_2^{(1)}=\cos(0.235619x)$$

$$\varphi_1^{(1)}=1841.18[1-0.927556\cosh(0.0785398y)]$$

$$\varphi_2^{(1)}=-68.1917[1-0.562422\cosh(0.235619y)] \tag{14}$$

$$\begin{Bmatrix} f_1^{(2)} \\ f_2^{(2)} \end{Bmatrix}=\begin{Bmatrix} 0.944394 \\ 0.484892 \end{Bmatrix}+\begin{bmatrix} -0.0108305 & 5.74659\cdot 10^{-9} \\ -0.0340327 & 2.53523\cdot 10^{-8} \end{bmatrix} \times\begin{Bmatrix} \cosh(0.314165x) \\ \cosh(1.01693x) \end{Bmatrix}$$

$$\begin{Bmatrix} \varphi_1^{(2)}/1841.18 \\ \varphi_2^{(2)}/(-68.1917) \end{Bmatrix}=\begin{Bmatrix} 0.750775 \\ 3.88 \end{Bmatrix}+\begin{bmatrix} -0.678393 & 5.83246\cdot 10^{-5} \\ -3.43504 & -6.99961\cdot 10^{-3} \end{bmatrix} \times\begin{Bmatrix} \cosh(0.0919757y) \\ \cosh(0.613275y) \end{Bmatrix}.$$

An excellent agreement with the exact solution is reached by the second and third iterations.

The results of three-term approximation are shown in Fig. 4. The first, second, and third iterations are

$$\Psi^{(1)}=\sum_{i=1}^{3} f_i^{(1)}(x)\varphi_i^{(1)}(y), \quad \Psi^{(2)}=\sum_{i=1}^{3} f_i^{(2)}(x)\varphi_i^{(1)}(y), \quad \Psi^{(3)}=\sum_{i=1}^{3} f_i^{(2)}(x)\varphi_i^{(2)}(y) \tag{15}$$

where the closed-form solution for the associated functions is given by

$$f_1^{(1)}=\cos(0.0785398x), \quad f_2^{(1)}=\cos(0.235619x), \quad f_3^{(1)}=\cos(0.392699x)$$

$$\varphi_1^{(1)}=1841.18[1-0.927556\cosh(0.0785398y)]$$

$$\varphi_2^{(1)}=-68.1917[1-0.562422\cosh(0.235619y)] \tag{16}$$

$$\varphi_3^{(1)}=14.7294[1-0.275309\cosh(0.392699y)]$$

$$\begin{Bmatrix} f_1^{(2)} \\ f_2^{(2)} \\ f_3^{(2)} \end{Bmatrix}=\begin{Bmatrix} 0.986349 \\ 0.775494 \\ 0.288386 \end{Bmatrix}+\begin{bmatrix} -0.0193973 & 2.3365\cdot 10^{-7} & -9.2446\cdot 10^{-16} \\ -0.0933343 & 1.56731\cdot 10^{-6} & -6.45344\cdot 10^{-15} \\ -0.0587884 & 1.46645\cdot 10^{-6} & -6.4915\cdot 10^{-15} \end{bmatrix} \times\begin{Bmatrix} \cosh(0.314159x) \\ \cosh(0.945081x) \\ \cosh(1.89988x) \end{Bmatrix}$$

$$\begin{Bmatrix} \varphi_1^{(2)}/1841.18 \\ \varphi_2^{(2)}/(-68.1917) \\ \varphi_3^{(2)}/14.7294 \end{Bmatrix}=\begin{Bmatrix} 0.813996 \\ 3.65549 \\ 2.61704 \end{Bmatrix}+\begin{bmatrix} -0.741732 & 1.8073\cdot 10^{-4} & -9.04282\cdot 10^{-9} \\ -3.18749 & -0.0303879 & 1.18256\cdot 10^{-6} \\ -1.75802 & -0.134276 & 2.07411\cdot 10^{-6} \end{bmatrix} \times\begin{Bmatrix} \cosh(0.0881224y) \\ \cosh(0.464141y) \\ \cosh(1.6822y) \end{Bmatrix}.$$

Note that the first iteration (15), which is equivalent to keeping the first three terms in series (7), results in a large discrepancy with the exact solution (7) while the maximum error for the third iteration is less than three percent.

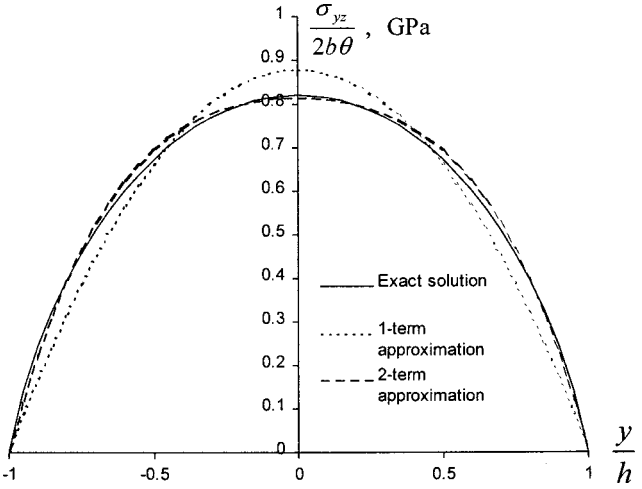

Fig. 5 Comparison of second iterations for one and two-term approximations with exact solution for orthotropic beam torsion

The following three observations can be made. First, one-term approximation predicts the correct trend information. Second, two-term approximation is accurate and therefore higher order approximations are not necessary. Third, the convergence of the iteration procedure is fast: Two iterations are sufficient for an accurate modeling.

These observations are not specific to the choice of the system of trial functions in Eq. (3). Consider the following first approximation,

$$\Psi^{(1)}=\sum_{i=1}^{N}\left[1-\left(\frac{x}{b}\right)^{2i}\right]\varphi_i^{(1)}(y). \tag{17}$$

The second iterations for one and two-term approximations are compared with the exact solution (7) in Fig. 5. Comparison of shear stress predictions in Fig. 5 with the one and two-term approximations in Figs. 2 and 3 shows that the solutions based on the trial functions (17) and (3) have similar trend.

Elasticity Equations for Composite Laminates. The theory of elasticity of an anisotropic body in the three-dimensional state of strain dependent on two coordinates is well documented in Lekhnitski [8]. The governing equations are provided in the following.

Consider a laminated beam with a rectangular cross section shown in Fig. 1. The laminate is undergoing a uniform axial strain ϵ_0, a constant twist rate θ, and constant bending curvatures κ_1 and κ_2. The engineering strain-displacement relations are written as [8]

$$\begin{gathered}\epsilon_{xx}=U_{,x}\quad \epsilon_{yy}=V_{,y}\quad \epsilon_{zz}=\epsilon_0+\kappa_1 x+\kappa_2 y\\ \gamma_{yz}=\theta x+W_{,y}\quad \gamma_{xz}=-\theta y+W_{,x}\quad \gamma_{xy}=U_{,y}+V_{,x}\end{gathered} \tag{18}$$

where U, V, and W are functions of x and y. Subscript commas denote partial derivatives.

The following compatibility equations can be obtained from Eqs. (18)

$$\epsilon_{xx,yy}+\epsilon_{yy,xx}-\gamma_{xy,xy}=0\quad \gamma_{xz,y}-\gamma_{yz,x}=-2\theta. \tag{19}$$

The laminate consists of plies which are represented by strips made of continuous fibers and a matrix. All fibers in a ply are aligned parallel to the (x,z)-plane at an angle with the longitudinal z-axis. This angle defines the ply orientation and can be different for each ply. An off-axis ply is modeled as a homogeneous medium with 13 nonzero elastic constants, 9 of which are independent [3]. This 13-constant system is generally different from ply to ply. Therefore, each ply in the laminate has an independent set of field variables. The boundary conditions, namely, continuity of the displacements and the interlaminar stresses, are established at the ply interfaces.

For an off-axis ply, the general constitutive relationships, defined in Lekhnitski [8], are simplified to

$$\sigma^{zz}=\frac{1}{\alpha_{33}}(\epsilon_{zz}-\alpha_{13}\sigma^{xx}-\alpha_{23}\sigma^{yy}-\alpha_{35}\sigma^{xz}) \tag{20}$$

$$\begin{gathered}\begin{Bmatrix}\epsilon_{xx}\\ \epsilon_{yy}\\ \gamma_{xz}\end{Bmatrix}=\begin{bmatrix}\beta_{11}&\beta_{12}&\beta_{15}\\ \beta_{12}&\beta_{22}&\beta_{25}\\ \beta_{15}&\beta_{25}&\beta_{55}\end{bmatrix}\begin{Bmatrix}\sigma^{xx}\\ \sigma^{yy}\\ \sigma^{xz}\end{Bmatrix}+\begin{Bmatrix}\alpha_{13}\\ \alpha_{23}\\ \alpha_{35}\end{Bmatrix}\frac{\epsilon_{zz}}{\alpha_{33}}\\ \begin{Bmatrix}\gamma_{yz}\\ \gamma_{xy}\end{Bmatrix}=\begin{bmatrix}\beta_{44}&\beta_{46}\\ \beta_{46}&\beta_{66}\end{bmatrix}\begin{Bmatrix}\sigma^{yz}\\ \sigma^{xy}\end{Bmatrix}.\end{gathered} \tag{21}$$

The stress functions identically satisfying the equilibrium equations are defined as follows:

$$\begin{gathered}\sigma^{xx}=F_{,yy}\quad \sigma^{yy}=F_{,xx}\quad \sigma^{xy}=-F_{,xy}\\ \sigma^{xz}=\Psi_{,y}\quad \sigma^{yz}=-\Psi_{,x}.\end{gathered} \tag{22}$$

Substitute Eqs. (22) and (21) into the compatibility Eqs. (19) to obtain

$$\begin{aligned}&\beta_{22}F_{,xxxx}+(2\beta_{12}+\beta_{66})F_{,xxyy}+\beta_{11}F_{,yyyy}+(\beta_{25}+\beta_{46})\Psi_{,xxy}\\ &\quad+\beta_{15}\Psi_{,yyy}=0\end{aligned} \tag{23}$$

$$(\beta_{25}+\beta_{46})F_{,xxy}+\beta_{15}F_{,yyy}+\beta_{44}\Psi_{,xx}+\beta_{55}\Psi_{,yy}=-2\theta+\frac{\alpha_{35}}{\alpha_{33}}\kappa_2. \tag{24}$$

The traction-free edge boundary conditions result in the following expressions:

$$x=\pm b,\quad F=F_{,x}=\Psi=0 \tag{25}$$

$$y=\pm h,\quad F=F_{,y}=\Psi=0. \tag{26}$$

The following quantities are continuous at the ply interfaces due to the continuity of the interlaminar stresses and the displacements:

$$\begin{gathered}F,\quad F_{,y},\quad \Psi,\\ \beta_{11}F_{,yy}+\beta_{12}F_{,xx}+\beta_{15}\Psi_{,y}+\frac{\alpha_{13}}{\alpha_{33}}(\epsilon_0+\kappa_1 x+\kappa_2 y),\\ \beta_{11}F_{,yyy}+(\beta_{12}+\beta_{66})F_{,xxy}+\beta_{15}\Psi_{,yy}+\beta_{46}\Psi_{,xx}+\frac{\alpha_{13}}{\alpha_{33}}\kappa_2,\\ \beta_{15}F_{,yy}+\beta_{25}F_{,xx}+\beta_{55}\Psi_{,y}+\frac{\alpha_{35}}{\alpha_{33}}(\epsilon_0+\kappa_1 x+\kappa_2 y)+\theta y.\end{gathered} \tag{27}$$

Approximate Solution. In order to apply the developed iteration procedure to the boundary value problem, the following weak form of Eqs. (23) and (24) is constructed

$$\begin{aligned}&\int_{h_1}^{h_2}dy\int_{-b}^{b}[\beta_{22}F_{,xxxx}+(2\beta_{12}+\beta_{66})F_{,xxyy}+\beta_{11}F_{,yyyy}\\ &\quad+(\beta_{25}+\beta_{46})\Psi_{,xxy}+\beta_{15}\Psi_{,yyy}]\delta F\,dx=0\end{aligned} \tag{28}$$

$$\begin{aligned}&\int_{h_1}^{h_2}dy\int_{-b}^{b}\Big[(\beta_{25}+\beta_{46})F_{,xxy}+\beta_{15}F_{,yyy}+\beta_{44}\Psi_{,xx}\\ &\quad+\beta_{55}\Psi_{,yy}+2\theta-\frac{\alpha_{35}}{\alpha_{33}}\kappa_2\Big]\delta\Psi\,dx=0\end{aligned} \tag{29}$$

where h_1 and h_2 denote the lower and upper boundaries of the associated ply (or sublaminate if the adjacent plies are treated as one group). The form of the approximate solution is

$$F=\sum_{i=1}^{N} f_{xi}(x)f_{yi}(y), \quad \Psi=\sum_{i=1}^{N} \psi_{xi}(x)\psi_{yi}(y) \tag{30}$$

To simplify the calculations, the x-dependent functions $f_{xi}(x)$ and $\psi_{xi}(x)$ in Eqs. (30) do not change from ply to ply. There are no conceptual difficulties in considering different $f_{xi}(x)$ and $\psi_{xi}(x)$ for each sublaminate. The functions of y in Eqs. (30) are independent for each sublaminate. The following first approximations, satisfying the free-edge boundary conditions (25), are selected:

$$F^{(1)}=\sum_{i=1}^{N} f_{xi}^{(1)}f_{yi}^{(1)}=\sum_{i=1}^{N}\left(\cos\xi_i\frac{x}{b}-\frac{\cos\xi_i}{\cosh\xi_i}\cosh\xi_i\frac{x}{b}\right)f_{yi}^{(1)} \tag{31}$$

$$\Psi^{(1)}=\sum_{i=1}^{N} \psi_{xi}^{(1)}\psi_{yi}^{(1)}=\sum_{i=1}^{N}\frac{1}{\sqrt{hb}}\left(1-\frac{\cosh\xi_i\frac{x}{b}}{\cosh\xi_i}\right)\psi_{yi}^{(1)}$$

where ξ_i are roots of the following characteristic equation:

$$\cos\xi_i\sinh\xi_i+\sin\xi_i\cosh\xi_i=0. \tag{32}$$

The boundary conditions for the y-dependent functions f_{yi} and ψ_{yi} are established in the following.

Equations (26) result in the following conditions at the edges $y=\pm h$

$$y=\pm h, \quad f_{yi}=\frac{df_{yi}}{dy}=\psi_{yi}=0. \tag{33}$$

Since f_{xi} and ψ_{xi} do not change from ply to ply, the first three conditions (27), which express the continuity of the interlaminar stresses at the ply interfaces, are satisfied by enforcing

$$f_{yi}, \quad \frac{df_{yi}}{dy}, \quad \text{and} \quad \psi_{yi} \tag{34}$$

to be continuous at the ply interfaces. The last three continuity conditions (27) cannot be satisfied due to the presence of independent functions. Consistent with Eqs. (28) and (29), a weak form of these conditions needs to be obtained. If the complementary virtual work of surface tractions at the ply interfaces is considered, the following expressions are continuous at the ply interfaces:

$$\int_{-b}^{b} U\delta\sigma^{xy}dx, \quad \int_{-b}^{b} V\delta\sigma^{yy}dx, \quad \int_{-b}^{b} W\delta\sigma^{yz}dx, \tag{35}$$

in addition to the interlaminar stress continuity. Substitute Eqs. (22) into (35), integrate by parts, and use Eqs. (18), (21), (22), and (25) to obtain the following continuity conditions:

$$\int_{-b}^{b}\left[\beta_{11}F_{,yy}+\beta_{12}F_{,xx}+\beta_{15}\Psi_{,y}+\frac{\alpha_{13}}{\alpha_{33}}(\epsilon_0+\kappa_1 x+\kappa_2 y)\right]\delta F_{,y}dx,$$

$$\int_{-b}^{b}\left[\beta_{11}F_{,yyy}+(\beta_{12}+\beta_{66})F_{,xxy}+\beta_{15}\Psi_{,yy}+\beta_{46}\Psi_{,xx}+\frac{\alpha_{13}}{\alpha_{33}}\kappa_2\right]\delta F dx, \tag{36}$$

$$\int_{-b}^{b}\left[\beta_{15}F_{,yy}+\beta_{25}F_{,xx}+\beta_{55}\Psi_{,y}+\frac{\alpha_{35}}{\alpha_{33}}(\epsilon_0+\kappa_1 x+\kappa_2 y)+\theta y\right]\delta\Psi dx.$$

According to Eqs. (30), and continuity conditions (34) and (36), the following quantities are continuous at the ply interfaces:

$$f_{yi}^{(1)}, \quad \frac{df_{yi}^{(1)}}{dy}, \quad \psi_{yi}^{(1)},$$

$$\beta_{11}\left(\int_{-b}^{b} f_{xi}^{(1)}f_{xj}^{(1)}dx\right)\frac{d^2f_{yi}^{(1)}}{dy^2}+\beta_{12}\left(\int_{-b}^{b} f_{xi}^{(1)}\frac{d^2f_{xj}^{(1)}}{dx^2}dx\right)f_{yi}^{(1)}$$
$$+\beta_{15}\left(\int_{-b}^{b} f_{xi}^{(1)}\psi_{xj}^{(1)}dx\right)\frac{d\psi_{yi}^{(1)}}{dy}$$
$$+\frac{\alpha_{13}}{\alpha_{33}}\left([\epsilon_0+\kappa_2 y]\int_{-b}^{b} f_{xi}^{(1)}dx+\kappa_1\int_{-b}^{b} x f_{xi}^{(1)}dx\right),$$

$$\beta_{11}\left(\int_{-b}^{b} f_{xi}^{(1)}f_{xj}^{(1)}dx\right)\frac{d^3f_{yj}^{(1)}}{dy^3}+(\beta_{12}+\beta_{66})\left(\int_{-b}^{b} f_{xi}^{(1)}\frac{d^2f_{xj}^{(1)}}{dx^2}dx\right)$$
$$\times\frac{df_{yj}^{(1)}}{dy}+\beta_{15}\left(\int_{-b}^{b} f_{xi}^{(1)}\psi_{xj}^{(1)}dx\right)\frac{d^2\psi_{yj}^{(1)}}{dy^2}$$
$$+\beta_{46}\left(\int_{-b}^{b} f_{xi}^{(1)}\frac{d^2\psi_{xj}^{(1)}}{dx^2}dx\right)\psi_{yj}^{(1)}+\frac{\alpha_{13}}{\alpha_{33}}\kappa_2\int_{-b}^{b} f_{xi}^{(1)}dx, \tag{37}$$

$$\beta_{15}\left(\int_{-b}^{b} \psi_{xi}^{(1)}f_{xj}^{(1)}dx\right)\frac{d^2f_{yj}^{(1)}}{dy^2}+\beta_{25}\left(\int_{-b}^{b} \psi_{xi}^{(1)}\frac{d^2f_{xj}^{(1)}}{dx^2}dx\right)f_{yj}^{(1)}$$
$$+\beta_{55}\left(\int_{-b}^{b} \psi_{xi}^{(1)}\psi_{xj}^{(1)}dx\right)\frac{d\psi_{yj}^{(1)}}{dy}+\left(\frac{\alpha_{35}}{\alpha_{33}}[\epsilon_0+\kappa_2 y]+\theta y\right)$$
$$\times\int_{-b}^{b} \psi_{xi}^{(1)}dx+\frac{\alpha_{35}}{\alpha_{33}}\kappa_1\int_{-b}^{b} x\psi_{xi}^{(1)}dx,$$

$$i,j=1,\ldots,N$$

where summation over the repeated index j is assumed.

Substitute the first approximations (31) for the stress functions into Eqs. (28) and (29) to obtain a system of ordinary linear differential equations with constant coefficients. The closed-form solution of such a system is straightforward. Satisfying the boundary conditions (33) and (37) results in a system of linear algebraic equations of order six times the number of terms N in the approximate solution times the number of sublaminates.

Since the functions $f_{xi}(x)$ and $\psi_{xi}(x)$ in Eqs. (30) do not change from ply to ply, the weak forms (28) and (29) are integrated over the total thickness of the cross section for the second iteration

$$\int_{-b}^{b} dx\int_{-h}^{h}[\beta_{22}F_{,xxxx}+(2\beta_{12}+\beta_{66})F_{,xxyy}+\beta_{11}F_{,yyyy}+(\beta_{25}+\beta_{46})\Psi_{,xxy}+\beta_{15}\Psi_{,yyy}]\delta F dy=0 \tag{38}$$

$$\int_{-b}^{b} dx\int_{-h}^{h}\left[(\beta_{25}+\beta_{46})F_{,xxy}+\beta_{15}F_{,yyy}+\beta_{44}\Psi_{,xx}+\beta_{55}\Psi_{,yy}+2\theta-\frac{\alpha_{35}}{\alpha_{33}}\kappa_2\right]\delta\Psi dy=0. \tag{39}$$

This is equivalent to averaging the weak forms (28) and (29) through the thickness. The functions $f_{xi}(x)$ and $\psi_{xi}(x)$ have to satisfy the free-edge boundary conditions

$$x=\pm b, \quad f_{xi}=\frac{df_{xi}}{dx}=\psi_{xi}=0. \tag{40}$$

The odd iterations (third, fifth, etc.) are carried out in exactly the same way as the first iteration, the even iteration procedure is identical to the second iteration.

In order to obtain a nonzero even iteration for the special cases of axial extension or in-plane bending, the following weak form of Eqs. (23) and (24) is constructed based upon the principle of complementary virtual work:

$$\int_{-b}^{b} dx \int_{-h}^{h} \Bigg[\Bigg(\beta_{11} F_{,yy} + \beta_{12} F_{,xx} + \beta_{15} \Psi_{,y} + \frac{\alpha_{13}}{\alpha_{33}} [\epsilon_0 + \kappa_1 x + \kappa_2 y] \Bigg) \delta F_{,yy} + (\beta_{12} F_{,xxyy} + \beta_{22} F_{,xxxx} + \beta_{25} \Psi_{,xxy}) \delta F - (\beta_{46} \Psi_{,xx} + \beta_{66} F_{,xxy}) \delta F_{,y} \Bigg] dy = 0 \quad (41)$$

$$\int_{-b}^{b} dx \int_{-h}^{h} \Bigg[\Bigg(\beta_{15} F_{,yy} + \beta_{25} F_{,xx} + \beta_{55} \Psi_{,y} + \frac{\alpha_{35}}{\alpha_{33}} [\epsilon_0 + \kappa_1 x + \kappa_2 y] \Bigg) \delta \Psi_{,y} - (\beta_{44} \Psi_{,xx} + \beta_{46} F_{,xxy}) \delta \Psi \Bigg] dy = 0. \quad (42)$$

Otherwise, the system of ordinary differential equations derived from the weak forms (38) and (39) together with the free-edge boundary conditions would result in a trivial solution.

For the special case of uniform axial extension, only half of the laminate, above the middle surface, is considered due to symmetry [3]. The boundary conditions at the middle surface are

$$y = 0, \quad \frac{df_{yi}}{dy} = \psi_{yi} = \beta_{11} \Bigg(\int_{-b}^{b} f_{xi} f_{xj} dx \Bigg) \frac{d^3 f_{yj}}{dy^3} + \beta_{15} \Bigg(\int_{-b}^{b} f_{xi} \psi_{xj} dx \Bigg) \frac{d^2 \psi_{yj}}{dy^2} = 0 \qquad i, j = 1, \ldots, N \quad (43)$$

where the summation over j is implied.

Results

Axial Extension. In this section, the approximate analytical solution is compared with the numerical results of Pipes and Pagano [3] and Wang and Choi [4,5] for stresses in a symmetric, $[+45/-45]_x$, graphite-epoxy laminate under axial extension. The thickness-to-width ratio is 0.25, and the material properties are provided in Table 2. The stresses predicted by Pipes and Pagano [3] and Wang and Choi [4,5] at the $+45/-45$ ply interface are compared with one-term approximation in Figs. 6 and 7. The peel stress, σ_{yy}, and the shear stress σ_{xy} distributions are not recoverable from the plots of Pipes and Pagano [3]. The in-plane normal stress σ_{xx} data are not provided in the work of Wang and Choi [4,5]. Despite numerical discrepancies, one-term approximation predicts the correct trend for all stress components, except for the in-plane normal stress σ_{xx}.

According to Pipes and Pagano [3], the σ_{xx}-stress is tensile (positive), and its maximum magnitude is five times larger than the maximum tensile peel stress, σ_{yy}, magnitude as evaluated from the corresponding plot of Wang and Choi [4,5]. A better accuracy is achieved by two-term approximation as illustrated in Figs. 8 and 9 where a close agreement with the predictions of Pipes and Pagano [3] and Wang and Choi [4,5] is shown for all stresses.

Three-term approximation was also performed. The comparison for the second iterations of one, two, and three-term approximations is presented in Figs. 10 and 11. While the discrepancy between the predictions of three and two-term approximate solutions is small, the order of the system of linear algebraic equations resulting from three-term approximation is 36 compared to 24 for the two-term approximation.

The distribution of the interlaminar shear stress σ_{yz} at the free edge is shown in Fig. 12 where the three iterations for one, two, and three-term approximations are compared with the results of Pipes and Pagano [3] and Wang and Choi [4,5]. While one-term approximation gives an accurate estimate at $x = 0.89b$, two and three-term approximations are accurate at both $x = 0.89b$ and b.

Torsion. Predictions of the interlaminar shear stress σ_{yz} at the free edge are compared with the finite element results of Sen

Table 2 Properties of graphite-epoxy material system [3]

$E_{33} = 20.0$ Msi (137.9 GPa)
$E_{11} = E_{22} = 2.1$ Msi (14.48 GPa)
$G_{13} = G_{23} = G_{12} = 0.85$ Msi (5.86 GPa)
$\nu_{31} = \nu_{32} = \nu_{12} = 0.21$

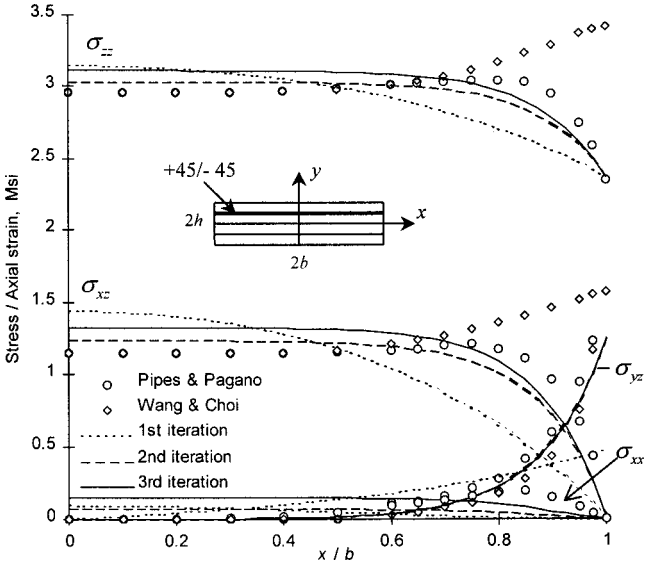

Fig. 6 One-term approximation. Comparison of stress predictions at +45/−45 ply interface for axial extension of $[+45/-45]_s$ laminate.

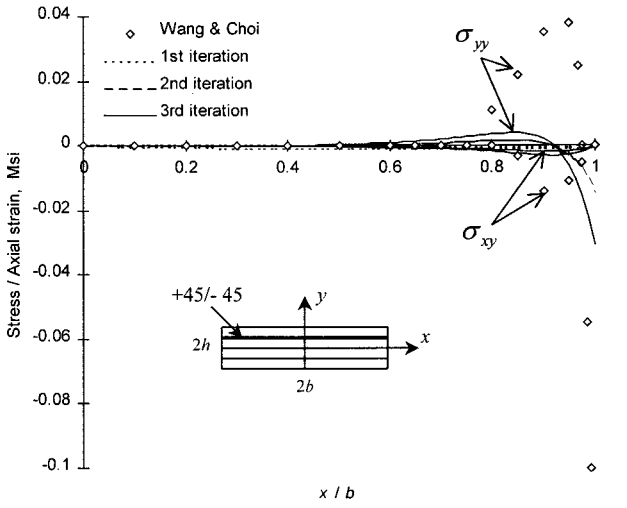

Fig. 7 One-term approximation. Comparison of stress predictions at +45/−45 ply interface for axial extension of $[+45/-45]_s$ laminate.

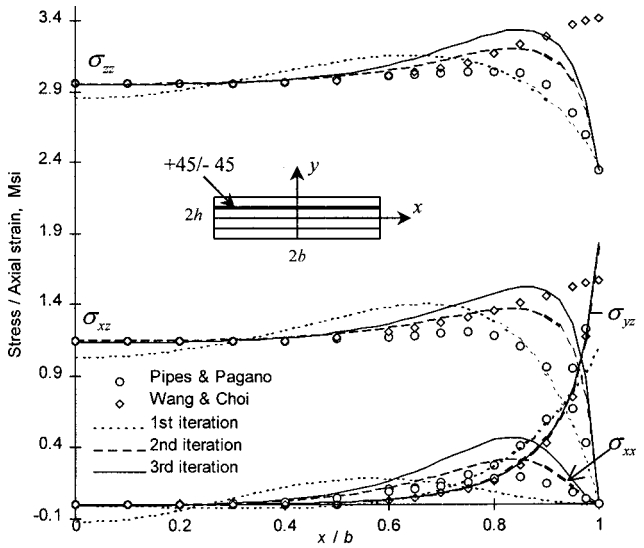

Fig. 8 Two-term approximation. Comparison of stress predictions at +45/−45 ply interface for axial extension of $[+45/-45]_s$ laminate.

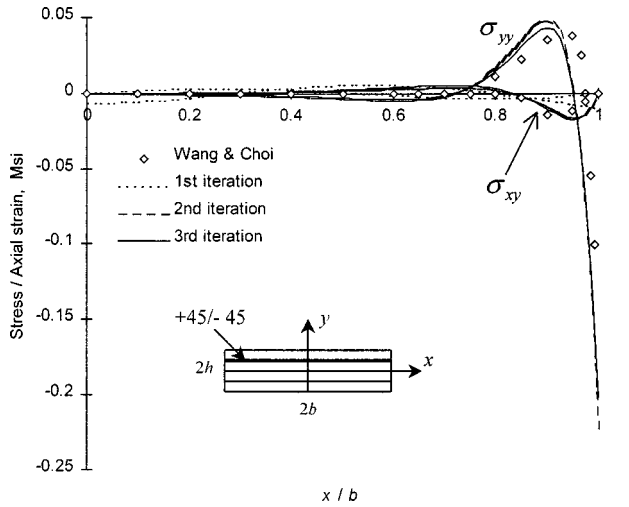

Fig. 9 Two-term approximation. Comparison of stress predictions at +45/−45 ply interface for axial extension of $[+45/-45]_s$ laminate.

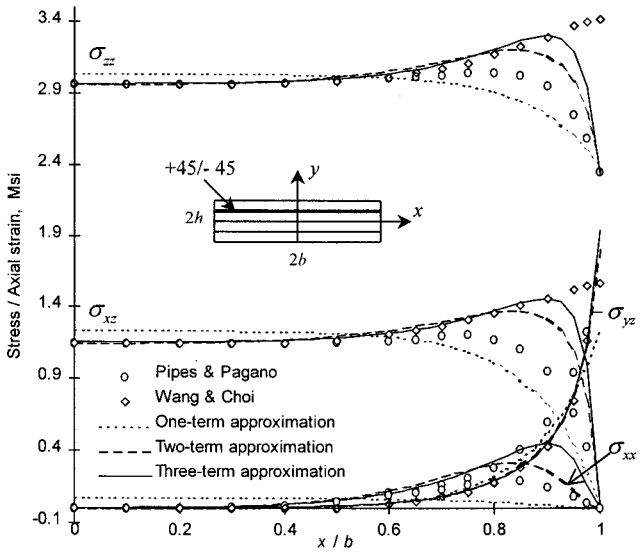

Fig. 10 Comparison of stress predictions at +45/−45 ply interface for axial extension of $[+45/-45]_s$ laminate

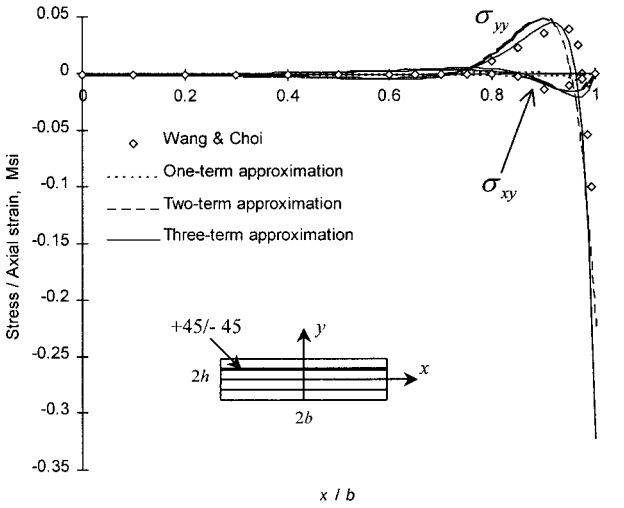

Fig. 11 Comparison of stress predictions at +45/−45 ply interface for axial extension of $[+45/-45]_s$ laminate

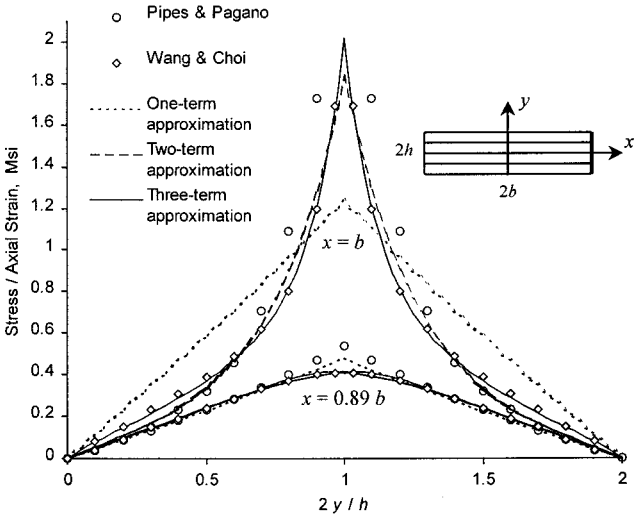

Fig. 12 Comparison of interlaminar shear stress predictions at the free edge for axial extension of $[+45/-45]_s$ laminate

and Fish [2] for the torsion of a 32-ply $[0_{12}/\pm 30_2]_s$ S2/F584 glass-epoxy flexbeam laminate configuration. The width of the laminate is 38 mm, the thickness is 7.296 mm, and the material properties are provided in Table 1. The interlaminar shear stress was evaluated at a 27-deg twist angle per 114.3 mm length, corresponding to the measured failure twist angle for this laminate [2]. One-term approximation predictions are shown in Fig. 13. The third iteration predicts the correct trend with a nine percent discrepancy compared to the finite element result for the maximum stress value. The predictions of two-term approximation, appearing in Fig. 14, show a maximum value discrepancy of less than one percent for the third iteration. One-term approximation requires solution of 54 linear algebraic equations at the first and the third iterations. Two-term approximation results in 108 linear algebraic equations at each odd iteration.

Conclusion

An iterative method for the approximate analytical solution of elasticity problems for composite laminates is presented. The stresses in laminates subjected to uniform axial extension and torsion are evaluated. A good agreement with the numerical

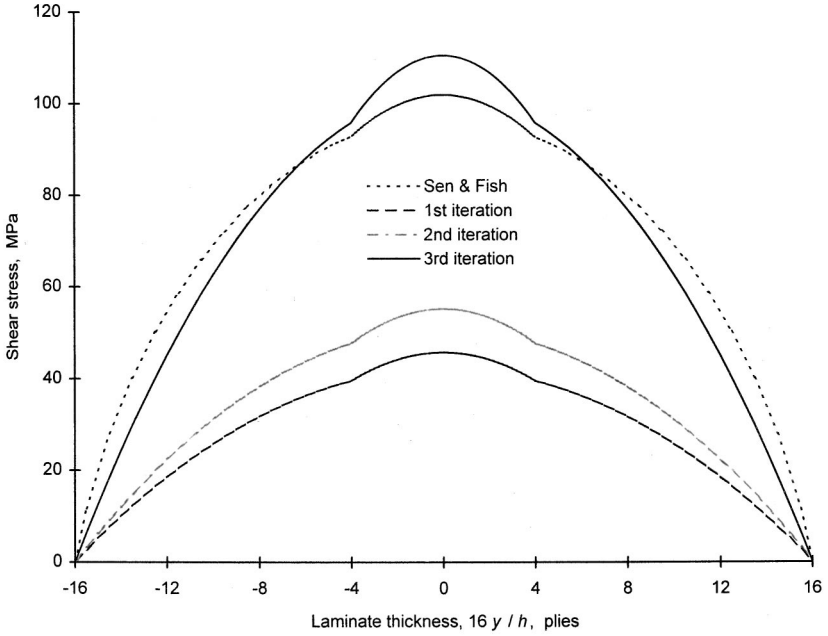

Fig. 13 One-term approximation. Comparison of interlaminar shear stress predictions at the free edge $x=b$ for torsion of $[0_{12}/\pm 30_2]_s$ laminate.

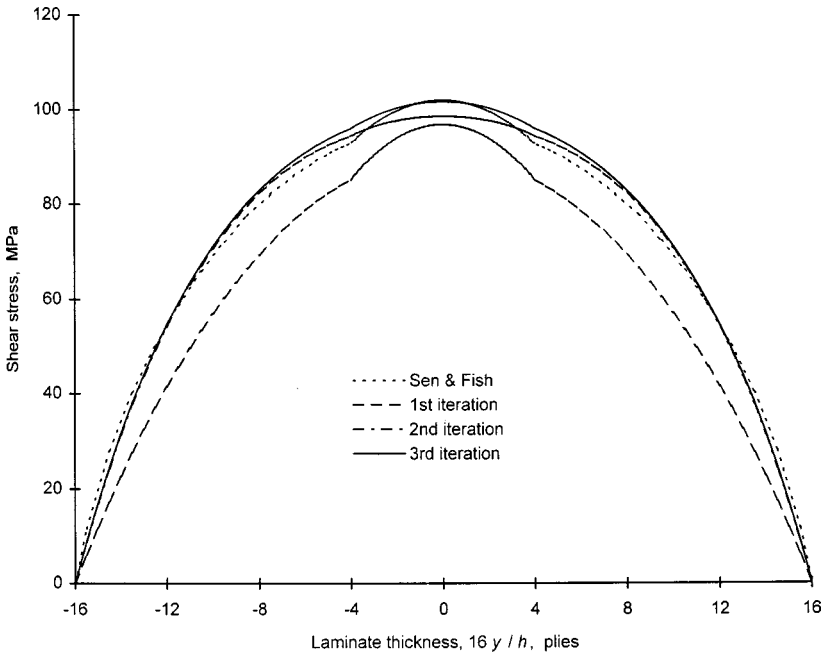

Fig. 14 Two-term approximation. Comparison of interlaminar shear stress predictions at the free edge $x=b$ for torsion of $[0_{12}/\pm 30_2]_s$ laminate.

solution of Pipes and Pagano [3], and analytical predictions of Wang and Choi [4,5] for the case of axial extension, and the finite element results of Sen and Fish [2] for the torsion case illustrates the validity of the method. For the examples considered in this study, one-term approximation predicts a correct trend information, and two-term approximation provides a good numerical accuracy. Only two or three iterations are sufficient for an accurate modeling of the stress state. An advantage of the method over existing numerical or analytical models is its simplicity, which makes the method appealing for parametric design studies.

Acknowledgments

This work is sponsored by the National Rotorcraft Technology Center under Grant NCC2-945. This support is gratefully acknowledged. The authors would also like to acknowledge Dr. Joyanto K. Sen for providing the finite element results.

References

[1] Sen, J. K., and Fish, J. C., 1995, ''Fracture of Glass-Epoxy Laminates Under Torsional and Combined Tension-Torsion Loads,'' *Composite Materials: Fa-*

tigue and Fracture, Fifth Volume, R. H. Martin, ed., ASTM STP 1230, ASTM, Philadelphia, PA, pp. 440–466.
[2] Sen, J. K., and Fish, J. C., 1996, ''Failure Prediction of Composite Laminates under Torsion,'' *Key Engineering Materials Vols. 121-122, Fracture of Composites*, E. Armanios, ed., Transtec Publications, Zuerich-Uetikon, Switzerland, pp. 285–306.
[3] Pipes, R. B., and Pagano, N. J., 1970, ''Interlaminar Stresses in Composite Laminates Under Uniform Axial Extension,'' J. Compos. Mater., **4**, pp. 538–548.
[4] Wang, S. S., and Choi, I., 1982, ''Boundary-Layer Effects in Composite Laminates: Part 1—Free-Edge Stress Singularities,'' ASME J. Appl. Mech., **49**, pp. 541–548.
[5] Wang, S. S., and Choi, I., 1982. ''Boundary-Layer Effects in Composite Laminates: Part 2—Free-Edge Stress Solutions and Basic Characteristics.'' ASME J. Appl. Mech., **49**, pp. 549–560.
[6] Makeev, A., 1997, ''Geometrically Nonlinear Analysis of Laminated Composites With Extension-Twist Coupling,'' Ph.D. thesis, Georgia Institute of Technology, Atlanta, GA.
[7] Makeev, A., and Armanios, E. A., 1998, ''A Simple Elasticity Solution for Predicting Interlaminar Stresses in Composite Flexbeams,'' *Proceedings of the American Helicopter Society 54th Annual Forum*, AHS International, Washington, DC, pp. 977–985.
[8] Lekhnitski, S. G., 1981, *Theory of Elasticity of an Anisotropic Body*, Mir Publishers, Moscow.
[9] Timoshenko, S. P., 1959, *Theory of Plates and Shells*, 2nd Ed., McGraw-Hill, New York.

J. Y. Chen
Department of Mechanical Engineering
and Engineering Mechanics,
Michigan Technological University,
Houghton, MI 49931

Y. Huang
Department of Mechanical
and Industrial Engineering,
University of Illinois,
Urbana, IL 61801

K. C. Hwang
Department of Engineering Mechanics,
Tsinghua University,
Beijing 100084, China

Z. C. Xia
Ford Research Laboratory,
P.O. Box 2053, MD 3135/SRL,
Dearborn, MI 48121

Plane-Stress Deformation in Strain Gradient Plasticity

A systematic approach is proposed to derive the governing equations and boundary conditions for strain gradient plasticity in plane-stress deformation. The displacements, strains, stresses, strain gradients and higher-order stresses in three-dimensional strain gradient plasticity are expanded into a power series of the thickness h in the out-of-plane direction. The governing equations and boundary conditions for plane stress are obtained by taking the limit $h \to 0$. It is shown that, unlike in classical plasticity theories, the in-plane boundary conditions and even the order of governing equations for plane stress are quite different from those for plane strain. The kinematic relations, constitutive laws, equilibrium equation, and boundary conditions for plane-stress strain gradient plasticity are summarized in the paper. [S0021-8936(00)02301-1]

1 Introduction

Ductile materials display strong size effects when the characteristic length scale is on the order of microns. For example, in micro- and nano-indentation experiments, the measured indentation hardness of metallic materials increases by a factor of two to three as the width of the indenter decrease from 10 μm to 1 μm ([1–6]). In torsion of thin copper wires, Fleck et al. [7] observed that the scaled shear strength increases by a factor of three as the wire diameter decreases from 170 μm to 12 μm, while the increase of work hardening in tension is negligible. In bending of thin nickel beams, Stolken and Evans [8] found a significant increase in the plastic work hardening as the beam thickness decreases from 100 μm to 12.5 μm. In an aluminum-silicon matrix composite reinforced by silicon carbide particles, Lloyd [9] observed a substantial strength increase when the particle diameter was reduced from 16 μm to 7.5 μm with the particle volume fraction fixed at 15 percent.

The classical plasticity theories cannot predict this size dependence of material behavior at the micron scale because their constitutive models do not possess an internal length scale. In order to extend the continuum J_2-deformation or J_2-flow plasticity theories to micron scale, strain gradient plasticity theories have been developed. Aifantis [10] and Muhlhaus and Aifantis [11] have modified the constitutive model of classical plasticity by introducing the Laplacian of plastic strain in the flow stress-plastic strain relation. Recently, Fleck and Hutchinson [12,13] and Fleck et al. [7] developed a phenomenological strain gradient plasticity theory. Its point of departure is that the plastic work hardening of materials is due to the storage of both statistically stored dislocations (e.g., [14]) and geometrically necessary dislocations, and the latter are related to the gradients of plastic shear in a material ([14–16]). The theory fits the mathematical framework of higher-order continuum theory of elasticity ([17–20]), and satisfies the Clausius-Duhem thermodynamic restrictions on the constitutive law for second deformation gradients ([21–23]). The theory introduces three material lengths, two scale with rotation gradients of deformation, while the other scales with the stretch gradients of deformation. Begley and Hutchinson [24] determined three material lengths by fitting Fleck et al.'s [7] microtorsion data, Stolken and Evans' [8] microbending data as well as micro-indentation data ([1–6]). They found that the material lengths associated with the rotation gradients of deformation are approximately 4 μm for copper and 6 μm for nickel, while the length associated with the stretch gradients of deformation is much smaller, ranging from 0.22 μm to 0.6 μm.

Nix and Gao [25] used Taylor's model to connect the geometrically necessary dislocations to strain gradient plasticity. They identified the intrinsic material lengths l in strain gradient plasticity as $l = L_S^2/b$, where L_S is the average dislocation spacing, and b is the Burgers vector. In terms of the shear modulus G and yield stress σ_Y in uniaxial tension, the intrinsic material lengths is given by $3\alpha^2(G/\sigma_Y)^2 b$, and is indeed on the order of microns, where α is a constant in Taylor's model, ranging between 0.2 to 0.5 for various materials. Nix and Gao's [25] analysis predicts a linear relation between the square of micro-indentation hardness and the inverse of indent depth. This linear relation agrees remarkably well with McElhaney et al.'s [6] microindentation hardness data for single crystal and cold worked polycrystalline copper, as well as with Ma and Clarke's [4] micro-indentation hardness data for single crystal silver and Poole et al.'s [5] data for annealed and work-hardened copper polycrystals.

Motivated by the remarkable agreement between Nix and Gao's [25] analysis and micro-indentation data, Gao et al. [26] and Huang et al. [27] developed a mechanism-based theory of strain gradient plasticity (MSG). A multiscale framework is proposed to link the microscale notion of statistically stored and geometrically necessary dislocations to the mesoscale notion of plastic strain and strain gradient. The microscale at which dislocation interaction is considered is distinguished from the mesoscale at which the plasticity theory is formulated. On the microscale, the Taylor's hardening model is adopted as a founding principle to govern dislocation interactions at the microscale. On the mesoscale, the constitutive equations are constructed by averaging microscale plasticity laws over a representative cell. An expression for the effective strain gradient is obtained by considering models of geometrically necessary dislocations associated with bending, torsion, and two-dimensional axisymmetric void growth.

The strain gradient plasticity theories have been used in analyz-

Contributed by the Applied Mechanics Division of THE AMERICAN SOCIETY OF MECHANICAL ENGINEERS for publication in the ASME JOURNAL OF APPLIED MECHANICS. Manuscript received by the ASME Applied Mechanics Division, July 9, 1998; final revision, July 23, 1999. Associate Technical Editor: K. T. Ramesh. Discussion on the paper should be addressed to the Technical Editor, Professor Lewis T. Wheeler, Department of Mechanical Engineering, University of Houston, Houston, TX 77204-4792, and will be accepted until four months after final publication of the paper itself in the ASME JOURNAL OF APPLIED MECHANICS.

ing microscale phenomena, such as micro-indentation ([24,28]), microtorsion ([7,27]), and microbending experiments ([8,27,29]) void growth and cavitation instability ([13,27]), and fracture near a crack tip ([27,30–37]). All these studies are limited to plane-strain, axisymmetric, or antiplane shear deformation. There is no study on plane-stress deformation in strain gradient plasticity due to the difficulty that, unlike in plane strain, the governing equations for plane stress cannot be directly obtained from the three-dimensional governing equations in strain gradient plasticity. Moreover, even the order of the governing equations and in-plane traction-prescribed boundary conditions turn out to be different for plane stress and plane strain, which is rather different from classical plasticity theories.

We propose a systematic approach to derive the governing equations and boundary conditions for plane-stress deformation in strain gradient plasticity. The displacements, strains, stresses, strain gradients, and higher-order stresses in three-dimensional strain gradient plasticity are expanded into power series of the thickness h in the out-of-plane direction. As the thickness h approaches zero, the governing equations and boundary conditions for plane-stress deformation are obtained. A summary of Fleck and Hutchinson's [13] three-dimensional strain gradient plasticity is given in Section 2, while the plane-stress strain gradient plasticity is derived in Section 3. For readers who would like to bypass the details of derivations, the kinematic relations, constitutive law, equilibrium equation, and boundary conditions for plane-stress strain gradient plasticity are summarized in Section 4.

2 The Fleck-Hutchinson Phenomenological Strain Gradient Plasticity Theory

The Fleck-Hutchinson [13] phenomenological strain gradient plasticity theory has accounted for the effects from both rotation gradients and stretch gradients of deformation. It is summarized in this section for deformation theory. For simplicity, the elastic deformation is neglected such that the material is incompressible. In the following, all Roman subscripts (e.g., i, j, k) range from 1 to 3, while Greek letters (e.g., α, β, γ) are 1 or 2.

The strains ε_{ij} and strain gradients η_{ijk} are related to displacements u_i by

$$\varepsilon_{ij}=\frac{1}{2}(u_{i,j}+u_{j,i}), \tag{1}$$

$$\eta_{ijk}=u_{k,ij}. \tag{2}$$

Incompressibility of the deformation field requires

$$\varepsilon_{kk}=0, \quad \eta_{ikk}=0. \tag{3}$$

The work conjugates of strains and strain gradients are (symmetric) stresses σ_{ij} $(=\sigma_{ji})$ and (symmetric) higher-order stresses τ_{ijk} $(=\tau_{jik})$, respectively. The constitutive law of the deformation theory of strain gradient plasticity can be written in terms of the strain energy density W as

$$\sigma'_{ij}=\frac{\partial W}{\partial \varepsilon_{ij}}, \quad \tau'_{ijk}=\frac{\partial W}{\partial \eta_{ijk}}, \tag{4}$$

where $\sigma'_{ij}=\sigma_{ij}-1/3\sigma_{kk}\delta_{ij}$ are deviatoric stresses, and $\tau'_{ijk}=\tau_{ijk}-1/4(\tau_{ipp}\delta_{jk}+\tau_{jpp}\delta_{ik})$ are deviatoric higher-order stresses. Fleck and Hutchinson [13] assumed that the strain energy density W depends only on second-order invariants of strains and strain gradients for an incompressible solid, and W takes the same form as in uniaxial tension

$$W=\frac{n}{n+1}\Sigma_0 E_0\left(\frac{E}{E_0}\right)^{(n+1)/n}, \tag{5}$$

where n is the plastic work hardening exponent, Σ_0 is the tensile yield stress, E_0 is the yield strain $(=\Sigma_0/\text{Young's modulus})$, and E is a combined measure of effective strain and effective strain gradient and is given by

$$E=\sqrt{\varepsilon_e^2+c_1\eta_{iik}\eta_{jjk}+c_2\eta_{ijk}\eta_{ijk}+c_3\eta_{ijk}\eta_{kji}}. \tag{6}$$

Here, $\varepsilon_e=\sqrt{2/3\varepsilon_{ij}\varepsilon_{ij}}$ is the effective strain in classical plasticity, $\eta_{iik}\eta_{jjk}$, $\eta_{ijk}\eta_{ijk}$, and $\eta_{ijk}\eta_{kji}$ are three invariants of the strain gradient tensor, and c_1, c_2, and c_3 are three material parameters scaling with the above three invariants of the strain gradient tensor. Smyshlyaev and Fleck [38] showed that c_1, c_2, and c_3 can be equivalently written in terms of three lengths l_1, l_2, and l_3 as

$$c_1=-\frac{l_1^2}{15}-\frac{l_2^2}{3}+\frac{2}{5}l_3^2, \quad c_2=\frac{l_1^2}{3}+\frac{2}{3}l_2^2, \quad c_3=\frac{2}{3}l_1^2-\frac{2}{3}l_2^2. \tag{7}$$

Begley and Hutchinson [24] proposed to determine the lengths l_1, l_2, and l_3 by fitting experimental data such as microbend ([8]) microtorsion ([7]) and micro-indentation data ([1–6]). Based on the fitting, they suggested that

$$l_1=\frac{l}{16}\sim\frac{l}{8}, \quad l_2=\frac{l}{2}, \quad l_3=\sqrt{\frac{5}{24}}l, \tag{8}$$

where l is considered as an intrinsic material length, and is approximately 4 μm for copper and 6 μm for nickel. The choice in Eq. (8) give parameters c_1, c_2, and c_3 as

$$c_1=-0.0010l^2\sim-0.0026l^2, \quad c_2=0.17l^2, \quad c_3=-0.16l^2. \tag{9}$$

Gao et al. [26] and Huang et al. [27] on the other hand, determined the parameters c_1, c_2, and c_3 from the relation between the effective strain gradient and the density of geometrically necessary dislocations. Based on three dislocation models for pure bending, pure torsion, and void growth, they established three parameters c_1, c_2, and c_3 as

$$c_1=0, \quad c_2=\frac{l^2}{4}, \quad c_3=0, \tag{10}$$

or equivalently,

$$l_1=l_2=l_3=\frac{l}{2}, \tag{11}$$

where the intrinsic material length l has been identified from Taylor's model to be on the order of the square of dislocation spacing over Burgers vector, L_S^2/b, by Nix and Gao [25]. In terms of macroscopic quantities, the material length l is given by

$$l=3\alpha^2\left(\frac{\mu}{\Sigma_0}\right)^2 b, \tag{12}$$

where μ is the shear modulus, Σ_0 is the yield stress in uniaxial tension, b is the Burgers vector, and α is an empirical parameter in Taylor's model, ranging from 0.2 and 0.5 for various materials. For typical ductile materials, the material length l is indeed on the order of microns, consistent with Fleck and Hutchinson's [13] and Begley and Hutchinson's [24] estimates.

Based on Taylor's model, Gao et al. [26] and Huang et al. [27] proposed a mechanism-based strain gradient (MSG) plasticity theory. It differs from Fleck and Hutchinson's [13] phenomenological strain gradient plasticity not only in the coefficients c_1, c_2, and c_3 as in Eq. (10), but also in the constitutive relations (4)–(6). However, in the present study, we will derive the governing equations and boundary conditions for plane-stress deformation only in Fleck-Hutchinson's phenomenological strain gradient plasticity ([13]). Equations (4)–(6) give the constitutive law as

$$\sigma'_{ij}=\frac{2}{3}\frac{\Sigma_0}{E_0}\left(\frac{E}{E_0}\right)^{1/n-1}\varepsilon_{ij}, \tag{13}$$

$$\tau'_{ijk}=\frac{\Sigma_0}{E_0}\left(\frac{E}{E_0}\right)^{1/n-1}\left[c_1\eta_{ppk}\delta_{ij}+c_2\eta_{ijk}+\frac{c_3}{2}(\eta_{kji}+\eta_{kij})\right.$$
$$\left.-\frac{1}{4}\left(c_1+\frac{c_3}{2}\right)\eta_{ppi}\delta_{jk}-\frac{1}{4}\left(c_1+\frac{c_3}{2}\right)\eta_{ppj}\delta_{ik}\right]. \quad (14)$$

We emphasize that σ'_{ij} and τ'_{ijk} in the above expressions are indeed symmetric and deviatoric, i.e., $\sigma'_{ij}=\sigma'_{ji}$, $\sigma'_{kk}=0$, $\tau'_{ijk}=\tau'_{jik}$, and $\tau'_{ikk}=0$.

The equilibrium equations for an incompressible solid in the higher-order continuum theory are ([13])

$$\sigma'_{ik,i}-\tau'_{ijk,ij}+H_{,k}=0, \quad (15)$$

where

$$H=\frac{1}{3}\sigma_{kk}-\frac{1}{2}\tau_{ikk,i} \quad (16)$$

is a combined measure of hydrostatic stress and hydrostatic higher-order stress for an incompressible solid. For a three-dimensional problem, there are five independent traction-prescribed boundary conditions, including three independent stress tractions $\hat{t}_k$ and two independent high-order stress tractions $\hat{r}_k$ on the surface ([13]),

$$\hat{t}_k=Hn_k+n_i(\sigma'_{ik}-\tau'_{ijk,j})+D_k(n_in_jn_p\tau'_{ijp})-D_j(n_i\tau'_{ijk})$$
$$+(n_in_j\tau'_{ijk}-n_kn_in_jn_p\tau'_{ijp})(D_qn_q), \quad (17)$$

$$\hat{r}_k=n_in_j\tau'_{ijk}-n_kn_in_jn_p\tau'_{ijp}, \quad (18)$$

where $\mathbf{n}$ is the unit normal of the boundary surface, $D_j\equiv(\delta_{jk}-n_jn_k)\partial/\partial x_k$ is the surface gradient, and $\hat{r}_k$ are not independent because $n_k\hat{r}_k=0$. For the special case where the surface of the body has edges, there is a line traction $\hat{p}_k$ that must be taken into account ([13]). Suppose the surface has an edge C, formed by the intersection of two smooth surface segments S_1 and S_2. The line traction $\hat{p}_k$ is

$$\hat{p}_k=\sum(n_ik_j\tau'_{ijk}-k_kn_in_jn_p\tau'_{ijp}), \quad (19)$$

where the summation is over both surface S_1 and S_2 at edge C, $\mathbf{n}$ is the unit normal of each segment of surface, and $\mathbf{c}$ is the unit tangent along the edge defined with each segment to the left, $\mathbf{k}=\mathbf{c}\times\mathbf{n}$. (As pointed out by Huang [27], Eq. (19) corrects the misprint in Fleck and Hutchinson's [13] expression for the line traction $\hat{p}_k$.) There can also be five independent displacement-prescribed boundary conditions. Since the displacement-prescribed boundary conditions in a two-dimensional problem can be obtained straightforwardly from the three-dimensional relations, the present study focuses on traction-prescribed boundary conditions.

For a two-dimensional problem in the (x_1,x_2) plane, the equilibrium Eq. (15) can be categorized to the in-plane equations

$$\sigma'_{\alpha\gamma,\alpha}+\sigma'_{3\gamma,3}-\tau'_{\alpha\beta\gamma,\alpha\beta}-2\tau'_{3\alpha\gamma,\alpha3}-\tau'_{33\gamma,33}+H_{,\gamma}=0, \quad (20)$$

and out-of-plane equations

$$\sigma'_{\alpha3,\alpha}+\sigma'_{33,3}-\tau'_{\alpha\beta3,\alpha\beta}-2\tau'_{\alpha33,\alpha3}-\tau'_{333,33}+H_{,3}=0. \quad (21)$$

The in-plane traction boundary conditions can be obtained by replacing the unit normal n_k in Eqs. (17) and (18) with n_γ, i.e.,

$$\hat{t}_\gamma=Hn_\gamma+n_\alpha(\sigma'_{\alpha\gamma}-\tau'_{\alpha\beta\gamma,\beta})+D_\gamma(n_\alpha n_\beta n_\delta\tau'_{\alpha\beta\delta})-D_\beta(n_\alpha\tau'_{\alpha\beta\gamma})$$
$$+(n_\alpha n_\beta\tau'_{\alpha\beta\gamma}-n_\gamma n_\alpha n_\beta n_\delta\tau'_{\alpha\beta\delta})(D_\zeta n_\zeta)-2n_\alpha\tau'_{3\alpha\gamma,3}, \quad (22)$$

$$\hat{t}_3=n_\alpha(\sigma'_{\alpha3}-\tau'_{\alpha\beta3,\beta})+n_\alpha n_\beta n_\delta\tau'_{\alpha\beta\delta,3}-D_\beta(n_\alpha\tau'_{\alpha\beta3})$$
$$+n_\alpha n_\beta\tau'_{\alpha\beta3}(D_\zeta n_\zeta)-2n_\alpha\tau'_{\alpha33,3}, \quad (23)$$

$$\hat{r}_\gamma=n_\alpha n_\beta\tau'_{\alpha\beta\gamma}-n_\gamma n_\alpha n_\beta\eta_\delta\tau'_{\alpha\beta\delta}, \quad (24)$$

$$\hat{r}_3=n_\alpha n_\beta\tau'_{\alpha\beta3}, \quad (25)$$

where $\hat{r}_\gamma$ satisfies $n_\gamma\hat{r}_\gamma=0$. The out-of-plane traction boundary conditions can be obtained by replacing the unit normal n_k in Eqs. (17) and (18) with $\mathbf{n}=(0,0,1)$, i.e.,

$$\hat{t}_\gamma=\sigma'_{3\gamma}-2\tau'_{3\beta\gamma,\beta}-\tau'_{33\gamma,3}+\tau'_{333,\gamma}, \quad (26)$$

$$\hat{t}_3=H+\sigma'_{33}-2\tau'_{\beta33,\beta}-\tau'_{333,3}, \quad (27)$$

$$\hat{r}_\gamma=\tau'_{33\gamma}. \quad (28)$$

For a plane-strain problem, Eqs. (20), (22), and (24) rigorously degenerate to a two-dimensional problem since deviatoric stresses and deviatoric higher-order stresses in the out-of-plane direction (with the subscript 3) all vanish after enforcing the plane-strain condition $u_\alpha=u_\alpha(x_1,x_2)$ and $u_3=0$. The out-of-plane Eq. (21) and boundary conditions (23), (25), (26), and (28) also become identically zero, while Eq. (27) gives the combined measure H of hydrostatic stress and hydrostatic higher-order stress. For a plane-stress problem, however, it is unclear which higher-order stresses are zero. In fact, as shown later, deviatoric higher-order stresses $\tau'_{\alpha33}$ and the derivatives of $\tau'_{\alpha\beta3}$ and $\tau'_{3\alpha\beta}$ with respect to x_3 are not zero. In the following, a systematic approach is proposed to derive the governing equations and boundary conditions for plane-stress deformation in strain gradient plasticity.

The stress and higher-order stress tractions in the x_3-direction must vanish in a plane-stress problem. Therefore, Eqs. (26)–(28) become

$$\sigma'_{3\gamma}-2\tau'_{3\beta\gamma,\beta}-\tau'_{33\gamma,3}+\tau'_{333,\gamma}=0, \quad x_3=\pm\frac{h}{2}, \quad (29)$$

$$H+\sigma'_{33}-2\tau'_{\beta33,\beta}-\tau'_{333,3}=0, \quad x_3=\pm\frac{h}{2}, \quad (30)$$

$$\tau'_{33\gamma}=0, \quad x_3=\pm\frac{h}{2}, \quad (31)$$

where h is the thickness in the out-of-plane direction.

3 Plane-Stress Deformation in Strain Gradient Plasticity

In plane-stress deformation, the thickness h in the out-of-plane direction (x_3) is much smaller than the characteristic wave length in x_1-x_2 plane. In order to capture the variation of displacements along the x_3-direction, a rescaled coordinate ς is introduced:

$$\varsigma=\frac{x_3}{h}. \quad (32)$$

The derivative with respect to the out-of-plane direction can be written as $\partial/\partial x_3=1/h(\partial/\partial\varsigma)$. The two lateral surfaces correspond to $\varsigma=\pm1/2$.

For plane-stress deformation, the displacement u_3 in the out-of-plane direction is linearly proportional to x_3. Therefore, the in-plane and out-of-plane displacement can be expanded in a power series of thickness h as

$$u_\alpha(x_1,x_2,x_3)=u_\alpha^{(0)}(x_1,x_2,\varsigma)+h^2u_\alpha^{(2)}(x_1,x_2,\varsigma)+O(h^4), \quad (33)$$

$$u_3(x_1,x_2,x_3)=hu_3^{(1)}(x_1,x_2,\varsigma)+h^3u_3^{(3)}(x_1,x_2,\varsigma)+O(h^5), \quad (34)$$

where the superscript denotes the order of h in the power series, and the in-plane displacement u_α and out-of-plane displacement u_3 have even and odd powers of h, respectively, consistent with those in classical elasticity ([39]).

From the strain-displacement relation (1), strains are given by

$$\varepsilon_{\alpha\beta}=\frac{1}{2}\left(\frac{\partial u_\alpha^{(0)}}{\partial x_\beta}+\frac{\partial u_\beta^{(0)}}{\partial x_\alpha}\right)+O(h^2), \tag{35}$$

$$\varepsilon_{33}=\frac{\partial u_3^{(1)}}{\partial \varsigma}+O(h^2), \tag{36}$$

$$\varepsilon_{\alpha 3}=\frac{1}{2h}\frac{\partial u_\alpha^{(0)}}{\partial \varsigma}+\frac{h}{2}\left(\frac{\partial u_\alpha^{(2)}}{\partial \varsigma}+\frac{\partial u_3^{(1)}}{\partial x_\alpha}\right)+O(h^3). \tag{37}$$

Since strains must be finite as the out-of-plane thickness h approaches 0 in a plane-stress problem, Eq. (37) requires

$$\frac{\partial u_\alpha^{(0)}}{\partial \varsigma}=0 \quad \text{or} \quad u_\alpha^{(0)}=u_\alpha^{(0)}(x_1,x_2). \tag{38}$$

This means the leading terms of the in-plane displacements $u_\alpha^{(0)}$ are independent of ς (or x_3). The incompressibility statement $\varepsilon_{\alpha\alpha}+\varepsilon_{33}=0$ and Eqs. (35) and (36) require

$$\frac{\partial u_3^{(1)}}{\partial \varsigma}=-\frac{\partial u_\alpha^{(0)}}{\partial x_\alpha} \quad \text{or} \quad u_3^{(1)}=-\varsigma\frac{\partial u_\alpha^{(0)}}{\partial x_\alpha}. \tag{39}$$

The strains in Eqs. (35)–(37) can then be written as

$$\varepsilon_{\alpha\beta}=\varepsilon_{\alpha\beta}^{(0)}+O(h^2)=\frac{1}{2}\left(\frac{\partial u_\alpha^{(0)}}{\partial x_\beta}+\frac{\partial u_\beta^{(0)}}{\partial x_\alpha}\right)+O(h^2), \tag{35$'$}$$

$$\varepsilon_{33}=\varepsilon_{33}^{(0)}+O(h^2)=-\frac{\partial u_\beta^{(0)}}{\partial x_\beta}+O(h^2), \tag{36$'$}$$

$$\varepsilon_{\alpha 3}=O(h). \tag{37$'$}$$

Here the zeroth-order terms in strains $\varepsilon_{\alpha\beta}^{(0)}$ and $\varepsilon_{33}^{(0)}$ are independent of the out-of-plane coordinate ς (or x_3). Using Eqs. (38) and (39), the strain gradients can be found from strain gradient-displacement relation (2) as

$$\eta_{\alpha\beta\gamma}=\eta_{\alpha\beta\gamma}^{(0)}+O(h^2)=\frac{\partial^2 u_\gamma^{(0)}}{\partial x_\alpha \partial x_\beta}+O(h^2), \tag{40}$$

$$\eta_{\alpha 33}=\eta_{\alpha 33}^{(0)}+O(h^2)=-\frac{\partial^2 u_\beta^{(0)}}{\partial x_\alpha \partial x_\beta}+O(h^2), \tag{41}$$

$$\eta_{33\alpha}=\eta_{33\alpha}^{(0)}+O(h^2)=\frac{\partial^2 u_\alpha^{(2)}}{\partial \varsigma^2}+O(h^2), \tag{42}$$

$$\eta_{\alpha\beta 3}=O(h), \quad \eta_{3\alpha\beta}=O(h), \quad \eta_{333}=O(h). \tag{43}$$

It should be pointed out that the leading term of strain gradient $\eta_{33\alpha}$ in Eq. (42) comes from the second-order displacement $u_\alpha^{(2)}$. As will be shown later, this term can be determined by the leading term of in-plane strain gradients $\eta_{\alpha\beta\gamma}^{(0)}$ from the plane-stress condition. Therefore, all leading terms of strain gradients $\eta_{\alpha\beta\gamma}^{(0)}$, $\eta_{33\alpha}^{(0)}$, and $\eta_{\alpha 33}^{(0)}$ are independent of ς (or x_3).

The constitutive Eq. (13) gives the deviatoric stresses as

$$\sigma'_{\alpha\beta}=\sigma'^{(0)}_{\alpha\beta}+O(h^2)=\frac{2}{3}\frac{\Sigma_0}{E_0^{1/n}}(E^{(0)})^{1/n-1}\varepsilon_{\alpha\beta}^{(0)}+O(h^2), \tag{44}$$

$$\sigma'_{33}=\sigma'^{(0)}_{33}+O(h^2)=-\frac{2}{3}\frac{\Sigma_0}{E_0^{1/n}}(E^{(0)})^{1/n-1}\varepsilon_{\alpha\alpha}^{(0)}+O(h^2), \tag{45}$$

$$\sigma'_{\alpha 3}=h\sigma'^{(1)}_{\alpha 3}=O(h), \tag{46}$$

where $E^{(0)}$ is the leading term in the combined measure E of effective strain and effective strain gradient in Eq. (6), and is given by

$$E^{(0)^2}=\frac{2}{3}(\varepsilon_{\alpha\beta}^{(0)}\varepsilon_{\alpha\beta}^{(0)}+\varepsilon_{\alpha\alpha}^{(0)}\varepsilon_{\beta\beta}^{(0)})+c_1(\eta_{\alpha\alpha\gamma}^{(0)}+\eta_{33\gamma}^{(0)})(\eta_{\beta\beta\gamma}^{(0)}+\eta_{33\gamma}^{(0)})$$
$$+c_2(\eta_{\alpha\beta\gamma}^{(0)}\eta_{\alpha\beta\gamma}^{(0)}+\eta_{33\gamma}^{(0)}\eta_{33\gamma}^{(0)}+2\eta_{\gamma\alpha\alpha}^{(0)}\eta_{\gamma\beta\beta}^{(0)})+c_3(\eta_{\alpha\beta\gamma}^{(0)}\eta_{\gamma\beta\alpha}^{(0)}$$
$$-2\eta_{\alpha\beta\beta}^{(0)}\eta_{33\alpha}^{(0)}+\eta_{\gamma\alpha\alpha}^{(0)}\eta_{\gamma\beta\beta}^{(0)}). \tag{47}$$

It is once again emphasized that, as shown later, $\eta_{33\alpha}^{(0)}$ can be related to the leading terms of in-plane strain gradients $\eta_{\alpha\beta\gamma}^{(0)}$ from the plane-stress condition. Therefore, $E^{(0)}$ is independent of ς (or x_3). Similarly, the deviatoric higher-order stresses are obtained from the constitutive Eq. (14) as

$$\tau'_{\alpha\beta\gamma}=\tau'^{(0)}_{\alpha\beta\gamma}+O(h^2)$$
$$=\frac{\Sigma_0}{E_0^{1/n}}(E^{(0)})^{1/n-1}\Bigg[c_1(\eta_{\delta\delta\gamma}^{(0)}+\eta_{33\gamma}^{(0)})\delta_{\alpha\beta}+c_2\eta_{\alpha\beta\gamma}^{(0)}$$
$$+\frac{c_3}{2}(\eta_{\gamma\beta\alpha}^{(0)}+\eta_{\gamma\alpha\beta}^{(0)})-\frac{1}{4}\left(c_1+\frac{c_3}{2}\right)(\eta_{\delta\delta\alpha}^{(0)}+\eta_{33\alpha}^{(0)})\delta_{\beta\gamma}$$
$$-\frac{1}{4}\left(c_1+\frac{c_3}{2}\right)(\eta_{\delta\delta\beta}^{(0)}+\eta_{33\beta}^{(0)})\delta_{\alpha\gamma}\Bigg]+O(h^2), \tag{48}$$

$$\tau'_{33\alpha}=\tau'^{(0)}_{33\alpha}+O(h^2)$$
$$=\frac{\Sigma_0}{E_0^{1/n}}(E^{(0)})^{1/n-1}[c_1\eta_{\delta\delta\alpha}^{(0)}+(c_1+c_2)\eta_{33\alpha}^{(0)}-c_3\eta_{\alpha\delta\delta}^{(0)}]$$
$$+O(h^2), \tag{49}$$

$$\tau'_{\alpha 33}=\tau'^{(0)}_{\alpha 33}+O(h^2)$$
$$=\frac{\Sigma_0}{E_0^{1/n}}(E^{(0)})^{1/n-1}\Bigg[-\left(c_2+\frac{c_3}{2}\right)\eta_{\alpha\delta\delta}^{(0)}-\frac{1}{4}\left(c_1-\frac{3}{2}c_3\right)\eta_{33\alpha}^{(0)}$$
$$-\frac{1}{4}\left(c_1+\frac{c_3}{2}\right)\eta_{\delta\delta\alpha}^{(0)}\Bigg]+O(h^2), \tag{50}$$

$$\tau'_{\alpha\beta 3}=h\tau'^{(1)}_{\alpha\beta 3}=O(h), \quad \tau'_{3\alpha\beta}=h\tau'^{(1)}_{3\alpha\beta}=O(h),$$
$$\tau'_{333}=h\tau'^{(1)}_{333}=O(h). \tag{51}$$

It can be shown that the zeroth-order terms $\sigma'^{(0)}_{\alpha\beta}$, $\sigma'^{(0)}_{33}$, $\tau'^{(0)}_{\alpha\beta\gamma}$, $\tau'^{(0)}_{33\alpha}$, and $\tau'^{(0)}_{\alpha 33}$ are independent of ς (or x_3), while the first-order terms $\sigma'^{(1)}_{\alpha 3}$, $\tau'^{(1)}_{\alpha\beta 3}$, $\tau'^{(1)}_{3\alpha\beta}$, and $\tau'^{(1)}_{333}$ are linearly proportional to ς (or x_3).

We analyze the equilibrium equations and traction-prescribed boundary conditions in the following. We start with the out-of-plane direction. The leading terms of the out-of-plane equilibrium Eq. (21) now become

$$\frac{1}{h}\frac{\partial}{\partial \varsigma}\left(\sigma'^{(0)}_{33}-2\tau'^{(0)}_{\alpha 33,\alpha}-\frac{\partial \tau'^{(1)}_{333}}{\partial \varsigma}+H^{(0)}\right)=0, \tag{52}$$

where the combined measure H of hydrostatic stress and hydrostatic higher-order stress has been expanded as

$$H=H^{(0)}+O(h^2). \tag{53}$$

The leading terms of out-of-plane boundary condition $\hat{t}_3=0$ in Eq. (30) give

$$\sigma'^{(0)}_{33}-2\tau'^{(0)}_{\alpha 33,\alpha}-\frac{\partial \tau'^{(1)}_{333}}{\partial \varsigma}+H^{(0)}=0, \quad \text{at} \quad \varsigma=\pm\frac{1}{2}. \tag{54}$$

Comparison of Eqs. (52) and (54) gives $H^{(0)}$ in the entire field as

$$H^{(0)}=-\sigma'^{(0)}_{33}+2\tau'^{(0)}_{\alpha 33,\alpha}+\frac{\partial \tau'^{(1)}_{333}}{\partial \varsigma}, \tag{55}$$

which is also independent of ς (or x_3). The leading terms of the other out-of-plane boundary conditions $\hat{t}_\gamma=0$ in Eq. (29) and $\hat{r}_\gamma=0$ in Eq. (31) give

$$\frac{\partial \tau'^{(0)}_{33\gamma}}{\partial \varsigma}=0, \quad \tau'^{(0)}_{33\gamma}=0, \quad \text{at} \quad \varsigma=\pm\frac{1}{2}. \tag{56}$$

It should be pointed out that, once the leading terms vanish, relations among some second-order terms become important. For example, the second-order terms of $\hat{t}_\gamma=0$ in Eq. (29) give

$$\sigma'^{(1)}_{3\gamma}-2\tau'^{(1)}_{3\beta\gamma,\beta}-\frac{\partial \tau'^{(2)}_{33\gamma}}{\partial \varsigma}+\tau'^{(1)}_{333,\gamma}=0, \quad \text{at} \quad \varsigma=\pm\frac{1}{2}, \tag{57}$$

where $\tau'^{(2)}_{33\gamma}$ is the second-order term of $\tau'_{33\gamma}$, i.e., $\tau'_{33\gamma}=\tau'^{(0)}_{33\gamma}+h^2\tau'^{(2)}_{33\gamma}+O(h^4)$.

We now analyze the in-plane equilibrium equations and boundary conditions. The leading terms of the in-plane equilibrium Eqs. (20) become

$$-\frac{1}{h^2}\frac{\partial^2 \tau'^{(0)}_{33\gamma}}{\partial \varsigma^2}=0. \tag{58}$$

In conjunction with Eq. (56), the above equation gives that the leading terms of $\tau'_{33\gamma}$ are identically zero, i.e.,

$$\tau'^{(0)}_{33\gamma}\equiv 0. \tag{59}$$

This, together with the constitutive relation (49), gives $\eta^{(0)}_{33\alpha}$ in terms of the in-plane strain gradients $\eta^{(0)}_{\alpha\beta\gamma}$, i.e.,

$$\eta^{(0)}_{33\alpha}=\frac{1}{c_1+c_2}(c_3\eta^{(0)}_{\alpha\delta\delta}-c_1\eta^{(0)}_{\delta\delta\alpha}). \tag{60}$$

Once the leading terms in in-plane equilibrium Eq. (20) vanish, the next order terms become important and give the governing equation for plane-stress deformation as

$$\sigma'^{(0)}_{\alpha\gamma,\alpha}-\tau'^{(0)}_{\alpha\beta\gamma,\alpha\beta}+H^{(0)}_{,\gamma}+\frac{\partial}{\partial \varsigma}\left(\sigma'^{(1)}_{3\gamma}-2\tau'^{(1)}_{3\alpha\gamma,\alpha}-\frac{\partial \tau'^{(2)}_{33\gamma}}{\partial \varsigma}\right)=0. \tag{61}$$

Since the zeroth-order terms are independent of ς, we can integrate the above equation from $\varsigma=-1/2$ to $\varsigma=1/2$ (over the thickness) to give the governing equations only in terms of the in-plane deviatoric stress and deviatoric higher-order stresses,

$$\sigma'^{(0)}_{\alpha\gamma,\alpha}-\tau'^{(0)}_{\alpha\beta\gamma,\alpha\beta}+(\sigma'^{(0)}_{\beta\beta}-2\tau'^{(0)}_{\alpha\beta\beta,\alpha})_{,\gamma}=0, \tag{62}$$

where Eqs. (55) and (57) have been used. Equation (62) gives two fourth-order differential equations for the two in-plane displacements, $u^{(0)}_1$ and $u^{(0)}_2$. Therefore, four independent boundary conditions should be prescribed on any boundaries within x_1-x_2 plane.

The in-plane stress-traction boundary condition (22) becomes

$$\begin{aligned}\hat{t}_\gamma=&H^{(0)}n_\gamma+n_\alpha(\sigma'^{(0)}_{\alpha\gamma}-\tau'^{(0)}_{\alpha\beta\gamma,\beta})+D_\gamma(n_\alpha n_\beta n_\delta\tau'^{(0)}_{\alpha\beta\delta})\\&-D_\beta(n_\alpha\tau'^{(0)}_{\alpha\beta\gamma})+(n_\alpha n_\beta\tau'^{(0)}_{\alpha\beta\gamma}-n_\gamma n_\alpha n_\beta n_\delta\tau'^{(0)}_{\alpha\beta\delta})(D_\zeta n_\zeta)\\&-2n_\alpha\frac{\partial \tau'^{(1)}_{3\alpha\gamma}}{\partial \varsigma},\end{aligned} \tag{63}$$

where, as shown in the Appendix, the last term on the right-hand side can be written in terms of in-plane strains and strain gradients as

$$\begin{aligned}\frac{\partial \tau'^{(1)}_{3\alpha\gamma}}{\partial \varsigma}=&\frac{\Sigma_0}{E_0^{1/n}}(E^{(0)})^{1/n-1}\left[c_2\eta^{(0)}_{33\gamma,\alpha}+\frac{c_3}{2}(\eta^{(0)}_{33\alpha,\gamma}-\varepsilon^{(0)}_{\beta\beta,\alpha\gamma})\right.\\&\left.+\frac{1}{4}\left(c_1+\frac{c_3}{2}\right)(\eta^{(0)}_{33\beta,\beta}+\varepsilon^{(0)}_{\beta\beta,\delta\delta})\delta_{\alpha\gamma}\right],\end{aligned} \tag{64}$$

while $H^{(0)}$ in Eq. (63) can be evaluated from Eq. (55) as (see Appendix for details)

$$\begin{aligned}H^{(0)}\equiv&\sigma'^{(0)}_{\beta\beta}-2\tau'^{(0)}_{\alpha\beta\beta,\alpha}-\frac{\Sigma_0}{E_0^{1/n}}(E^{(0)})^{1/n-1}\left[\left(\frac{c_1}{2}-\frac{c_3}{4}\right)\varepsilon^{(0)}_{\beta\beta,\alpha\alpha}\right.\\&\left.+\left(\frac{c_1}{2}+c_2+\frac{3}{4}c_3\right)\eta^{(0)}_{33\alpha,\alpha}\right].\end{aligned} \tag{65}$$

The in-plane higher-order stress-traction boundary condition (24) gives

$$\hat{r}_\gamma=n_\alpha n_\beta\tau'^{(0)}_{\alpha\beta\gamma}-n_\gamma n_\alpha n_\beta n_\delta\tau'^{(0)}_{\alpha\beta\delta}. \tag{66}$$

The other two traction boundary conditions in Eqs. (23) and (25), however, are on the order of $O(h)$ and therefore do not provide nontrivial boundary conditions for the leading terms in deformation. It is observed that Eqs. (63) and (66) give only three boundary conditions. This is quite puzzling because the governing Eq. (62) require four independent boundary conditions, as discussed before. This ''missing'' boundary condition represents a unique feature of plane-stress deformation in strain gradient plasticity since it does not occur in plane strain nor in three-dimensional deformation. In fact, this ''missing'' boundary condition comes from the line traction in Eq. (19). At the intersection of lateral surface $x_3=h/2(\varsigma=1/2)$ (unit normal $\mathbf{n}=(0,0,1)$) and the in-plane boundary with unit normal $\mathbf{n}=(n_\alpha,n_\beta,0)$, the line tractions $\hat{p}_k$ are given by

$$\hat{p}_\gamma=O(h), \tag{67}$$

$$\hat{p}_3=-2n_\alpha\tau'_{\alpha\beta\beta}-n_\alpha n_\beta n_\gamma\tau'_{\alpha\beta\gamma}. \tag{68}$$

The in-plane line tractions $\hat{p}_\gamma$ do not contribute to the leading terms in in-plane deformation because Eq. (67) vanish as h approaches zero. The leading terms of Eq. (68), however, do not automatically vanish. Therefore, the requirement of $\hat{p}_3=0$ for plane-stress deformation gives the ''missing'' fourth boundary condition as

$$2n_\alpha\tau'^{(0)}_{\alpha\beta\beta}+n_\alpha n_\beta n_\gamma\tau'^{(0)}_{\alpha\beta\gamma}=0. \tag{69}$$

This completes our systematic approach to derive the governing equations and boundary conditions for plane-stress deformation in strain gradient plasticity.

4 Summary

We have adopted a systematic approach to derive the governing equations and boundary conditions for plane-stress deformation in strain gradient plasticity. It has been shown that three-dimensional governing equations and boundary conditions are satisfied up to the order of $O(1)$, i.e., terms neglected are on the order of $O(h)$ or higher, which vanish as the thickness h in the out-of-plane direction approaches zero. The governing equations and traction-prescribed boundary conditions are summarized in the following, and the superscript 0 for the leading terms are omitted.

Kinematic Relations.

$$\varepsilon_{\alpha\beta}=\frac{1}{2}(u_{\alpha,\beta}+u_{\beta,\alpha}), \tag{70}$$

$$\eta_{\alpha\beta\gamma}=u_{\gamma,\alpha\beta}. \tag{71}$$

Constitutive Law.

$$\sigma'_{\alpha\beta}=\frac{2}{3}\frac{\Sigma_0}{E_0}\left(\frac{E}{E_0}\right)^{1/n-1}\varepsilon_{\alpha\beta}, \tag{72}$$

$$\tau'_{\alpha\beta\gamma}=\frac{\Sigma_0}{E_0}\left(\frac{E}{E_0}\right)^{1/n-1}\left[\frac{c_1}{c_1+c_2}(c_2\eta_{\delta\delta\gamma}+c_3\eta_{\gamma\delta\delta})\delta_{\alpha\beta}+c_2\eta_{\alpha\beta\gamma}\right.$$
$$+\frac{c_3}{2}(\eta_{\gamma\beta\alpha}+\eta_{\gamma\alpha\beta})-\frac{2c_1+c_3}{8(c_1+c_2)}(c_2\eta_{\delta\delta\alpha}+c_3\eta_{\alpha\delta\delta})\delta_{\beta\gamma}$$
$$\left.-\frac{2c_1+c_3}{8(c_1+c_2)}(c_2\eta_{\delta\delta\beta}+c_3\eta_{\beta\delta\delta})\delta_{\alpha\gamma}\right] \tag{73}$$

where Eq. (60) has been used to eliminate $\eta_{33\alpha}$, and the combined measure E of effective strain and effective strain gradient is given by

$$E^2=\frac{2}{3}(\varepsilon_{\alpha\beta}\varepsilon_{\alpha\beta}+\varepsilon_{\alpha\alpha}\varepsilon_{\beta\beta})+\frac{c_1}{(c_1+c_2)^2}(c_2\eta_{\alpha\alpha\gamma}+c_3\eta_{\gamma\alpha\alpha})$$
$$\times(c_2\eta_{\beta\beta\gamma}+c_3\eta_{\gamma\beta\beta})+c_2\left[\eta_{\alpha\beta\gamma}\eta_{\alpha\beta\gamma}+2\eta_{\gamma\alpha\alpha}\eta_{\gamma\beta\beta}\right.$$
$$\left.+\frac{1}{(c_1+c_2)^2}(c_1\eta_{\alpha\alpha\gamma}-c_3\eta_{\gamma\alpha\alpha})(c_1\eta_{\beta\beta\gamma}-c_3\eta_{\gamma\beta\beta})\right]$$
$$+c_3\left(\eta_{\alpha\beta\gamma}\eta_{\gamma\beta\alpha}+\frac{c_1+c_2-2c_3}{c_1+c_2}\eta_{\gamma\alpha\alpha}\eta_{\gamma\beta\beta}\right.$$
$$\left.+\frac{2c_1}{c_1+c_2}\eta_{\gamma\alpha\alpha}\eta_{\beta\beta\gamma}\right). \tag{74}$$

Equilibrium Equations.

$$\sigma'_{\alpha\gamma,\alpha}-\tau'_{\alpha\beta\gamma,\alpha\beta}+(\sigma'_{\beta\beta}-2\tau'_{\alpha\beta\beta,\alpha})_{,\gamma}=0. \tag{75}$$

Traction-Prescribed Boundary Conditions.

$$\hat{t}_\gamma=Hn_\gamma+n_\alpha(\sigma'_{\alpha\gamma}-\tau'_{\alpha\beta\gamma,\beta})+D_\gamma(n_\alpha n_\beta n_\delta\tau'_{\alpha\beta\delta})-D_\beta(n_\alpha\tau'_{\alpha\beta\gamma})$$
$$+(n_\alpha n_\beta\tau'_{\alpha\beta\gamma}-n_\gamma n_\alpha n_\beta n_\delta\tau'_{\alpha\beta\delta})(D_\zeta n_\zeta)-2n_\alpha A_{\alpha\gamma}, \tag{76}$$
$$\hat{r}_\gamma=n_\alpha n_\beta\tau'_{\alpha\beta\gamma}-n_\gamma n_\alpha n_\beta n_\delta\tau'_{\alpha\beta\delta}, \tag{77}$$
$$0=2n_\alpha\tau'_{\alpha\beta\beta}+n_\alpha n_\beta n_\gamma\tau'_{\alpha\beta\gamma}, \tag{78}$$

where H is the combined measure of hydrostatic stress and hydrostatic higher-order stress and is given by

$$H\equiv\sigma'_{\beta\beta}-2\tau'_{\alpha\beta\beta,\alpha}-\frac{\Sigma_0}{E_0}\left(\frac{E}{E_0}\right)^{1/n-1}\frac{(3c_3-2c_1)(c_2+c_3)}{4(c_1+c_2)}\varepsilon_{\beta\beta,\alpha\alpha}, \tag{79}$$

and the tensor $A_{\alpha\gamma}$ in Eq. (76) is given by

$$A_{\alpha\gamma}=\frac{\Sigma_0}{E_0}\left(\frac{E}{E_0}\right)^{1/n-1}\left[\frac{c_3(c_2+c_3-c_1)}{2(c_1+c_2)}\varepsilon_{\beta\beta,\alpha\gamma}-\frac{c_1c_2}{c_1+c_2}\eta_{\delta\delta\gamma,\alpha}\right.$$
$$\left.-\frac{c_1c_3}{2(c_1+c_2)}\eta_{\delta\delta\alpha,\gamma}+\frac{(2c_1+c_3)(c_2+c_3)}{8(c_1+c_2)}\varepsilon_{\beta\beta,\delta\delta}\delta_{\alpha\gamma}\right]. \tag{80}$$

It is observed that the constitutive law (73), the expression (74) of combined measure E of effective strain and effective strain gradient, equilibrium Eq. (75), the boundary condition (76) for plane-stress deformation in strain gradient plasticity are much more complicated than their counterparts in plane-strain condition. Moreover, the boundary condition (78) is imposed for plane-stress deformation only. However, for dislocation-model-based strain gradient plasticity ([26,27]) in which $c_1=c_3=0$, the governing equations and boundary conditions take some rather simple forms that are similar to their counterparts in plane strain. For example, Eq. (73) becomes

$$\tau'_{\alpha\beta\gamma}=\frac{\Sigma_0}{E_0}\left(\frac{E}{E_0}\right)^{1/n-1}c_2\eta_{\alpha\beta\gamma}, \tag{73'}$$

where the combined measure E of effective strain and effective strain gradient in Eq. (74) is simplified to

$$E^2=\frac{2}{3}(\varepsilon_{\alpha\beta}\varepsilon_{\alpha\beta}+\varepsilon_{\alpha\alpha}\varepsilon_{\beta\beta})+c_2(\eta_{\alpha\beta\gamma}\eta_{\alpha\beta\gamma}+2\eta_{\gamma\alpha\alpha}\eta_{\gamma\beta\beta}). \tag{74'}$$

The boundary condition (76) also becomes simpler because the last term $A_{\alpha\gamma}$ vanishes; similarly, the last term in Eq. (79) vanishes such that the combined measure of hydrostatic stress and hydrostatic higher-order stress takes a simple form

$$H=\sigma'_{\beta\beta}-2\tau'_{\alpha\beta\beta,\alpha}. \tag{79'}$$

Therefore, strain gradient plasticity based on dislocation models gives a much simpler form than phenomenological strain gradient plasticity.

Acknowledgments

The work of Y. H. was supported by the NSF through grant CMS-98-96285 and NSF of China. The work of K. C. H. was supported by NSF of China.

Appendix

Similar to the derivation of Eqs. (48), (49), and (50), it can be established from the constitutive Eq. (14) that

$$\tau'^{(1)}_{3\alpha\gamma}=\frac{\Sigma_0}{E_0^{1/n}}(E^{(0)})^{1/n-1}\left[c_2\eta^{(1)}_{3\alpha\gamma}+\frac{c_3}{2}(\eta^{(1)}_{\gamma\alpha3}+\eta^{(1)}_{3\gamma\alpha})\right.$$
$$\left.-\frac{1}{4}\left(c_1+\frac{c_3}{2}\right)(\eta^{(1)}_{\beta\beta3}+\eta^{(1)}_{333})\delta_{\alpha\gamma}\right], \tag{A1}$$

$$\tau'^{(1)}_{333}=\frac{\Sigma_0}{E_0^{1/n}}(E^{(0)})^{1/n-1}\left[\left(\frac{c_1}{2}-\frac{c_3}{4}\right)\eta^{(1)}_{\beta\beta3}+\left(\frac{c_1}{2}+c_2+\frac{3}{4}c_3\right)\eta^{(1)}_{333}\right]. \tag{A2}$$

Their derivatives respect to ς can be written in terms of displacements as

$$\frac{\partial\tau'^{(1)}_{3\alpha\gamma}}{\partial\varsigma}=\frac{\Sigma_0}{E_0^{1/n}}(E^{(0)})^{1/n-1}\left[c_2\frac{\partial^2u^{(2)}_{\gamma,\alpha}}{\partial\varsigma^2}+\frac{c_3}{2}\left(-u^{(0)}_{\beta,\alpha\beta\gamma}+\frac{\partial^2u^{(2)}_{\alpha,\gamma}}{\partial\varsigma^2}\right)\right.$$
$$\left.+\frac{1}{4}\left(c_1+\frac{c_3}{2}\right)\left(u^{(0)}_{\beta,\beta\delta\delta}+\frac{\partial^2u^{(2)}_{\beta,\beta}}{\partial\varsigma^2}\right)\delta_{\alpha\gamma}\right], \tag{A3}$$

$$\frac{\partial\tau'^{(1)}_{333}}{\partial\varsigma}=\frac{\Sigma_0}{E_0^{1/n}}(E^{(0)})^{1/n-1}\left[-\left(\frac{c_1}{2}-\frac{c_3}{4}\right)u^{(0)}_{\beta,\beta\alpha\alpha}\right.$$
$$\left.-\left(\frac{c_1}{2}+c_2+\frac{3}{4}c_3\right)\frac{\partial^2u^{(2)}_{\beta,\beta}}{\partial\varsigma^2}\right], \tag{A4}$$

where incompressibility (39) and $\partial u^{(3)}_3/\partial\varsigma=\partial u^{(2)}_\beta/\partial x_\beta$ have been used. The substitution of Eqs. (35′) and (42) into Eq. (*A*3) yields the expression of $\partial\tau'^{(1)}_{3\alpha\gamma}/\partial\varsigma$ given in Eq. (64). Similarly, the substitution of Eqs. (35′) and (42) into Eq. (*A*4) provides the expression of $\partial\tau'^{(1)}_{333}/\partial\varsigma$, which is further substituted into Eq. (55) to give the combined measure $H^{(0)}$ of hydrostatic stress and hydrostatic higher-order stress in Eq. (65).

References

[1] Nix, W. D., 1989, ''Mechanical Properties of Thin Films,'' Metall. Trans. A, **20A**, pp. 2217–2245.
[2] De Guzman, M. S., Newbauer, G., Flinn, P., and Nix, W. D., 1993, ''The Role of Indentation Depth on the Measured Hardness of Materials,'' *Materials Research Symposium Proceedings*, **308**, pp. 613–618.
[3] Stelmashenko, N. A., Walls, A. G., Brown, L. M., and Milman, Y. V., 1993, ''Microindentations on W and Mo Oriented Single Crystals: An STM Study,'' Acta Metall. Mater., **41**, pp. 2855–2865.
[4] Ma, Q., and Clarke, D. R., 1995, ''Size Dependent Hardness of Silver Single Crystals,'' J. Mater. Res., **10**, pp. 853–863.
[5] Poole, W. J., Ashby, M. F., and Fleck, N. A., 1996, ''Micro-Hardness of

Annealed and Work-Hardened Copper Polycrystals,'' Scr. Metall. Mater., **34**, pp. 559–564.
[6] McElhaney, K. W., Vlassak, J. J., and Nix, W. D., 1998, ''Determination of Indenter Tip Geometry and Indentation Contact Area for Depth-Sensing Indentation Experiments,'' J. Mater. Res., **13**, pp. 1300–1306.
[7] Fleck, N. A., Muller, G. M., Ashby, M. F., and Hutchinson, J. W., 1994, ''Strain Gradient Plasticity: Theory and Experiment,'' Acta Metall. Mater., **42**, pp. 475–487.
[8] Stolken, J. S., and Evans, A. G., 1998, ''A Microbend Test Method for Measuring the Plasticity Length Scale,'' Acta Metall., **46**, pp. 5109–5115.
[9] Lloyd, D. J., 1994, ''Particle Reinforced Aluminum and Magnesium Matrix Composites,'' Int. Mater. Rev., **39**, pp. 1–23.
[10] Aifantis, E. C., 1984, ''On the Microstructural Origin of Certain Inelastic Models,'' J. Eng. Mater. Technol., **106**, pp. 326–330.
[11] Muhlhaus, H. B., and Aifantis, E. C., 1991, ''A Variational Principle for Gradient Plasticity,'' Int. J. Solids Struct., **28**, pp. 845–857.
[12] Fleck, N. A., and Hutchinson, J. W., 1993, ''A Phenomenological Theory for Strain Gradient Effects in Plasticity,'' J. Mech. Phys. Solids, **41**, pp. 1825–1857.
[13] Fleck, N. A., and Hutchinson, J. W., 1997, ''Strain Gradient Plasticity,'' *Advances in Applied Mechanics*, J. W. Hutchinson, and T. Y. Wu, eds., Vol. 33, Academic Press, San Diego, CA, pp. 295–361.
[14] Ashby, M. F., 1970, ''The Deformation of Plastically Non-homogeneous Alloys,'' Philos. Mag., **21**, pp. 399–424.
[15] Nye, J. F., 1953, ''Some Geometrical Relations in Dislocated Crystals,'' Acta Metall., **1**, pp. 153–162.
[16] Cottrell, A. H., 1964, *The Mechanical Properties of Materials*, John Wiley and Sons, New York, p. 277.
[17] Toupin, R. A., 1962, ''Elastic Materials With Couple Stresses,'' Arch. Ration. Mech. Anal., **11**, pp. 385–414.
[18] Koiter, W. T., 1964, ''Couple Stresses in the Theory of Elasticity, I and II,'' *Proceedings. Koninklijke Nederlandse Akademie van Wetenschappen (B)*, **67**, pp. 17–44.
[19] Mindlin, R. D., 1964, ''Micro-Structure in Linear Elasticity,'' Arch. Ration. Mech. Anal., **16**, pp. 51–78.
[20] Mindlin, R. D., 1965, ''Second Gradient of Strain and Surface Tension in Linear Elasticity,'' Int. J. Solids Struct., **1**, pp. 417–438.
[21] Curtin, M. E., 1965, ''Thermodynamics and the Possibility of Spatial Interaction in Elastic Materials,'' Arch. Ration. Mech. Anal., **19**, pp. 339–352.
[22] Acharya, A., and Shawki, T. G., 1995, ''Thermodynamic Restrictions on Constitutive Equations for Second-Deformation-Gradient Inelastic Behavior,'' J. Mech. Phys. Solids, **43**, pp. 1751–1772.
[23] Acharya, A., and Bassani, J. L., 1996, ''On Non-local Flow Theories That Preserve the Classical Structure of Incremental Boundary Value Problems,'' *Proceedings of the IUTAM Symposium on Micromechanics of Plasticity and Damage at Multiphase Materials*, A. Pineau and A. Zaoui, eds., Kluwer Academic Press, Dordrecht, The Netherlands, pp. 3–10.
[24] Begley, M. R., and Hutchinson, J. W., 1998, ''The Mechanics of Size-dependent Indentation,'' J. Mech. Phys. Solids, **46**, pp. 2049–2068.
[25] Nix, W. D., and Gao, H., 1998, ''Indentation Size Effects in Crystalline Materials: A Law for Strain Gradient Plasticity,'' J. Mech. Phys. Solids, **46**, pp. 411–425.
[26] Gao, H., Huang, Y., Nix, W. D., and Hutchinson, J. W., 1999, ''Mechanism-Based Strain Gradient Plasticity—I. Theory,'' J. Mech. Phys. Solids, **47**, pp. 1239–1263.
[27] Huang, Y., Gao, H., Nix, W. D., and Hutchinson, J. W., 2000, ''Mechanism-Based Strain Gradient Plasticity—II. Analysis,'' J. Mech. Phys. Solids, **48**, pp. 99–128.
[28] Shu, J. Y., and Fleck, N. A., 1998, ''The Prediction of a Size-Effect in Microindentation,'' Int. J. Solids Struct., **35**, pp. 1363–1383.
[29] Wang, W., Huang, Y., Hsia, K. J., Hu, K. X., Yeh, C. P., and Chandra, A., 1999, ''A Study of Ultra-thin Beams by Strain Gradient Plasticity,'' submitted for publication.
[30] Huang, Y., Zhang, L., Guo, T. F., and Hwang, K.-C., 1995, ''Near-Tip Fields for Cracks in Materials With Strain Gradient Effects,'' *IUTAM Symposium on Nonlinear Analysis of Fracture*, J. R. Willis, ed., Cambridge University, Sept. 3–7, pp. 231–243.
[31] Huang, Y., Zhang, L., Guo, T. F., and Hwang, K.-C., 1997, ''Fracture of Materials With Strain Gradient Effects,'' *Advances in Fracture Research*, Ninth International Conference of Fracture, Sydney, Australia, Apr. 1–5, pp. 2275–2286.
[32] Huang, Y., Zhang, L., Guo, T. F., and Hwang, K. C., 1997, ''Mixed Mode Near-Tip Fields for Cracks in Materials With Strain Gradient Effects,'' J. Mech. Phys. Solids, **45**, pp. 439–465.
[33] Huang, Y., Hwang, K. C., and Guo, T. F., 1998, ''Fracture of Materials at the Microscale, Mechanical Problems of Advanced Engineering Materials'' M. Senoo, B. Y. Xu, M. Tokuda, and B. Bundara, eds., *Third International Symposium on Microstructures and Mechanical Properties of New Engineering Materials*, Mei University Press, Tsu, Japan, pp. 3–12.
[34] Huang, Y., Chen, J. Y., Guo, T. F., Zhang, L., and Hwang, K. C., 2000, ''Analytical and Numerical Studies on Mode I and Mode II Fracture in Elastic-plastic Materials With Strain Gradient Effects,'' Int. J. Fract., in press.
[35] Xia, Z. C., and Hutchinson, J. W., 1996, ''Crack Tip Fields in Strain Gradient Plasticity,'' J. Mech. Phys. Solids, **44**, pp. 1621–1648.
[36] Wei, Y., and Hutchinson, J. W., 1997, ''Steady-State Crack Growth and Work of Fracture for Solids Characterized by Strain Gradient Plasticity,'' J. Mech. Phys. Solids, **45**, pp. 1253–1273.
[37] Chen, J. Y., Huang, Y., and Hwang, K. C., 1998, ''Mode I and Mode II Plane-Stress Near-Tip Fields for Cracks in Materials With Strain Gradient Effects,'' Key Eng. Mater., **145**, pp. 19–28.
[38] Smyshlyaev, V. P., and Fleck, N. A., 1996, ''The Role of Strain Gradients in the Grain Size Effect for Polycrystals,'' J. Mech. Phys. Solids, **44**, pp. 465–495.
[39] Love, A. E. H., 1927, *A Treatise of Mathematical Theory of Elasticity*, Cambridge University Press, Cambridge, UK.

P. Vielsack
Professor

H. Spiess
Graduate Student

Institute fur Mechanik,
Universitat Karlsruhe,
Postfach 6980,
76049 Karlsruhe,Germany
e-mail: Mechanik@bau-verm.uni-karlsruhe.de

Sliding of a Mass on an Inclined Driven Plane With Randomly Varying Coefficient of Friction

Investigated are sliding motions of a rigid body on a harmonically driven inclined plane. Coulomb's law with a random coefficient of friction is assumed. The mean sliding velocity in a steady state of deterministic motions is taken as a measure to compare deterministic with stochastic behavior. Not only do the random parameters influence the deviation in the results but strongly influence the typical features of the different motions themselves. [S0021-8936(00)01701-3]

1 Introduction

Systematic investigations of dry friction problems have been made available in the last decade. They are focused either on microscopic approaches concerning correlation processes between two bodies in contact or on macroscopic friction laws. Most friction laws are phenomenological in their character and do not consider micromechanical mechanisms. Comprehensive literature can be found in the review paper of Ibrahim [1]. Mainly Coulomb's law or various modified versions are used for calculations. Their peculiar feature is the assumption of a constant coefficient of friction along the sliding path. In reality, randomly distributed interface irregularities due to contamination, surface finish, roughness, and waviness of the contact surface should be taken into account. Experimental data always exhibit a randomly varying friction force along the sliding path. As will be shown, the use of a constant coefficient of friction does not only involve an uncertain parameter in the calculation of a distinct motion but it neglects the interaction of the solution with typical characteristics of the sliding motion itself.

2 Mechanical System

Consider a mass m on a rough plane with an angle of inclination $\alpha \geqslant 0$. (See Fig. 1).

The drive of the plane

$$y = a \sin \Omega t \tag{1}$$

is harmonic with support displacement amplitude a and angular frequency Ω. The relative coordinate x gives the position of the mass which can either slide or have lockups on the plane. To describe the sliding path a length coordinate

$$ds = |dx| \tag{2}$$

is introduced. This separation between the mass trajectory s and the relative position x is necessary because of the specific features of the motion. The mass will slide back and forth. A material point on the contact surface can be touched more than one time. A dependency of the friction coefficient on the relative position x is inconsistent because of two reasons. First, a reversal in the direction of sliding may lead to different friction at the same point x. The simplest intuitive example is a brushed carpet, having low resistance when moving a mass in direction to the unidirectional oriented fibers and high resistance in the opposite direction. Second, each sliding process alters the friction properties of the interface. A reversal of direction therefore always meets a new situation.

Both facts can be proved by calculating the exceptional case of the motion on an ideal horizontal plane ($\alpha = 0$). Deterministic friction exhibits stationary, periodic oscillations with constant amplitude. Stochastic friction, depending on the relative position x, also leads to equivalent features of the stationary motion. The distribution of the friction coefficient along the sliding path becomes periodic. This contradicts reality.

Coulomb's law of kinetic friction gives the active tangential contact force

$$R_a = \mu mg \cos \alpha \operatorname{sgn} \dot{x}. \tag{3}$$

The normal compressive force $mg \cos \alpha$ remains constant for all times.

During sliding the friction coefficient $\mu(s)$ depends on the surface properties along the sliding path. Kilburn [2] conducted an experimental investigation which indicates that friction behaves like a random process. Its constant component is most significant and nearly identical to the coefficient of friction. This allows the assumption

$$\mu(s) = \mu_0 + f(s) \tag{4}$$

with a constant mean value μ_0 superimposed by a random field $f(s)$. Solutions in the deterministic case $f(s) \equiv 0$ have already been derived by Vielsack [3]. The choice of the deviation $f(s)$ is rather intuitive. It is oriented by Soom and Chen [4], who simulated the effective roughness in terms of a wave number spectrum but without taking friction into account. In contrast, a constant waviness of the contact surface will be considered in the following. This implies the existence of a definite material pattern at the interface. Apparently, sand paper with a definite granulation is the most simple example. Then, the interface parameter Δ is achieved by subdividing the sliding coordinate s into constant steps. The random field $f(s)$ reads

$$f(s) = X_n, \quad s \in [n\Delta, (n+1)\Delta], \quad n = 0,1,2, \ldots \tag{5}$$

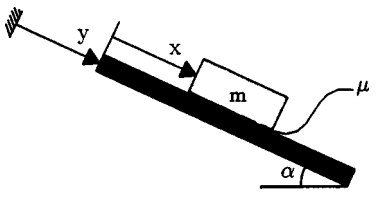

Fig. 1 Rigid mass on an inclined, moving, rough plane

Contributed by the Applied Mechanics Division of THE AMERICAN SOCIETY OF MECHANICAL ENGINEERS for publication in the ASME JOURNAL OF APPLIED MECHANICS. Manuscript received by the ASME Applied Mechanics Division, Nov. 6, 1998; final revision, July 9, 1999. Associate Technical Editor: J. T. Jenkins. Discussion on the paper should be addressed to the Technical Editor, Professor Lewis T. Wheeler, Department of Mechanical Engineering, University of Houston, Houston, TX 77204-4792, and will be accepted until four months after final publication of the paper itself in the ASME JOURNAL OF APPLIED MECHANICS.

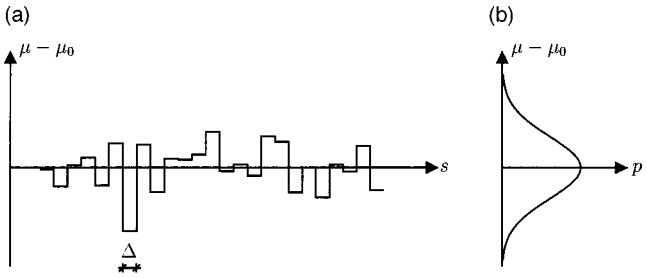

Fig. 2 Friction coefficient: (*a*) versus sliding path, (*b*) Gaussian distribution

where X_n are real numbers, normally distributed (Gaussian) with mean value zero and standard deviation σ. They are generated by a standard computer program. These assumptions lead to a Gaussian distribution of the friction coefficient along the sliding path as illustrated in Fig. 2.

The interface parameter Δ cannot be correlated with the real geometry of the interface. This is conditioned by Coulomb's law being independent of the shape of the contact area, as well as by the rigid-body model having no distinct geometrical dimension. Therefore, Δ can only be used as a relative measure. The question is, how does the mechanical system behave if the interface parameter Δ tends to zero without changing the standard deviation σ.

Sliding is determined by the motion equation

$$m\ddot{x} + R_a = mg \sin\alpha + ma\Omega^2 \sin\Omega t. \tag{6}$$

During sticking a passive tangential contact force

$$R_p = mg \sin\alpha + ma\Omega^2 \sin\Omega t \tag{7}$$

exists. The quantities

$$\begin{aligned} \tau &= \Omega t \\ A &= \tan\alpha/\mu_0 \\ B &= a\Omega^2/(\mu_0 g \cos\alpha) \\ \rho_p &= R_p/(\mu_0 mg \cos\alpha) \\ \rho_a &= R_a/(\mu_0 mg \cos\alpha) \\ \xi &= Bx/a \\ \delta &= B\Delta/a \\ c_n &= X_n/\mu_0 \end{aligned} \tag{8}$$

allow a dimensionless representation of (3), (6), and (7) in the form

$$\left.\begin{aligned} \rho_a &= (1+c_n)\operatorname{sgn}\xi' \\ \xi'' &= -\rho_a + A + B\sin\tau \end{aligned}\right\} \quad \xi' \neq 0 \tag{9}$$

for sliding, and

$$\left.\begin{aligned} \rho_p &= A + B\sin\tau \\ \xi &\equiv \xi_0 \end{aligned}\right\} \quad \xi' \equiv 0 \tag{10}$$

for sticking. The random number c_n must be generated after each sliding step δ. The constant displacement ξ_0 characterizes a distinct state of sticking. During the course of time, the contact force

$$\rho = \begin{cases} \rho_a; & \xi' \neq 0 \\ \rho_p; & \xi' \equiv 0 \end{cases} \tag{11}$$

is intermittent between active and passive. The separation points are called switching times. They are the inherent unknowns of the nonsmooth dynamical problem under consideration.

3 Integration of Motion

The motion can consist of a sequence of three possible smooth partial states, i.e., relative sliding down ($\xi' > 0$), relative sliding up ($\xi' < 0$), and states of sticking ($\xi' \equiv 0$). The partial states are enumerated by $k = 0,1,2,\ldots$. The type and the duration of the kth smooth part ($k = 0,1,2,\ldots$) depend on the excitation parameters A and B and are not known a priori. Therefore, in addition to Eqs. (9) and (10) further information is needed indicating the end of a certain state (switching condition) and predicting the type of the following state (switching decision).

3.1 State ''Sticking''. Assume $\tau = \tau_{k-1}$ to be a known switching time at which a partial state ''sticking'' starts. The previous history of motion at the time $\tau_{k-1} - 0$ yields the coordinate $\xi(\tau_{k-1} - 0) = \xi_0$ and the velocity $\xi'(\tau_{k-1} - 0) = 0$. They form the constant relative displacement $\xi(\tau) \equiv \xi_0$ and the vanishing relative velocity $\xi'(\tau) \equiv 0$ during the existence of this state in a time interval $\tau_{k-1} < \tau < \tau_k$. The unknown switching time τ_k characterizes the change to the next partial state. The passive contact force ρ_p can be calculated from Eq. (10) at any time $\tau > \tau_{k-1}$. Sticking is finished as soon as the value of the passive contact force ρ_p reaches the threshold for sliding, which means

$$|\rho_p(\tau)| = |\rho_a|. \tag{12}$$

The value of the active friction force ρ_a is known from the end of the last sliding process at τ_{k-1} and is kept constant during $\tau_{k-1} < \tau < \tau_k$. Equation (12) is called a switching condition. As $\rho_p(\tau)$ is a known function in time, the switching time τ_k follows from the search for the first root of the algebraic expression (12) in the open interval $(\tau_{k-1}, \tau[$. If no root exists, the mechanical system remains in a state of lockup for all times. Otherwise, sticking is followed by sliding. Knowing the switching time τ_k, the switching decision

$$\operatorname{sgn}(\xi') = \operatorname{sgn}(\rho_p(\tau_k - 0)) \tag{13}$$

rules the direction of sliding. At the switching time τ_k, the contact force (11) changes from passive to active continuously, but not continuously differentiably.

3.2 States ''Sliding''. Assume $\tau = \tau_{k-1}$ to be a known switching time at which a partial state ''sliding'' with a known direction of velocity ξ' starts. The previous history yields the generalized coordinates $\xi(\tau_{k-1} - 0)$ and $\xi'(\tau_{k-1} - 0) = 0$ at the time $\tau_{k-1} - 0$. They form the initial conditions

$$\begin{aligned} \xi(\tau_{k-1} + 0) &= \xi(\tau_{k-1} - 0) \\ \xi'(\tau_{k-1} + 0) &= 0 \end{aligned} \tag{14}$$

for the equation of motion (9) with a random number c_n known from the previous partial state. The sign of the velocity ξ' is known at $\tau_{k-1} + 0$ from history. Therefore, Eq. (9) becomes linear. Taking (14) into account, its explicit solution can be given. Because of its simplicity it shall be omitted in the following. A numerical integration is not needed.

The procedure of solving a state ''sliding'' consists of two loops. The outer loop concerns the jump of the deviation $f(s)$ in Eq. (4). The intervals δ on the total sliding path are enumerated by $n = 0,1,2,\ldots$.

During sliding the active contact force ρ_a will change its value after each length step δ. Assume τ_{n-1} to be a known switching time at which the value of ρ_a changes from $1 + c_{n-1}$ to $1 + c_n$. Then c_n has to be generated as a new random number. The initial conditions for the solution of Eq. (9) in the open interval $(\tau_{n-1}, \tau[$ read

$$\begin{aligned} \xi(\tau_{n-1} + 0) &= \xi(\tau_{n-1} - 0), \\ \xi'(\tau_{n-1} + 0) &= \xi'(\tau_{n-1} - 0). \end{aligned} \tag{15}$$

The value of the active contact force $\rho_a = 1 + c_n$ is limited to a time interval $\tau_{n-1} < \tau < \tau_n$ with unknown upper bound. It is finished when the ratio

$$\int_0^{\xi} \frac{|d\xi(\tau)|}{\delta} = n; n \in \mathbf{N} \tag{16}$$

becomes the natural number n. As $\xi(\tau)$ is known explicitly, the switching condition (16) is an algebraic expression which allows for calculation of the unknown switching time τ_n.

The inner loop controls the existence of the kth smooth state, which actually is assumed to be ''sliding'' by inspecting all successive intervals δ one by one.

A partial state ''sliding'' consists of a sequence of solutions of Eq. (9) with different values of ρ_a. Altogether sliding exists in a time range $\tau_{k-1} < \tau < \tau_k$. The unknown switching time τ_k characterizes the transition to a new state. Sliding in one direction is finished when the velocity ξ' becomes zero. The search for the first root of the switching condition

$$\xi'(\tau) = 0 \tag{17}$$

in the open interval $(\tau_{k-1}, \tau[$ leads to the switching time τ_k. This is again an algebraic task. If no root exists, the mechanical system remains in a unidirectional sliding process for all times. Otherwise, one has to decide about the new state starting at $\tau_k + 0$. First, sticking is assumed. The passive contact force $\rho_p(\tau_k + 0)$ follows from Eq. (10). If the switching decision

$$|\rho_p(\tau_k + 0)| < |\rho_a| \tag{18}$$

is valid, sticking really exists in the open interval $(\tau_k, \tau[$. If, on the other hand,

$$|\rho_p(\tau_k + 0)| > |\rho_a|, \tag{19}$$

there exists an immediate reversal of motion to opposite sliding

$$\operatorname{sgn}(\xi') = -\operatorname{sgn}(\xi'(\tau_k - 0)). \tag{20}$$

At the end of each sliding process, the contact force ρ is discontinuous.

The problem of integration is reduced to an algebraic task. This is the determination of all switching times on the basis of the switching conditions (12), (16), and (17), which will be performed by numerical means as described by Vielsack and Hartung [5]. The total motion consists of a sequence of different states, which are valid during time intervals of different lengths. The end of a certain state determines the following one. The total solution is pieced together analytically. The process is strongly history dependent.

Despite the fact that no numerical integration is necessary, all calculations are extremely time-consuming. The reasons lie in the iterative determination of all transition points between successive length intervals δ to get the sequence $n = 0,1,2, \ldots$ and of all switching times between all intermittent states ''sliding'' and ''sticking'' to get the sequence $k = 0,1,2, \ldots$. Moreover, the time range $\tau > 0$ for the calculations must be chosen very large to obtain sufficiently large numbers of samples because the durations of the sliding periods are random. In reality, to get one probability distribution, about 15 hours are needed on a Pentium II, 400 MHz PC.

4 Results

The main interest is focused on the consequences of stochastic friction on the system's response. It is obvious that only a limited number of examples can be considered. Their choice is rather heuristic. But the aim is to compare a ''normal'' situation with two ''exceptional'' ones. This implies the appropriate choice of three sets of parameters A and B. The question is whether equal stochastic properties δ and σ have the same influence on the responses in all three sets, or not.

4.1 Deterministic Dry Friction. Both parameters A and B contain implicitly the constant mean value μ_0 of the coefficient of friction. The absolute value of the active friction force is normalized to $|\rho_a| = 1$. The intensity of the harmonic drive is captured by $B \geqslant 0$. The inclination of the plane is given by $A \geqslant 0$. A constellation $0 \leqslant A \leqslant 1$ and $B = 0$ corresponds to the trivial lockup of a mass on an inclined unmoveable plane. $A > 1$ leads to unidirectional accelerated sliding down. Within the range $0 \leqslant A < 1$ and $B > 0$ (sufficiently large to exceed the threshold value of Eq. (11)) the mass performs different types of steady-state motions. Their response period 2π always equals the dimensionless excitation period. A constant mean velocity

$$\xi'_m = [\xi(\tau + 2\pi) - \xi(\tau)]/2\pi \tag{21}$$

exists for all types. This quantity will be taken for now to characterize the main property of a distinct response.

Figure 3 shows phase curves of three steady states during two response periods. Figure 3(*a*) depicts a ''normal'' situation with alternating sliding up and down without sticking. The amount of velocity in a state ''sliding down'' is about three times larger than for ''sliding up.'' This leads to a drift $\xi(\tau + 2\pi) - \xi(\tau) = 6.11$ during one response period. The value $A = 0.99$ for the motion plotted in Fig. 3(*b*) is near to the critical inclination $A = 1.0$. Even low excitation $B = 0.4$ is sufficient to induce a steady-state motion with a considerable drift $\xi(\tau + 2\pi) - \xi(\tau) = 2.34$. The response consists of successive states of unidirectional sliding down with intermediate states of sticking. Their duration of about ten percent of a period is not visible because time is eliminated in the trajectory. Figure 3(*c*) depicts the fact of an approximately horizontal plane with $A = 0.01$. Despite the strong excitation $B = 4.0$, the drift $\xi(\tau + 2\pi) - \xi(\tau) = 0.36$ is very small. The response consists of a sequence of alternating sliding without sticking. The velocity distribution in both directions is nearly the same.

4.2 Stochastic Dry Friction. In addition to the system parameters A and B two more parameters δ and σ are needed to describe the friction properties of the contact surface. Its interface property is measured by δ. Three values $\delta = 0.1$, $\delta = 0.01$, and $\delta = 0.001$ will be considered in the following. The standard deviation $\sigma = 0.1$ of the random numbers in Eq. (9) will be the same for all problems. To compare stochastic effects with the corresponding deterministic result, the probability density function $p(e)$ of the true relative error

$$e = [\xi'_m(A,B) - \xi'_m(A,B,\delta,\sigma)]/\xi'_m(A,B) \tag{22}$$

of the mean velocity for a given set of parameters is needed. The procedure is as follows: The deterministic value $\xi'_m(A,B)$ is calculated once. The stochastic value $\xi'_m(A,B,\delta,\sigma)$ changes from

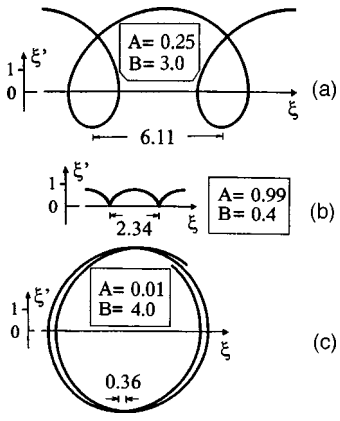

Fig. 3 Trajectories of steady-state motions: (*a*) ''normal'' situation, (*b*) near to critical inclination, (*c*) near the horizontal plane

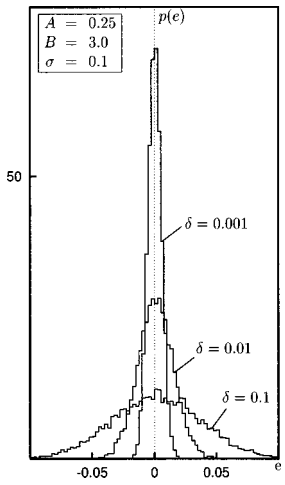

Fig. 4 Probability density of the relative error in the mean velocity of a ''normal'' motion

period to period. All results for the first 100 response periods are omitted to exclude transient effects. Then every tenth result is stored. This distance of time seems to be enough to obtain independent samples. Altogether, 10,000 samples are calculated for all cases.

Figure 4 shows the reduction of the error arising at the set $A=0.25$, $B=3.0$ when decreasing the interface parameter δ. It is considerably small even for the large relative value $\delta=0.1$. The integrals of the probability density functions are equal to unity.

This behavior of a ''normal'' motion has also been confirmed by additional calculations where A was sufficiently far away from the exceptional cases $A=0$ and $A=1.0$. The transition of the stochastic response to the deterministic one for decreasing δ can be explained by considering the course of the contact force (11) during time (see Fig. 5). The time interval $1000\cdot 2\pi \leqslant \tau \leqslant 1005\cdot 2\pi$ is chosen arbitrarily.

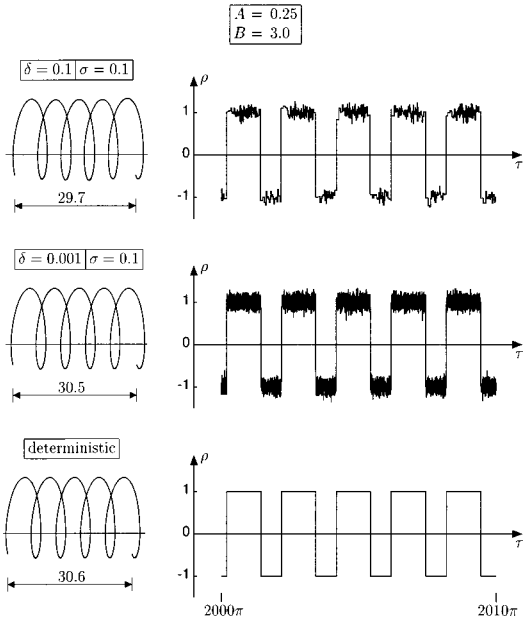

Fig. 5 Five response periods of a ''normal'' motion with different interface parameter. Left: trajectories; right: contact forces versus time

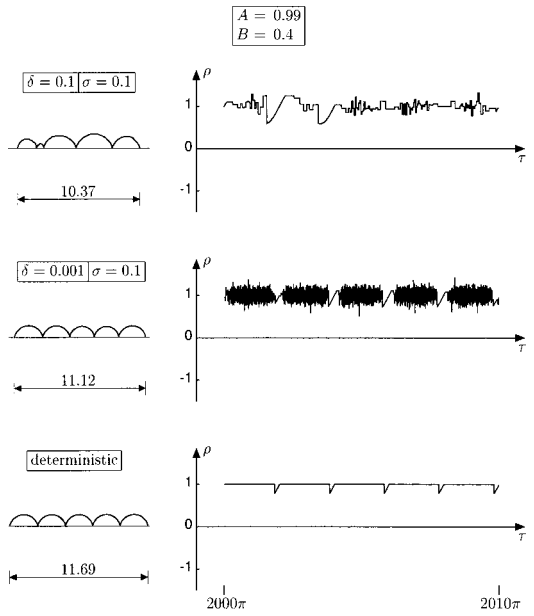

Fig. 6 Five response periods of a motion near the critical inclination of the plane. Left: trajectories; right: contact forces versus time.

Knowing $\rho=\rho(\tau)$ the problem could be rewritten by only one equation $\xi''=-\rho(\tau)+A+B\sin\tau$. Each integration to get ξ' and ξ is equivalent to a smoothening effect which is well known from experimental investigations. Even a very noisy signal of the acceleration leads to a smooth signal for the displacement. The smaller δ for a fixed value σ, the better is the approach to the deterministic solution, which can be seen from the corresponding phase curves. However, this intuitively expected property gives no quantitative information about the influence of the stochastic parameter on different types of motion.

Figure 6 shows phase curves and contact forces for the exceptional motion near to the critical inclination of the plane. The

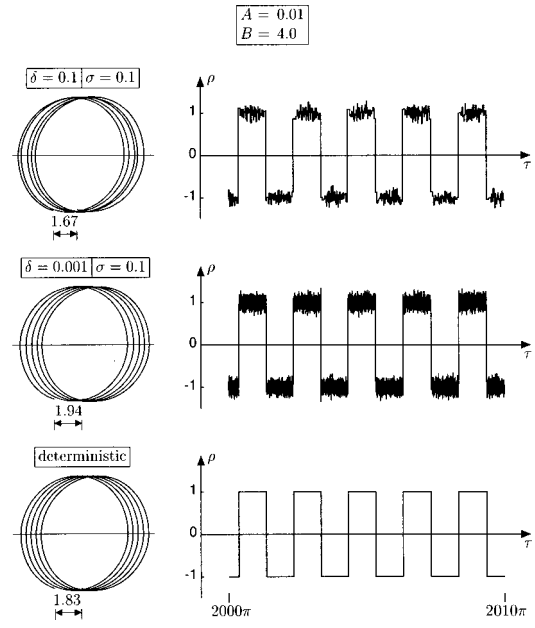

Fig. 7 Five response periods of a motion on an approximately horizontal plane. Left: trajectories; right: contact forces versus time.

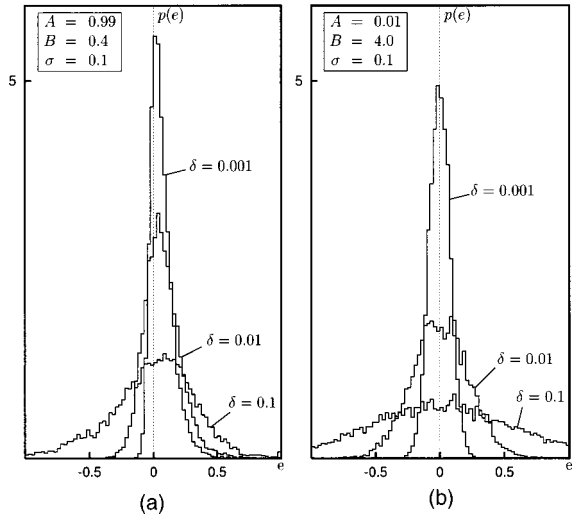

Fig. 8 Probability density of the relative error in the mean velocity; (*a*) motion near to the critical inclination of the plane, (*b*) motion on an approximately horizontal plane

property of the contact surface is the same as before. Now, even a small value $\delta = 0.001$ affects the result considerably compared with the deterministic one. (Note: scales of the trajectories differ from Fig. 5.) On the other hand, a large value $\delta = 0.1$ give rise to sliding periods, which can be longer than the exciting period. Moreover, it can happen at a point of separation from sliding to sticking that the active contact force ρ_a becomes so large that the switching condition (12) is never reached during sticking. The system remains in a lockup position for all times. In such a situation the program is restarted to obtain a sufficient number of samples for the error in the mean velocity.

The second exceptional case is a motion on an approximately horizontal plane. Here Fig. 7 shows a similar situation as before. (Note: Scales of the trajectories differ from Fig. 6.) The stochastic results differ considerably from the deterministic one.

The error distributions for both exceptional motions confirm the above statements. Note that the scale on both axes in Fig. 8 are altered with respect to Fig. 4, by a factor 10 on the abscissae and a factor of 0.1 on the ordinate.

In both cases, the error is enlarged by one order of magnitude compared with the situation of a ''normal'' motion.

Moreover, the probability distribution is non-Gaussian in the case $A = 0.99$. Its mean value is unequal to zero. The distinction to the result for a ''normal'' motion is remarkable and has an important consequence. The mean sliding velocity of the mass on the plane is an easily observable quantity when performing experiments. It seems obvious to use its value for a determination of a constant coefficient of friction by averaging some experimental data. But despite the fact that the frictional properties at the interface are unaltered, the apparent friction coefficient will change when changing the type of motion. Considering a completely different mechanical situation Adams [6] has pointed out a similar discrepancy. The coefficient of friction at the interface can also differ from the apparent coefficient at a large distance due to interface stick-slip.

All results are based on a constant value $\sigma = 0.1$ of the standard deviation. Dividing σ in half and recalculation of all examples leads to probability densities with less deviation and double maximum values than those given in Figs. 4 and 8. Apparently the mechanical problem becomes deterministic when the deviation σ tends to zero.

5 Conclusions

Considered are sliding motions of a mass on an inclined moving plane. The influence of both different angles of inclination and harmonic excitations on the response of the mass are investigated. The contact force is modeled under the assumption of Coulomb's law. In the deterministic case, the friction coefficient remains constant along the whole sliding path. In contrast, a relative interface parameter and a deviation from the constant friction coefficient is introduced to capture stochastic properties of the contact surface.

In the deterministic case, all responses show a common feature in the steady state. This is a constant mean velocity depending on both the inclination and the excitation. To characterize the influence of the stochastic parameters, the probability density of the relative error in the mean velocity is taken as a measure.

An intuitively expected result is valid for all kinds of motions: When decreasing the interface parameter of the contact surface, all stochastic responses approach to the corresponding deterministic ones. The error, however, is strongly influenced not only by the stochastic parameter but also by the considered motion itself. Depending on this sensitivity concerning the type of motion, a classical deterministic calculation based on the mean value of the friction coefficient can include an unpredictable error with respect to reality. This statement is confirmed by Kikuchi and Oden [7]: ''It is known that even for the same combination of both contact materials, changes only in the dynamic properties of the experimental setup or the driving velocity produce dramatic changes in the observed friction characteristics.''

References

[1] Ibrahim, R. A., 1994, ''Friction-Induced Vibration, Chatter, Squeal, and Chaos, Part II: Dynamics and Modeling,'' ASME Appl. Mech. Rev., **47**, pp. 227–253.

[2] Kilburn, R. F., 1974, ''Friction Viewed as a Random Process,'' ASME J. Lubr. Technol., **96**, pp. 291–299.

[3] Vielsack, P., 1996, ''Regularisierung des Haftzustandes bei Coulombscher Reibung,'' Z. Angew. Math. Mech., **76**, pp. 439–446.

[4] Soom, A., and Chen, J. W., 1986, ''Simulation of Random Surface Roughness-Induced Contact Vibrations at Hertzian Contacts During Steady Sliding,'' ASME J. Tribol., **108**, pp. 123–127.

[5] Vielsack, P., and Hartung, A., 1999, ''An example for the Orbital Stability of Permanently Disturbed Non-Smooth Motions,'' Z. Angew. Math. Mech., **79**, pp. 389–397.

[6] Adams, G. G., 1998, ''Steady sliding of Two Elastic Half-Spaces With Friction Reduction due to Interface Stick-Slip,'' ASME J. Appl. Mech., **65**, pp. 470–475.

[7] Kikuchi, N., and Oden, F. T., 1988, ''Contact Problems in Elasticity: A Study of Variational Inequalities and Finite Element Methods,'' SIAM.

A. J. Paris[1]
Visiting Assistant Professor,
Mem. ASME

G. A. Costello
Professor Emeritus,
Fellow ASME

Theoretical and Applied Mechanics,
University of Illinois at Urbana-Champaign,
Urbana, IL 61801

Bending of Cord Composite Cylindrical Shells

An analytical method for determining the load-deformation behavior of cord composite cylindrical shells is developed by considering the mechanics of the matrix, the cords, and the shell. To illustrate the method, a circular cylindrical shell with a single ply of uniformly spaced cords parallel to the shell axis is considered. The differential equations for the displacements are derived. These equations are solved analytically in closed form for a shell with the cords on the middle surface and subjected to axisymmetric loading. The deformations are strongly dependent upon the properties of the constituents, including the extension-twist coupling of the cords, and the geometry, boundary conditions, and loading. [S0021-8936(00)02701-X]

Introduction

An analytical method for determining the load-deformation behavior of cord composite cylindrical shells is developed.

A cord composite consists of cords embedded in a matrix. Current applications of cord composites include pneumatic tires, air springs, hoses, sleeves, couplings, belts, bladders, diaphragms, and various membrane structures. The cords have high axial stiffness and high axial strength, as well as small bending stiffness and long fatigue life. The matrix separates and protects the cords, and a rubber matrix can sustain large strains and resist wear. In addition, the matrix provides a web between the cords to carry or contain loose material, such as gravel on a conveyer belt, or to contain liquids or gases inside such structures as bladders, tanks, hoses, tires, air springs, and diaphragms.

The most common application of a cord composite shell is the automobile or truck steel-belted radial tire, where steel cords are embedded in a rubber matrix. It is the combination of the properties of the steel cords and the rubber matrix that allows tire survival after striking rocks and potholes. Engineers in the tire industry believe that the performance of tires still can be significantly increased through improved structural analysis. One aspect of performance of a tire is the load-deformation relations. Currently, new designs are evaluated by the long and costly process of building a prototype and determining its properties. To expedite the development process, an improved analytical model for the load-deformation relations is needed.

In the literature, attempts have been made to determine the behavior of cord composites by experimental, finite element, and analytical methods. Reviews of cord composites are given by Walter [1] and Walter and Patel [2]. While many papers contain a brief discussion of cylindrical shells, toroidal shells, tires, or air-rubber springs, only a few contain a geometrical analysis of the shell structure. Typically, the approach to determine the load-deformation relations for cord composites has been similar to the approach used for conventional composites ([3]); a cord has been modeled by an isotropic-rod approximation, a cord composite lamina by the rule of mixtures, and a cord composite laminate by classical lamination theory. The extension-twist coupling of the cords ([4]) was ignored. More recently, this coupling has been taken into account. Paris, Lin, and Costello [5] presented the first analysis of a cord composite that included the extension-twist coupling of the cord. It was not until an analysis of the static response of cord composite plates was presented in the doctoral thesis by Kittredge [6] and in three papers by Shield (Kittredge) and Costello [7–9] that the mechanics of the cords was included in the analysis of cord composite plates. Paris [10] considered cord-reinforced cylindrical shells.

The objective is to assess the effects of changes in the geometry and/or constituents of a cord composite shell on the load-deformation relations. These relations are developed analytically by considering the mechanics of the matrix, the cords, and the shell. The matrix is modeled as linear-elastic ([11]). The theory that is used to model the cords was developed by Costello [4] and includes the extension-twist coupling of the cords. For the shell, differential equations for the displacements are derived using the analysis of the bending of circular cylindrical shells by Flügge [12]. These equations are solved for a shell with axisymmetric loading and the cords on the middle surface. The response due to uniformly distributed axisymmetric end loads and uniform internal pressure is found for both a semi-infinite cylinder and a finite cylinder. Other solutions are given by Paris [10]. The resulting load-deformation relations are strongly dependent upon the properties of the constituents, including the extension-twist coupling of the cords, and the geometry, boundary conditions, and loading of the cord composite shell.

Formulation

The differential equations for the displacements of a cord composite cylindrical shell due to the loads are developed by considering the mechanics of the matrix material, the cords, and the shell. A circular cylindrical shell with a single ply of uniformly spaced cords, with the cord axes parallel to the axis of the shell is considered.

The matrix is assumed to be homogeneous, linear-elastic, and isotropic. The stress-strain relations and the strain-displacement relations in cylindrical coordinates can be found in the book by Love [11].

Costello [4] showed that the cord axial force and twisting moment are linearly proportional to the axial strain and twist of the cord, and that the cord bending moment is linearly proportional to the curvature of the cord. The theory of Costello most recently has been verified by Jiang, Yao and Walton [13], where a finite element model, experimental results, and the theory of Costello are compared. The transverse load-carrying capacity of the cords is neglected. Although the axial response of the cords is different in tension than in compression ([14]), these bimodular characteristics are neglected.

The shell is modeled following the theory for the bending of circular cylindrical shells by Flügge [12]. It is assumed that lines

[1]To whom all correspondence should be addressed.

Contributed by the Applied Mechanics Division of THE AMERICAN SOCIETY OF MECHANICAL ENGINEERS for publication in the ASME JOURNAL OF APPLIED MECHANICS. Manuscript received by the ASME Applied Mechanics Division, Dec. 23, 1998; final revision, Sept. 10, 1999. Associate Technical Editor: R. C. Benson. Discussion on the paper should be addressed to the Technical Editor, Professor Lewis T. Wheeler, Department of Mechanical Engineering, University of Houston, Houston, TX 77204-4792, and will be accepted until four months after final publication of the paper itself in the ASME JOURNAL OF APPLIED MECHANICS.

straight and normal to the middle surface before deformation are straight and normal to the middle surface after deformation, and that the change in the length of any line normal to the middle surface is negligible. In addition, the shell is assumed to be thin and the strains, displacements, and rotations are assumed to be small. These assumptions are often referred to as the Kirchhoff-Love hypothesis. In the current theory, it is assumed that the cords are perfectly bonded to the matrix and that the volume fraction of the cords is small.

Equilibrium Equations. Figure 1 shows a cord composite cylindrical shell with a single ply of uniformly spaced cords with the cord axes parallel to the axis of the shell. Figure 2 shows a typical element for the shell. The radius of the middle surface is denoted by a, the thickness by h, the cylindrical coordinates by x, φ, and z, the arc length along the φ-axis by s, and the element dimensions in the x and φ-directions by Δx and $a\Delta\varphi$. The x-axis is parallel to the longitudinal direction, the φ-axis is parallel to the circumferential direction, where the x and φ-axes lie on the middle surface, and the z-axis is an inward normal to the middle surface of the shell such that the x, φ, and z-axes form a right-handed orthogonal coordinate system.

Figure 3 shows a typical element for the shell with (a) the tractions and the force resultants and (b) the moment resultants. The tractions in the x, φ, and z-directions are denoted by p_x, p_φ, and p_z, the force resultants by N_x, $N_{x\varphi}$, $N_{\varphi x}$, N_φ, Q_x, and Q_φ,

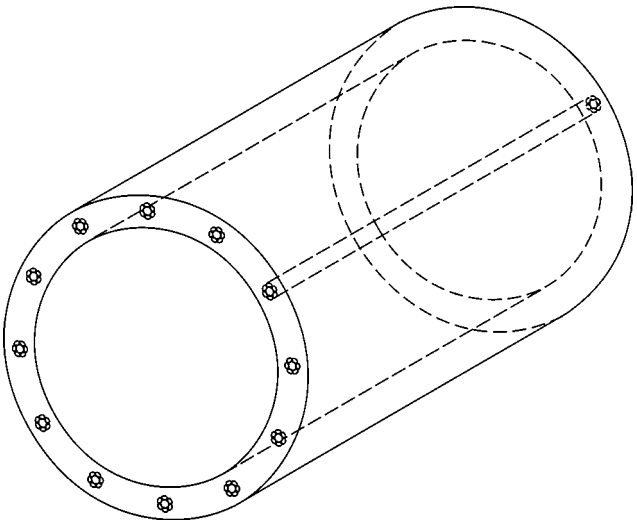

Fig. 1 A cord composite cylindrical shell

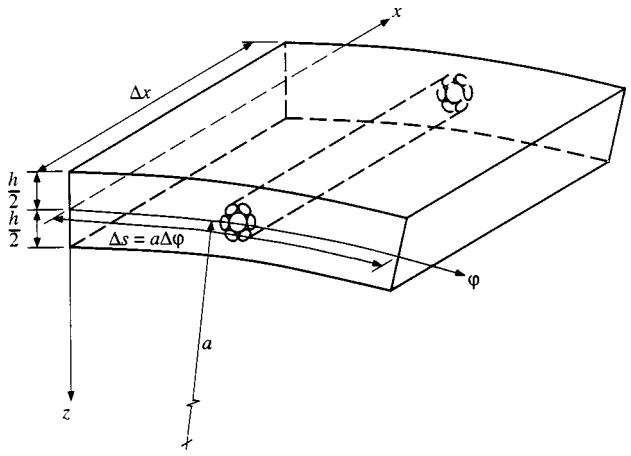

Fig. 2 A typical element for the shell

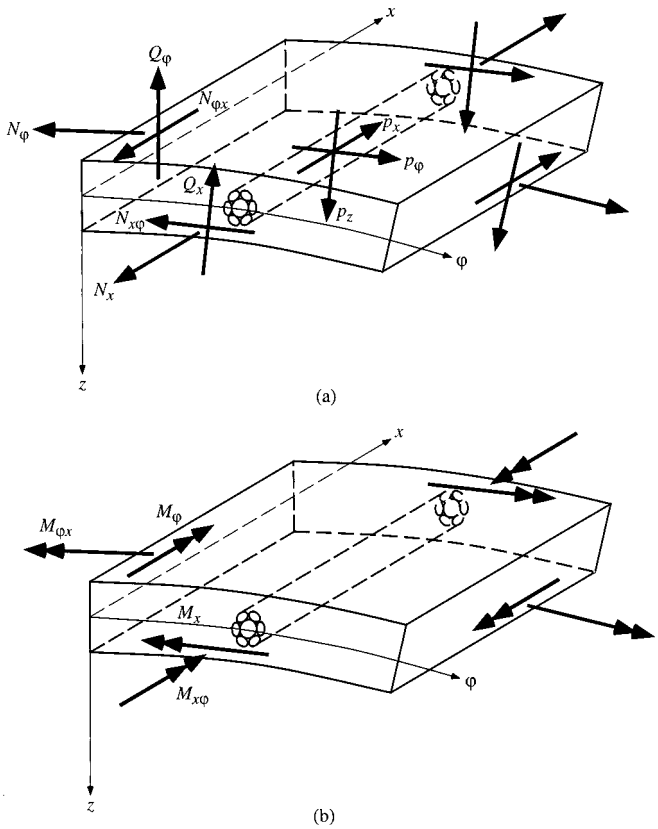

Fig. 3 A typical element for the shell with (*a*) the tractions and the force resultants and (*b*) the moment resultants

and the moment resultants by M_x, $M_{x\varphi}$, $M_{\varphi x}$, and M_φ. It is assumed that the force and moment resultants may be represented by a Taylor series. The equilibrium equations for the element in terms of the tractions, force, and moment resultants are found by setting the sum of the forces equal to zero and the sum of the moments equal to zero. Setting the sum of the forces equal to zero and setting the sum of the moments equal to zero yields

$$\frac{\partial N_x}{\partial x}+\frac{1}{a}\frac{\partial N_{\varphi x}}{\partial \varphi}+p_x=0, \tag{1}$$

$$\frac{\partial N_{x\varphi}}{\partial x}+\frac{1}{a}\frac{\partial N_\varphi}{\partial \varphi}+p_\varphi-\frac{Q_\varphi}{a}=0, \tag{2}$$

$$\frac{\partial Q_x}{\partial x}+\frac{1}{a}\frac{\partial Q_\varphi}{\partial \varphi}+p_z+\frac{N_\varphi}{a}=0, \tag{3}$$

$$\frac{\partial M_{x\varphi}}{\partial x}+\frac{1}{a}\frac{\partial M_\varphi}{\partial \varphi}-Q_\varphi=0, \tag{4}$$

$$\frac{\partial M_x}{\partial x}+\frac{1}{a}\frac{\partial M_{\varphi x}}{\partial \varphi}-Q_x=0, \tag{5}$$

and

$$N_{x\varphi}-N_{\varphi x}+\frac{M_{\varphi x}}{a}=0. \tag{6}$$

Solving Eqs. (4) and (5) for Q_φ and Q_x, respectively, yields

$$Q_\varphi=\frac{\partial M_{x\varphi}}{\partial x}+\frac{1}{a}\frac{\partial M_\varphi}{\partial \varphi} \tag{7}$$

and

$$Q_x=\frac{\partial M_x}{\partial x}+\frac{1}{a}\frac{\partial M_{\varphi x}}{\partial \varphi}. \tag{8}$$

Substituting Eqs. (7) and (8) into Eqs. (1)–(3) and (6), yields

$$\frac{\partial N_x}{\partial x}+\frac{1}{a}\frac{\partial N_{\varphi x}}{\partial \varphi}+p_x=0, \tag{9}$$

$$\frac{\partial N_{x\varphi}}{\partial x}+\frac{1}{a}\frac{\partial N_{\varphi}}{\partial \varphi}-\frac{1}{a}\frac{\partial M_{x\varphi}}{\partial x}-\frac{1}{a^2}\frac{\partial M_{\varphi}}{\partial \varphi}+p_{\varphi}=0, \tag{10}$$

$$\frac{\partial^2 M_x}{\partial x^2}+\frac{1}{a}\frac{\partial^2 M_{x\varphi}}{\partial x\partial \varphi}+\frac{1}{a}\frac{\partial^2 M_{\varphi x}}{\partial x\partial \varphi}+\frac{1}{a^2}\frac{\partial^2 M_{\varphi}}{\partial \varphi^2}+\frac{N_{\varphi}}{a}+p_z=0, \tag{11}$$

and

$$N_{x\varphi}-N_{\varphi x}+\frac{M_{\varphi x}}{a}=0. \tag{12}$$

Equations (9)–(12) are the differential equations for the force and moment resultants N_x, $N_{x\varphi}$, $N_{\varphi x}$, N_{φ}, M_x, $M_{x\varphi}$, $M_{\varphi x}$, and M_{φ}. There are four coupled, linear, nonhomogenous, partial differential equations with constant coefficients in terms of eight unknowns, and the problem is statically indeterminate.

Kinematics. Figure 4 shows exaggerated displacements and rotations for the shell (*a*) in the *xz*-plane and (*b*) in the φz-plane. The shell undergoes a deformation, and point *A* moves from *A* to *A′*. The displacements of *A* in the *x*, φ, and *z*-directions are denoted by u_A, v_A and w_A. The displacements of the middle surface of the shell in the *x*, φ, and *z*-directions are denoted by *u*, *v*, and *w*, respectively. Using the Kirchhoff-Love hypothesis to express u_A, v_A, and w_A in terms of *u*, *v*, and *w* yields

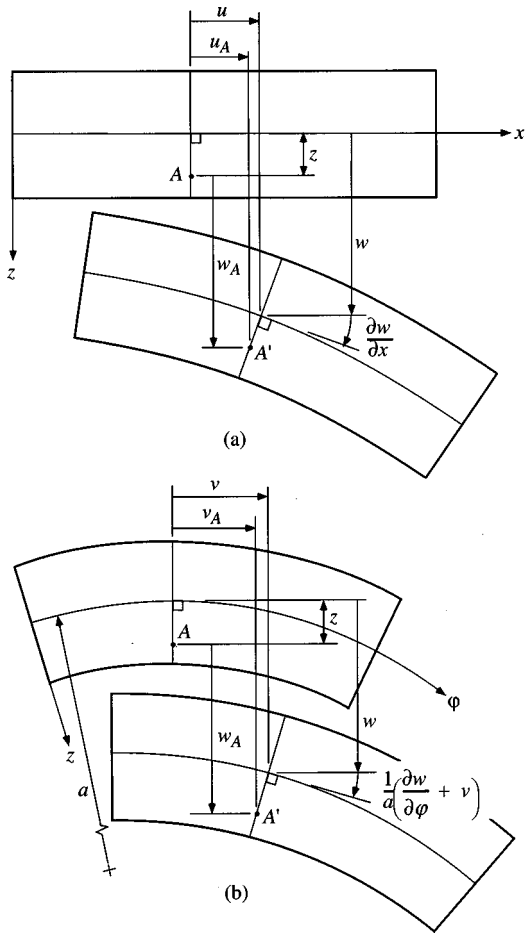

Fig. 4 Exaggerated displacements and rotations for the shell (*a*) in the *xz*-plane and (*b*) in the φz-plane

$$u_A=u-z\frac{\partial w}{\partial x}, \tag{13}$$

$$v_A=\left(\frac{a-z}{a}\right)v-\frac{z}{a}\frac{\partial w}{\partial \varphi}, \tag{14}$$

and

$$w_A=w, \tag{15}$$

where $u=u(x,\varphi)$, $v=v(x,\varphi)$ and $w=w(x,\varphi)$.

Strain-Displacement Relations. The normal strains in the *x* and φ-directions are denoted by ε_x and ε_{φ}, respectively, and the shearing strain corresponding with the directions of the axes of *x* and φ is denoted by $\gamma_{x\varphi}$. The strain-displacement relations are

$$\varepsilon_x=\frac{\partial u_A}{\partial x}, \tag{16}$$

$$\varepsilon_{\varphi}=\frac{1}{r}\left(\frac{\partial v_A}{\partial \varphi}-w_A\right), \tag{17}$$

and

$$\gamma_{x\varphi}=\frac{1}{r}\frac{\partial u_A}{\partial \varphi}+\frac{\partial v_A}{\partial x}, \tag{18}$$

where $r=a-z$.

Matrix Force and Moment Resultants. The normal stresses in the *x* and φ-directions are denoted by σ_x and σ_{φ}, respectively, and the shearing stress corresponding with the directions of the axes of *x* and φ is denoted by $\tau_{x\varphi}$. The stress-strain relations are

$$\sigma_x=\frac{E_m}{1-\nu_m^2}(\varepsilon_x+\nu_m\varepsilon_{\varphi}), \tag{19}$$

$$\sigma_{\varphi}=\frac{E_m}{1-\nu_m^2}(\varepsilon_{\varphi}+\nu_m\varepsilon_x), \tag{20}$$

and

$$\tau_{x\varphi}=\frac{E_m}{2(1+\nu_m)}\gamma_{x\varphi}, \tag{21}$$

where E_m is the modulus of elasticity and ν_m is the Poisson's ratio of the matrix material. The subscripts *m* and *c* will be used to denote variables related to the matrix and cord, respectively.

The matrix force resultants are found by integrating the stresses over the thickness of the shell and the moment resultants are found by integrating the first moment of the stresses over the thickness of the shell. Figure 5 shows a typical element for the shell with the in-plane stresses. The stresses σ_x and $\tau_{x\varphi}$ act on a differential area $(a-z)\Delta\varphi dz$ of the surface of the element with a normal in the *x*-direction and the stresses σ_{φ} and $\tau_{x\varphi}$ act on a differential area $\Delta x dz$ of the surface of the element with a normal in the φ direction, all at a distance *z* from the middle surface. The matrix force resultants are denoted by N_{xm}, $N_{x\varphi m}$, $N_{\varphi xm}$, $N_{\varphi m}$, Q_{xm}, and $Q_{\varphi m}$, and the matrix moment resultants are denoted by M_{xm}, $M_{x\varphi m}$, $M_{\varphi xm}$, and $M_{\varphi m}$. The matrix force and moment resultants are

$$N_{xm}=\frac{1}{a\Delta\varphi}\int_{-h/2}^{h/2}\sigma_x(a-z)\Delta\varphi dz, \tag{22}$$

$$N_{x\varphi m}=\frac{1}{a\Delta\varphi}\int_{-h/2}^{h/2}\tau_{x\varphi}(a-z)\Delta\varphi dz, \tag{23}$$

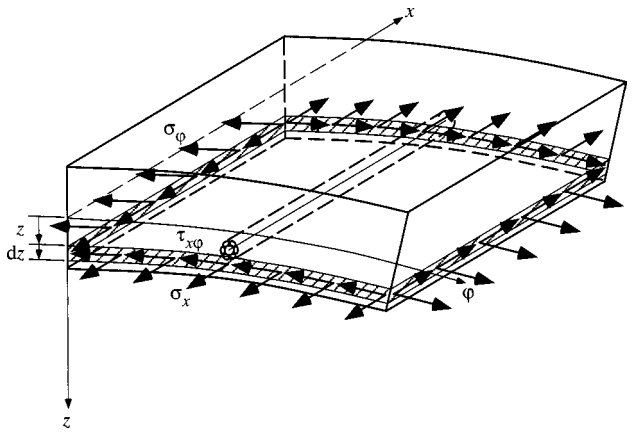

Fig. 5 A typical element for the shell with the in-plane matrix stresses

$$M_{xm}=\frac{1}{a\Delta\varphi}\int_{-h/2}^{h/2}\sigma_x(a-z)\Delta\varphi z dz, \tag{24}$$

$$M_{x\varphi m}=\frac{1}{a\Delta\varphi}\int_{-h/2}^{h/2}\tau_{x\varphi}(a-z)\Delta\varphi z dz, \tag{25}$$

$$N_{\varphi m}=\frac{1}{\Delta x}\int_{-h/2}^{h/2}\sigma_\varphi\Delta x dz, \tag{26}$$

$$N_{\varphi xm}=\frac{1}{\Delta x}\int_{-h/2}^{h/2}\tau_{x\varphi}\Delta x dz, \tag{27}$$

$$M_{\varphi m}=\frac{1}{\Delta x}\int_{-h/2}^{h/2}\sigma_\varphi\Delta x z dz, \tag{28}$$

and

$$M_{\varphi xm}=\frac{1}{\Delta x}\int_{-h/2}^{h/2}\tau_{x\varphi}\Delta x z dz. \tag{29}$$

The change in these integrals due to the cross-sectional area of the cords is neglected.

Equations (13)–(29) yield

$$N_{xm}=C\left(\frac{\partial u}{\partial x}+\frac{\upsilon_m}{a}\frac{\partial v}{\partial\varphi}-\frac{\upsilon_m}{a}w\right)+\frac{D}{a}\frac{\partial^2 w}{\partial x^2}, \tag{30}$$

$$N_{\varphi m}=C\left(\frac{1}{a}\frac{\partial v}{\partial\varphi}+\upsilon_m\frac{\partial u}{\partial x}-\frac{w}{a}\right)-\frac{D}{a^3}\left(w+\frac{\partial^2 w}{\partial\varphi^2}\right), \tag{31}$$

$$N_{x\varphi m}=\frac{1-\upsilon_m}{2}C\left(\frac{\partial v}{\partial x}+\frac{1}{a}\frac{\partial u}{\partial\varphi}\right)+\frac{1-\upsilon_m}{2}\frac{D}{a^2}\left(\frac{\partial v}{\partial x}+\frac{\partial^2 w}{\partial x\partial\varphi}\right), \tag{32}$$

$$N_{\varphi xm}=\frac{1-\upsilon_m}{2}C\left(\frac{\partial v}{\partial x}+\frac{1}{a}\frac{\partial u}{\partial\varphi}\right)+\frac{1-\upsilon_m}{2}\frac{D}{a^2}\left(\frac{1}{a}\frac{\partial u}{\partial\varphi}-\frac{\partial^2 w}{\partial x\partial\varphi}\right), \tag{33}$$

$$M_{xm}=-\frac{D}{a^2}\left(a^2\frac{\partial^2 w}{\partial x^2}+\upsilon_m\frac{\partial^2 w}{\partial\varphi^2}+a\frac{\partial u}{\partial x}+\upsilon_m\frac{\partial v}{\partial\varphi}\right), \tag{34}$$

$$M_{\varphi m}=-\frac{D}{a^2}\left(\frac{\partial^2 w}{\partial\varphi^2}+\upsilon_m a^2\frac{\partial^2 w}{\partial x^2}+w\right), \tag{35}$$

$$M_{x\varphi m}=-(1-\upsilon_m)\frac{D}{a^2}\left(a\frac{\partial^2 w}{\partial x\partial\varphi}+a\frac{\partial v}{\partial x}\right), \tag{36}$$

and

$$M_{\varphi xm}=-(1-\upsilon_m)\frac{D}{a^2}\left(a\frac{\partial^2 w}{\partial x\partial\varphi}+\frac{a}{2}\frac{\partial v}{\partial x}-\frac{1}{2}\frac{\partial u}{\partial\varphi}\right), \tag{37}$$

where terms of $O(h/a)^5$ have been neglected, C is the extensional rigidity of the matrix and is defined to be

$$C=\frac{E_m h}{1-\upsilon_m^2}, \tag{38}$$

and D is the flexural rigidity or bending stiffness of the matrix and is defined to be

$$D=\frac{E_m h^3}{12(1-\upsilon_m^2)}. \tag{39}$$

Cord Force and Moment Resultants. Figure 6 shows a cord loaded by an axial force and twisting moment, where F_c is the axial force, M_{tc} is the twisting moment, R_i is the radius of the inner wire, R_o is the radius of the outer wires, R_c is the outside radius of the cord, m is the number of outer wires, and α is the helix angle of the outer wires. The cord axial force F_c and twisting moment M_{tc} may be expressed as

$$\frac{F_c}{A_c E_c}=C_1\varepsilon_c+C_2 R_c\tau_c, \tag{40}$$

and

$$\frac{M_{tc}}{E_c R_c^3}=C_3\varepsilon_c+C_4 R_c\tau_c, \tag{41}$$

where A_c is the metallic cross sectional area, E_c is the modulus of elasticity of the material, ε_c is the axial strain, τ_c is the twist per unit length, and C_1, C_2, C_3, and C_4 are constants which can be determined analytically [4]. Figure 7 shows a cord (a) undeformed

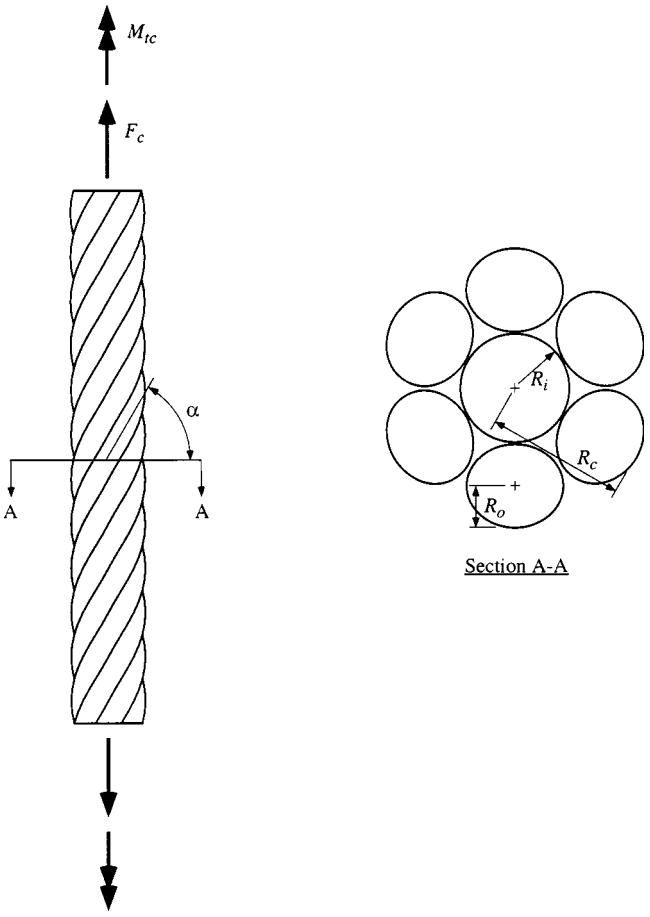

Fig. 6 A cord loaded by an axial force and twisting moment

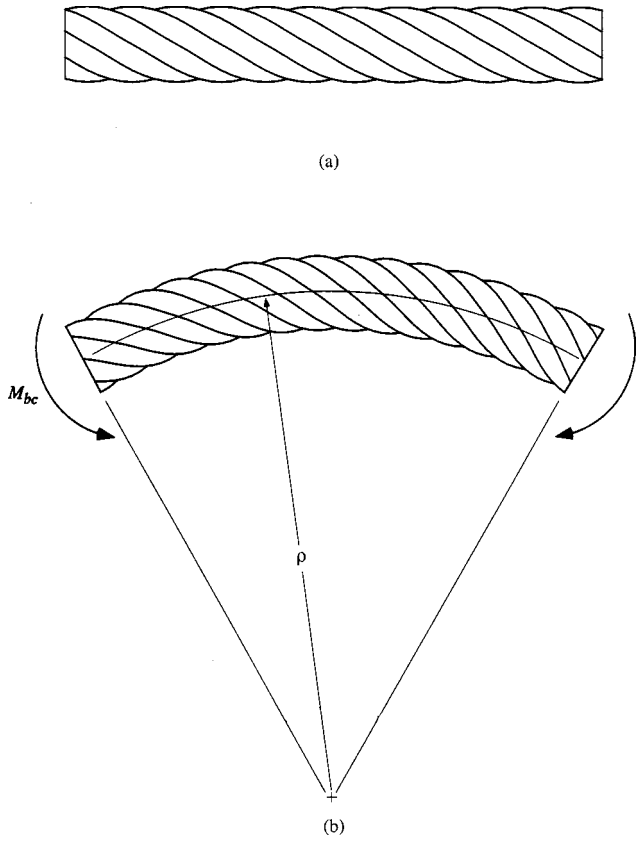

Fig. 7 A cord (*a*) undeformed and (*b*) deformed in pure bending

and (b) deformed in pure bending, where M_{bc} is the cord bending moment, and ρ_c is the radius of curvature of the cord. The cord bending moment M_{bc} may be expressed as

$$\frac{M_{bc}}{E_c R_c^3} = C_5 R_c \kappa_c , \tag{42}$$

where $\kappa_c = 1/\rho_c$ is the curvature and C_5 is a constant which can be determined analytically ([4]).

Figure 8 shows a typical element for the shell with the cord axial force, twisting moment, and bending moment. The z-coordinate of the cord axis is denoted as z_c. The axial strain, change in curvature, and twist per unit length of the cord may be expressed in terms of the strains, change in curvatures, and twist of the middle surface. Using Eqs. (13)–(15) to express ε_c, κ_c, and τ_c yields

$$\varepsilon_c = \left[\frac{\partial u_A}{\partial x}\right]_{z=z_c}, \tag{43}$$

$$\kappa_c = \frac{1}{\rho_c} = \left[\frac{\partial^2 w_A}{\partial x^2}\right]_{z=z_c}, \tag{44}$$

and

$$\tau_c = \left\{\frac{\partial}{\partial x}\left[\frac{1}{2}\left(\frac{v_A}{r} + \frac{1}{r}\frac{\partial w_A}{\partial \varphi} - \frac{\partial v_A}{\partial z}\right)\right]\right\}_{z=z_c}. \tag{45}$$

Figure 3 shows a typical element for the shell with (*a*) the tractions and the force resultants and (*b*) the moment results. Figure 8 shows a typical element for the shell with the cord axial force, twisting moment, and bending moment. The transverse load-carrying capacity of the cords is assumed to be negligible. The axial force, twisting moment, and bending moment in the

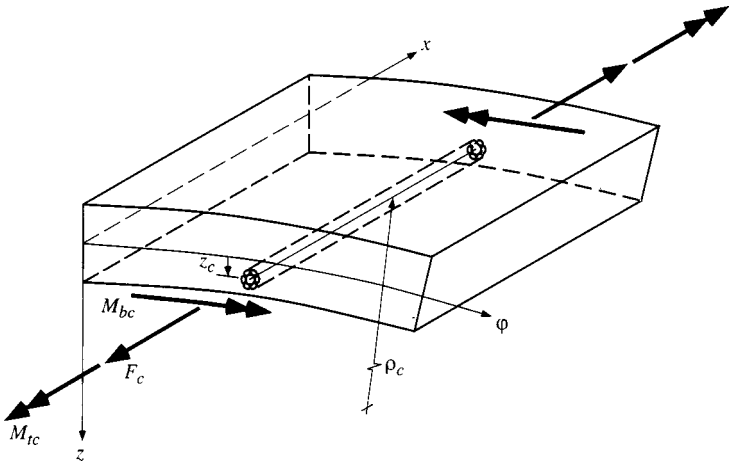

Fig. 8 A typical element for the shell with the cord axial force, twisting moment, and bending moment

cord may be divided by the spacing of the cords and resolved into the force and moment resultants in the shell. The cord force resultants are denoted by N_{xc}, $N_{x\varphi c}$, $N_{\varphi xc}$, $N_{\varphi c}$, Q_{xc}, and $Q_{\varphi c}$, and the cord moment resultants are denoted by M_{xc}, $M_{x\varphi c}$, $M_{\varphi xc}$, and $M_{\varphi c}$. Referring to Figs. 3 and 8 and comparing the force and moment resultants with the cord axial force, twisting moment, and bending moment yields

$$N_{\varphi c} = N_{x\varphi c} = Q_x = Q_\varphi = N_{\varphi xc} = M_{\varphi c} = M_{\varphi xc} = 0, \tag{46}$$

$$N_{xc} = \frac{F_c}{b}, \tag{47}$$

$$M_{xc} = \frac{F_c z_c - M_{bc}}{b} \tag{48}$$

and

$$M_{x\varphi c} = -\frac{M_{tc}}{b} \tag{49}$$

where b is the spacing of the cords. Equations (40)–(49) yield

$$N_{xc} = \frac{A_c C_1 E_c}{b}\left(\frac{\partial u}{\partial x} - z_c\frac{\partial^2 w}{\partial x^2}\right) + \frac{A_c C_2 E_c R_c}{ab}\left(\frac{\partial v}{\partial x} + \frac{\partial^2 w}{\partial x \partial \varphi}\right), \tag{50}$$

$$M_{xc} = \frac{A_c C_1 E_c z_c}{b}\frac{\partial u}{\partial x} - \left(\frac{A_c C_1 E_c z_c^2}{b} + \frac{C_5 E_c R_c^4}{b}\right)\frac{\partial^2 w}{\partial x^2} + \frac{A_c C_2 E_c R_c z_c}{ab}\left(\frac{\partial v}{\partial x} + \frac{\partial^2 w}{\partial x \partial \varphi}\right), \tag{51}$$

and

$$M_{x\varphi c} = -\frac{C_3 E_c R_c^3}{b}\left(\frac{\partial u}{\partial x} - z_c\frac{\partial^2 w}{\partial x^2}\right) - \frac{C_4 E_c R_c^4}{ab}\left(\frac{\partial v}{\partial x} + \frac{\partial^2 w}{\partial x \partial \varphi}\right). \tag{52}$$

Note that by dividing the cord axial force, twisting moment, and bending moment by the spacing of the cords that the cord is smeared out in the circumferential direction (φ-direction) but not in the radial direction (z-direction). The position of the cord in the radial direction is significant where bending is considered. It is assumed that the spacing of the cords b is sufficiently small to yield accurate results.

Total Force and Moment Resultants. The total force and moment resultants are the sum of the force and moment resultants of the matrix and of the cords. The total force and moment resultants may be expressed as

$$N_x = N_{xm} + N_{xc}, \tag{53}$$

$$N_\varphi = N_{\varphi m} + N_{\varphi c}, \tag{54}$$

$$N_{x\varphi} = N_{x\varphi m} + N_{x\varphi c}, \tag{55}$$

$$N_{\varphi x} = N_{\varphi x m} + N_{\varphi x c}, \tag{56}$$

$$M_x = M_{xm} + M_{xc}, \tag{57}$$

$$M_\varphi = M_{\varphi m} + M_{\varphi c}, \tag{58}$$

$$M_{x\varphi} = M_{x\varphi m} + M_{x\varphi c}, \tag{59}$$

and

$$M_{\varphi x} = M_{\varphi x m} + M_{\varphi x c}. \tag{60}$$

Equations (30)–(37), (46), and (50)–(60) yield

$$N_x = \left(C + \frac{A_c C_1 E_c}{b}\right)\frac{\partial u}{\partial x} + \frac{A_c C_2 E_c R_c}{ab}\frac{\partial v}{\partial x} + \frac{\nu_m C}{a}\frac{\partial v}{\partial \varphi} - \frac{\nu_m C}{a} w + \left(\frac{D}{a} - \frac{A_c C_1 E_c z_c}{b}\right)\frac{\partial^2 w}{\partial x^2} + \frac{A_c C_2 E_c R_c}{ab}\frac{\partial^2 w}{\partial x \partial \varphi}, \tag{61}$$

$$N_\varphi = \nu_m C \frac{\partial u}{\partial x} + \frac{C}{a}\frac{\partial v}{\partial \varphi} - \left(\frac{C}{a} + \frac{D}{a^3}\right) w - \frac{D}{a^3}\frac{\partial^2 w}{\partial \varphi^2}, \tag{62}$$

$$N_{x\varphi} = \frac{(1-\nu_m)C}{2a}\frac{\partial u}{\partial \varphi} + \frac{1-\nu_m}{2}\left(C + \frac{D}{a^2}\right)\frac{\partial v}{\partial x} + \frac{(1-\nu_m)D}{2a^2}\frac{\partial^2 w}{\partial x \partial \varphi}, \tag{63}$$

$$N_{\varphi x} = \frac{1-\nu_m}{2a}\left(C + \frac{D}{a^2}\right)\frac{\partial u}{\partial \varphi} + \frac{(1-\nu_m)C}{2}\frac{\partial v}{\partial x} - \frac{(1-\nu_m)D}{2a^2}\frac{\partial^2 w}{\partial x \partial \varphi}, \tag{64}$$

$$M_x = \left(-\frac{D}{a} + \frac{A_c C_1 E_c z_c}{b}\right)\frac{\partial u}{\partial x} + \frac{A_c C_2 E_c R_c z_c}{ab}\frac{\partial v}{\partial x} - \frac{\nu_m D}{a^2}\frac{\partial v}{\partial \varphi} - \left(D + \frac{C_5 E_c R_c^4}{b} + \frac{A_c C_1 E_c z_c^2}{b}\right)\frac{\partial^2 w}{\partial x^2} + \frac{A_c C_2 E_c R_c z_c}{ab}\frac{\partial^2 w}{\partial x \partial \varphi} - \frac{\nu_m D}{a^2}\frac{\partial^2 w}{\partial \varphi^2}, \tag{65}$$

$$M_\varphi = -\frac{D}{a^2}\left(w + \nu_m a^2 \frac{\partial^2 w}{\partial x^2} + \frac{\partial^2 w}{\partial \varphi^2}\right), \tag{66}$$

$$M_{x\varphi} = -\frac{C_3 E_c R_c^3}{b}\frac{\partial u}{\partial x} - \left[\frac{(1-\nu_m)D}{a} + \frac{C_4 E_c R_c^4}{ab}\right]\frac{\partial v}{\partial x} + \frac{C_3 E_c R_c^3 z_c}{b}\frac{\partial^2 w}{\partial x^2} - \left[\frac{C_4 E_c R_c^4}{ab} + \frac{(1-\nu_m)D}{a}\right]\frac{\partial^2 w}{\partial x \partial \varphi}, \tag{67}$$

and

$$M_{\varphi x} = -\frac{(1-\nu_m)D}{a^2}\left(-\frac{1}{2}\frac{\partial u}{\partial \varphi} + \frac{a}{2}\frac{\partial v}{\partial x} + a\frac{\partial^2 w}{\partial x \partial \varphi}\right). \tag{68}$$

Equations (61)–(68) are the total force and total moment resultants. Substituting Eq. (61)–(68) into Eqs. (7) and (8) yields

$$Q_x = \left(-\frac{D}{a} + \frac{A_c C_1 E_c z_c}{b}\right)\frac{\partial^2 u}{\partial x^2} + \frac{(1-\nu_m)D}{2a^3}\frac{\partial^2 u}{\partial \varphi^2} + \frac{A_c C_2 E_c R_c z_c}{ab}\frac{\partial^2 v}{\partial x^2} - \frac{(1+\nu_m)D}{2a^2}\frac{\partial^2 v}{\partial x \partial \varphi} + \frac{A_c C_2 E_c R_c z_c}{ab} \times \frac{\partial^3 w}{\partial x^2 \partial \varphi} - \left(D + \frac{C_5 E_c R_c^4}{b} + \frac{A_c C_1 E_c z_c^2}{b}\right)\frac{\partial^3 w}{\partial x^3} - \frac{D}{a^2}\frac{\partial^3 w}{\partial x \partial \varphi^2} \tag{69}$$

and

$$Q_\varphi = -\frac{C_3 E_c R_c^3}{b}\frac{\partial^2 u}{\partial x^2} - \left[\frac{(1-\nu_m)D}{a} + \frac{C_4 E_c R_c^4}{ab}\right]\frac{\partial^2 v}{\partial x^2} + \frac{C_3 E_c R_c^3 z_c}{b}\frac{\partial^3 w}{\partial x^3} - \left(\frac{D}{a} + \frac{C_4 E_c R_c^4}{ab}\right)\frac{\partial^3 w}{\partial x^2 \partial \varphi} - \frac{D}{a^3}\frac{\partial w}{\partial \varphi} - \frac{D}{a^3}\frac{\partial^3 w}{\partial \varphi^3}. \tag{70}$$

Differential Equations for the Displacements of the Middle Surface. The differential equations for the displacements of the middle surface of the shell are found. Substituting Eqs. (61)–(68) into Eqs. (9)–(12) yields

$$\left(C + \frac{A_c C_1 E_c}{b}\right)\frac{\partial^2 u}{\partial x^2} + \frac{1-\nu_m}{2a^2}\left(C + \frac{D}{a^2}\right)\frac{\partial^2 u}{\partial \varphi^2} + \frac{A_c C_2 E_c R_c}{ab}\frac{\partial^2 v}{\partial x^2} + \frac{(1+\nu_m)C}{2a}\frac{\partial^2 v}{\partial x \partial \varphi} - \frac{\nu_m C}{a}\frac{\partial w}{\partial x} + \left(\frac{D}{a} - \frac{A_c C_1 E_c z_c}{b}\right)\frac{\partial^3 w}{\partial x^3} - \frac{(1-\nu_m)D}{2a^3}\frac{\partial^3 w}{\partial x \partial \varphi^2} + \frac{A_c C_2 E_c R_c}{ab}\frac{\partial^3 w}{\partial x^2 \partial \varphi} + p_x = 0, \tag{71}$$

$$\frac{C_3 E_c R_c^3}{ab}\frac{\partial^2 u}{\partial x^2} + \frac{(1+\nu_m)C}{2a}\frac{\partial^2 u}{\partial x \partial \varphi} + \left[\frac{(1-\nu_m)C}{2} + \frac{3(1-\nu_m)D}{2a^2} + \frac{C_4 E_c R_c^4}{a^2 b}\right]\frac{\partial^2 v}{\partial x^2} + \frac{C\partial^2 v}{a^2 \partial \varphi^2} - \frac{C_3 E_c R_c^3 z_c}{ab}\frac{\partial^3 w}{\partial x^3} - \frac{C}{a^2}\frac{\partial w}{\partial \varphi} + \left[\frac{(3-\nu_m)D}{2a^2} + \frac{C_4 E_c R_c^4}{a^2 b}\right]\frac{\partial^3 w}{\partial x^2 \partial \varphi} + p_\varphi = 0, \tag{72}$$

$$\frac{\nu_m C}{a}\frac{\partial u}{\partial x} + \left(\frac{A_c C_1 E_c z_c}{b} - \frac{D}{a}\right)\frac{\partial^3 u}{\partial x^3} - \frac{C_3 E_c R_c^3}{ab}\frac{\partial^3 u}{\partial x^2 \partial \varphi} + \frac{(1-\nu_m)D}{2a^3}\frac{\partial^3 u}{\partial x \partial \varphi^2} + \frac{A_c C_2 E_c R_c z_c}{ab}\frac{\partial^3 v}{\partial x^3} - \left[\frac{(3-\nu_m)D}{2a^2} + \frac{C_4 E_c R_c^4}{a^2 b}\right]\frac{\partial^3 v}{\partial x^2 \partial \varphi} + \frac{C}{a^2}\frac{\partial v}{\partial \varphi} - \left(\frac{C}{a^2} + \frac{D}{a^4}\right) w - \left(D + \frac{A_c C_1 E_c z_c^2}{b} + \frac{C_5 E_c R_c^4}{b}\right)\frac{\partial^4 w}{\partial x^4} + \left(\frac{A_c C_2 E_c R_c z_c}{ab} + \frac{C_3 E_c R_c^3 z_c}{ab}\right)\frac{\partial^4 w}{\partial x^3 \partial \varphi} - \left(\frac{2D}{a^2} + \frac{C_4 E_c R_c^4}{a^2 b}\right)\frac{\partial^4 w}{\partial x^2 \partial \varphi^2} - \frac{2D}{a^4}\frac{\partial^2 w}{\partial \varphi^2} - \frac{D}{a^4}\frac{\partial^4 w}{\partial \varphi^4} + p_z = 0, \tag{73}$$

and Eq. (12) is identically satisfied. Equations (71)–(73) are three linear, coupled, nonhomogenous, partial differential equations with constant coefficients for the three displacements u, v, and w. The coupling is due in part to the extension-twist coupling of the cords.

Results

Axisymmtric Loading. Closed-form solutions are found for a shell with the cords on the middle surface, axisymmetric loading, and the in-plane tractions equal to zero. First, a general solution for the displacements from the loads is developed. Second, the solution for a semi-infinite cylinder loaded by a uniform in-

ternal pressure and by end loads is developed. Third, the solution for a finite cylinder loaded by a uniform internal pressure and by end loads is developed.

The shell has the cords on the middle surface, axisymmetric loading, and the in-plane tractions equal to zero. Therefore,

$$p_x=0, \quad p_\varphi=0, \quad p_z=p_z(x), \text{ and } z_c=0. \tag{74}$$

Since the loads are functions of x only, Eq. (74), the displacements of the middle surface will also be functions of x only and may be expressed as

$$u=u(x), \quad v=v(x), \text{ and } w=w(x). \tag{75}$$

Note that although the loading is axisymmetric, the displacement in the φ direction v is not assumed to be zero. Since the loads and the displacements are functions of x only, Eqs. (74) and (75), all derivatives with respect to φ are zero.

General Solution. Solving Eqs. (71) and (72) for d^2u/dx^2 and d^2v/dx^2 and integrating once with respect to x yields

$$\frac{du}{dx}=\frac{\dfrac{1-\nu_m}{2}\left(C+\dfrac{3D}{a^2}\right)+\dfrac{C_4E_cR_c^4}{a^2b}}{\left(C+\dfrac{C_1E_cA_c}{b}\right)\left[\dfrac{1-\nu_m}{2}\left(C+\dfrac{3D}{a^2}\right)+\dfrac{C_4E_cR_c^4}{a^2b}\right]-\dfrac{C_2C_3E_c^2R_c^4A_c}{a^2b^2}}\left(\frac{C\nu_m}{a}w-\frac{D}{a}\frac{d^2w}{dx^2}\right)+B_1, \tag{76}$$

and

$$\frac{dv}{dx}=\frac{-\dfrac{C_3E_cR_c^3}{ab}}{\left(C+\dfrac{C_1E_cA_c}{b}\right)\left[\dfrac{1-\nu_m}{2}\left(C+\dfrac{3D}{a^2}\right)+\dfrac{C_4E_cR_c^4}{a^2b}\right]-\dfrac{C_2C_3E_c^2R_c^4A_c}{a^2b^2}}\left(\frac{C\nu_m}{a}w-\frac{D}{a}\frac{d^2w}{dx^2}\right)+B_2, \tag{77}$$

where B_1 and B_2 are constants of integration to be determined.

Substituting Eqs. (76) and (77) into Eq. (73) yields

$$A_1\frac{d^4w}{dx^4}+A_2\frac{d^2w}{dx^2}+A_3w=p, \tag{78}$$

where

$$A_1=D+\frac{C_5E_cR_c^4}{b}-\left(\frac{D}{a}\right)^2\left\{\frac{\dfrac{1-\nu_m}{2}\left(C+\dfrac{3D}{a^2}\right)+\dfrac{C_4E_cR_c^4}{a^2b}}{\left(C+\dfrac{C_1E_cA_c}{b}\right)\left[\dfrac{1-\nu_m}{2}\left(C+\dfrac{3D}{a^2}\right)+\dfrac{C_4E_cR_c^4}{a^2b}\right]-\dfrac{C_2C_3E_c^2R_c^4A_c}{a^2b^2}}\right\}, \tag{79}$$

$$A_2=\frac{2\nu_mCD}{a^2}\left\{\frac{\dfrac{1-\nu_m}{2}\left(C+\dfrac{3D}{a^2}\right)+\dfrac{C_4E_cR_c^4}{a^2b}}{\left(C+\dfrac{C_1E_cA_c}{b}\right)\left[\dfrac{1-\nu_m}{2}\left(C+\dfrac{3D}{a^2}\right)+\dfrac{C_4E_cR_c^4}{a^2b}\right]-\dfrac{C_2C_3E_c^2R_c^4A_c}{a^2b^2}}\right\}, \tag{80}$$

$$A_3=\frac{C}{a^2}+\frac{D}{a^4}-\left(\frac{\nu_mC}{a}\right)^2\left\{\frac{\dfrac{1-\nu_m}{2}\left(C+\dfrac{3D}{a^2}\right)+\dfrac{C_4E_cR_c^4}{a^2b}}{\left(C+\dfrac{C_1E_cA_c}{b}\right)\left[\dfrac{1-\nu_m}{2}\left(C+\dfrac{3D}{a^2}\right)+\dfrac{C_4E_cR_c^4}{a^2b}\right]-\dfrac{C_2C_3E_c^2R_c^4A_c}{a^2b^2}}\right\}, \tag{81}$$

and

$$p=\frac{\nu_mC}{a}B_1+p_z. \tag{82}$$

Equation (78) is a fourth-order, linear, nonhomogeneous, ordinary differential equation with constant coefficients for w and has the solution

$$w=e^{-\beta x}[B_3\cos(\alpha x)+B_4\sin(\alpha x)]+e^{\beta x}[B_5\cos(\alpha x)+B_6\sin(\alpha x)]+w_p(x), \tag{83}$$

where

$$\alpha=\left[\frac{1}{2}\left(\frac{A_3}{A_1}\right)^{1/2}+\frac{A_2}{4A_1}\right]^{1/2} \tag{84}$$

and

$$\beta=\left[\frac{1}{2}\left(\frac{A_3}{A_1}\right)^{1/2}-\frac{A_2}{4A_1}\right]^{1/2}, \tag{85}$$

B_3, B_4, B_5, and B_6 are constants of integration to be determined, and $w_p(x)$ is the particular solution that depends on the transverse loading $p_z(x)$. An alternate form of the solution to Eq. (78) is

$$w=D_1\cosh(\beta x)\cos(\alpha x)+D_2\cosh(\beta x)\sin(\alpha x)+D_3\sinh(\beta x)\cos(\alpha x)+D_4\sinh(\beta x)\sin(\alpha x)+w_p(x), \tag{86}$$

where α and β are as given above by Eqs. (84) and (85), D_1, D_2, D_3, and D_4 are constants of integration to be determined, and $w_p(x)$ is the particular solution that depends on the transverse loading $p_z(x)$. The type of problem will determine which form of the solution is most convenient.

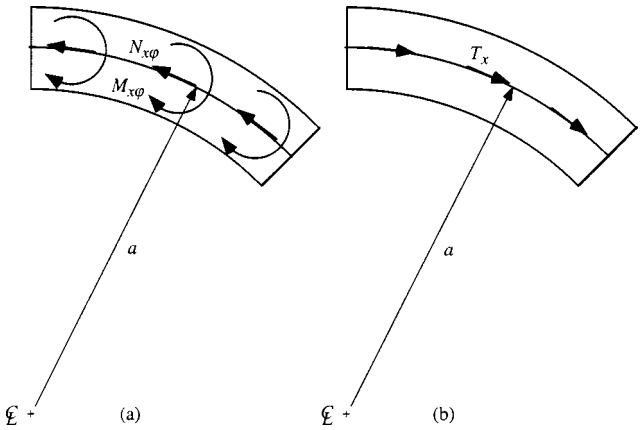

Fig. 9 An element of the end of a cylindrical shell with (*a*) the loads with a moment about the centerline and (*b*) the equivalent shear force resultant

Consider the loads that may be applied to the end of a cylindrical shell. The force and moment resultants acting on the end of the cylindrical shell are N_x, $N_{x\varphi}$, Q_x, M_x, and $M_{x\varphi}$. These are the traction boundary conditions. Now consider the net moment of these force and moment resultants about the centerline of the cylindrical shell. Figure 9(*a*) shows an element of the end of a cylindrical shell with the loads with a moment about the centerline. The sum of the moments about the centerline is

$$\Sigma M_{CL}=M_{x\varphi}\Delta s-a(N_{x\varphi}\Delta s). \tag{87}$$

The force resultant $N_{x\varphi}$ and moment resultant $M_{x\varphi}$ can be resolved into an equivalent shear force resultant T_x acting on the end of the cylindrical shell. Figure 9(*b*) shows an element of the end of a cylindrical shell with the equivalent shear force resultant. Dividing both sides of Eq. (87) by $a\Delta s$ yields the equivalent shear force resultant T_x is

$$T_x=\frac{\Sigma M_{CL}}{a\Delta s}=\frac{M_{x\varphi}}{a}-N_{x\varphi}. \tag{88}$$

When the transverse traction is $p_z=p_o+p_1x$, where p_o and p_1 are constants, the forcing term p given by Eq. (82) becomes

$$p=\frac{\nu_m C}{a}B_1+p_o+p_1x. \tag{89}$$

The particular solution w_p of Eq. (78) for the forcing term p given by Eq. (89) is

$$w_p=\frac{1}{A_3}\left(\frac{\nu_m C}{a}B_1+p_o+p_1x\right). \tag{90}$$

The particular solution w_p given by Eq. (90) is valid regardless of the boundary conditions. Therefore, it is valid for both a semi-infinite cylinder with end loads and a finite cylinder with end loads.

Semi-Infinite Cylinder With End Loads. Consider a semi-infinite cylinder with a uniform internal pressure p_o and end loads. The boundary conditions at $x=0$ are $N_x=N$, $M_x=M$, $Q_x=Q$, and $T_x=T$, and the transverse traction is $p_z=p_o$, where p_o is a constant. It is most convenient to use the form of the solution for w given by Eq. (83). The displacement w is bounded in x and therefore B_5 and B_6 must be zero. The forcing term p is given by Eq. (89), where $p_1=0$. The particular solution w_p is given by Eq. (90), again where $p_1=0$.

Applying the boundary conditions $N_x=N$ and $T_x=T$ at $x=0$ to Eqs. (61), (63), (67), (76), (77), and (88), and solving for the constants of integration B_1 and B_2 yields

$$B_1=\frac{\left[\frac{1-\nu_m}{2}\left(C+\frac{3D}{a^2}\right)+\frac{C_4E_cR_c^4}{a^2b}\right]N+\frac{C_2E_cA_cR_c}{ab}T}{\left(C+\frac{C_1E_cA_c}{b}\right)\left[\frac{1-\nu_m}{2}\left(C+\frac{3D}{a^2}\right)+\frac{C_4E_cR_c^4}{a^2b}\right]-\frac{C_2C_3E_c^2R_c^4A_c}{a^2b^2}} \tag{91}$$

and

$$B_2=\frac{-\frac{C_3E_cR_c^3}{ab}N-\left(C+\frac{C_1E_cA_c}{b}\right)T}{\left(C+\frac{C_1E_cA_c}{b}\right)\left[\frac{1-\nu_m}{2}\left(C+\frac{3D}{a^2}\right)+\frac{C_4E_cR_c^4}{a^2b}\right]-\frac{C_2C_3E_c^2R_c^4A_c}{a^2b^2}}. \tag{92}$$

Applying the boundary conditions $M_x=M$ and $Q_x=Q$ at $x=0$ to Eqs. (65), (69), (76), (77), (83)–(85), and (90) and solving for the constants of integration B_3 and B_4 yields

$$B_3=-\frac{M+B_1\left(\frac{D}{a}+\frac{A_2C\nu_m}{2aA_3}\right)+\frac{A_2p_o}{2A_3}}{2\alpha^2A_1}-\frac{Q}{2\alpha^2\beta A_1} \tag{93}$$

and

$$B_4=\frac{M+B_1\left(\frac{D}{a}+\frac{A_2C\nu_m}{2aA_3}\right)+\frac{A_2p_o}{2A_3}}{2\alpha\beta A_1}. \tag{94}$$

The constants of integration B_1, B_2, B_3, B_4, B_5, and B_6 have been determined in terms of the loads, and therefore du/dx, dv/dx, and w have been determined in terms of the loads. The displacements u and v can easily be found by integrating the equations for du/dx and dv/dx, respectively, once with respect to x. The equations for u and v will have two new constants of integration. The constants represent rigid-body displacements and may be set equal to zero.

Finite Cylinder With End Loads. Consider a finite cylinder of length $2L$ with end loads and a uniform internal pressure p_o. The transverse traction is $p_z=p_o$, where p_o is a constant. The boundary conditions are $N_x=N$ at $x=\pm L$, $M_x=M$ at $x=\pm L$, $Q_x=Q$ at $x=-L$, $Q_x=-Q$ at $x=L$, and $T_x=T$ at $x=\pm L$.

It is most convenient to use the form of the solution for w given by Eq. (86). Since the transverse traction $p_z=p_o$, then $p_1=0$ in Eq. (90). The cylinder is symmetric about the φz-plane, and there-

fore the transverse displacement w must also be symmetric and the constants of integration D_2 and D_3 must be zero.

Applying the boundary conditions $N_x=N$ and $T_x=T$ at $x=\pm L$ to Eqs. (61), (63), (67), (76), (77), and (88) and solving for the constants of integration B_1 and B_2 yields Eqs. (91) and (92), the same as for a semi-infinite cylinder.

Equations (65), (69), (76), (77), (84)–(86), and (90) and applying the boundary conditions $Q_x=-Q$ and $M_x=M$ at $x=L$ and solving for constants of integration D_1 and D_4 yields

$$D_1=\frac{A_8(M-A_6)+A_5Q}{A_4A_8+A_5A_7} \tag{95}$$

and

$$D_4=\frac{-A_7(M-A_6)+A_4Q}{A_4A_8+A_5A_7}, \tag{96}$$

where

$$A_4=2\alpha\beta A_1\sin(\alpha L)\sinh(\beta L), \tag{97}$$

$$A_5=2\alpha\beta A_1\cos(\alpha L)\cosh(\beta L), \tag{98}$$

$$A_6=-\frac{B_1}{a}\left(D+\frac{A_2Cv_m}{2A_3}\right)-\frac{p_oA_2}{2A_3}, \tag{99}$$

$$A_7=2\alpha\beta A_1[\alpha\cos(\alpha L)\sinh(\beta L)+\beta\sin(\alpha L)\cosh(\beta L)], \tag{100}$$

and

$$A_8=2\alpha\beta A_1[\alpha\sin(\alpha L)\cosh(\beta L)-\beta\cos(\alpha L)\sinh(\beta L)]. \tag{101}$$

The constants of integration B_1, B_2, D_1, D_2, D_3, and D_4 have been determined in terms of the loads, and therefore du/dx, dv/dx, and w have been determined in terms of the loads. The displacements u and v can easily be found by integrating the equations for du/dx and dv/dx, respectively, once with respect to x. The equations for u and v will have two new constants of integration. The constants represent rigid-body displacements and may be set equal to zero.

Selected results are compared with the solutions given by Gough-Tangorra and Akasaka-Hirano for a cord composite cylindrical shell. In each case the cords are on the middle surface and are parallel to the shell axis. First, the results for an axially loaded semi-infinite shell are examined. Second, the results for a semi-infinite shell loaded by an edge moment are examined. Third, the results for an axially loaded finite shell are examined. The authors are not aware of any published experimental data on the load-deformation behavior of cord composite cylindrical shells to compare with the analytical solutions.

A concise review of the solutions by Gough-Tangorra and Akasaka-Hirano is given by Walter and Patel [2]. Classical lamination theory ([3]) is used to find the stiffnesses of the lamina. The solution given by Paris [10] is used to find the force and moment resultants, and deformations of the shell.

The Gough-Tangorra equations for the in-plane material properties are

$$E_1=E_cV_c+E_m(1-V_c). \tag{102}$$

$$E_2=\frac{4E_m(1-V_c)[E_cV_c+E_m(1-V_c)]}{3E_cV_c+4E_m(1-V_c)}, \tag{103}$$

$$G_{12}=G_m(1-V_c), \tag{104}$$

$$\nu_{12}=0.5, \tag{105}$$

and

$$\nu_{21}=\nu_{12}\frac{E_2}{E_1}, \tag{106}$$

where E is the tensile modulus, G is the shear modulus, V is the Poisson's ratio, and subscripts 1 and 2 indicate the in-plane material properties parallel to and perpendicular to the cord direction, respectively.

The cord volume fraction V_c is defined as

$$V_c=\frac{A_c}{bh}. \tag{107}$$

The Akasaka-Hirano equations for the in-plane material properties are

$$E_1=E_cV_c, \tag{108}$$

$$E_2=\frac{4E_m}{3}, \tag{109}$$

$$G_{12}=G_m, \tag{110}$$

$$\nu_{12}=0.5, \tag{111}$$

and

$$\nu_{21}=0. \tag{112}$$

The properties of the constituents and the geometry of the cord composite cylindrical shell are

Steel cord:	$R_i=0.15$ mm
	$R_o=0.14$ mm
	$m=6$
	$\alpha=81.4$ deg
	$R_c=R_i+2R_o=0.430$ mm
	$E_c=200$ GPa
	$\nu_c=0.25$
	$A_c=0.440$ mm^2
	$C_1=0.967$
	$C_2=0.0828$
	$C_3=0.187$
	$C_4=0.0723$
	$C_5=0.0638$
Rubber matrix	$E_m=10$ MPa
	$\nu_m=0.5$
Shell:	$h=4R_c=1.71$ mm
	$a=0.318$ m
	$\nu_c=0.3$
Finite cylinder:	$2L=2a=0.635$ m

Consider a semi-infinite cylinder with an axial load $N=C$. Figure 10 shows the normalized displacements u/a, v/a, and w/a versus the normalized coordinate x/a. The curves for the normalized displacement u/a are indistinguishable for the current solution, Gough-Tangorra, and Akasaka-Hirano. For the solutions of Gough-Tangorra and Akasaka-Hirano, the normalized displace-

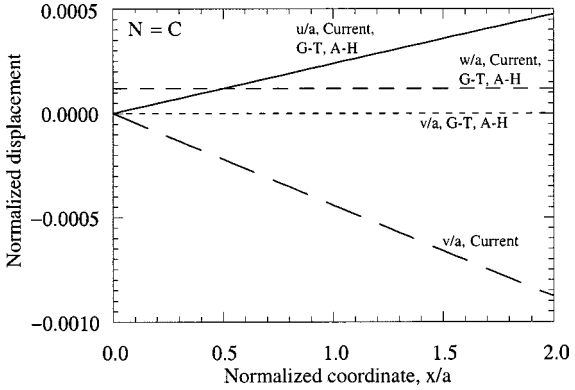

Fig. 10 Normalized displacements u/a, v/a, and w/a versus normalized coordinate x/a

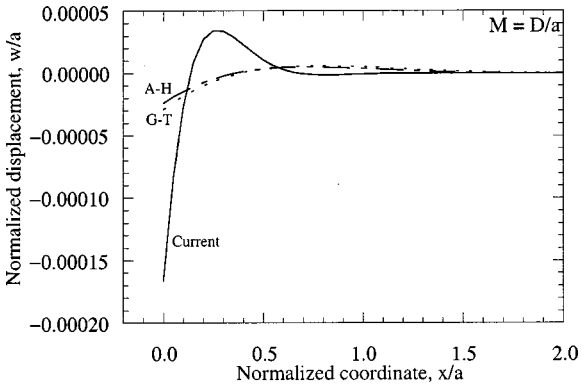

Fig. 11 Normalized displacement w/a versus normalized coordinate x/a

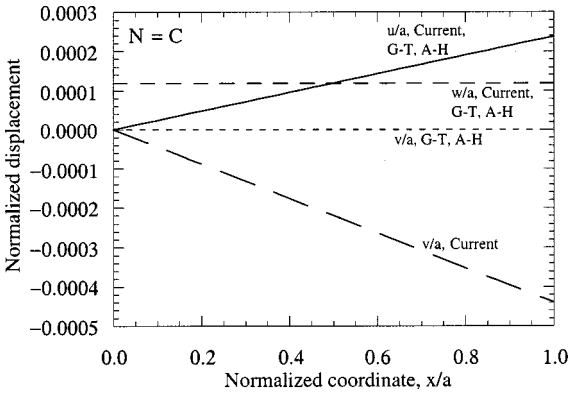

Fig. 13 Normalized displacements u/a, v/a, and w/a versus normalized coordinate x/a

ment v/a is zero. However, for the current solution, the normalized displacements u/a and v/a are of the same order of magnitude. The magnitude of the normalized displacement v/a is almost twice the magnitude of u/a. The sign of the normalized displacement v/a is dependent upon the lay of the cords: here the cords are right lay and the sign of the normalized displacement v/a is negative; if the cords were left lay, the sign of v/a would be positive. The curves for w/a are indistinguishable for the current solution and the solutions of Gough-Tangorra and Akasaka-Hirano. The shell has significant extension-twist coupling due to the extension-twist coupling of the cords.

Consider a semi-infinite cylinder with an edge moment $M = D/a$. Figure 11 shows the normalized displacement w/a versus normalized coordinate x/a. The curves for the normalized displacement w/a for the current solution is dramatically different from the solutions of both Gough-Tangorra and Akasaka-Hirano. The curves for the normalized displacement w/a for the solutions of Gough-Tangorra and Akasaka-Hirano are very close. At the end of the shell, where the normalized coordinate x/a is zero, the normalized displacement w/a for the current solution is one order of magnitude greater than those for the solutions of Gough-Tangorra and Akasaka-Hirano. A larger displacement indicates a smaller bending stiffness. The bending stiffness for the Gough-Tangorra and Akasaka-Hirano solutions is larger than the bending stiffness for the current solution since the Gough-Tangorra and Akasaka-Hirano solutions smear out the cord over the thickness of the shell and the current solution does not. The normalized displacement w/a decays exponentially and has nearly vanished when the normalized coordinate $x/a > 1$ for the current solution, and when $x/a > 2$ for the solutions of Gough-Tangorra and Akasaka-Hirano. Figure 12 shows the normalized moment resultant M_x/M versus the normalized coordinate x/a. Again, the curve for the current solution is dramatically different from the solutions of both Gough-Tangorra and Akasaka-Hirano. The curves for the solutions of Gough-Tangorra and Akasaka-Hirano are very close. The normalized moment resultant M_x/M decays exponentially and has nearly vanished when the normalized coordinate $x/a > 1$ for the current solution, and when $x/a > 2$ for the solutions of Gough-Tangorra and Akasaka-Hirano. The normalized displacement w/a and moment resultant M_x/M decay much more rapidly for the current solution than for the solutions of Gough-Tangorra and Akasaka-Hirano.

Consider a finite cylinder with an axial load $N = C$. This is an intermediate length shell based upon the analysis of a semi-infinite shell with an edge moment above. Figure 13 shows the normalized displacements u/a, v/a, and w/a versus the normalized coordinate x/a. These results for an axially loaded finite cylinder are similar to those for a semi-infinite cylinder above. The following discussion follows the discussion for a semi-infinite cylinder above. The curves for the normalized displacement u/a are indistinguishable for the current solution, Gough-Tangorra, and Akasaka-Hirano. For the solutions of Gough-Tangorra and Akasaka-Hirano, the normalized displacement v/a is zero. However, for the current solution the normalized displacements u/a and v/a are of the same order of magnitude. The magnitude of the normalized displacement v/a is almost twice the magnitude of the normalized displacement u/a. The curves for the normalized displacement w/a are indistinguishable for the current solution, Gough-Tangorra and Akasaka-Hirano. The shell has significant extension-twist coupling due to the extension-twist coupling of the cords.

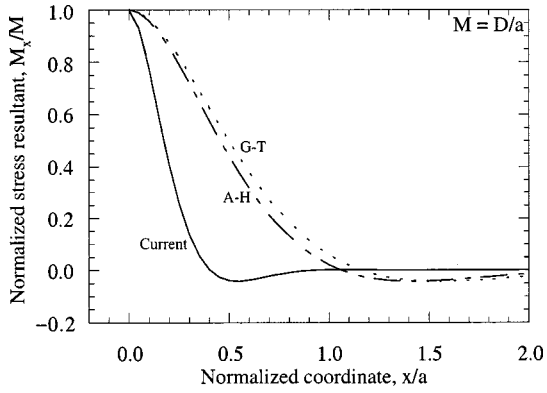

Fig. 12 Normalized stress resultant M_x/M versus normalized coordinate x/a

Summary and Conclusions

An analytical method for determining the load-deformation behavior of cord composite cylindrical shells was developed by considering the mechanics of the matrix, the cords, and the shell. The differential equations for the displacements were found for a shell with a single ply of uniformly spaced cords with the cord axes parallel to the shell axis. The equations were solved analytically in closed form for a shell with the cords on the middle surface. The response due to uniformly distributed axisymmetric end loads and uniform internal pressure was found for both a semi-infinite cylinder and a finite cylinder.

In general, the effect of the extension-twist coupling of the cords on the displacements of a cord composite cylindrical shell depends upon the shell constituents, geometry, boundary conditions, and loading. The results show that the axially loaded cord composite cylindrical shells considered have significant extension-twist coupling.

Acknowledgments

The authors would like to thank the Department of Theoretical and Applied Mechanics of the University of Illinois at Urbana-Champaign for supporting this work, Carol Kittredge Shield for the many conversations regarding the mechanics of cords and cord composite materials, Robert E. Miller for the many conversations regarding the mechanics of shells, and James W. Phillips, Sarah E. Zeller, and W. Earl Anderson for their comments and suggestions regarding this manuscript.

References

[1] Walter, J. D., 1978, ''Cord-Rubber Tire Composites: Theory and Applications,'' Rubber Chem. Technol., **51**, No. 3, pp. 524–576.
[2] Walter, J. D., and Patel, H. P., 1979, ''Approximate Expressions for the Elastic Constants of Cord-Rubber Laminates,'' Rubber Chem. Technol., **52**, No. 4, pp. 710–724.
[3] Jones, R. M., 1998, *Mechanics of Composite Materials*, 2nd ed., Taylor and Francis, Philadelphia.
[4] Costello, G. A., 1997, *Theory of Wire Rope*, 2nd ed., Springer-Verlag, New York.
[5] Paris, A. J., Lin, C. C., and Costello, G. A., 1992, ''Simple Cord Composites,'' J. Eng. Mech., **118**, No. 9, pp. 1939–1948.
[6] Kittredge, C. A., 1991, ''Static Response of Cord Composite Plates,'' Ph.D. thesis, Department of Theoretical and Applied Mechanics, University of Illinois at Urbana-Champaign, Urbana, IL.
[7] Shield, C. K., and Costello, G. A., 1994, ''The Effect of Wire Rope Mechanics on the Mechanical Response of Cord Composite Laminates: An Elasticity Approach,'' ASME J. Appl. Mech., **61**, pp. 1–8.
[8] Shield, C. K., and Costello, G. A., 1994, ''The Effect of Wire Rope Mechanics on the Mechanical Response of Cord Composite Laminates: An Energy Approach,'' ASME J. Appl. Mech., **61**, pp. 9–15.
[9] Shield, C. K., and Costello, G. A., 1994, ''Bending of Cord Composite Plates,'' J. Eng. Mech., **120**, No. 4, pp. 876–892.
[10] Paris, A. J., 1997, ''Cord-Reinforced Cylindrical Shells,'' Ph.D. thesis, Department of Theoretical and Applied Mechanics, University of Illinois at Urbana-Champaign, Urbana, IL.
[11] Love, A. E. H., 1934, *A Treatise on the Mathematical Theory of Elasticity*, 4th ed., Cambridge University Press, London.
[12] Flügge, W., 1966, *Stresses in Shells*, Springer-Verlag, New York.
[13] Jiang, W. G., Yao, M. S., and Walton, J. M., 1999, ''A Concise Finite Element Model for Simple Straight Wire Rope Strand,'' Int. J. Mech. Sci., **41**, pp. 143–161.
[14] Prakash, A., Conway, T. A., and Costello, G. A., 1992, ''Compression of a Cord,'' ASME J. Appl. Mech., **59**, pp. S213–S216.

V. Madhavan
Assoc. Mem. ASME
Department of Industrial and Manufacturing Engineering,
Wichita State University,
Wichita, KS 6720-0035

S. Chandrasekar
Mem. ASME
School of Industrial Engineering,
Purdue University,
West Lafayette, IN 47907

T. N. Farris
Mem. ASME
School of Aeronautics and Astronautics,
Purdue University,
West Lafayette, IN 47907

Machining as a Wedge Indentation

A case is made for the consideration of single-point machining of ductile metals as a special type of wedge indentation process. A general-purpose finite element analysis of machining using iterative rezoning is developed based on this analogy. The accuracy of this analysis, which does not incorporate any separation criterion, is limited only by our knowledge of the material properties and the friction conditions at the tool-chip interface. Strain hardening, strain rate effects, and the temperature dependence of the properties of the work material can be taken into consideration. While Coulomb friction is assumed at the chip-tool interface in the present model, it can easily be reformulated to include more complicated frictional interactions such as adhesion. An analysis of the cutting/indentation of an isotropic work-hardening material at slow speeds under two different friction conditions is presented. It is shown that many of the important features of machining processes are consistently reproduced by the analysis. [S0021-8936(00)03501-7]

1 Introduction

The main reason for developing machining models is the need to predict outputs of the machining process such as cutting forces, residual stresses, and the tool life for a given set of input parameters like feed, speed, depth of cut, and tool geometry. Such models will help us address the inverse problem of determining the inputs for achieving certain values of the output parameters. Various models of machining at varying levels of complexity have been proposed by different researchers. These models can be broadly classified into (i) slip line field models, (ii) finite element models and (iii) atomistic models. A careful review of these models suggests that finite element models are best suited for accurate prediction of machining parameters.

Based on similarities between experimentally observed deformation patterns in machining and indentation of ductile metals, and on atomistic analyses of these two processes, it is concluded that they are equivalent and that finite element models of machining of ductile materials (with production of continuous chips) do not have to incorporate separation or failure criteria for the work material. An iterative finite element model of machining which is capable of simulating machining by periodic remeshing of the workpiece (to offset mesh distortions due to deformation caused by the infeed of the tool) is described. Due to its closer representation of the actual machining process, such a model is more accurate than conventional Lagrangian finite element models that incorporate a separation criterion. This model is used to analyze machining and gives results which are consistent with experimental observations pertaining to cutting and wedge indentation.

2 Background

2.1 Finite Element Analysis. Finite element studies of the machining process have been carried out by a number of researchers. Klamecki's model ([1]) was limited to the incipient cutting stage. Usui and Shirakash [2] also assumed a steady-state chip geometry and advanced the tool only incrementally. The first analysis of orthogonal metal cutting where the tool was moved into the workpiece to generate a chip which separates from the workpiece along a previously defined ''parting line'' was due to Strenkowski and Carroll [3]. In their analysis, the nodes along the parting line were ''unhooked'' when the effective strain at these nodes exceeded 0.5. Subsequently they adopted an Eulerian analysis in which finite element equations were formulated in an Eulerian reference frame ([4]). This approach allows the mesh to be fixed in space and the material to flow through the mesh, thereby avoiding problems of mesh distortion and the need for a predefined parting line. The procedure required iterative modification of the chip geometry so as to satisfy the velocity boundary conditions and since a purely viscoplastic material model was assumed, it could not give information about residual stresses. Various other researchers ([5–8]) have carried out Lagrangian analyses of metal cutting process by incorporating the concept of the parting line along which nodes initially tied together are separated as the tool advances into the work. The criteria used for this ''unhooking'' have included limiting values of strain, distance to the tool tip, etc. All of these criteria are completely arbitrary and have a major influence on the residual stresses in the chip and the machined surface ([3]). Though there is no inherent difference in the nature of chip formation while cutting with negative and positive rake angle tools, these analyses could not simulate cutting with large negative rake angle tools suggesting that the modeling of the process is not accurate. Another source of error was the coarseness of the mesh even in regions of intense plastic deformation. These models require tremendous computational resources to effectively model the cutting process because of the need for a fine mesh of elements all along the parting line.

It can be argued that finite element analyses which incorporate node separation along a parting line, simulate a process more akin to the splitting of wood than to the machining of ductile metals. Unhooking the nodes when they are a small distance away from the cutting edge, results in a small crack in the work material ahead of the tool. It is a well-acknowledged fact that there is no such crack propagating ahead of the tool in the machining of ductile metals ([9–10]). Though material ''separation'' occurs along a plane in the workpiece, it is more accurate to picture such separation as due to plastic flow of the material rather than due to tensile rupture. The presence or absence of a crack ahead of the cutting edge is a big factor in determining the actual mechanics of the process. From consideration of the distribution of the hydrostatic stress along the shear zone, given by Roth and Oxley [11] and reproduced here in Fig. 1, it can be seen that the hydrostatic stress close to the cutting edge is compressive. Such compressive stresses cannot produce tensile rupture of the work material. It is also evident that if this small compressively stressed zone is re-

Contributed by the Applied Mechanics Division of THE AMERICAN SOCIETY OF MECHANICAL ENGINEERS for publication in the ASME JOURNAL OF APPLIED MECHANICS. Manuscript received by the ASME Applied Mechanics Division, Oct. 2, 1997; final revision, Feb. 23, 1998. Associate Technical Editor: M. Ortiz. Discussion on the paper should be addressed to the Technical Editor, Professor Lewis T. Wheeler, Department of Mechanical Engineering, University of Houston, Houston, TX 77204-4792, and will be accepted until four months after final publication of the paper itself in the ASME JOURNAL OF APPLIED MECHANICS.

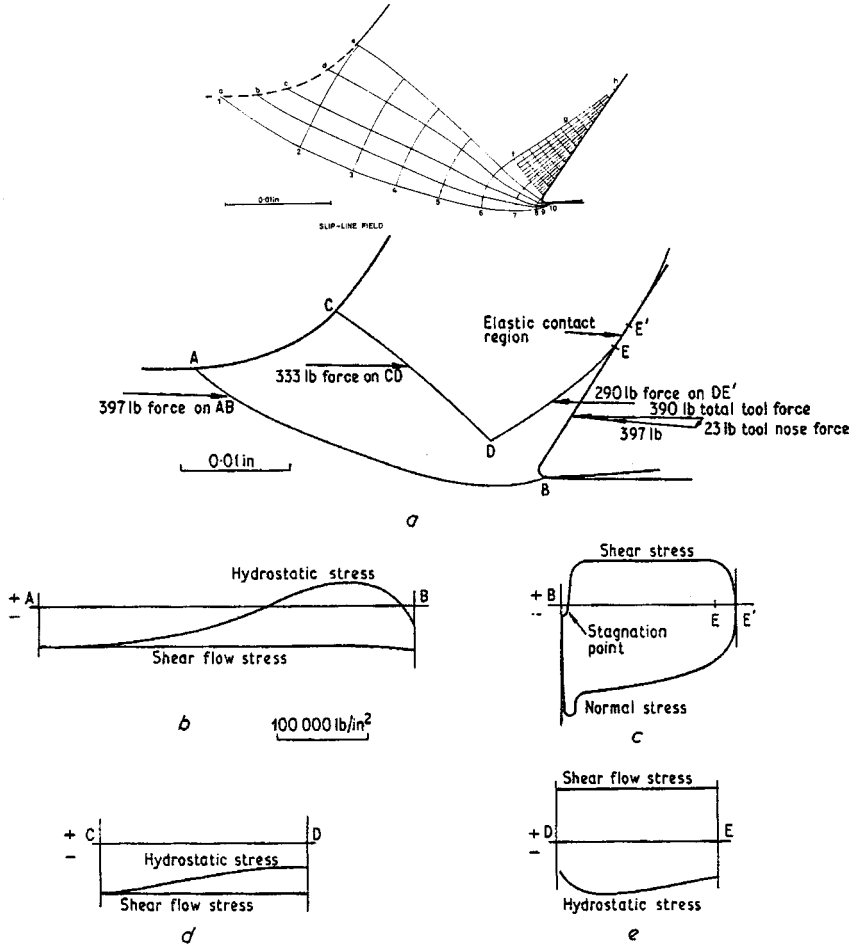

Fig. 1 Variation of hydrostatic stress along the shear plane as given by Oxley et al. [11]

placed by a crack, the tensile stress beyond this zone can be used to drive the crack ahead of the cutting edge of the tool. The reason for the inability of such finite element analyses to simulate machining with large negative rake angle tools is that even when a crack is artificially introduced ahead of the tool, the stresses due to machining tend to close this crack rather than open it. Thus the results obtained by finite element method studies where the nodes are unhooked along a parting line ([3,5,8,7]) neither reflect the true nature nor the magnitude of the stresses and strains found close to the cutting edge in machining.

Two new analyses ([12–13]) have overcome such limitations of previous analyses by continual remeshing of the workpiece and chip material in the deformation zones. Sekhon and Chenot [12] have used a velocity approach in which velocities are the unknowns at the nodes and the workpiece material is treated like an incompressible viscous fluid. Thus elastic effects are ignored and so residual stresses cannot be estimated. However, their coupled thermomechanical analysis does take into consideration the thermal aspects of the process.

Marusich and Ortiz [13] have developed a Lagrangian finite element model of machining using continual remeshing and an explicit solution technique. Their model incorporates thermal effects as well as fracture criteria for the material and is able to predict localized shear deformation in the case of high-speed machining. Analysis of quasi-static processes is not possible by these explicit solution techniques. Both this and the previous analysis mentioned ([12]) use proprietary codes for the finite element analysis.

2.2 Atomic Analysis of Machining. Recently there has been some work directed at modeling the machining process at the level of the individual atoms of the workpiece and the tool ([14–19]). The aim of such analyses has been to study the mechanism of chip formation in ultra precision machining, deduce limits to the depth of cut achievable, and investigate the integrity of the machined surface. The tool and the workpiece are modeled as separate collections of atoms. Each atom interacts with its neighbors according to assumed force laws which express the interatomic forces as functions of the interatomic spacing. The thermal vibrations of the atoms are also taken into account in the models.

Cutting is simulated by forcing the atoms comprising the tool into the workpiece. No separation criterion for the atoms is used in these simulations. Plastic deformation of the work material occurs when the lattice strain energy exceeds a critical level upon which it is energetically favorable for the atoms to rearrange themselves (in a manner akin to that considered in theoretical calculations of the ultimate shear stress) in a different configuration of lower energy. Thus dislocations are generated and move in a zig-zag path from the cutting edge to the free surface resulting in a broad zone of shear (as opposed to a shear plane). Upon continued infeed of the tool, a succession of progressive shearing motions are found to result in the formation of a chip. These analyses have yielded useful information about the strain distribution in the chip and the subsurface of the machined layer. But extension of these results to the macroscopic dimensions of most cutting processes is difficult.

In this study, experimental observations from prior studies as

well as finite element analysis of machining are used to obtain a better understanding of the mechanics of separation of material into the workpiece and the chip at the cutting edge. A compelling case is presented for considering machining (cutting) of ductile metals as a wedge indentation process. This insight is then applied to develop a finite element analysis of machining without recourse to separation criteria, purely by periodic remeshing of the workpiece.

3 Equivalence of Machining and Indentation

Early researchers were fully aware of the similarities between machining and wedge indentation. By using sequences from motion pictures of the indentation of a paraffin block by a wedge-shaped tool pressed into the middle of the block, and the cutting action initiated when the tool is pressed into the block close to an edge, Ernst [9] was able to conclude that machining is equivalent to asymmetric indentation with an inclined wedge. Bhattacharyya [20] has also highlighted the similarities between machining and indentation. Due to the difficulty of analysis of the inclined wedge indentation model, and the simplicity of the shear-plane model of chip formation, the latter has probably found favor as the model for analysis of machining. When detailed information about the cutting process is required, the simple straight shear-plane model has been found to be inadequate and extensive modifications have been proposed resulting in systems which are hard to analyze ([21,11]). In this context it is worthwhile to revisit the machining problem as a special case of indentation.

Texture or flow lines are produced in any deformation process as a result of elongation of the grains of the material in the direction of maximum tensile strain. These lines can be further stretched, compressed, and rotated by subsequent strains imposed on the material. Chaudhri [22] has recently investigated the subsurface deformation produced in mild steel specimens indented with tungsten carbide cones by studying the deformation of naturally occurring texture lines (formed by the alignment of pearlite grains produced by prior cold drawing). Figure 2 shows an etched cross-section through the center of such an indentation produced by a 45-deg tungsten carbide cone. It is seen clearly that the texture lines are not ruptured by the penetration of the indenter, but are actually bent around the tip of the indenter. In machining, flow lines form as a consequence of the shear deformation occurring along the primary shear zone. These lines are then stretched and rotated due to the secondary deformation taking place along the rake face of the tool. Thus the flow lines in the chip and the workpiece also contain similar information as the flow lines around the indentation in Fig. 2, and can be used for comparing the deformation patterns in the two processes. Furthermore, machining with sticking friction along the tool-chip interface also shows flow lines bent around the tip of the tool as seen in Fig. 3. In the case of frictionless indentation of a semi-infinite solid with a wedge, the theory of Hill et al. [23] predicts that the material ahead of the indenter and along the axis of loading ''ruptures'' as the edge of the indenter is moved in. This has been found to be roughly true in experiments where split lead specimens with grids imprinted on the surfaces of the split were indented with lubricated steel wedges. A similar ''rupture'' of the flow lines can indeed be observed in etched cross sections of quick-stop specimens of machining when the chip slides over the tool rake face as in Fig. 4.

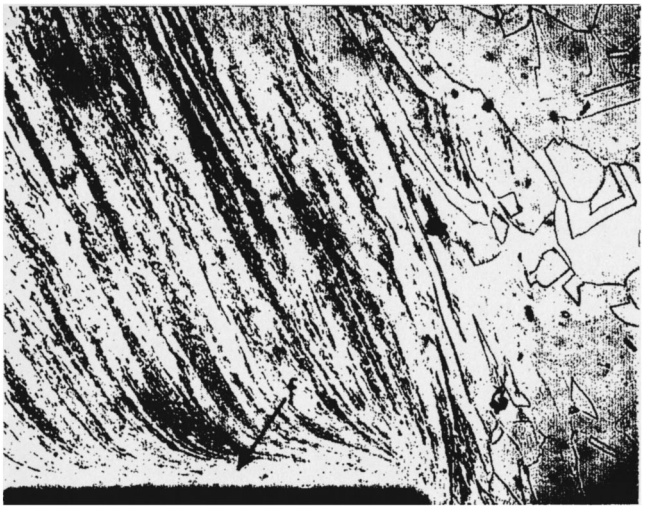

Fig. 3 Etched cross section through a machining quick-stop specimen involving sticking between the chip and the rake face of the tool ([29]). The texture lines are curved around the cutting edge of the tool.

Further evidence of the similarities between machining and wedge indentation comes from Hutchings's [24] study of the deformation produced in mild steel surfaces by the oblique impact of square plates made of hardened tool steel. A regime of deformation intermediate between normal wedge indentations and cutting was observed in these experiments, which is consistent with the orientation and the direction of motion of the indenter in the experiments being intermediate between normal indentation and machining. These experimentally observed similarities in the deformation pattern in machining and indentation have motivated the

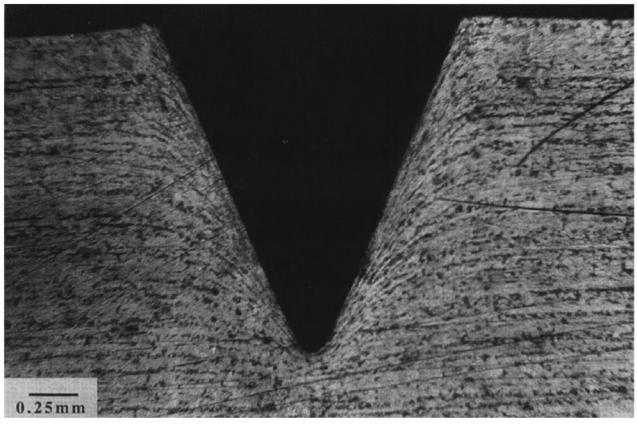

Fig. 2 Etched cross section through the center of a conical indentation in mild steel showing deformation of texture lines ([22]). Note that the texture lines are not cut by the tip of the indenter.

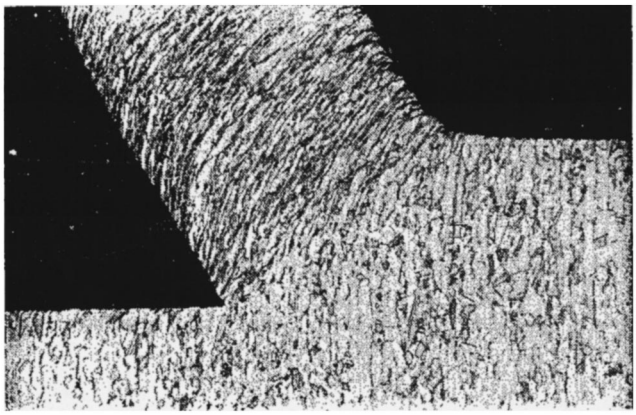

Fig. 4 Etched cross section of a machining quick-stop specimen involving sliding of the chip over the rake face ([10]). Note that the flow lines are cut by the cutting edge of the tool.

view that machining is indeed a special type of wedge indentation in which the indentation is made close to one of the edges of the surface being indented with the wedge positioned asymmetrically with respect to the surface normal and the direction of motion of the indenter is controlled. Similarity between machining and indentation is also evident from atomistic analyses of the two processes where only the shape, location, and the direction of motion of the tool/indenter are found to be different while all the physical phenomena modeled are the same. Using this analogy between machining and indentation, it is easy to picture machining as a process whereby a chip is generated from the workpiece by a process of pure shear. Thus machining can be analyzed by iterative finite element analysis, without the need for any criterion for material failure ahead of the cutting edge to produce the chip.

The real difficulty encountered in finite element analyses of machining is that points in the workpiece which start out close to each other may end up being very far apart if some of them form part of the chip and others constitute part of the machined surface. Such ''local'' deformation of the material cannot be accommodated in conventional Lagrangian finite element analysis. This, coupled with the idea that there was ''separation'' or ''fracture'' of the material close to the cutting edge of the tool in machining, has led to the incorporation of artificial failure criteria in machining models which enforce separation of initially continuous material into a chip and a machined surface along a predetermined parting line. Such models cannot represent the true nature of the machining process.

The atomistic analyses of machining processes reviewed earlier indicate that even in the case of tools so sharp that their cutting edge radii are less than a few nanometers, the deformation in the workpiece produced as a result of dislocations being generated and moved along the shear zone can be considered to be a shear deformation. This suggests that when the scale at which the workpiece is modeled is such that the elements representing the workpiece material close to the cutting edge of the tool are much smaller than the radius of curvature of the cutting edge, the elements can be assumed to deform purely by shear with no tensile rupture being involved. It is thus clear that machining can be analyzed accurately by an iterative finite element method so long as the size of the elements are small enough to realistically represent the stress state in the workpiece near the cutting edge, and the workpiece is periodically remeshed in order to replace distorted elements with undistorted elements. The next section describes such an iterative finite element analysis of the machining process.

4 Iterative Finite Element Analysis of Machining

The Lagrangian finite element analysis described here uses iterative rezoning, by which the mesh representing the discretization of the workpiece and the chip for an interval of time, is replaced by a different mesh for the next interval of time. The distribution of stresses and strains represented by the old mesh is interpolated onto the new mesh. Thus the new mesh is a different discretization of the exact same body with the same stress and strain fields. The difference is that the new mesh does not retain any of the distortions the old mesh underwent due to the incremental infeed of the tool during the time for which it was used to represent the workpiece and the chip. This technique of continual remeshing in between displacement increments of the tool avoids problems due to excessive mesh distortion, namely inaccurate results and, in extreme cases, the inability of the solution procedure to converge to an equilibrium stress state. It should be noted that only in order to circumvent these problems did most of the previous analyses report to unhooking the nodes along the parting line.

4.1 Analysis Methodology. Figure 5 shows the configuration of the cutting process being analyzed. The analysis performed is a two-dimensional plane strain analysis. The tool is idealized as a rigid body having a rake angle of 0 deg and a clearance angle of 10 deg with a curvature at the corner representing the radius of curvature of the cutting edge, 250 μm in this case. There is no

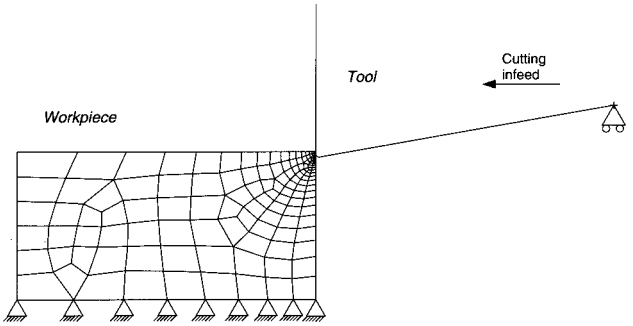

Fig. 5 Configuration of workpiece and tool for the finite element simulation of machining

inherent limitation imposed by the model on the values of the rake angle and this can be varied arbitrarily. In fact, even in the present study, the local rake angle near the cutting edge of the tool is highly negative, though the nominal rake angle of the tool is 0 deg. The workpiece is a rectangular piece of metal 50 mm long$\times$25 mm deep, held rigidly along its bottom edge. The tool and the workpiece surfaces (edges in 2-d) are connected together by contact elements along the interface which transmit sufficient forces to prevent interpenetration of one body into another. Friction and adhesion are also modeled for the contact region. The model of friction adopted is shear limited Coulomb friction with the maximum shear stress at the tool-workpiece interface limited to 150 MPa. The tool is positioned so that it will interfere with the workpiece when moved. The depth of cut was chosen to be 0.45 mm in the present case. This small value, $<$2.0, of the ratio of the depth of cut to the cutting edge radius of the tool was deliberately chosen in order to clearly illustrate the similarities between machining and indentation.

Cutting is simulated by forcing the tool to move into the workpiece in small increments. After a predetermined value of the equivalent plastic strain (chosen to be 0.25 in this case as this corresponds to a pure shear strain of less than 30 deg) is exceeded at any point in the workpiece, a new mesh is automatically generated to represent the deformed configuration of the workpiece. It is observed in our simulations that the results are insensitive to the remeshing criterion, when the equivalent plastic strain increment between remeshing increments is varied up to 0.33. After interpolation of the stresses and strains onto the new mesh, the analysis is restarted by further infeed of the tool. During the automatic remeshing, adaptive mesh refinement is accomplished by making the mesh finer in the regions of high gradients of stresses and strains and in regions of high plastic strain increments. This is done by fixing the minimum and maximum element sizes and allowing the sizes of the individual elements to vary within these limits depending on the above criteria. Mesh refinement is carried out only in regions where the fine details of the stress distribution have to be resolved.

The model described above has been implemented using a combination of two commercial finite element method packages. The automated creation and refinement of the meshes (pre-processing) and the processing of the results (post-processing) are both done using the P3/PATRAN package. PATRAN was chosen because it offers the Patran Command Language (PCL) in which these tasks could be programmed efficiently and because of its ability to create input files for a range of solvers. The actual solution of each step in the simulation when the tool is moved incrementally into the workpiece is performed in ABAQUS/STANDARD. CPE4 constant strain quadrilateral plane-strain elements are used to discretize the workpiece. ABAQUS was chosen as the solver because of its ability to automatically interpolate values of the variables

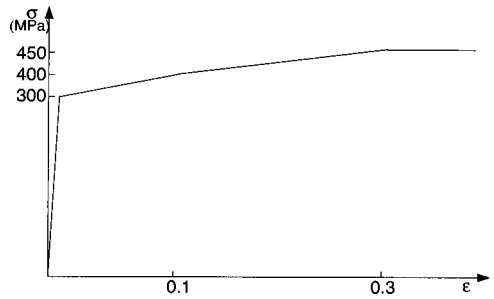

Fig. 6 Strain-hardening characteristic of the work material

from the old mesh onto the new mesh, the flexibility provided in the contact elements, and because of its reputedly superior handling of plasticity problems.

5 Results and Discussion

The finite element analysis described above has been used to study the cutting process for two values of the coefficient of friction (μ=0.2 and 0.8) at the chip-tool interface. In both cases, the rake angle is 0 deg, the radius of curvature of the cutting edge of the tool is 250 μm and the depth of cut is 452 μm. The hardening characteristic assumed for the work material is shown in Fig. 6 with initial yield beginning at an effective stress of 350 MPa. The maximum shear stress along the tool-chip interface is limited to 150 MPa, which is less than the shear strength of the work material even in its unhardened state. In the analysis, the minimum mesh size (50 μm) is chosen to be one-fifth of the radius of curvature of the cutting edge.

Figures 7 and 8 show the stages in the formation of the chip as cutting proceeds, for the two cases (μ=0.2 and μ=0.8). Equivalent plastic strain contours are also plotted in these figures. Figure 9 shows the steady state distribution of the von Mises stress after approximately 5 mm of cutting (i.e., infeed of the tool) by which time a constant curl of the chip is established. Similar plots for the three components of stresses (σ_{xx}, σ_{yy}, and σ_{xy}) are shown in Figs. 10–12. The main features of the machining process as evidenced by these figures are summarized below.

5.1 Stress and Strain Distributions in the Chip. A region of fairly concentrated shear (Fig. 7) separates the nearly unstrained work material from the fully strained chip. This region can be approximated as a parallel sided shear zone as shown schematically in Fig. 13. There is another region of secondary deformation (where the Mises stress is around 450 MPa) close to the rake face of the tool which is evident in Figs. 9(*a*) and 9(*b*). This region can be approximated as a triangular region as indicated in Figs. 1 and 13. The existence of such a triangular secondary shear zone has been commonly postulated by a number of investigators ([25,26,11,27]). The fact that secondary shear occurs even though the shear strength of the chip-tool interface is less than the shear strength of the chip, implies that the slip lines in this zone are not parallel to the interface. Such secondary shear can result in curvature of the flowlines close to the rake face of the cutting tool even though the chip may actually be sliding (i.e., not sticking) over the rake face of the tool.

A zone of plastic deformation extends underneath the machined surface. The depth of subsurface plastic deformation is found to be nearly equal to the radius of curvature of the cutting edge. This subsurface deformation results in compressive stresses in the machined surface. Though the stress patterns shown are those with the load applied by the tool still present, elastic recovery caused by unloading of the tool is not expected to significantly change the stress distribution close to the free surface and so σ_{xx} at the surface can be taken to be the residual stress. The residual stress is compressive with a magnitude greater than 200 MPa, which is more than half the uniaxial yield stress of the material. The plastic strains in the machined surface are as high as 5.0. The elastic springback of the machined surface after it passes underneath the tool is found to be $\approx$2 μm which is less than one percent of the radius of curvature of the cutting edge.

The plastic strain in most of the chip formed during steady state cutting is found to be between 1.3 and 2.0. It is much higher close to the chip-tool interface (up to 7.3). Most of the strain in this layer close to the interface occurs when the material passes near the cutting edge of the tool. The increase in the strain as the chip moves along the rake face of the tool is negligible. The strain gradient along the chip-tool interface is also low and therefore the adaptive remeshing criterion used, based upon strain gradients and strain rate as noted above, results in fairly large elements in the chip in this region.

The cutting and thrust forces stabilize very early in the analysis even before a steady-state curvature of the chip is attained. The cutting forces, for a 1-cm wide workpiece, are 4600N for μ=0.2 and 5400N for μ=0.8. The cutting pressure defined as the ratio of the cutting force to the interference area (which is the product of the uncut chip thickness and the width of cut), represents the average pressure required to deform the material in the interference zone. It is found to be close to three times the yield strength of the material for μ=0.2 and is around 3.4 times the yield strength for μ=0.8. The thrust force is between 0.5 and 0.6 times the cutting force. It is interesting to note here that the indentation pressure or hardness value for most metals is about three times the yield strength of the solid ([28]).

From Fig. 10, the length of contact between the chip and the tool is estimated as 0.866 mm for the case of μ=0.2 and 1.21 mm for the case of μ=0.8. It can be seen (Fig. 12) that for μ=0.8 the shear stress at the chip-tool interface (σ_{xy}) is nearly constant at 150 MPa, for most of the length of contact between the rake face of the tool and the chip. Close to the end of chip tool contact, this shear stress along the rake face rapidly decreases to zero. A similar feature is also observed in the distribution of σ_{xx} (Fig. 10) which remains constant at around 500 MPa for most of the contact length and then rapidly decreases to zero at the end of contact. Another interesting observation from Fig. 10 is that the maximum contact pressure at the chip-tool interface is 819 MPa for μ=0.2 while it is only 700 MPa for μ=0.8.

The variation of the hydrostatic and shear stresses along the shear plane can be directly inferred from the plots of σ_{xx} and σ_{yy}. For μ=0.2 the hydrostatic stress close to the cutting edge is ≈ -475 MPa. This decreases to ≈ -175 MPa in the middle of the shear zone and rises to ≈ -325 MPa near the exit of the shear plane (i.e., near the free surface of the workpiece). For μ=0.8 the three corresponding values are -575 MPa, -190 MPa, and -330 MPa.

The back surface of the chip is found to be wrinkled. This is a result of concentrated shear occurring in the region where the shear plane exits the work material. This is observed even in studies with much finer meshes, so long as material workhardening and strain-rate effects are minimal.

5.2 Chip Curl. From Figs. 11 and 10, it is seen that the stress along the free surface (back) of the chip is highly tensile. It is also tensile along the surface of the chip which has moved out of contact with the tool rake face (front side of the chip). σ_{yy} in the middle of the chip is compressive. Such a distribution of stresses was seen to develop early on in the formation of the chip.

The hypotheses propounded by various researchers to explain the curvature of the chip include (i) the cutting moment causes the chip to bend; (ii) the ''crushing'' of the chip in the secondary shear zone and the resultant acceleration of the work material in moving through the secondary shear zone causes the chip to lengthen along this side (the front side). This results in a curvature of the chip, similar to the curvature of a bimetallic strip; (iii) the shear plane is curved in such a way that the shear plane angle is

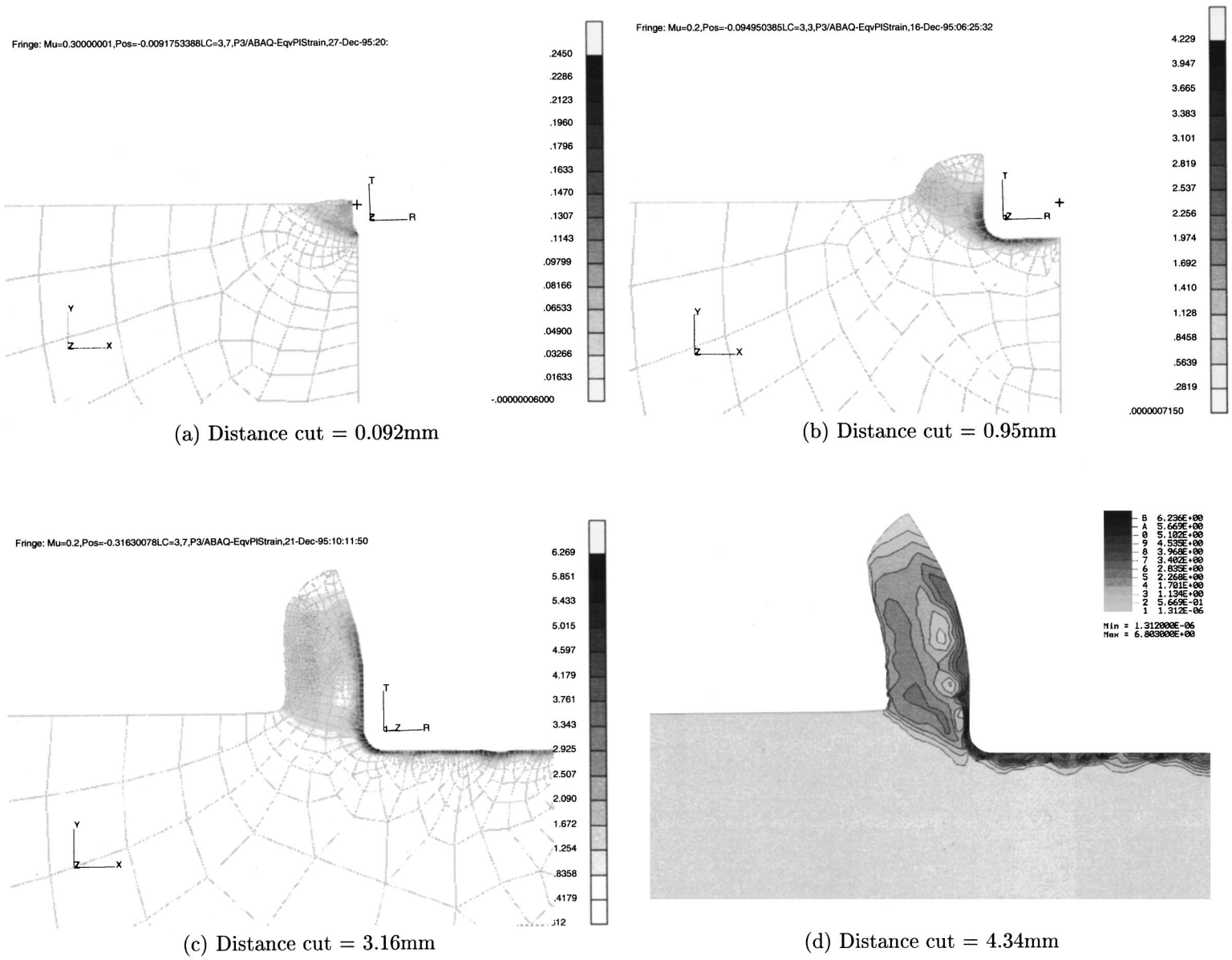

(a) Distance cut = 0.092mm

(b) Distance cut = 0.95mm

(c) Distance cut = 3.16mm

(d) Distance cut = 4.34mm

Fig. 7 Chip formation and distribution of equivalent plastic strain (μ=0.2)

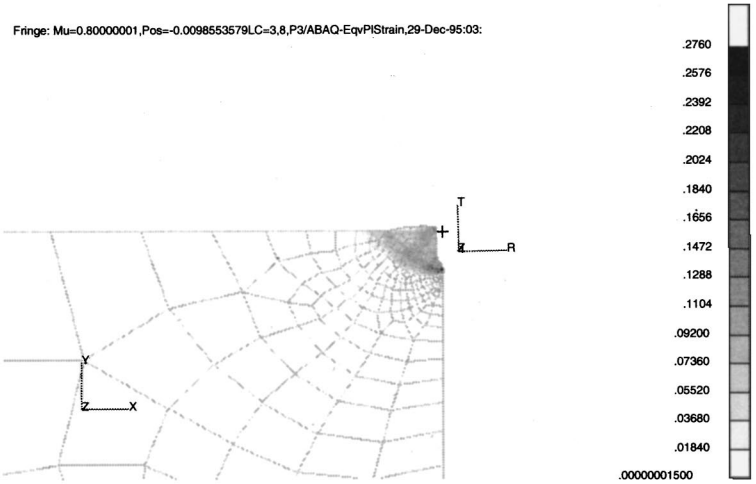

(a) Distance cut = 0.099mm

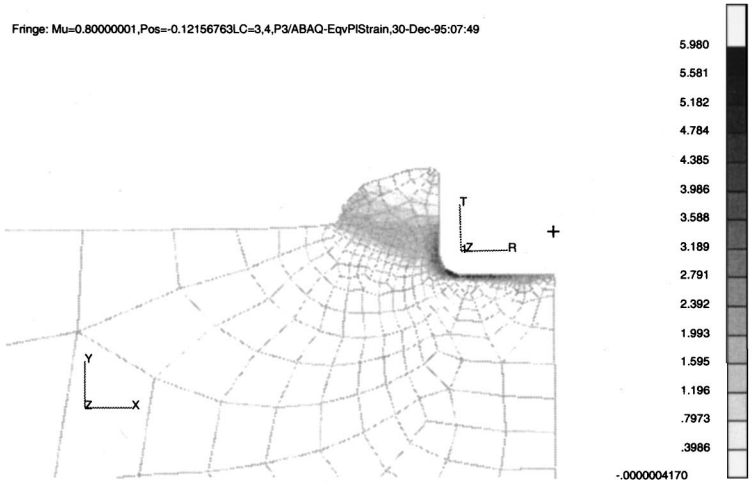

(b) Distance cut = 1.22mm

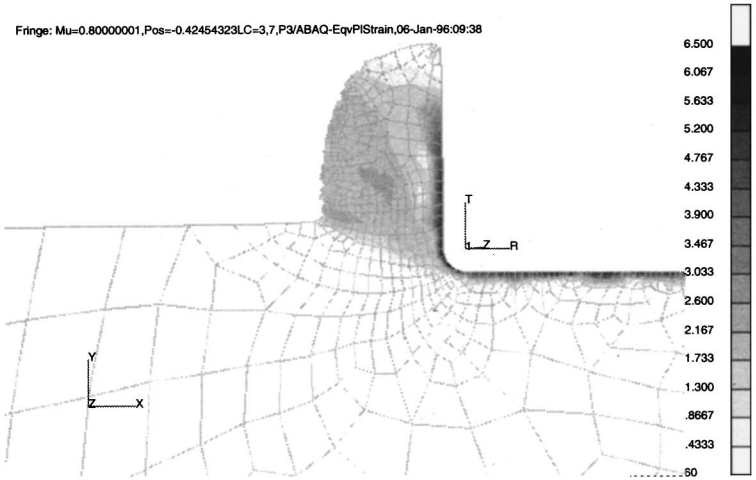

(c) Distance cut = 4.25mm

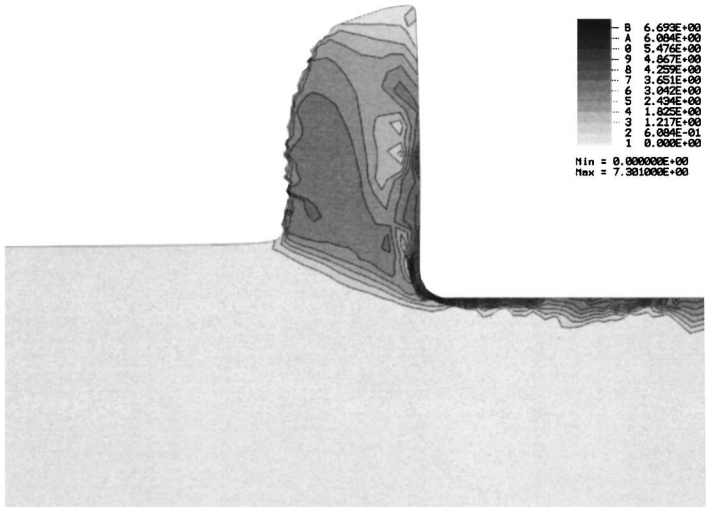

(d) Distance cut = 5.14mm

Fig. 8 Chip formation and distribution of equivalent plastic strain (μ=0.8)

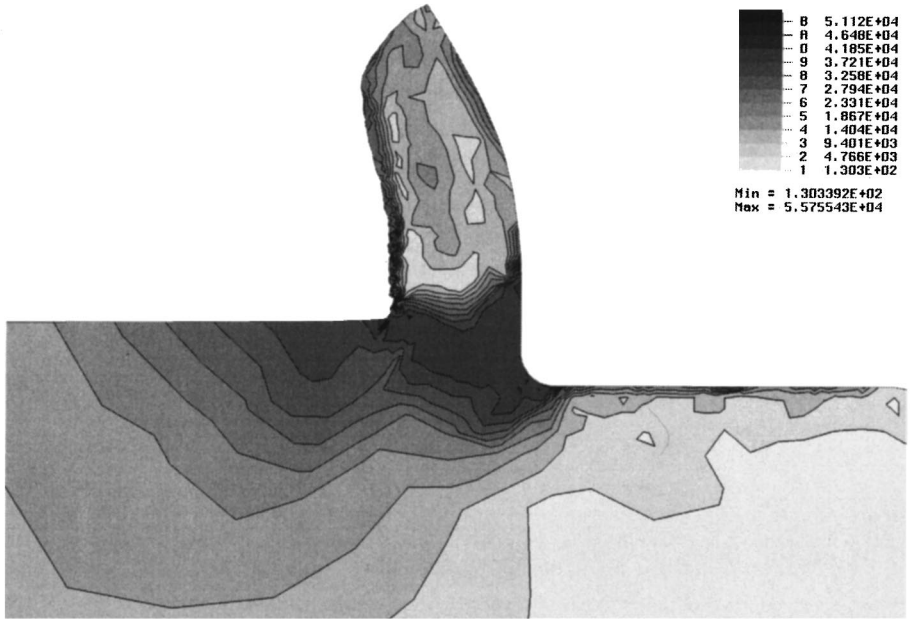

(a) $\mu = 0.2$; Distance cut = 4.34mm

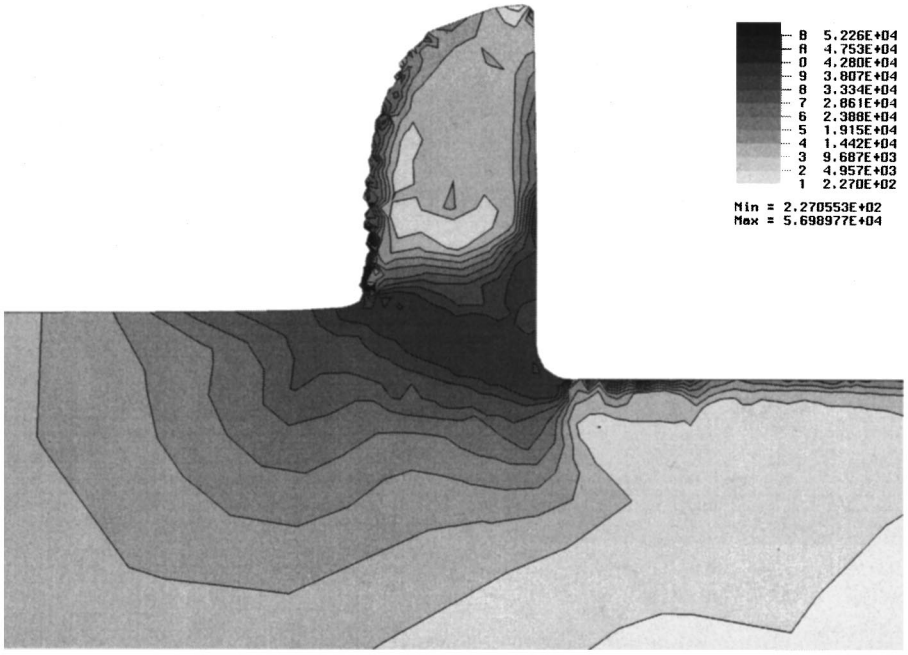

(b) $\mu = 0.8$; Distance cut = 5.14mm

Fig. 9 Steady-state von Mises stress distribution. Hundred units of stress equals one MPa.

smaller near the exit of the shear plane. Thus the chip velocity on the outside is smaller than the average chip velocity causing the chip to curl.

The stress distributions which would be expected in the chip if each of these three hypotheses are true are indicated in Fig. 14. The bending moment on the chip considered as a beam would result in compressive stresses along the free surface (back) of the chip if hypothesis (i) was true. Crushing of the chip in the secondary shear zone will result in compressive σ_{yy} in the front of the chip, whereas the observed stress is tensile. Only a curved shear plane would result in a stress distribution similar to that given by the finite element analysis, while simultaneously accounting for curl of the chip. It should be noted that though the chip does accelerate (due to secondary shear) as it flows along the rake face of the tool, this is just an accessory to chip curl and not the cause of chip curl.

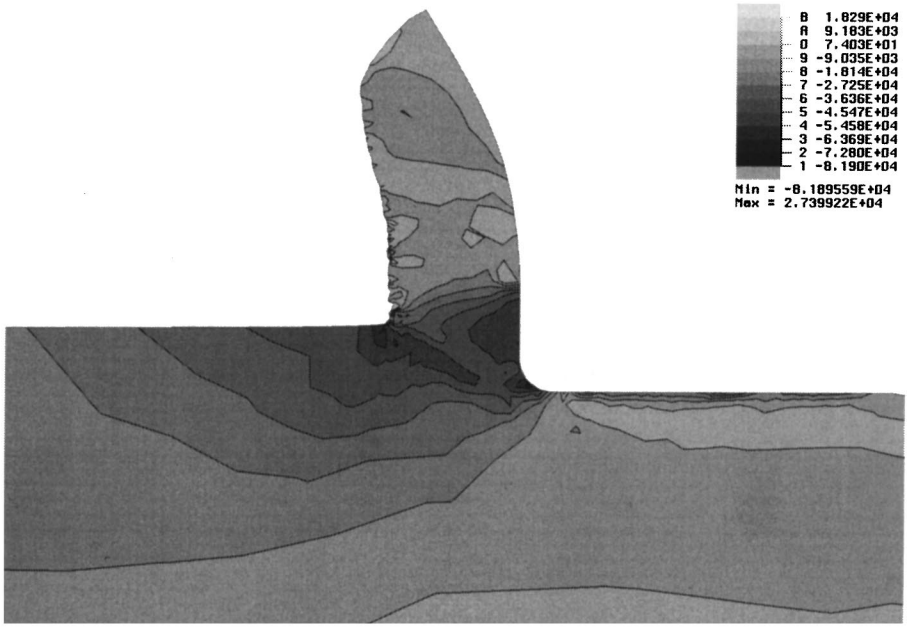

(a) $\mu = 0.2$; Distance cut = 4.34mm

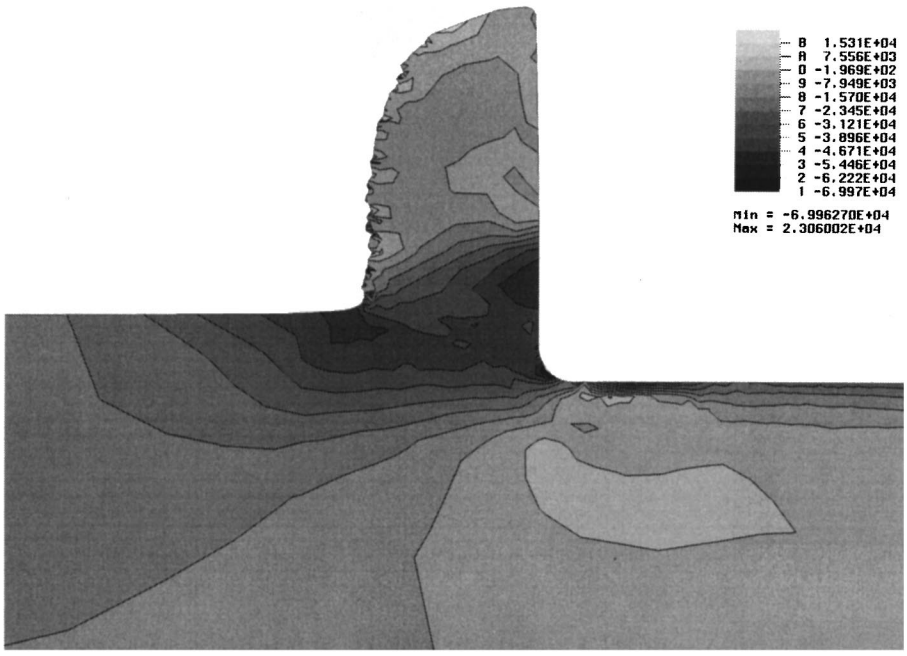

(b) $\mu = 0.8$; Distance cut = 5.14mm

Fig. 10 Steady-state distribution of σ_{xx}. Hundred units of stress equals one MPa.

The reason for the curvature of the shear plane can be found from a detailed analysis of the stress distribution in the zone of plastic deformation. Work in this direction, utilizing finer meshes, is in progress.

5.3 Differences Due to the Two Different Friction Coefficients. The main difference between the stress distributions in the two cases is found in the values of σ_{xy} at the chip-tool interface. For μ=0.2, σ_{xy} is less than 150 MPa (ranges between 30 and 130 MPa) along most of the chip-tool contact length, whereas for μ=0.8 σ_{xy} is nearly constant at 150 MPa, the maximum value allowed by the shear limited Coulomb friction used in the analysis, along the contact length (Fig. 12).

The chip thickness ratio is approximately 2.0 for μ=0.2 while it is 2.5 for μ=0.8. This indicates the trend towards stubby chips for high friction coefficients. The reason for the relatively small change in the chip thickness ratio is the fact that for the case of μ=0.8, the chip-tool interface friction is limited by the shear

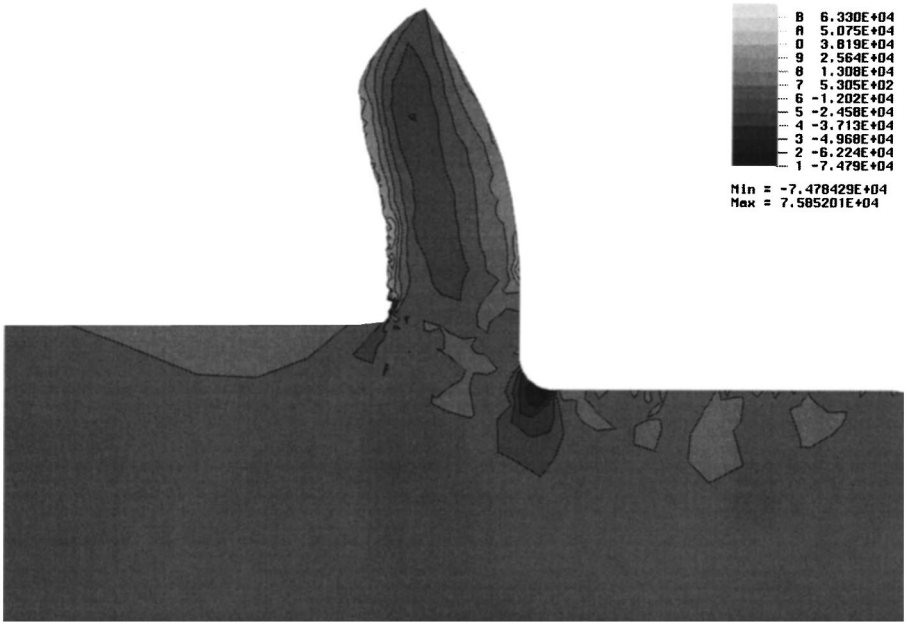

(a) $\mu = 0.2$; Distance cut = 4.34mm

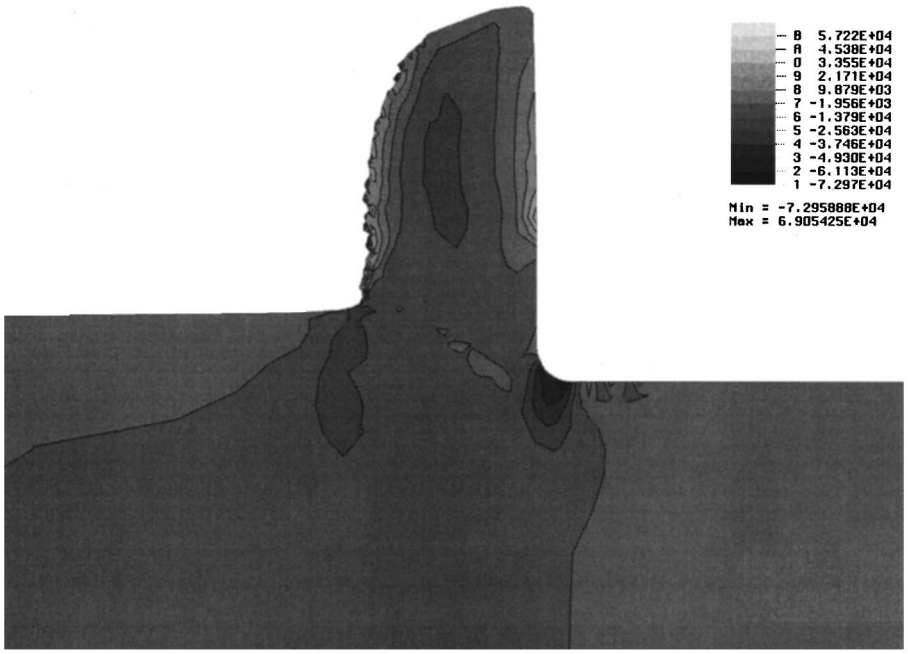

(b) $\mu = 0.8$; Distance cut = 5.14mm

Fig. 11 Steady-state distribution of σ_{yy}. Hundred units of stress equals one MPa.

strength of the interface. The maximum plastic strain is found to occur in the chip for μ=0.2 while the maximum strains are found in the machined surface for μ=0.8. There is a dramatic difference in the chip curl for the two cases. The chip curl is higher for the case of lower friction at the chip tool interface.

The variation in the cutting and thrust force components between different iterations after steady state is reached was quite small for μ=0.2 (<2 percent for the cutting force and <1 percent for the thrust force). The variation in the cutting force for μ=0.8 was higher (up to three percent), while the variation in thrust force was even greater (up to ten percent). The computed stress values are estimated to be correct to within 15 percent of the yield stress of the material. This estimate on the accuracy is determined from the stress values reported at free surfaces, and the values of von Mises stress reported above the maximum possible von Mises stress according to the definition of the work-hardening characteristics of the material. As in all other finite element analysis, errors at boundaries will be minimized if finer meshes are used.

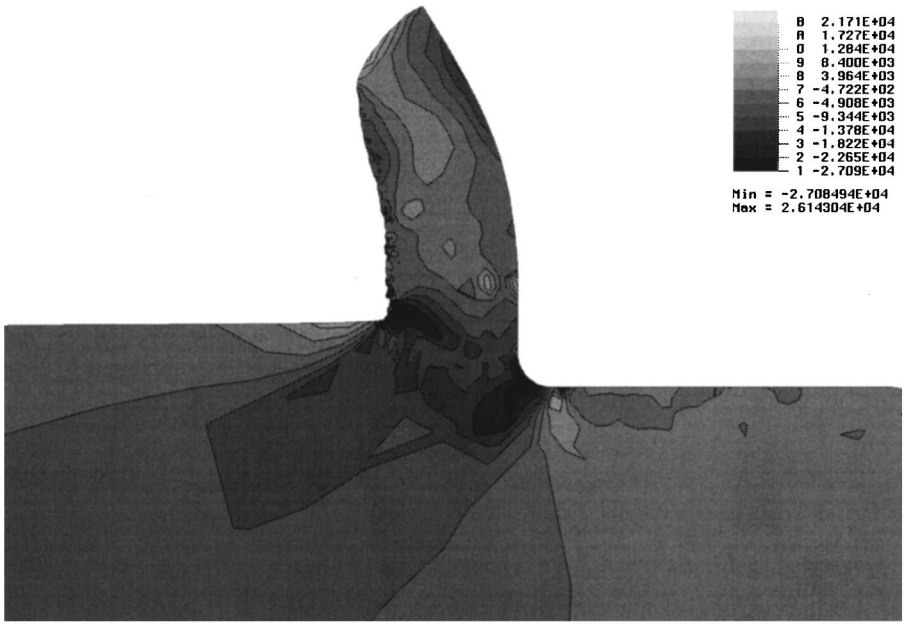

(a) $\mu = 0.2$; Distance cut $= 4.34$mm

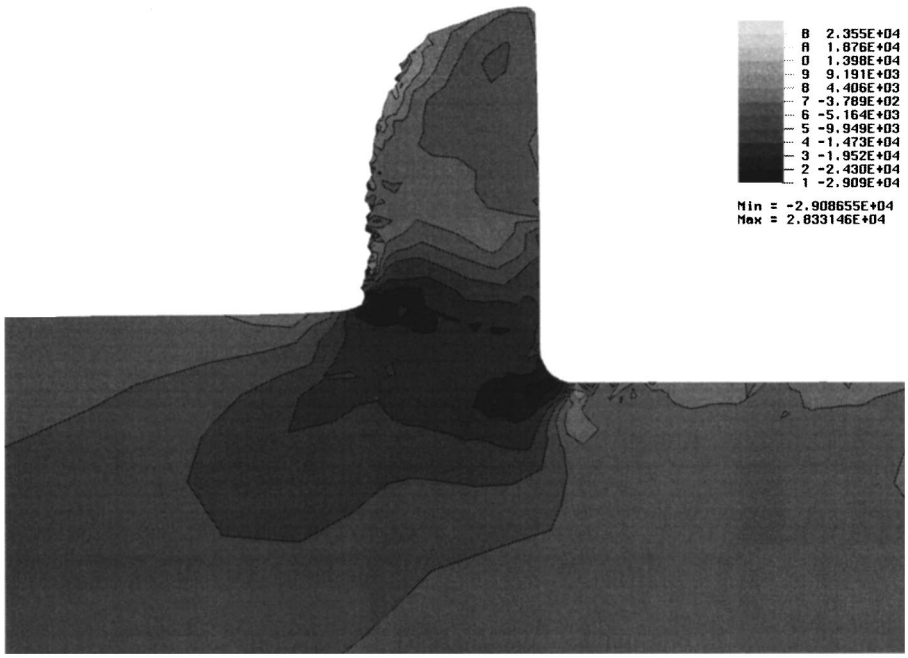

(b) $\mu = 0.8$; Distance cut $= 5.14$mm

Fig. 12 Steady-state distribution of σ_{xy}. Hundred units of stress equals one MPa.

6 Conclusions

It has been demonstrated that machining can be simulated as a special type of wedge indentation using Lagrangian finite element analysis provided that the mesh near the cutting edge is fine enough to represent the stress and strain gradients faithfully. The mesh representing the workpiece should be periodically regenerated in order to preclude solution inaccuracies due to distortion of the mesh.

The principal zones where deformation occurs are in a parallel-sided primary shear zone and a triangular secondary shear zone near the rake face, similar to that postulated by various other researchers. The residual stress in the workpiece, when thermal effects are ignored in the analysis, is found to be compressive. The normal stress on the tool rake face is found to be uniformly high along the rake face except near the end of chip-tool contact where it rapidly decreases to zero. The hydrostatic stress is found to be highly compressive near the cutting edge of the tool. The effects caused by variation of the coefficient of friction have also

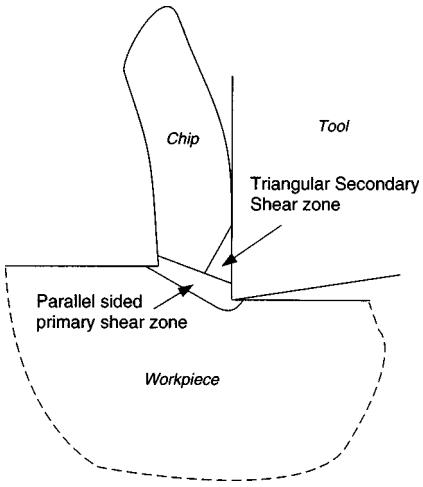

Fig. 13 Schematic representation of the primary and secondary shear zones

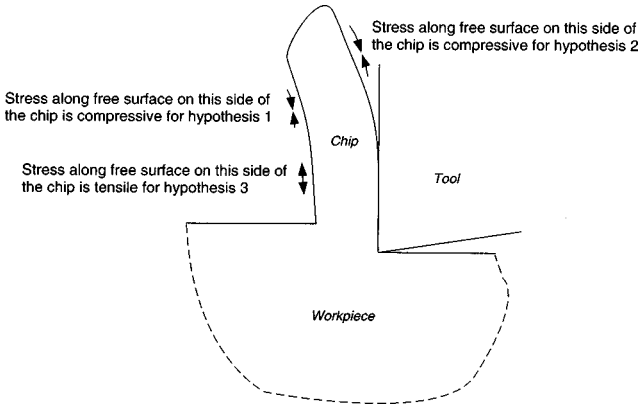

Fig. 14 Schematic representation of stress distributions necessitated by different hypotheses for explaining chip curl

been studied. The results of the simulations are consistent with many observations pertaining to deformation occurring in the chip and the work surface.

Investigations are underway to conduct a wider range of analyses with finer meshes, to better understand the mechanics of the process. Special emphasis will be placed on understanding the reasons for the curvature of the shear plane, which has been shown to be the cause of the curvature of the chip.

Acknowledgments

This work has been supported by NSF grants DDM 9057916 (to S.C.) and CMS 9057082 (to T.N.F). We would like to thank Dr. M. M. Chaudhri of Cambridge University for many insightful comments during the formative phases of the work.

References

[1] Klamecki, B. E., 1973, ''Incipient Chip Formation in Metal Cutting—A Three Dimension Finite Element Analysis,'' Ph.D. thesis, University of Illinois at Urbana-Champaign, Urbana, IL.
[2] Usui, E., and Shirakashi, T., 1982, ''Mechanics of Machining—From Description to Predictive Theory,'' *On the Art of Cutting Metals—75 Years Later*, ASME, New York, pp. 13–35.
[3] Strenkowski, J. S. and Carroll, J. T., 1985, ''A Finite Element Model of Orthogonal Metal Cutting,'' J. Eng. Ind., **109**, pp. 349–353.
[4] Carroll, J. T. and Strenkowski, J. S., 1988, ''Finite Element Models of Orthogonal Cutting With Application to Single Point Diamond Turning,'' Int. J. Mech. Sci., **30**, No. 2, pp. 899–920.
[5] Shih, J. M., Chandrasekar, S., and Yang, T. Y., 1990, ''Finite Element Simulation of Metal Cutting Process With Strain Rate and Temperature Effects,'' *Proc. ASME Symposium on Fundamental Issues in Machining*, ASME, New York, p. 11.
[6] Komvopoulos, K. and Erpenbeck, S. A., 1991, ''Finite Element Modeling of Orthogonal Metal Cutting,'' J. Eng. Ind., **113**, pp. 253–267.
[7] Lin, Z.-C., Chu, K.-T., and Pan, W.-C., 1994, ''Study of the Stress, Strain, and Temperature Distributions of a Machined Workpiece Using a Thermo-Elastic-Plastic Coupled Model,'' J. Mater. Process. Technol., **41**, No. 3, pp. 291–310.
[8] Zhang, B. and Bagchi, A., 1994, ''Finite Element Simulation of Chip Formation and Comparison With Machining Experiment,'' J. Eng. Ind., **116**, No. 3, pp. 289–297.
[9] Ernst, H., 1938, ''Physics of Metal Cutting,'' *Machining of Metals*, Amer. Soc. for Metals, pp. 1–34.
[10] Finnie, I., 1956, ''Review of the Metal-Cutting Analyses of the Past Hundred Years,'' Mech. Eng., **78**, pp. 715–721.
[11] Roth, R. N. and Oxley, P. L. B., 1972, ''A Slip-Line Field Analysis for Orthogonal Machining Based on Experimental Flow Fields,'' J. Mech. Eng. Sci., **14**, pp. 85–97.
[12] Sekhon, G. S. and Chenot, J. L., 1993, ''Numerical Simulation of Continuous Chip Formation During Non-Steady Orthogonal Cutting,'' Eng. Comput., **10**, pp. 31–48.
[13] Marusich, T. D., and Ortiz, M., 1994, ''Finite Element Simulation of High-Speed Machining,'' *Proc. ASME Symposium on Mechanics in Materials Processing and Manufacturing*, ASME, New York, pp. 137–149.
[14] Belak, J. F., and Stowers, I. F., 1990, ''A Molecular Dynamics Model of the Orthogonal Cutting Process,'' *ASPE Annual Conference*, ASPE, Rochester, NY, pp. 259–264.
[15] Inamura, T. and Takezawa, N., 1992, ''Atomic-Scale Cutting in a Computer Using Crystal Models of Copper and Diamond,'' Annu. CIRP, **41**, No. 1, pp. 121–124.
[16] Ikawa, N., Shimada, S., Tanaka, H., and Ohmori, G., 1991, ''An Atomistic Analysis of Nanometric Chip Removal as Affected by Tool-Work Interaction in Diamond Turning,'' Annu. CIRP, **40**, No. 1, pp. 551–554.
[17] Inamura, T., Takezawa, N., and Kumaki, Y., 1993, ''Mechanics and Energy Dissipation in Nanoscale Cutting,'' Annu. CIRP, **42**, No. 1, pp. 79–82.
[18] Shimada, S., Ikawa, N., Tanaka, H., Ohmori, G., and Uchikoshi, J., 1993, ''Feasibility Study on Ultimate Accuracy in Microcutting Using Molecular Dynamics Simulation,'' Annu. CIRP, **42**, No. 1, pp. 91–94.
[19] Rentsch, R. and Inasaki, I., 1995, ''Investigation of Surface Integrity by Molecular Dynamics Simulation,'' Annu. CIRP, **44**, No. 1, pp. 295–298.
[20] Bhattacharyya, A., 1984, *Metal Cutting*, Central Book Publishers, Bombay.
[21] Enahoro, H. E. and Oxley, P. L. B., 1966, ''Flow Along the Chip-Tool Interface in Orthogonal Metal Cutting,'' J. Mech. Eng. Sci., **8**, pp. 36–41.
[22] Chaudhri, M. M., 1993, ''Subsurface Deformation Patterns Around Indentations in Work-Hardened Mild Steel,'' Philos. Mag. Lett., **67**, No. 2, pp. 107–115.
[23] Hill, R., Lee, E. H., and Tupper, S. J., 1947, ''The Theory of Wedge Indentation of Ductile Materials,'' Proc. R. Soc. London, Ser. A, **188**, pp. 273–289.
[24] Hutchings, I. M., 1976, ''Deformation of Metal Surfaces by the Oblique Impact of Square Plates,'' Int. J. Mech. Sci., **19**, pp. 45–52.
[25] Palmer, W. B., and Oxley, P. L. B., 1959, ''Mechanics of Metal Cutting,'' Proc. Inst. Mech. Eng., **173**, pp. 623–638.
[26] Kudo, H., 1965, ''Some New Slip-Line Solutions for Two-Dimensional Steady-State Machining,'' Int. J. Mech. Sci., **7**, pp. 43–55.
[27] Childs, T. H. C. and Rowe, G. W., 1973, ''Physics in Metal Cutting,'' Rep. Prog. Phys., **36**, pp. 223–288.
[28] Tabor, D., 1951, *The Hardness of Metals*, Clarendon Press, Oxford,
[29] Wright, P. K., Horne, J. G., and Tabor, D., 1979, ''Boundary Conditions at the Chip-Tool Interface in Machining: Comparisons Between Seizure and Sliding Friction,'' Wear, **54**, pp. 371–390.

H. C. Chan
Department of Civil and Structural Engineering,
The University of Hong Kong,
Pokfulam Road,
Hong Kong

C. W. Cai
Department of Mechanics,
Zhongshan University,
Guangzhou 510275,
P. R. China

Y. K. Cheung
Department of Civil and Structural Engineering,
The University of Hong Kong,
Pokfulam Road,
Hong Kong

Forced Vibration Analysis for Damped Periodic Systems With One Nonlinear Disorder

The steady-state responses of damped periodic systems with finite or infinite degrees-of-freedom and one nonlinear disorder to harmonic excitation are investigated by using the Lindstedt-Poincare method and the U-transformation technique. The perturbation solutions with zero-order and first-order approximations, which involve a parameter n, i.e., the total number of subsystems, as well as the other structural parameters, are derived. When n approaches infinity, the limiting solutions are applicable to the system with infinite number of subsystems. For the zero-order approximation, there is an attenuation constant which denotes the ratio of amplitudes between any two adjacent subsystems. The attenuation constant is derived in an explicit form and calculated for several values of the damping coefficient and the ratio of the driving frequency to the lower limit of the pass band. [S0021-8936(00)01101-6]

1 Introduction

A detailed review of the dynamics of both linear periodic and disordered periodic structures was given by Li and Benaroya [1]. The studies on the dynamic responses of harmonically excited nonlinear systems can be found in [2] and in references of the book by Vakakis et al. [3]. A geometric theory was proposed to analyze the mode localization and frequency loci veering without reference to any specific systems ([4]). The nonlinear localized modes in a perfectly cyclic periodic system was examined with the averaging method of multiple scales by Vakakis et al. [5]. Forced localization in a periodic chain of nonlinear oscillators was examined by using a ''continuum approximation'' ([6]). The *U*-transformation technique ([7,8]) was applied to analyze the disordered periodic systems with an infinite number of subsystems for localized modes ([9]). Recently, the localized modes of undamped periodic systems with infinite degrees-of-freedom and having one or two nonlinear disorders were investigated ([10]) by using the Lindstedt-Poincare (L-P) method ([11]) and the *U*-transformation technique.

In the present study, the primary resonance of the damped periodic systems with finite or infinite degrees-of-freedom and one nonlinear disorder is investigated by using the L-P method and the *U*-transformation technique. By applying the *U*-transformation to the governing equation, the new governing equation in terms of the generalized displacements takes the standard form where the linear terms are uncoupled. Then by applying the L-P method to the simultaneous equations with the standard form, the zero-order and first-order perturbation solutions can be found in explicit form.

2 Governing Equations and Perturbation Solutions

Consider the system shown in Fig. 1(*a*) which consists of n number of subsystems connected to each other by means of a linear spring having stiffness ϵk_c. Each subsystem is made up of a mass M connected to both a dashpot with a nondimensional damping coefficient $\epsilon\zeta_0$ and a spring with linear stiffness K (for ordered subsystems) or nonlinear stiffness $K+\epsilon\gamma_0 x^2$ (for disordered one), where ϵ is a positive small parameter. In Fig. 1(*a*), s denotes the ordinal number of the disordered subsystem and x_j denotes the longitudinal displacement of the jth mass.

In order to apply the *U*-transformation to uncouple the linear terms of the governing equation, an equivalent system with cyclic periodicity must be created. It is necessary to extend the original system by its symmetrical image and apply the antisymmetric loading on the corresponding extended part as shown in Fig. 1(*b*) in which the first and last ($2n$th) masses are imaginarily jointed by a spring with stiffness ϵk_c. This imaginary spring is not subjected to any load for antisymmetric vibration. If and only if the dynamic response of the extended system is antisymmetric, two extreme end conditions of the original system are satisfied in the extended one, i.e., the extended system is equivalent to the original one. The response of the first half (i.e., substructures $1\sim n$) of the equivalent system is the same as that of the original system.

Applying Newton's second law to every mass in the equivalent system, one can write the differential equations of motion as follows:

$$M\ddot{x}_j+2M\omega_0\epsilon\zeta_0\dot{x}_j+(K+2\epsilon k_c)x_j-\epsilon k_c(x_{j+1}+x_{j-1})=\epsilon F_j \qquad j=1,2,\ldots,2n \tag{2.1}$$

and

$$F_j=F_{j0}\cos\Omega t \quad j\neq s,\ 2n-s+1$$
$$F_j=F_{j0}\cos\Omega t-\gamma_0 x_j^3 \quad j=s,\ 2n-s+1 \tag{2.2}$$

where the superior dot denotes the derivative with respect to the time variable t, ω_0 denotes the natural frequency for the single-ordered subsystem and $x_{2n+1}\equiv x_1$, $x_0\equiv x_{2n}$ due to cyclic periodicity, ϵF_{j0} denotes the amplitude of the harmonic force acting on the jth mass Ω denotes the driving frequency, and $\epsilon\gamma_0$ is the coefficient of the cubic term of the nonlinear stiffness in the disordered subsystem. The external excitation for the equivalent system must satisfy the antisymmetry condition, i.e.,

$$F_{2n-j+1,0}=F_{j,0} \quad j=1,2,\ldots,n \tag{2.3}$$

where $F_{1,0}\sim F_{n,0}$ indicate the real excitation acting on the original system.

If the initial conditions are antisymmetric, then the dynamic displacements are also antisymmetric, i.e.,

Contributed by the Applied Mechanics Division of THE AMERICAN SOCIETY OF MECHANICAL ENGINEERS for publication in the ASME JOURNAL OF APPLIED MECHANICS. Manuscript received by the ASME Applied Mechanics Division, June 10, 1998; final revision, Dec. 28, 1998. Associate Technical Editor: W. K. Liu. Discussion on the paper should be addressed to the Technical Editor, Professor Lewis T. Wheeler, Department of Mechanical Engineering, University of Houston, Houston, TX 77204-4792, and will be accepted until four months after final publication of the paper itself in the ASME JOURNAL OF APPLIED MECHANICS.

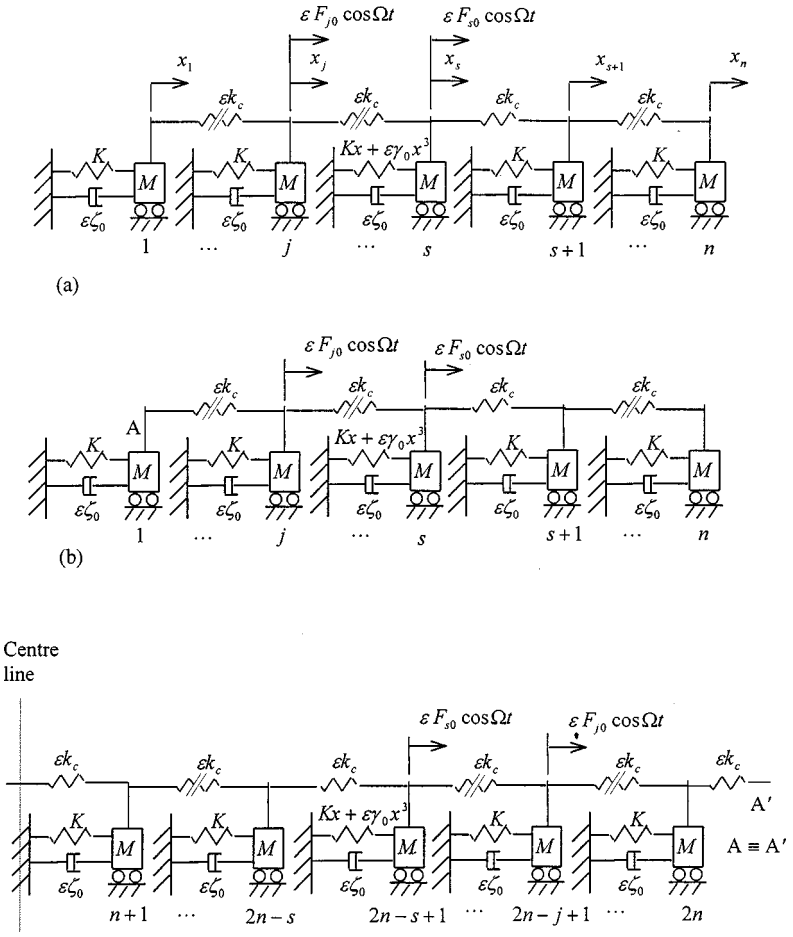

Fig. 1 Damped periodic system with a nonlinear disorder; (*a*) original system with *n* number of subsystems, (*b*) equivalent system with cyclic periodicity and 2*n* number of subsystems

$$x_{2n-j+1}=x_j \quad j=1,2,\ldots,n. \tag{2.4}$$

One can now apply the *U*-transformation to the governing Eq. (2.1). The *U* and inverse *U*-transformations may be expressed as

$$x_j=\frac{1}{\sqrt{2n}}\sum_{m=1}^{2n} e^{i(j-1)m\psi}q_m \quad j=1,2,\ldots,2n \tag{2.5a}$$

and

$$q_m=\frac{1}{\sqrt{2n}}\sum_{j=1}^{2n} e^{-i(j-1)m\psi}x_j \quad m=1,2,\ldots,2n \tag{2.5b}$$

with $\psi=\pi/n$ and $i=\sqrt{-1}$, where $2n$ denotes the total number of subsystems for the equivalent system. Noting that the displacements are always real variables, it can be proved that the generalized displacements $q_m(m=1,2,\ldots,2n)$ have the following property:

$$q_{2n-m}=\overline{q}_m \quad m=1,2,\ldots,2n \tag{2.6}$$

and q_n, q_{2n} must be real variables, in which the superior bar denotes the complex conjugation.

By using the *U*-transformation, i.e., premultiplying both sides of Eq. (2.1) by the operator $1/\sqrt{2n}\Sigma_{j=1}^{2n}e^{-i(j-1)m\psi}$, Eq. (2.1) becomes

$$\ddot{q}_m+2\omega_0\epsilon\zeta_0\dot{q}_m+\omega_m^2 q_m=\frac{\epsilon f_m}{M} \tag{2.7}$$

where

$$f_m=\frac{2e^{i(1/2)m\psi}}{\sqrt{2n}}\left[\left(\sum_{j=1}^{n}\cos\left(j-\frac{1}{2}\right)m\psi F_{j,0}\right)\cos\Omega t - \cos\left(s-\frac{1}{2}\right)m\psi\gamma_0 x_s^3(q_1,q_2,\ldots,q_{2n})\right] \tag{2.8}$$

$$\omega_m^2=\frac{K+2\epsilon k_c(1-\cos m\psi)}{M} \tag{2.9}$$

$\omega_m(m=0,1,2,\ldots,n-1)$ is the $(m+1)$th natural frequency for the undamped periodic system without any disorder. The lower and upper bounds of the passband can be expressed, respectively, as

$$\omega_L=\omega_0=\sqrt{\frac{K}{M}}, \qquad \omega_U=\sqrt{\frac{K+4\epsilon k_c}{M}}=\omega_0\sqrt{1+4\frac{\epsilon k_c}{K}}. \tag{2.10}$$

Introducing the time substitution

$$\Omega t=\tau+\varphi \tag{2.11}$$

into Eq. (2.7) results in

$$q_m''+\nu_m^2 q_m=\epsilon\left(\frac{f_m}{M\Omega^2}-\frac{2\omega_0\zeta_0}{\Omega}q_m'\right) \quad m=1,2,\ldots,2n \tag{2.12}$$

and

$$\nu_m^2=\frac{\omega_m^2}{\Omega^2}=\frac{\omega_0^2}{\Omega^2}+\epsilon\frac{2k_c(1-\cos m\psi)}{M\Omega^2} \tag{2.13}$$

where the prime symbol designates differentiation with respect to the new time variable τ and φ is an unknown phase angle.

Consider now the case of primary resonance, i.e., $\Omega\approx\omega_0$. By letting

$$\frac{\omega_0^2}{\Omega^2}=1+\epsilon\eta_0. \tag{2.14}$$

Equation (2.13) can be written as

$$\nu_m^2=1+\epsilon\eta_m \tag{2.15}$$

where

$$\eta_m=\eta_0+\frac{2k_c(1-\cos m\psi)}{M\Omega^2}. \tag{2.16}$$

Inserting Eq. (2.15) in Eq. (2.12) gives

$$q_m''+q_m=\epsilon G_m \quad m=1,2,\ldots,2n \tag{2.17}$$

in which

$$G_m=\frac{2e^{i(1/2)m\psi}}{M\Omega^2\sqrt{2n}}\left[\left(\sum_{j=1}^{n}\cos\left(j-\frac{1}{2}\right)m\psi F_{j,0}\right)\cos(\tau+\varphi)-\cos\left(s-\frac{1}{2}\right)m\psi\gamma_0 x_s^3(q_1,q_2,\ldots,q_{2n})\right]-\frac{2\omega_0\zeta_0}{\Omega}q_m'-\eta_m q_m. \tag{2.18}$$

According to the perturbation method ([11]), we seek a solution of Eq. (2.17) in the form of a power series in ϵ, not only for $q_m(\tau)$, but also for φ. Hence, let

$$q_m(\tau)=q_{m0}(\tau)+\epsilon q_{m1}(\tau)+\epsilon^2 q_{m2}(\tau)+\cdots \tag{2.19}$$

and

$$\varphi=\varphi_0+\epsilon\varphi_1+\epsilon^2\varphi_2+\cdots. \tag{2.20}$$

Equation (2.19) is equivalent to

$$x_j(\tau)=x_{j0}(\tau)+\epsilon x_{j1}(\tau)+\epsilon^2 x_{j2}(\tau)+\cdots \tag{2.21}$$

with

$$x_{jr}(\tau)=\frac{1}{\sqrt{2n}}\sum_{m=1}^{2n}e^{i(j-1)m\psi}q_{mr} \quad r=0,1,2,\ldots. \tag{2.22}$$

Substituting Eqs. (2.19) and (2.20) into Eqs. (2.17) and (2.18), the coefficients of equal powers of ϵ on both sides of Eq. (2.17) must be equal, i.e.,

$$q_{m0}''+q_{m0}=0 \tag{2.23a}$$

$$q_{m1}''+q_{m1}=\frac{2e^{i(/2)m\psi}}{M\Omega^2\sqrt{2n}}\left[\left(\sum_{j=1}^{n}F_{j0}\cos\left(j-\frac{1}{2}\right)m\psi\right)\cos(\tau+\varphi_0)-\cos\left(s-\frac{1}{2}\right)m\psi\gamma_0 x_{s0}^3\right]-\frac{2\omega_0\zeta_0}{\Omega}q_{m0}'-\eta_m q_{m0} \tag{2.23b}$$

$$q_{m2}''+q_{m2}=\frac{2e^{i(/2)m\psi}}{M\Omega^2\sqrt{2n}}\left[\left(\sum_{j=1}^{n}F_{j0}\cos\left(j-\frac{1}{2}\right)m\psi\right)\times(-\varphi_1\sin(\tau+\varphi_0))-\cos\left(s-\frac{1}{2}\right)m\psi(3\gamma_0 x_{s0}^2 x_{s1})\right]-\frac{2\omega_0\zeta_0}{\Omega}q_{m1}'-\eta_m q_{m1}. \tag{2.23c}$$

.....

The solution of Eq. (2.23*a*) may be expressed as

$$q_{m0}=a_{m0}\cos\tau+b_{m0}\sin\tau \quad m=1,2,\ldots,2n \tag{2.24}$$

with $a_{2n-m,0}=\overline{a}_{m,0}$ and $b_{2n-m,0}=\overline{b}_{m,0}$ due to $q_{2n-m,0}=\overline{q}_{m,0}$, where a_{m0} and b_{m0} $(m=1,2,\ldots,2n)$ are complex constants to be determined.

The physical displacements corresponding to q_{m0} shown in Eq. (2.24) can be obtained from Eq. (2.22) with $r=0$ as

$$x_{j0}=A_{j0}\cos\tau+B_{j0}\sin\tau \quad j=1,2,\ldots,2n \tag{2.25a}$$

where

$$A_{j0}=\frac{1}{\sqrt{2n}}\sum_{m=1}^{2n}e^{i(j-1)m\psi}a_{m0},\qquad B_{j0}=\frac{1}{\sqrt{2n}}\sum_{m=1}^{2n}e^{i(j-1)m\psi}b_{m0}. \tag{2.25b}$$

A_{j0} and B_{j0} are real numbers and $A_{2n-j,0}=A_{j0}$, $B_{2n-j,0}=B_{j0}$, which leads to $x_{2n-j,0}=x_{j,0}$.

Without loss of generality, we can assume that the initial velocity for the disordered subsystem is zero besides the antisymmetry for both initial displacement and velocity, which leads to

$$B_{s0}=0 \tag{2.26}$$

and

$$x_{s0}=A_{s0}\cos\tau. \tag{2.27}$$

In order to prevent secular terms, the coefficients of $\cos\tau$ and $\sin\tau$ on the right side of Eq. (2.23*b*) must be zero. Introducing Eqs. (2.24) and (2.27) into Eq. (2.23*b*), letting the coefficients of $\cos\tau$ and $\sin\tau$ be equal to zero, gives

$$\frac{2e^{i(1/2)m\psi}}{M\Omega^2\sqrt{2n}}\left[\left(\sum_{j=1}^{n}F_{j0}\cos\left(j-\frac{1}{2}\right)m\psi\right)\cos\varphi_0-\cos\left(s-\frac{1}{2}\right)m\psi\frac{3\gamma_0}{4}A_{s0}^3\right]-\frac{2\omega_0\zeta_0}{\Omega}b_{m0}-\eta_m a_{m0}=0 \tag{2.28}$$

$$\frac{2e^{i(1/2)m\psi}}{M\Omega^2\sqrt{2n}}\left[-\left(\sum_{j=1}^{n}F_{j0}\cos\left(j-\frac{1}{2}\right)m\psi\right)\sin\varphi_0\right]+\frac{2\omega_0\zeta_0}{\Omega}a_{m0}-\eta_m b_{m0}=0 \quad m=1,2,\ldots,2n.$$

Consider now a specific loading condition as that there is no excitation acting on each subsystem except the disordered one, i.e.,

$$F_{j0}=0 \quad j\neq s \quad \text{and} \quad j=1,2,\ldots,n \quad F_{s0}\neq 0. \tag{2.29}$$

Introducing Eq. (2.29) into Eq. (2.28), the solution for a_{m0} and b_{m0} of simultaneous Eqs. (2.28) can be expressed as

$$a_{m0}=\frac{1}{2k_c}\frac{2}{\sqrt{2n}}e^{i(1/2)m\psi}\cos\left(s-\frac{1}{2}\right)m\psi\frac{(D+1-\cos m\psi)I_1+CI_2}{(D+1-\cos m\psi)^2+C^2}$$

$$b_{m0}=\frac{1}{2k_c}\frac{2}{\sqrt{2n}}e^{i(1/2)m\psi}\cos\left(s-\frac{1}{2}\right)m\psi\frac{CI_1-(D+1-\cos m\psi)I_2}{(D+1-\cos m\psi)^2+C^2} \tag{2.30}$$

in which

$$I_1=F_{s0}\cos\varphi_0-\frac{3}{4}\gamma_0A_{s0}^3,\quad I_2=F_{s0}\sin\varphi_0 \tag{2.31a}$$

$$C=\frac{M\Omega\omega_0\zeta_0}{k_c}=\frac{\Omega}{\omega_0}\frac{\epsilon\zeta_0}{(\epsilon k_c/K)}$$
$$D=\frac{K-M\Omega^2}{2\epsilon k_c}=\left[1-\left(\frac{\Omega}{\omega_0}\right)^2\right]\Big/\left(2\frac{\epsilon k_c}{K}\right) \tag{2.31b}$$

C and D are two nondimensional parameters. They are dependent on the nondimensional frequency, stiffness, and damping constant, i.e., Ω/ω_0, $\epsilon k_c/K$, and $\epsilon\zeta_0$. In Eq. (2.31*a*), A_{s0} and φ_0 are unknown variables.

Substituting Eq. (2.30) into Eq. (2.25*b*) results in

$$A_{j0}=\frac{1}{2k_c}(\alpha_jI_1+\beta_jI_2)$$
$$B_{j0}=\frac{1}{2k_c}(\beta_jI_1-\alpha_jI_2)\quad j=1,2,\ldots,2n \tag{2.32}$$

where

$$\alpha_j=\frac{1}{2n}\sum_{m=1}^{2n}\left[2\cos\left(j-\frac{1}{2}\right)m\psi\cos\left(s-\frac{1}{2}\right)m\psi\times\frac{D+1-\cos m\psi}{(D+1-\cos m\psi)^2+C^2}\right]$$
$$\beta_j=\frac{1}{2n}\sum_{m=1}^{2n}\left[2\cos\left(j-\frac{1}{2}\right)m\psi\cos\left(s-\frac{1}{2}\right)m\psi\times\frac{C}{(D+1-\cos m\psi)^2+C^2}\right]. \tag{2.33}$$

Consider now the sth set of simultaneous equations in Eq. (2.32). Inserting $j=s$ and Eq. (2.26) in Eq. (2.32) yields

$$I_1=\frac{2k_c\alpha_sA_{s0}}{\alpha_s^2+\beta_s^2},\quad I_2=\frac{2k_c\beta_sA_{s0}}{\alpha_s^2+\beta_s^2}. \tag{2.34}$$

Noting the definitions of I_1 and I_2, shown in Eqs. (2.31*a*) and (2.34), may be rewritten as

$$F_{s0}\cos\varphi_0=\frac{3}{4}\gamma_0A_{s0}^3+\frac{2k_c\alpha_sA_{s0}}{\alpha_s^2+\beta_s^2}$$
$$F_{s0}\sin\varphi_0=\frac{2k_c\beta_sA_{s0}}{\alpha_s^2+\beta_s^2}. \tag{2.35}$$

From the above equation, we can find the phase angle with zero-order approximation as

$$\varphi_0=\tan^{-1}\frac{2k_c\beta_s}{2k_c\alpha_s+\frac{3}{4}\gamma_0A_{s0}^2(\alpha_s^2+\beta_s^2)} \tag{2.36}$$

and the frequency response curve as

$$\left(\frac{F_{s0}}{A_{s0}}\right)^2=\frac{4k_c^2}{\alpha_s^2+\beta_s^2}+\frac{4k_c\alpha_s}{\alpha_s^2+\beta_s^2}\left(\frac{3}{4}\gamma_0A_{s0}^2\right)+\left(\frac{3}{4}\gamma_0A_{s0}^2\right)^2 \tag{2.37}$$

in which α_s and β_s are dependent on Ω. They can be expressed as

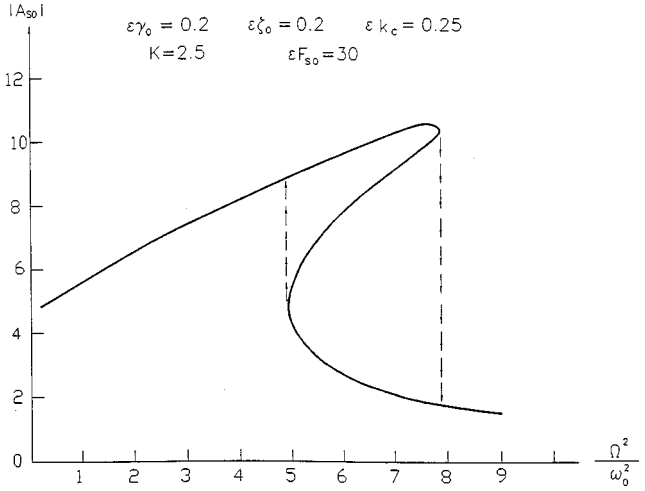

Fig. 2 The frequency response ($|A_{s0}|-\Omega/\omega_0$) curve

$$\alpha_s=\frac{1}{2n}\sum_{m=1}^{2n}2\cos^2\left(s-\frac{1}{2}\right)m\psi\frac{D+1-\cos m\psi}{(D+1-\cos m\psi)^2+C^2}$$
$$\beta_s=\frac{1}{2n}\sum_{m=1}^{2n}2\cos^2\left(s-\frac{1}{2}\right)m\psi\frac{C}{(D+1-\cos m\psi)^2+C^2}, \tag{2.38}$$

where C and D are dependent on Ω/ω_0 besides the structural parameters as shown in Eq. (2.31*b*).

If the parameters of the system and loading are given, the response A_{s0} for the loaded subsystem can be calculated from Eq. (2.37), and the other A_{j0} and B_{j0} can be obtained by substituting Eq. (2.34) into Eq. (2.32) as

$$A_{j0}=\frac{\alpha_j\alpha_s+\beta_j\beta_s}{\alpha_s^2+\beta_s^2}A_{s0}$$
$$B_{j0}=\frac{\beta_j\alpha_s-\alpha_j\beta_s}{\alpha_s^2+\beta_s^2}A_{s0}\quad j=1,2,\ldots,2n. \tag{2.39}$$

The characteristic of the frequency response ($|A_{s0}|-(\Omega/\omega_0)$) curve is similar to that for the single nonlinear subsystem, i.e., the jump phenomenon may occur. For the specific case of $\epsilon\gamma_0=0.2$, $\epsilon\zeta_0=0.2$, $\epsilon k_c=0.25$, $K=2.5$, and $\epsilon F_{s0}=30$ with n approaching infinity, the frequency response curve is as shown in Fig. 2.

Introducing Eqs. (2.27) and (2.24) into Eq. (2.23*b*) and noting the coefficients of $\cos\tau$ and $\sin\tau$ on the right-hand side of Eq. (2.23*b*) vanishing, yields

$$q''_{m1}+q_{m1}=-\frac{2e^{i(1/2)m\psi}}{M\Omega^2\sqrt{2n}}\cos\left(s-\frac{1}{2}\right)m\psi\frac{\gamma_0}{4}A_{s0}^3\cos3\tau. \tag{2.40}$$

The solution for q_{m1} of Eq. (2.40) can be expressed as

$$q_{m1}=a_{m1}\cos\tau+b_{m1}\sin\tau+\frac{\gamma_0A_{s0}^3}{16M\Omega^2\sqrt{2n}}e^{i(1/2)m\psi}\cos\left(s-\frac{1}{2}\right)m\psi\cos3\tau. \tag{2.41}$$

Substituting Eq. (2.41) into Eq. (2.22) with $r=1$ results in

$$x_{j1}=A_{j1}\cos\tau+B_{j1}\sin\tau+\frac{\gamma_0 A_{s0}^3}{16M\Omega^2}\frac{1}{2n}\times\sum_{m=1}^{2n}e^{i(j-1/2)m\psi}\cos\left(s-\frac{1}{2}\right)m\psi\cos 3\tau\quad j=1,2,\ldots,2n \tag{2.42}$$

where

$$A_{j1}=\frac{1}{\sqrt{2n}}\sum_{m=1}^{2n}e^{i(j-1)m\psi}a_{m1},\qquad B_{j1}=\frac{1}{\sqrt{2n}}\sum_{m=1}^{2n}e^{i(j-1)m\psi}b_{m1}. \tag{2.43}$$

Noting the initial velocity vanishing for the nonlinear subsystem and $\Sigma_{m=1}^{2n}\cos^2(s-\frac{1}{2})m\psi\equiv n$, inserting $j=s$ into Eq. (2.42) gives

$$x_{s1}=A_{s1}\cos\tau+\frac{\gamma_0 A_{s0}^3}{32M\Omega^2}\cos 3\tau \tag{2.44}$$

and

$$B_{s1}=\frac{1}{\sqrt{2n}}\sum_{m=1}^{2n}e^{i(s-1)m\psi}b_{m1}=0. \tag{2.45}$$

Substituting Eqs. (2.41), (2.44), and (2.27) into Eq. (2.23*c*), and letting the coefficients of $\cos\tau$ and $\sin\tau$ on the right side of Eq. (2.23*c*), being equal to zero, gives

$$a_{m1}=\frac{1}{2k_c\sqrt{2n}}2e^{i(1/2)m\psi}\cos\left(s-\frac{1}{2}\right)m\psi\times\frac{(D+1-\cos m\psi)I_1^*+CI_2^*}{(D+1-\cos m\psi)^2+C^2}$$
$$b_{m1}=\frac{1}{2k_c\sqrt{2n}}2e^{i(1/2)m\psi}\cos\left(s-\frac{1}{2}\right)m\psi\times\frac{CI_1^*-(D+1-\cos m\psi)I_2^*}{(D+1-\cos m\psi)^2+C^2} \tag{2.46}$$

in which

$$I_1^*=-\varphi_1\sin\varphi_0F_{s0}-\frac{3}{4}\gamma_0A_{s0}^2\left(3A_{s1}+\frac{\gamma_0A_{s0}^3}{32M\Omega^2}\right)$$
$$I_2^*=\varphi_1\cos\varphi_0F_{s0}. \tag{2.47}$$

Introducing Eq. (2.46) into Eq. (2.43) results in

$$A_{j1}=\frac{1}{2k_c}(\alpha_jI_1^*+\beta_jI_2^*)$$
$$B_{j1}=\frac{1}{2k_c}(\beta_jI_1^*-\alpha_jI_2^*) \tag{2.48}$$

in which the definitions of α_j and β_j are as shown in Eq. (2.33)

Recalling Eq. (2.45) and inserting $j=s$ into Eq. (2.48), yields

$$I_1^*=\frac{2k_c\alpha_sA_{s1}}{\alpha_s^2+\beta_s^2},\quad I_2^*=\frac{2k_c\beta_sA_{s1}}{\alpha_s^2+\beta_s^2}. \tag{2.49}$$

Introducing Eq. (2.47) into Eq. (2.49), gives

$$A_{s1}=-\frac{3\gamma_0^2A_{s0}^5}{128M\Omega^2}\Big/\left[\frac{9}{4}\gamma_0A_{s0}^2+\frac{2k_c}{\alpha_s^2+\beta_s^2}(\alpha_s+\beta_s\tan\varphi_0)\right] \tag{2.50a}$$

$$\varphi_1=\frac{2k_c\beta_sA_{s1}}{(\alpha_s^2+\beta_s^2)F_{s0}\cos\varphi_0}=\frac{A_{s1}}{A_{s0}}\tan\varphi_0. \tag{2.50b}$$

Inserting Eq. (2.49) into Eq. (2.48) yields

$$A_{j1}=\frac{\alpha_j\alpha_s+\beta_j\beta_s}{\alpha_s^2+\beta_s^2}A_{s1},\quad B_{j1}=\frac{\beta_j\alpha_s-\alpha_j\beta_s}{\alpha_s^2+\beta_s^2}A_{s1}. \tag{2.51}$$

The forced response with first-order approximation can be obtained by substituting Eqs. (2.25*a*), (2.39), (2.42), and (2.51) into Eq. (2.21), as

$$x_j=\frac{\alpha_j\alpha_s+\beta_j\beta_s}{\alpha_s^2+\beta_s^2}(A_{s0}+\epsilon A_{s1})\cos\tau+\frac{\beta_j\alpha_s-\alpha_j\beta_s}{\alpha_s^2+\beta_s^2}(A_{s0}+\epsilon A_{s1})\sin\tau+\epsilon\frac{\gamma_0A_{s0}^3}{16M\Omega^2}\times\left[\frac{1}{2n}\sum_{m=1}^{2n}\cos\left(j-\frac{1}{2}\right)m\psi\cos\left(s-\frac{1}{2}\right)m\psi\right]\cos 3\tau$$
$$j=1,2,\ldots,2n \tag{2.52}$$

with $\tau=\Omega t-(\varphi_0+\epsilon\varphi_1)$.

Consider now the sum of series in the square brackets as follows:

$$\frac{1}{2n}\sum_{m=1}^{2n}\cos\left(j-\frac{1}{2}\right)m\psi\cos\left(s-\frac{1}{2}\right)m\psi=\frac{1}{4n}\sum_{m=1}^{2n}[\cos(j+s-1)m\psi+\cos(j-s)m\psi]$$
$$=\begin{cases}0 & j\neq s,\quad 2n-s+1\\ \dfrac{1}{2} & j=s,\quad 2n-s+1.\end{cases} \tag{2.53}$$

Introducing the above result into Eq. (2.52), and noting $\alpha_{2n-j+1}=\alpha_j$ and $\beta_{2n-j+1}=\beta_j$ yields

$$x_{2n-j+1}=x_j=\frac{\alpha_j\alpha_s+\beta_j\beta_s}{\alpha_s^2+\beta_s^2}(A_{s0}+\epsilon A_{s1})\cos\tau+\frac{\beta_j\alpha_s-\alpha_j\beta_s}{\alpha_s^2+\beta_s^2}(A_{s0}+\epsilon A_{s1})\sin\tau$$
$$j=1,2,\ldots,n\ \text{ and }\ j\neq s \tag{2.54a}$$

$$x_{2n-s+1}=x_s=(A_{s0}+\varepsilon A_{s1})\cos\tau+\frac{\varepsilon\gamma_0A_{s0}^3}{32M\Omega^2}\cos 3\tau. \tag{2.54b}$$

It is obvious that the forced vibration shown in Eqs. (2.54*a*,*b*) satisfies the antisymmetric condition shown in Eq. (2.4), i.e., the solution $x_j(j=1,2,\ldots,n)$ is applicable to the original system.

In Eq. (2.54*a*), α_j and β_j are dependent on the total number of subsystems besides the parameters C and D. Consider now the periodic system with an infinite number of subsystems. By letting n approach infinity, the limit of the series summation on the right sides of Eq. (2.33) become the definite integral ([7]), respectively, i.e.,

$$\alpha_j=\frac{1}{2\pi}\int_0^{2\pi}2\cos\left(j-\frac{1}{2}\right)\theta\cos\left(s-\frac{1}{2}\right)\theta\times\frac{D+1-\cos\theta}{(D+1-\cos\theta)^2+C^2}d\theta$$
$$=\frac{1}{2\pi}\int_0^{2\pi}[\cos(j+s-1)\theta+\cos(j-s)\theta]\times\frac{D+1-\cos\theta}{(D+1-\cos\theta)^2+C^2}d\theta \tag{2.55a}$$

and

Table 1 Attenuation constant $\xi_1(\xi_2)$ for $\varepsilon k_c/K=0.1$. *a*) The numerical results in the round brackets denote ξ_2; *b*) Case of $\Omega=\omega_L$; *c*) Case of $\Omega=\omega_U$.

$\varepsilon\zeta_0$ / Ω^2/ω_0^2	0.00001	0.00100	0.01000	0.10000	0.20000
0.8	0.2679491920 (0.2679491920)[a]	0.2679450672 (0.2679450672)	0.2675379778 (0.2675379778)	0.2360679775 (0.2360679775)	0.1867233484 (0.1867233484)
0.9	0.3819660094 (0.3819660094)	0.3819475651 (0.3819475651)	0.3801450670 (0.3801450670)	0.2892626024 (0.2892626024)	0.2042325086 (0.2042325086)
1.0[b]	0.9900497512 (0.9900497512)	0.9047621882 (0.9047621882)	0.7270194833 (0.7270194833)	0.3460143392 (0.3460143392)	0.2168453354 (0.2168453354)
1.1	0.9998789013 (0.9998789013)	0.9879630216 (0.9879630216)	0.8864552245 (0.8864552245)	0.3833046482 (0.3833046482)	0.2215530221 (0.2215530221)
1.2	0.9998904637 (0.9998904593)	0.9891055471 (0.9891055471)	0.8964375957 (0.8964375957)	0.3877945824 (0.3877945824)	0.2174286857 (0.2174286857)
1.3	0.9998683525 (0.9998683525)	0.9869214264 (0.9869214264)	0.8772952844 (0.8772952844)	0.3612922949 (0.3612922949)	0.2058395544 (0.2058395544)
1.4[c]	0.9891812677 (0.9891812677)	0.8968356116 (0.8968356116)	0.7066092868 (0.7066092868)	0.3130958493 (0.3130958493)	0.1895643223 (0.1895643223)
1.5	0.3819660082 (0.3819660082)	0.3819352703 (0.3819352703)	0.3789568507 (0.3789568507)	0.2599562179 (0.2599562179)	0.1715728753 (0.1715728753)
1.6	0.2679491916 (0.2679491916)	0.2679409423 (0.2679409423)	0.2671293807 (0.2671293807)	0.2149005549 (0.2149005549)	0.1540711857 (0.1540711857)

a) The numerical results in the round brackets denote ξ_2;

b) Case of $\Omega=\omega_L$;

c) Case of $\Omega=\omega_U$.

$$\beta_j=\frac{1}{2\pi}\int_0^{2\pi}[\cos(j+s-1)\theta+\cos(j-s)\theta]\times\frac{C}{(D+1-\cos\theta)^2+C^2}\,d\theta. \tag{2.55b}$$

Since an infinite periodic system is an idealization, the important question is when a finite structure can be approximated by the infinite idealization. This question was first addressed by Skudrzyk [12,13]. Igusa and Tang [14] later determined a relation between the total number and damping of the substructures and the accuracy of the Riemann integral idealization.

When a finite periodic system is considered, i.e., n is a finite number, α_j and β_j can be expressed exactly as the series forms shown in Eq. (2.33). The series form can be regarded as the rectangular integration formula for the definite integral shown in Eqs. (2.55*a*) and (2.55*b*), where the integration interval $[0, 2\pi]$ is divided into $2n$ subintervals, i.e., each subinterval is ψ. If the integral form is adopted instead of the series form, the error is in agreement with that for rectangular integral formula, i.e., $O(n^{-1})$.

Generally, there are infinite subsystems between the disordered subsystem and the extreme one at infinity, i.e., $(j+s-1)$ is an infinite number. Introducing the Riemann lemma into Eqs. (2.55*a*) and (2.55*b*) yields

$$\alpha_{s+k}=\frac{1}{2\pi}\int_0^{2\pi}\cos k\theta\,\frac{D+1-\cos\theta}{(D+1-\cos\theta)^2+C^2}\,d\theta,\quad k=0,\pm1,\pm2,\ldots \tag{2.56a}$$

$$\beta_{s+k}=\frac{1}{2\pi}\int_0^{2\pi}\cos k\theta\,\frac{C}{(D+1-\cos\theta)^2+C^2}\,d\theta,\quad k=0,\pm1,\pm2,\ldots. \tag{2.56b}$$

The above definite integrals can be expressed in terms of elementary functions, such as

$$\begin{gathered}\alpha_s=(D+1)E_0-E_1,\quad \beta_s=CE_0\\ \alpha_{s-1}=\alpha_{s+1}=[(D+1)^2+C^2]E_0-(D+1)E_1-1\\ \beta_{s-1}=\beta_{s+1}=CE_1\\ \cdots\cdots\end{gathered} \tag{2.57}$$

where

$$\begin{aligned}E_0&\equiv\frac{1}{2\pi}\int_0^{2\pi}\frac{d\theta}{(D+1-\cos\theta)^2+C^2}\\ &=[2(D^2+2D+C^2+\sqrt{[(2+D)^2+C^2](D^2+C^2)})]^{-1/2}\\ &\quad\times\left(\frac{1}{\sqrt{D^2+C^2}}+\frac{1}{\sqrt{(2+D)^2+C^2}}\right)\end{aligned} \tag{2.58a}$$

Table 2 Difference of phase angles $\Delta\theta_1(\Delta\theta_2)$ (degree) for $\varepsilon k_c/K=0.1$. *a*) The numerical results in the round brackets denote $\Delta\theta_2$; *b*) Case of $\Omega=\omega_L$; *c*) Case of $\Omega=\omega_U$.

$\varepsilon\zeta_0$ / Ω^2/ω_0^2	0.00001	0.00100	0.01000	0.10000	0.20000
0.8	0.0029587412	0.2958701883	2.954809549	26.56505118	43.80251522
	(0.0029587414)[a]	(0.2958701883)	(2.954809549)	(26.56505118)	(43.80251522)
0.9	0.0048617080	0.4861451448	4.836423380	36.79497241	53.97312668
	(0.0048617081)	(0.4861451448)	(4.836423380)	(36.79497241)	(53.97312668)
1.0[b]	0.5729530204	5.724792592	17.96423592	51.82729237	65.53019948
	(0.5729530204)	(5.724792592)	(17.96423592)	(51.82729237)	(65.53019948)
1.1	60.00000024	60.00242543	60.23852969	70.47593457	77.80809134
	(60.00000025)	(60.00242543)	(60.23852969)	(70.47593457)	(77.80809139)
1.2	90.00000000	90.00000000	90.00000000	90.00000000	90.00000000
	(90.00000000)	(90.00000000)	(90.00000000)	(90.00000000)	(90.00000000)
1.3	119.9999997	119.9971337	119.7189490	108.6373579	101.3892055
	(119.9999995)	(119.9971337)	(119.7189490)	(108.6373579)	(101.3892055)
1.4[c]	179.3767671	173.7737712	160.4907647	124.7702433	111.4677448
	(179.3767671)	(173.7737712)	(160.4907647)	(124.7702433)	(111.4677448)
1.5	179.9937236	179.3724114	173.7774321	136.9286010	120.0000000
	(179.9937236)	(179.3724114)	(173.7774321)	(136.9286010)	(120.0000000)
1.6	179.9958157	179.5815819	175.8267916	145.2509396	127.0128869
	(179.9958157)	(179.5815819)	(175.8267916)	(145.2509396)	(127.0128869)

a) The numerical results in the round brackets denote $\Delta\theta_2$;

b) Case of $\Omega=\omega_L$;

c) Case of $\Omega=\omega_U$.

$$E_1\equiv\frac{1}{2\pi}\int_0^{2\pi}\frac{\cos\theta d\theta}{(D+1-\cos\theta)^2+C^2}$$
$$=[2(D^2+2D+C^2+\sqrt{[(2+D)^2+C^2](D^2+C^2)})]^{-1/2}$$
$$\times\left(\frac{1}{\sqrt{D^2+C^2}}-\frac{1}{\sqrt{(2+D)^2+C^2}}\right). \tag{2.58b}$$

All of $\alpha_{s\pm k}$ and $\beta_{s\pm k}(k=1,2,\dots)$ can be expressed as the linear combination of E_0 and E_1. Let us investigate the localized property of the forced vibration mode. The periodic response with zero-order approximation shown in Eq. (2.25*a*) can be written as

$$x_j=A_{j0}\cos\tau+B_{j0}\sin\tau=X_j\cos(\tau-\theta_j)\quad j=1,2,\dots,\infty \tag{2.59}$$

where

$$X_j=\sqrt{\frac{\alpha_j^2+\beta_j^2}{\alpha_s^2+\beta_s^2}}A_{s0} \tag{2.60a}$$

$$\theta_j=\tan^{-1}\frac{\beta_j\alpha_s-\alpha_j\beta_s}{\alpha_j\alpha_s+\beta_j\beta_s}. \tag{2.60b}$$

It is clear that

$$X_s=A_{s0}\ \text{ and }\ \theta_s=0. \tag{2.61}$$

Because of $\alpha_{s-j}=\alpha_{s+j}$ and $\beta_{s-j}=\beta_{s+j}$, we have

$$X_{s-j}=X_{s+j}\ \text{ and }\ \theta_{s-j}=\theta_{s+j} \tag{2.62}$$

which indicate the symmetry of the forced vibration about the nonlinear subsystem.

The localized level of the mode is dependent on the attenuation rate of the amplitudes. Let

$$\xi_k\equiv\frac{X_{s+k}}{X_{s+k-1}}=\sqrt{\frac{\alpha_{s+k}^2+\beta_{s+k}^2}{\alpha_{s+k-1}^2+\beta_{s+k-1}^2}}\quad k=1,2,\dots \tag{2.63a}$$

and

$$\Delta\theta_k\equiv\theta_{s+k}-\theta_{s+k-1}\quad k=1,2,\dots. \tag{2.63b}$$

$\Delta\theta_k$ indicates the phase difference between the corresponding displacements in $(s+k)$th and $(s+k-1)$th subsystems. ξ_k and $\Delta\theta_k$ are only dependent on three nondimensional parameters, i.e., Ω/ω_0, $\varepsilon k_c/K$, and $\varepsilon\zeta_0$, and independent from the nonlinear parameter $\varepsilon\gamma_0$. The numerical results are given as shown in Tables 1 and 2.

The accurate numerical results show that

$$\xi\equiv\xi_1=\xi_2=\cdots \tag{2.64a}$$

$$\Delta\theta_1=\Delta\theta_2=\cdots, \tag{2.64b}$$

which are in agreement with those obtained from the linear periodic system.

By using the results shown in Eqs. (2.64*a*) and (2.64*b*), Eq. (2.59) can be written as

$$x_{s-k}=x_{s+k}=\xi^k A_{s0}\cos(\tau-k\Delta\theta_1) \quad k=0,1,2,\ldots . \tag{2.65}$$

$|\xi|$ is always less than one except that $\varepsilon\zeta_0=0$ and Ω lie in the passband as shown in Table 1. The case of $|\xi|=1$ indicates that the corresponding mode is not localized.

Moreover let us consider the forced vibration with first-order approximation. By using the above results, Eqs. (2.54*a*) and (2.54*b*) can be expressed as

$$x_{s-k}=x_{s+k}=\xi^k(A_{s0}+\varepsilon A_{s1})\cos(\tau-k\Delta\theta_1)+\frac{\varepsilon\gamma_0 A_{s0}^3}{32M\Omega^2}\cos 3\tau\,\delta_{k0} \tag{2.66}$$

where $\tau=\Omega t-(\varphi_0+\varepsilon\varphi_1)$ and δ_{k0} denote the Kronecker symbol.

For the zero-order approximation shown in Eq. (2.65), the amplitudes decay exponentially on either side of the nonlinear disorder and for the first-order approximation shown in Eq. (2.66), the same conclusion can be obtained, except for the nonlinear subsystem. From the above property, the forced mode for the considered system looks like the linear one. On the other hand, the frequency response curve for every subsystem has the nonlinear property as shown in Fig. 2.

Finally, let us discuss the results shown in Tables 1 and 2. Table 1 points to the following conclusions: (1) when Ω lies far from the passband, ξ is much less than one and the effect of damping on ξ is very weak; (2) when Ω lies in the passband and $\varepsilon\zeta_0$ is very small, ξ is approximately equal to one but ξ decreases rapidly with increasing $\varepsilon\zeta_0$. From Table 2, one comes to the conclusion that, (3), when $\Omega^2=\omega_0^2(1+(2\varepsilon k_c/K))$, $\Delta\theta_1$ is identically equal to 90°, which can be proved mathematically as follows: Inserting $\Omega^2=\omega_0^2(1+(2\varepsilon k_c/K))$ into Eqs. (2.31*b*) and (2.58*a*), yields $D=-1$ and $E_1=0$, leading to $\alpha_s=0$ and $\beta_{s+1}=0$, then introducing these results into Eq. (2.60*b*) gives $\Delta\theta_1\equiv\theta_{s+1}=90°$, which is independent of the damping; (4) when $\Omega^2<\omega_0^2(1+(2\varepsilon k_c/K))$, $\Delta\theta_1$ increases with increasing $\varepsilon\zeta_0$; and when $\Omega^2>\omega_0^2(1+(2\varepsilon k_c/K))$, $\Delta\theta_1$ decreases with increasing $\varepsilon\zeta_0$.

3 Conclusions

The primary resonance of the damped periodic systems with an arbitrary number of subsystems and one nonlinear disorder has been analyzed by using the *L-P* method. Applying the *U*-transformation to the governing equation beforehand leads to the standard form of simultaneous differential equations. The perturbation solutions with zero-order and first-order approximations have been derived. The solutions include explicitly the total number of subsystems as well as the other structural parameters. The total number of subsystems, i.e., *n*, may be finite or infinite. By letting *n* approach infinity, the limit of a solution is applicable to a system with an infinite number of subsystems. It is interesting to note that the expression of the limiting solution is simpler than that for the system with a finite number of subsystems.

The system considered possesses the properties of both the nonlinear and linear systems, i.e., there are jump phenomena in the nonlinear system and the wave propagation constant in the linear periodic system, which may be expressed as $\ln\xi-i\Delta\theta_1$.

The effect of the damping and driving frequency on the wave propagation constant has been examined numerically. It may be concluded that the effect is similar to that of a perfect periodic system.

References

[1] Li, D., and Benaroya, H., 1992, ''Dynamics of Periodic and Near-Periodic Structures,'' ASME Appl. Mech. Rev., **45**, pp. 447–459.

[2] Nayfeh, A. H., and Mook, D. T., 1984, *Nonlinear Oscillations*, Wiley, New York.

[3] Vakakis, A. F., Manvetich, L. I., Mikhlin, Y. V., Pilipchuk, V. N. and Zevin, A. A., 1996, *Normal Modes and Localization in Nonlinear Systems*, Wiley, New York.

[4] Liu, J. K., Zhao, L. C., and Fang, T., 1995, ''A Geometric Theory in Investigation on Mode Localization and Frequency Loci Veering Phenomena,'' ACTA Mech. Solida Sinica, **8**, pp. 349–355.

[5] Vakakis, A. F., Nayfeh, T. A., and King, M. E., 1993, ''A Multiple-Scales Analysis of Nonlinear Localized Modes in a Cyclic Periodic System,'' ASME J. Appl. Mech., **60**, pp. 388–397.

[6] Vakakis, A. F., King, M. E., and Pearlstein, A. J., 1994, ''Forced Localization in a Periodic Chain of Nonlinear Oscillators,'' Int. J. Non-Linear Mech., **29**, pp. 429–447.

[7] Cai, C. W., Cheung, Y. K., and Chan, H. C., 1988, ''Dynamic Response of Infinite Continuous Beams Subjected to a Moving Force—An Exact Method,'' J. Sound Vib., **123**, pp. 461–472.

[8] Cai, C. W., Cheung, Y. K., and Chan, H. C., 1990, ''Uncoupling of Dynamic Equations for Periodic Structures,'' J. Sound Vib., **139**, pp. 253–263.

[9] Cai, C. W., Cheung, Y. K., and Chan, H. C., 1995, ''Mode Localization Phenomena in Nearly Periodic Systems,'' ASME J. Appl. Mech., **62**, pp. 141–149.

[10] Cai, C. W., Chan, H. C., and Cheung, Y. K., 1997, ''Localized Modes in Periodic Systems With Nonlinear Disorders,'' ASME J. Appl. Mech., **64**, pp. 940–945.

[11] Meirovitch, L., 1975, *Elements of Vibration Analysis*, McGraw-Hill, New York.

[12] Skudrzyk, E. J., 1968, *Simple and Complex Vibratory Systems*, Pennsylvania State University Press, University Park, PA.

[13] Skudzryk, E. J., 1980, ''The Mean Value Method of Predicting the Dynamic Response of Complex Vibrators,'' J. Acoust. Soc. Am., **67**, pp. 1105–1135.

[14] Igusa, T., and Tang, Y., 1992, ''Mobilities of Periodic Structures in Terms of Asympotic Modal Properties,'' AIAA J., **30**, pp. 2520–2525.

Equilibrium Solutions and Existence for Traveling, Arbitrarily Sagged Elastic Cables

A. C. J. Luo[1]
Assistant Professor,
Department of Mechanical and
Industrial Engineering,
Southern Illinois University,
Edwardsville, IL 62034-1805
Mem. ASME

C. D. Mote, Jr.
Glen L. Martin Professor of Engineering,
Office of the President,
Main Administration Building,
University of Maryland,
College Park, MD 20742
Honorary Mem. ASME

The exact, closed-form, three-dimensional solutions for the steady motion of traveling, sagged, elastic cables under arbitrarily distributed and concentrated loading are developed in this paper. Three components of displacement describing two equilibrium states of an extensible traveling elastic cable are derived. These exact solutions apply to straight and sagged cables traveling under their own weight and uniformly distributed loading. The exact solutions are also used to investigate the steady motion of three-dimensional traveling cables under the uniformly distributed and concentrated loading. Traveling elastic cables with large sag can be modeled approximately through the inextensible cable model when both the loading and the translation speed are very small. A slightly sagged cable must be modeled as extensible, rather than inextensible, even though both the loading and transport speed are very small. These solutions can be applied to multispan cable structures. [S0021-8936(00)02601-5]

1 Introduction

The equilibrium configuration, tension, and displacement of elastic cables under arbitrary loading are needed in the design of cable structures. Rohrs [1] first modeled the vibration of a uniform, inextensible suspended chain hanging freely under its own weight and obtained the approximate natural frequencies and responses of the cable. Routh [2] considered the symmetric transverse vibration of a heterogeneous chain hanging in the form of a cycloid, and application of this chain model to the uniform chain yielded the Rohrs model when the sag ratio is small. The chain was still modeled as inextensible. Pugsley [3] developed a semiempirical theory for the in-plane natural frequencies of the first three modes of a uniform, inextensible suspended chain. Saxon and Cahn [4] developed an asymptotic method for the natural frequencies of the chain for large sag to span ratios. Simpson [5] investigated the in-plane vibration of a stretched cable through its equilibrium and also determined the natural frequencies of multispan, sagged transmission lines using the transfer matrix method. Irvine and Caughey [6] used a similar approach to investigate the free vibrations of a sagged, stretched cable hanging under its own weight. Hagedorn and Schafer [7] showed that geometrical nonlinearity is significant in the computation of natural frequencies of in-plane vibration of an elastic cable. Luongo et al. [8] analyzed the planar, nonlinear free vibrations of sagged cables through a perturbation method. Perkins [9] considered the three-dimensional nonlinear vibrations of elastic, sagged cables analytically and experimentally, and gave a brief review of recent developments in cable dynamics. For translating cables, Simpson [10] investigated planar oscillations through the linearized equations of motion around the equilibrium. Triantafyllou [11] used an alternative approach to derive the linearized equations of motion at the equilibrium. Perkins and Mote [12,13] developed a three-dimensional cable theory for traveling elastic cables. The natural modes for the vibration and stability of translating cable at equilibria were obtained from the eigensolutions of discretized continuum models, and also some experimental results were reported.

The nonstraight equilibria have been determined by approximate means. For stationary cables/strings, Dickey [14] investigated a nonlinear string under a vertical force and gave tensile and compressive equilibrium solutions. Antman [15] extended the Dickey investigation and investigated comprehensively the existence, multiplicity, and qualitative behavior of equilibrium for nonlinear elastic strings under different loads, and the translating, sagged string possesses two nontrivial equilibrium states because of centrifugal loading. O'Reilly and Varadi [16] investigated the equilibria of translating elastic cables. In 1996 O'Reilly showed that if one used an observation due to Routh [2] for inextensible strings, then the work of Antman [15] and Dickey [14] on static equilibria for strings can be extended to examine the steady motions of these strings. Healey and Papadopoulos [17] extended the inextensible cable results to all the elastic strings. O'Reilly [18] obtained the steady motion and stability of elastic and inextensible strings, and it was also shown that multiple steady motions were possible. In the quantitative investigation of elastic cables, Irvine [19] used the method of Dickey [14] to determine the exact equilibrium configuration and the approximate displacements of two-dimensional cables under positive tension. For a single concentrated vertical load, the predicted displacement is constrained by the assumption that the equilibrium configuration is parabolic and that the ends of the cable are fixed. For multiple concentrated masses, the solutions given by Irvine [19] require specificity of the initial configuration. To overcome these limitations, Yu et al. [20] followed Irvine's procedure and computed the tension and equilibrium configuration in three dimensions under uniform and concentrated transverse loading. The aforementioned exact solutions describe the equilibrium but not the response because the initial configuration is not known.

The exact closed-form solution for the steady-state motion of a traveling, arbitrarily sagged elastic cable will be derived under distributed and concentrated static loading in this paper. The closed-form solutions under the uniformly distributed and concentrated loading will be formulated, and discontinuity in tension and equilibrium configuration caused by concentrated forces will be discussed as well.

2 Modeling

2.1 Equation of Motion. Consider a traveling, sagged elastic cable passing through two eyelets, as illustrated in Fig. 1. The

[1]To whom correspondence should be addressed.

Contributed by the Applied Mechanics Division of THE AMERICAN SOCIETY OF MECHANICAL ENGINEERS for publication in the ASME JOURNAL OF APPLIED MECHANICS. Manuscript received by the ASME Applied Mechanics Division, Oct. 16, 1998; final revision, Aug. 10, 1999. Associate Technical Editor: N. C. Perkins. Discussion on the paper should be addressed to the Technical Editor, Professor Lewis T. Wheeler, Department of Mechanical Engineering, University of Houston, Houston, TX 77204-4792, and will be accepted until four months after final publication of the paper itself in the ASME JOURNAL OF APPLIED MECHANICS.

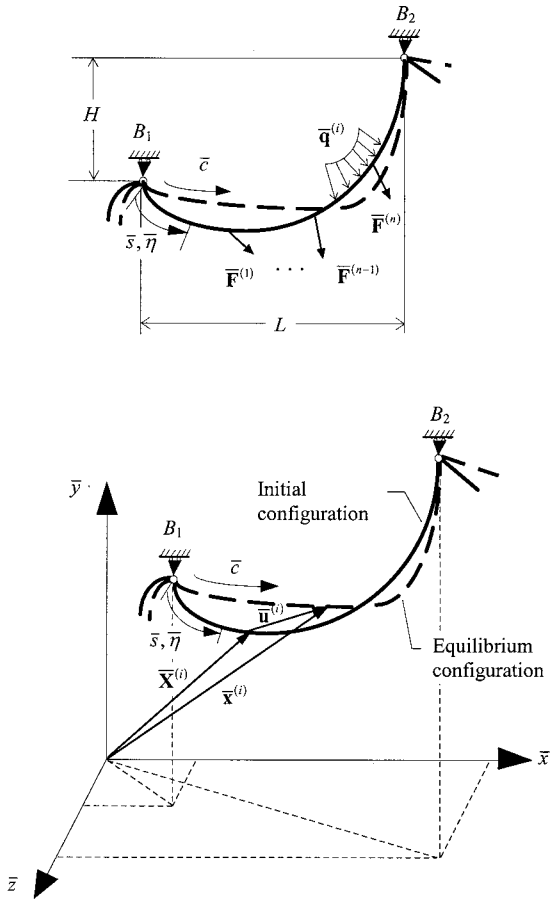

Fig. 1 Equilibrium and deformation of a traveling sagged cable under arbitrary loading

horizontal and vertical separations of the eyelets are L and H, respectively, and the length of cable is S. This cable travels at a constant speed $\bar{c}$. $\bar{x}$, $\bar{y}$, and $\bar{z}$ are fixed rectangular Cartesian coordinates; $\bar{y}$ is colinear with gravitational acceleration. The fixed end points B_1 and B_2 are positioned arbitrarily. $\bar{\mathbf{q}}^{(i)}=\{\bar{q}_x^{(i)},\bar{q}_y^{(i)},\bar{q}_z^{(i)}\}=\{\bar{q}_k^{(i)}\}$ and $\bar{\mathbf{F}}^{(i)}=\{\bar{F}_x^{(i)},\bar{F}_y^{(i)},\bar{F}_z^{(i)}\}=\{\bar{F}_k^{(i)}\}$ for the ith segment are distributed and concentrated forces on the cable, and $\bar{\mathbf{u}}^{(i)}=\{\bar{u}^{(i)},\bar{v}^{(i)},\bar{w}^{(i)}\}=\{\bar{u}_k^{(i)}\}$ is the displacement from the initial configuration $\bar{\mathbf{X}}^{(i)}=\{\bar{X}^{(i)},\bar{Y}^{(i)},\bar{Z}^{(i)}\}=\{\bar{X}_k^{(i)}\}$ to equilibrium $\bar{\mathbf{x}}^{(i)}=\{\bar{x}^{(i)},\bar{y}^{(i)},\bar{z}^{(i)}\}=\{\bar{x}_k^{(i)}\}$. $\sqrt{\bar{X}_{k,s}^{(i)}\bar{X}_{k,s}^{(i)}}=1$ and $\bar{u}_k^{(i)}=\bar{x}_k^{(i)}-\bar{X}_k^{(i)}$. For straight cables, $\bar{s}=\bar{X}_1^{(i)}(\bar{s})$ and $\bar{X}_2^{(i)}=\bar{X}_3^{(i)}=0$. The strain of equilibrium under initial tension $\bar{T}_0$ is

$$\varepsilon^{(i)}=\varepsilon_0^{(i)}+[\sqrt{(\bar{X}_{j,s}^{(i)}+\bar{u}_{j,s}^{(i)})(\bar{X}_{j,s}^{(i)}+\bar{u}_{j,s}^{(i)})}-1],\quad(\text{summation on } j) \tag{1}$$

where $(\cdot)_{,\bar{s}}=\partial(\cdot)/\partial\bar{s}$, $\varepsilon_0^{(i)}=\bar{T}_0/EA$, and E, A, and $\bar{s}$ are Young's modulus, the cross-sectional area, and the arc length of the cable in the initial configuration. For inextensible cables ($EA\to\infty$), $\varepsilon^{(i)}=0$ because $\sqrt{X_{k,s}^{(i)}X_{k,s}^{(i)}}=1$ and $\bar{u}_k^{(i)}=0$, $\{\bar{X}_k^{(i)}\}$ depends on the external loading except the initial tension. The tension in the cable at equilibrium is

$$\bar{T}^{(i)}(\bar{s})=\bar{T}_0+EA[\sqrt{(\bar{X}_{j,s}^{(i)}+\bar{U}_{j,s}^{(i)})(\bar{X}_{j,s}^{(i)}+\bar{u}_{j,s}^{(i)})}-1]. \tag{2}$$

For the sake of general solutions, the nondimensionalizations

$$\left.\begin{aligned}
&s=\frac{\bar{s}}{S},x_k^{(i)}=\frac{\bar{x}_k^{(i)}}{S},X_k^{(i)}=\frac{\bar{X}_k^{(i)}}{S},u_k^{(i)}=\frac{\bar{u}_k^{(i)}}{S},q_k^{(i)}=\frac{\bar{q}_k^{(i)}}{\rho Ag},\\
&F_k^{(i)}=\frac{\bar{F}_k^{(i)}}{\rho AgS},t=\frac{c_q\bar{t}}{S},\\
&c_p=\frac{1}{c_q}\sqrt{\frac{E}{\rho}},c_0=\frac{1}{c_q}\sqrt{\frac{\bar{T}_0}{\rho A}},\\
&c=\frac{\bar{c}}{c_q},c_q=\sqrt{gS},T^{(i)}=\frac{\bar{T}^{(i)}}{\rho AgS},T_0^{(i)}=\frac{\bar{T}_0^{(i)}}{\rho AgS};
\end{aligned}\right\} \tag{3}$$

are introduced. The material is linear elastic, and the exact nonlinear strain is modeled. Hence, as in Luo et al. [21], the equations of motion for a cable segment $[s_{i-1},s_i]$ between concentrated forces $\mathbf{F}^{(i-1)}$ and $\mathbf{F}^{(i)}$ $(i=1,...,n,n+1)$, are obtained through force balances of the deformed cable, and when the geometrical relations are used, the equations of motion become

$$(X_k^{(i)}+u_k^{(i)})_{,tt}=q_k^{(i)}+\left\{\frac{c_0^2+c_p^2[\sqrt{(X_{j,s}^{(i)}+u_{j,s}^{(i)})(X_{j,s}^{(i)}+u_{j,s}^{(i)})}-1]}{\sqrt{(X_{j,s}^{(i)}+u_{j,s}^{(i)})(X_{j,s}^{(i)}+u_{j,s}^{(i)})}}(X_{k,s}^{(i)}+u_{k,s}^{(i)})\right\}_{,s}. \tag{4}$$

The reactions at ends $B_1(s_0=s_{B_1}=0)$ and $B_2(s_{n+1}=s_{B_2}=1)$ are $\mathbf{F}^{(0)}$ and $\mathbf{F}^{(n+1)}$. For traveling cables, the variable η is used as a fixed coordinate system and s as a traveling coordinate system. Therefore, transformation of s to η

$$\eta=s+ct, \tag{5}$$

results in equations of motion for segment $[\eta_{i-1},\eta_i]$ mapped from $[s_{i-1},s_i]$

$$\rho u_{k,tt}^{(i)}+2cu_{k,\eta t}^{(i)}+c^2(X_{k,\eta\eta}^{(i)}+u_{k,\eta\eta}^{(i)})=q_k^{(i)}+\left\{\left[c_p^2+\frac{c_0^2-c_p^2}{\sqrt{(X_{j,\eta}^{(i)}+u_{j,\eta}^{(i)})(X_{j,\eta}^{(i)}+u_{j,\eta}^{(i)})}}\right](X_{k,\eta}^{(i)}+u_{k,\eta}^{(i)})\right\}. \tag{6}$$

When $s=X_1^{(i)}=x$ and $X_2^{(i)}=X_3^{(i)}=0$, Eq. (6) reduces to the two-dimensional straight cable model. The boundary conditions for the equilibrium displacement and initial configuration are

$$u_k^{(0)}|_{\eta=0}=a_k,u_k^{(n+1)}|_{\eta=1}=b_k\ \text{ and }\ X_k^{(0)}|_{\eta=0}=A_k,X_k^{(n+1)}|_{\eta=1}=B_k. \tag{7}$$

From (7) the ratio of the chord to arc length of the cable at initial configuration is determined through the nondimensionalized variable $x_B=\sqrt{(A_k-B_k)(A_k-B_k)}$. Continuity requires

$$u_k^{(i)}|_{\eta=\eta_i}=u_k^{(i+1)}|_{\eta=\eta_i}\ \text{ and }\ X_k^{(i)}|_{\eta=\eta_i}=X_k^{(i+1)}|_{\eta=\eta_i}. \tag{8}$$

2.2 Equilibrium

2.2.1 Existence. With vanishing of the time variations in (6), integration over $[\eta_{i-1},\eta_i]$ gives

$$\left[\frac{c_0^2-c_p^2}{\sqrt{(X_{j,\eta}^{(i)}+u_{j,\eta}^{(i)})(X_{j,\eta}^{(i)}+u_{j,\eta}^{(i)})}}+(c_p^2-c^2)\right](X_{k,\eta}^{(i)}+u_{k,\eta}^{(i)})=-\int q_k^{(i)}d\eta+c_k^{(i)}, \tag{9}$$

where $c_k^{(i)}(k=1,2,3)$ are integration constants. With the tension (2), (9) reduces to the model of Yu et al. [20] when $q_1^{(i)}=c=0$ and $q_k^{(i)}(k\neq1)$ are uniformly distributed. The Irvine two-dimensional model is also a special case of (9) obtained by $q_1^{(i)}=q_3^{(i)}=c=0$.

The squaring of both sides of (9) for each k and summing of them for all k leads to

$$\sqrt{(X^{(i)}_{j,\eta}+u^{(i)}_{j,\eta})(X^{(i)}_{j,\eta}+u^{(i)}_{j,\eta})}=\frac{1}{c_p^2-c^2}\left[(c_p^2-c_0^2)\pm\sqrt{\left(\int q^{(i)}_j d\eta-c^{(i)}_j\right)\left(\int q^{(i)}_j d\eta-c^{(i)}_j\right)}\right]. \quad (10)$$

The translating cable in (10) possesses two equilibria. When the translation speed equals the wave speed (i.e., $c=\sqrt{E/\rho}$), resonance occurs and the stretch ratio $\sqrt{(X^{(i)}_{j,\eta}+u^{(i)}_{j,\eta})(X^{(i)}_{j,\eta}+u^{(i)}_{j,\eta})}$ becomes infinite. In (10) the stretch ratio increases with increasing c for $c<c_p$.

The substitution of (10) into (2) with (3) leads to

$$T^{(i)}=\frac{1}{c_p^2-c^2}\left[c^2(c_p^2-c_0^2)\pm c_p^2\sqrt{\left(\int q^{(i)}_j d\eta-c^{(i)}_j\right)\left(\int q^{(i)}_j d\eta-c^{(i)}_j\right)}\right] \quad (11)$$

showing that the tension increases monotonically with c for $c<c_p$. For stationary cables, setting $c=0$ in (11) and choosing $T^{(i)}>0$ for all the segments gives

$$T^{(i)}=\sqrt{\left(\int q^{(i)}_j d\eta-c^{(i)}_j\right)\left(\int q^{(i)}_j d\eta-c^{(i)}_j\right)}. \quad (12)$$

In the inextensible cable, $\sqrt{(X^{(i)}_{k,\eta}+u^{(i)}_{k,\eta})(X^{(i)}_{k,\eta}+u^{(i)}_{k,\eta})}=1$ (or $u^{(i)}_k=0$), the stiffness in (9) becomes $(T_0-\rho Ac^2)$ identical to Routh [2], and the tension is

$$T^{(i)}=c^2\pm\sqrt{\left(\int q^{(i)}_j d\eta-c^{(i)}_j\right)\left(\int q^{(i)}_j d\eta-c^{(i)}_j\right)}. \quad (13)$$

Cable/string models require positive tension, i.e., $T^{(i)}>0$. Therefore, a condition of existence of steady motion from (11) is

$$c_0^2<c_p^2\left[1\pm\frac{1}{c^2}\sqrt{\left(\int q^{(i)}_j d\eta-c^{(i)}_j\right)\left(\int q^{(i)}_j d\eta-c^{(i)}_j\right)}\right]. \quad (14)$$

A critical condition for the existence of steady motion is obtained at $T^{(i)}=0$ or equality in (14).

2.2.2 Displacement. Substitution of (10) into (9) and integration gives three components of displacement

$$u^{(i)}_k=d^{(i)}_k-X^{(i)}_k\int\left\{\frac{-\int q^{(i)}_k d\eta+c^{(i)}_k}{(c_p^2-c^2)}\times\left[1\pm\frac{c_p^2-c_0^2}{\sqrt{(\int q^{(i)}_j d\eta-c^{(i)}_j)(\int q^{(i)}_j d\eta-c^{(i)}_j)}}\right]\right\}d\eta, \quad (15)$$

where $d^{(i)}_k (k=1,2,3)$ are constants. The boundary conditions (7), displacement continuity (8), and force balances at each $\mathbf{F}^{(i)}$ are used to determine all coefficients in (9) and (15). The force balances are

$$\left(-\int q^{(i)}_k d\eta+c^{(i)}_k\right)\Big|_{\eta=\eta_i}-F^{(i)}_k=\left(-\int q^{(i+1)}_k d\eta+c^{(i+1)}_k\right)\Big|_{\eta=\eta_i}. \quad (16)$$

The inextensible cable requires $c_p\to\infty$, and (10) gives $\sqrt{X^{(i)}_{k,\eta}X^{(i)}_{k,\eta}}=1$ indicating $u^{(i)}_k=0$. Substitution of the c_p and $u^{(i)}_k$ into (15) gives the equilibrium configuration $\hat{X}^{(i)}_k$.

$$\hat{X}^{(i)}_k=\pm\int\left[\frac{-\int q^{(i)}_k d\eta+\hat{c}^{(i)}_k}{\sqrt{(\int q^{(i)}_j d\eta-\hat{c}^{(i)}_j)(\int q^{(i)}_j d\eta-\hat{c}^{(i)}_j)}}\right]d\eta+\hat{d}^{(i)}_k. \quad (17)$$

Similarly, $\hat{c}^{(i)}_k$ and $\hat{d}^{(i)}_k$ can be determined. Equation (16) and (17) show that $\hat{X}^{(i)}_k$ is independent of the initial tension. For the inextensible and elastic cables under the same loading, it is assumed that the two cables possess the same initial configuration. For the inextensible cable, its displacement is zero (i.e., $u^{(i)}_k=0$), which implies that the equilibrium of the inextensible cable is the initial configuration (i.e., $X^{(i)}_k(\eta)=\hat{X}^{(i)}_k(\eta)$. Therefore from (15) and (17) the displacement of the elastic cable is

$$u^{(i)}_k=\int\left\{\frac{-\int q^{(i)}_k d\eta+c^{(i)}_k}{(c_p^2-c^2)}\times\left[1\pm\frac{c_p^2-c_0^2}{\sqrt{(\int q^{(i)}_j d\eta-c^{(i)}_j)(\int q^{(i)}_j d\eta-c^{(i)}_j)}}\right]\right\}d\eta+d^{(i)}_k \mp\int\left[\frac{-\int q^{(i)}_k d\eta+\hat{c}^{(i)}_k}{\sqrt{(\int q^{(i)}_j d\eta-\hat{c}^{(i)}_j)(\int q^{(i)}_j d\eta-\hat{c}^{(i)}_j)}}\right]d\eta-\hat{d}^{(i)}_k. \quad (18)$$

3 Applications

3.1 Uniformly Distributed Loading. Consider a sagged cable traveling at constant speed c. The cable is subjected to a uniformly distributed load $\mathbf{q}=\{q_x,q_y,q_z\}$. The chord ratio of the cable is x_B and a constant, initial tension is T_0. The superscripts denoting the particular segment have been dropped. The boundary conditions are

$$u_k|_{\eta=0}=u_k|_{\eta=1}=0,\ X_k|_{\eta=0}=A_k=0 \text{ and } X_k|_{\eta=1}=B_k. \quad (19)$$

The displacement is given by (18)

$$u_k=\frac{1}{(c_p^2-c^2)}\left(-\frac{1}{2}q_k\eta^2+c_k\eta\right)\pm\frac{(c_p^2-c_0^2)}{(c_p^2-c^2)}\left\{-\frac{q_k}{q}\Theta(\eta)+\frac{(c_kq_j-c_jq_k)q_j}{q^3}\log[\Xi(\eta)+\Theta(\eta)]\right\}+d_k \mp\left\{-\frac{q_k}{q}\hat{\Theta}(\eta)+\frac{(\hat{c}_kq_j-\hat{c}_jq_k)q_j}{q^3}\log[\hat{\Xi}(\eta)+\hat{\Theta}(\eta)]\right\}-\hat{d}_k, \quad (20)$$

where

$$\left.\begin{aligned}\Theta(\eta)&=\sqrt{\eta^2-2\frac{c_jq_j}{q^2}\eta+\frac{c_jc_j}{q^2}},\\ \Xi(\eta)&=\eta-\frac{c_jq_j}{q^2},\ q=\sqrt{q_jq_j}\\ \hat{\Theta}(\eta)&=\sqrt{\eta^2-2\frac{\hat{c}_jq_j}{q^2}\eta+\frac{\hat{c}_j\hat{c}_j}{q^2}},\ \hat{\Xi}(\eta)=\eta-\frac{\hat{c}_jq_j}{q^2}.\end{aligned}\right\} \quad (21)$$

The boundary conditions (19) with (20) give

$$d_k=\mp\frac{c_p^2-c_0^2}{(c_p^2-c^2)}\left\{-\frac{q_k}{q}\Theta(0)+\frac{(c_kq_j-c_jq_k)q_j}{q^3}\log[\Xi(0)+\Theta(0)]\right\}, \quad (22)$$

$$c_k\pm\frac{(c_p^2-c_0^2)(c_kq_j-c_jq_k)q_j}{q^3}\log\left[\frac{\Xi(1)+\Theta(1)}{\Xi(0)+\Theta(0)}\right]=B_k(c_p^2-c^2)+\frac{1}{2}q_k\pm\frac{(c_p^2-c_0^2)q_k}{q}[\Theta(1)-\Theta(0)]. \quad (23)$$

The c_k and d_k in (20) are determined through solution of the nonlinear algebraic Eq. (22) and (23), and the $\hat{c}_k$ and $\hat{d}_k$ for the inextensible cable are determined from

$$\hat{d}_k = \mp\left\{ -\frac{q_k}{q}\hat{\Theta}(0) + \frac{(\hat{c}_k q_j - \hat{c}_j q_k)q_j}{q^3}\log[\hat{\Xi}(0)+\hat{\Theta}(0)]\right\}, \quad (24)$$

$$\pm\frac{(\hat{c}_k q_j - \hat{c}_j q_k)q_j}{q^3}\log\left[\frac{\hat{\Xi}(1)+\hat{\Theta}(1)}{\hat{\Xi}(0)+\hat{\Theta}(0)}\right] = B_k \pm \frac{q_k}{q}[\hat{\Theta}(1)-\hat{\Theta}(0)]. \quad (25)$$

The exact displacement solution is complete. The tension and the equilibrium configuration are

$$T(\eta) = \frac{1}{c_p^2 - c^2}[c^2(c_p^2 - c_0^2) \pm c_p^2 q\Theta(\eta)]. \quad (26)$$

$$x_k = X_k + u_k = \frac{(-\frac{1}{2}q_k\eta^2 + c_k\eta)}{(c_p^2-c^2)} + d_k \pm \frac{(c_p^2-c_0^2)}{(c_p^2-c^2)} \times\left\{ -\frac{q_k}{q}\Theta(\eta) + \frac{(c_k q_j - c_j q_k)q_j}{q^3}\log[\Xi(\eta)+\Theta(\eta)]\right\}. \quad (27)$$

For the inextensible cable, the equilibrium configuration is

$$\hat{X}_k(\eta) = \hat{d}_k \pm \left\{ -\frac{q_k}{q}\hat{\Theta}(\eta) + \frac{(\hat{c}_k q_j - \hat{c}_j q_k)q_j}{q^3}\log[\hat{\Xi}(\eta)+\hat{\Theta}(\eta)]\right\}. \quad (28)$$

3.1.1 Special Cases. Consider a two-dimensional traveling cable with $\overline{q_x}=0$, $\overline{q_y}=-\rho Ag=W/S$, $B_x=L/S$ and $B_y=H/S$. The substitution of (3), (22), and (23) into (27) and use of inverse hyperbolic functions leads to the equilibrium of the two-dimensional deformed cable,

$$\left.\begin{aligned}
\overline{x}(\overline{\eta}) &= \frac{\overline{c_1}}{(E-\rho\overline{c}^2)A}\left\{\overline{\eta} \pm \frac{EA-\overline{T}_0}{\overline{q}_y}\left[\sinh^{-1}\left(\frac{\overline{c}_2}{\overline{c}_1}\right) - \sinh^{-1}\left(\frac{\overline{c}_2 - \overline{q}_y\overline{\eta}}{\overline{c}_1}\right)\right]\right\},\\
\overline{y}(\overline{\eta}) &= \frac{1}{(E-\rho\overline{c}^2)A}\left\{\left(-\frac{1}{2}\overline{q}_y\overline{\eta}^2 + c_2\overline{\eta}\right) \pm \frac{(EA-\overline{T}_0)\overline{c}_1}{\overline{q}_y}\left[\sqrt{1+\left(\frac{\overline{c}_2}{\overline{c}_1}\right)^2} - \sqrt{1+\left(\frac{\overline{c}_2-\overline{q}_y\overline{\eta}}{\overline{c}_1}\right)^2}\right]\right\}.
\end{aligned}\right\} \quad (29)$$

The bar indicates dimensional variables and parameters. For the stationary cable ($\overline{c}=0$), let $\overline{T}_0=0$ and neglect the solution with $\overline{T}\leqslant 0$, (29) becomes

$$\left.\begin{aligned}
\overline{x}(\overline{\eta}) &= \frac{\overline{c}_1}{EA}\overline{\eta} + \frac{\overline{c}_1 S}{W}\left[\sinh^{-1}\left(\frac{\overline{c}_2}{\overline{c}_1}\right) - \sinh^{-1}\left(\frac{\overline{c}_2 - W\overline{\eta}/S}{\overline{c}_1}\right)\right],\\
\overline{y}(\overline{\eta}) &= \left[\frac{W\overline{\eta}}{EA}\left(\frac{\overline{c}_2}{W} - \frac{\overline{\eta}}{2S}\right) + \frac{\overline{c}_1 S}{W}\left(\sqrt{1+\left(\frac{\overline{c}_2}{\overline{c}_1}\right)^2} - \sqrt{1+\left(\frac{\overline{c}_2 - W\overline{\eta}/S}{\overline{c}_1}\right)^2}\right)\right].
\end{aligned}\right\} \quad (30)$$

which is the solution of Irvine [19].

The inextensible, axially moving cable is obtained from (29) by setting $EA\to\infty$.

$$\left.\begin{aligned}
\overleftarrow{X}(\eta) &= \pm\frac{\overline{c}_1}{\overline{q}_y}\left[\sinh^{-1}\left(\frac{\overline{c}_2}{\overline{c}_1}\right) - \sinh^{-1}\left(\frac{\overline{c}_2 - \overline{q}_y\overline{\eta}}{\overline{c}_1}\right)\right],\\
\hat{Y}(\eta) &= \pm\frac{\overline{c}_1}{\overline{q}_y}\left(\sqrt{1+\left(\frac{\overline{c}_2}{\overline{c}_1}\right)^2} - \sqrt{1+\left(\frac{\overline{c}_2 - \overline{q}_y\overline{\eta}}{\overline{c}_1}\right)^2}\right);
\end{aligned}\right\} \quad (31)$$

where $\overline{c}_1$ and $\overline{c}_2$ are determined through the boundary condition at $\overline{\eta}=S$. The equilibrium under nonpositive tension in (31) is unstable. Setting $\overleftarrow{X}_0 = \overline{c}_1/\overline{q}_y \sinh^{-1}(\overline{c}_2/\overline{c}_1)$, (31) becomes

$$\overleftarrow{Y}(\overleftarrow{X}) = \pm\frac{\overline{c}_1}{\rho Ag}\left[\cosh\left(\frac{\rho Ag}{\overline{c}_1}(\overleftarrow{X} - \overleftarrow{X}_0)\right) - \cosh\left(\frac{\rho Ag}{\overline{c}_1}\overleftarrow{X}_0\right)\right]. \quad (32)$$

Letting $\overleftarrow{T}_1(0) = \pm\overleftarrow{\overline{c}_1} = \pm[\overleftarrow{T}_0(0) - \rho A\overline{c}^2]\cos\theta(0)$ where $d\overleftarrow{X}/d\overline{\eta} = \cos\theta(\overline{\eta})$, (32) is given by O'Reilly [18] (see p. 188). $\overleftarrow{X}_0$ is determined by the boundary condition at $\overline{\eta}=S$. If the inextensible cable is sufficiently straight that $\cos\theta\approx 1$ and $\overline{c}_1 \gg \overline{c}_2$, then $\overleftarrow{X}_0 \approx 0$ and (32) becomes

$$\left.\begin{aligned}
\overleftarrow{X}(\overline{\eta}) &= \pm\frac{\overline{c}_1}{\overline{q}_y}\sinh^{-1}\left(\frac{\overline{q}_y\overline{\eta}}{\overline{c}_1}\right),\\
\overleftarrow{Y}(\overline{\eta}) &= \pm\frac{\overline{c}_1}{\overline{q}_y}\left(1 - \sqrt{1+\left(\frac{\overline{q}_y\overline{\eta}}{\overline{c}_1}\right)^2}\right)\\
&= \mp\frac{\overline{c}_1}{\overline{q}_y}\left[\cosh\left(\frac{\overline{q}_y\overline{\eta}}{\overline{c}_1}\right) - 1\right].
\end{aligned}\right\} \quad (33)$$

This stable solution is given by Simpson [10]. However, (33) does not provide the equilibrium solution of the inextensible cable because the boundary conditions are not satisfied. The linear model of the straight cable gives

$$u = -\frac{q_x}{2(c_p^2-c^2)}(\eta-1)\eta, \quad v = -\frac{q_y}{2(c_0^2-c^2)}(\eta-1)\eta. \quad (34)$$

3.1.2 Illustrations. In all the figures to be referenced next, the solid and dash lines represent the upper (+) and lower (−) branches of the equilibrium configurations, respectively, and the dotted line denotes the unstable equilibrium of the cable when $T\leqslant 0$. The longitudinal and transverse wave speeds are $c_p=740.87$ and $c_0=0$.

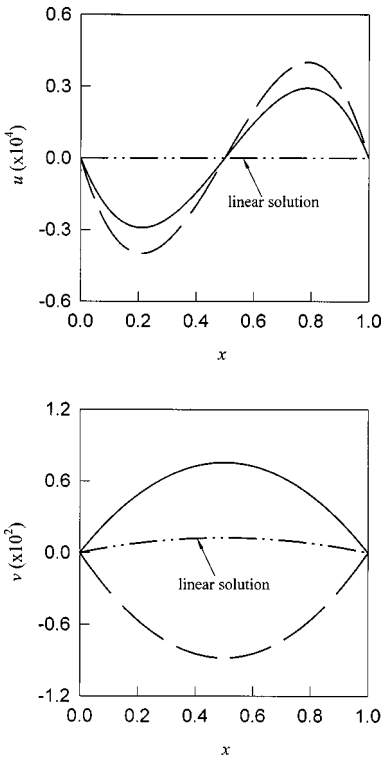

Fig. 2 Longitudinal (upper) and transverse (lower) equilibrium displacements of a *straight elastic* cable under $q_x=0$ and $q_y=-1$ for $c=10$: $c_p=740.87$ and $c_0=0$

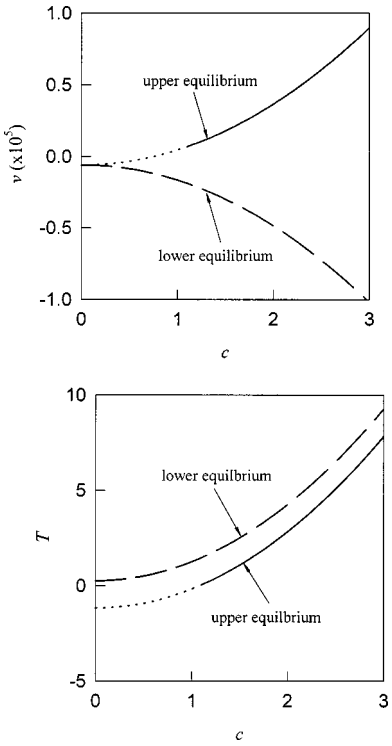

Fig. 3 Displacement (upper) and tension (lower) versus traveling speed of a sagged *elastic* cable ($x_B=0.8$) for $q_x=q_y=-1$ with various transverse loads: $c_p=740.87$ and $c_0=0$

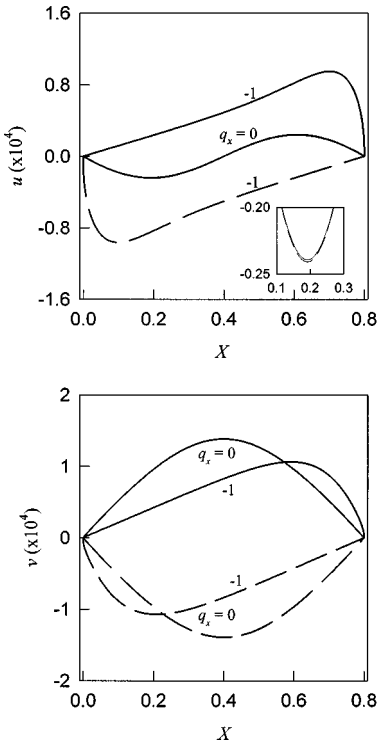

Fig. 5 Longitudinal (upper) and transverse (lower) displacements of a sagged *elastic* cable at equilibrium ($x_B=0.8$) under its own weight ($q_y=-1$) and various longitudinal loads for $c=10$: $c_p=740.87$ and $c_0=0$

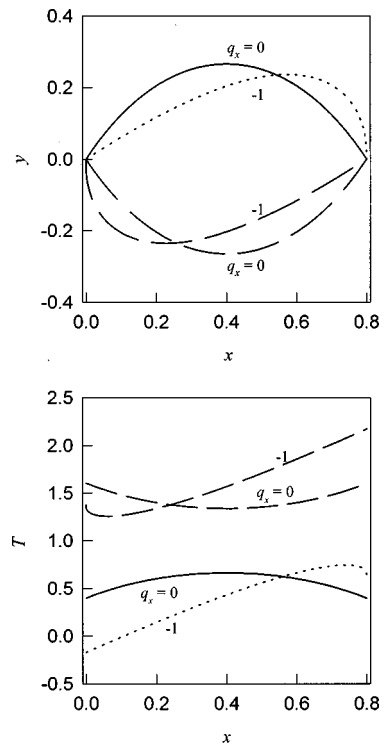

Fig. 4 Multiple equilibrium configurations (upper) and tension distributions (lower) of a sagged *elastic* cable ($x_B=0.8$) under its own weight ($q_y=-1$) and various longitudinal loads for $c=1$: $c_p=740.87$ and $c_0=0$

Consider a two-dimensional horizontal straight cable ($B_x=x_B=1$, $B_y=B_z=0$) hanging under its own weight ($q_x=0$, $q_y=-1$). Two components of displacement $u=x(\eta)-\eta$ and $v=y(\eta)$ computed from (20) at $c=10$ are shown in Fig. 2. The chain line denotes the linear prediction of displacement from (34). The maximum longitudinal displacement is 3.998×10^{-5} (lower branch) and 2.923×10^{-5} (upper branch) at $\eta=0.21$ and 0.79. The linear prediction of the longitudinal displacement is zero because of $q_x=0$. The maximum transverse displacement is 8.828×10^{-3} (lower branch) and 7.547×10^{-3} (upper branch), but 1.25×10^{-3} for the linear prediction. For the inextensible cable, two components of displacement are zero.

The maximum transverse displacement and minimum tension in the two-dimensional sagged elastic cable ($B_x=x_B$, $B_y=B_z=0$) for $q_x=-1$ is plotted in Fig. 3 when the chord ratio is $x_B=0.8$. The lower branch of the equilibrium configuration for any traveling speed always exists, and the displacement and tension increase with the transverse load and transport speed. The upper branch of equilibrium configuration is stable only when the transport creates positive tension.

The equilibrium configuration and tension of a cable under its own weight ($q_y=-1$) and the longitudinal loads ($q_x=0,-1$) are illustrated in Fig. 4 at $x_B=0.8$ and $c=1$. The equilibrium configurations and tension distributions are symmetric for $q_x=0$. The longitudinal and transverse displacements from the initial configuration to equilibrium of the sagged elastic cable are illustrated in Fig. 5. Unlike the straight cable in Fig. 2, the longitudinal displacement of the sagged cable is the same order of magnitude as the transverse displacement.

The maximum transverse displacement and the related tension versus the chord ratio are illustrated in Fig. 6 at $c=10$. The maxima occur at $x_B=1$. The results indicates that slightly sagged cables ($x_B=0.9\sim1$) must be modeled as extensible to achieve the

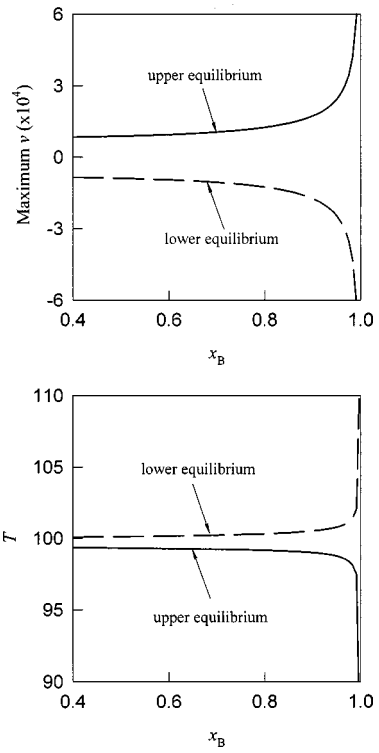

Fig. 6 Displacement (upper) and tension (lower) versus chord ratio of a sagged *elastic* cable with various transverse loads for $c=10:c_p=740.87$ and $c_0=0$

accuracy for most applications. The sagged cable model reduces to the straight cable model at $x_B=1$.

3.2 Concentrated Loading. Consider a three-dimensional sagged traveling cable carrying $n-1$ concentrated loads $F_k^{(i)}$ ($i=1,2,...,n-1$ and $k=1,2,3$ for x, y, z) which divide the cable into n segments. $q_k^{(i)}(i=1,2,...,n)$ are uniformly distributed loads and c_0^2 is a constant initial tension. The boundary conditions satisfy (19). Three components of displacement from (19) are computed through (20) and (21) when $\{u_k,q_k,c_k,d_k,\Xi,\Theta,q\}$ and $\{\hat{c}_k,\hat{d}_k,\hat{\Xi},\hat{\Theta}\}$ are replaced by $\{u_k^{(i)},q_k^{(i)},c_k^{(i)},d_k^{(i)},\Xi^{(i)},\Theta^{(i)},q^{(i)}\}$ and $\{\hat{c}_k^{(i)},\hat{d}_k^{(i)},\hat{\Xi}^{(i)},\hat{\Theta}^{(i)}\}$.

The corresponding boundary condition in (19) at $\eta=0$ becomes

$$d_k^{(1)}=\mp\frac{c_p^2-c_0^2}{(c_p^2-c^2)}\left\{-\frac{q_k^{(1)}}{q^{(1)}}\Theta(0)+\frac{(c_k^{(1)}q_j^{(1)}-c_j^{(1)}q_k^{(1)})q_j^{(1)}}{(q^{(1)})^3}\log[\Xi^{(1)}(0)+\Theta^{(1)}(0)]\right\}. \quad (35)$$

The displacement continuity between the ith and $(i+1)$th segments $(i=1,2,...,n-1)$ is

$$\pm\frac{(c_k^{(i)}q_j^{(i)}-c_j^{(i)}q_k^{(i)})q_j^{(i)}}{(q^{(i)})^3}\log[\Xi^{(i)}(\eta_i)+\Theta^{(i)}(\eta_i)]\mp\frac{q_k^{(i)}}{q^{(i)}}\Theta^{(i)}(\eta_i)+\frac{1}{c_p^2-c_0^2}\left(c_k^{(i)}\eta_i-\frac{1}{2}q_k^{(i)}\eta_i^2\right)$$
$$=\pm\frac{(c_k^{(i+1)}q_j^{(i+1)}-c_j^{(i+1)}q_k^{(i+1)})q_j^{(i+1)}}{(q^{(i+1)})^3}\times\log[\Xi^{(i+1)}(\eta_i)+\Theta^{(i+1)}(\eta_i)]\mp\frac{q_k^{(i+1)}}{q^{(i+1)}}\Theta^{(i+1)}(\eta_i)+\frac{1}{c_p^2-c_0^2}\left(c_k^{(i+1)}\eta_i-\frac{1}{2}q_k^{(i+1)}\eta_i^2\right)+\frac{c_p^2-c^2}{c_0^2-c^2}(d_k^{(i+1)}-d_k^{(i)}), \quad (36)$$

and force balances in (16) give

$$-q_k^{(i)}\eta_i+c_k^{(i)}-F_k^{(i)}=-q_k^{(i+1)}\eta_i+c_k^{(i+1)}. \quad (37)$$

The boundary condition in (19) at $\eta=1$ produces

$$\pm\frac{(c_k^{(n)}q_j^{(n)}-c_j^{(n)}q_k^{(n)})q_j^{(n)}}{(q^{(n)})^3}\log[\Xi^{(n)}(1)+\Theta^{(n)}(1)]+(d_k^{(n)}+c_k^{(n)})\frac{1}{c_p^2-c_0^2}=B_k\frac{c_p^2-c^2}{c_p^2-c_0^2}+\frac{1}{c_p^2-c_0^2}\frac{q_k^{(n)}}{2}\pm\frac{q_k^{(n)}}{q^{(n)}}\Theta^{(n)}(1). \quad (38)$$

The $c_k^{(i)}$ and $d_k^{(i)}$ are determined by solving $6\times n$ nonlinear algebraic Eq. (35)–(38). Similarly, the $\hat{c}_k$ and $\hat{d}_k$ for the inextensible cable are determined by the following $6\times n$ nonlinear equations:

$$\hat{d}_k^{(1)}=\mp\left\{-\frac{q_k^{(1)}}{q^{(1)}}\hat{\Theta}(0)+\frac{(\hat{c}_k^{(1)}q_j^{(1)}-\hat{c}_j^{(1)}q_k^{(1)})q_j^{(1)}}{(q^{(1)})^3}\times\log[\hat{\Xi}^{(1)}(0)+\hat{\Theta}^{(1)}(0)]\right\}, \quad (39)$$

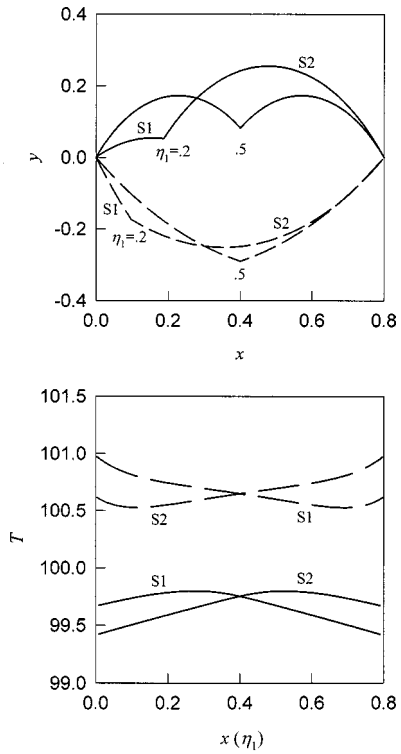

Fig. 7 Equilibrium configuration (upper) and tension-jump from segment 1 to segment 2 (lower) of a sagged *elastic* cable ($x_B=0.8$) under its own weight ($q_y=-1$) and a concentrated force ($F_y=-2$) for $c=10:c_p=740.87$ and $c_0=0$

$$\pm\frac{(\hat{c}_k^{(i)}q_j^{(i)}-\hat{c}_j^{(i)}q_k^{(i)})q_j^{(i)}}{(q^{(i)})^3}\log[\hat{\Xi}^{(i)}(\eta_i)+\hat{\Theta}^{(i)}(\eta_i)]\mp\frac{q_k^{(i)}}{q^{(i)}}\hat{\Theta}^{(i)}(\eta_i)$$

$$+\hat{d}_k^{(i)}=\pm\frac{(\hat{c}_k^{(i+1)}q_j^{(i+1)}-\hat{c}_j^{(i+1)}q_k^{(i+1)})q_j^{(i+1)}}{(q^{(i+1)})^3}\log[\hat{\Xi}^{(i+1)}(\eta_i)$$

$$+\hat{\Theta}^{(i+1)}(\eta_i)]\mp\frac{q_k^{(i+1)}}{q^{(i+1)}}\hat{\Theta}^{(i+1)}(\eta_i)+\hat{d}_k^{(i+1)}, \tag{40}$$

$$-q_k^{(i)}\eta_i+\hat{c}_k^{(i)}-F_k^{(i)}=-q_k^{(i+1)}\eta_i+\hat{c}_k^{(i+1)}, \tag{41}$$

$$\pm\frac{(\hat{c}_k^{(n)}q_j^{(n)}-\hat{c}_j^{(n)}q_k^{(n)})q_j^{(n)}}{(q^{(n)})^3}\log[\hat{\Xi}^{(n)}(1)+\hat{\Theta}^{(n)}(1)]+\hat{d}_k^{(n)}$$

$$=B_k\pm\frac{q_k^{(n)}}{q^{(n)}}\hat{\Theta}^{(n)}(1). \tag{42}$$

The exact closed form displacement for the equilibrium configuration of traveling sagged cables under the uniformly distributed and concentrated loading is complete. The computation of tension equilibrium configuration for each segment of elastic and inextensible cables can be carried out from (26)–(28).

To illustrate the equilibrium configuration and tension distribution under concentrated loading, consider a two-dimensional sagged cable ($B_x=x_B$, $B_y=B_z=0$) under its own weight and a concentrated load $F_x=0$, $F_y=-2$ when $c=10$ and $x_B=0.8$. The equilibrium configurations and the tension from segment 1 (S1) to segment 2 (S2) for the concentrated loading at $\eta_1=0.2$ and 0.5 are plotted in Fig. 7. If the concentrated force is at the middle of cable ($\eta_1=0.5$), the jump in tension vanishes. The slopes of the configuration and tension are discontinuous at the location of the concentrated force.

4 Conclusion

The exact closed-form displacements, configuration, and tension for the steady-state motion of traveling, three-dimensional sagged elastic cables under arbitrary loading are developed. Traveling cables with large sag can be modeled approximately through the inextensible cable model when the loading and traveling speed are very small. However, a slightly sagged cable must be modeled as extensible even if both loading and transport speed are very small. For a stationary cable with large sag subjected to its own weight, the equilibrium configuration and tension distribution can be approximated by the ones of the inextensible cable model.

Acknowledgments

The authors would like to thank the National Science Foundation, NSERC (Canada) postdoctoral fellowship for their support in this work.

References

[1] Rohrs, J. H., 1851, ''On the Oscillations of a Suspension Cable,'' Trans. Cambridge Philos. Soc., **9**, pp. 379–398.
[2] Routh E. J., 1884, *The Advanced Part of a Treatise on the Dynamics of a System of Rigid Bodies*, 4th Ed., MacMillan and Co., London.
[3] Pugsley, A. G., 1949, ''On Natural Frequencies of Suspension Chain,'' Q. J. Mech. Appl. Math., **2**, pp. 412–418.
[4] Saxon, D. S., and Cahn, A. S., 1953, ''Modes of Vibration of a Suspended Chain,'' Q. J. Mech. Appl. Math., **6**, pp. 273–285.
[5] Simpson, A., 1966, ''Determination of the Inplane Natural Frequencies of Multispan Transmission Lines by a Transfer Matrix Method,'' Proc. Inst. Electr. Eng., **113**, pp. 870–878.
[6] Irvine, H. M., and Caughey, T. K., 1974, ''The Linear Theory of Free Vibrations of a Suspended Cable,'' Proc. R. Soc. London, Ser. A, **341A**, pp. 299–315.
[7] Hagedorn, P., and Schafer, B., 1980, ''On Nonlinear Free Vibrations of an Elastic Cable,'' Int. J. Non-Linear Mech., **15**, pp. 333–340.
[8] Luongo, A., Rega, G., and Vestroni, F., 1984, ''Planar Non-linear Free Vibrations of an Elastic Cable,'' Int. J. Non-Linear Mech., **19**, pp. 39–52.
[9] Perkins, N. C., 1992, ''Modal Interactions in the Nonlinear Response of Elastic Cables Under Parametric/External Excitation,'' Int. J. Non-Linear Mech., **27**, No. 2, pp. 233–250.
[10] Simpson, A., 1972, ''On the Oscillatory Motions of Translating Elastic Cables,'' J. Sound Vib., **20**, No. 2, pp. 177–189.
[11] Triantafyllou, M. S., 1985, ''The Dynamics of Translating Cables,'' J. Sound Vib., **103**, No. 2, pp. 171–182.
[12] Perkins, N. C., and Mote, Jr., C. D., 1987, ''Three-Dimensional Vibration of Traveling Elastic Cables,'' J. Sound Vib., **114**, No. 3, pp. 325–340.
[13] Perkins, N. C., and Mote, Jr., C. D., 1989, ''Theoretical and Experimental Stability of Two Translating Cable Equilibria,'' J. Sound Vib., **128**, No. 3, pp. 397–410.
[14] Dickey, R. W., 1969, ''The Nonlinear String Under a Vertical Force,'' SIAM (Soc. Ind. Appl. Math.) J. Appl. Math., **17**, No. 1, pp. 172–178.
[15] Antman, S. S., 1979, ''Multiple Equilibrium States of Nonlinear Elastic Strings,'' SIAM (Soc. Ind. Appl. Math.) J. Appl. Math., **37**, No. 3, pp. 588–604.
[16] O'Reilly, O. M., and Varadi, P., 1995, ''Elastic Equilibria of Translating Cables,'' Acta Mech., **108**, pp. 189–206.
[17] Healey, T. J., and Papadopoulos, J. N., 1990, ''Steady Axial Motions of Strings,'' ASME J. Appl. Mech., **57**, pp. 785–787.
[18] O'Reilly, O. M., 1996, ''Steady Motions of a Drawn Cable,'' ASME J. Appl. Mech., **63**, pp. 180–189.
[19] Irvine, H. M., 1974, *Cable Structures*, The MIT Press, Cambridge, MA.
[20] Yu, P., Wong, P. S., and Kaempffer, F., 1995, ''Tension of Conductor Under Concentrated Loads,'' ASME J. Appl. Mech., **62**, pp. 802–809.
[21] Luo, A. C. J., Han, R. P. S., Tyc, G., Modi, V. J., and Misra, A. K., 1996, ''Analytical Vibration and Resonant Motion of a Stretched, Spinning, Nonlinear Tether,'' AIAA J. Guidance, Control Dyn., **19**, No. 5, pp. 1162–1171.

Mold Surface Wavelength Effect on Gap Nucleation in Solidification

L. G. Hector, Jr.
Surface Science Division,
Alcoa Technical Center,
Alcoa Center, PA 15069

J. A. Howarth
Department of Applied Mathematics,
University of Hull,
Hull HU6 7RX, England

O. Richmond
Alcoa Technical Center,
Alcoa Center, PA 15069
Mem. ASME

W.-S. Kim
Department of Mechanical Engineering,
Hanyang University,
Seoul 133, Korea

A theoretical model that predicts the time and position of gap nucleation along the metal-shell interface during solidification of a pure metal on a sinusoidal mold surface is presented. The ratio of the mold surface amplitude to its wavelength is assumed to be much less than one and hence it is used as a perturbation parameter in the analysis. The molten metal perfectly wets the mold surface prior to the beginning of solidification, and this leads to a corresponding undulation of the metal shell thickness. A nonuniform distortion develops in the shell due to the lateral temperature gradient induced by the modest spatial variation of the mold surface. This causes a variation in the contact pressure so that the growing shell pushes harder on the mold in some places, but in other places it starts to pull away from the mold. Gap nucleation is assumed to occur when the contact pressure falls to zero. The conditions for gap nucleation in the surface troughs are examined since a corresponding increase in pressure at the crests signals the possibility of a growth instability in the shell at later stages of the process. A series expansion for the contact pressure is presented which is appropriate for early solidification times. This reveals how the contact pressure varies with the mold surface wavelength. This solution is compared with a numerical solution for the contact pressure that is not limited to early solidification times. Gap nucleation times are calculated for pure aluminum and iron shells for selected mold surface wavelengths. The associated mean shell thicknesses are calculated as a function of wavelength at selected mean molten metal pressures. [S0021-8936(00)02901-9]

1 Introduction

The most critical region during the earliest stages of metal casting processes is the mold-shell interface. It is through this interface that heat is extracted from the molten metal resulting in the growth of the metal shell. Some of the most difficult process-related problems are gap nucleation and subsequent gap growth, and remelting of the shell along the mold-shell interface. There is indeed a substantial body of experimental literature that considers the nucleation and growth of gaps during solidification processes (see, for example, [1]).

Gap nucleation is largely caused by irregular thermomechanical distortion of the shell which leads to localized separation from the mold surface. The nonuniform thermal field that gives rise to irregular distortion can result from spatial variations in the heat extraction profile along the mold-shell interface (due, for example, to mold surface topography, release agents, oxides, etc). Evidence of nonuniform shell growth due to irregular distortion is found as raised ''humps'' along the internal surface of the shell which are apparent when solidification is interrupted and the residual molten metal is decanted. The humps are a macromorphological phenomenon reaching several centimeters in span. They are a clear indication of a shell growth instability which is most prominent during the early to intermediate stages of casting. This type of irregular growth has been linked to a variety of problems with cast ingot surface quality, among the most significant of which are a microstructure that is unsuitable for subsequent processing (such as hot rolling) and surface cracks.

Previous experimental work on this cellular undulation phenomenon has led to the suggestion that the humps grow as a result of gap nucleation at regions of the mold surface that lie beneath the thinnest regions of the shell (see, for example, [2–5]). It is likely that this is but one of several contributing factors to solidification growth instability since process-related phenomena, such as superheat, mold velocity, mold distortion, meniscus behavior, and fluid flow play prominent roles in the process ([6]).

Richmond et al. [7] developed a beam theory model to explore the onset of the proposed macroscale growth instability mechanism assuming that thickness nonuniformity of a pure metal shell was due to a periodic heat extraction profile. This assumption was based upon the premise that small scale disturbances in the heat extraction profile at the mold-shell interface led to larger scale shell thickness nonuniformities via gap nucleation and growth. It was proposed that gap nucleation occurred when the contact pressure along the mold-shell interface fell to zero. Richmond et al. [7] found that gap nucleation occurred beneath the thinnest regions of the shell, which presumably diminished further growth of these regions, with a corresponding increase in contact pressure beneath the thickest regions of the shell, the thicker regions subsequently growing at a faster rate. The mismatch in growth rates along the shell is what leads to the humps discussed above. Beyond gap nucleation time, their model was no longer valid since it could not account for continued growth of the gaps and the shell. Li and Barber [8] extended this work using a stress function approach and found that the Richmond model was appropriate for the earliest stages of the casting when the shell is very thin. Their model assumed that the temperature and stress fields in the growing shell were coupled along the mold-shell interface through a pressure-dependent thermal contact resistance. Additional models, which address such added complexities as strain rate relaxation due to viscous creep ([9]), Stefan number ([10]), and mold distortion ([11]), have subsequently been developed.

All of the preceding theoretical work on the growth instability problem has assumed a perfectly smooth mold surface with a superposed periodic cooling profile. In practice, no surface is per-

Contributed by the Applied Mechanics Division of THE AMERICAN SOCIETY OF MECHANICAL ENGINEERS for publication in the ASME JOURNAL OF APPLIED MECHANICS. Manuscript received by the ASME Applied Mechanics Division, Jan. 12, 1999; final revision, Oct. 12, 1999. Associate Technical Editor: J. R. Barber. Discussion on the paper should be addressed to the Technical Editor, Professor Lewis T. Wheeler, Department of Mechanical Engineering, University of Houston, Houston, TX 77204-4792, and will be accepted until four months after final publication of the paper itself in the ASME JOURNAL OF APPLIED MECHANICS.

fectly smooth. Most ground finishes (for example) can be thought of as nothing more than a mixture of spatial frequencies each of which has an amplitude that is a perturbation on a smooth background surface. It is therefore the purpose of the present work to reformulate the model originally proposed by Richmond et al. [7] for a pure metal solidifying on a sinusoidal mold surface of low aspect ratio (i.e., the ratio of the amplitude to wavelength is much less than one). The stress function formalism of Li and Barber [8] is followed which leads to solutions for the temperature and stress fields in the metal shell and the contact pressure along the mold-shell interface. A series solution for the mold-shell contact pressure at early times in the solidification process is derived from the stress field in order to reveal how the contact pressure depends upon key process parameters. This solution is compared with a numerical solution for the contact pressure that is not limited to early solidification times. Gap nucleation in pure aluminum and iron shells is explored for selected process parameters. The variation of the mean shell thickness with mold surface wavelength at gap nucleation time is examined at selected mean molten metal pressures.

2 The Thermal Problem

The system to be modeled is shown in Fig. 1. A pure metal shell solidifies from a quiescent bath of molten metal that has perfectly wet a sinusoidal mold surface. In the planar reference coordinates, the mold surface is given by $y=a\cos(2\pi x/\lambda)$, where a is the surface amplitude, and λ is the wavelength or center-to-center spacing between adjacent crests. The mold, which is assumed to be a rigid, perfect conductor, is held at a temperature T_m, where $T_m<T_f$, and T_f is the fusion temperature of the molten metal.

The temperature problem in the shell is

$$\frac{\partial^2 T}{\partial x^2}+\frac{\partial^2 T}{\partial y^2}=\frac{1}{k}\frac{\partial T}{\partial t} \tag{1}$$

$$\frac{\partial T}{\partial y}=\frac{Q}{K} \quad \text{at } y=l\epsilon\cos(mx) \tag{2}$$

$$T=T_f \quad \text{at } y=s \tag{3}$$

$$\frac{\partial T}{\partial y}=\frac{\rho L}{K}\frac{\partial s}{\partial t} \quad \text{at } y=s \tag{4}$$

$$s=l\epsilon\cos(mx) \quad \text{at } t=0 \tag{5}$$

where

$$QR=T \quad \text{at } y=l\epsilon\cos(mx). \tag{6}$$

Note that

$$R(x,t)=R(P(x,t)) \tag{7}$$

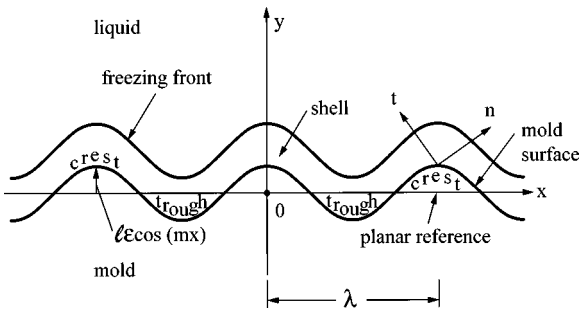

Fig. 1 Pure metal shell solidifying on a rigid mold with a sinusoidal surface

is the thermal contact resistance (wherein we have assumed that $T_m=0$ without loss of generality) and $P(x,t)$ is the contact pressure along the mold-casting interface. We define

$$\epsilon=a/l \tag{8}$$

as the mold surface aspect ratio, where $l=\lambda/2\pi=1/m$. The aspect ratio is a convenient perturbation parameter since we assume $\epsilon\ll 1$. This is not an unrealistic assumption since a ground finish in practice might have (nominally) $a\approx 1.0\,\mu$m and $\lambda\approx 5.0$ mm, and hence, $\epsilon=2\times 10^{-4}$. We assume a negligible Stefan number material, in which case Eq. (1) reduces to the steady-state heat equation.

Note that Eq. (2) is more appropriately written as

$$\mathbf{n}\cdot\nabla T=\frac{Q}{K} \tag{9}$$

where $\mathbf{n}$ is the unit normal vector to the mold surface at any point. However, the difference between Eqs. (2) and (9) can be shown to be $O(\epsilon^2)$ (this relies in part on the fact that the unperturbed solution is independent of x). A similar comment also applies to Eq. (4). The following perturbation analysis will only keep track of terms to $O(\epsilon)$, and hence we may retain Eq. (2) without loss of generality.

2.1 Perturbation of the Thermal Problem. We assume the following forms for T, Q, and s:

$$T(x,y,t)=T_o(y,t)+T_1(x,y,t) \tag{10}$$

$$Q(x,y,t)=Q_o(t)+Q_1(x,y,t) \tag{11}$$

$$s(x,t)=s_o(t)+s_1(x,t) \tag{12}$$

where terms with suffix 1 are implicitly $O(\epsilon)$. We insert Eq. (10) into Eq. (1) and separate the zeroth-order and first-order governing thermal equations. We then expand Eqs. (2) and (6) in a Taylor series about $y=l\epsilon\cos(mx)$ to $O(\epsilon)$ and group terms corresponding to the zeroth-order and first-order conditions. After proceeding in a similar fashion with the other conditions, we separate expressions corresponding to the zeroth-order and first-order thermal problems, which are written as follows:

The Zeroth-Order Problem.

$$\frac{\partial^2 T_o}{\partial y^2}=0 \tag{13}$$

$$\frac{\partial T_o}{\partial y}=\frac{Q_o}{K} \quad \text{at } y=0 \tag{14}$$

$$T=T_f \quad \text{at } y=s_o \tag{15}$$

$$\frac{\partial T_o}{\partial y}=\frac{\rho L}{K}\frac{ds_o}{dt} \quad \text{at } y=s_o \tag{16}$$

$$s_o=0 \quad \text{at } t=0 \tag{17}$$

where

$$Q_oR_o=T_o \quad \text{at } y=0 \tag{18}$$

The First-Order Problem.

$$\frac{\partial^2 T_1}{\partial x^2}+\frac{\partial^2 T_1}{\partial y^2}=0 \tag{19}$$

$$\frac{\partial T_1}{\partial y}=\frac{Q_1}{K} \quad \text{at } y=0 \tag{20}$$

$$s_1\frac{\partial T_o}{\partial y}+T_1=0 \quad \text{at } y=s_o \tag{21}$$

$$s_1 \frac{\partial^2 T_o}{\partial y^2} + \frac{\partial T_1}{\partial y} = \frac{\rho L}{K} \frac{\partial s_1}{\partial t} \quad \text{at } y = s_o \tag{22}$$

$$s_1 = l\epsilon \cos(mx) \quad \text{at } t = 0 \tag{23}$$

where

$$Q_1(x,0,t) = \frac{1}{R_o}\left[l\epsilon \frac{\partial T_o}{\partial y} \cos(mx) + T_1 - Q_o R_1 \right] \quad \text{at } y = 0 \tag{24}$$

$$R_1 = \frac{1}{Q_o}(T_1 - Q_1 R_o). \tag{25}$$

2.2 The Zeroth-Order Solution. The procedure for solving the zeroth-order problem may be found in Li and Barber [8]. We therefore summarize the solution without proof:

$$T_o(y,t) = T_f\left[\frac{y + KR_o}{s_o(t) + KR_o}\right] \quad ; \quad 0 \leqslant y \leqslant s_o(t) \tag{26}$$

$$Q_o(t) = \left[\frac{KT_f}{s_o(t) + KR_o}\right] \tag{27}$$

$$s_o(t) = -KR_o + \sqrt{K^2 R_o^2 + \frac{2KT_f t}{\rho L}}. \tag{28}$$

Using Eq. (28), we define $t_o(y)$ as the time when the mean melt line reaches the position y; thus

$$t_o(y) = \frac{y\rho L}{2KT_f}(y + 2KR_o). \tag{29}$$

2.3 The First-Order Solution. The solution to the first-order thermal problem may be written as

$$T_1(x,y,t) = [A(t)\cosh(my) + B(t)\sinh(my)]\cos(mx) \tag{30}$$

where $A(t)$ and $B(t)$ are unknown time functions. Application of Eq. (20) to Eq. (30) gives

$$B(t)\cos(mx) = \frac{Q_1(x,0,t)}{mK}. \tag{31}$$

Application of Eq. (21) to Eq. (30) gives

$$[A(t)\cosh(ms_o) + B(t)\sinh(ms_o)]\cos(mx) = -\left[\frac{s_1(x,t)T_f}{s_o(t) + KR_o}\right]. \tag{32}$$

At this point, the following definitions are convenient:

$$Q_1(x,0,t) = Q_1(t)\cos(mx) \tag{33}$$

$$s_1(x,t) = s_1(t)\cos(mx) \tag{34}$$

$$T_1(x,y,t) = T_1(y,t)\cos(mx) \tag{35}$$

$$R_1(0,P(x,t)) = R' P_1(t)\cos(mx) \tag{36}$$

$$P(x,t) = P_o + P_1(t)\cos(mx) \tag{37}$$

where the same symbol is retained for each of the perturbation quantities on the right-hand sides of Eqs. (33)–(37). Note that Eq. (36) comes from the Taylor series expansion

$$\begin{aligned} R(P(x,t)) &= R(P_o + P_1(t)\cos(mx)) \\ &= R(P_o) + R'(P_o)P_1(t)\cos(mx) \end{aligned} \tag{38}$$

and

$$R_o = R(P_o) \quad ; \quad R' = \frac{dR(P_o)}{dP}. \tag{39}$$

Equation (24) may therefore be written as

$$Q_1(t) = \frac{1}{R_o}\left[l\epsilon \frac{\partial T_o(0,t)}{\partial y} + T_1(0,t) - Q_o(t) R' P_1(t) \right]. \tag{40}$$

Substitution of Eqs. (26), (27), and (31) into Eq. (40) gives

$$A(t) - mKR_o B(t) = \frac{KT_f R' P_1(t)}{s_o(t) + KR_o} - \frac{l\epsilon T_f}{s_o(t) + KR_o}. \tag{41}$$

We next insert Eq. (30) into Eq. (22):

$$A(t)\sinh(ms_o) + B(t)\cosh(ms_o) = \left(\frac{\rho L}{m}\right)\frac{ds_1(t)}{dt}. \tag{42}$$

Solving Eq. (32) for $B(t)$ and substituting the result into Eq. (42) gives $A(t)$, and $B(t)$ follows. Substitution of $A(t)$ and $B(t)$ into Eq. (41) gives

$$\begin{aligned} &[s_o(t) + KR_o][mKR_o \cosh(ms_o) + \sinh(ms_o)]\dot{s}_1(t) \\ &\quad + \frac{mKT_f}{\rho L}[mKR_o \sinh(ms_o) + \cosh(ms_o)]s_1(t) \\ &\quad = \frac{\epsilon KT_f}{\rho L} - \frac{mK^2 T_f R' P_1(t)}{\rho L} \end{aligned} \tag{43}$$

which is a linear first-order differential equation in $s_1(t)$.

3 The Mechanical Problem

Based upon the form of the temperature field, we assume that the total stress field in the shell and the resulting contact pressure at the mold-shell interface have the following forms:

$$\sigma_{ij}(x,y,t) = \sigma_{ij_o}(y,t) + \sigma_{ij_1}(y,t)\cos(mx) \tag{44}$$

$$P(x,t) = P_o + P_1(t)\cos(mx) \tag{45}$$

where

$$P_o = -\sigma_{yy_o} \quad ; \quad P_1(t)\cos(mx) = -\sigma_{yy_1} \tag{46}$$

at $y = l\epsilon\cos(mx)$, and P_o is the mean pressure from the molten metal. The mechanical boundary conditions for frictionless contact at the mold surface are

$$\sigma_{nt} = 0 \quad ; \quad y = l\epsilon\cos(mx) \tag{47}$$

$$\dot{u}_n = 0 \quad ; \quad y = l\epsilon\cos(mx) \tag{48}$$

where σ_{nt} is the shear stress in the (n,t) coordinate system that rides along the mold surface (see Fig. 1) and $\dot{u}_n$ is the normal velocity. Equation (47) is appropriate for situations where the shear strength of the interface is negligible, such as when a thin lubricating film is applied to the interface. Note that Eq. (48) can only be stated in terms of a time derivative since there is no reference state for displacement of the shell. Solidification at the freezing front is assumed to occur in a state of hydrostatic stress

$$\sigma_{xx} = \sigma_{yy} = -P_o \quad , \quad \sigma_{xy} = 0 \quad ; \quad y = s(x,t). \tag{49}$$

Once the stress field is determined, then $P_1(t)$ is obtained from Eq. (46).

3.1 The Particular Solution. The stress field corresponding to the particular solution can be constructed in the form (see [12])

$$2\mu\mathbf{u} = \nabla\psi \tag{50}$$

where the scalar displacement potential, $\psi(x,y,t)$, satisfies

$$\nabla^2\psi = \frac{2\mu\alpha(1+\nu)T}{(1-\nu)} \quad ; \quad \mu = \frac{E}{2(1+\nu)} \tag{51}$$

and T is given by the sum of Eqs. (26) and (30). The stress and displacement fields corresponding to the particular solution are then derived from

$$\sigma^p_{xx_1} = -\frac{\partial^2 \psi}{\partial y^2} \quad ; \quad \sigma^p_{xy_1} = \frac{\partial^2 \psi}{\partial x \partial y} \quad ;$$
$$\sigma^p_{yy_1} = -\frac{\partial^2 \psi}{\partial x^2} \quad ; \quad \dot{u}^p_{y_1} = \frac{1}{2\mu}\frac{\partial}{\partial t}\left(\frac{\partial \psi}{\partial y}\right) \tag{52}$$

where the rate-dependent form of Eq. (50) has been used (as previously discussed) and the subscript ''1'' denotes a first-order component. A particular integral of Eq. (51) is

$$\psi = \frac{\mu\alpha(1+\nu)}{m(1-\nu)}\left[\frac{my^2 T_f}{3}\left(\frac{y+3KR_o}{s_o(t)+KR_o}\right) + y\{A(t)\sinh(my) + B(t)\cosh(my)\}\cos(mx)\right]. \tag{53}$$

We can simplify the problem somewhat by adjusting Eq. (53) so that the component of Eq. (48) corresponding to the particular solution, $\dot{u}^p_n$, is satisfied automatically. We first express the displacement normal to the mold surface in the planar reference coordinates via the following transformation equation:

$$\dot{u}^p_{n_1} = \dot{u}^p_{y_1}\cos(\phi) - \dot{u}^p_{x_1}\sin(\phi) \tag{54}$$

where

$$\phi = \frac{dy}{dx} = -\epsilon\sin(mx). \tag{55}$$

Since $\phi \ll 1$, Eq. (54) can be written as

$$\dot{u}^p_{n_1} = \dot{u}^p_{y_1} + \epsilon\dot{u}^p_{x_1}\sin(mx). \tag{56}$$

Since the zeroth-order solution requires that $\dot{u}^p_{n_1} = \dot{u}^p_{y_1}$, it is true that $\dot{u}^p_{x_1}$ is at least of $O(\epsilon)$ and hence the second term in Eq. (56) is at least of $O(\epsilon^2)$. We may therefore write

$$\dot{u}^p_{n_1} \approx \dot{u}^p_{y_1} \quad ; \quad y = l\epsilon\cos(mx) \tag{57}$$

since we are only interested in terms to $O(\epsilon)$. Using the expression for $\dot{u}^p_{y_1}$ from Eqs. (52), along with Eqs. (53) and (57), we obtain

$$\dot{u}^p_y|_{l\epsilon\cos(mx)} = \frac{\alpha(1+\nu)}{2m(1-\nu)}\frac{d}{dt}\left[\frac{2\epsilon KR_o T_f}{s_o(t)+KR_o} + B(t)\right]\cos(mx) \tag{58}$$

which results after we expand the hyperbolic functions in a Taylor series about $y = l\epsilon\cos(mx)$ and retain terms to $O(\epsilon)$. We can eliminate this unwanted velocity by superposing a suitable harmonic function onto ψ in Eq. (53). Let

$$\psi_i = C(t)\sinh(my)\cos(mx) \tag{59}$$

where $C(t)$ is an unknown function of time. The expression for $\dot{u}^p_{y_1}$ from Eqs. (52) gives

$$\dot{u}^p_{y_i} = \frac{d}{dt}\left[\frac{mC(t)}{2\mu}\cosh(my)\cos(mx)\right]. \tag{60}$$

In order to eliminate the term on the right-hand side of Eq. (58), we write

$$C(t) = -\frac{\mu\alpha(1+\nu)}{m(1-\nu)}\left[\frac{2l\epsilon KR_o T_f}{s_o(t)+KR_o} + \frac{B(t)}{m}\right] \tag{61}$$

and hence

$$\dot{u}^p_{y_i}|_{l\epsilon\cos(mx)} = -\frac{\alpha(1+\nu)}{2m(1-\nu)}\frac{d}{dt}\left[\frac{2\epsilon KR_o T_f}{s_o(t)+KR_o} + B(t)\right]\cos(mx) \tag{62}$$

since $\cosh(\epsilon\cos(mx)) \approx 1$. When Eq. (59) is superposed onto Eq. (53), there results

$$\psi = \frac{\mu\alpha(1+\nu)}{m(1-\nu)}\left[\frac{my^2 T_f}{3}\left(\frac{y+3KR_o}{s_o(t)+KR_o}\right) - \left(\frac{2l\epsilon KR_o T_f}{s_o(t)+KR_o}\right)\sinh(my)\cos(mx) + \left\{A(t)y\sinh(my) + B(t)\left[y\cosh(my) - \frac{\sinh(my)}{m}\right]\right\}\cos(mx)\right], \tag{63}$$

which provides a velocity field (corresponding to the particular solution) that automatically satisfies Eq. (48). The stress field corresponding to the particular solution, $\sigma^p_{ij_1}$, can now be derived via Eqs. (52) and (63).

3.2 The Homogeneous Solution. We pose the following form of the zeroth-order homogeneous solution

$$\sigma^h_{yy_o} = -P_o \quad ; \quad \sigma^h_{xx_o} = F^*(y) \quad ; \quad \sigma^h_{xy_o} = 0 \tag{64}$$

where $F^*(y)$ is an unknown function of position. It is convenient to transfer the zeroth-order term from σ^p_{xx} (determined from Eqs. (52) and (63)) to $F^*(y)$ by writing

$$\sigma^h_{xx_o} = -\frac{2\mu\alpha T_f(1+\nu)}{(1-\nu)}\left[\frac{y+KR_o}{s_o(t)+KR_o}\right] + F(y) \tag{65}$$

where $F(y)$ is also an unknown function of position. From Eqs. (49), we have $\sigma^h_{xx_o}(s_o) = -P_o$. Hence,

$$F(y) = -P_o + \frac{2\mu\alpha T_f(1+\nu)}{(1-\nu)} \tag{66}$$

and the zeroth-order lateral stress corresponding to the homogeneous solution is

$$\sigma^h_{xx_o} = -P_o + \frac{2\mu\alpha T_f(1+\nu)}{(1-\nu)}\left[\frac{s_o(t)-y}{s_o(t)+KR_o}\right]. \tag{67}$$

Also

$$\sigma^h_{xy_o} = 0 \quad ; \quad \sigma^h_{yy_o} = -P_o. \tag{68}$$

The first-order stress field corresponding to the homogeneous solution is derived from

$$\sigma^h_{xx_1} = \frac{\partial^2 \Phi}{\partial y^2} \quad ; \quad \sigma^h_{xy_1} = -\frac{\partial^2 \Phi}{\partial x \partial y} \quad ; \quad \sigma^h_{yy_1} = \frac{\partial^2 \Phi}{\partial x^2} \tag{69}$$

where Φ is the Airy stress function, which is written as

$$\Phi = [\{b_1(t)y + b_2(t)\}\cosh(my) + \{b_3(t)y + b_4(t)\}\sinh(my) + g(y)]\cos(mx). \tag{70}$$

Note that the b_i are unknown functions of time and $g(y)$ is a time-independent function that represents residual stress (or the stress field in the shell when it is cooled to a uniform temperature and relieved of all boundary tractions). The stress field corresponding to the homogeneous solution, $\sigma^h_{ij_1}$, can now be derived via Eqs. (69) and (70) in terms of the unknown $b_i(t)$. The components of the total stress field are obtained through superposition of the particular and homogeneous stress fields via Eq. (44).

3.3 Determination of the b_i. The $b_i(t)$ in the $\sigma^h_{ij_1}$ are determined by requiring the total stress field to satisfy Eqs. (47) and (49) and the homogeneous stress field to satisfy Eq. (48). The total shear stress in the mold surface system may be written in terms of the planar reference via

$$\sigma_{nt} = \sigma_{xy}(\cos^2(\phi) - \sin^2(\phi)) + (\sigma_{yy} - \sigma_{xx})\sin(\phi)\cos(\phi) \tag{71}$$

which, using Eq. (55), may be written as

$$\sigma_{nt} = \sigma_{xy} - (\sigma_{yy} - \sigma_{xx})\epsilon\sin(mx). \tag{72}$$

Equations (47), (52), (63), (72) and that for $\sigma^h_{xy_1}$ give

$$b_1(t)+mb_4(t)+g'(0)=-\frac{2\mu\alpha\epsilon T_f(1+\nu)}{m(1-\nu)} \tag{73}$$

where we have retained terms to $O(\epsilon)$. The elastic constitutive law for plane strain (where the associated rigid-body displacements have been neglected) is

$$\dot{u}^h_{y_1}=\frac{1+\nu}{E}\left[(1-\nu)\int \dot{\sigma}^h_{yy_1}dy-\nu\int \dot{\sigma}^h_{xx_1}dy\right]. \tag{74}$$

Application of $\dot{u}^h_n=0$ at $y=l\epsilon\cos(mx)$ from Eq. (48), using $\sigma^h_{xx_1}$ and $\sigma^h_{yy_1}$, gives $b_1(t)$. Equations (74) and that for $b_1(t)$ give $b_4(t)$. Application of the boundary conditions at the freezing front, Eqs. (49), provides expressions for $b_2(t)$, $b_3(t)$ and $g(y)$. We expand each of Eqs. (49) in a Taylor series about the mean position of the freezing front, s_o, beginning with σ_{xx}. Hence

$$\sigma_{xx}(s)=\sigma_{xx}(s_o)+(s-s_o)\frac{\partial\sigma_{xx}(x,s_o,t)}{\partial y}+\cdots=-P_o. \tag{75}$$

We have

$$\frac{\partial\sigma_{xx}(x,s_o,t)}{\partial y}=-\frac{2\mu\alpha T_f(1+\nu)}{(1-\nu)\{s_o+KR_o\}}+O(\epsilon) \tag{76}$$

where $\sigma_{xx}=\sigma^p_{xx}+\sigma^h_{xx}$ is derived from Eqs. (52) and (63). Equation (75) may therefore be written thus

$$\sigma_{xx}(s)=\sigma_{xx}(s_o)-\frac{2\mu\alpha s_1T_f(1+\nu)}{(1-\nu)\{s_o+KR_o\}}\cos(mx)=-P_o. \tag{77}$$

Substitution of the sum of σ^p_{xx} and σ^h_{xx} into Eq. (77) gives

$$\left[\frac{2b_1(t)}{m}+b_3(t)s_o+b_4(t)\right]\sinh(ms_o)+\left[b_1(t)s_o+b_2(t)+\frac{2b_3(t)}{m}\right]\cosh(ms_o)+\frac{g''(s_o)}{m^2}$$
$$=\frac{\mu\alpha\epsilon(1+\nu)}{m^2(1-\nu)}\left[2T_f\left\{\frac{s_1(t)-\epsilon KR_o\sinh(ms_o)}{s_o+KR_o}\right\}+\{2\cosh(ms_o)+ms_o\sinh(ms_o)\}A(t)+\{\sinh(ms_o)+ms_o\cosh(ms_o)\}B(t)\right]. \tag{78}$$

Following the same procedure for σ_{xy} and σ_{yy} gives, respectively,

$$\left[\frac{b_1(t)}{m}+b_3(t)s_o+b_4(t)\right]\cosh(ms_o)+\left[b_1(t)s_o+b_2(t)+\frac{b_3(t)}{m}\right]\sinh(ms_o)+\frac{g'(s_o)}{m}$$
$$=\frac{\mu\alpha(1+\nu)}{m^2(1-\nu)}\left[\begin{array}{c}\{\sinh(ms_o)+ms_o\cosh(ms_o)\}A(t)+ms_oB(t)\sinh(ms_o)\\ -\left\{\dfrac{2\epsilon T_fKR_o}{s_o+KR_o}\right\}\cosh(ms_o)\end{array}\right] \tag{79}$$

$$[b_1(t)s_o+b_2(t)]\cosh(ms_o)+[b_3(t)s_o+b_4(t)]\sinh(ms_o)+g(s_o)$$
$$=-\frac{\mu\alpha(1+\nu)}{m^2(1-\nu)}\left[\left\{\frac{2\epsilon T_fKR_o}{s_o+KR_o}-ms_oA(t)\right\}\sinh(ms_o)-\{ms_o\cosh(ms_o)-\sinh(ms_o)\}B(t)\right]. \tag{80}$$

Elimination of $b_2(t)$ between Eqs. (78) and (80) gives $b_3(t)$. Substitution of $b_3(t)$ into Eq. (80) gives $b_2(t)$. Note that $b_2(t)$ and $b_3(t)$ are not reported here due to their lengths.

3.4 Differential Equations for $P_1(t)$ and $s_1(t)$. Substitution of $b_2(t)$ and $b_3(t)$ into Eq. (79) gives a single differential equation relating the unknown functions $g(s_0)$ and $s_1(t)$. By definition,

$$P_1(t)\cos(mx)=-\sigma_{yy}(x,0,t). \tag{81}$$

Using Eqs. (44), (52), (63), and that for $\sigma^h_{yy_1}$, we find

$$P_1(t)=m^2\{b_2(t)+g(0)\}. \tag{82}$$

Substitution of Eq. (82) for $P_1(t)$ into Eq. (43) gives a second differential equation that relates $g(s_o)$ and $s_1(t)$. We shall present each of these equations in dimensionless form in the following section since this will facilitate subsequent algebraic and numerical manipulations.

3.5 Dimensionless Formulation for Perturbation Quantities. It will be necessary to examine each of the perturbation quantities (i.e., P_1, Q_1, T_1, and s_1) at sufficiently long times (in the absence of a mean pressure). Each quantity must tend smoothly to zero as time increases since the mold-shell interface will have a diminishing impact on the freezing front morphology as the shell thickens. Once it is verified that each perturbation quantity vanishes at sufficiently long times after the start of solidification, then we can proceed with confidence to examine the short-time behavior of the contact pressure and what it implies about the gap nucleation process for pure metals.

The coupled differential equations mentioned in the previous section may be written in terms of the following dimensionless variables:

$$\tau=\frac{m^2KT_f}{\rho L}t \quad ; \quad \eta=ms_o(t_o(y))=my \quad ;$$

$$\overline{s_1}(\tau_o(\eta))=\frac{ms_1(t_o(y))}{\epsilon}$$

$$\overline{g}(\eta)=\frac{m^2(1-\nu)}{E\alpha\epsilon T_f}g(y) \quad ; \quad \overline{R_o}=mKR_o \quad ; \quad \overline{R'}=\frac{E\alpha T_fR'}{(1-\nu)R_o}$$

$$\overline{P_1}(\eta)=\frac{(1-\nu)}{E\alpha\epsilon T_f}P_1(t) \quad ; \quad \overline{b_2}(\eta)=\frac{m^2(1-\nu)}{E\alpha\epsilon T_f}b_2(t) \quad ;$$

$$\overline{w}=\tanh(\eta)$$

$$\overline{Q_o}(\eta)=\frac{Q_o(t)}{mKT_f} \quad ; \quad \overline{Q_1}(\eta)=\frac{R_oQ_1(t)}{\epsilon T_f} \quad ; \quad \overline{T_1}(0,\eta)=\frac{T_1(0,t)}{\epsilon T_f}. \tag{83}$$

Hence

$$\frac{1}{2}(\eta\overline{w}^2-\eta-\overline{w})\overline{g}''(\eta)+\overline{g}'(\eta)-\frac{1}{2}(\eta\overline{w}^2+\overline{w}-\eta)\overline{g}(\eta)$$

$$=-\frac{1}{2}\left[\left\{\frac{\eta\overline{w}}{\eta+\overline{R}_o}\right\}\overline{s}_1'(\eta)+\left\{\frac{\eta+\overline{w}}{\eta+\overline{R}_0}\right\}\overline{s}_1(\eta)\right.$$

$$\left.-\frac{\{2(1-\nu)-\eta\overline{w}\}}{(1-\nu)\cosh(\eta)}+\frac{2\overline{R}_o}{(\eta+\overline{R}_o)\cosh(\eta)}\right] \tag{84}$$

$$\left[\frac{\eta\overline{w}\overline{R}'}{2\cosh(\eta)}\right]\overline{g}''(\eta)-\frac{\overline{R}'}{\cosh(\eta)}\left[1+\frac{\eta\overline{w}}{2}\right]\overline{g}(\eta)$$

$$=\left[\frac{\overline{w}\overline{R}_o\overline{R}'}{\eta+\overline{R}_o}+\left\{\frac{\overline{R}'}{2\cosh(\eta)}\left(\frac{\cosh(\eta)\sinh(\eta)-\eta}{\eta+\overline{R}_o}\right)\right.\right.$$

$$\left.-\cosh(\eta)-\frac{\sinh(\eta)}{\overline{R}_o}\right\}\overline{s}_1'(\eta)$$

$$+\left\{\frac{\overline{R}'\overline{w}\sinh(\eta)}{2(\eta+\overline{R}_o)}-\sinh(\eta)-\frac{\cosh(\eta)}{\overline{R}_o}\right\}\overline{s}_1(\eta)+\frac{1}{\overline{R}_o}$$

$$\left.-\frac{\overline{R}'}{2(1-\nu)}\{\eta\,\mathrm{sech}^2(\eta)+\overline{w}(1-2\nu)\}\right] \tag{85}$$

where the primes on $\overline{g}(\eta)$ and $\overline{s}_1(\eta)$ denote differentiation with respect to η, and we have used

$$\left(\frac{d\overline{s}_1(\tau)}{d\tau}\right)\Bigg|_{\tau=\tau_o(\eta)}=\frac{\overline{s}_1'(\eta)}{\eta+R_o}. \tag{86}$$

Note that we have set $\overline{g}(0)=\overline{g}'(0)=0$ since these are arbitrary and will not affect the final results. The contact pressure perturbation is determined from

$$\overline{P}_1(\eta)=\overline{b}_2(\eta) \tag{87}$$

where $\overline{b}_2(\eta)$ is listed in Appendix A.

An analytical solution is available for $\overline{s}_1(\eta)$ from Eq. (85) in the uncoupled case ($\overline{R}'=0$). Subsequently, $\overline{g}(\eta)$ can be obtained from Eq. (84) by the method of Variation of Parameters in terms of indefinite integrals. However, the form of this is lengthy and complicated, and in practice it is easier to solve Eq. (84) numerically.

4 Small η Solution for $\overline{P}_1(\eta)$

We seek an early time form of $\overline{P}(\eta)$ using Eq. (87). This can be derived from Eqs. (84), (85), and (*A*1) by assuming the following truncated Taylor series expansions for $\overline{s}_1(\eta)$ and $\overline{g}(\eta)$:

$$\overline{s}_1(\eta)=1+\sum_{i=1}^{N}\hat{A}_i\eta^i \tag{88}$$

$$\overline{g}(\eta)=\sum_{i=1}^{N}\hat{B}_{i+1}\eta^{i+1} \tag{89}$$

where $\eta\ll 1$. Note that the time-independent term in Eq. (88) implies that the thin shell is compliant to the mold surface at initial time. The unknown constant coefficients, $\hat{A}_i$ and $\hat{B}_i$, are obtained by first inserting Eqs. (88) and (89) into Eqs. (84) and (85), and then replacing each transcendental function with its series form, and finally by writing

$$\frac{1}{\eta+\overline{R}_o}=\frac{1}{\overline{R}_o}\left(1-\frac{\eta}{\overline{R}_o}+\frac{\eta^2}{\overline{R}_o^2}-\cdots\right). \tag{90}$$

For $N=5$, this gives (using Eqs. (87), (88)–(90), (*A*1), and (*B*1)) the early time form of $\overline{P}_1(\eta)$

$$\overline{P}_1(\eta)=\frac{\eta^2}{2\overline{R}_o}-\frac{\eta^3}{2\overline{R}_o^2}+\frac{(6-\overline{R}_o^2)\eta^4}{12\overline{R}_o^3}-\frac{(15-2\overline{R}_o^2)\eta^5}{30\overline{R}_o^4}$$

$$+\frac{(720-5(4+9\overline{R}')\overline{R}_o^2+32\overline{R}_o^4)\eta^6}{1440\overline{R}_o^5}+\cdots. \tag{91}$$

The $\hat{A}_i$ and $\hat{B}_i$ used to generate Eq. (91) are listed in Appendix B. Note that $\hat{B}_2$ was eliminated in the course of calculating $\overline{P}_1$.

5 Gap Nucleation at Early Solidification Times

In many casting processes, the molten metal pressure is insufficient to prevent gap nucleation during the earliest stages of solidification when the shell is very thin. It is therefore of interest to determine the conditions for gap nucleation to occur. This can be achieved through examination of P^{tr}, which is the ratio of the total (dimensional) contact pressure in the troughs, P, to the mean pressure, P_o, at the mold surface troughs. Hence

$$P^{tr}=\frac{P}{P_o}=1-\frac{P_1}{P_o}. \tag{92}$$

Gap nucleation at the troughs will indicate the possibility of irregular growth of the shell since contact will simultaneously increase at the crests (the sign in front of P_1 will be positive, rather than negative, due to the cos(*mx*) term in Eq. (45)). Writing Eq. (91) in dimensional form using Eqs. (83), and inserting the result into Eq. (92), we obtain

$$P^{tr}=1-\frac{2E\alpha T_f a}{KR_oP_o(1-\nu)}\left(\frac{\overline{s}_o}{\Lambda}\right)^2$$

$$\times\left[1-\overline{s}_o+\left(\frac{3-2/\Lambda^2}{3}\right)\overline{s}_o^2-\left(\frac{15-8/\Lambda^2}{15}\right)\overline{s}_o^3\right.$$

$$\left.+\left(\frac{720-20\{4+9\overline{R}'\}/\Lambda^2+512/\Lambda^4}{720}\right)\overline{s}_o^4-\cdots\right] \tag{93}$$

where

$$\overline{s}_o=\frac{s_o}{KR_o}\ll 1\quad;\quad\Lambda=\frac{\lambda}{\pi KR_o}. \tag{94}$$

If one neglects all terms except the lowest order term in $\overline{s}_o$, then it is possible to make some cursory observations about the effect that key process parameters have on P^{tr} for a specific $\overline{s}_o$ (or set time). For example, an increase in λ (holding all other parameters constant), causes a decrease in P_1, and a corresponding increase in P^{tr}. An increase in a (holding all other parameters constant) causes an increase in P_1, and a corresponding decrease in P^{tr}. An increase in R_o (holding all other parameters constant) causes a decrease in P_1 and a corresponding increase in P^{tr}. An increase in the mean molten metal pressure, P_o, causes a decrease in P_1, and a corresponding increase in P^{tr}. The contact resistance sensitivity, $\overline{R}'$, first appears in the coefficient of $\overline{s}_o^6$. Hence, for early solidification times, the contact pressure variation with time at the mold surface troughs is essentially controlled through uncoupled physics since the sensitivity is more of a longer time effect. The remaining perturbation quantities are written in dimensional form in Appendix C.

Gap nucleation occurs when

$$P^{tr}=0. \tag{95}$$

If $P^{tr}>0$ during the time frame of interest, then gaps will not nucleate in the troughs.

At gap nucleation, we require that each of the perturbation quantities be much less than one, except for P_1, which must be of the same order as P_o. This requires that Eq. (95) be subject to the following restriction via perturbation of Eq. (6):

$$-\frac{R' P_o}{R_o} \ll 1 \tag{96}$$

(the derivation of Eq. (96) is found in Appendix D). This limits the present analysis to either weakly coupled systems, or the extreme case of a fully uncoupled system.

6 Results and Discussion

Prior to conducting an examination of gap nucleation for pure metal systems, we verified that at sufficiently long times, the dimensionless perturbation quantities $\overline{s_1}$, $\overline{P_1}$, $\overline{Q_1}$, and $\overline{T_1}$ tend smoothly to zero. Following the method of Li and Barber [8], each quantity was numerically evaluated as a function of the dimensionless time variable, $\tau_o(\eta)$ (which is the dimensionless form of Eq. (29)), for selected mean contact resistances, $\overline{R_o}$, over a range of $0.1<\overline{R_o}<50$, for a fixed value of the dimensionless contact resistance sensitivity, $\overline{R'}$. It was verified that each quantity tended smoothly to zero for sufficiently large $\tau_o(\eta)$. As a second test, each perturbation quantity was evaluated for a fixed value of $\overline{R_o}$, running through a range of $\overline{R'}$ from $-0.1>\overline{R'}>-300$. Again, each of the perturbation quantities tended smoothly to zero at sufficiently large values of $\tau_o(\eta)$. This provided the confidence we needed to proceed to the gap nucleation analysis.

We wish to examine gap nucleation during the solidification of pure aluminum and iron shells. In particular, it is of interest to examine how the mold surface wavelength affects gap nucleation time and the mean shell thickness at gap nucleation for these two materials. In order to accomplish this, we propose to fix the amplitude, a, of the mold surface and vary the wavelength. As a consequence, a variation of the wavelength results in a variation in the aspect ratio, ϵ, given by Eq. (8), and hence a variation in the slope of the asperities relative to the planar reference results (see Eq. (55)). The following question then remains: Why not fix the wavelength, λ, and vary the amplitude, a? In practice, either approach could be followed. From a theoretical standpoint, Eq. ($C2$) shows that an increase in λ (holding the other process parameters fixed) results in a corresponding decrease in the lowest-order term of the heat flux perturbation, Q_1. A similar effect is at hand when the amplitude, a, is decreased. However, it has generally been the case in the experimental literature on mold surface topography design, wherein groove-type surface morphologies are applied, that the wavelength is varied while the amplitude of the topography is held fixed (see, for example, [13]). This is perhaps an attempt to avoid inducing failure sites into thin molds that are common to many commercial casting processes. In practice, the molten metal will not perfectly wet the mold surface (i.e., it will not completely fill the trough regions) due to surface tension effects, and hence we anticipate a diminishing return from variation of a.

Since the contact resistance sensitivity, R', appears in the sixth-order term in Eq. (93), indicating that it is a longer time effect, we choose to limit our analysis to the case of fully uncoupled systems. The elevated temperature material properties used in the calculations are specified in Table 1.

Figure 2 shows the variation of P^{tr} versus t as predicted by the short time solution and that due to numerical solution of Eqs. (84) and (85) (followed by conversion to dimensional coordinates via Eqs. (83)), for selected wavelengths (in millimeters), during solidification of pure aluminum. The solid curves are those due to the short time solution, given by Eq. (93), and the dashed curves are those due to the numerical solution. The process parameters used to generate this figure were $P_o=8000$ Pa, $a=1$ μm, and $R_o=10^{-3}$ m^2 sec°C/J. Note that the turn around in each of the short time curves, which denotes the limit of validity of the short time solution, is more sudden at the shorter wavelengths (over the chosen time range). Each of the curves predicted by the long time solution, however, proceeds to decrease in a linear fashion. Their intersections with the $P^{tr}=0$ axis denote a gap nucleation time (negative values of P^{tr} have no meaning in the present context). For design purposes, reasonable estimates of the gap nucleation times can be obtained from the series solution by simply ignoring the turnarounds, and subsequently extending the linear portion on the curves toward the $P^{tr}=0$ axis. The resulting values overestimate the gap nucleation time (with the estimates becoming progressively worse with increasing λ) compared with their counterparts from the numerical solution.

Table 1 Material properties for pure aluminum and iron

	Material		
		Fe	
Property	Al	Value	Fe Reference
T_f (°C)	660	1536	[14]
$K\ \left(\frac{\mathrm{W}}{\mathrm{m\cdot °C}}\right)$	229.4	36.2	[15]
$\rho\ \left(\frac{\mathrm{kg}}{\mathrm{m}^3}\right)$	2650	7265	[16]
$L\ \left(10^5\frac{\mathrm{J}}{\mathrm{kg}}\right)$	3.9	2.7	[17]
E (10^{10} Pa)	6.0	14.4	[18]
α (10^{-6} °C^{-1})	37.8	23.4	[19]
ν	0.33	0.33	[18]

Figure 3 shows the numerical solution for P^{tr} versus t for pure aluminum and selected wavelengths. The process parameters are $P_o=10{,}000$ Pa, $a=1$ μm, and $R_o=10^{-3}$ m^2 sec°C/J. The smaller wavelengths lead to faster gap nucleation, while larger wavelengths, such as $\lambda=50.0$ mm, do not lead to gap nucleation over the time frame of interest. If metallurgical requirements are such that the shell must retain contact with the mold during the first two

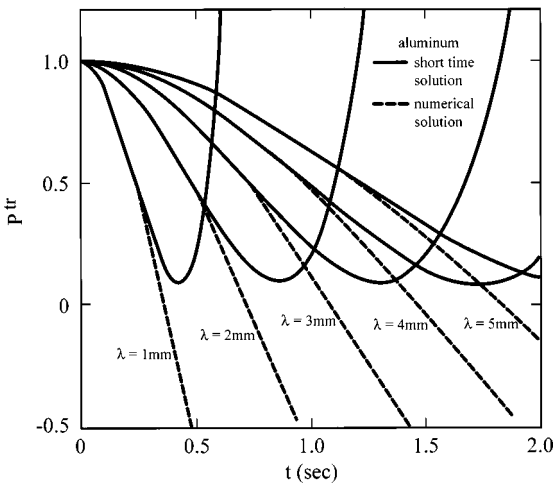

Fig. 2 Evolution of P^{tr} at selected λ for pure aluminum as predicted by short time solution and numerical solution. $P_o=8000$ Pa, $a=1.0$ μm, and $R_o=10^{-3}$ m^2 sec°C/J. Note that the short time solution predicts a fictitious turn around in P^{tr} for all cases.

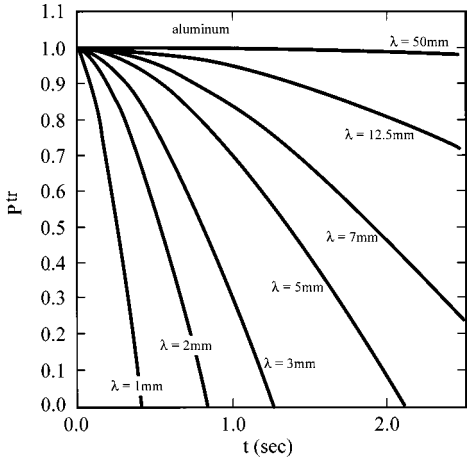

Fig. 3 Evolution of P^{tr} at selected λ for pure aluminum solidification with P_o=10,000 Pa, a=1.0 μm, R_o=10^{-3} m^2 sec°C/J (numerical solution)

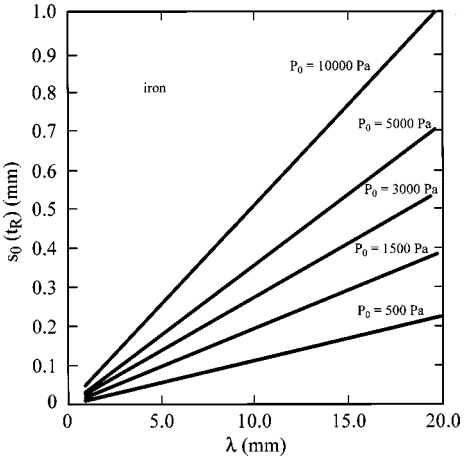

Fig. 6 Mean shell thickness variation with λ for pure iron solidification at selected P_o for a=1.0 μm, R_o=10^{-3} m^2 sec°C/J (numerical solution)

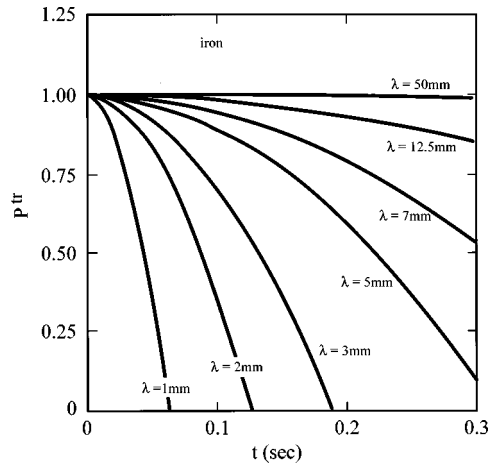

Fig. 4 Evolution of P^{tr} at selected λ for pure iron solidification with P_o=10,000 Pa, a=1.0 μm, R_o=10^{-3} m^2 sec°C/J (numerical solution)

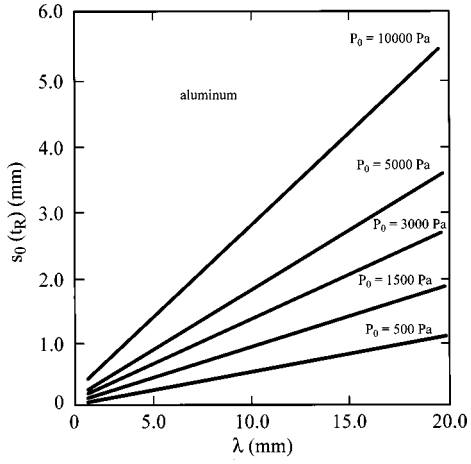

Fig. 5 Mean shell thickness variation with λ for pure aluminum solidification at selected P_o for a=1.0 μm, R_o=10^{-3} m^2 sec°C/J (numerical solution)

seconds or so, then the present theory suggests that a mold surface having a wavelength of λ = 12.5 mm (or greater) might be a reasonable choice.

Figure 4 shows the numerical solution for P^{tr} versus t for pure iron with the same process conditions used for Fig. 3. It is interesting to note that while the same observations made for Fig. 3 are applicable to Fig. 4, there is one important difference between pure aluminum and pure iron that is highlighted by Fig. 4: The time to gap nucleation for pure iron is nearly an order-of-magnitude smaller than that for pure aluminum. This difference is largely controlled by the quantity $E\alpha T_f/K$ for fixed a/P_oR_o (see Eq. (93) and Table 1).

Figures 5 and 6 show s_o evaluated at the gap nucleation time as a function of λ, at selected P_o. Note that $s_o(0)=0$ for all cases. A linear variation with λ is predicted for any given value of P_o. Shell growth is improved at higher pressures and longer wavelengths. Note that under the same process conditions, s_o for the pure aluminum shell is of the order of millimeters, whereas s_o for the pure iron shell is of the order of hundreds of microns.

7 Conclusions

A model of pure metal solidification on a sinusoidal mold surface was developed for the purpose of examining the gap nucleation process at the mold/shell interface. Gap nucleation was assumed to occur when the contact pressure locally fell to zero. The contact pressure was found to consist of a superposition of the mean pressure from the molten metal and a time and position-dependent perturbation which led to changes in the contact pressure due to the evolving distortion. The evolving distortion of the metal shell was initiated by the small lateral component of heat flux due to the geometry of the mold surface.

A series expansion for the contact pressure at the mold surface troughs, which was limited to early solidification times, was derived and compared with a numerical solution which was appropriate for all times. The numerical solution predicted that the contact pressure always falls to zero at the troughs. However, the series solution was only valid over a limited time range prior to gap nucleation since it suffered a turnaround toward increasing values of the contact pressure. It was concluded that the series solution could still provide an estimate of gap nucleation time for preliminary design purposes through a linear extrapolation to the time axis. An additional insight provided by the series solution was that coupling between the thermal and mechanical fields at the metal-shell interface becomes important at longer solidification times.

It was found that increasing the mold surface wavelength (while fixing the amplitude) led to longer gap nucleation times. Also, the mean shell thickness increased with increasing wavelength under the same conditions. Gap nucleation was faster for the iron shell than it was for the aluminum shell under identical process conditions.

Although in the sinusoidal case the pressure perturbation first becomes zero at a trough, there is no reason why this should necessarily be the case for a non-sinusoidal profile. In this more general case, a different criterion might be relevant (for example the point of greatest curvature), which happens to coincide with a profile trough in the special sinusoidal case examined in this paper.

The linearization of the resistance relation introduces a fairly severe restriction on the extent to which we can examine the coupling process at shorter times. With a slightly more numerical treatment in the present theoretical framework, however, it should be possible to implement a more realistic expression for the contact resistance variation with pressure during directional solidification. This could be achieved from data via experiments such as those reported by Nishida and Matsubara [20].

The present theory assumes that the metal shell is hypoelastic. Although the constitutive law can be modified to account for strain relaxation due to viscous creep, it is anticipated that, during the early stages of solidification, creep effects will introduce higher order corrections to the contact pressure similar to that due to the contact resistance sensitivity in the present model. We suspect that same to be true for the case of finite thermal diffusivity (and hence nonzero Stefan number).

Acknowledgments

The authors wish to express their gratitude to F. Yigit of King Saud University, J. R. Barber of the University of Michigan and D. Weirauch of Alcoa Technical Center for providing critical reviews of the manuscript. The authors are grateful to W. R. D. Wilson of the University of Washington for several stimulating discussions on the mold surface wavelength effect in casting processes.

Appendix A

Expression for $\bar{b}_2(\eta)$.

$$\bar{b}_2(\eta)=\frac{1}{2\cosh(\eta)}\left[\begin{array}{c}\left(\dfrac{1-2\nu}{1-\nu}\right)\left[\dfrac{\eta\,\mathrm{sech}(\eta)}{1-2\nu}+\sinh(\eta)\right]+\eta\bar{w}[\bar{g}''(\eta)-\bar{g}(\eta)]-2\bar{g}(\eta)\\ -\dfrac{1}{(\eta+\bar{R}_o)}\{\eta\overline{ws_1}(\eta)+2\bar{R}_o\sinh(\eta)+[\bar{s}_1(\eta)\sinh(\eta)+\bar{s}_1'(\eta)\cosh(\eta)][\sinh(\eta)-\eta\,\mathrm{sech}(\eta)]\}\end{array}\right] \tag{A1}$$

Appendix B

Coefficients of Eqs. (88) and (89) for $N=5$.

$$\hat{A}_1=0\quad;\quad \hat{A}_2=-\frac{1}{2}\quad;\quad \hat{A}_3=\frac{2-\bar{R}'}{6\bar{R}_o}\quad;\quad \hat{A}_4=-\left(\frac{8-5\bar{R}_o^2-7\bar{R}'}{24\bar{R}_o^2}\right)$$

$$\hat{A}_5=\frac{40-12(3-\bar{R}')\bar{R}_o^2-47\bar{R}'}{120\bar{R}_o^3}\quad;\quad \hat{B}_2\rightarrow Arbitrary\quad;\quad \hat{B}_3=\frac{1}{6(1-\nu)}$$

$$\hat{B}_4=\frac{2\hat{B}_2\bar{R}_o-1}{12\bar{R}_o}\quad;\quad \hat{B}_5=\frac{18+3\bar{R}_o^2-5\bar{R}'-\nu(18-5\bar{R}')}{180(1-\nu)\bar{R}_o^2}\quad \hat{B}_6=\frac{300-8\bar{R}_o^2-155\bar{R}'-24\hat{B}_2\bar{R}_o^3}{2880\bar{R}_o^3} \tag{B1}$$

Appendix C

Expression for s_1, Q_1, and $T_1(0,t)$.

$$s_1=a\left[1-2\left(\frac{\bar{s}_o}{\Lambda}\right)^2\left\{1-\left(\frac{2-\bar{R}'}{3}\right)\bar{s}_o+\left(\frac{8-7\bar{R}'-20/\Lambda^2}{12}\right)\bar{s}_o^2-\left(\frac{40-47\bar{R}'-48\{3-\bar{R}'\}/\Lambda^2}{60}\right)\bar{s}_o^3\right\}+\cdots\right] \tag{C1}$$

$$Q_1=\frac{4T_f a}{KR_o^2}\left(\frac{\bar{s}_o}{\Lambda}\right)^2\left[\left(1-\frac{\bar{R}'}{2}\right)-\left(\frac{7-5\bar{R}'}{3}\right)\bar{s}_o+\left(\frac{96-8\{8-\bar{R}'\}/\Lambda^2-87\bar{R}'}{24}\right)\bar{s}_o^2-\left(\frac{3\{240-259\bar{R}'\}-4\{256-70\bar{R}'\}/\Lambda^2}{120}\right)\bar{s}_o^3\right.$$
$$\left.+\left(\frac{8640-10044\bar{R}'-4\{2512-370\bar{R}'-45\bar{R}'^2\}/\Lambda^2-32\{155+16\bar{R}'\}/\Lambda^4}{1440}\right)\bar{s}_o^4-\cdots\right] \tag{C2}$$

$$T_1(0,t)=-\frac{aT_f}{KR_o}\left[1+(1-4/\Lambda^2)\bar{s}_o^2-\left(\frac{3-4\{7-2\bar{R}'\}/\Lambda^2}{3}\right)\bar{s}_o^3+\left(\frac{6-\{96-51\bar{R}'\}/\Lambda^2+64/\Lambda^4}{6}\right)\bar{s}_o^4\right.$$
$$\left.-\left(\frac{30-3\{240-179\bar{R}'\}/\Lambda^2+16/\Lambda^4}{30}\right)\bar{s}_o^5+\left(\frac{90-9\{240-179\bar{R}'\}/\Lambda^2+2\{1256-67\bar{R}'\}/\Lambda^4+1240/\Lambda^6}{90}\right)\bar{s}_o^6-\cdots\right] \tag{C3}$$

Appendix D

Derivation of Eq. (96). Differentiation of the resistance relation Eq. (6) gives

$$T_1 = Q_1 R(P_o) + Q_o R' P_1 . \tag{D1}$$

Substitution of the following ratios

$$\tilde{Q} = \frac{Q_1}{Q_o} \quad \tilde{P} = \frac{P_1}{P_o} \quad \tilde{T} = \frac{T_1}{T_o} \tag{D2}$$

into Eq. (*D*1) gives

$$T_o \tilde{T} = Q_o \tilde{Q} R_o + Q_o R' \tilde{P} P_o . \tag{D3}$$

Dividing Eq. (*D*3) by T_o, and using Eq. (18) gives

$$\tilde{T} = \tilde{Q} + \frac{R' P_o \tilde{P}}{R_o} . \tag{D4}$$

We impose the conditions that $\tilde{T} \ll 1, \tilde{Q} \ll 1$, but $\tilde{P} = -1$ since P_1 is to be of the same order as P_o. Based on these conditions, Equation (*D*4) gives

$$-\frac{R' P_o}{R_o} \ll 1. \tag{D5}$$

References

[1] Nishida, Y., Droste, W., and Engler, S., 1986, ''The Air-Gap Formation Process at the Casting-Mold Interface and the Heat Transfer Mechanism through the Gap,'' Metall. Trans. B, **17**, pp. 833–844.

[2] Neymark, V. Y., 1955, ''Influence and Inoculants and Crystallization Conditions on the Quality of the Skin of the Ingot,'' *Transactions of the First All-Union Conference on Continuous Steel Casting*, Izd-vo Akademii Nauk SSSR (Russian Academy of Sciences), Moscow, pp. 222–240.

[3] Cisse, J., Cole, G. S., and Bolling, G. F., 1971, ''Freezing Front Asymmetry During Ingot Solidification of Aluminum and Its Alloys,'' AFS Cast Met. Res. J., **7**, pp. 158–161.

[4] Singh, S. N., and Blazek, K. E., 1974, ''Heat Transfer and Skin Formation in a Continuous-Casting Mold as a Function of Carbon Content,'' J. Met., **26**, pp. 17–27.

[5] Wray, P. J., 1977 ''Non-Uniform Growth of a Plate on a Chilled Surface,'' presented at the Annual Meeting of AIME, Atlanta, GA, Mar. 6–10.

[6] Weirauch, Jr., D. A., and Giron, A., 1999, ''The Early Stages of Aluminum Solidification in the Presence of a Moving Meniscus,'' *Proceedings on the Integration of Material, Process and Product Design—A Conference dedicated to the 70th birthday of Owen Richmond*, A. A. Balkema Publishers, Rotterdam, Netherlands, pp. 183–191.

[7] Richmond, O., Hector, Jr., L. G., and Fridy, J. M., 1990, ''Growth Instability During Nonuniform Directional Solidification of Pure Metals,'' ASME J. Appl. Mech., **57**, pp. 529–536.

[8] Li, N.-Y., and Barber, J. R., 1991, ''Thermoelastic Instability in Planar Solidification,'' Int. J. Mech. Sci., **33**, pp. 945–959.

[9] Hector, Jr., L. G., Li, N.-Y., and Barber, J. R., 1994, ''Strain Rate Relaxation Effect on Freezing Front Growth Stability During Planar Solidification of Pure Metals. Part 1. Uncoupled Theory,'' J. Thermal Stresses, **17**, pp. 619–646.

[10] Yigit, F., and Barber, J. R., 1992, ''Effect of Thermal Capacity on the Development of Sinusoidal Perturbation During the Unidirectional Solidification of Pure Metals,'' *Micro/Macro Scale Phenomena in Solidification*, ASME, New York, pp. 141–150.

[11] Yigit, F., 1997, ''Effect of Mold Properties on Thermoelastic Instability in Unidirectional Planar Solidification,'' J. Thermal Stresses, **21**, No. 1, pp. 55–81.

[12] Westergaard, H. M., 1964, *Theory of Elasticity and Plasticity*, Dover, New York.

[13] Murakami, H., Suzuki, M., Kitagawa, T., and Miyahara, S., 1992, ''Control of Uneven Solidification of Hypoperitectic Carbon Steels in Continuous Casting Molds,'' Tetsu to Hagane, **78**, pp. 105–112.

[14] Bolz, R. E., and Tuve, G. L., 1984, *CRC Handbook of Tables for Applied Engineering and Science*, 2nd Ed., CRC Press, Boca Raton, FL.

[15] Touloukian, Y. S., Powell, R. W., Ho, C. Y., and Klemens, P. G., 1970, *Thermophysical Properties of Matter, Thermal Conductivity*, Vol. 1, IFI/Plenum, New York.

[16] Lucas, L. D., 1972, ''Density of Metals at High Temperatures in the Solid and Molten States. Part 1,'' Mem. Sci. Rev. Met., **69**, No. 5, pp. 395–409.

[17] Baumeister, T., Avallone, E. A., and Baumeister, III, T., 1978, *Mark's Standard Handbook for Mechanical Engineers*, 8th ed., McGraw-Hill, New York.

[18] Wawra, H. H., 1974, ''The Elastomechanical Properties of Pure Iron and FeS_2 in Different Crystallographic Directions as a Function of Temperature and Pressure,'' Arch. Eisenhuettenwes., **45**, No. 5, pp. 317–320.

[19] Touloukian, Y. S., Kirby, R. K., Taylor, R. E., and Desai, P. D., 1978, *Thermophysical Properties of Matter, Thermal Expansion*, Vol. 12, IFI/Plenum, New York.

[20] Nishida, Y., and Matsubara, H., 1976, ''Effect of Pressure on Heat Transfer at the Metal Mould-Casting Interface,'' British Foundryman, **69**, No. 11, pp. 274–278.

Interaction Between a Semi-Infinite Crack and a Screw Dislocation in a Piezoelectric Material

Kang Yong Lee

Won Gyu Lee[1]

Department of Mechanical Engineering,
Yonsei University,
Seoul 120-749, Korea

Y. Eugene Pak

Micro Systems Laboratory,
System and Control Sector,
Samsung Advanced Institute
of Technology and CRI,
P.O. Box 111,
Suwon 440-600, Korea

The interaction between a semi-infinite crack and a screw dislocation under antiplane mechanical and in-plane electrical loading in a linear piezoelectric material is studied in the framework of linear elasticity theory. A straight dislocation with the Burgers vector normal to the isotropic basal plane near a semi-infinite crack tip is considered. In addition to having a discontinuous electric potential across the slip plane, the dislocation is subjected to a line-force and a line-charge at the core. The explicit solution for the model is derived by means of complex variable and conformal mapping methods. The classical $1/\sqrt{r}$ singularity is observed for the stress, electric displacement, and electric field at the crack tip. The force on a screw dislocation due to the existence of a semi-infinite crack subjected to external electromechanical loads is calculated. Also, the effect of the screw dislocation with the line-force and line-charge at the core on the crack-tip fields is observed through the field intensity factors and the crack extension force.
[S0021-8936(00)01501-4]

1 Introduction

Due to their intrinsic electromechanical coupling phenomenon, piezoelectric materials are used widely in the device applications such as high-power sonar transducers, electromechanical actuators, and piezoelectric power supplies. It is well known that defects, such as dislocations, cracks, cavities, and inclusions, can adversely influence the performance of such piezoelectric devices. These defects carrying charges in piezoelectric semiconductors, for example, can be sources of internal electro-elastic fields ([1]). Therefore, to predict the performance and integrity of these devices, it is important that the behavior of various defects in electrical and mechanical fields is analyzed. Deeg [2] examined the effect of a dislocation, a crack, and an inclusion on the coupled response of piezoelectric solids theoretically. Pak [3] considered the problem of a finite crack in an unbounded piezoelectric medium subjected to far-field antiplane electromechanical loads. In the paper, it was shown that the traditional square root stress singularities exist near the crack tip. Sosa and Pak [4] did a three-dimensional eigenfunction analysis of a semi-infinite crack in a piezoelectric material, while Pak [5] considered a screw dislocation in a material and derived the generalized Peach-Koehler forces acting on a screw dislocation subjected to external loads. Kuo and Barnett [6] and Suo et al. [7] studied the singularities of interfacial cracks in bonded anisotropic piezoelectric media. Recently, efforts have been made to develop inclusion models in a piezoelectric material ([8–12]). The results on the interaction between defects in the piezoelectric media are very rare. Meguid and Deng [13] discussed the electro-elastic interaction between a screw dislocation and an elliptical inhomogeneity in piezoelectric media. But they obtained only the distributions of the fields, not the direct interaction of forces acting on each other.

In the purely elastic case, however, many researchers considered such defect interaction problems. For example, Majumdar and Burns [14] considered the screw dislocations positioned near the crack tip, while Ohr et al. [15] studied the condition for the emission of dislocations from a semi-infinite wedge crack to determine the ductile versus brittle fracture behavior in metals.

Considered in this paper is a simple continuum model of a single screw dislocation near a semi-infinite crack in a hexagonal piezoelectric crystal subjected to antiplane mechanical and in-plane electrical loading. The analysis is carried out in the framework of linear elasticity theory without consideration of nonlinear response due to domain wall motion in ferroelectric materials ([16,17]). The dislocation line is assumed to be straight and is located perpendicular to the isotropic basal plane in a hexagonal crystal exhibiting 6-mm symmetry. An infinitely long screw dislocation suffering a finite discontinuity in the displacement and in the electric potential across the slip plane is modeled. The displacement jump across the slip plane corresponds to the Burgers vector **b**, which is perpendicular to the basal plane. The jump in the electric potential (''electric-potential-dislocation'') corresponds to the electric dipole layer along the slip plane. The dislocation core is subjected to a line-force and a line-charge.

In this work, conformal mapping and complex variable approach are used to solve the governing equations. Using the generalized Peach-Koehler force, we will calculate the forces acting on a piezoelectric screw dislocation near the semi-infinite crack, and discuss the effect of a screw dislocation and a line-force/charge on the field intensity factors and the crack extension force acting on the crack tip. The relation between the crack extension force and the field intensity factors will be presented.

2 A Screw Dislocation Near a Semi-Infinite Crack

Let us examine a piezoelectric material containing a charged screw dislocation near a semi-infinite crack, wherein the crack front is parallel to the *z*-axis as shown in Fig. 1. Consider a screw dislocation located at a point (x_0, y_0), which is assumed to be straight and infinitely long in the *z*-direction, suffering a finite discontinuity in the displacement and electric potential across the

[1]Presently at Daewoo Motor Technical Center, 199 Chongchon-Dong, Pupyong-Gu, Inchon 403-714, Korea.

Contributed by the Applied Mechanics Division of THE AMERICAN SOCIETY OF MECHANICAL ENGINEERS for publication in the ASME JOURNAL OF APPLIED MECHANICS. Manuscript received by the ASME Applied Mechanics Division, July 7, 1999; final revision, Sept. 21, 1999. Associate Technical Editor: J. R. Barber. Discussion on the paper should be addressed to the Technical Editor, Professor Lewis T. Wheeler, Department of Mechanical Engineering, University of Houston, Houston, TX 77204-4792, and will be accepted until four months after final publication of the paper itself in the ASME JOURNAL OF APPLIED MECHANICS.

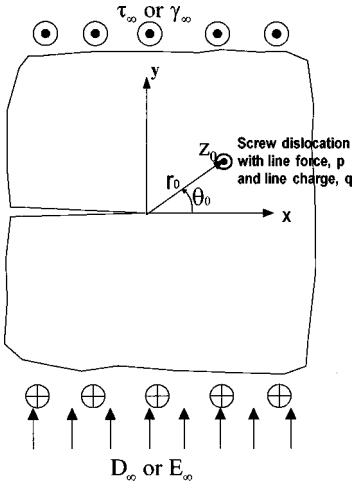

Fig. 1 A screw dislocation with a line-force and a line-charge near a semi-infinite crack in a piezoelectric material

slip plane. The dislocation has a line-force and a line-charge along its core. In this configuration, the piezoelectric boundary value problem is simplified considerably because only the out-of-plane displacement and the in-plane electric fields exist such that

$$u_x=u_y=0, \quad u_z=u_z(x,y),$$
$$E_x=E_x(x,y), \quad E_y=E_y(x,y), \quad E_z=0. \tag{1}$$

In this case the constitutive relations become

$$\sigma_{zx}=c_{44}\frac{\partial u_z}{\partial x}+e_{15}\frac{\partial \phi}{\partial x}, \quad D_x=e_{15}\frac{\partial u_z}{\partial x}-\epsilon_{11}\frac{\partial \phi}{\partial x},$$
$$\sigma_{zy}=c_{44}\frac{\partial u_z}{\partial y}+e_{15}\frac{\partial \phi}{\partial y}, \quad D_y=e_{15}\frac{\partial u_z}{\partial y}-\epsilon_{11}\frac{\partial \phi}{\partial y} \tag{2}$$

where σ_{kz}, D_k, $(k=x,y)$, c_{44}, ϵ_{11}, e_{15} and ϕ are the stress tensor, the electric displacement vector, the elastic modulus measured in a constant electric field, the dielectric permittivity measured at a constant strain, the piezoelectric constant and the electric potential, respectively.

The governing equations are simplified to

$$c_{44}\nabla^2 u_z+e_{15}\nabla^2\phi=0$$
$$e_{15}\nabla^2 u_z-\epsilon_{11}\nabla^2\phi=0. \tag{3}$$

These simplified governing equations can be made in the forms

$$\nabla^2 u_z=0, \quad \nabla^2\phi=0. \tag{4}$$

We will consider four possible cases of far-field boundary conditions as follows:

$$\text{Case 1: } \sigma_{zy}=\tau_\infty \text{ and } D_y=D_\infty,$$
$$\text{Case 2: } \gamma_{zy}=\gamma_\infty \text{ and } E_y=E_\infty,$$
$$\text{Case 3: } \sigma_{zy}=\tau_\infty \text{ and } E_y=E_\infty,$$
$$\text{Case 4: } \gamma_{zy}=\gamma_\infty \text{ and } D_y=D_\infty. \tag{5}$$

where τ_∞, γ_∞, D_∞, and E_∞ are an uniform shear traction, shear strain, electric displacement, and electric field, respectively. The boundary condition on the upper and the lower surfaces of the crack is free of the surface traction and the surface charge for all cases of far-field loading conditions ([3])

$$\sigma_{zy}=0, \qquad D_y=0 \text{ at } x<0, \ y=0. \tag{6}$$

The solution for the governing Eq. (4) can be found by letting u_z and ϕ be the real parts of some analytic functions such that

$$u_z=\mathrm{Re}\,U(Z), \qquad \phi=\mathrm{Re}\,\Phi(Z), \tag{7}$$

where

$$U(Z)=A_1\log(\sqrt{Z}-\sqrt{Z_0})(\sqrt{Z}+\sqrt{\overline{Z_0}})$$
$$+A_2 i\log\frac{\sqrt{Z}-\sqrt{Z_0}}{\sqrt{Z}+\sqrt{\overline{Z_0}}}+Ci\sqrt{Z},$$
$$\Phi(Z)=B_1\log(\sqrt{Z}-\sqrt{Z_0})(\sqrt{Z}+\sqrt{\overline{Z_0}}) \tag{8}$$
$$+B_2 i\log\frac{\sqrt{Z}-\sqrt{Z_0}}{\sqrt{Z}+\sqrt{\overline{Z_0}}}+Di\sqrt{Z}.$$

The first term corresponds to the line-force/charge and its image, the second to the dislocation and its image, and the third to the uniform external loads. A_1, A_2, B_1, B_2, C, and D are all real constants which are determined by the displacement and electric potential jump conditions across the slip plane, the force and charge balance conditions at the core, and the far-field loading conditions at infinity. $Z(=x+iy)$ is a complex variable.

The strains, the electric fields, the stresses, and the electric displacements can then be expressed in the forms

$$\gamma_{zx}=\frac{\partial u_z}{\partial x}=\frac{\partial u_z}{\partial Z}=\mathrm{Re}\,U'(Z),$$
$$\gamma_{zy}=\frac{\partial u_z}{\partial y}=i\left(\frac{\partial u_z}{\partial Z}\right)=-\mathrm{Im}\,U'(Z),$$
$$E_x=-\frac{\partial \phi}{\partial x}=-\frac{\partial \phi}{\partial Z}=-\mathrm{Re}\,\Phi'(Z), \tag{9}$$
$$E_y=-\frac{\partial \phi}{\partial y}=-i\left(\frac{\partial \phi}{\partial Z}\right)=\mathrm{Im}\,\Phi'(Z).$$
$$\sigma_{zx}=\mathrm{Re}[c_{44}U'(Z)+e_{15}\Phi'(Z)],$$
$$\sigma_{zy}=-\mathrm{Im}[c_{44}U'(Z)+e_{15}\Phi'(Z)],$$
$$D_x=\mathrm{Re}[e_{15}U'(Z)-\epsilon_{11}\Phi'(Z)], \tag{10}$$
$$D_y=-\mathrm{Im}[e_{15}U'(Z)-\epsilon_{11}\Phi'(Z)].$$

Consider a contour C with the outer normal unit vector, n_i, surrounding the dislocation core. The z-component of the Burgers vector is equal to the jump in the displacement across the slip plane $(x>x_0, \ y=y_0)$:

$$b=\Delta u_z=u_z(x,y_0^-)-u_z(x,y_0^+)=\mathrm{Re}[\Delta U(Z)], \tag{11}$$

where Δ denotes the jump across the slip plane. Similarly, the jump in the electric potential, $\Delta\phi$, across the slip plane is

$$\Delta\phi=\phi(x,y_0^-)-\phi(x,y_0^+)=\mathrm{Re}[\Delta\Phi(Z)]. \tag{12}$$

From the Eqs. (10)–(12), we obtain

$$A_2=-\frac{b}{2\pi}, \qquad B_2=-\frac{\Delta\phi}{2\pi}. \tag{13}$$

The z-component of the traction integrated along the contour C must balance the line-force, p, applied at the core in the z-direction:

$$-p=\oint_C \sigma_{zj}n_j dl. \tag{14}$$

From an infinitely narrow rectangle contour C containing the dislocation, we obtain

$$p = -2\pi[c_{44}A_1 + e_{15}B_1]. \tag{15}$$

Similarly for the charge balance we obtain

$$q = \oint_C D_i n_i dl = 2\pi[e_{15}A_1 - \epsilon_{11}B_1]. \tag{16}$$

From these balance conditions we obtain

$$A_1 = \frac{-\epsilon_{11}p + e_{15}q}{2\pi(c_{44}\epsilon_{11} + e_{15}^2)}, \qquad B_1 = -\frac{e_{15}p + c_{44}q}{2\pi(c_{44}\epsilon_{11} + e_{15}^2)}. \tag{17}$$

Extending the traditional concept of stress intensity factor, K^σ, to other field variables, we introduce the electric field intensity factor, K^E, the strain intensity factor, K^s and the electric displacement intensity factor, K^D. Using these field intensity factors, we can represent the far-field loads as follows:

$$\begin{aligned} E_y = E_\infty &= -\mathrm{Im}\left[-\frac{iK^E}{\sqrt{2\pi Z}}\right], \quad \gamma_{zy} = \gamma_\infty = -\mathrm{Im}\left[-\frac{iK^s}{\sqrt{2\pi Z}}\right], \\ \sigma_{zy} = \tau_\infty &= -\mathrm{Im}\left[-\frac{iK^\sigma}{\sqrt{2\pi Z}}\right], \quad D_y = D_\infty = -\mathrm{Im}\left[-\frac{iK^D}{\sqrt{2\pi Z}}\right], \end{aligned} \quad \text{as } Z \to \infty. \tag{18}$$

At infinity we obtain

$$U'(Z) = \frac{Ci}{2\sqrt{Z}}, \qquad \Phi'(Z) = \frac{Di}{2\sqrt{Z}}, \quad \text{as } Z \to \infty. \tag{19}$$

Substituting Eqs. (18) and (19) into Eqs. (9) and (10), we obtain

$$\text{Case 1: } C = -\sqrt{\frac{2}{\pi}}\frac{\epsilon_{11}K^\sigma + e_{15}K^D}{c_{44}\epsilon_{11} + e_{15}^2}, \qquad D = -\sqrt{\frac{2}{\pi}}\frac{e_{15}K^\sigma - c_{44}K^D}{c_{44}\epsilon_{11} + e_{15}^2} \tag{20}$$

$$\text{Case 2: } C = -\sqrt{\frac{2}{\pi}}K^s, \qquad D = \sqrt{\frac{2}{\pi}}K^E \tag{21}$$

$$\text{Case 3: } C = -\sqrt{\frac{2}{\pi}}\frac{K^\sigma + e_{15}K^E}{c_{44}}, \qquad D = \sqrt{\frac{2}{\pi}}K^E \tag{22}$$

$$\text{Case 4: } C = -\sqrt{\frac{2}{\pi}}K^s, \qquad D = -\sqrt{\frac{2}{\pi}}\frac{e_{15}K^s - K^D}{\epsilon_{11}}. \tag{23}$$

From these four results, we can define the relations $K^\sigma = c_{44}K^s - e_{15}K^E$ and $K^D = e_{15}K^s + \epsilon_{11}K^E$.

Substituting Eqs. (13), (17), and (20) into Eq. (10) and using Eqs. (9) and (10), we can obtain the following field variables for Case 1:

$$\sigma_{zx} = \mathrm{Re}\left[-\frac{p}{2\pi}L(Z) - \frac{c_{44}b + e_{15}\Delta\phi}{2\pi}iM(Z) - K^\sigma iN(Z)\right], \tag{24}$$

$$\sigma_{zy} = -\mathrm{Im}\left[-\frac{p}{2\pi}L(Z) - \frac{c_{44}b + e_{15}\Delta\phi}{2\pi}iM(Z) - K^\sigma iN(Z)\right],$$

$$\gamma_{zx} = \mathrm{Re}\left[\frac{-\epsilon_{11}p + e_{15}q}{2\pi(c_{44}\epsilon_{11} + e_{15}^2)}L(Z) - \frac{b}{2\pi}iM(Z) - \frac{\epsilon_{11}K^\sigma + e_{15}K^D}{c_{44}\epsilon_{11} + e_{15}^2}iN(Z)\right], \tag{25}$$

$$\gamma_{zy} = -\mathrm{Im}\left[\frac{-\epsilon_{11}p + e_{15}q}{2\pi(c_{44}\epsilon_{11} + e_{15}^2)}L(Z) - \frac{b}{2\pi}iM(Z) - \frac{\epsilon_{11}K^\sigma + e_{15}K^D}{c_{44}\epsilon_{11} + e_{15}^2}iN(Z)\right],$$

$$D_x = \mathrm{Re}\left[\frac{q}{2\pi}L(Z) - \frac{e_{15}b - \epsilon_{11}\Delta\phi}{2\pi}iM(Z) - K^D iN(Z)\right], \tag{26}$$

$$D_y = -\mathrm{Im}\left[\frac{q}{2\pi}L(Z) - \frac{e_{15}b - \epsilon_{11}\Delta\phi}{2\pi}iM(Z) - K^D iN(Z)\right],$$

$$E_x = -\mathrm{Re}\left[-\frac{e_{15}p + c_{44}q}{2\pi(c_{44}\epsilon_{11} + e_{15}^2)}L(Z) - \frac{\Delta\phi}{2\pi}iM(Z) - \frac{e_{15}K^\sigma - c_{44}K^D}{c_{44}\epsilon_{11} + e_{15}^2}iN(Z)\right],$$

$$E_y = \mathrm{Im}\left[-\frac{e_{15}p + c_{44}q}{2\pi(c_{44}\epsilon_{11} + e_{15}^2)}L(Z) - \frac{\Delta\phi}{2\pi}iM(Z) - \frac{e_{15}K^\sigma - c_{44}K^D}{c_{44}\epsilon_{11} + e_{15}^2}iN(Z)\right], \tag{27}$$

where

$$L(Z) = \left(\frac{1}{\sqrt{\bar{Z}_0}} - \frac{1}{\sqrt{Z_0}}\right)\frac{1}{2\sqrt{Z}} + \frac{1}{2\sqrt{Z_0}}\frac{1}{\sqrt{Z} - \sqrt{Z_0}} - \frac{1}{2\sqrt{\bar{Z}_0}}\frac{1}{\sqrt{Z} + \sqrt{\bar{Z}_0}},$$

$$M(Z) = -\left(\frac{1}{\sqrt{Z_0}} + \frac{1}{\sqrt{\bar{Z}_0}}\right)\frac{1}{2\sqrt{Z}} + \frac{1}{2\sqrt{Z_0}}\frac{1}{\sqrt{Z} - \sqrt{Z_0}} + \frac{1}{2\sqrt{\bar{Z}_0}}\frac{1}{\sqrt{Z} + \sqrt{\bar{Z}_0}}. \tag{28}$$

$$N(Z) = \frac{1}{\sqrt{2\pi Z}}.$$

In Eqs. (24)–(27), the first term is related to the line-loads, the second to the screw dislocation and the third to the external loads. The field variables of the Eqs. (24)–(27) reveal the classical $1/\sqrt{Z}$ (or $1/\sqrt{r}$ in the real coordinates) type of singularity near the crack tip.

3 Force on a Dislocation

The forces acting on a dislocation S with a line-force and a line-charge due to the stresses and the electrical fields generated by a crack T are obtained from the following relations ([5]):

$$F_x = b\sigma_{zy}^T + \Delta\phi D_y^T + p\gamma_{zx}^T + qE_x^T$$
$$F_y = -b\sigma_{zx}^T - \Delta\phi D_x^T + p\gamma_{zy}^T + qE_y^T. \tag{29}$$

The expressions for γ_{zi}^T, σ_{zi}^T, E_i^T, and D_i^T can be obtained by subtracting the fields generated by the dislocation from Eqs. (24)–(27) in the forms

$$\gamma_{zx}^T = \frac{1}{4r_0}\left\{\frac{-\epsilon_{11}p + e_{15}q}{2\pi(c_{44}\epsilon_{11}+e_{15}^2)}\tan\frac{\theta_0}{2}\sin\theta_0 + \frac{b}{2\pi}\left(\sin\theta_0 + \tan\frac{\theta_0}{2}\right)\right\} - \frac{\epsilon_{11}K^\sigma + e_{15}K^D}{c_{44}\epsilon_{11}+e_{15}^2}\frac{\sin\frac{\theta_0}{2}}{\sqrt{2\pi r_0}},$$
$$\gamma_{zy}^T = \frac{1}{4r_0}\left\{\frac{\epsilon_{11}p - e_{15}q}{2\pi(c_{44}\epsilon_{11}+e_{15}^2)}\tan\frac{\theta_0}{2}\cos\theta_0 - \frac{b}{2\pi}(\cos\theta_0+1)\right\} + \frac{\epsilon_{11}K^\sigma + e_{15}K^D}{c_{44}\epsilon_{11}+e_{15}^2}\frac{\cos\frac{\theta_0}{2}}{\sqrt{2\pi r_0}}, \tag{30}$$

$$\sigma_{zx}^T = \frac{1}{4r_0}\left\{-\frac{p}{2\pi}\tan\frac{\theta_0}{2}\sin\theta_0 + \frac{c_{44}b + e_{15}\Delta\phi}{2\pi}\left(\sin\theta_0 + \tan\frac{\theta_0}{2}\right)\right\} - K^\sigma\frac{\sin\frac{\theta_0}{2}}{\sqrt{2\pi r_0}},$$
$$\sigma_{zy}^T = \frac{1}{4r_0}\left\{\frac{p}{2\pi}\tan\frac{\theta_0}{2}\cos\theta_0 - \frac{c_{44}b + e_{15}\Delta\phi}{2\pi}(\cos\theta_0+1)\right\} + K^\sigma\frac{\cos\frac{\theta_0}{2}}{\sqrt{2\pi r_0}}, \tag{31}$$

$$E_x^T = \frac{1}{4r_0}\left\{\frac{e_{15}p + c_{44}q}{2\pi(c_{44}\epsilon_{11}+e_{15}^2)}\tan\frac{\theta_0}{2}\sin\theta_0 - \frac{\Delta\phi}{2\pi}\left(\sin\theta_0 + \tan\frac{\theta_0}{2}\right)\right\} + \frac{e_{15}K^\sigma - c_{44}K^D}{c_{44}\epsilon_{11}+e_{15}^2}\frac{\sin\frac{\theta_0}{2}}{\sqrt{2\pi r_0}},$$
$$E_y^T = \frac{1}{4r_0}\left\{-\frac{e_{15}p + c_{44}q}{2\pi(c_{44}\epsilon_{11}+e_{15}^2)}\tan\frac{\theta_0}{2}\cos\theta_0 + \frac{\Delta\phi}{2\pi}(\cos\theta_0+1)\right\} - \frac{e_{15}K^\sigma - c_{44}K^D}{c_{44}\epsilon_{11}+e_{15}^2}\frac{\cos\frac{\theta_0}{2}}{\sqrt{2\pi r_0}}, \tag{32}$$

$$D_x^T = \frac{1}{4r_0}\left\{\frac{q}{2\pi}\tan\frac{\theta_0}{2}\sin\theta_0 + \frac{e_{15}b - \epsilon_{11}\Delta\phi}{2\pi}\left(\sin\theta_0 + \tan\frac{\theta_0}{2}\right)\right\} - K^D\frac{\sin\frac{\theta_0}{2}}{\sqrt{2\pi r_0}},$$
$$D_y^T = \frac{1}{4r_0}\left\{-\frac{q}{2\pi}\tan\frac{\theta_0}{2}\cos\theta_0 - \frac{e_{15}b - \epsilon_{11}\Delta\phi}{2\pi}(\cos\theta_0+1)\right\} + K^D\frac{\cos\frac{\theta_0}{2}}{\sqrt{2\pi r_0}}. \tag{33}$$

In the purely elastic case, Eqs. (30)–(33) are reduced to the relations of Ohr et al. [15]. From Eqs. (29)–(33), we obtain

$$F_x = \frac{c_{44}q^2 + 2e_{15}pq - \epsilon_{11}p^2}{4\pi r_0(c_{44}\epsilon_{11}+e_{15}^2)}\sin^2\frac{\theta_0}{2} - \frac{c_{44}b^2 + 2e_{15}b\Delta\phi - \epsilon_{11}\Delta\phi^2}{4\pi r_0}\cos^2\frac{\theta_0}{2} + \frac{pb - q\Delta\phi}{4\pi r_0}\sin\theta_0 - \frac{p(\epsilon_{11}K^\sigma + e_{15}K^D) + q(c_{44}K^D - e_{15}K^\sigma)}{\sqrt{2\pi r_0}(c_{44}\epsilon_{11}+e_{15}^2)}\sin\frac{\theta_0}{2} + \frac{bK^\sigma + \Delta\phi K^D}{\sqrt{2\pi r_0}}\cos\frac{\theta_0}{2}, \tag{34}$$

$$F_y = -\frac{c_{44}q^2 + 2e_{15}pq - \epsilon_{11}p^2}{8\pi r_0(c_{44}\epsilon_{11}+e_{15}^2)}\cos\theta_0\tan\frac{\theta_0}{2} - \frac{c_{44}b^2 + 2e_{15}b\Delta\phi - \epsilon_{11}\Delta\phi^2}{8\pi r_0}\left(\sin\theta_0 + \tan\frac{\theta_0}{2}\right) - \frac{pb - q\Delta\phi}{4\pi r_0}\cos\theta_0 + \frac{p(\epsilon_{11}K^\sigma + e_{15}K^D) + q(c_{44}K^D - e_{15}K^\sigma)}{\sqrt{2\pi r_0}(c_{44}\epsilon_{11}+e_{15}^2)}\cos\frac{\theta_0}{2} + \frac{bK^\sigma + \Delta\phi K^D}{\sqrt{2\pi r_0}}\sin\frac{\theta_0}{2} \tag{35}$$

where a negative term contributes to the attractive force and a positive to the repulsive. In Eqs. (34) and (35) the first term is the interaction between the line-loads and the free surface of the crack; the second, the interaction between a screw dislocation and the crack surface; the third, the effect of the crack surface on the force generated by the line-loads acting on the screw dislocation; and the fourth and the fifth are, respectively, the effects of the external loads on the interactions between the crack tip and the line-loads, and between the crack tip and the screw dislocation. In case of no electrical and mechanical loads, Eqs. (34) and (35) can be reduced to the solutions of Majumdar and Burns [14]. Also, in case of no crack, the Eqs. (34) and (35) can be reduced to the solutions of Pak [5].

Let us consider the case of a screw dislocation with the line-loads near the free surface parallel to the *y*-axis, wherein the forces can be calculated without using the conformal mapping technique. The results are

$$F_x = -\frac{c_{44}b^2 + 2e_{15}b\Delta\phi - \epsilon_{11}\Delta\phi^2}{4\pi d} + \frac{c_{44}q^2 + 2e_{15}pq - \epsilon_{11}p^2}{4\pi d} + b\tau_\infty + \Delta\phi D_\infty, \tag{36}$$

$$F_y = \frac{p(\epsilon_{11}\tau_\infty + e_{15}D_\infty) + q(c_{44}D_\infty - e_{15}\tau_\infty)}{c_{44}\epsilon_{11}+e_{15}^2}. \tag{37}$$

The interaction between the line-loads and the free surface shows up in F_x, but vanishes in F_y. The third terms in Eqs. (34) and (35) do not appear in this case. Equations (36) and (37) are reduced to the solutions of Pak [5] in the absence of external loads.

4 Stress and Electric Displacement Intensity Factors

The resultant stress and electric displacement intensity factors can be calculated by the following relations, respectively,

$$K_R^\sigma = \lim_{Z\to 0}[\sqrt{2\pi Z}\sigma_{zy}], \qquad K_R^D = \lim_{Z\to 0}[\sqrt{2\pi Z}D_y]. \tag{38}$$

Substituting Eqs. (24) and (26) into Eq. (38), we obtain

$$K_R^\sigma = K_L^\sigma + K_d^\sigma + K^\sigma, \tag{39}$$

$$K_R^D = K_L^D + K_d^D + K^D, \tag{40}$$

Table 1 Crack-tip shielding effect induced by a line-force, a line-charge, and a screw dislocation when $b, \Delta\phi, p, q$ are positive(+) (⊖:shielding, ⊕:anti-shielding)

Position	$-\pi < \theta_0 < 0$				$\theta_o = 0$				$0 < \theta_o < \pi$			
variables / intensity factors	p	q	b	$\Delta\phi$	p	q	b	$\Delta\phi$	p	q	b	$\Delta\phi$
K_R^σ	⊖	×	⊖	⊖	×	×	⊖	⊖	⊕	×	⊖	⊖
K_R^D	×	⊕	⊖	⊕	×	×	⊖	⊕	×	⊖	⊖	⊕

where

$$K_L^\sigma = \frac{p}{\sqrt{2\pi r_0}}\sin\frac{\theta_0}{2}, \quad K_L^D = -\frac{q}{\sqrt{2\pi r_0}}\sin\frac{\theta_0}{2},$$

$$K_d^\sigma = -\frac{1}{\sqrt{2\pi r_0}}(c_{44}b + e_{15}\Delta\phi)\cos\frac{\theta_0}{2}, \tag{41}$$

$$K_d^D = -\frac{1}{\sqrt{2\pi r_0}}(e_{15}b - \epsilon_{11}\Delta\phi)\cos\frac{\theta_0}{2}.$$

In the purely elastic case, K_d^σ in Eq. (41) becomes the solutions of Majumdar and Burns [14].

Examining Eqs. (39) and (40) one can observe the crack-tip shielding effect due to the line-force, the line-charge and the screw dislocation. In case of the Burgers vector, b, the electric potential jump, $\Delta\phi$, the line-force and the line-charge to be all positive, K_R^σ and K_R^D are not affected by the line-charge and the line-force, respectively, as shown in Table 1. The line-force increases the crack- tip antishielding effect in the upper-half plane ($0 < \theta_0 < \pi$), since it adds to the far-field mechanical load. But it decreases K_R^σ in the lower-half plane ($-\pi < \theta_0 < 0$). The screw dislocation (b and $\Delta\phi$) decreases K_R^σ in any position, which is same as the result of Majumdar and Burns [14] in the purely elastic case. On the contrary, the line-charge, q, placed in the upper half-plane ($0 < \theta_0 < \pi$) decreases K_R^D, since the line-charge induces an adverse electric field to the applied electrical load near the crack tip. But, in the lower-half plane it increases K_R^D. Regardless of the location of the dislocation, b decreases K_R^D but $\Delta\phi$ increases it.

5 Crack Extension Force

The crack extension force can be obtained by considering the work done in closing the crack tip over an infinitesimal distance δ:

$$\Delta W = 2\int_0^\delta \frac{1}{2}\sigma_{zy}\Delta u_{z,\delta}dx + 2\int_0^\delta \frac{1}{2}D_y\Delta\phi_\delta dx, \tag{42}$$

where $\Delta u_{z,\delta}$ and $\Delta\phi_\delta$ represent the change in the displacement and the electric potential due to the virtual extension of the crack, respectively,

$$\Delta u_{z,\delta} = u_z(x-\delta) - u_z(x), \quad \Delta\phi_\delta = \phi(x-\delta) - \phi(x). \tag{43}$$

The crack extension force, G, can then be calculated as follows:

$$G = \lim_{\delta\to 0}\frac{\Delta W}{\delta}. \tag{44}$$

To simplify the calculation, we first consider the screw dislocation positioned at a distance, d, along the x-axis from the crack tip. The changes in the displacement and the electric potential are

$$\Delta u_{z,\delta} = A_1\log\left(1+\frac{\delta}{d-x}\right) + 2A_2\tan^{-1}\sqrt{\frac{\delta-x}{d}} + C'\sqrt{\frac{2}{\pi}}\sqrt{\delta-x},$$
$$\Delta\phi_\delta = B_1\log\left(1+\frac{\delta}{d-x}\right) + 2B_2\tan^{-1}\sqrt{\frac{\delta-x}{d}} + D'\sqrt{\frac{2}{\pi}}\sqrt{\delta-x}. \tag{45}$$

The stress and the electric displacement are

$$\sigma_{zy} = \frac{c_{44}b + e_{15}\Delta\phi}{2\pi}\frac{\sqrt{d}}{\sqrt{x}(x-d)} + \frac{K^\sigma}{\sqrt{2\pi x}},$$
$$D_y = \frac{e_{15}b - \epsilon_{11}\Delta\phi}{2\pi}\frac{\sqrt{d}}{\sqrt{x}(x-d)} + \frac{K^D}{\sqrt{2\pi x}}. \tag{46}$$

From Eqs. (42)–(46) along with Eq. (34), we obtain the crack extension force in the form

$$G = -F_x + \frac{\epsilon_{11}K^{\sigma^2} + 2e_{15}K^DK^\sigma - c_{44}K^{D^2}}{2(c_{44}\epsilon_{11} + e_{15}^2)}. \tag{47}$$

The second term is the crack extension force due to the external loads in the absence of the dislocation. For the purely elastic case, Eq. (47) becomes the solution of linear elastic fracture mechanics:

$$G = \frac{K^{\sigma^2}}{2\mu}. \tag{48}$$

Letting $\theta_0 = 0$ and $r_0 = d$ in Eqs. (39) and (40), G can be rearranged from Eq. (47) as follows:

$$G = \frac{\epsilon_{11}K_R^{\sigma^2} + 2e_{15}K_R^DK_R^\sigma - c_{44}K_R^{D^2}}{2(c_{44}\epsilon_{11} + e_{15}^2)}. \tag{49}$$

This result is in the same form as the second term in Eq. (47). Therefore, this is the general relation between the crack extension force and the field intensity factors in linear piezoelectric material. From Eq. (47) or (49), we can now obtain the crack extension force in the case of a screw dislocation at any position near a crack tip in the form

$$\begin{aligned} G = &-\frac{c_{44}q^2 + 2e_{15}pq - \epsilon_{11}p^2}{4\pi r_0(c_{44}\epsilon_{11} + e_{15}^2)}\sin^2\frac{\theta_0}{2} \\ &+ \frac{c_{44}b^2 + 2e_{15}b\Delta\phi - \epsilon_{11}\Delta\phi^2}{4\pi r_0}\cos^2\frac{\theta_0}{2} - \frac{pb - q\Delta\phi}{4\pi r_0}\sin\theta_0 \\ &+ \frac{(p\epsilon_{11} - qe_{15})K^\sigma + (pe_{15} + qc_{44})K^D}{\sqrt{2\pi r_0}(c_{44}\epsilon_{11} + e_{15}^2)}\sin\frac{\theta_0}{2} \\ &- \frac{bK^\sigma + \Delta\phi K^D}{\sqrt{2\pi r_0}}\cos\frac{\theta_0}{2} + \frac{\epsilon_{11}K^{\sigma^2} + 2e_{15}K^DK^\sigma - c_{44}K^{D^2}}{2(c_{44}\epsilon_{11} + e_{15}^2)}. \end{aligned} \tag{50}$$

A lead zirconate titante (PZT-5H) ferroelectric piezoceramic is considered. The material properties are given by ([3]):

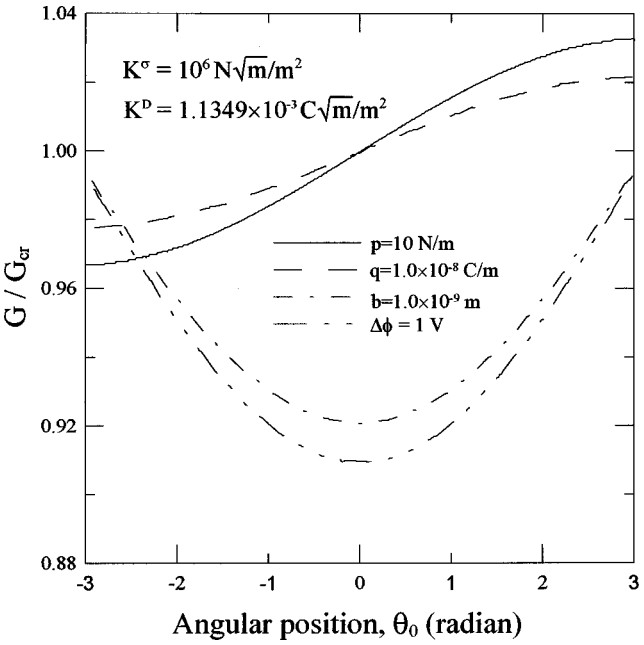

Fig. 2 The effect of the line-loads, the Burgers vector, and the electric potential jump on the resultant crack extension force

$$c_{44}=3.53\times 10^{10}\ \frac{\mathrm{N}}{\mathrm{m}^2},$$

$$e_{15}=17.0\ \frac{\mathrm{C}}{\mathrm{m}^2},$$

$$\epsilon_{11}=151\times 10^{-10}\ \frac{\mathrm{C}}{\mathrm{Vm}},$$

$$G_{\mathrm{cr}}=5.0\ \frac{\mathrm{N}}{\mathrm{m}}, \tag{51}$$

where N is the force in Newtons, C is the charge in coulombs, V is the electric potential in volts, m is the length in meters, and G_{cr} is the critical crack extension force.

Assuming that $r_0=1\ \mu$m, $K^{\sigma}=10^6$ N$\sqrt{\mathrm{m}}$/m^2 and $K^D=1.1349\times 10^{-3}$ C$\sqrt{\mathrm{m}}$/m^2 so that the value of the sixth term in Eq. (50) is the same as the one of G_{cr} and the line-loads, and the Burgers vector, or the electric potential jump is a positive value, the ratio of G to G_{cr} with respect to the angle θ_0 is plotted in Fig. 2. It does not represent the coupled effect of p, q, b, and $\Delta\phi$ because we give only one parameter a positive value and set others to zero. It is noted that the fourth, fifth, and sixth terms in Eq. (50) have the dominant effect on the resultant crack extension force and, in the result, G/G_{cr} varies linearly with p, q, b, and $\Delta\phi$. The fifth term shows that a positive screw dislocation always decreases the crack extension force when the positive external load is applied. Its effect is very small because there is only one screw dislocation in this analysis. However, since a realistic zone of a crack tip consists of a number of dislocations, its effect is expected to be considerably large.

By ignoring the first, second, and third terms and differentiating G with respect to the angle of the position, we obtain the location of the dislocation, $\theta_0^{\min}$, at which the crack extension force becomes minimum in the form

$$\theta_0^{\min}=2\ \mathrm{Arctan}\left[\frac{(bK^{\sigma}+\Delta\phi K^D)(c_{44}\epsilon_{11}+e_{15}^2)}{(p\epsilon_{11}-qe_{15})K^{\sigma}+(pe_{15}+qc_{44})K^D}\right]-\pi. \tag{52}$$

With no line-force-charge ($p=0$, $q=0$), the position for the minimum is $\theta_0^{\min}=0$. As the values of the Burgers vector and electric potential jump increase, $\theta_0^{\min}$ approaches zero, while it approaches $-\pi$ with increase of the line-loads.

6 Conclusions

A theoretical analysis was performed for a screw dislocation with a line-force and a line-charge near a semi-infinite crack in a hexagonal piezoelectric crystal subjected to far-field antiplane mechanical and in-plane electrical loads. The solution was obtained by complex variable and conformal mapping technique. The classical $1/\sqrt{r}$ singularity was observed for stress, electric displacement, and electric field near the crack tip. The forces acting on the dislocation were obtained, which were in agreement with the previous works. The effects of the screw dislocation and the line-loads on the stress and the electric displacement intensity factors were calculated. The crack extension force was also calculated, which consists of the force obeying the law of action-reaction and the force acting on the crack directly by the external loads. The general relation between the crack extension force and the field intensity factors was presented. In the limiting case of vanishing electrical quantities, all the results obtained in this paper was reduced to those for the purely elastic case.

Acknowledgment

The authors are grateful for the support provided by the Brain Korea 21 Project and by a grant from the Korean Science Engineering Foundation (KOSEF) and Safety and Structural Integrity Research Center at the Sungkyunkwan University.

References

[1] Faivre, G., and Saada, G., 1972, ''Dislocations in Piezoelectric Semiconductors,'' Phys. Status Solidi B, **52**, p. 127.
[2] Deeg, W. F., 1980, ''The Analysis of Dislocation, Crack, and Inclusion Problems in Piezoelectric Solids,'' Ph.D. thesis, Stanford University, Stanford, CA.
[3] Pak, Y. E., 1990, ''Crack Extension force in a Piezoelectric Material,'' ASME J. Appl. Mech., **57**, pp. 647–653.
[4] Sosa, H. A., and Pak, Y. E., 1990, ''Three-Dimensional Eigenfunction Analysis of a Crack in a Piezoelectric Material,'' Int. J. Solids Struct., **26**, pp. 1–15.
[5] Pak, Y. E., 1990, ''Force on a Piezoelectric Screw Dislocation,'' ASME J. Appl. Mech., **57**, pp. 863–869.
[6] Kuo, C.-M., and Barnett, D. M., 1991, *Modern Theory of Anisotropic Elasticity and Applications*, J. J. Wu, T. C. T. Ting, and D. M. Barnett, eds., SIAM Proceedings, pp. 35–50.
[7] Suo, Z., Kuo, C.-M., Barnett, D. M., and Willis, J. R., 1992, ''Fracture Mechanics for Piezoelectric Ceramics,'' J. Mech. Phys. Solids, **26**, pp. 739–765.
[8] Wang, B., 1992, ''Three-Dimensional Analysis of an Ellipsoidal Inclusion in Piezoelectric Material,'' Int. J. Solids Struct., **29**, pp. 293–308.
[9] Chen, T., 1993, ''The Rotation of a Rigid Inclusion Embedded in an Anisotropic Piezoelectric Medium,'' Int. J. Solids Struct., **30**, pp. 1983–1995.
[10] Liang, J., Han, J.-C., Wang, B., and Du, S., 1995, ''Electroelastic Modeling of Anisotropic Piezoelectric Materials With an Elliptic Inclusion,'' Int. J. Solids Struct., **32**, pp. 2989–3000.
[11] Chung, M. Y., and Ting, T. C. T., 1996, ''Piezoelectric Solid With an Elliptical Inclusion or Hole,'' Int. J. Solids Struct., **33**, pp. 3343–3361.
[12] Zhong, Z., and Meguid, S. A., 1997, ''Interfacial Debonding of a Circular Inhomogeneity in Piezoelectric Materials,'' Int. J. Solids Struct., **34**, pp. 1965–1984.
[13] Meguid, S. A., and Deng, Wei, 1998, ''Electro-Elastic Interaction Between a Screw Dislocation and an Elliptical Inhomogeneity in Piezoelectric Materials,'' Int. J. Solids Struct., **35**, pp. 1467–1482.
[14] Majumdar, B. S., and Burns, S. J., 1981, ''Crack Tip Shielding—An Elastic Theory of Dislocations and Dislocation Arrays Near a Sharp Crack,'' Acta Metall., **29**, pp. 579–588.
[15] Ohr, S. M., Chang, S.-J., and Thomson, R., 1985, ''Elastic Interaction of a Wedge Crack With a Screw Dislocation,'' J. Appl. Phys., **57**, pp. 1839–1843.
[16] Damjanovic, D., 1997, ''Stress and Frequency Dependence of the Direct Piezoelectric Effect in Ferroelectric Ceramics,'' J. Appl. Phys., **82**, pp. 1788–1797.
[17] Pertsev, N. A., 1988, ''Changed Dislocations in Ferroelectrics,'' Sov. Phys. Solid State, **30**, pp. 1616–1621.

Stability of Rectangular Plates With Free Side-Edges in Two-Dimensional Inviscid Channel Flow

C. Q. Guo[1]

M. P. Paidoussis[2]
Fellow ASME

Department of Mechanical Engineering,
McGill University,
817 Sherbrooke Street West,
Montreal, Quebec H3A 2K6, Canada

The linear stability of rectangular plates with free side-edges in inviscid channel flow is studied theoretically. The Galerkin method and Fourier transform technique are employed to solve the plate and potential flow equations. A new approach is introduced to treat the mixed fluid-plate interaction boundary condition, which leads to a singular integral equation. Divergence, single-mode flutter, and coupled-mode flutter are found for plates supported differently at the leading and trailing edges. In some cases, single-mode flutter at vanishingly small flow velocity is predicted. The effects of mass ratio and channel-height-to-plate-length ratio on critical velocity are studied. An energy balance analysis shows how different types of instability arise for plates with different supports. [S0021-8936(00)01801-8]

1 Introduction

Stability of plates in axial flow is a problem of practical importance in aerospace and nuclear engineering and has been examined by many investigators. For parallel-plate assemblies used as core elements in some nuclear research and power reactors, a theory was first presented by Miller [1] for predicting the critical flow velocity for divergence, later improved by Johansson [2] and many others ([3]). Other investigators have studied the flutter of a panel in subsonic or incompressible flow; e.g., Dugundji et al. [4], Dowell [5], Weaver and Unny [6,7], and Epstein et al. [8]. More recently, a plate in axial flow has even been chosen as a model to study human snoring ([9])!

However, compared with the stability of pipes conveying fluid, a similar problem now becoming a paradigm in dynamics ([10]), our understanding of the stability of plates in axial flow is far from complete, and some controversial problems such as postdivergence flutter still remain to be resolved ([11]). No theory is available to explain why and under what conditions different types of instability exist in different cases.

The purpose of this paper is to investigate some fundamental characteristics of the instability of plates in axial flow. To concentrate on the fundamental aspects of the problem, we consider a finite length rectangular plate with free side-edges in a channel (Fig. 1), and treat the plate as one-dimensional and the channel flow as two-dimensional (a three-dimensional model has been presented by the authors for a similar problem; see [3]). In the analysis, the Galerkin method is employed to solve the plate equation, while the Fourier transform technique is used to obtain the perturbation pressure from the potential flow equations. The mixed fluid-plate interaction boundary condition along the plate and its up and downstream extensions leads to a singular integral equation, which is solved numerically. Investigated in this paper are (i) types of instability for plates with different support conditions at the leading and trailing edges and (ii) effects of fluid density and channel height on the critical flow velocity.

2 Governing Equations and Boundary Conditions

The one-dimensional equation of motion of an elastic plate is given by

$$D\frac{\partial^4 w}{\partial x^4}+\rho_p h_p\frac{\partial^2 w}{\partial t^2}+p=0, \tag{1}$$

where $D=Eh_p^3/[12(1-\nu^2)]$ is the plate stiffness, E being Young's modulus, ν Poisson's ratio, h_p the plate thickness, ρ_p the plate density, $w\equiv w(x,t)$ its lateral deflection, and $p\equiv p(x,t)$ the net load per unit area on the plate, equal to the difference between the perturbation pressures on the upper and lower surfaces of the plate caused by its deflection. Because of antisymmetry with respect to the plate, these perturbation pressures must be equal in magnitude but opposite in sign.

Assuming an inviscid, incompressible two-dimensional flow, the perturbation pressures can be given by the unsteady Bernoulli equation,

$$p=-2\rho\left[\frac{\partial\varphi}{\partial t}+U\frac{\partial\varphi}{\partial x}\right]_{z=0}, \tag{2}$$

where ρ is the fluid density, and U the unperturbed flow velocity in the channel. The perturbation velocity potential φ must satisfy the Laplace equation

$$\frac{\partial^2\varphi}{\partial x^2}+\frac{\partial^2\varphi}{\partial z^2}=0. \tag{3}$$

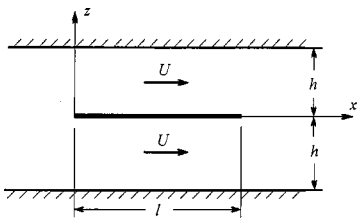

Fig. 1 Schematic of a plate in two-dimensional channel flow

[1]Visiting scholar from Central-South Institute of Technology, Hengyang, Hunan, P. R. China.

[2]To whom all correspondence should be addressed. e-mail: maryf@MechEng.McGill.ca.

Contributed by the Applied Mechanics Division of THE AMERICAN SOCIETY OF MECHANICAL ENGINEERS for publication in the JOURNAL OF APPLIED MECHANICS. Manuscript received by the ASME Applied Mechanics Division, Apr. 15, 1999; final revision, Sept. 12, 1999. Associate Technical Editor: N. C. Perkins. Discussion on the paper should be addressed to the Technical Editor, Professor Lewis T. Wheeler, Department of Mechanical Engineering, University of Houston, Houston, TX 77204-4792, and will be accepted until four months after final publication of the paper itself in the JOURNAL OF APPLIED MECHANICS.

To put these equations in dimensionless form and to analyze the problem in the frequency domain, we let

$$x=l\bar{x},\quad z=h\bar{z},\quad c=\frac{h}{l},\quad \mu=\frac{\rho l}{\rho_p h_p},$$
$$\omega=\frac{1}{l^2}\sqrt{\frac{D}{\rho_p h_p}}\,\bar{\omega},\quad U=\frac{1}{l}\sqrt{\frac{D}{\rho_p h_p}}\,\bar{U},$$
$$\varphi(x,z,t)=\sqrt{\frac{D}{\rho_p h_p}}\,\bar{\varphi}(\bar{x},\bar{z})e^{i\omega t},\quad p(x,t)=\frac{D}{l^3}\bar{p}(\bar{x})e^{i\omega t},\tag{4}$$
$$w(x,t)=l\bar{w}(\bar{x})e^{i\omega t}.$$

Inserting these into (1)–(3), and dropping the overbars for simplicity (only valid in this section and in Section 3), we obtain the dimensionless governing equations of the problem in the frequency domain:

$$\frac{d^4w}{dx^4}-\omega^2 w+p=0,\tag{5}$$

$$p=-2\mu\left[i\omega\varphi+U\frac{\partial\varphi}{\partial x}\right]_{z=0},\tag{6}$$

$$\frac{\partial^2\varphi}{\partial x^2}+\frac{1}{c^2}\frac{\partial^2\varphi}{\partial z^2}=0.\tag{7}$$

The boundary conditions for solving φ are given as

$$\varphi|_{x\to\pm\infty}=0,\tag{8}$$

$$\left.\frac{\partial\varphi}{\partial z}\right|_{z=1}=0,\tag{9}$$

$$\frac{1}{c}\left.\frac{\partial\varphi}{\partial z}\right|_{z=0}=i\omega w+U\frac{dw}{dx},\quad 0\leqslant x\leqslant 1,\tag{10a}$$

$$p=-2\mu\left[i\omega\varphi+U\frac{\partial\varphi}{\partial x}\right]_{z=0}=0,\quad x<0,\quad x>1,\tag{10b}$$

in which the antisymmetry with respect to the plate (and its extensions to infinity) is taken into account.

3 Solution

Galerkin's method is used to solve the plate Eq. (5). The dimensionless plate deflection is expressed as

$$w(x)=\sum_{m=1}^{M}A_m w_m(x),\tag{11}$$

where $w_m(x)$ are the beam eigenfunctions satisfying the plate boundary conditions at the leading and trailing edges.

Because the perturbation pressure p is dependent on the plate deflection w through (6)–(10), to solve Eq. (5), we must first determine their relationship.

3.1 Solution for Perturbation Pressure. For a given plate deflection $w(x)$, we must now find the corresponding perturbation pressure $p(x)$.

By applying the Fourier transform to $\varphi(x,z)$ with respect to the variable x, Eq. (7) and boundary condition (9) become

$$\frac{1}{c^2}\frac{\partial^2\tilde{\varphi}(\alpha,z)}{\partial z^2}-\alpha^2\tilde{\varphi}(\alpha,z)=0,\tag{12}$$

$$\left.\frac{\partial\tilde{\varphi}(\alpha,z)}{\partial z}\right|_{z=1}=0,\tag{13}$$

where

$$\tilde{\varphi}(\alpha,z)=\frac{1}{2\pi}\int_{-\infty}^{\infty}\varphi(x,z)e^{-l\alpha x}dx.\tag{14}$$

The solution of (12) satisfying (13) is given by

$$\tilde{\varphi}(\alpha,z)=B(\alpha)[e^{-c|\alpha|z}+e^{c|\alpha|(z-2)}].\tag{15}$$

Taking the inverse Fourier transform for (15), we get

$$\varphi(x,z)=\int_{-\infty}^{\infty}B(\alpha)[e^{-c|\alpha|z}+e^{c|\alpha|(z-2)}]e^{i\alpha x}d\alpha.\tag{16}$$

With this expression, condition (8) is satisfied automatically, and only the mixed boundary condition (10) is yet to be satisfied.

Inserting (16) into (6), we obtain the expression of perturbation pressure,

$$p(x)=\int_{-\infty}^{\infty}B(\alpha)(-2\mu)i(\omega+\alpha U)(1+e^{-2c|\alpha|})e^{i\alpha x}d\alpha.\tag{17}$$

Substitution of (17) into (10) yields a pair of dual integral equations for the unknown $B(\alpha)$. In order to reduce the dual integral equations to a single one, we use $p'(x)$ as the basic unknown. From (17), it follows that

$$p'(x)=\int_{-\infty}^{\infty}B(\alpha)(2\mu)\alpha(\omega+\alpha U)(1+e^{-2c|\alpha|})e^{i\alpha x}d\alpha.\tag{18}$$

Taking the inverse Fourier transform of (18), incorporating (10*b*), we obtain

$$B(\alpha)=\frac{1}{4\pi\mu\alpha(\omega+\alpha U)(1+e^{-2c|\alpha|})}\int_0^1 p'(\xi)e^{-i\alpha\xi}d\xi.\tag{19}$$

From (16) and (19), we have

$$\frac{1}{c}\left.\frac{\partial\varphi}{\partial z}\right|_{z=0}=\int_{-\infty}^{\infty}B(\alpha)|\alpha|(-1+e^{-2c|\alpha|})e^{i\alpha x}d\alpha$$
$$=\int_0^1 H(x,\xi)p'(\xi)d\xi,\tag{20}$$

where

$$H(x,\xi)=-\frac{1}{4\pi\mu}\int_{-\infty}^{\infty}\frac{|\alpha|\tanh(c|\alpha|)}{\alpha(\omega+\alpha U)}e^{i\alpha(x-\xi)}d\alpha.\tag{21}$$

Substitution of (20) into (10*a*) yields an integral equation for $p'(x)$:

$$\int_0^1 H(x,\xi)p'(\xi)d\xi=i\omega w(x)+Uw'(x),\quad 0\leqslant x\leqslant 1.\tag{22}$$

Premultiplying Eq. (22) by $i\omega+U(d/dx)$, we have

$$\int_0^1 G(x,\xi)p'(\xi)d\xi=-\omega^2 w(x)+i2\omega Uw'(x)+U^2w''(x),$$
$$(0\leqslant x\leqslant 1),\tag{23}$$

in which

$$G(x,\xi)=i\omega H(x,\xi)+U\frac{\partial H(x,\xi)}{\partial x}$$
$$=-\frac{i}{4\pi\mu}\int_{-\infty}^{\infty}\frac{|\alpha|\tanh(c|\alpha|)}{\alpha}e^{i\alpha(x-\xi)}d\alpha$$
$$=\frac{1}{2\pi\mu}\left\{\frac{1}{x-\xi}+\int_0^{\infty}[\tanh(c\alpha)-1]\sin\alpha[(x-\xi)]d\alpha\right\}. \quad (24)$$

Equation (23) is a Cauchy-type singular integral equation, from which $p'(x)$ can be obtained numerically by the Gauss-Chebyshev method ([12]). Then $p(x)$ can be obtained by integrating $p'(x)$.

The perturbation pressure $p(x)$ can be expressed as

$$p(x)=-\omega^2 p^{(M)}(x)+i2\omega U p^{(G)}(x)+U^2 p^{(K)}(x), \quad (25)$$

in which $p^{(M)}(x)$, $p^{(G)}(x)$, and $p^{(K)}(x)$ are the components of $p(x)$ obtained by retaining on the right-hand side of Eq. (23) terms associated with $w(x)$, $w'(x)$, and $w''(x)$, respectively.

3.2 Solution for Plate Deflection. Applying Galerkin's method to Eq. (5) gives

$$\int_0^1\sum_{m=1}^{M}A_m[w_m''''(x)-\omega^2 w_m(x)+p_m(x)]w_r(x)dx=0,$$
$$(r=1,2,\ldots,M), \quad (26)$$

in which $p_m(x)$ is the perturbation pressure corresponding to $w_m(x)$.

Inverting the integration and summation order and rearranging, we can rewrite (26) as

$$\sum_{m=1}^{M}[-\omega^2(M_{mr}^{(p)}+M_{mr}^{(f)})+i2\omega U G_{mr}^{(f)}+K_{mr}^{(p)}+U^2K_{mr}^{(f)}]A_m=0,$$
$$(r=1,2,\ldots,M), \quad (27)$$

in which

$$M_{mr}^{(p)}=\int_0^1 w_m(x)w_r(x)dx, \quad K_{mr}^{(p)}=\int_0^1 w_m''''(x)w_r(x)dx,$$
$$M_{mr}^{(f)}=\int_0^1 p_m^{(M)}(x)w_r(x)dx, \quad G_{mr}^{(f)}=\int_0^1 p_m^{(G)}(x)w_r(x)dx, \quad (28)$$
$$K_{mr}^{(f)}=\int_0^1 p_m^{(K)}(x)w_r(x)dx.$$

The first two integrals in (28) can be evaluated analytically and the last three numerically.

4 Numerical Results and Discussion

To obtain an overall understanding of the problem, we have studied plates with every possible combination of classical supports at the leading and trailing edges: clamped-clamped, pinned-pinned, free-free, clamped-pinned, pinned-clamped, clamped-free, free-clamped, pinned-free, and free-pinned. For clamped-clamped, pinned-pinned, clamped-free, and free-clamped plates in the limit of large channel height, some results have been obtained previously by Dowell [13] and Kornecki et al. [14].

To test for the convergence of the Galerkin solution, the lowest three eigenfrequencies at zero flow velocity and the critical velocity for first-mode divergence, of a clamped-pinned plate, were calculated with a different number of terms in Eq. (11). The results show that both the eigenfrequencies and the critical velocity converge rapidly. Even with only one term, the accuracy for the first-mode eigenfrequency and the critical velocity of first-mode divergence is fairly good (to within 0.2 percent). In spite of this, we have taken ten terms in the calculations.

For symmetrically supported (clamped-clamped, pinned-pinned, and free-free) plates, we have obtained four complex conjugate modes for the eigenvalue parameter, $\lambda=i\omega$; otherwise, only two have been found. This conclusion can be proved mathematically from Eq. (27). In the figures, only those modes with a non-negative ω_R have been plotted.

4.1 Clamped-Clamped, Pinned-Pinned, and Clamped-Pinned Plates. Figure 2 is a typical diagram of the first and second-mode dimensionless complex eigenfrequencies $\bar{\omega}$ versus the dimensionless flow velocity $\bar{U}$ for a clamped-clamped plate. The solid and dotted lines represent the real and imaginary parts of the complex eigenfrequencies, respectively. It is clear that the plate first diverges in the first mode, it is then restabilized and, shortly after that, it undergoes coupled-mode flutter involving the first and second modes. For a pinned-pinned plate, results very similar to Fig. 2 have been obtained.

Figure 3 is for a clamped-pinned plate. It is different from Fig. 2 in two respects: (i) the imaginary parts are nonzero prior to divergence and (ii) after first-mode divergence, the first and second modes interact in some way, but they do not combine into one, so it is hard to say whether the flutter is single or coupled-mode.

Calculations have shown that clamped-clamped and pinned-pinned plates lose stability by first-mode divergence for any mass ratio μ and channel-height-to-length ratio c. This is also true for clamped-pinned plates with relatively large μ and c; otherwise, stability is lost by single-mode flutter at vanishingly small flow velocity.

For divergence, the dimensionless critical velocity $\bar{U}_{cr}$ is in-

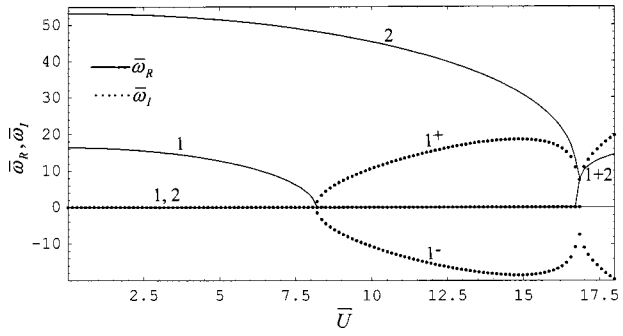

Fig. 2 Dimensionless complex eigenfrequencies versus flow velocity for a clamped-clamped plate; $c=1$, $\mu=1$

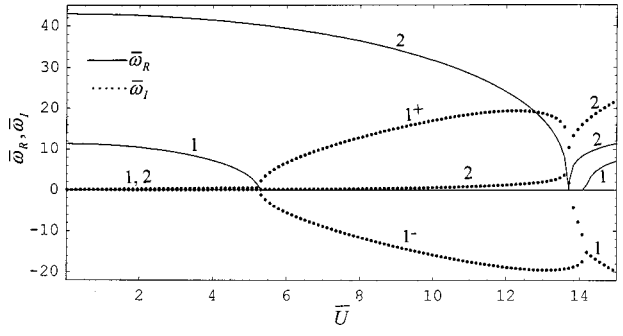

Fig. 3 Dimensionless complex eigenfrequencies versus flow velocity for a clamped-pinned plate; $c=1$, $\mu=1$

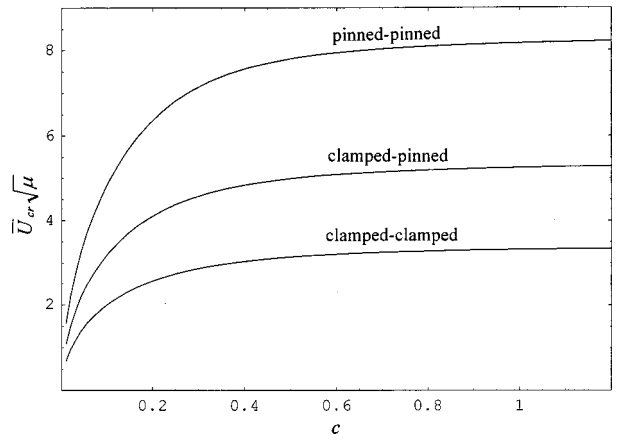

Fig. 4 Critical flow velocity of first-mode divergence versus channel-height-to-plate-length ratio for clamped-clamped, clamped-pinned, and pinned-pinned plates

versely proportional to $\sqrt{\mu}$. $\overline{U}_{cr}\sqrt{\mu}$ increases with increasing c, and then tends asymptotically to a constant as c tends to infinity, as seen in Fig. 4.

4.2 Free-Free Plate. Figure 5 shows the complex eigenfrequencies for a free-free plate. If we do not consider the rigid-body modes (the eigenvalue frequency corresponding to the rigid-body mode in translation is zero, and that in rotation is pure imaginary, ω_I is positive and proportional to the flow velocity), a free-free plate loses stability by coupled-mode (classical) flutter. Which modes are involved depends on the parameters. Figure 6 shows the lowest flutter critical velocity as a function of $\mu/(1+\mu)$ and c. $\overline{U}_{cr}\sqrt{\mu}$ does not change monotonically with either $\mu/(1+\mu)$ or

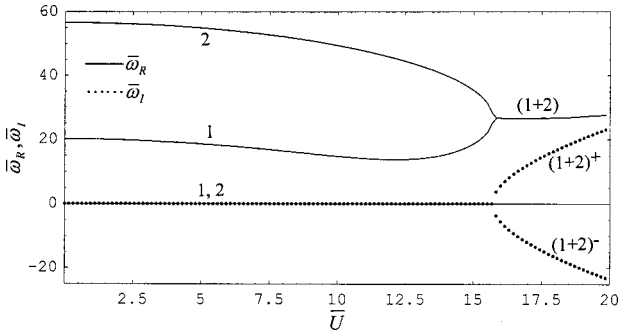

Fig. 5 Dimensionless complex eigenfrequencies versus flow velocity for a free-free plate; $c=1$, $\mu=1$

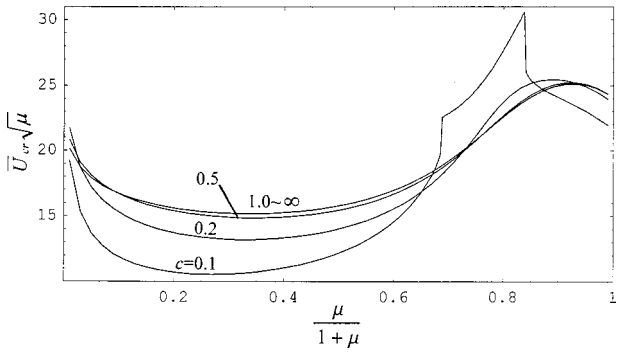

Fig. 6 Critical flow velocity versus mass ratio for a free-free plate with different channel-height-to-plate-length ratios

c; however, it tends to a constant as c tends to infinity. The ''jump'' and ''plummet'' on the curve for $c=0.1$ are due to a change in the modes involved in flutter, which are the second and third ones for $0.69<\mu/(1+\mu)<0.84$, and the first and second for the rest. For $c\geq 0.2$, the lowest flutter velocity is always that of coupled-mode flutter involving the first and second modes.

4.3 Clamped-Free and Pinned-Free Plates. Figure 7 shows that a clamped-free plate loses stability by single-mode flutter. Although the real part of the first-mode eigenfrequency becomes zero at some ''critical'' velocity, no divergence occurs because the two branches of the bifurcated imaginary part remain positive. The imaginary part of the second-mode eigenfrequency changes sign as flow velocity increases. The lowest velocity at which it changes from positive to negative is the critical velocity for single-mode flutter. For clamped-free plates, second-mode flutter is prevalent. For pinned-free plates, the diagrams are similar, but first-mode flutter occurs most often.

Figure 8 shows the lowest flutter critical velocity as a function of $\mu/(1+\mu)$ and c for clamped-free plates. The S-shaped jumps of the critical velocity are also due to the shift of modes involved in the flutter. $\overline{U}_{cr}\sqrt{\mu}$ increases with increasing $\mu/(1+\mu)$ and tends to a constant as c tends to infinity. For pinned-free plates, similar results have been obtained.

It can be seen from Fig. 8 that if the fluid density is small enough, the critical velocity becomes zero! Calculations have shown that this kind of zero-critical-velocity instability is very weak because the imaginary part of the eigenfrequency of the fluttering mode is very small, so it disappears when damping is taken into account, as shown in Fig. 9, in which γ is the viscoelas-

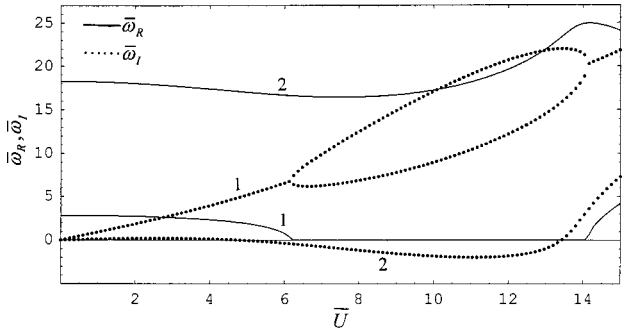

Fig. 7 Dimensionless complex eigenfrequencies versus flow velocity for a clamped-free plate; $c=1$, $\mu=1$

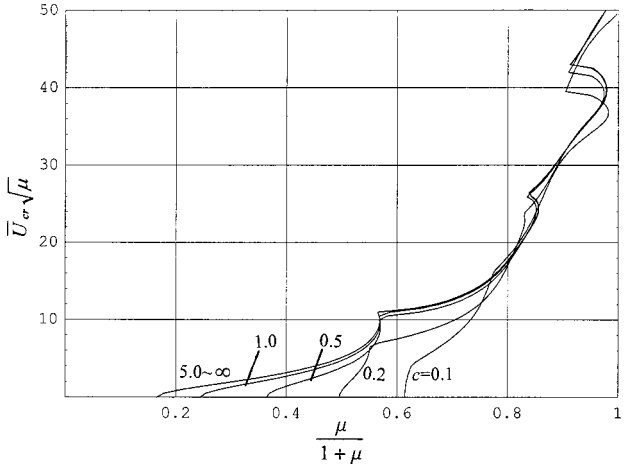

Fig. 8 Critical flow velocity versus mass ratio for a clamped-free plate with different channel-height-to-plate-length ratios

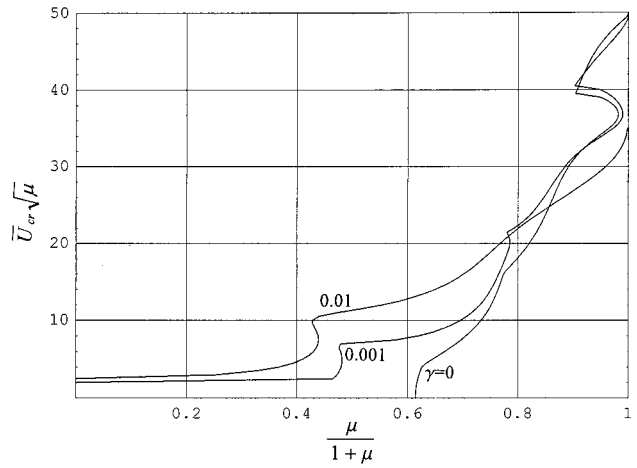

Fig. 9 Effect of viscoelastic damping on critical flow velocity for a clamped-free plate; $c=1$

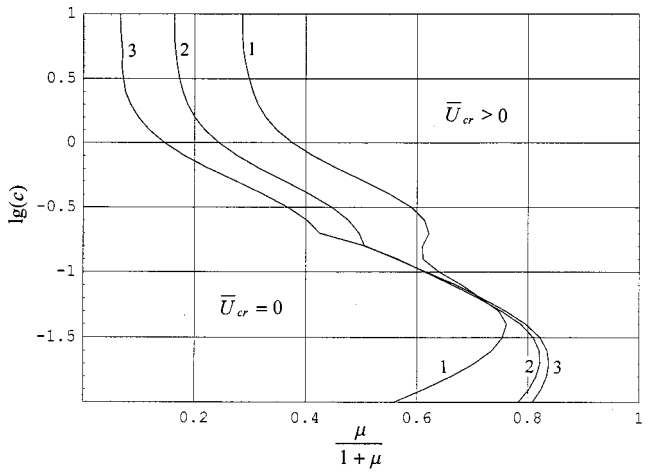

Fig. 10 Stability boundaries for (1) clamped-pinned, (2) clamped-free, and (3) pinned-free plates

tic damping coefficient (in this case, a factor $(1+i\omega\gamma)$ should be added in front of $K_{mr}^{(p)}$ in Eq. (27). This phenomenon no doubt is related to the limitations of inviscid flow theory. A similar result related to ''aspirating'' pipes (originally thought to lose stability at vanishingly small flow velocity) was resolved ([15])—but viscous flow theory was used all along.

This same phenomenon also exists in the case of clamped-pinned plates. In Fig. 10 are given the boundaries separating the zero-critical-velocity flutter region and nonzero-critical-velocity region in the plane of parameters $\lg(c)$ and $\mu/(1+\mu)$, for the aforementioned three types of plates.

4.4 Pinned-Clamped, Free-Clamped, and Free-Pinned Plates. For pinned-clamped, free-clamped, and free-pinned plates, calculations have shown that the eigenfrequencies are conjugates of those of clamped-pinned, clamped-free, and pinned-free plates, respectively, with the same parameters and at the same flow velocity. For a clamped-pinned, clamped-free, or pinned-free plate at any flow velocity, there exists at least one mode with a positive imaginary part of eigenfrequency, therefore, a pinned-clamped, free-clamped, or free-pinned plate will flutter at vanishing flow velocity. When external viscous damping or internal viscoelastic damping is taken into account, calculations have shown that the critical velocity is nonzero, proportional to the damping coefficient, inversely proportional to μ, and that increases with increasing c; see also other comments in Section 4.3.

5 Energy Balance Analysis of Instability

From Eq. (23), we can express $\overline{p}(\overline{x})$ (using again overbars for dimensionless terms) as

$$\overline{p}(\overline{x})=-\overline{\omega}^2\overline{m}_1(\overline{x})\overline{w}(\overline{x})+i2\overline{\omega}\overline{U}\overline{m}_2(\overline{x})\overline{w}'(\overline{x})+\overline{U}^2\overline{m}_3(\overline{x})\overline{w}''(\overline{x}), \tag{29}$$

in which $\overline{m}_1(\overline{x})$, $\overline{m}_2(\overline{x})$, and $\overline{m}_3(\overline{x})$, depend on the shapes of $\overline{w}(\overline{x})$, $\overline{w}'(\overline{x})$, and $\overline{w}''(\overline{x})$, respectively; from (24), they are proportional to μ. The perturbation pressure can be expressed as

$$p(x,t)=m_1(x)\frac{\partial^2 w}{\partial t^2}+2Um_2(x)\frac{\partial^2 w}{\partial x\partial t}+U^2m_3(x)\frac{\partial^2 w}{\partial x^2}; \tag{30}$$

the three terms on the right-hand side are the inertial, Coriolis and centrifugal forces of the fluid on the plate, consecutively. With Eq. (30) as the expression for $p(x,t)$, Eq. (1) is similar to the equation of motion of a pipe conveying fluid ([15]), except that, for the latter, $m_1(x)=m_2(x)=m_3(x)=m_0=$ real constant.

The rate of work done on the plate by the fluid-dynamic forces, the only possible source of energy input, is given by

$$\frac{dW}{dt}=-\int_0^l p(x,t)\frac{\partial w(x,t)}{\partial t}dx. \tag{31}$$

For periodic oscillation, we express $w(x,t)$ in real form

$$w(x,t)=w_c(x)\cos\omega t+w_s(x)\sin\omega t; \tag{32}$$

then, the perturbation pressure is

$$\begin{aligned}p(x,t)=&[-\omega^2m_{c1}w_c+2\omega Um_{s2}w_s'+U^2m_{c3}w_c'']\cos\omega t\\&+[-\omega^2m_{s1}w_s-2\omega Um_{c2}w_c'+U^2m_{s3}w_s'']\sin\omega t.\end{aligned} \tag{33}$$

Hence the work done by the fluid forces over a cycle of periodic oscillation of period $T=2\pi/\omega$ is

$$\begin{aligned}\Delta W=&-\int_0^T\int_0^l p(x,t)\frac{\partial w(x,t)}{\partial t}dxdt\\=&-\pi\Bigg[-\omega^2\int_0^l(m_{c1}-m_{s1})w_cw_sdx\\&+2\omega U\int_0^l(m_{c2}w_c'w_s+m_{s2}w_s'w_c)dx\\&+U^2\int_0^l(m_{c3}w_c''w_s-m_{s3}w_s''w_c)dx\Bigg].\end{aligned} \tag{34}$$

If the constraints at the leading and trailing edges of the plate are the same, then one of $w_c(x)$, $w_s(x)$ is symmetric and the other antisymmetric with respect to $x=l/2$. From Eqs. (23), (24), and (30), it can be concluded that $m_{c1}(x),\ldots,m_{s3}(x)$ are symmetric with respect to $x=l/2$. Hence, $\Delta W=0$. Thus, in these cases, no single-mode flutter (Hopf bifurcation) can occur. Divergence (pitchfork bifurcation) and coupled-mode flutter (either a Hamiltonian Hopf bifurcation or so-called Païdoussis flutter) may exist.

For other cases, generally ΔW does not vanish. If for some modes and at some velocities, $\Delta W<0$, then the vibrations of these modes will be damped out; if $\Delta W>0$, the plate will gain energy from the fluid and single-mode flutters will occur.

If we exchange the constraints at the leading and trailing edges of the plate, or, more easily, change the direction of the flow, then $w_c(x)$ and $w_s(x)$ will exchange their positions in Eq. (32). Changing the sign of U and exchanging the subscript c with s in Eq.

(34), we get the opposite sign in ΔW. So, if a plate with clamped-pinned or clamped-free constraints at the leading and trailing edges is stable at very low velocities, then a pinned-clamped or free-clamped plate is unstable, even when the velocity tends to zero—at least according to inviscid theory!

These conclusions can also be reached via Eq. (27). If we change the sign of the flow velocity U, the sign of the imaginary part of eigenfrequency ω will also change. Then, if the plate is symmetrically supported, there are only two possibilities regarding the roots of ω in Eq. (27): (i) the imaginary part is zero, which represents neutral stability; or (ii) a pair of conjugates exist, which represents coupled-mode flutter (for $\omega_R \neq 0$) or divergence (for $\omega_R = 0$).

For a pipe conveying fluid, if the ends of the pipe are positively supported (clamped or pinned), one obtains $\Delta W = 0$ ([15]). Therefore, for a clamped-pinned or pinned-clamped pipe, the vibrations will be neither damped nor amplified, and single-mode flutter will not occur. But for a clamped-pinned or pinned-clamped *plate*, and also most probably for other similar structures such as cylinders and shells in external axial flow, both are possible ([16]).

6. Conclusions

Different types of instability exist for plates with different supports at the leading and trailing edges. Divergence and coupled-mode flutter may occur for plates with any type of end supports, while single-mode flutter only arises for nonsymmetrically supported plates. For clamped-clamped and pinned-pinned plates, first-mode divergence always occurs prior to other types of instability. For clamped-pinned plates, if the mass ratio μ and the channel-height-to-length ratio c are relatively large, the first-mode divergence is also the predominant type of instability. Free-free plates always lose stability by coupled-mode flutter, mostly involving the first and second modes. Clamped-free and pinned-free plates lose stability by single-mode flutter, usually in their second mode for the former and the first mode for the latter. If μ or c are small, clamped-pinned, clamped-free, and pinned-free plates may experience very weak single-mode flutter at very small velocity (the critical velocity is zero). Pinned-clamped, free-clamped, and free-pinned plates always lose stability by single-mode flutter at very low flow velocity, at least according to inviscid flow theory.

For divergence, the dimensionless critical velocity $\overline{U}_{cr}$ is inversely proportional to $\sqrt{\mu}$ and increases with increasing c. For single-mode flutter, $\overline{U}_{cr}\sqrt{\mu}$ generally increases with increasing μ and c. For coupled-mode flutter, $\overline{U}_{cr}\sqrt{\mu}$ does not change monotonically with either μ or c. However, for all types of instability, $\overline{U}_{cr}\sqrt{\mu}$ tends asymptotically to a constant as c tends to infinity ($c = 1 \sim 5$ is a fairly good approximation for $c \rightarrow \infty$).

Acknowledgments

The authors gratefully acknowledge the support of NSERC of Canada, FCAR of Quebec, and CSC of P.R. China.

References

[1] Miller, D. R., 1960, ''Critical Flow Velocities for Collapse of Reactor Parallel-Plate Fuel Assemblies,'' ASME J. Eng. Power, **82**, pp. 83–95.

[2] Johansson, R. B., 1960, ''Hydraulic Instability of Reactor Parallel Plate Fuel Assemblies,'' *Nuclear Engineering Science Conference*, Apr. 4–7, Preprint Paper No. 57.

[3] Guo, C. Q., and Païdoussis, M. P., 1999, ''Analysis of Hydroelastic Instabilities of Rectangular Parallel-Plate Assemblies,'' *Flow-Induced Vibration*, ASME, New York, pp. 191–198.

[4] Dugundji, J., Dowell, E., and Perkin, B., 1963, ''Subsonic Flutter of Panels on Continuous Elastic Foundations,'' AIAA J., **1**, pp. 1146–1154.

[5] Dowell, E. H., 1966, ''Flutter of Infinitely Long Plates and Shells. Part I: Plates,'' AIAA J., **4**, pp. 1370–1377.

[6] Weaver, D. S., and Unny, T. E., 1970, ''The Hydroelastic Stability of a Flat Plate,'' ASME J. Appl. Mech., **37**, pp. 823–827.

[7] Weaver, D. S., and Unny, T. E., 1972, ''The Influence of a Free Surface on the Hydroelastic Stability of a Flat Panel,'' ASME J. Appl. Mech., **39**, pp. 53–58.

[8] Epstein, R. J., Srinivasan, R., and Dowell, E. H., 1995, ''Flutter of an Infinitely Long Panel in a Duct,'' AIAA J., **33**, pp. 109–115.

[9] Huang, L., 1995, ''Flutter of Cantilevered Plates in Axial Flow,'' J. Fluids Struct., **9**, pp. 127–147.

[10] Païdoussis, M. P. and Li, G. X., 1993, ''Pipes Conveying Fluid: A Model Dynamical Problem,'' J. Fluids Struct., **7**, pp. 137–204.

[11] Matsuzaki, Y., 1981, ''Reexamination of Stability of a Two-Dimensional Finite Panel Exposed to an Incompressible Flow,'' ASME J. Appl. Mech., **48**, pp. 472–478.

[12] Erdogan, F., and Gupta, G. D., 1972, ''On the Numerical Solution of Singular Integral Equations,'' Q. Appl. Math., **29**, pp. 525–534.

[13] Dowell, E. H., 1974, *Aeroelasticity of Plates and Shells*, Martinus Nijhoff Publishers, Dordrecht, The Netherlands, Appendix II.

[14] Kornecki, A., Dowell, E. H., and O'Brien, J., 1976, ''On the Aeroelastic Instability of Two-Dimensional Panels in Uniform Incompressible Flow,'' J. Sound Vib., **47**, pp. 163–178.

[15] Païdoussis, M. P., 1998, *Fluid-Structure Interactions: Slender Structures and Axial Flow*, Vol. 1, Academic Press, London, pp. 59–276.

[16] Horáček, J., and Zolotarev, I., 1984, ''Influence of Fixing the Edges of a Cylindrical Shell Conveying Fluid on its Dynamic Characteristics,'' Sov. Appl. Mech., **20**, pp. 756–765.

Aerodynamic Characteristics of Pressure-Pad Air Bars

Y. B. Chang
e-mail: ybae@okstate.edu
Mem. ASME

P. M. Moretti
Mem. ASME

School of Mechanical and Aerospace Engineering,
Oklahoma State University,
Stillwater, OK 74078

Air-flotation ovens are widely used for noncontact support and drying of coated paper and plastic films (generically called webs). The main components in typical air-flotation ovens are air bars which have slot nozzles or holes through which hot air jets are ejected. Problems in air-flotation drying techniques include sideward motion of the web, web flutter, and contact between the web and air bars. The key to analyzing these problems is to determine the aerodynamic forces on the web. This paper discusses the aerodynamic forces generated by pressure-pad-type air bars, each of which has two slot nozzles. Ground-effect theories, which were originally developed for the design of hovercraft, are re-examined. The theories are compared with the measured values of the aerodynamic forces for typical air bars. It is shown that ground effect theories can be applied to pressure-pad-type air bars if we properly define the equivalent values of the ground effect variables, which include thickness of the air jet, flotation height, ejection angle of the air jet, and the effective total pressure of the air jet. [S0021-8936(00)02801-4]

Introduction

When web materials such as paper and plastic films are coated, they need to be dried without contact while they are continuously moving. A variety of aerodynamic methods have been developed for effective drying without damaging the coatings. One method is to use air-flotation ovens having two (upper and lower) rows of air bars, as sketched in Fig. 1. Each air bar has two slot nozzles through which hot air is ejected toward the translating web. Air bars of this type are called pressure-pad air bars because of the nearly uniform cushion pressure developed between the air bar and the web. Hot air jets are used for both drying and noncontact support of the web. Typically, air bars are arranged in such a way that the web path in an oven is sinusoidal. The depth of the sinusoidal curve (amplitude of vertical deformation of the web) depends on the width and arrangement of the air bars, bending stiffness of the web, and operating conditions, such as supply air pressure and web tension. For example, thick aluminum foils or steel plates stay nearly flat in an oven. Bezella [1], Fraser [2,3], and Krizek [4] provide good summaries of applications of air-flotation ovens.

Aerodynamic forces (pressure distributions) on a rigid stationary web were measured by Pinnamaraju [5] for various air bars. He studied the effects of flotation height (distance between the air bar surface and the rigid web) on the aerodynamic forces and explained the out-of-plane stability characteristics of an air-floated web. Nisankararao [6] repeated and extended Pinnamaraju's experiments, and studied the effects of cross-directional tilt angle of a rigid web. Even though these tests were limited to a rigid and stationary web, the results help us understand the aerodynamic characteristics of air bars and the behavior of air-floated webs.

In this paper, ground effect theories, which were originally developed in connection with the development of hovercraft in the 1950s and 1960s, are re-examined and applied to pressure-pad-type air bars. The theories and the air bar test results are compared, and it is shown that ground effect theories can be useful tools for the analysis of the aerodynamic characteristics of air-flotation bars.

Contributed by the Applied Mechanics Division of THE AMERICAN SOCIETY OF MECHANICAL ENGINEERS for publication in the ASME JOURNAL OF APPLIED MECHANICS. Manuscript received by the ASME Applied Mechanics Division, Jan. 1, 1999; final revision, Sept. 10, 1999. Associate Technical Editor: R. C. Benson. Discussion on the paper should be addressed to the Technical Editor, Professor Lewis T. Wheeler, Department of Mechanical Engineering, University of Houston, Houston, TX 77204-4792, and will be accepted until four months after final publication of the paper itself in the ASME JOURNAL OF APPLIED MECHANICS.

Ground Effect Theories

Thin Jet Model. The basic ground effect model is shown in Fig. 2 and Fig. 3. For hovercraft, Fig. 2 represents the cross section of a circular or elliptical three-dimensional body. Our main interest, however, is in air bars, so that Fig. 2 should be understood as the cross section of a two-dimensional body. This model assumes that the thickness of jet flow is much smaller than the flotation height ($b/h \ll 1$), the thickness of jet flow does not change along the path of the jet, the flow profile across the jet is uniform, the jet speed does not change along the path of the jet, the path of the jet flow has a constant curvature and is tangent to the ground, and the pressure in the region surrounded by the two streams of air jet is constant.

The validity of these assumptions and the derivation of the ground effect equations are discussed in Mair [7], Jaumotte and Kiedrzynski [8], and Davies and Wood [9]. The key concepts involved in the classical thin jet model are briefly explained below. The horizontal force balance for the air jet requires

$$\rho b V_j^2 (1+\cos\theta) = p_c h \tag{1}$$

where ρ is the air density, b is the width of the air jet, V_j is the velocity of the air jet, and p_c is the cushion pressure (page pressure). The effective total pressure (gage pressure) of the air jet after the nozzle is

$$p_j = \frac{p_c}{2} + \frac{\rho V_j^2}{2} \tag{2}$$

where the static pressure is assumed to be the average of the ambient pressure and the cushion pressure because these two pressures are acting on the two sides of the air jet. From Eqs. (1) and (2) we obtain the pressure ratio

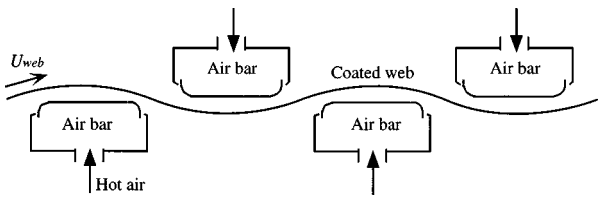

Fig. 1 Cross section of air bars and the web in oven

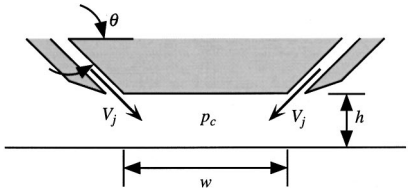

Fig. 2 Schematic of ground effect model

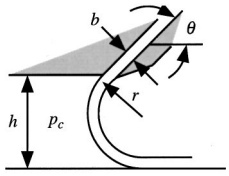

Fig. 3 Thin jet model

$$\frac{p_c}{p_j}=\frac{2(1+\cos\theta)}{h/b+1+\cos\theta}. \tag{3}$$

Note that all pressures are gage pressures. The lift force per unit length of air bar is

$$F=p_c w+2\rho b V_j^2\sin\theta \tag{4}$$

where w indicates the distance between the two slot nozzles. The last term in the above equation is the change of momentum of the two air jets in the vertical direction. By eliminating p_c and $\rho b V_j^2$ from Eq. (4) using Eqs. (1) and (3), we obtain

$$\frac{F}{p_j b}=\frac{p_c}{p_j}\left(\frac{w}{b}+\frac{h}{b}\frac{2\sin\theta}{1+\cos\theta}\right). \tag{5}$$

Recall that the flotation height h is assumed much larger than the jet thickness b. We can show that, when $(b/h)(1+\cos\theta)>1$, Eq. (3) predicts a cushion pressure higher than the total pressure of the air jet. As an extreme case, when the flotation height approaches zero, Eq. (3) predicts $p_c/p_j=2$.

Thick Jet Models. Following Crewe and Eggington [10], if we assume that the static pressure varies across the air jet, the force balance for an infinitesimal element shown in Fig. 4 can be written as

$$\frac{dp}{dr}=\frac{\rho V_j^2}{r} \tag{6}$$

where the radius r is a variable, and the flow velocity is assumed to be uniform. The total pressure at radius r can be written as

$$p_j=p+\frac{\rho V_j^2}{2} \tag{7}$$

From Eqs. (6) and (7),

$$\int_0^{p_c}\frac{dp}{p_j-p}=\int_{r_o}^{r_o+b}\frac{2dr}{r}. \tag{8}$$

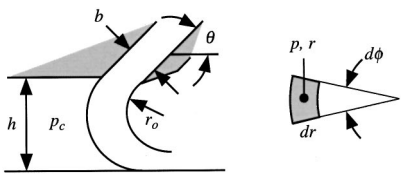

Fig. 4 Thick jet model

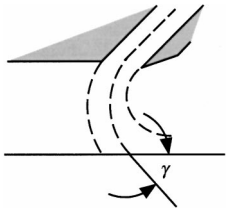

Fig. 5 Definition of angle γ

By performing the integrations and using the geometrical relationship $h=b+r_o(1+\cos\theta)$, we obtain

$$\frac{p_c}{p_j}=1-\left(\frac{h/b-1}{h/b+\cos\theta}\right)^2. \tag{9}$$

This pressure ratio approaches 1 when the ratio h/b approaches 1. When the flotation height is very small, Eq. (9) predicts that the cushion pressure can be negative.

Another thick jet model is obtained when we treat r in Eq. (8) as a constant and write the right-hand side term as $2b/r$ ([8]). This concept does not seem to be accurate, but yields the following cushion pressure equation which agrees well with Stanton Jones' experimental results cited by Mair [7]:

$$\frac{p_c}{p_j}=1-e^{-2(b/h)(1+\cos\theta)} \tag{10}$$

The pressure ratio predicted by Eq. (10) approaches 1 when the flotation height approaches zero. Even though none of these theories accounts for the case where the flotation height is smaller than the nozzle opening (jet thickness), Eq. (10) seems to be a reasonable choice if we want to analyze ground-effect problems in a wide range of flotation height. Strand [11] provides additional discussion of a thick jet model.

Other Ground Effect Models. Alexander [12] attempted to improve the ground effect models mentioned above for the case where the flotation height is small; that is, when $h/b<1$. Alexander's inviscid theory assumes that the total pressure of the air jet does not change even after it touches the wall. This assumption results in an equation which predicts the cushion pressure always higher than the earlier thin jet model, which already overpredicts the cushion pressure when h/b is small. Alexander's equation is

$$\frac{p_c}{p_j}=\frac{2(1+\cos\theta)}{\frac{h}{b}+\frac{1}{2}+\cos\theta}. \tag{11}$$

Another attempt was made by Bradbury [13] to improve the earlier ground effect models. Bradbury's analytical model takes into account the mixing phenomenon and is based on the study of reattachment of a plane jet to an adjacent surface ([14]). The resulting equation is

$$\frac{p_c}{p_j}=\frac{2(\cos\theta+\cos\gamma)}{\frac{h}{b}+\frac{1}{2}\cos\theta+\cos\gamma} \tag{12}$$

where γ is the angle that the extended jet centerline makes with the horizontal plane as shown in Fig. 5. Unlike the jet ejection angle θ which is a geometric property of the nozzle, the angle γ is difficult to determine. The equation overpredicts the cushion when the ratio h/b is smaller than approximately 4.

Comparison of Theories. Effects of flotation height and ejection angle of the air jet on the cushion pressure are plotted in Fig. 6 and Fig. 7, respectively, for the various theories presented above. In Fig. 6, the ejection angle of the air jet is assumed to be 60 deg. The differences among the different theories are small

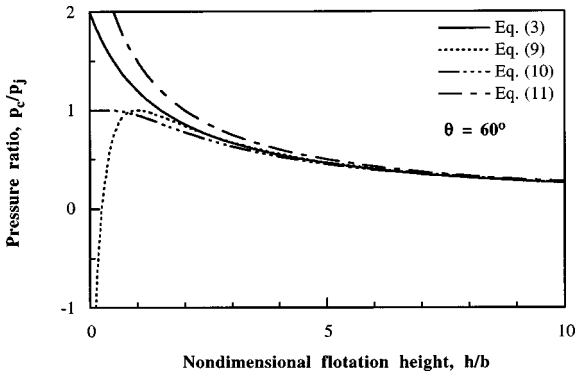

Fig. 6 Effects of flotation height on cushion pressure

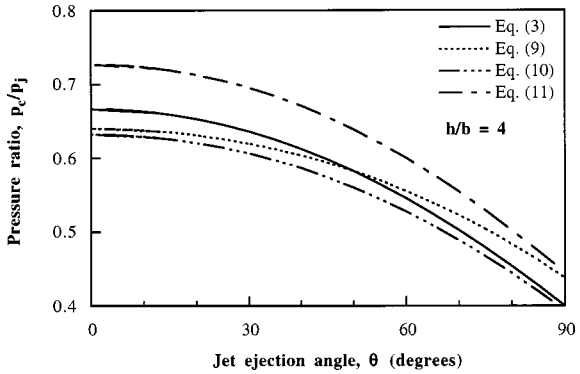

Fig. 7 Effects of jet ejection angle on cushion pressure

when $h/b>4$. It is apparent that Eqs. (3) and (11) overpredict the cushion pressure when the flotation height is small. Among the two thick jet equations, Eq. (10) appears to be more reasonable to use for a wide range of flotation heights because Eq. (9) predicts a sudden drop (to a negative value) of cushion pressure when the flotation height approaches zero. Figure 7 shows that the effect of the ejection angle of the air jet on the cushion pressure is weak when the angle is small, but its effect becomes prominent as it approaches 90 deg.

Air Bars With Vent Holes. Some commercial air bars have vent holes through which the air in the gap between the web and the air bar can escape to the ambient. The air bar used in this study has two rows of holes as sketched in Fig. 8 and Fig. 9. The vent holes are connected to a large channel, the two ends of which are open to the ambient. For a typical air bar, the channel area is approximately 250 times larger than the area of a hole. When the flotation height is large, the effects of the vent holes on the cushion pressure profile may be negligible because the cushion pressure is low and the pressure gradient along the width of the air bar is small even if a small amount of air escapes through the vent holes. When the flotation height is small, on the other hand, a large pressure gradient is developed along the width of the air bar, and the cushion pressure profile can be strongly affected by the vent holes. If we assume that the flotation height is uniform and small, and the flow in the gap between the web and the air bar is laminar, the pressure drop in the gap can be expressed as ([15])

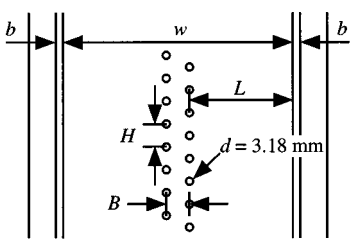

b = 3.30 mm, w = 127 mm, B = H = 12.7 mm, L = 57.2 mm
(w/b = 39.5, B/b = H/b = 3.95, L/b = 17.3)

Fig. 8 Down view of typical air bar with vent holes

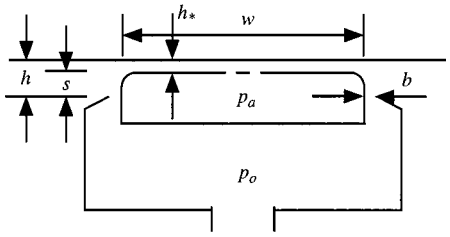

b = s = 3.30 mm, w = 127 mm (s/b = 1, w/b = 39.5)

Fig. 9 Cross section of typical air bar with vent holes

$$\Delta p_1 = \frac{12\mu QL}{h_*^3} \tag{13}$$

where Q is the flow rate in the gap per unit length the air bar (or per unit width of the web), L is the distance between the nozzle and the vent holes, and h^* is the height of the gap. The air flow through the vent holes can be approximated as ([15])

$$Q = NC_d \frac{\pi d^2}{4} \sqrt{\frac{2\Delta p_2}{\rho}} \tag{14}$$

where Δp_2 is the pressure drop across the vent holes, N is the number of holes in a row per unit length of air bar, C_d is the discharge coefficient, and d is the diameter of the holes (Fig. 8 and Fig. 9). The cushion pressure near the nozzle is the sum of the two pressure losses:

$$p_c = \Delta p_1 + \Delta p_2 . \tag{15}$$

Since the flow rate in the gap between the web and the air bar must be the same as the total flow rate through one row of holes, the value of Q must be the same in Eqs. (13) and (14). If we eliminate Q and Δp_2 from Eqs. (13), (14), and (15), the pressure drop in the gap (Δp_1) becomes

$$\frac{\Delta p_1}{p_c} = \frac{p_*}{p_c}\left(\sqrt{1+2\frac{p_c}{p_*}} - 1 \right) \tag{16}$$

where

$$p_* = \frac{1}{\rho}\left(\frac{3\pi NC_d d^2 \mu L}{h_*^3} \right)^2 . \tag{17}$$

The lift force per unit length of air bar is

$$F = (p_c - \Delta p_1)(w-2L) + (p_c - \Delta p_1/2)2L + 2\rho b V_j^2 \sin\theta$$
$$= p_c w + \Delta p_1 (L-w) + 2\rho b V_j^2 \sin\theta. \tag{18}$$

If we assume that the cushion pressure near the nozzle is not affected by the vent holes, and only a small fraction of the air ejected from the nozzle is vented through the holes, then the cushion pressure near the nozzle is predicted by Eq. (10). The lift force can be rewritten in nondimensional form, by combining Eq. (18) and Eq. (1), as

$$\frac{F}{bp_j} = \frac{p_c}{p_j}\left(\frac{w}{b} + \frac{h}{b}\frac{2\sin\theta}{1+\cos\theta} + \frac{L-w}{b}\frac{\Delta p_1}{p_c} \right) \tag{19}$$

where p_c/p_j is given by Eq. (10) and $\Delta p_1/p_c$ is given by Eq. (16).

Comparison of Theories and Air Bar Experiments

The experimental data reviewed in this paper are from Pinnamaraju [5] and Nisankararao [6]. Two air bars, schematically shown in Fig. 10, were used for the measurement of the air pressure profile on a rigid stationary web. The two air bars are different mainly in their widths (w) and nozzle openings (b), and they are approximately 0.36 m (14 in.) in length. A rigid plate, 12.7-mm thick piece of Plexiglas, was placed against the working surface of the air bar. The plate was mounted on slide bearings so that the pressure profile could be measured while the plate was traversed. The plate was larger than it appears in Fig. 10 so that it covered the whole surface area of the air bar at all locations of the plate. The main test variable is the distance between the rigid web and an air bar. The blower used for air supply could deliver 1740 Pa (seven inches of water) of air pressure when the flow rate was zero, and the flow rate was approximately 0.028 m^3/min (580 CFM) when the blower's inlet and outlet were open to the ambient. The flow valve was always fully open during the tests, and the flow rate was not controlled.

Typical pressure measurement results are shown in Fig. 11 and Fig. 12. Note that $x=0$ corresponds to the center of the air bar. The air pressure on the web is nearly uniform in a wide region surrounded by the air jets, and high peak pressures appear near the slot nozzles. When the air gap between an air bar and the web is large, a drop of cushion pressure is observed adjacent to the high peak pressures. This pressure drop implies that the main stream of jet flow induces a strong vortex in the pressurized region.

Comparison of the test results with the ground effect theories requires some care, because the geometry of the tested air bars is different from the basic geometry of the ground effect model. In order to compare the theories with the test results, we need to define equivalent values of the ground effect variables, which include thickness of the air jet, the ejection angle of the air jet, flotation height, and the total pressure of jet flow at the nozzle. First, the thickness of the air jet can be defined as the nozzle opening. Second, the ejection angle of the air jet and the location of flow separation on the air bar surface are uncertain for the tested air bars. As sketched in Fig. 10, the surface of each tested air bar has curved corners near the slot nozzles. Note that there are various types of commercial air bars having geometries different from the air bars discussed in this paper. It is believed that when the flotation height is large (when the cushion pressure is small) the air stream follows the curved surface up to a certain point and then separates from the air bar surface with an angle smaller than 90 deg. When the flotation height is small, however, the air jet may separate from the air bar surface with an angle of nearly 90 deg. For comparison with the theories, it is assumed that the ejection angle of the air jet is 90 deg for all cases. Definition of the flotation height is also uncertain because the exit of the air jet is lower than the top surface of the air bar. It seems reasonable to define the flotation height as the distance between the web and the exit of the jet (h) rather than the distance between the web and the top surface of the air bar (h_*). The effective total pressure of the air jet is described by a nozzle coefficient, which is defined as the ratio of the effective total pressure of the air jet after the nozzle to the total pressure inside the air bar ($C \equiv p_j / p_o$). It is easy to measure the supply air pressure inside the air bar, but the effective total pressure of the air jet after the nozzle cannot be determined by simply measuring the total pressure at the nozzle. The nozzle coefficient accounts for the effects of flow contraction and the effects of mixing and surface friction. It is found that the mean squared error between Eq. (10) and the test data becomes minimum when $C \equiv p_j / p_o = 0.85$. If we consider the thin jet theory,

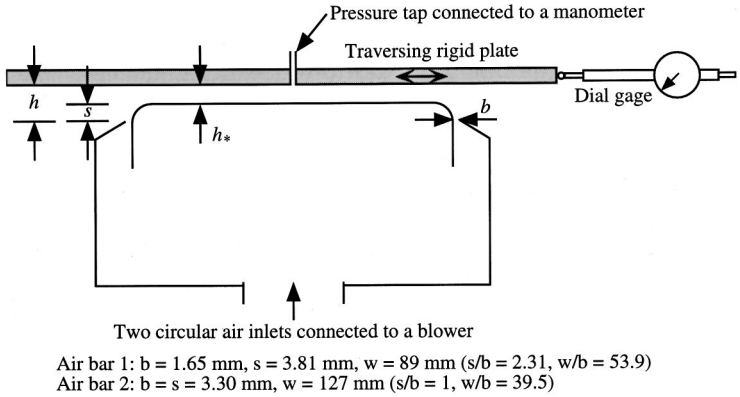

Fig. 10 Schematic of test setup

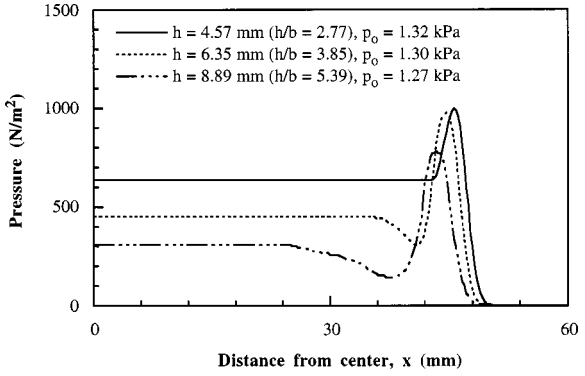

Fig. 11 Effects of flotation height on pressure distribution for air bar 1

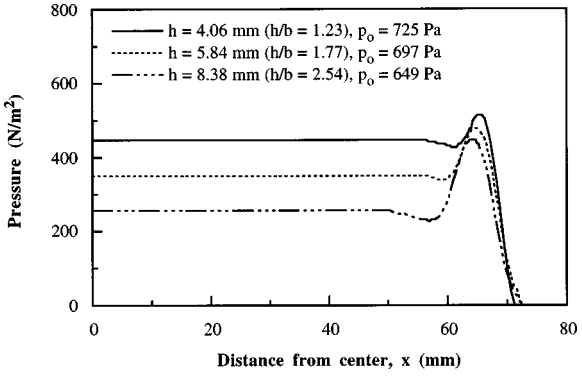

Fig. 12 Effects of flotation height on pressure distribution for air bar 2

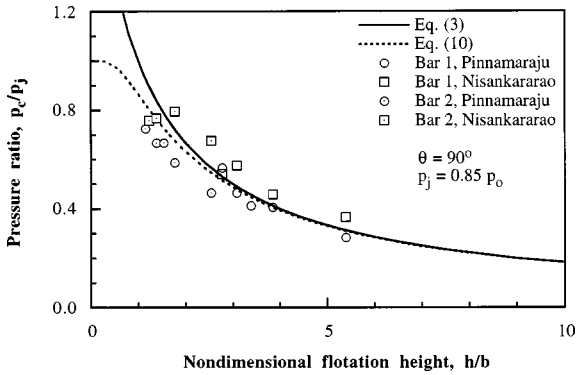

Fig. 13 Comparison of theories and experiments for cushion pressure

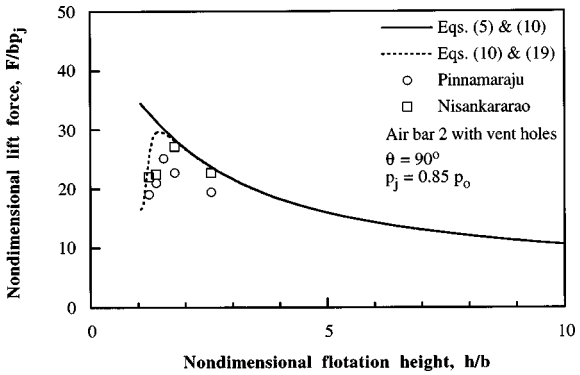

Fig. 16 Lift force per unit length of air bar with vent holes

Eq. (3), the error becomes minimum when the nozzle coefficient is 0.80. In Figs. 13, 14, and 15 it is assumed that the nozzle coefficient is 0.85.

The effects of vent holes on pressure profile and lift force were measured. The geometric properties of the tested air bar are $w=0.127$ m $(w/b=38.5)$, $b=s=0.0033$ m $(s/b=1)$, $d=0.0032$ m $(d/b=0.97)$, $B=H=0.0127$ m, and $N=78.7$ holes per meter (for each row). The discharge coefficient C_d is a function of Reynolds number, which in turn depends on Δp_2. For simplicity, we will assume $C_d=0.6$, which is a reasonable approximation when $\mathrm{Re}_d=\rho V_{\mathrm{vent}} d/\mu>20$ or $V_{\mathrm{vent}}>0.1$ m/s, where V_{vent} is the flow velocity at the holes. As shown in Fig. 16, the thick jet model far overpredicts the lift force when the flotation height is small where the vent holes play an important role. The analytical model for air bars with vent holes (Eq. (19)) follows the trend of the measurement data, but it seems to predict the upper limit of measured lift force. Note that h is the distance between the plate and the exit of air jet, and the plate is in contact with the air bar surface $(h_*=0)$ when $h/b=1$ for the tested air bar. It was observed in a pilot air-flotation oven that, when a flexible web under tension was pushed by hand toward an air bar with vent holes, the web suddenly contacted the whole surface area of the air bar. When the web was pushed away from the air bar by hand, it suddenly popped up, away from the air bar surface. This phenomenon could not be observed with any air bars without vent holes. These observations agree, qualitatively, with the prediction model and the rigid web experiments.

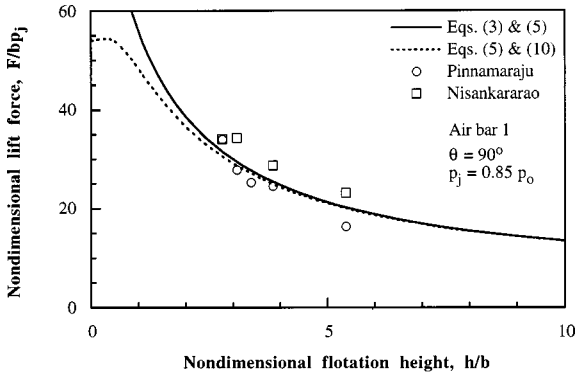

Fig. 14 Comparison of theories and experiments for lift force

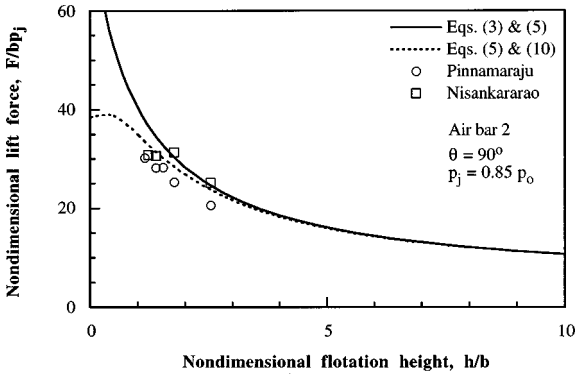

Fig. 15 Comparison of theories and experiments for lift force

Discussion

Richardson et al. [16] measured the effects of Reynolds number $(\rho V_j b/\mu)$ and nozzle opening (b) on the cushion pressure. Their results show that the inviscid theory overestimates the cushion pressure up to 40 percent at small jet thicknesses, low Reynolds numbers, and large flotation heights. The error is reduced to about five percent (still the theory overestimates) at large jet thicknesses, high Reynolds numbers, and small flotation heights. The nozzle sizes for our air bar experiments were 1.65 mm and 3.30 mm $(h/b=1.2-5.4$ and $h_*/b=0.15-3.0)$ while Richardson's nozzle sizes were 2.54 mm and 5.08 mm $(h/b=0.3-6.0$ and h_*/b = undefined). The Reynolds number for our air bar experiments ranged approximately from 4000 to 6000, which is close to the lower limit of Richardson's test range. The ranges of the air bar test parameters fall on the side where Richardson observed the biggest differences between the theoretical prediction and measurement of cushion pressure. Crewe and Eggington [10] also report that their measured cushion pressure is lower than the predicted, and that the error increases as the air nozzle thickness is reduced. They attribute the error to a ''scale effect'' related to the development of boundary layers inside the nozzle. A good correlation was obtained when they corrected the total pressure of the air jet at the nozzle as $p_j'=p_j(1-\Delta b/b)$, where b is the nozzle thickness and $\Delta b=1.27$ mm. For our air bar experiments, where the two air bars have much different nozzle openings $(b=1.65$ mm and 3.30 mm), only the nozzle coefficient $(C\equiv p_j/p_o)$ needed to be introduced as correction factor.

Hope-Gill [17] analyzed the effects of high-speed jet flow and found that the coefficient of cushion pressure decreases as the Mach number increases. For example, when the flotation height to jet thickness ratio h/b is 2 and 4, the coefficient of cushion pressure at sonic speed of jet flow is reduced by two percent and four percent respectively, compared to the values at low subsonic cases. For our air bar experiments, the flow speed was lower than 42 m/s $(M=0.12)$. In most cases, the air speed at the nozzle of an air bar is less than 100 m/s $(M=0.29)$. Therefore, the effect of Mach number is negligible for most air-flotation applications.

Closing Remarks

Ground effect theories are proved to be useful tools for analyzing the aerodynamic characteristics of pressure-pad air bars. The aerodynamic characteristics of pressure-pad air bars are determined by four factors: the ejection angle of the air jet, thickness of the air jet, width of the air bar, and the effective total pressure of the air jet after the nozzle. By properly defining the equivalent values of these variables we can predict the aerodynamic forces on the web floated by an air bar. The effect of the vent holes on pressure-pad air bars is analyzed, and the proposed simple model is found to agree reasonably well with rigid-web test results.

Acknowledgment

The research was funded by the Web Handling Research Center (WHRC) at Oklahoma State University and its supporting companies. The authors are grateful to the anonymous reviewers for their invaluable suggestions.

Nomenclature

b = width of air jet; width of slot nozzle
C = nozzle coefficient, p_j/p_o
C_d = discharge coefficient of vent holes on air bar surface
d = diameter of vent holes
F = lift force per unit length of air bar
h = effective flotation height
h_* = gap between top surface of air bar and rigid web
L = channel length; distance between slot nozzle and the closest row of vent holes
M = Mach number
N = number of vent holes in each row of holes per unit length of air bar
p = pressure (gage pressure)
p_c = cushion pressure (gage pressure)
p_j = effective total pressure of air jet (gage pressure)
p_o = supply pressure measured inside air bar (gage pressure)
Q = flow rate per unit length
r = radius of curvature
V_j = speed of jet flow
w = width of air bar; distance between two slot nozzles
γ = angle between extended jet centerline and horizontal plane
μ = dynamic viscosity of air
θ = jet ejection angle
ρ = air density

References

[1] Bezella, G. L., 1976, ''Application of Floater Dryers to the Paper Industry,'' Tappi J., **59**, No. 4, pp. 92–96.
[2] Fraser, W. A. R., 1983, ''Air Flotation Systems: Theoretical Considerations & Practical Applications, Part I,'' Paper, Film, Foil Converter, May, pp. 162–165.
[3] Fraser, W. A. R., 1983, ''Air Flotation Systems: Theoretical Considerations & Practical Applications, Part II,'' Paper, Film, Foil Converter, June, pp. 112–118.
[4] Krizek, F., 1986, ''Impinging Jet Systems to Support and Dry Paper,'' Drying Technol., **4**, No. 2, pp. 271–294.
[5] Pinnamaraju, R., 1992, ''Measurements on Air Bar/Web Interaction for the Determination of Lateral Stability of a Web in Flotation Ovens,'' M.S. report, Oklahoma State University, Stillwater, OK.
[6] Nisankararao, K., 1994, ''An Experimental Study of Aerodynamic Forces of Air Bars,'' M. S. thesis, Oklahoma State University, Stillwater, OK.
[7] Mair, W. A., 1964, ''The Physical Principles of Hovercraft,'' Hovering Craft Hydrofoils, **4**, No. 3, pp. 5–13.
[8] Jaumotte, A., and Kiedrzynski, A., 1965, ''Theory and Experiments on Air Cushion Vehicles at Zero Speed,'' Hovering Craft Hydrofoils, **4**, pp. 4–25.
[9] Davies, M. J., and Wood, D. H., 1983, ''The Basic Aerodynamics of Flotation,'' ASME J. Fluids Eng., **105**, pp. 323–328.
[10] Crewe, P. R., and Eggington, W. J., 1960, ''The Hovercraft—A New Concept in Maritime Transport,'' Trans. R. Inst. Naval Arch., **102**, pp. 315–356.
[11] Strand, T., 1961, ''Inviscid-Incompressible-Flow Theory of Static Peripheral Jets in Proximity to the Ground,'' J. Aerosp. Sci., **28**, No. 1, pp. 27–33.
[12] Alexander, A. J., 1966, ''The Momentum Equation for a Static Hovercraft at Zero Incidence,'' J. R. Aeronaut. Soc., **70**, p. 363.
[13] Bradbury, L. J. S., 1967, ''A Mixing Theory for the Hovering of Peripheral-Jet Air Cushion Vehicles,'' J. R. Aeronaut. Soc., **71**, pp. 53–54.
[14] Bourque, C., and Newman, B. G., 1960, ''Reattachment of a Two-Dimensional Incompressible Jet to an Adjacent Flat Plate,'' Aeronaut. Q., **11**, pp. 201–232.
[15] Rouse, H., 1946, *Elementary Mechanics of Fluids*, Wiley, New York (Dover edition published in 1978).
[16] Richardson, H. H., Ribich, W. A., and Ercan, Y., 1968, ''Pressure-Flow-Displacement Characteristics of a Peripheral Jet Fluid Suspension,'' Report DSR 76110-7, MIT.
[17] Hope-Gill, C. D., 1970, ''Analysis of High-Speed Peripheral Jet for AVC Applications,'' J. Hydronaut., **4**, pp. 80–85.

The Tip Region of a Fluid-Driven Fracture in an Elastic Medium

D. Garagash

E. Detournay[1]
e-mail: detou001@tc.umn.edu

Department of Civil Engineering,
University of Minnesota,
500 Pillsbury Drive SE,
Minneapolis, MN 55455

The focus of this paper is on constructing the solution for a semi-infinite hydraulic crack for arbitrary toughness, which accounts for the presence of a lag of a priori unknown length between the fluid front and the crack tip. First, we formulate the governing equations for a semi-infinite fluid-driven fracture propagating steadily in an impermeable linear elastic medium. Then, since the pressure in the lag zone is known, we suggest a new inversion of the integral equation from elasticity theory to express the opening in terms of the pressure. We then calculate explicitly the contribution to the opening from the loading in the lag zone, and reformulate the problem over the fluid-filled portion of the crack. The asymptotic forms of the solution near and away from the tip are then discussed. It is shown that the solution is not only consistent with the square root singularity of linear elastic fracture mechanics, but that its asymptotic behavior at infinity is actually given by the singular solution of a semi-infinite hydraulic fracture constructed on the assumption that the fluid flows to the tip of the fracture and that the solid has zero toughness. Further, the asymptotic solution for large dimensionless toughness is derived, including the explicit dependence of the solution on the toughness. The intermediate part of the solution (in the region where the solution evolves from the near tip to the far from the tip asymptote) of the problem in the general case is obtained numerically and relevant results are discussed, including the universal relation between the fluid lag and the toughness. [S0021-8936(00)02401-6]

Introduction

The problem of a fluid-driven fracture propagating in rock arises in hydraulic fracturing, a technique used widely in the oil and gas industry to enhance the recovery of hydrocarbons from underground reservoirs, as well as in the formation of intrusive dykes in the earth crust and in the transport of magma in the lithosphere by means of fractures.

The conditions under which fluid-driven fractures propagate in rock vary widely and are usually not well defined. In that respect, mathematical modeling of the propagation of such fractures becomes an important tool for predicting the evolution of fluid pressure, fracture opening, and fracture geometry and for understanding the dependence of the process on rock properties (fracture toughness and elastic constants), *in situ* stresses, fracturing fluid properties (essentially viscosity) and boundary conditions.

Mathematical modeling of fluid-driven fractures has attracted numerous contributions since the 1950s (see, e.g., [1–11]). These models require simultaneous consideration of fluid and solid mechanics: on the one hand, the lubrication equation to characterize the flow of fluid in the fracture (and, in the case of a permeable medium, a time-dependent equation that governs the exchange of fluid between the fracture and the rock); on the other hand, the elasticity equations to describe the deformation and propagation of the fracture. Such models are notoriously difficult to develop because of the strong nonlinear coupling between the lubrication and elasticity equations and the nonlocal character of the elastic response of the fracture. Furthermore, constructing the solution for the near-tip region represents in itself a formidable challenge which has motivated a series of dedicated research efforts ([9,12–20]).

Interest in the tip region stems not only from a basic quest to find the correct structure of the solution (in particular to determine the unknown lag between the fluid front and the crack tip), but also from the recognition that the strong fluid-solid coupling is mainly confined to a small region near the tip of the advancing fracture (small compared to the overall fracture dimension), where rapid variation of the fluid pressure is taking place. More importantly, however, the tip solution holds the key for understanding the propagation regime of a fluid-driven fracture. Two limiting regimes exist ([21–23]): in the viscosity-dominated regime, the toughness of the solid is ''small'' enough that the solution of a hydraulic fracture can be approximated by the zero toughness solution ([8,10]); while in the toughness-dominated regime the fluid can be assumed to be inviscid as in the solution of Huang et al. ([24]).

For a hydraulic fracture propagating in a zero toughness solid ($K_{Ic}=0$, viscosity-dominated solution), it was recently recognized that the fluid-solid coupling in the near-tip region of the fracture actually corresponds to an exact matching singularity between the lubrication and elasticity equations under the assumptions that the fluid flows up to the tip of the fracture and that the solid has zero toughness ([7,9,15]). For a Newtonian fluid, this matching singularity is characterized by a crack opening ω varying as $x^{2/3}$ (where x is distance from the tip), and not as $x^{3/2}$ as predicted by linear elastic fracture mechanics for the case of zero toughness, and the fluid pressure p as $-x^{-1/3}$. This singularity is thus associated with a negative infinite fluid pressure at the tip of the fracture. It should be noted that the singular asymptotes of the fluid pressure and fracture opening near the tip, provide the exact solution for a *semi-infinite* fluid-driven fracture propagating steadily in impermeable elastic solid of zero toughness ([15]). The new tip singularity was used by Carbonell and Detournay [10] and by Savitski and Detournay [11] to construct self-similar solutions for a finite hydraulic fracture propagating in a zero toughness elastic solid under plane-strain and axisymmetric conditions, respectively.

For a hydraulic fracture propagating in a solid with toughness $K_{Ic}>0$, it can readily be shown that a lag λ is required between the fluid front and the crack tip to ensure coherence of the mathematical solution ([22]). Indeed, under the condition of $\lambda=0$ (no

[1]To whom correspondence should be addressed.

Contributed by the Applied Mechanics Division of THE AMERICAN SOCIETY OF MECHANICAL ENGINEERS for publication in the ASME JOURNAL OF APPLIED MECHANICS. Manuscript received by the ASME Applied Mechanics Division, Aug. 14, 1998; final revision, June 22, 1999. Associate Technical Editor: W. J. Drugan. Discussion on the paper should be addressed to the Technical Editor, Professor Lewis T. Wheeler, Department of Mechanical Engineering, University of Houston, Houston, TX 77204-4792, and will be accepted until four months after final publication of the paper itself in the ASME JOURNAL OF APPLIED MECHANICS.

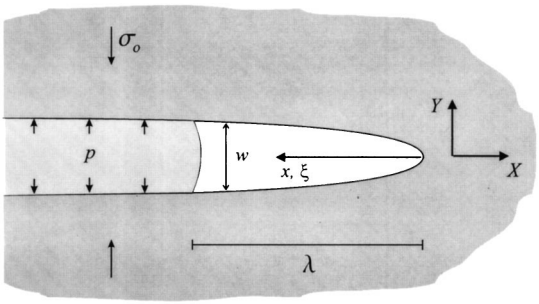

Fig. 1 Semi-infinite fluid driven crack with the lag zone adjacent to the tip

lag), combination of the lubrication equation with the linear elastic fracture mechanics asymptotic fracture opening $w \sim x^{1/2}$ implies that the fluid pressure has a logarithmic singularity, $p \sim \ln x$, which is mathematically inconsistent with the assumed eigensolution. Hence, the presence of the lag removes the singularity in the fluid pressure, and at the same time enables the classical square root stress singularity of linear elastic fracture mechanics to take place. It could also be argued that a lag also necessarily forms even if $K_{Ic}=0$, since the fluid cannot sustain an arbitrary large negative pressure. (Such an argument is obviously akin to the question of the existence of a process zone or a plastic zone to ensure finiteness of the stress at the crack tip.) Although the assumption of zero lag does not lead to any mathematical inconsistency for $K_{Ic}=0$ (contrary to the case $K_{Ic}>0$), a lag must necessarily exist if the supplementary condition of a minimum fluid pressure (here taken to be zero) is introduced. In which case, the solution for $K_{Ic}>0$ can be expected to be continued in the limit $K_{Ic}=0$, but this then raises the question of the meaning of the zero toughness singular solution.

In this paper, we construct the solution of the near-tip region for the case of arbitrary toughness (including the limit $K_{Ic}=0$), by analyzing the problem of a semi-infinite hydraulic crack propagating at constant velocity V in an impermeable linear elastic medium (see Fig. 1). The elastic solid is characterized by the plane-strain modulus $E'=E/(1-\nu^2)$, where E is the Young's modulus and ν the Poisson's ratio, and the material toughness K_{Ic}; and the Newtonian fluid (assumed to be incompressible) by the viscosity μ. There is a far-field confining stress σ_o acting perpendicular to the fracture.

We assume that a fluid lag exists adjacent to the crack tip. Since the crack propagation is stationary, the fluid front propagates with the same velocity as the crack tip V. The length λ of the tip cavity is thus constant, but is unknown and is part of the solution. This tip cavity is filled by evaporated fracturing fluid under a constant pressure which is assumed, however, to be negligibly small compared to the far-field stress σ_o and is therefore set equal to zero. But for the presence of the unknown lag λ and the pressure boundary condition $p=0$, the problem considered here is identical to the one treated by Desroches et al. [15] for the zero toughness case.

The paper is organized as follows. First, we formulate the governing equations and derive a dimensionless form of these equations which only depends on one number κ, having the meaning of a dimensionless toughness. The asymptotic forms of the solution near and away from the tip are then discussed. It is shown that the solution is not only consistent with linear elastic fracture mechanics at the tip, but that its asymptotic behavior at infinity is actually given by the zero toughness singular solution of a semi-infinite hydraulic fracture obtained by Desroches et al. [15]. The intermediate part of the solution (in the region where the solution evolves from the near tip to the far from the tip asymptote) of the problem is obtained numerically. We also formulate the asymptotic solution for large dimensionless toughness κ, and derive the explicit dependence of this asymptotic solution on κ. Finally, relevant results are presented and discussed, including the universal relationship between the scaled fluid lag Λ and the toughness κ.

Governing Equations

The flow of a viscous incompressible fluid in the crack is described by the equations of lubrication theory ([25]); i.e., the continuity equation

$$\frac{\partial w}{\partial t}+\frac{\partial q}{\partial X}=0 \tag{1}$$

and Poiseuille law

$$q=-\frac{w^3}{12\mu}\frac{\partial p}{\partial X} \tag{2}$$

where p is the fluid pressure, w the crack opening, and q the fluid flow rate per unit width of the crack. These field quantities are function of both the spatial coordinate X (with the fixed reference X-axis chosen to be parallel to the fracture), and the time t.

The other equation relating the net loading on the crack defined as $p-\sigma_o$ and the crack-opening w is given by elasticity theory (e.g., [26])

$$p(X,t)-\sigma_o=\frac{E'}{4\pi}\int_{-\infty}^{X_{\text{tip}}}\frac{\partial w(s,t)}{\partial s}\frac{ds}{X-s} \tag{3}$$

where the integral is taken in the sense of a Cauchy principal value. In (3), $X_{\text{tip}}=Vt$ denotes the tip position.

After performing the transformation from a fixed to moving with the crack-tip coordinate system $x=X_{\text{tip}}-X=Vt-X$, making use of the condition of steady propagation and upon integrating the continuity Eq. (1), the lubrication equations reduce to ([15]),

$$w^2(x)\frac{dp}{dx}=12\mu V \quad \text{for } x\in\,]\lambda,\infty[. \tag{4}$$

In the lag region, the condition on p is simply

$$p=0 \quad \text{for } x\in[0,\lambda]. \tag{5}$$

Also the elasticity Eq. (3) transforms as

$$p(x)-\sigma_o=\frac{E'}{4\pi}\int_0^{\infty}\frac{dw(s)}{ds}\frac{ds}{x-s}. \tag{6}$$

To be complete, the system of Eqs. (4)–(6) has to be supplemented by the criterion for crack propagation

$$K_I=K_{Ic} \tag{7}$$

where K_I is the stress intensity factor of the crack and K_{Ic} is the material toughness. Noting the asymptotic expression for opening w close to the crack tip (linear elastic fracture mechanics singular region) in terms of K_I (e.g., [26]) and using (7) we write

$$w=\frac{4K_{Ic}}{E'}\left(\frac{2x}{\pi}\right)^{1/2}+O(x^{3/2}). \tag{8}$$

Henceforth, we will use (8), which also prescribes the asymptotic behavior of w, rather than (7) for the condition of crack propagation.

Scaling and Dimensionless Formulation

The problem depends on five dimensional parameters μ, V, σ_o, E', and K_{Ic}. First, we define two lengthscales L_μ and L_κ, and a small parameter ϵ

$$L_\mu=\frac{12\mu VE'^2}{\sigma_o^3}, \quad L_\kappa=\frac{8}{\pi}\left(\frac{K_{Ic}}{\sigma_o}\right)^2, \quad \epsilon=\frac{\sigma_o}{E'} \tag{9}$$

The lengthscale L_μ is associated with viscous dissipation ([15]), while L_κ characterizes the dissipation due to fracturing of the solid. Next, we introduce the dimensionless crack opening Ω, the net pressure Π and the moving coordinate ξ

$$\Omega=\frac{w}{\epsilon L_\mu},\quad \Pi=\frac{p-\sigma_o}{\sigma_o},\quad \xi=\frac{x}{L_\mu} \tag{10}$$

The system (4)–(6) and (8) then takes the form

$$\Omega^2(\xi)\Pi'(\xi)=1 \quad \text{for } \xi\in]\Lambda,\infty[\tag{11}$$

$$\Pi(\xi)=-1 \quad \text{for } \xi\in[0,\Lambda] \tag{12}$$

$$\Pi(\xi)=\frac{1}{4\pi}\int_0^\infty \Omega'(\eta)\frac{d\eta}{\xi-\eta} \tag{13}$$

$$\Omega(\xi)=\kappa\xi^{1/2}+O(\xi^{3/2}) \tag{14}$$

where (12) specifies the pressure in the lag region. In the above, Λ and κ denote the dimensionless coordinate of the fluid front and the dimensionless toughness, respectively, defined as

$$\Lambda=\frac{\lambda}{L_\mu},\quad \kappa=2\left(\frac{L_\kappa}{L_\mu}\right)^{1/2}. \tag{15}$$

Thus, (11)–(14) completely defines the crack-opening $\Omega(\xi;\kappa)$ and the net pressure $\Pi(\xi;\kappa)$ for the semi-infinite fracture ($0\leqslant\xi<\infty$), as well as the position of the fluid front $\Lambda(\kappa)$. Note that, the normalized system of equations and boundary conditions (11)–(14) depends on one number κ (and not on two numbers, according to dimensional analysis considerations only).

Elastic Expression for the Crack Opening

Equation (13) expresses the net loading $\Pi(\xi)$ as a convolution integral of the dislocation density $\Omega'(\xi)$ with the singular Cauchy kernel. The Cauchy convolution integral on the semi-infinite interval $\xi\in[0,\infty[$ has the inverse given by

$$\Omega'(\xi)=\frac{C}{2\xi^{1/2}}-\frac{4}{\pi}\int_0^\infty\left(\frac{\xi}{\eta}\right)^{1/2}\frac{\Pi(\eta)}{\xi-\eta}d\eta \tag{16}$$

where C is an arbitrary constant and the integral in (16) is taken in the sense of a Cauchy principal value. Details of the derivation of the inverse (16) are given in Appendix A. Note that this inversion formula is different from the classical form used for semi-infinite crack in linear elastic fracture mechanics (e.g., [26]) which requires $\Pi(\xi)$ to vanish at infinity as $\xi^{-\alpha}$ with $\alpha>1/2$ in order for it to converge, whereas the inversion formula (16) has the more relaxed requirement $\alpha>0$ for $\Pi(\xi)$.

Since, the net loading is known along the lag zone (12), we can split the integral in (16) in two integrals on the intervals $(0,\Lambda)$ and (Λ,∞), respectively,

$$\Omega'(\xi)=\frac{C}{2\xi^{1/2}}+\Omega'_\Lambda(\xi)+\Omega'_r(\xi) \tag{17}$$

$$\Omega'_\Lambda(\xi)=\frac{4}{\pi}\ln\left|\frac{\xi^{1/2}+\Lambda^{1/2}}{\xi^{1/2}-\Lambda^{1/2}}\right|,\quad \Omega'_r(\xi)=-\frac{4}{\pi}\int_\Lambda^\infty\left(\frac{\xi}{\eta}\right)^{1/2}\frac{\Pi(\eta)}{\xi-\eta}d\eta \tag{18}$$

where Ω_Λ and Ω_r are the contributions of the net loading in the lag and in the rest of the crack to the crack-opening Ω, respectively. The unknown constant C is peculiar to the semi-infinite crack and is part of the solution of the problem. However, it is completely defined by the near-tip crack-opening asymptote (14). Indeed, with the help of (14) the dimensionless toughness can be expressed as

$$\kappa=C-\kappa_\Lambda-\kappa_r$$

where κ_Λ and κ_r are the contributions of the net-loading in the lag zone and the net-loading in the rest of the crack to the dimensionless stress intensity factor, respectively,

$$\kappa_\Lambda\equiv\lim_{\xi\to0}2\xi^{1/2}\Omega'_\Lambda(\xi)\qquad \kappa_r\equiv\lim_{\xi\to0}2\xi^{1/2}\Omega'_r(\xi). \tag{19}$$

According to (18) and definitions (19), these contributions are zero, $\kappa_\Lambda=\kappa_r=0$. Therefore,

$$C=\kappa. \tag{20}$$

Integration of (17) over ξ with the condition of zero opening at the tip and (20) yields

$$\Omega(\xi)=\kappa\xi^{1/2}+\Omega_\Lambda(\xi)+\Omega_r(\xi) \tag{21}$$

where

$$\Omega_\Lambda(\xi)=\frac{4}{\pi}\left(2\sqrt{\Lambda\xi}+(\xi-\Lambda)\ln\left|\frac{\xi^{1/2}+\Lambda^{1/2}}{\xi^{1/2}-\Lambda^{1/2}}\right|\right),$$
$$\Omega_r(\xi)=\frac{4}{\pi}\int_\Lambda^\infty K(\xi,\eta)\Pi(\eta)d\eta \tag{22}$$

with the kernel $K(\xi,\eta)$ in (22) given by

$$K(\xi,\eta)=\ln\left|\frac{\xi^{1/2}+\eta^{1/2}}{\xi^{1/2}-\eta^{1/2}}\right|-2\left(\frac{\xi}{\eta}\right)^{1/2}. \tag{23}$$

It follows from the above considerations that the solution is now reduced to finding the lag $\Lambda(\kappa)$, the net pressure $\Pi(\xi;\kappa)$ and the crack-opening $\Omega(\xi;\kappa)$ along the semi-infinite interval $\xi\in[\Lambda,\infty[$. The solution must satisfy (11) and (21)–(23) with the boundary conditions

$$\Pi(\Lambda)=-1,\quad \Pi(\infty)=0. \tag{24}$$

It is worth noting that the paradoxical property of this solution, namely that the crack-opening Ω is positive while the net pressure Π is everywhere negative, is a direct consequence of the semi-infinite length of the crack. The classical elastic eigensolution $\Omega\sim\xi^{1/2}$ corresponding to $\Pi=0$ for a semi-infinite crack is of a similar nature.

Near-Tip and Far-Field Asymptotic Behavior

Near-Tip Asymptote. The near-tip asymptote of the crack-opening $\Omega(\xi;\kappa)$ is given by (14) for the case of nonzero toughness. One can actually assign a region adjacent to the tip of the crack, $\xi\in[0,\xi_o(\kappa;\epsilon)]$, where (14) holds to a certain specified degree of accuracy ϵ; in other words $|\Omega/\kappa\xi^{1/2}-1|\leqslant\epsilon$ for $\xi\in[0,\xi_o(\kappa;\epsilon)]$. This region is said to be dominated by the linear elastic fracture mechanics $\xi^{1/2}$ behavior. The upper limit ξ_o of this region is expected to be an increasing function of the dimensionless toughness κ. Accordingly, the linear elastic fracture mechanics region should lie inside the lag entirely for small enough values of the toughness, while this region should extend beyond the fluid lag for large enough toughness. In the latter case, $\xi_o(\kappa)>\Lambda(\kappa)$, and, consequently, from (14) and the lubrication Eq. (11), we derive the following logarithmic distribution for the fluid pressure:

$$\Pi(\xi;\kappa)\simeq\Pi_o(\xi;\kappa)=-1+\frac{1}{\kappa^2}\ln\frac{\xi}{\Lambda},\quad \xi\in[\Lambda(\kappa),\xi_o(\kappa)]. \tag{25}$$

The asymptotic expression (25) is strictly valid only for large enough values of toughness κ and small enough values of fluid lag Λ. It can indeed be shown that (25) holds provided that $\kappa^2/a\Lambda\gg1$, where a is the coefficient of the next order term in (14), i.e., $\Omega\simeq\kappa\xi^{1/2}+a\xi^{3/2}$. As we will see further, the fluid lag decreases exponentially with κ^2; thus the ratio Λ/κ^2 is negligibly small for $\kappa\sim1$, causing the linear elastic fracture mechanics region to extend beyond the fluid lag and therefore ensuring the validity of (25).

Far-Field Asymptote. In the *zero toughness* singular solution of a *semi-infinite* crack ([15]), the fluid is assumed to flow up to the crack tip; hence, the lubrication Eq. (11) is valid along the whole crack length, $\xi\in]0,\infty[$, and no boundary condition is imposed on the net-pressure at the tip, $\Pi(0)$. Since the opening of the crack goes to zero at the tip $\Omega(0)=0$, validity of (11) near the tip leads to a singularity in the fluid pressure there. It can be shown that the condition of exact matching singularity between the lubrication (11) and elasticity (13) equations uniquely prescribes the form of this singularity as well as the whole self-similar solution ([15])

$$\Omega_\infty(\xi)=\frac{1}{2\sqrt{3}}(36\xi)^{2/3},\quad \Pi_\infty(\xi)=-(36\xi)^{-1/3}. \tag{26}$$

The solution (26) has a weaker singularity than the one (14) predicted by linear elastic fracture mechanics. Consistency of (26) requires, therefore, the toughness K_{Ic} to be zero ($\kappa=0$). It is important to note, that (26) cannot be the solution of the system (11)–(14) as the fluid lag goes to zero $\Lambda\to 0$. Indeed, the net pressure Π is singular at the tip according to (26), whereas the solution Π of (11)–(14) is finite at the tip in view of boundary condition (24). However, as proven in Appendix B, (26) gives the exact asymptotic behavior of the solution of (11)–(14) at infinity

$$\Pi(\xi;\kappa)=\Pi_\infty(\xi),\quad \Omega(\xi;\kappa)=\Omega_\infty(\xi),\quad \text{as}\ \ \xi\to\infty. \tag{27}$$

It is important to note that the asymptotic behavior at infinity is independent of κ; the distance from the tip, ξ_∞, at which this asymptotic solution is applicable within a given degree of accuracy ϵ is, however, expected to be a function of κ. In other words, $|\Omega/\Omega_\infty-1|\leqslant\epsilon$ for $\xi\in[\xi_\infty(\kappa;\epsilon),\infty[$.

Solution

Numerical Solution for Arbitrary κ. The unknown solution for an arbitrary nonzero toughness κ behaves according to linear elastic fracture mechanics in the near-tip region $\xi\in[0,\xi_o(\kappa)]$ (see (14), (12) and 25)), and asymptotically as the zero toughness singular solution (26) at large enough distance from the tip, $\xi\in[\xi_\infty(\kappa),\infty[$. In the transition zone, $\xi\in[\xi_o(\kappa),\xi_\infty(\kappa)]$, the intermediate solution has to be obtained numerically.

The system of equations to be solved on the semi-infinite interval $\xi\in]\Lambda,\infty[$ is the lubrication Eq. (11), the integral Eqs. (21)–(23), the boundary conditions (24), and the asymptotic expression for Π at infinity (27). Also recall that for large enough values of toughness the near fluid lag asymptote (25) is applicable. The solution (which include the lag Λ) is a function of only one dimensionless parameter, κ.

The numerical algorithm used to calculate the solution is described in Appendix C. We only point out here that in the numerical solution, the lag length Λ is prescribed rather than κ, and that κ is obtained as part of the solution which then depends only on Λ.

Although results will be discussed in detail in a later section, we report here the calculated dependence on the toughness κ of the bounds ξ_o and ξ_∞ of the regions dominated, respectively, by the near-tip and the far-field asymptotes. The variation of ξ_o and ξ_∞ with κ (computed for a relative error $\epsilon=0.01$), as well as the variation of Λ with κ is shown in Fig. 2. (The dashed lines correspond to the large κ asymptotes which are discussed below.) According to Fig. 2, the bounds $\xi_o(\kappa)$ and $\xi_\infty(\kappa)$ are increasing functions of κ for κ large enough. This result is expected since the region dominated by the linear elastic fracture mechanics tip singularity extends with the strength of this singularity, namely κ, whereas the region where the solution is given by far-field asymptote is pushed further away to infinity. The peculiar evolution of ξ_o and ξ_∞ in the range $\Lambda\in[10^{-3},10^{-2}]$ (nonmonotonic behavior) is linked to the fact that the asymptotic solution at infinity $\Pi_\infty(\xi)$ fulfills the pressure at the fluid interface $\Pi=-1$ exactly at $\xi=\Lambda=1/36$. Therefore, we can expect that for this particular value of the lag, the far-field asymptote is valid over the largest portion of the crack, almost up to the fluid front (compared to other values of the lag); in other words, $\xi_\infty(\Lambda)$ has a minimum at $\Lambda=1/36$, as can be seen in Fig. 2.

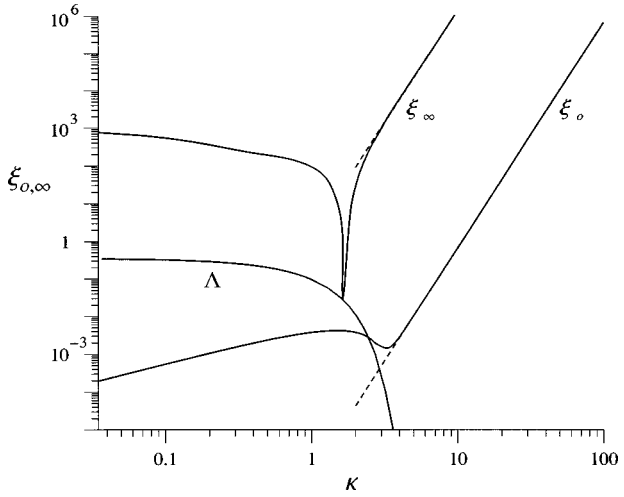

Fig. 2 Bounds ξ_o and ξ_∞ of the regions where solution is dominated by corresponding asymptotes, and lag Λ versus dimensionless toughness κ in log-log scale. (Dashed lines show the large κ asymptotes of $\xi_o(\kappa)$, $\xi_\infty(\kappa)$.)

An examination of the curves $\xi_o(\kappa)$ and $\Lambda(\kappa)$ in Fig. 2 shows that they intersect at about $\kappa\simeq 2.55$. Thus for κ smaller than this value, the linear elastic fracture mechanics region lies inside the lag entirely (within an accuracy $\epsilon=0.01$); this value of κ also marks the onset of the applicability of the near-tip asymptotic expression (25) for the fluid pressure.

Asymptotic Solution for Large κ. In order to capture the asymptotic behavior of the solution for large κ, and motivated by the numerical results shown in Fig. 2, we introduce the rescaled field coordinate

$$\tilde{\xi}=\kappa^{-\beta_\xi}\xi \tag{28}$$

and look for a large κ asymptotic solution of the system (11), (21)–(23) with (25), (27) of the form

$$\Pi(\xi;\kappa)=\kappa^{\beta_\Pi}\tilde{\Pi}(\tilde{\xi}),\quad \Omega(\xi;\kappa)=\kappa^{\beta_\Omega}\tilde{\Omega}(\tilde{\xi}). \tag{29}$$

The power-law exponents β_ξ, β_Π, β_Ω are determined as follows. Substitution of (28) and (29) in the lubrication Eq. (11), and in the near-tip (25) and the far-field (27) asymptotic expressions for pressure yields

$$\tilde{\Omega}^2\frac{d\tilde{\Pi}}{d\tilde{\xi}}=\kappa^{\beta_\xi-2\beta_\Omega-\beta_\Pi} \tag{30}$$

$$\tilde{\Pi}(\tilde{\xi})=\kappa^{-\beta_\Pi}\Pi_o(\xi;\kappa)=\kappa^{-\beta_\Pi-2}\left(-\kappa^2+\ln\frac{\kappa^{\beta_\xi}}{\Lambda}+\ln\tilde{\xi}\right),\quad \tilde{\xi}\to 0 \tag{31}$$

$$\tilde{\Pi}(\tilde{\xi})=\kappa^{-\beta_\Pi}\Pi_\infty(\xi)=\kappa^{-\beta_\Pi-\beta_\xi/3}\Pi_\infty(\tilde{\xi}),\quad \tilde{\xi}\to\infty. \tag{32}$$

In order for $\tilde{\Omega}(\tilde{\xi})$ and $\tilde{\Pi}(\tilde{\xi})$ to be independent of κ, necessarily

$$\begin{gathered}2\beta_\Omega+\beta_\Pi-\beta_\xi=0,\quad \beta_\Pi=-2,\\ \beta_\Pi+\beta_\xi/3=0\quad -\kappa^2+\ln\frac{\kappa^{\beta_\xi}}{\Lambda}=\text{const.}\end{gathered} \tag{33}$$

It follows therefore that the large κ asymptotic representation (29) with (28) of Π and Ω exists for the power-law exponents $\beta_\xi=6$, $\beta_\Pi=-2$, $\beta_\Omega=4$, i.e.,

$$\Pi(\xi;\kappa)=\kappa^{-2}\tilde{\Pi}(\tilde{\xi}),\quad \Omega(\xi;\kappa)=\kappa^{4}\tilde{\Omega}(\tilde{\xi}),\quad \xi=\kappa^{6}\tilde{\xi},\quad (34)$$

and provided that the asymptotic form of the relation $\Lambda=\Lambda(\kappa)$ is given by

$$\Lambda=\Lambda_{*}\kappa^{6}e^{-\kappa^{2}} \quad (35)$$

with Λ_{*} is a yet undetermined constant.

Note that it has been assumed that the near-tip asymptotic expression for the pressure (25) holds, in deriving (34) and (35). This assumption is supported by the asymptotic form (35) of the relation $\Lambda(\kappa)$ which shows that the fluid lag indeed decreases with increasing toughness κ; it will be further justified below.

The unknown functions $\tilde{\Pi}(\tilde{\xi})$, $\tilde{\Omega}(\tilde{\xi})$ and the constant Λ_{*} are the solution of the following system of equations:

$$\tilde{\Omega}^{2}\frac{d\tilde{\Pi}}{d\tilde{\xi}}=1,\quad \tilde{\xi}\in[l_o,\infty[\quad (36)$$

$$\tilde{\Omega}(\tilde{\xi})=\tilde{\xi}^{1/2}+\tilde{\Omega}_r(\tilde{\xi}),$$
$$\tilde{\Omega}_r(\tilde{\xi})=\frac{4}{\pi}\left\{\int_0^{l_o}K(\tilde{\xi},\tilde{\eta})\tilde{\Pi}_o(\tilde{\eta})d\tilde{\eta}+\int_{l_o}^{\infty}K(\tilde{\xi},\tilde{\eta})\tilde{\Pi}(\tilde{\eta})d\tilde{\eta}\right\} \quad (37)$$

where

$$\tilde{\Pi}\simeq\tilde{\Pi}_o(\tilde{\xi})=\ln\frac{\tilde{\xi}}{\Lambda_{*}}\quad\text{and}\quad \tilde{\Omega}(\tilde{\xi})\simeq\tilde{\xi}^{1/2},\quad \tilde{\xi}\in[0,l_o] \quad (38)$$

$$\tilde{\Pi}(\tilde{\xi})=\Pi_{\infty}(\tilde{\xi})\quad\text{and}\quad \tilde{\Omega}(\tilde{\xi})=\Omega_{\infty}(\tilde{\xi}),\quad \tilde{\xi}\to\infty. \quad (39)$$

In the above equations l_o is an arbitrary number smaller than or equal to $\tilde{\xi}_o$ (to be prescribed in the numerical solution of (36)–(39)), that provides a ''safe'' bound to the near-tip region where the asymptotic behavior is given by (38).

The scaled contribution from the loading on the lag to the opening is

$$\tilde{\Omega}_{\Lambda}(\tilde{\xi})\equiv\kappa^{-4}\Omega_{\Lambda}(\xi;\kappa)=\frac{16}{\pi}\kappa^{-4}(\xi\Lambda)^{1/2}\leqslant\kappa^{2}e^{-\kappa^{2}/2},$$

$$\text{for}\quad \tilde{\xi}\leqslant 1\quad\text{and}\quad \kappa\gg 1.$$

Hence, $\tilde{\Omega}_{\Lambda}(\xi)$ can be neglected in the expression for $\tilde{\Omega}(\xi)$, (see (37)). The exponential decay of the lag Λ with κ (34) also allows us to shift the lower bound of the first integral in $\tilde{\Omega}_r(\tilde{\xi})$ (see (37)) to zero, since the convolution integral of $\tilde{\Pi}_o$ over $\tilde{\xi}\in[0,\tilde{\Lambda}]$, $\tilde{\Lambda}=\Lambda_{*}e^{-\kappa^{2}}$, is negligible.

The system of Eqs. (36)–(39) is solved numerically for $\tilde{\Pi}(\tilde{\xi})$, $\tilde{\Omega}(\tilde{\xi})$ and Λ_{*} within the framework of the algorithm devised for the general case of arbitrary κ, $0\leqslant\kappa<\infty$ (see Appendix C). In particular, it is found that

$$\Lambda_{*}\simeq 4.36\cdot 10^{-3}. \quad (40)$$

The numerical solution also provides the constant (κ-independent) bounds $\tilde{\xi}_o$ and $\tilde{\xi}_{\infty}$, $\tilde{\xi}_o<\tilde{\xi}_{\infty}$, for which the asymptotic behaviors, (38) and (39), are reached by $\tilde{\Omega}(\tilde{\xi})$ to a certain degree of accuracy

$$\tilde{\xi}_o\simeq 6.58\cdot 10^{-7},\quad \tilde{\xi}_{\infty}\simeq 1.37,\quad \text{for}\ \epsilon=0.01. \quad (41)$$

Consequently, the asymptotic formulas for the bounds in the original scaling, $\xi_o(\kappa)$ and $\xi_{\infty}(\kappa)$, are

$$\xi_o(\kappa)=\tilde{\xi}_o\kappa^{6},\quad \xi_{\infty}(\kappa)=\tilde{\xi}_{\infty}\kappa^{6},\quad \kappa\gg 1. \quad (42)$$

Comparison between the bounds ξ_o and ξ_{∞} computed for the general case and the asymptotic expressions (42) with (41) is shown in Fig. 2. It can be seen that the asymptotic behavior of these two bounds is virtually reached for $\kappa=4$ (the relative error is of order one percent or less for $\kappa\geqslant 4$).

Results

Fluid Lag and Toughness. Figure 3 shows the variation in semi-logarithmic scale of the fluid lag length Λ with the toughness κ computed numerically, as well as the large κ asymptote (35), with Λ_{*} given by (40). The fluid lag can be seen to be a decreasing function of toughness, attaining a maximum value $\Lambda_o\approx 0.3574$ at $\kappa=0$. This value of Λ_o is actually very close to the value computed (in a different scaling) by Lister [9], using a perturbation technique, for the problem of a buoyancy-driven hydraulic fracture. Note that for $\Lambda>\Lambda_o$, $\kappa<0$ and a (physically inadmissible) overlapping of the crack faces occurs in the region adjacent to the tip. As the toughness κ increases the lag reaches the large κ asymptote (shown in Fig. 3 as a dashed line) and decays exponentially to zero. The computed fluid lag length Λ is given by the asymptote (35) for $\kappa\geqslant 4.2$ with one percent or less error.

It is of interest to compute the maximum dimension of the lag, $\lambda_o=\Lambda_o L_{\mu}$, for some typical values of the physical parameters. Consider the following set: $E'=3\cdot 10^{4}$ MPa, $\mu=10^{-7}$ MPa·s (100 cp), $\sigma_o=10$ MPa, and $V=1$ m/s. Then, the characteristic length $L_{\mu}=1.08$ m and $\lambda_o\simeq 0.39$ m. The fluid lag reduces to $\lambda\simeq 0.27$ m for a toughness $K_{Ic}=1$ MPa·m$^{1/2}$, according to Fig. 3 ($\Lambda\simeq 0.25$ for $\kappa=0.31$).

Recently published results of laboratory scale hydraulic fracturing experiments carried out at the Delft University of Technology ([27]) also provide an opportunity to test the theoretical prediction of the fluid lag size. In an experiment involving the propagation of a penny-shaped hydraulic fracture in a cement block, the position of both the fracture tip and the fluid front position were measured continuously by ultrasonic diffraction. For example, these measurements give a fracture radius $R\approx 0.1$ m, and a fluid lag length $\lambda\approx 10^{-3}$ m at a particular time t, and a fracture propagation velocity $V\approx 4\cdot 10^{-6}$ m/s (estimated from the evolution of R with time t). Given V and the following set of parameters $E'=1.92\cdot 10^{4}$ MPa, $K_{Ic}=0.5$ MPa·m$^{1/2}$, $\mu=5\cdot 10^{-4}$ MPa·s and $\sigma_o=8$ MPa, the predicted fluid lag is $\lambda\approx 0.8\cdot 10^{-3}$ m which is in relatively good agreement with the experimental value. We should emphasize that the semi-infinite crack model is applicable to the near-tip region of a finite fracture provided that $L_{\mu}\ll R$ (which also ensures that the plane strain condition is met since R is equal to the local radius of curvature for a penny-shape crack). Here the characteristic length $L_{\mu}\approx 0.02$ m is only one order of magnitude smaller than the radius of the fracture R. It appears, however, that

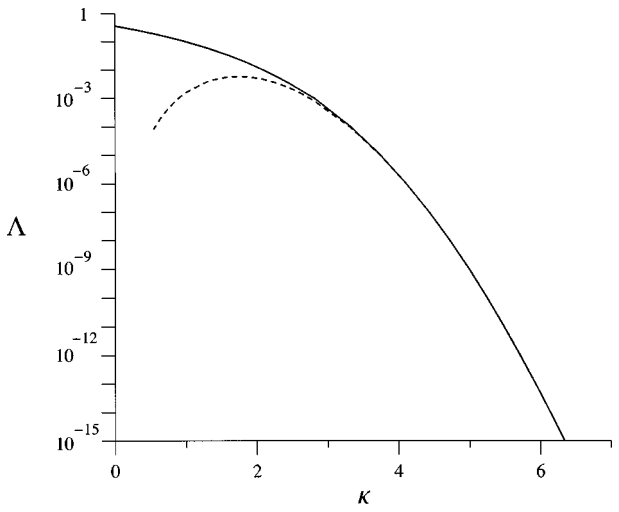

Fig. 3 Dimensionless lag length Λ versus dimensionless toughness κ (solid line), together with the large κ asymptote (dashed line)

there is a reasonable agreement between the predicted and experimental values of λ provided that the ratio L_μ/R is less than ten percent ([28]).

Crack Opening and Fluid Pressure. Figures 4 and 5 give the profiles of the net-loading in linear and semi-logarithmic scales, respectively, for various values of κ. It can be seen that the pressure increases rapidly from its value $\Pi=-1$ at the fluid front $\xi=\Lambda$, and that it tends towards the far-field asymptote (indicated by dashed line) for large ξ. The value of the fluid lag Λ corresponding to each pressure profile on Fig. 5 is given by the intersection of the curve with the ξ-axis.

Figures 6 and 7 show in log-log and linear scale the crack opening Ω along the crack for various values of κ (and thus of Λ, see Table 1). The dashed line corresponds to the asymptotic solution at infinity, $\Omega_\infty(\xi)$. Figure 7 shows the shape of the crack in the near-tip region for the dimensionless toughness κ varying from 0 to 4.11. It can be seen that for zero or near zero toughness the crack has a ''sharp'' tip ($\Omega\sim\xi^{3/2}$) as opposed to nonzero toughness when the crack tip is ''blunt'' ($\Omega\sim\xi^{1/2}$). Figure 6 provides transparent evidence that the solution (in terms of Ω) behaves as $\xi^{1/2}$ (or as $\Omega_o(\xi)$, classical linear elastic fracture mechanics type, but as $\xi^{3/2}$ for $\kappa=0$) in the region immediately adjacent to the tip and as $\xi^{2/3}$ (or as $\Omega_\infty(\xi)$) further away from the tip. There is a transition zone between these two types of behavior, which can be identified as $\xi\in[\xi_o(\kappa),\xi_\infty(\kappa)]$, where ξ_o and ξ_∞ are the bounds (introduced earlier) of the regions dominated by the corresponding asymptote.

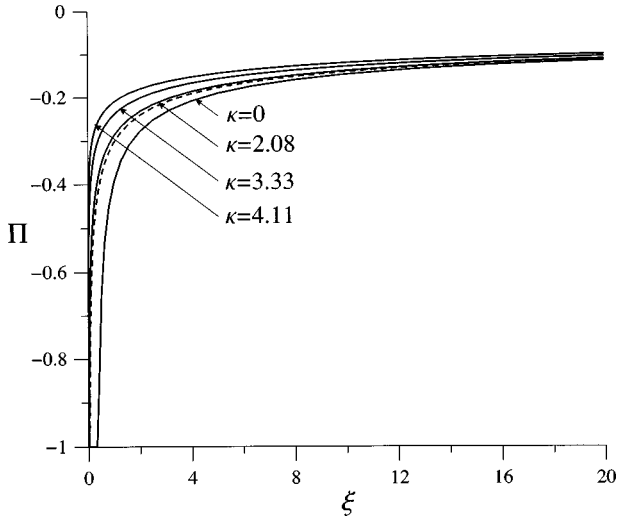

Fig. 4 Dimensionless net-loading Π along the crack for κ=0, 2.08, 3.33, 4.11. The dashed line corresponds to $\Pi_\infty(\xi)$.

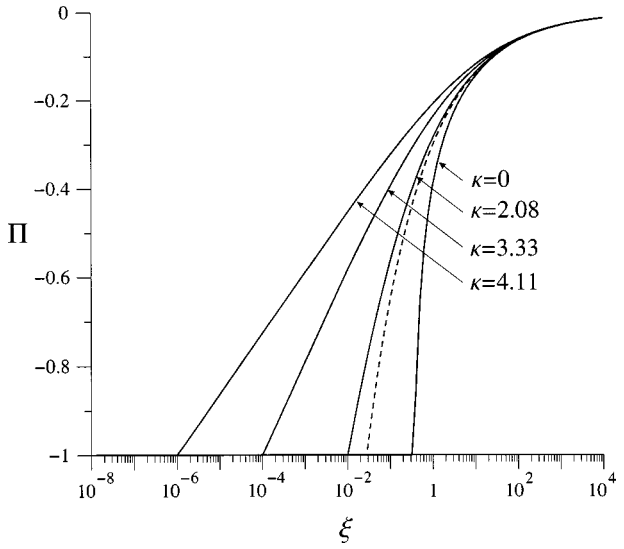

Fig. 5 Dimensionless fluid pressure Π along the crack for κ=0, 2.08, 3.33, 4.11 in semi-log scale. Corresponding values of fluid lag Λ are given by the intersection of a curve with the ξ-axis. The dashed line corresponds to $\Pi_\infty(\xi)$.

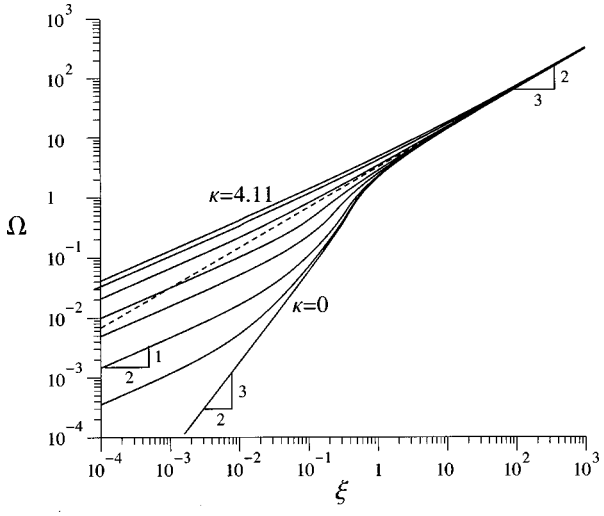

Fig. 6 The dimensionless crack opening Ω along the crack in log-log scale for dimensionless toughness varying from κ=0 ($\Lambda\simeq$0.3574) to κ=4.1 ($\Lambda=10^{-6}$), (see Table 1). The dashed line corresponds to the asymptotic solution at infinity, $\Omega_\infty(\xi)$.

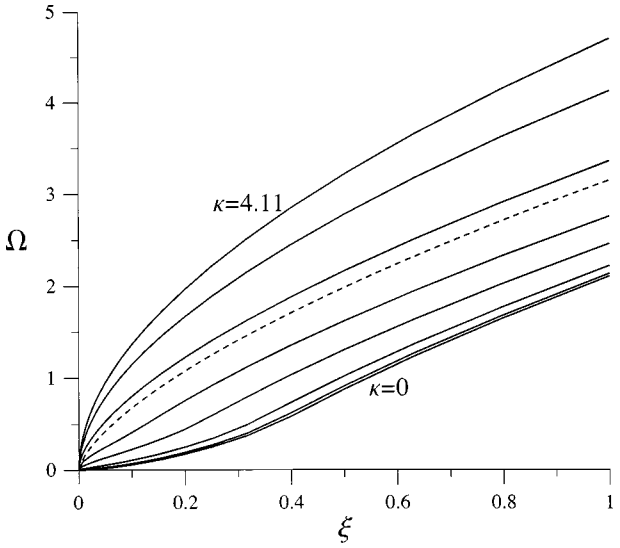

Fig. 7 The opening Ω along the crack in near tip region for κ varying from κ=0 ($\Lambda\simeq$0.3574) to κ=4.1 ($\Lambda=10^{-6}$), (see Table 1). The dashed line corresponds to $\Omega_\infty(\xi)$.

Table 1 Table of corresponding values of the pair (κ,Λ)

κ	0	0.05	0.145	0.49	0.99	2.084	3.327	4.11
Λ	0.3574	0.3445	0.306	0.203	0.1	0.01	1E-4	1E-6

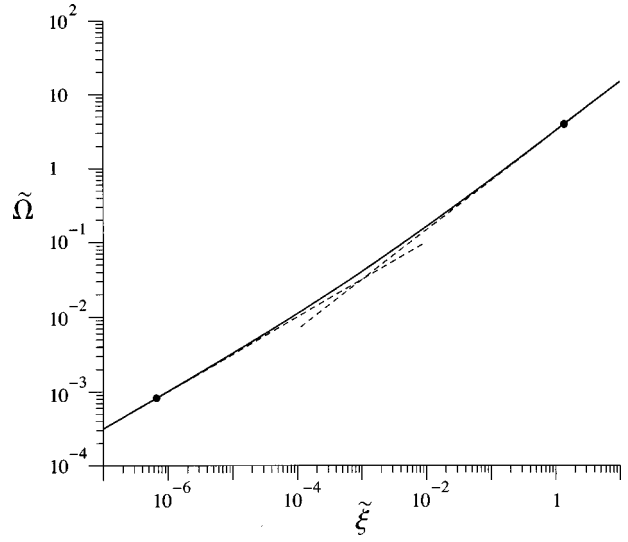

Fig. 8 Scaled opening $\tilde{\Omega}$ along the crack in log-log scales. Dashed lines correspond to the solution asymptotes and black dots to $\tilde{\xi}_o$ and $\tilde{\xi}_\infty$.

The solution for the pressure Π and the opening Ω for $\kappa=4.11$ ($\Lambda=10^{-6}$) (see Figs. 4, 5 and 7, 6) matches the large κ asymptotic solution (34) with a maximum error of order 0.1 percent and 1 percent (which is about the accuracy of the numerical method itself) for pressure and opening, respectively. Thus, the solution of the semi-infinite fluid-driven crack is given by its large toughness asymptote (34) for $\kappa \geqslant 4$. Also, the plot of the pressure profile in the semi-logarithmic scale (see Fig. 5) confirms the logarithmic distribution (25) for the range of toughness $\kappa \geqslant 3$, according to Fig. 3.

Finally, the large κ asymptotic solution for the fluid pressure and the crack opening, i.e., the scaled opening $\tilde{\Omega}(\tilde{\xi})$ and pressure $\tilde{\Pi}(\tilde{\xi})$, is shown in Figs. 8 and 9 (with the dots indicating the position of the bounds $\tilde{\xi}_o$ and $\tilde{\xi}_\infty$ corresponding to a relative error $\epsilon=0.01$).

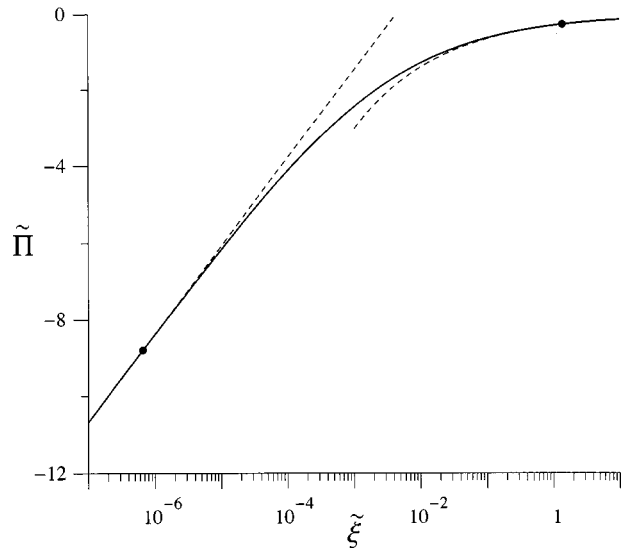

Fig. 9 Scaled pressure $\tilde{\Pi}$ along the crack in semi-logarithmic scales. Dashed lines correspond to the solution asymptotes and black dots to $\tilde{\xi}_o$ and $\tilde{\xi}_\infty$.

Conclusions

In this paper, we have constructed the solution for a semi-infinite fluid-driven fracture steadily propagating in an impermeable elastic solid. The particularity of this solution is that it accounts for the existence of a fluid lag, of a priori unknown length. The existence of this lag (where the pressure is essentially zero) allows the construction of a solution for arbitrary material toughness which has a near crack-tip behavior consistent with linear elastic fracture mechanics. Indeed, the assumption that the fluid reaches the tip of the fracture implies a singularity in the fluid pressure and a crack-tip behavior which is incompatible with linear elastic fracture mechanics. The singular solution of a semi-infinite fracture built on the assumption of zero lag ([15]) was shown, however, to correspond to the asymptotic behavior at infinity. It was demonstrated that the solution depends only on the dimensionless toughness κ, which is an aggregate of all the parameters of the problem. A large κ asymptotic solution whose dependance on κ is explicit was also derived; this asymptotic solution was shown to be applicable for $\kappa>4$, with an error less than one percent. An important outcome of this solution is the universal relation between the fluid lag Λ and the toughness κ. According to this relation, the lag is a decreasing function of the toughness κ; it is maximum at zero toughness and vanishes exponentially for large κ.

The characteristic length of the near tip processes, L_μ, is typically several orders of magnitude smaller than the length of hydraulic fractures ($10-10^3$ m). This difference in scales suggests that this solution of a semi-infinite fracture can actually be used to describe the near-tip asymptotic solution of a finite hydraulic fracture. A consistent solution of a finite two-dimensional fluid-driven fracture propagating in an impermeable solid of nonzero toughness can actually be constructed in the spirit of a singular perturbation technique ([23]), using the solution derived in this paper as the ''inner'' solution and the zero-toughness self-similar solution for a finite crack ([10]) as the ''outer'' solution.

Acknowledgments

One of the authors (D. G.) would like to acknowledge the partial support of this research by the Graduate School of the University of Minnesota in the form of a Doctoral Research Fellowship (1997–1998).

Appendix A

Inversion Formulae on a Semi-Infinite Interval

1 Introduction. This Appendix is concerned with the inversion of

$$\Pi(\xi)=\frac{1}{4\pi}\int_0^\infty \Omega'(\eta)\,\frac{d\eta}{\xi-\eta} \tag{A1}$$

which is usually given by (see, e.g., [26])

$$\Omega'(\xi)=-\frac{4}{\pi}\int_0^\infty \left(\frac{\eta}{\xi}\right)^{1/2}\frac{\Pi(\eta)}{\xi-\eta}\,d\eta. \tag{A2}$$

Here we derive an alternative inversion formula as there are situations regarding the behavior of the functions $\Pi(\xi)$ and $\Omega'(\xi)$ at infinity, for which (*A*1) exists but not its inverse (*A*2).

Consider the condition of existence of an integral on the semi-infinite interval $\eta\in[0,\infty[$ in regards to the behavior of its integrand at infinity; the integral obviously exists if the integrand behaves as $\xi^{-1-\alpha}$ for large ξ and if $\alpha>0$. Consequently, the integral in (*A*1) exists if $\Omega'(\xi)\sim\xi^{-\alpha}$ as $\xi\to\infty$ and if $\alpha>0$. Similarly the integral in (*A*2) converges provided that $\alpha>1/2$ if $\Pi(\xi)\sim\xi^{-\alpha}$ as $\xi\to\infty$. It then follows that there are situations when Π can be evaluated using (*A*1) but when the inverse (*A*2) does not exist. Indeed, consider the case where $\Omega'(\xi)$ behaves as $\xi^{-\alpha}$ at

infinity, with α in the open interval]0, 1/2[. It can then be shown that the corresponding $\Pi(\xi)$ according to, i.e., (*A*1) behaves also at infinity as $\xi^{-\alpha}$ with the same exponent α (see Appendix B for a proof of the particular case $\alpha=1/3$). Obviously, the inverse (*A*2) does not exist. As an example, consider the particular function $\Omega'_\alpha=\xi^{-\alpha}$, $0<\alpha<1/2$. Then, according to (*A*1), the corresponding pressure $\Pi_\alpha=\xi^{-\alpha}/(4\ \tan\ \pi\alpha)$. Note that $\Omega'_{1/2}=\xi^{-1/2}$ is an eigensolution for the plane problem of a semi-infinite crack and that $\Pi_{1/2}=0$.

The inversion formula (*A*2) is thus not applicable to the problem considered in this paper, since the expected behavior for Π at infinity is characterized by $\alpha=1/3$. In this Appendix, we derive inversion formulae applicable to that problem. First, we show that there is a family of inversion formulae that are equivalent to the conventional inversion formula, whenever the latter exists. Next, we prove that the new formulae are also applicable when $\Pi(\xi)$ behaving at infinity as $\xi^{-\alpha}$ with $\alpha>0$, although the conventional formula (*A*2) exists only for $\alpha>1/2$.

2 Alternative Inversion Formulae. To construct an inversion with relaxed requirements on $\Pi(\xi)$ at infinity, we start by simultaneously adding to and substracting from the right-hand side of (*A*2) the term $C/2\xi^{1/2}$, where C is for the time being an arbitrary constant which we choose to express as

$$C=\frac{8}{\pi}\int_0^\infty \frac{\eta^{1/2}\Pi(\eta)}{f(\eta)}\,d\eta. \tag{A3}$$

The function $f(\eta)$ in (*A*3) is presently restricted to behave in such a way that the constant C is bounded. The inversion formula (*A*2) then becomes

$$\Omega'(\xi)=\frac{C}{2\xi^{1/2}}-\frac{4}{\pi}\int_0^\infty\left(\frac{\eta}{\xi}\right)^{1/2}\frac{[\xi-\eta+f(\eta)]\Pi(\eta)}{(\xi-\eta)f(\eta)}\,d\eta. \tag{A4}$$

In order to relax the requirements on the behavior of $\Pi(\xi)$ at infinity to ensure convergence of the integral (compared to those for (*A*2)), the aggregate $[\xi-\eta+f(\eta)]/f(\eta)$ in (*A*4) must vanish at infinity as some negative power of η. This can be achieved if and only if $f(\eta)=\eta+D$, where D is an arbitrary constant. Indeed, for this case, the inversion (*A*4) takes the form

$$\Omega'(\xi)=\frac{C}{2\xi^{1/2}}-\frac{4}{\pi}\int_0^\infty\left(\frac{\eta}{\xi}\right)^{1/2}\left(\frac{\xi+D}{\eta+D}\right)\frac{\Pi(\eta)}{\xi-\eta}\,d\eta \tag{A5}$$

and the integral in (*A*5) exists if $\Pi(\xi)$ behaves at infinity as $\xi^{-\alpha}$ with $\alpha>0$ (actually with $\alpha>-1/2$, but as discussed below the case $-1/2<\alpha\leqslant 0$ is of no interest since (*A*1) does not exist then). Note that this inversion formula with $D=1/2$ is quoted by Srivastava and Buschman [29].

Although D can be chosen arbitrarily, we will use the particular value $D=0$. Hence (*A*5) becomes

$$\Omega'(\xi)=\frac{C_0}{2\xi^{1/2}}-\frac{4}{\pi}\int_0^\infty\left(\frac{\xi}{\eta}\right)^{1/2}\frac{\Pi(\eta)}{\xi-\eta}\,d\eta \tag{A6}$$

with

$$C_0=\frac{8}{\pi}\int_0^\infty\frac{\Pi(\eta)}{\eta^{1/2}}\,d\eta. \tag{A7}$$

Obviously C is bounded if $\Pi(\xi)$ behaves at infinity as $\xi^{-\alpha}$ with $\alpha>1/2$. Actually, the constant C_0 is the scaled stress intensity factor and it can readily be recognized that (*A*7) is the classical expression for the stress intensity factor as an integral of the net loading over the semi-infinite crack (e.g., [26]). It can also be proven that there is no contribution to the term $\xi^{-1/2}$ of $\Omega'(\xi)$ from the integral in (*A*6). (There is a contribution to that term from the integral in (*A*5) if $D\neq 0$; however, the combination of that contribution and the term $C/2\xi^{1/2}$ of (*A*5) with C computed from (*A*3) is identical to the term $C_0/2\xi^{1/2}$ of (*A*6) with C_0 computed from (*A*7).)

Although we have focused on a net loading $\Pi(\xi)$ behaving at infinity as $\xi^{-\alpha}$ with $\alpha>1/2$, the general inversion formula (*A*5) together with (*A*3), and in particular (*A*6) with (*A*7), applies whenever (*A*2) exists. As an example consider the classical problem where $\Pi=1$, $0<\xi<1$ and zero elsewhere. Then (*A*2) gives

$$\Omega'(\xi)=\frac{8}{\pi\xi^{1/2}}-\frac{4}{\pi}\ln\left|\frac{1+\xi^{1/2}}{1-\xi^{1/2}}\right| \tag{A8}$$

and (*A*6) yields

$$\Omega'(\xi)=\frac{C}{2\xi^{1/2}}-\frac{4}{\pi}\ln\left|\frac{1+\xi^{1/2}}{1-\xi^{1/2}}\right| \tag{A9}$$

with $C=16/\pi$ according to (*A*7). The two inversion formulas (*A*2) and (*A*6) give therefore identical results.

3 General Case of $\Pi(\xi)\sim\xi^{-\alpha}$ at Large ξ, with $0<\alpha<1/2$. The inversion formula (*A*5) was derived from the conventional (*A*2) and, therefore, at this stage is proven to be the valid inverse of (*A*1) under the same conditions imposed on the loading at infinity as for the conventional one. Actually, as proven next, (*A*5) or (*A*6) gives the inverse of (*A*1) for any $\Pi(\xi)$ behaving at infinity as $\xi^{-\alpha}$ with $\alpha>0$. However, in that case, C becomes an arbitrary constant which cannot be determined by (*A*3) or (*A*7) anymore since the integral in these equations does not exist.

Consider first the particular loading $\Pi_\alpha(\xi)=-\xi^{-\alpha}/(4\tan\pi\alpha)$ for $\xi\in[0,\infty[$. The corresponding dislocation density integral $\Omega'_\alpha(\xi)$ is given by (*A*5)

$$\Omega'_\alpha(\xi)=\frac{C-2\csc(\pi\alpha)D^{1/2-\alpha}}{2\xi^{1/2}}+\xi^{-\alpha}. \tag{A10}$$

Note that (*A*10) provides a $\Omega'_\alpha(\xi)$ obtained by integration of $\Pi_\alpha(\xi)$ according to (*A*5) as long as $\alpha>-1/2$. However, the pair $\Pi_\alpha(\eta)$ and $\Omega'_\alpha(\xi)$ satisfy (*A*1) identically only for $\alpha>0$, which, as noted earlier, is the condition of existence of the integral in (*A*1). Therefore, (*A*5) is the exact inverse of (*A*1) for the considered type of loading with $\alpha>0$. Recall also that the term $\xi^{-1/2}$ does not contribute to Π in (*A*1), as it is an eigensolution.

In the problem of interest, the loading $\Pi(\eta)$ can be expressed as

$$\Pi(\eta)=\sum_{i=1}^{n}A_i\Pi_{\alpha_i}(\eta)+\Pi_r(\eta) \tag{A11}$$

where $0<\alpha_i\leqslant 1/2$ and $\Pi_r(\eta)\sim\eta^{-\beta}$ with $\beta>1/2$ at infinity. Applying (*A*5) to the loading $\Pi(\eta)$ specified by (*A*11), we obtain the corresponding $\Omega'(\xi)$

$$\Omega'(\xi)=\sum_{i=1}^{n}A_i\Omega'_{\alpha_i}(\xi)+\Omega'_r(\eta) \tag{A12}$$

where $\Omega'_r(\eta)$ is the result of (*A*5) applied to $\Pi_r(\eta)$. Since each pair $(\Pi_{\alpha_i}(\eta),\Omega'_{\alpha_i}(\xi))$ and $(\Pi_r(\eta),\Omega'_r(\eta))$ satisfy (*A*1) identically and due to linearity of (*A*1), $\Pi(\eta)$ and $\Omega'(\xi)$ given by (*A*11) and (*A*12), respectively, satisfy (*A*1) identically. Therefore, formula (*A*5) gives the exact inverse of (*A*1) for any loading $\Pi(\eta)$ behaving at infinity as $\eta^{-\alpha}$ with $\alpha>0$.

Note finally that the inversion (*A*6) corresponding to $D=0$ is used in this paper.

Appendix B

Asymptotic Behavior at Infinity. In this Appendix, we prove that the zero toughness singular solution (26) gives the asymptotic behavior of the solution of (11)–(14) at infinity, see (27). To prove (27), we start by assuming that the asymptotic behavior of Π at infinity is indeed given by (26)

$$\Pi(\xi)=\Pi_\infty(\xi)+O(\xi^{-1/3-\alpha}),\quad \alpha>0,\quad \text{as}\quad \xi\to\infty. \tag{B1}$$

We can choose $\xi_\infty(\kappa)<\infty$ such that the asymptotic formula (B1) is valid for any prescribed degree of accuracy for $\xi\in[\xi_\infty,\infty[$ or, in other words, the terms of order $O(\xi^{-1/3-\alpha})$ in (B1) are negligible and can be dropped.

It follows from (18) that the contribution $\Omega'_\Lambda(\xi)$ from the lag loading to the derivative of the opening $\Omega'(\xi)$ is of order $\xi^{-1/2}$ as $\xi\to\infty$. Let us find the asymptotic behavior at infinity for the contribution $\Omega'_r(\xi)$ from the loading on the rest of the crack to $\Omega'(\xi)$. First, we split the integral in the expression (18) for $\Omega'_r(\xi)$ in two integrals $I_1(\xi)$ and $I_2(\xi)$ over the intervals $\xi\in[\Lambda,\xi_\infty]$ and $\xi\in[\xi_\infty,\infty[$, respectively:

$$\Omega'_r(\xi)=I_1(\xi)+I_2(\xi) \tag{B2}$$

where

$$I_1(\xi)=-\frac{4}{\pi}\int_\Lambda^{\xi_\infty}\left(\frac{\xi}{\eta}\right)^{1/2}\frac{\Pi(\eta)}{\xi-\eta}\,d\eta$$
$$I_2(\xi)=-\frac{4}{\pi}\int_{\xi_\infty}^{\infty}\left(\frac{\xi}{\eta}\right)^{1/2}\frac{\Pi(\eta)}{\xi-\eta}\,d\eta. \tag{B3}$$

Consider first the asymptotic behavior of $I_1(\xi)$ as $\xi\to\infty$. Behavior at infinity of the integral $I_1(\xi)$ is constrained by the following two inequalities:

$$m_{\min}\xi^{-1/2}+O(\xi^{-1})\leqslant I_1(\xi)\leqslant m_{\max}\xi^{-1/2}+O(\xi^{-1})\quad \text{as}\quad \xi\to\infty \tag{B4}$$

where $m_{\min}$ and $m_{\max}$ are finite non-negative numbers defined as

$$m_{\max}=\frac{8}{\pi}(\sqrt{\xi_\infty}-\sqrt{\Lambda})\qquad m_{\min}=-\Pi(\xi_\infty)m_{\max}. \tag{B5}$$

Indeed, the net-loading $\Pi(\eta)$ is bounded on the interval $\eta\in[\Lambda,\xi_\infty]$, $\Pi\in[-1,\Pi(\xi_\infty)]$. Consider first the minimum value for Π on the interval under consideration, $\Pi(\Lambda)=-1$. Since $\xi>\xi_\infty$ and $\Pi<0$, I_1 is positive and an upper bound for I_1 is obtained by substituting the function $\Pi(\eta)$ by $\Pi(\Lambda)$

$$I_1(\xi)\leqslant\frac{4}{\pi}\int_\Lambda^{\xi_\infty}\left(\frac{\xi}{\eta}\right)^{1/2}\frac{1}{\xi-\eta}\,d\eta=\frac{4}{\pi}\ln\left|\frac{\sqrt{\xi}+\sqrt{\xi_\infty}}{\sqrt{\xi}-\sqrt{\xi_\infty}}\,\frac{\sqrt{\xi}-\sqrt{\Lambda}}{\sqrt{\xi}+\sqrt{\Lambda}}\right|. \tag{B6}$$

Hence,

$$I_1(\xi)\leqslant m_{\max}\xi^{-1/2}+O(\xi^{-1})\quad \text{as}\quad \xi\to\infty. \tag{B7}$$

Thus, (B7) proves the right inequality in (B4), which provides an upper bound for $I_1(\xi)$. The other inequality, which gives the lower bound for $I_1(\xi)$, can be proved in a similar fashion by considering the upper net-loading bound $\Pi(\xi_\infty)$.

Consider next the asymptotic behavior of the integral $I_2(\xi)$. Since ξ_∞ is chosen sufficiently large, such that the asymptotic expression (B1) for $\Pi(\xi)$ is valid on the interval $\xi\in[\xi_\infty,\infty[$ to any chosen degree of accuracy, the first term of the asymptotic expansion for $I_2(\xi)$ as $\xi\to\infty$ is determined by substituting Π_∞ to Π in the integrand of I_2 defined in (B3)

$$I_2(\xi)=i_2(\xi,\infty)-i_2(\xi,\xi_\infty) \tag{B8}$$

with

$$i_2(\xi,\zeta)\equiv-\frac{4}{\pi}\int_0^{\zeta}\left(\frac{\xi}{\eta}\right)^{1/2}\frac{\Pi_\infty(\eta)}{\xi-\eta}\,d\eta.$$

Evaluating the integral $i_2(\xi,\zeta)$ analytically and then calculating the first term of the asymptotic expansion of the resulting expression leads to

$$i_2(\xi,\infty)=b\xi^{-1/3}+O(\xi^{-1/2}),\quad i_2(\xi,\xi_\infty)=O(\xi^{-1/2}) \tag{B9}$$

where $b=2^{4/3}3^{-1/6}$. Combining (B2), (B4), and (B8) with (B9) yields

$$\Omega'_r(\xi)=b\xi^{-1/3}+O(\xi^{-1/2}). \tag{B10}$$

Upon integrating (B10), using (21), and noting that $\Omega_\Lambda(\xi)=O(\xi^{1/2})$, see (22), we obtain the asymptotic expansion of the opening of the crack as $\xi\to\infty$

$$\Omega(\xi)=\frac{3}{2}b\xi^{2/3}+O(\xi^{1/2})\quad \text{as}\quad \xi\to\infty. \tag{B11}$$

Noting that $3b\xi^{2/3}/2\equiv\Omega_\infty(\xi)$ (see (26)), we conclude that the asymptotic behavior of the solution $\Pi(\xi;\kappa)$ and $\Omega(\xi;\kappa)$ at infinity, (27), is consistent with the elasticity Eqs. (21)–(23). Furthermore, this asymptote (27) satisfies the lubrication Eq. (11) automatically. Therefore, if there exists a unique solution for any prescribed $\kappa\geqslant 0$, then the asymptotic behavior of this solution at infinity is given by (26).

Appendix C

Numerical Scheme. This Appendix outlines the numerical scheme used to solve the system (11), (21)–(23) on the semi-infinite interval $\xi\in[\Lambda,\infty[$ with the boundary condition (24) and the asymptotic behavior (27). As shown next, this numerical algorithm yields a system of nonlinear algebraic equations in terms of the fluid pressure at nodes inside the fluid-filled part of the crack and in terms of the toughness κ, given the lag Λ. (Although the length of the lag Λ is technically an unknown of the problem to be solved as a function of κ, the lag Λ—i.e., the geometry of the problem—is prescribed in the numerical solution and the corresponding κ solved numerically.)

Actually, we seek to determine numerically the transition between the near-tip (14) and the far-field asymptote (27), which are reached to a certain prescribed degree of accuracy for $\xi\in[0,\xi_o]$ and $\xi\in[\xi_\infty,\infty[$, respectively. Let us introduce L_o, $\Lambda<L_o<\xi_o$ ($L_o=\Lambda$ if $\xi_o\leqslant\Lambda$), and L_∞, $L_\infty>\xi_\infty$ and prescribe that $\Pi(\xi)=\Pi_o(\xi)$ for $\xi\in[\Lambda,L_o]$ (if $\xi_o>\Lambda$, otherwise $L_o=\Lambda$) and $\Pi(\xi)=\Pi_\infty(\xi)$ for $\xi\in[L_\infty,\infty[$. Note that if $\xi_o>\Lambda$ (which corresponds to the case of large toughness κ and small lag) we take into account the asymptotic behavior of the net-loading Π near the interface between the tip cavity and the rest of the crack, $\xi=\Lambda$, and at infinity; whereas if $\xi_o\leqslant\Lambda$ (corresponding to moderate and small toughness) the near interface asymptote $\Pi_o(\xi)$ is not valid and we only take into account the far-field asymptote (by imposing $L_o=\Lambda$). The constants L_o and L_∞ have the meaning of ''safe'' guesses for the bounds ξ_o and ξ_∞ and must be chosen in such a way that the resulting solution in terms of Π be equal to $\Pi_o(\xi)$ (if $L_o>\Lambda$) (be equal to $\Pi_\infty(\xi)$) on several intervals immediately succeeding (preceding) the interval $\xi\in[\Lambda,L_o]$($\xi\in[L_\infty,\infty[$). In other words, the intervals $[\Lambda,L_o]$ and $[L_\infty,\infty[$ have to lie within the region dominated by the corresponding asymptotes to provide a smooth transition between the intermediate numerical solution and the asymptotes.

We start by dividing the interval $\xi\in[L_o,L_\infty]$ into $n-1$ intervals (ξ_i,ξ_{i+1}), $i=1,\ldots,n-1$, where $\xi_1=L_o$, $\xi_n=L_\infty$ and prescribe the variation of pressure Π over each boundary element to be a linear function of $\Pi_\infty(\xi)$, i.e.,

$$\Pi(\xi)=a_i\Pi_\infty(\xi)+b_i,\quad \xi\in[\xi_i,\xi_{i+1}],\quad i=1,\ldots,n-1. \tag{C1}$$

Using (22), one can deduce the expression for Ω_r corresponding to the net-loading representation (C1)

$$\Omega_r(\xi)=[F_o(\xi,\eta)]_{\eta=\Lambda}^{\eta=\xi_1}+\sum_{j=1}^{n-1}[a_jF_\infty(\xi,\eta)+b_jF(\xi,\eta)]_{\eta=\xi_j}^{\eta=\xi_{j+1}}$$
$$+[F_\infty(\xi,\eta)]_{\eta=\xi_n}^{\eta=\infty} \tag{C2}$$

where the functions $F_o(\xi,\eta)$, $F_\infty(\xi,\eta)$, and $F(\xi,\eta)$ are defined as

$$F(\xi,\eta)\equiv\frac{4}{\pi}\int_0^\eta K(\xi,\eta)d\eta$$

$$F_\infty(\xi,\eta)\equiv\frac{4}{\pi}\int_0^\eta K(\xi,\eta)\Pi_\infty(\eta)d\eta$$

$$F_o(\xi,\eta)\equiv\frac{4}{\pi}\int_0^\eta K(\xi,\eta)\Pi_o(\eta)d\eta$$

$$=-F(\xi,\eta)+\frac{1}{\kappa^2}\{-\ln\Lambda F(\xi,\eta)+F_{\ln}(\xi,\eta)\}$$

$$F_{\ln}(\xi,\eta)\equiv\frac{4}{\pi}\int_0^\eta K(\xi,\eta)\ln\eta d\eta.$$

Functions $F_\infty(\xi,\eta)$, $F(\xi,\eta)$, and $F_{\ln}(\xi,\eta)$ in the above formula can be expressed in the following form:

$$F(\xi,\eta)=-\frac{4}{\pi}\left(2\sqrt{\xi\eta}+(\xi-\eta)\ln\left|\frac{\sqrt{\xi}+\sqrt{\eta}}{\sqrt{\xi}-\sqrt{\eta}}\right|\right)$$

$$F_\infty(\xi,\eta)=\frac{4}{\pi}\left(\frac{3}{256}\right)^{1/3}\xi^{2/3}\left\{4\zeta+2\sqrt{3}\arctan\left(\frac{1+2\zeta}{\sqrt{3}}\right)\right.$$
$$-2\sqrt{3}\arctan\left(\frac{1-2\zeta}{\sqrt{3}}\right)+\ln\frac{1-\zeta^3}{1+\zeta^3}\left(\frac{1+\zeta}{1-\zeta}\right)^3$$
$$\left.-\zeta^4\ln\left(\frac{1+\zeta^3}{1-\zeta^3}\right)^2\right\},\quad \zeta\equiv\left(\frac{\eta}{\xi}\right)^{1/6}$$

$$F_{\ln}(\xi,\eta)=\frac{4}{\pi}\left\{2\sqrt{\xi\eta}(1-\ln\eta)+(\xi-\eta(1-\ln\eta)\right.$$
$$-\xi\ln\eta)\ln\left|\frac{\sqrt{\xi}+\sqrt{\eta}}{\sqrt{\xi}-\sqrt{\eta}}\right|+\chi 2\xi\left(Li_2\left(\left(\frac{\eta}{\xi}\right)^{\chi/2}\right)\right.$$
$$\left.\left.-Li_2\left(-\left(\frac{\eta}{\xi}\right)^{\chi/2}\right)\right)\right\},$$
$$\chi\equiv\mathrm{sgn}(\xi-\eta)$$

and Li_2 and sgn denote the polylogarithmic function of order 2 and the sign function, respectively.

The coefficients in ($C1$) are determined by imposing continuity of $\Pi(\xi)$ at the grid points, i.e., $\Pi^i=\Pi(\xi_i)$

$$a_i=\frac{\Pi^{i+1}-\Pi^i}{\Pi_\infty^{i+1}-\Pi_\infty^i},\quad b_i=\Pi^i-a_i\Pi_\infty^i \qquad (C3)$$

where $\Pi_\infty^i=\Pi_\infty(\xi_i)$, and $\Pi_o^i=\Pi_o(\xi_i)$. The values of net pressure at the points ξ_1 and ξ_n are prescribed by the structure of sought solution

$$\Pi^1=\Pi_o(\xi_1)\quad(\text{or}\ -1\quad\text{if}\ \xi_1=\Lambda),\quad \Pi^n=\Pi_\infty(\xi_n). \qquad (C4)$$

Finally, the lubrication Eq. (11) can be evaluated at the midpoints of the intervals, using (21) for the crack-opening Ω, with $\Omega_r(\xi)$ expressed as a linear combination of the nodal values Π^i by means of ($C2$) and ($C3$)

$$\Omega^2(\xi_{j+1/2})\Pi'(\xi_{j+1/2})=1,\quad j=1,\ldots,n-1 \qquad (C5)$$

with the pressure gradient $\Pi'(\xi_{j+1/2})$ approximated as

$$\Pi'(\xi_{j+1/2})=\frac{\Pi_{j+1}-\Pi_j}{\xi_{j+1}-\xi_j}. \qquad (C6)$$

Taking into account the boundary conditions ($C4$), ($C5$) constitutes a system of $n-1$ nonlinear algebraic equations in terms of the $n-1$ unknowns $\Pi_2,\ldots,\Pi_{n-1}$ and κ. This nonlinear system of equations is solved using the Newton iteration procedure, which is built in the *Mathematica* computational software.

References

[1] Khristianovic, S. A., and Zheltov, Y. P., ''Formation of Vertical Fractures by Means of Highly Viscous Fluids,'' *Proc. 4th World Petroleum Congress*, Vol. II, pp. 579–586.

[2] Barenblatt, G. I., 1962, ''The Mathematical Theory of Equilibrium Cracks in Brittle Fracture,'' Adv. Appl. Mech., **VII**, pp. 55–129.

[3] Perkins, T. K., and Kern, L. R., 1961, ''Widths of Hydraulic Fractures,'' SPEJ, **222**, pp. 937–949.

[4] Nordgren, R. P., 1972, ''Propagation of Vertical Hydraulic Fracture,'' SPEJ, **253**, pp. 306–314.

[5] Abe, H., Mura, T., and Keer, L. M., 1976, ''Growth Rate of a Penny-Shaped Crack in Hydraulic Fracturing of Rocks,'' J. Geophys. Res., **81**, pp. 5335–5340.

[6] Geertsma, J., and Haafkens, R., 1979, ''A Comparison of the Theories for Predicting Width and Extent of Vertical Hydraulically Induced Fractures.'' ASME J. Energy Resour. Technol., **101**, pp. 8–19.

[7] Spence, D. A., and Sharp, P., 1985, ''Self-Similar Solution for Elastohydrodynamic Cavity Flow,'' Proc. R. Soc. London, Ser. A, **400**, pp. 289–313.

[8] Spence, D. A., and Turcotte, D. L., 1985, ''Magma-Driven Propagation Crack,'' J. Geophys. Res., **90**, pp. 575–580.

[9] Lister, J. R., 1990, ''Buoyancy-Driven Fluid Fracture: The Effects of Material Toughness and of Low-Viscosity Precursors,'' J. Fluid Mech., **210**, pp. 263–280.

[10] Carbonell, R. S., and Detournay, E., 2000, ''Self-Similar Solution of a Fluid Driven Fracture in a Zero Toughness Elastic Solid,'' Proc. R. Soc. London, Ser. A, to be submitted.

[11] Savitski, A., and Detournay, E., 1999, ''Similarity Solution of a Penny-Shaped Fluid-Driven Fracture in a Zero-Toughness Linear Elastic Solid,'' C. R. Acad. Sci. Paris, submitted for publication.

[12] Bui, H. D., and Parnes, R., 1992, ''A Reexamination of the Pressure at the Tip of a Fluid-Filled Crack,'' Int. J. Eng. Sci., **20**, No. 11, pp. 1215–1220.

[13] Medlin, W. L., and Masse, L., 1984, ''Laboratory Experiments in Fracture Propagation,'' SPEJ, pp. 256–268.

[14] Rubin, A. M., 1993, ''Tensile Fracture of Rock at High Confining Pressure: Implications for Dike Propagation,'' J. Geophys. Res., **98**, No. B9, pp. 15919–15935.

[15] Desroches, J., Detournay, E., Lenoach, B., Papanastasiou, P., Pearson, J. R. A., Thiercelin, M., and Cheng, A. H.-D., 1994 ''The Crack Tip Region in Hydraulic Fracturing,'' Proc. R. Soc. London, Ser. A, **447**, pp. 39–48.

[16] Lenoach, B., 1995, ''The Crack Tip Solution for Hydraulic Fracturing in a Permeable Solid,'' J. Mech. Phys. Solids, **43**, No. 7, pp. 1025–1043.

[17] Advani, S. H., Lee, T. S., Dean, R. H., Pak, C. K., and Avasthi, J. M., 1997, ''Consequences of Fluid Lag in Three-Dimensional Hydraulic Fractures,'' Int. J. Numer. Anal. Meth. Geomech., **21**, pp. 229–240.

[18] Papanastasiou, P., 1997, ''The Influence of Plasticity in Hydraulic Fracturing,'' Int. J. Fract., **84**, pp. 61–97.

[19] Garagash, D., and Detournay, E., 1998, ''Similarity Solution of a Semi-Infinite Fluid-Driven Fracture in a Linear Elastic Solid,'' C. R. Acad. Sci., Ser. II b, **326**, pp. 285–292.

[20] Detournay, E., and Garagash, D., 1999, ''The Tip Region of a Fluid-Driven Fracture in a Permeable Elastic Solid,'' J. Fluid Mech., submitted for publication.

[21] Carbonell, R., Desroches, J., and Detournay, E., 2000, ''A Comparison Between a Semi-analytical and a Numerical Solution of a Two-Dimensional Hydraulic Fracture,'' Int. J. Solids Struct., **36**, No. 31–32, pp. 4869–4888.

[22] Detournay, E., 1999, ''Fluid and Solid Singularities at the Tip of a Fluid-Driven Fracture,'' *Non-Linear Singularities in Deformation and Flow*, D. Durban and J. R. A. Pearson, eds., Kluwer Academic Publishers, Dordrecht, The Netherlands, pp. 27–42.

[23] Garagash, D., and Detournay, E., 2000, ''Plane Strain Propagation of a Hydraulic Fracture: Influence of Material Toughness, Fluid Viscosity, and Injection Rate,'' Proc. R. Soc. London, Ser. A, to be submitted.

[24] Huang, N., Szewczyk, A., and Li, Y., 1990, ''Self-Similar Solution in Problems of Hydraulic Fracturing,'' ASME J. Appl. Mech., **57**, pp. 877–881.

[25] Batchelor, G. K., 1967, *An Introduction to Fluid Mechanics*, Cambridge University Press, Cambridge, UK.

[26] Rice, J. R., 1968, ''Mathematical Analysis in the Mechanics of Fracture,'' *Fracture: An Advanced Treatise*, Vol II, Academic Press, San Diego, CA, pp. 191–311.

[27] van Dam, D. B., de Pater, C. J., and Romijn, R., 1998, ''Analysis of Hydraulic Fracture Closure in Laboratory Experiments, SPE/ISRM 47380. *Proc. Of Eu-Rock'98, Rock Mechanics in Petroleum Engineering*, SPE, Trondheim, Norway, pp. 365–374.

[28] van Dam, D. B., 1999, ''The Influence of Inelastic Rock Behaviour on Hydraulic Fracture Geometry,'' Ph.D. thesis, Delft Institute of Technology, Delft University Press, Delft, The Netherlands.

[29] Srivastava, H. M., and Buschman, R. G., 1992, *Theory and Applications of Convolution Integral Equations: Mathematics and Its Applications*, Kluwer Academic Publishers, Dordrecht, The Netherlands.

G. J. Rodin
Center for Mechanics of Solids Structures
and Materials,
Department of Aerospace Engineering
and Engineering Mechanics,
The University of Texas at Austin,
Austin, TX 78712

Continuum Damage Mechanics and Creep Life Analysis

It is shown that the original continuum damage mechanics model of Kachanov is better suited for creep life analysis of creep-brittle solids and structures than continuum damage mechanics models that take into account damage-induced softening.
[S0021-8936(00)03001-4]

1 Introduction

Continuum Damage Mechanics was introduced in 1958 by the late Prof. Lazar M. Kachanov. The premise of continuum damage mechanics is that by modeling the kinetics of damage accumulation one can predict the duration of the tertiary creep stage and thus estimate the creep life. The seminal idea of Kachanov has influenced many researchers, among others, Rabotnov [1], Hayhurst and Leckie with co-workers ([2]), and Chaboche and Lemaitre with co-workers ([3]). Presently, continuum damage mechanics is an umbrella for many phenomenological and micromechanical models concerned with distributed damage ([4,5]).

In this paper, we revisit one of the original themes of continuum damage mechanics—creep life analysis of creep-brittle (polycrystalline) solids and structures. Our approach is based on heuristic arguments rather than rigorous mathematical proofs, but it allows us to cover essentially the entire spectrum of continuum damage mechanics models. The principal result of this paper is that, as far as creep life analysis of creep-brittle solids and structures is concerned, the original model of Kachanov [6] appears to be more useful than more complicated models that take into account damage-induced softening.

The paper is organized as follows. In Section 2, we summarize the fundamentals of continuum damage mechanics. In Section 3, we compare engineering and continuum damage mechanics models for creep life predictions. Based on those comparisons, we argue that Kachanov's model is better suited for practical creep life analysis of creep-brittle solids and structures than continuum damage mechanics models that take into account damage induced softening. In Section 4, we briefly discuss several issues related to the principal result.

2 Continuum Damage Mechanics

In this section, we briefly summarize continuum damage mechanics fundamentals. We do not distinguish between micromechanical versus phenomenological models and scalar versus tensor damage variables, since those distinctions are neither useful nor necessary for our purposes.

2.1 Constitutive Equations. Continuum damage mechanics is based on evolution equations for the creep strain ϵ and damage variable ω. For isothermal creep of a cylindrical bar induced by a uniaxial stress σ, the evolution equations are

$$\dot{\epsilon}=f(\omega,\sigma) \tag{1}$$

and

$$\dot{\omega}=g(\omega,\sigma). \tag{2}$$

Equations (1) and (2) require the initial conditions

$$\epsilon=\epsilon_0 \quad \text{and} \quad \omega=\omega_0 \quad \text{at} \quad t=0 \tag{3}$$

and the termination condition

$$\omega=\omega_f \quad \text{at} \quad t=t_f. \tag{4}$$

In (3) and (4), ϵ_0, ω_0, and ω_f are prescribed data. The termination condition (4) is an implicit equation for the time to fracture (or the creep life) t_f of the bar.

Usually the continuum damage mechanics constitutive functions in (1) and (2) are calibrated using either uniaxial creep data or empirical equations that represent such data. For isothermal uniaxial creep data, there are two empirical equations that have been widely used in the engineering community. The first equation is a power-law relationship between the secondary (or minimum) creep rate and stress (or Norton's law)

$$\dot{\epsilon}_s=B\sigma^n. \tag{5}$$

The second equation is a power-law relationship between the secondary creep rate and time to fracture (or Monkman-Grant's formula)

$$\dot{\epsilon}_s^{\nu}t_f=C. \tag{6}$$

In (5) and (6) B, n, ν and C are material constants. Equations (5) and (6) can be combined as

$$\sigma^m t_f=D, \tag{7}$$

where

$$m=n\nu \quad \text{and} \quad D=B^{-\nu}C.$$

This paper is concerned with creep life analysis of creep-brittle solids and structures ([7]) for which, under isothermal uniaxial creep conditions, the ratio

$$\frac{\epsilon_f}{\dot{\epsilon}_s t_f}\leqslant 3.$$

Here ϵ_f is the strain at fracture. Such solids fail by accumulation of intergranular damage associated with relatively small creep strains. In contrast, creep-ductile solids, for which the ratio can exceed ten, fail as a result of intragranular damage associated with relatively large creep strains.

2.2 Boundary Value Problems. To formulate boundary value problems based on (1)–(4), one has to generalize the constitutive equations to three dimensions. Usually this is done by replacing σ in (1) and (2) with stress invariants that are linear combinations of either the Mises stress and the maximum principal stress ([2]) or the principal stresses ([8]).

In a typical continuum damage mechanics boundary value problem, one can identify the latent and propagation stages ([6]). The latent stage lasts from $t=0$ to the time t_l, when the first point reaches the state $\omega=\omega_f$, and the propagation stage consumes the

Contributed by the Applied Mechanics Division of THE AMERICAN SOCIETY OF MECHANICAL ENGINEERS for publication in the ASME JOURNAL OF APPLIED MECHANICS. Manuscript received by the ASME Applied Mechanics Division, Jan. 28, 1999; final revision, June 8, 1999. Associate Technical Editor: J. W. Ju. Discussion on the paper should be addressed to the Technical Editor, Professor Lewis T. Wheeler, Department of Mechanical Engineering, University of Houston, Houston, TX 77204-4792, and will be accepted until four months after final publication of the paper itself in the ASME JOURNAL OF APPLIED MECHANICS.

remainder of the creep life. For example, in a circular cylindrical bar subject to torsion, the ''fracture''of the outer layer signifies the end of the latent stage, and the remaining creep life involves propagation of the fracture front toward the center. This and similar problems have been considered by Kachanov [9].

Although formally one can use continuum damage mechanics equations for predicting the duration of the propagation stage, there are conceptual and practical difficulties with such predictions. From the conceptual perspective, we recall that continuum damage mechanics, as a continuum theory, is valid only at scales that are significantly larger than the microcrack size and therefore the field variations can be significant only over those, but not smaller scales. Most likely, this provision is violated near the fracture propagation front, where large damage and stress gradients are expected across the front. From the practical perspective, we recall that creep life predictions involve large margins of error ([10]), and therefore one should not extend the predicted creep life by adding to it the duration of the propagation stage. In the remainder of this paper we disregard the propagation stage and equate the creep life with the duration of the latent stage.

2.3 Kachanov's Model. Kachanov's model is recovered from (1)–(4) once we put

$$f(\omega,\sigma)=B\sigma^n, \tag{8}$$

$$g(\omega,\sigma)=\frac{1}{D(m+1)}\left(\frac{\sigma}{1-\omega}\right)^m, \tag{9}$$

and

$$\omega_0=0, \qquad \epsilon_0=0, \qquad \omega_f=1. \tag{10}$$

2.4 Models With Softening. The majority of continuum damage mechanics models include the softening effect of damage. In the phenomenological context, such models were introduced by Rabotnov [1] and advanced by Hayhurst and Leckie with co-workers ([2]), Lemaitre with co-workers ([3]), and others; related micromechanical models, applicable to structural creep life analysis, were developed by Ashby and Dyson [7] and Dib and Rodin [11].

The softening effect is included by choosing $f(\omega,\sigma)$ such that

$$\frac{\partial f(\omega,\sigma)}{\partial \omega}>0. \tag{11}$$

On the one hand, this is a sensible improvement of Kachanov's model as it captures the strain rate increase during tertiary creep, on the other hand, as will be shown in the next section, it appears to be a poor choice for practical creep life analysis of creep-brittle solids and structures.

For our purposes, it is not necessary to specify explicit expressions for $f(\omega,\sigma)$ and $g(\omega,\sigma)$. Instead, we prescribe $f(\omega,\sigma)$ and $g(\omega,\sigma)$ implicitly, in terms of inequalities they must satisfy. Namely, we assume that

$$f(\omega,\sigma)>0 \quad \text{and} \quad g(\omega,\sigma)>0, \tag{12}$$

and

$$\frac{\partial f(\omega,\sigma)}{\partial \sigma}>0, \quad \text{and} \quad \frac{\partial g(\omega,\sigma)}{\partial \sigma}>0. \tag{13}$$

The first pair of inequalities implies that there is no reverse creep or damage healing, and the second pair of inequalities implies that the strain and damage rates increase with stress. As far as I know, these conditions are satisfied by all continuum damage mechanics models.

3 Creep Life Analysis

In this section, we consider three models for creep life analysis. The first model represents engineering models ([10]), and in particular it was used by De Witte [12] for creep life analysis of a turbine rotor (see also [13]). We refer to this model as the engineering model and denote its attributes by the superscript *e*. The second model is due to Kachanov [6] and the third model is a generic continuum damage mechanics model with softening; their attributes are denoted by the superscripts *k* and *s*, respectively.

The objective in this section is twofold. First, we establish that, as far as creep life analysis is concerned, the engineering and Kachanov's models are equivalent. Second, we show that, for creep-brittle solids and structures, Kachanov's model is more conservative than continuum damage mechanics models with softening, and therefore should be preferred for creep life analysis. Furthermore, we argue that continuum damage mechanics models with softening are of little use for creep life analysis of creep-brittle solids and structures in cases when Kachanov's model is too conservative.

3.1 Engineering Versus Kachanov's Models. In the engineering model, the creep life is computed using Robinson's cumulative damage rule rather than an evolution equation for the damage variable ([14]). This model is based on the following steps:

- Compute the stress field using the standard power-law creep constitutive equations.
- Determine the maximum Mises stress $\bar{\sigma}^e_{\max}$.
- Compute the creep life as

$$t^e_f=D(\bar{\sigma}^e_{\max})^{-m}. \tag{14}$$

- For complex loading histories, one may choose several critical points and use

$$D=\int_0^{t^e_f}[\bar{\sigma}^e_{\max}(\tau)]^m d\tau \tag{15}$$

instead of (14).

The following observations about the engineering model are important:

- The engineering model does not include the propagation stage.
- The engineering and Kachanov's models predict the same creep life as long as Kachanov's model is extended to three dimensions by replacing σ with $\bar{\sigma}$. This statement holds for general stress histories ([14]).
- The conceptual difference between the engineering and Kachanov's models is that the former relies on real time while the latter uses ω as intrinsic material time. The advantage of the engineering model is in its simplicity. The advantage of Kachanov's model is that it allows one to correlate the creep life and microstructural observations of damage ([10]).

3.2 Kachanov's Model Versus Models With Softening. The objective in this section is to demonstrate that the creep life predicted with Kachanov's (or engineering) model is longer than the creep life predicted with models with softening. I cannot prove this statement rigorously. Therefore, first, we consider an example problem that demonstrates how damage-induced softening prolongs the creep life, and then we argue that this property of damage induced softening holds in general.

Consider a symmetric truss made of three vertical bars that are identical except that the inside bar is longer by a factor of α than the outside bars (Fig. 1). The upper ends of the bars are fixed whereas the lower ends are attached to a rigid plate that can move vertically only. The plate is loaded by a constant force *P* applied at its center. We consider two types of constitutive equations—the first type represents Kachanov's model and the second type represents models with softening.

For Kachanov's model, the constitutive equations are chosen as

$$\dot{\epsilon}^k=B\sigma^k \tag{16}$$

and

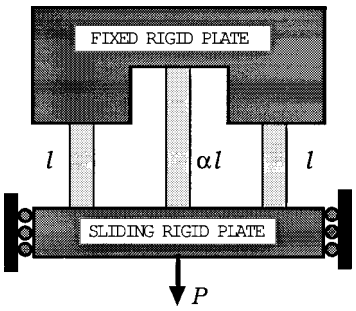

Fig. 1 Three-bar truss: The bars are identical except that the inside bar is longer than the outside bars by a factor of α

$$\dot{\omega}^k=\frac{1}{2D}\frac{\sigma^k}{1-\omega^k}. \tag{17}$$

For the model with softening, the constitutive equations are chosen as

$$\dot{\epsilon}^s=B\frac{\sigma^s}{1-\omega^s} \tag{18}$$

and

$$\dot{\omega}^s=\frac{1}{2D}\frac{\sigma^s}{1-\omega^s}. \tag{19}$$

For both models, we use $\epsilon_0=0$, $\omega_0=0$, and $\omega_f=1$.

The equilibrium and comparability equations for the given truss are

$$2\sigma_1 A+\sigma_2 A=P \tag{20}$$

and

$$\dot{\epsilon}_1=\alpha\dot{\epsilon}_2. \tag{21}$$

Here the subscript 1 refers to the outside bars, the subscript 1 refers to the inside bar, and A denotes the cross-sectional area of the bars.

For Kachanov's model, both σ_1 and σ_2 do not change with time (recall that the propagation stage is not considered in our analysis), and their values are determined once (20) and (21) are combined with (16):

$$\sigma_1^k=\frac{\alpha}{1+2\alpha}\frac{P}{A} \quad \text{and} \quad \sigma_2^k=\frac{1}{1+2\alpha}\frac{P}{A}. \tag{22}$$

Note that $\sigma_1^k\geqslant\sigma_2^k$ and therefore the creep life is computed as

$$t_f^k=\frac{D}{\sigma_1^k}. \tag{23}$$

For the model with softening, the expressions for σ_1 and σ_2 are rather cumbersome but the important point is that they can be represented in the form

$$\sigma_1^s(t)=\sigma_1^k h_1(t) \quad \text{and} \quad \sigma_2^s(t)=\sigma_2^k h_2(t), \tag{24}$$

where the functions $h_1(t)$ and $h_2(t)$ satisfy the inequality

$$h_2(t)\leqslant h_1(t)\leqslant 1. \tag{25}$$

This inequality implies that, on the one hand, the outside bars are exposed to a more severe stress history than the inside bar, and, on the other hand, the stress $\sigma_1^s(t)\leqslant\sigma_1^k$. The inequality $\sigma_1^s(t)\leqslant\sigma_1^k$ stems from the fact that damage accumulation and consequently softening is more active in the outside (more stressed) bars than in the inside (less stressed) bar, and therefore, with time, the stress is redistributed from the outside bars to the inside bar. This stress redistribution leads to the longer creep life:

$$\frac{t_f^s}{t_f^k}=1+\frac{\alpha-1}{2\alpha^2+\alpha}\geqslant 1 \quad (\alpha\geqslant 1).$$

Also, it is instructive to obtain this inequality from (25)

$$t_f^k=\frac{D}{\sigma_1^k}=\frac{1}{\sigma_1^k}\int_0^{t_f^s}\sigma_1^s(\tau)d\tau=\int_0^{t_f^s}h_1(\tau)d\tau\leqslant t_f^s.$$

Note that, if $\alpha=1$, the truss becomes essentially statically determinate and therefore the stress redistribution does not take place. In this case, $h_1(t)=h_2(t)=1$ and $t_f^s=t_f^k$.

The example problem demonstrates that the softening mechanism operates so that the stress is redistributed away from high-stress regions to low-stress regions, and therefore the stress distribution becomes less nonuniform. Obviously this property is not restricted to the example problem. Furthermore, this property is shared by all softening mechanisms, as long as instabilities (in our case the propagation stage) are absent. For example, power-law creep can be regarded as a softening mechanism that reduces stress concentrations induced by elastic deformation ([14]). In some sense, damage-induced softening endows the structure with adaptivity that adjusts its properties so that the stress is redistributed from high-stress/high-damage regions to low-stress/low-damage regions. As a result, the stress histories at the critical point(s) become less severe and the time to fracture increases.

I cannot establish rigorously the necessary and sufficient conditions on $f(\omega,\sigma)$ and $g(\omega,\sigma)$ associated with the inequality $t_f^s\geqslant t_f^k$. Conditions formulated in (12) and (13) may be sufficient since they require that creep strain and damage accumulate irreversibly (12) and the accumulation processes are most active in high-stress regions.

Considering the fact that creep life analysis involves large error margins, the engineer should prefer conservative estimates for t_f, provided that those estimates are not too conservative. In this regard, continuum damage mechanics models with softening could be useful if Kachanov's model is too conservative. This could happen if creep deformation induced by damage is significant. But, if this is the case, the structure under consideration is creep-ductile and one should consider models that emphasize intragranular damage and relatively large creep strains. A good example of such models is given by Dyson and Gibbons [15].

In conclusion of this section, it is proper to point out that in three dimensions the validity of $t_f^s\geqslant t_f^k$ can be challenged by arguing that the softening mechanism may affect one combination of the stress components whereas damage accumulation may be controlled by a different combination. For example, in phenomenological continuum damage mechanics theories ([2]) the strain rate is proportional to the deviatoric stresses and Mises stress, whereas the damage rate depends on the Mises stress and the maximum principal stress. I believe that this situation is highly unlikely but I cannot rule it out. Also, $t_f^s\geqslant t_f^k$ may not hold for composite structures because stress redistribution in one phase may adversely affect other phases.

4 Concluding Remarks

- The continuum damage mechanics models that take the softening effect of damage into account, and proposed as generalizations of the original model of Kachanov [6] appear to be of little use for practical creep life analysis of creep-brittle solids and structures.
- The conclusion that the importance of continuum damage mechanics models with softening may have been overestimated in the academic circles is indirectly supported by Viswanathan [10], who compiled a comprehensive collection of models used in practical creep life analysis. There continuum damage mechanics appears to be less prominent than various empirical equations, and it is used along the lines of Kachanov's model.

• Considering the broad range of topics presently covered by continuum damage mechanics one should not take the present results out of the proper context, as they are limited to creep life analysis of creep-brittle solids and structures.

Acknowledgment

This work was supported by the ALCOA Foundation and ONR grant N00014-92J1332, Program Director Yapa D. S. Rajapakse. I am grateful to Prof. Richard A. Schapery and Dimitris Lagoudas for comments and suggestions.

References

[1] Rabotnov, Y. N., 1969, *Creep Problems in Structural Members*, North-Holland, Amsterdam.
[2] Hayhurst, D. R., 1983, ''On the Role of Creep Continuum Damage in Structural Mechanics,'' *Engineering Approaches to High-Temperature Fracture*, B. Wilshire and D. R. J. Owen, eds., Pineridge Press, Swansea, UK, pp. 85–233.
[3] Lemaitre, J., 1992, *A Course on Damage Mechanics*, Springer-Verlag, Berlin.
[4] Kachanov, M., 1993, ''Elastic Solids with Many Cracks and Related Problems,'' *Advances in Applied Mechanics*, J. W. Hutchinson and T. Wu, eds., Academic Press, New York, pp. 259–445.
[5] Krajcinovic, D., 1996, *Damage Mechanics*, North-Holland, Amsterdam.
[6] Kachanov, L. M., 1958, ''On Creep Rupture Time,'' Proc. Acad. Sci., USSR, Div. Eng. Sci., **8**, pp. 26–31.
[7] Ashby, M. F., and Dyson, B. F., 1984, ''Creep Damage Mechanics and Micromechanisms,'' *Advances in Fracture Research'84*, Vol. 1, S. R. Valluri et al., eds., Pergamon Press, Oxford, pp. 3–30.
[8] Nix, W. D., Earthman, J. C., Eggeler, G., and Ilschner, B., 1989, ''The Principal Facet Stress as a Parameter for Predicting Creep Rupture Under Multiaxial Stresses,'' Acta Metall. Mater., **37**, pp. 1067–1077.
[9] Kachanov, L. M., 1986, *Introduction to Continuum Damage Mechanics*, Martinus Nijhoff Publishers, Dordrecht, The Netherlands.
[10] Viswanathan, R., 1989, *Damage Mechanisms and Life Assessment of High-Temperature Components*, ASM International, Metals Park, OH.
[11] Dib, M. W., and Rodin, G. J., 1993, ''Continuum Damage Mechanics of Constrained Intergranular Cavitation,'' Acta Metall. Mater., **41**, pp. 1567–1575.
[12] De Witte, M., 1989, ''Power Plant Life Estimation and Extension: The Belgian Experience From the User's Point of View,'' Int. J. Pressure Vessels Piping, **35**, pp. 41–61.
[13] Dib, M. W., and Rodin, G. J., 1992, ''A Micromechanical Creep Analysis of a Turbine Rotor,'' *Advances in Local Fracture Models*, J. H. Giovanola and A. K. Rosakis, eds., ASME, New York, pp. 3–13.
[14] Odquist, F. K. G., 1974, *Mathematical Theory of Creep and Creep Rupture*, Clarendon Press, Oxford, UK.
[15] Dyson, B. F., and Gibbons, T. B., 1987, ''Tertiary Creep in Nickel-Base Superalloys: Analysis of Experimental Data and Theoretical Synthesis,'' Acta Metall. Mater., **35**, pp. 2355–2369.

S. E. Bechtel
Mem. ASME

S. Vohra

Department of Mechanical Engineering,
The Ohio State University,
Columbus, OH 43210

K. I. Jacob
School of Textile and Fiber Engineering,
Georgia Institute of Technology,
Atlanta, GA 30332

C. D. Carlson
Mitsubishi Polyester Film, LLC,
2001 Hood Road, Box 1400,
Greer, SC 29652

The Stretching and Slipping of Belts and Fibers on Pulleys

We derive the equations of motion for an extensible belt on a pulley in which all effects of inertia, including (for the first time) acceleration due to stretching, are retained in the momentum balance. These equations are also valid for fibers and films on rollers undergoing cold draw. We apply our equations to the problem of torque transmission by a belt between two pulleys, and compare the resulting solution to solutions in which centrifugal acceleration is included but stretching acceleration is neglected (the common engineering practice), and the solution in which both centrifugal and stretching accelerations are neglected. We find that ignoring both centrifugal and stretching accelerations results in an overprediction of the maximum moment that can be transmitted, and, for a given transmitted moment, underprediction of the slip angles on the driving and driven pulleys and overprediction of belt strain rates and normal and frictional forces from the pulley on the belt in the slip zones. The common engineering practice of including the effects of centrifugal acceleration but neglecting stretching acceleration also results in errors, for example underpredicting the maximum moment that can be transmitted, overpredicting the slip angles, and underpredicting belt strain rates and normal and frictional forces on the driving pulley. The percentage error increases as the ratios of belt stiffness to centrifugal acceleration or initial belt tension decrease. [S0021-8936(00)01401-X]

1 Introduction

The stretching and sliding of belts on pulleys or fibers and films on rollers have significant industrial implications. Torque transmission between pulleys is affected by the stretching and slipping of the belt. In a fiber manufacturing process, polymeric fibers are drawn between feed and take-up rollers in order to improve their mechanical properties. In a cold draw process (i.e., where no external heat is supplied) the draw occurs on the rollers, accompanied by stretching and sliding of fibers. Similar behavior is also true for films. Although we address the problem of belts on pulleys and adopt this nomenclature, the formulation is equally applicable to the drawing of fibers and films.

Any examination of a belt-pulley system which takes into account the compliance or elasticity of the belt, for prediction of the slip angles on the pulleys, analysis of creep, etc., must, to be consistent, include the effects of changing belt stretch in the momentum equations. These analyses recognize that the belt tension is not uniform; there is a tight side and a slack side. The elastic characterization of the belt indicates that this change of tension is accompanied by a change of strain, so there must be a changing stretch in the belt. This rate of change of stretch is an acceleration that results in a change of momentum.

In Section 2 we derive the momentum equation for a moving, stretching belt on a pulley. We find that in the normal projection of the momentum equation there is a centrifugal acceleration term (Gv in Eq. $(3)_2$), and in the tangential projection there is a change of stretch term (Gdv in Eq. $(3)_1$). A review of the literature has revealed that some studies of stretching belts neglect both of these inertial terms in the momentum equations, and others incorporate only the centrifugal acceleration term in the normal projection. This paper is the first to include stretching acceleration in the tangential projection.

Without stretching acceleration, the two momentum projections reduce to a single differential equation for the evolution of belt tension with arclength, decoupled from belt stretch. When the stretching acceleration term is included, the two momentum projections become coupled differential equations for the evolution of both belt tension and belt stretch, and to close the mathematical problem statement one must adjoin a constitutive equation relating belt tension to belt stretch. For definiteness, in Section 3 we characterize the belt as linearly elastic.

In Section 5 we obtain and compare four solutions for the problem of torque transmission of a belt between two pulleys (after first presenting the governing equations for a belt in a free span in Section 4). The pulley radii, transmitted moment, angular velocity of the driving pulley, initial tension in the belt, stiffness of the belt, and coefficient of friction between the belt and the pulleys are considered to be specified, and the problem is solved for the angular velocity of the driven pulley, the angles over which the belt is slipping on the driving and driven pulleys, the belt tension and speed at all locations along the belt, and the normal and frictional forces per length from the pulleys on the belt at all locations of contact, as well as the maximum moment that can be transmitted by the belt-pulley system. The first solution is our new solution, which accounts for both stretching acceleration and centrifugal acceleration in the momentum equations. The next two solutions include centrifugal acceleration but neglect stretching acceleration (the common engineering practice). The fourth solution, recalled from the literature ([1]) neglects both centrifugal acceleration and stretching acceleration.

Beyond having a consistent mathematical formulation, there is a quantitative advantage to our solution. We find that the solution in the literature which neglects both centrifugal and stretching accelerations underpredicts the slip angles on the driving and driven pulleys, overpredicts the normal and frictional forces on the belt from the pulleys, overpredicts the strain rate of the belt in the slip zones, and overpredicts the maximum moment that can be transmitted. The common engineering simplification of including centrifugal acceleration but neglecting stretching acceleration decreases the magnitude of the errors, and reverses the direction of some. The quantitative differences between our solution and the common engineering practice is slight for most power transmission applications, but these differences increase as the stiffness of

Contributed by the Applied Mechanics Division of THE AMERICAN SOCIETY OF MECHANICAL ENGINEERS for publication in the ASME JOURNAL OF APPLIED MECHANICS. Manuscript received by the ASME Applied Mechanics Division, Feb. 24, 1999; final revision, Sept. 28, 1999. Associate Technical Editor: N. C. Perkins. Discussion on the paper should be addressed to the Technical Editor, Professor Lewis T. Wheeler, Department of Mechanical Engineering, University of Houston, Houston, TX 77204-4792, and will be accepted until four months after final publication of the paper itself in the ASME JOURNAL OF APPLIED MECHANICS.

the belt decreases and the speeds increase. It is essential to use the new equations in applications such as the drawing process in the manufacturing of polymer fibers and films, in which the stiffnesses are small and the speeds are great.

2 Equations of Mass and Momentum for Belts on Pulleys

Following Carlson [2], consider an extensible belt on a pulley with radius r and angular velocity ω. Without loss of generality we assign the direction of increasing arclength s of the belt, positive belt speed v, and positive pulley rotation ω to be the same. We adopt an Eulerian formulation with the point s fixed in space and assume the motion is steady so that the conditions at location s are independent of time. The mass per volume and cross-sectional area of the belt are ρ and A, respectively. For this steady motion, conservation of mass requires that the mass flow rate G is constant,

$$G=\rho A(s)v(s)=\text{constant}. \tag{1}$$

Figure 1 shows a free-body diagram of a space-fixed portion of the belt of length ds at location s, subtending an angle $d\theta$. The belt is in general extensible, so that the speed of the belt entering this domain at s is v and the speed exiting it at $s+ds$ is $v+dv$. The tension in the belt at s is T and at $s+ds$ is $T+dT$. f and n are the projections of the force per unit length from the pulley on the belt in the tangential and normal directions, respectively, as indicated in Fig. 1. We assign positive f to be in the direction of decreasing s and positive n to be radially outward; f can be positive, negative, or zero, depending on the velocity or impending velocity of the belt relative to the pulley. We ignore aerodynamic forces. Conservation of momentum projected in the tangential and normal direction are

$$\begin{aligned}
&-T\cos\left(\frac{d\theta}{2}\right)+(T+dT)\cos\left(\frac{d\theta}{2}\right)-frd\theta=Gdv\cos\left(\frac{d\theta}{2}\right),\\
&-T\sin\left(\frac{d\theta}{2}\right)-(T+dT)\sin\left(\frac{d\theta}{2}\right)+nds\\
&\qquad=-Gv\sin\left(\frac{d\theta}{2}\right)-G(v+dv)\sin\left(\frac{d\theta}{2}\right).
\end{aligned} \tag{2}$$

Using $|d\theta|\ll 1$ so that $\cos(d\theta/2)\approx 1$ and $\sin(d\theta/2)\approx d\theta/2$, Eqs. (2) reduce to

$$dT-fds=Gdv,\quad n=\frac{T-Gv}{r}, \tag{3}$$

where we have taken products of infinitesimal quantities to be negligible.

As is noted in Amijima [3], when adhesive forces are neglected the normal force per unit length n from the pulley on the belt must be compressive (nonnegative according to our sign convention), which in combination with Eq. $(3)_2$ demands

$$T-Gv\geqslant 0. \tag{4}$$

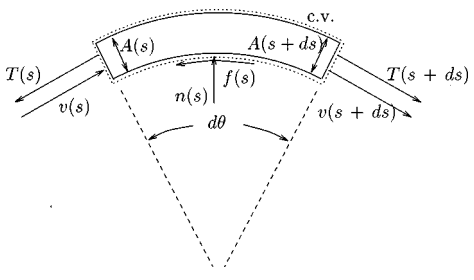

Fig. 1 Free-body diagram of a section of belt on a pulley

Hence, at any point on the belt there must be a tension greater than or equal to the mass flow rate of the belt times its speed. If not, the pulley would have to pull on the belt to keep it in contact and accelerating in a circular path. This the pulley cannot do, and the insufficiently tensioned belt will fly off the pulley.

Comparison With Belt Equations in the Literature. The mass and momentum equations for a deformable belt on a pulley are Eqs. (1) and (3). A review of the literature revealed that all studies employ the same mass Eq. (1), but all use momentum equations which are simplified forms of the momentum Eq. (3). For instance, Amijima [3,4], Rothbart [5], and Fazekas [6] employ

$$dT-fds=0,\quad n=\frac{T-Gv}{r}, \tag{5}$$

where, comparing Eqs. (5) with Eqs. (3), we see that the centrifugal term Gv is included in the normal projection $(5)_2$, but the inertia term Gdv is absent from the tangential projection $(5)_1$. Equations (5) are an exact special case of Eqs. (3) if and only if the stretch in the belt is uniform ($dv=0$). Johnson [1], Firbank [7], and all statics textbooks employ

$$dT-fds=0,\quad n=\frac{T}{r}, \tag{6}$$

where the inertia terms are absent from both projections. Equations (6) are an exact reduction of Eqs. (3) if and only if the belt is motionless ($v=0$, $dv=0$).

3 The Constitutive Model: A Linearly Elastic Belt

Unlike the momentum formulations (5) and (6), our formulation (3) couples the evolution dT of belt tension explicitly to the evolution dv of belt stretch. Hence belt tension along the pulley surface cannot be computed from momentum considerations alone; one must complement Eqs. (3) with a constitutive model relating the belt stretch to belt tension. Many such models are possible, depending on the application. Here we assume the belt is linearly elastic.

The axial strain ε at a point s of the belt is

$$\varepsilon(s)=\frac{dl(s)}{dl_{\text{ref}}}-1, \tag{7}$$

with $dl(s)$ the length of an infinitesimal section of the belt at location s and dl_{ref} the length of that section in some reference state. We consider a belt for which the tension at a point on the belt depends only on the belt's axial strain ε at that point (i.e., the belt is elastic), and further that this dependence is linear. Hence

$$T(s)=T_{\text{ref}}+k\varepsilon(s), \tag{8}$$

where k is the elastic modulus (units of force) and T_{ref} is the tension in the reference state. (The linearly elastic assumption is for the sake of definiteness; we could alternatively introduce a nonlinear elastic characterization, as in Amijima [3,4]).

At any point s along the belt, the strain $\varepsilon(s)$ is related to the belt speed $v(s)$ at that point and the speed v_{ref} of the belt in the reference state by

$$v(s)=v_{\text{ref}}\,(1+\varepsilon(s)). \tag{9}$$

The relation (9) between strain and speed in the belt implies that the tension may also be expressed as a function of belt speed, so that the constitutive assumption Eq. (8) becomes

$$T(s)=T_{\text{ref}}+k\left(\frac{v(s)}{v_{\text{ref}}}-1\right). \tag{10}$$

4 Equation of Momentum for Belts in Free Spans

In the next section we solve the torque transmission problem. Since the problem involves free spans of the belt, we first give the equations governing the belt behavior of such a span. Mass con-

Fig. 2 Control volume for a belt in a freespan

servation in a free span is given by Eq. (1). Figure 2 shows a free-body diagram of a differential belt element of length ds at s in the freespan. Conservation of momentum gives

$$(T+dT)-T=G(v+dv)-Gv, \tag{11}$$

or

$$dT=Gdv. \tag{12}$$

Integration gives

$$T=Gv+c, \tag{13}$$

where c is a constant of integration. For a linear elastic belt we must have the rewritten form of Eq. (10),

$$T=\left(\frac{k}{v_{\text{ref}}}\right)v+T_{\text{ref}}-k. \tag{14}$$

The mass flow rate G (which is dependent on the process) will not in general equal the elastic modulus divided by the reference velocity. Hence

$$T=\text{constant}, \quad v=\text{constant}, \tag{15}$$

is the relevant solution of Eq. (12) in the free span for isothermal motion.

5 The Torque Transmission Problem

We now solve the steady torque transmission problem of Fig. 3, with an extensible, linearly elastic belt, and pulleys mounted at fixed center distance. We solve the problem three ways: (*i*) using our momentum Eqs. (3) for the belt on the pulley, which account for both centrifugal acceleration and the acceleration due to stretching; (*ii*) using momentum equations in the form of Eqs. (5), where centrifugal acceleration is included but stretching acceleration is neglected; and (*iii*) using Eqs. (6) on the pulley surface, which neglect both accelerations. The quasi-static solution (*iii*) appears in the literature in Johnson [1]. It has long been held that the effect of centrifugal acceleration is significant, so that in belt applications solution (*ii*) is used, never (*iii*). It is also widely conjectured that the effect of the stretching inertia term is insignificant, although it has never before been computed. Our new solution (*i*) for the first time calculates this effect. We find

- computationally it is less problematic to retain both acceleration terms than to include one and neglect the other; Eqs. (5) and the elastic constitutive equation are inconsistent (the momentum Eqs. (5) predict that the tension is changing in the belt, and hence the elastic constitutive equation demands that the stretch of the belt is changing, but this changing stretch is absent from Eqs. (5)), resulting in an artificially decoupled and, as we shall see, ambiguous problem statement,
- for relatively stiff belts (in a sense we will make explicit later) solutions (*i*) and (*ii*) coincide, with solution (*iii*) noticeably different, supporting in such applications the common engineering wisdom that that the effect of centrifugal acceleration is significant and the effect stretching acceleration is insignificant, but
- for compliant belts, and fibers undergoing draw, solution (*i*) is significantly different from solution (*ii*), indicating that the effect of stretching in these applications is important.

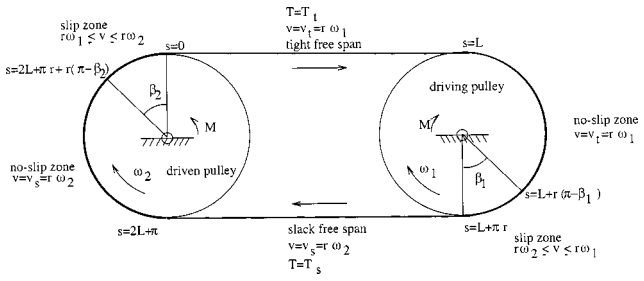

Fig. 3 Schematic diagram of a belt transmitting a torque *M* between two pulleys

The pulley radii r, transmitted moment M, driving pulley angular velocity ω_1, initial belt tension T_{init}, belt stiffness k, and coefficient of friction μ between the belt and the pulleys are assumed to be specified. The unknowns that constitute the solution are the angular velocity ω_2 of the driven pulley, the subtended angles β_1 and β_2 over which the belt is slipping on the driving and driven pulleys, respectively (see Fig. 3), the belt tension $T(s)$ and speed $v(s)$ at all locations s along the belt, and the normal and frictional forces per length $n(s)$ and $f(s)$ from the pulleys on the belt at all locations of contact. We will see that solutions (*i*) and (*ii*) depend on the specified quantities through the four dimensionless combinations

$$A=\frac{M}{2rk}, \quad B=\frac{T_{\text{init}}}{k}, \quad C=\frac{G\omega_1 r}{k}, \quad \mu. \tag{16}$$

Solution (*iii*) depends only on A, B, and μ. (We select combinations (16) rather than, say, $M/2rT_{\text{init}}, k/T_{\text{init}}, G\omega_1 r/T_{\text{init}}$, since it is commonly argued that the fractional change due to including the stretching acceleration is proportional to $Gv/k=G\omega_1 r/k$, or, stated differently, solution (*ii*) likely can be obtained from solution (*i*) by letting $G\omega_1 r \ll k$. Combinations (16) allow us to investigate this conjecture by considering the limit of small C.)

In the free spans the tensions and velocities are constant (see Eqs. (15)). When a constant torque M is transmitted between two pulleys of the same radius r as shown in Fig. 3, the tensions T_t in the tight free span and T_s in the slack free span are [1,8]

$$T_t=T_{\text{init}}+\frac{M}{2r}=T_{\text{init}}\left(1+\frac{A}{B}\right), \quad T_s=T_{\text{init}}-\frac{M}{2r}=T_{\text{init}}\left(1-\frac{A}{B}\right), \tag{17}$$

obtained by assuming the bearings are frictionless and summing the moments on either pulley to zero; T_{init} is the tensile force in the belt when the moment M is zero.

We assume, as do Amijima [8], Firbank [7], and Johnson [1], that the belt is not slipping on either the driving or driven pulleys where it first attaches, so that the speeds v_t and v_s of the tight and slack free spans are given by

$$v_t=r\omega_1, \quad v_s=r\omega_2. \tag{18}$$

We choose our reference state as the one in which the tension T_{ref} is zero, so that the linearly elastic constitutive Eq. (10) reduces to

$$T(s)=k\left(\frac{v(s)}{v_{\text{ref}}}-1\right), \tag{19}$$

the same constitutive equation employed by Johnson [1]. Evaluating this constitutive equation at the tight and slack free span speeds and recalling Eqs. (17) gives

$$k\left(\frac{r\omega_1}{v_{\text{ref}}}-1\right)=T_{\text{init}}\left(1+\frac{A}{B}\right), \quad k\left(\frac{r\omega_2}{v_{\text{ref}}}-1\right)=T_{\text{init}}\left(1-\frac{A}{B}\right). \tag{20}$$

These two equations can be inverted to give the angular velocity ω_2 of the driven pulley and the reference speed v_{ref} in terms of specified quantities,

$$\omega_2=\left(\frac{B-A+1}{B+A+1}\right)\omega_1, \quad v_{\text{ref}}=\frac{r\omega_1}{1+A+B}. \tag{21}$$

Note that $\omega_2<\omega_1$. Then the constitutive Eq. (19) can be recast as

$$T(s)=\frac{T_{\text{init}}}{B}\left[(1+A+B)\frac{v(s)}{r\omega_1}-1\right]. \tag{22}$$

In the torque transmission problem the belt passes through six zones. In the direction of increasing arclength s (clockwise), referring to Fig. 3, they are the tight free span, no-slip zone on the driving pulley, the slip zone on the driving pulley, the slack free span, the no-slip zone on the driven pulley, and the slip zone on the driven pulley. We select $s=0$ as the start of the tight free span. In the following subsections we obtain, for each of the three formulations, the belt tension, speed, and friction and normal force per length through these zones as a function of arclength s, as well as the angular extents β_1 and β_2 of the slip zones.

5.1 Full Solution Retaining all Inertia Terms. We first solve the problem using our Eqs. (3) when the belt is on the pulley.

The tight free span: Belt behavior is governed by Eqs. (15), so that

$$T(s)=T_t=T_{\text{init}}\left(1+\frac{A}{B}\right), \quad v=v_t=r\omega_1. \tag{23}$$

No-slip zone on the driving pulley: The belt attaches without slip to the driving pulley with the tight-span speed $v_t=r\omega_1$, and maintains this constant speed through a no-slip zone of yet-to-be-determined length. Since speed is constant so is strain, and hence in the elastic belt so is the tension, $T=T_t$. With constant speed ($dv=0$) and constant tension ($dT=0$), Eq. $(3)_1$ demands $f=0$: there is no friction between belt and pulley in the no-slip zone. The normal force per length n is computed using Eq. $(3)_2$. Summarizing,

$$T(s)=T_{\text{init}}\left(1+\frac{A}{B}\right), \quad v(s)=r\omega_1, \quad f(s)=0,$$
$$n(s)=\frac{T_{\text{init}}}{r}\left(1+\frac{A}{B}-\frac{C}{B}\right). \tag{24}$$

Slip zone on the driving pulley: Since the belt leaves the driving pulley with the slack-span speed $v_s=r\omega_2$ less than the tight-span speed $v_t=r\omega_1$ that it attaches (recall from Eq. $(21)_1$ that $\omega_1>\omega_2$), there must be a slip zone on the driving pulley. In this zone the friction is kinetic, and, since the belt is moving slower than the pulley surface, the direction of this friction is in the direction of motion. Therefore, according to our sign convention, $f=-\mu n$ (recall Fig. 1). Equations (1), (3), and this friction relation reduce to

$$\frac{d(T-Gv)}{T-Gv}=-\mu d\theta. \tag{25}$$

Integrating Eq. (25) over the entire slip zone yields a relation for the angle of slip β_1 on the driving pulley,

$$\beta_1=\frac{1}{\mu}\ln\left(\frac{T_t-Gr\omega_1}{T_s-Gr\omega_2}\right)=\frac{1}{\mu}\ln\left[\frac{B+A-C}{B-A-\left(\frac{B-A+1}{B+A+1}\right)C}\right]. \tag{26}$$

The boundary between the no-slip and slip zones on the driving pulley is therefore at $s=L+r(\pi-\beta_1)$, where L is the length of the free span. We integrate Eq. (25) from this boundary to arbitrary s within the slip zone:

$$T(s)-Gv(s)=(T_t-Gv_t)e^{-\mu(\bar{s}/r)}=T_{\text{init}}\left(1+\frac{A}{B}-\frac{C}{B}\right)e^{-\mu(\bar{s}/r)}, \tag{27}$$

where $\bar{s}=s-l-r(\pi-\beta_1)$ is the arclength from the start of the slip zone. To obtain the belt tension $T(s)$ and speed $v(s)$ in the slip zone separately as functions of arclength, we combine Eq. (27) with the elastic constitutive Eq. (22) to obtain

$$T(s)=T_{\text{init}}\left[\left(1+\frac{A}{B}-\frac{C/B}{B+A+1-C}\right)e^{-\mu(\bar{s}/r)}+\frac{C/B}{B+A+1-C}\right], \tag{28}$$

$$v(s)=r\omega_1\left[\left(1-\frac{1}{B+A+1-C}\right)e^{-\mu(\bar{s}/r)}+\frac{1}{B+A+1-C}\right].$$

The normal and frictional forces per length $n(s)$ and $f(s)$ are then obtained algebraically from $T(s)$ and $v(s)$ via Eq. $(3)_2$ and the friction relation:

$$n(s)=\frac{T(s)-Gv(s)}{r}=\frac{T_{\text{init}}}{r}\left(1+\frac{A}{B}-\frac{C}{B}\right)e^{-\mu(\bar{s}/r)},$$
$$f(s)=-\mu n(s)=-\mu\frac{T_{\text{init}}}{r}\left(1+\frac{A}{B}-\frac{C}{B}\right)e^{-\mu(\bar{s}/r)}. \tag{29}$$

Slack free span: In this zone, as in the tight free span, the speed and the tension remain constant.

$$T(s)=T_s=T_{\text{init}}\left(1-\frac{A}{B}\right), \quad v(s)=v_s=r\omega_2=\left(\frac{B-A+1}{B+A+1}\right)r\omega_1. \tag{30}$$

No-slip zone on the driven pulley: The belt attaches to the driven pulley at the slack-span speed $v_s=r\omega_2$ of the pulley surface. The belt continues with this speed for a yet-to-be-determined distance on the pulley. As in the no-slip zone on the driving pulley, there is no friction between belt and pulley. Summarizing,

$$T(s)=T_{\text{init}}\left(1-\frac{A}{B}\right), \quad v(s)=\left(\frac{B-A+1}{B+A+1}\right)r\omega_1,$$
$$f(s)=0, \quad n(s)=\frac{T_{\text{init}}}{r}\left[1-\frac{A}{B}-\left(\frac{B-A+1}{B+A+1}\right)\frac{C}{B}\right]. \tag{31}$$

Slip zone on the driven pulley: In this zone the belt speed increases from $r\omega_2$ to $r\omega_1$. The belt is moving faster than the pulley surface speed $r\omega_2$, so that according to our sign convention $f=\mu n$. Combining this friction relation with Eqs. (1) and (3) gives

$$\frac{d(T-Gv)}{T-Gv}=\mu d\theta. \tag{32}$$

Integrating over the slip zone yields (since the friction coefficients on both pulleys are the same) the same expression for the angle of slip β_2 on the driven pulley as we obtained in Eq. (26) for the angle β_1 on the driving pulley,

$$\beta_2=\beta_1=\frac{1}{\mu}\ln\left[\frac{B+A-C}{B-A-\left(\frac{B-A+1}{B+A+1}\right)C}\right]. \tag{33}$$

Within the slip zone of the driven pulley,

$$T(s)=T_{\text{init}}\left[\left(1-\frac{A}{B}-\frac{C/B}{B+A+1-C}\right)e^{\mu(s^*/r)}+\frac{C/B}{B+A+1-C}\right],$$

$$v(s)=r\omega_1\left[\left(\frac{B-A+1}{B+A+1}-\frac{1}{B+A+1-C}\right)e^{\mu(s^*/r)}+\frac{1}{B+A+1-C}\right], \tag{34}$$

$$n(s)=\frac{T_{\text{init}}}{r}\left(1-\frac{A}{B}-\left(\frac{B-A+1}{B+A+1}\right)\frac{C}{B}\right)e^{(\mu/r)s^*},$$

$$f(s)=\mu\frac{T_{\text{init}}}{r}\left(1-\frac{A}{B}-\left(\frac{B-A+1}{B+A+1}\right)\frac{C}{B}\right)e^{(\mu/r)s^*},$$

where $s^*=s-2l-\pi r-r(\pi-\beta_2)$ is the arclength measured from the start of the slip zone.

The maximum value $M_{\max}$ of torque that can be transmitted by the extensible belt is

$$M_{\max}=\frac{rT_{\text{init}}}{(e^{\mu\pi}+1)}\left\{(e^{\mu\pi}+1)\left(\frac{C-1}{B}\right)-2+\left[\left\{\left(\frac{1-C}{B}\right)^2+4\left(1+\frac{1}{B}\right)\left(1-\frac{C}{B}\right)\right\}e^{\mu\pi 2}+\left\{2\left(\frac{1-C}{B}\right)\left(2+\frac{1}{B}-\frac{C}{B}\right)\right\}e^{\mu\pi}+\left(\frac{1+C}{B}\right)^2\right]^{1/2}\right\}, \tag{35}$$

found by setting the angles $\beta_1=\beta_2$ of the slip zones equal to the maximum allowable value π in Eq. (26).

5.2 Formulations Neglecting Stretching Acceleration in the Momentum Equations. If the effect of centrifugal acceleration is included in the momentum equation, but not the tangential acceleration, i.e., if Eqs. (5) are employed instead of Eqs. (3), the mass conservation, momentum, and friction equations in the slip zones on the driving and driven pulleys reduce to

$$\frac{dT}{T-Gv}=-\mu d\theta, \quad \frac{dT}{T-Gv}=\mu d\theta, \tag{36}$$

respectively, rather than Eqs. (25) and (32). The modeling inconsistency of this approximation (assuming $dv=0$ in the momentum equations but coupling change of speed with change of tension in the elastic constitutive equation) allows for two possible ways to interpret Eqs. (36), and hence two different solutions.

5.2.1 The Engineering Solution. Consistent with the assumption in the momentum equation that change of speed dv is negligible, the common engineering practice is to consider v in Eqs. (36) to be the surface speed $r\omega_1$ of the driving pulley. Integrating over the slip zone of the driving pulley we obtain the angle of slip,

$$\beta_1=\frac{1}{\mu}\ln\left(\frac{T_t-Gr\omega_1}{T_s-Gr\omega_1}\right)=\frac{1}{\mu}\ln\left(\frac{B+A-C}{B-A-C}\right). \tag{37}$$

Then, Eq. $(36)_1$ is a decoupled differential equation for the evolution of belt tension in the slip zone of the driving pulley, which integrates to give

$$T(s)=(T_t-Gr\omega_1)e^{-\mu(\bar{s}/r)}+Gr\omega_1=T_{\text{init}}\left[\left(1+\frac{A}{B}-\frac{C}{B}\right)e^{-\mu(\bar{s}/r)}+\frac{C}{B}\right], \tag{38}$$

where $\bar{s}=s-l-r(\pi-\beta_1)$ is the arclength from the start of the slip zone. The belt normal force per length $n(s)$ and frictional force per length $f(s)$ are obtained algebraically from $T(s)$,

$$n(s)=\frac{1}{r}(T(s)-Gr\omega_1)=\frac{T_{\text{init}}}{r}\left(1+\frac{A}{B}-\frac{C}{B}\right)e^{-\mu(\bar{s}/r)},$$

$$f(s)=-\mu n(s)=-\mu\frac{T_{\text{init}}}{r}\left(1+\frac{A}{B}-\frac{C}{B}\right)e^{-\mu(\bar{s}/r)}. \tag{39}$$

If v is also set to $r\omega_1$ in the slip zone of the driven pulley, one obtains

$$\beta_2=\beta_1=\frac{1}{\mu}\ln\left(\frac{B+A-C}{B-A-C}\right),$$

$$T(s)=T_{\text{init}}\left[\left(1-\frac{A}{B}-\frac{C}{B}\right)e^{\mu(s^*/r)}+\frac{C}{B}\right],$$

$$n(s)=\frac{T_{\text{init}}}{r}\left(1-\frac{A}{B}-\frac{C}{B}\right)e^{\mu(s^*/r)}, \tag{40}$$

$$f(s)=\mu\frac{T_{\text{init}}}{r}\left(1-\frac{A}{B}-\frac{C}{B}\right)e^{\mu(s^*/r)},$$

where $s^*=s-2l-\pi r-r(\pi-\beta_2)$ is the arclength from the start of the slip zone.

Note that belt elasticity k does not appear in this solution unless one chooses to back out belt speed from the constitutive equation. (The problem for belt tension, normal force, and friction decouples from the constitutive equation; each of the nondimensional parameters A, B, C have k in their denominators, but solutions (38) and (39) depend only on the ratios A/B, C/B, so that there is no k dependence.)

The maximum torque that can be transmitted according to this solution is

$$M_{\max}=2rT_{\text{init}}\left(1-\frac{C}{B}\right)\left(\frac{e^{\mu\pi}-1}{e^{\mu\pi}+1}\right)=2r(T_{\text{init}}-Gr\omega_1)\left(\frac{e^{\mu\pi}-1}{e^{\mu\pi}+1}\right). \tag{41}$$

5.2.2 Alternate Solution. Although Eqs. (36) follow from setting $dv=0$ in the momentum equations, it is arguable that v in Eqs. (36) can be considered as a dependent variable, related to tension T through the constitutive Eq. (22). With this viewpoint, Eq. $(36)_1$ becomes

$$\frac{dT}{\left[\left(1-\frac{C}{B+A+1}\right)T-\frac{Gr\omega_1}{B+A+1}\right]}=-\mu d\theta. \tag{42}$$

Integrating this cumbersome expression over the slip zone produces the angle of slip on the driving pulley,

$$\beta_1=\frac{1}{\mu\left(1-\frac{C}{B+A+1}\right)}\ln\left(\frac{B+A-\frac{C}{B+A+1-C}}{B-A-\frac{C}{B+A+1-C}}\right), \tag{43}$$

and integrating to arbitrary location with the slip zone produces

$$T(s)=T_{\text{init}}\left[\left(1+\frac{A}{B}-\frac{C/B}{B+A+1-C}\right)e^{-\mu(1-C/(1+A+B))(\bar{s}/r)}+\frac{C/B}{B+A+1-C}\right], \tag{44}$$

where $\bar{s}=s-l-r(\pi-\beta_1)$ is the arclength from the start of the slip zone. Belt speed $v(s)$, normal force per length $n(s)$, and frictional force per length $f(s)$ in the slip zone are then obtained algebraically from $T(s)$ using the elastic constitutive equation, the normal projection of momentum, and the friction relation,

Table 1 Maximum moment M_{max} that can be transmitted by the stiff ($k=25$ N) and compliant ($k=0.2$ N) belts and corresponding critical values of the dimensionless parameter A, and the slip angles $\beta_1=\beta_2$ for the subcritical moment $M=2.0$ Nm, as predicted by the four solutions

Solution	$k=25$ kN			$k=0.2$ kN		
	M_{max} (Nm)	A_{max}	$\beta_1=\beta_2$ (deg)	M_{max} (Nm)	A_{max}	$\beta_1=\beta_2$ (deg)
Full (Sec. 5.1)	2.764	1.106×10^{-3}	113.488	2.993	1.500×10^{-1}	103.992
Engineering (Sec. 5.2.1)	2.761	1.104×10^{-3}	113.597	2.761	1.381×10^{-1}	113.597
Alternate (Sec. 5.2.2)	2.760	1.104×10^{-3}	113.545	2.910	1.455×10^{-1}	109.040
Capstan (Sec. 5.3)	3.682	1.473×10^{-3}	80.911	3.682	1.841×10^{-1}	80.911

$$v(s)=\omega_1 r\left[\left(1-\frac{1}{B+A+1-C}\right)e^{-\mu(1-C/(B+A+1))(\bar{s}/r)}+\frac{1}{B+A+1-C}\right],$$

$$n(s)=\frac{T_{init}}{r}\left(1+\frac{A}{B}-\frac{C}{B}\right)e^{-\mu(1-C/(B+A+1))(\bar{s}/r)},$$

$$f(s)=-\mu\frac{T_{init}}{r}\left(1+\frac{A}{B}-\frac{C}{B}\right)e^{-\mu(1-C/(B+A+1))(\bar{s}/r)}. \quad (45)$$

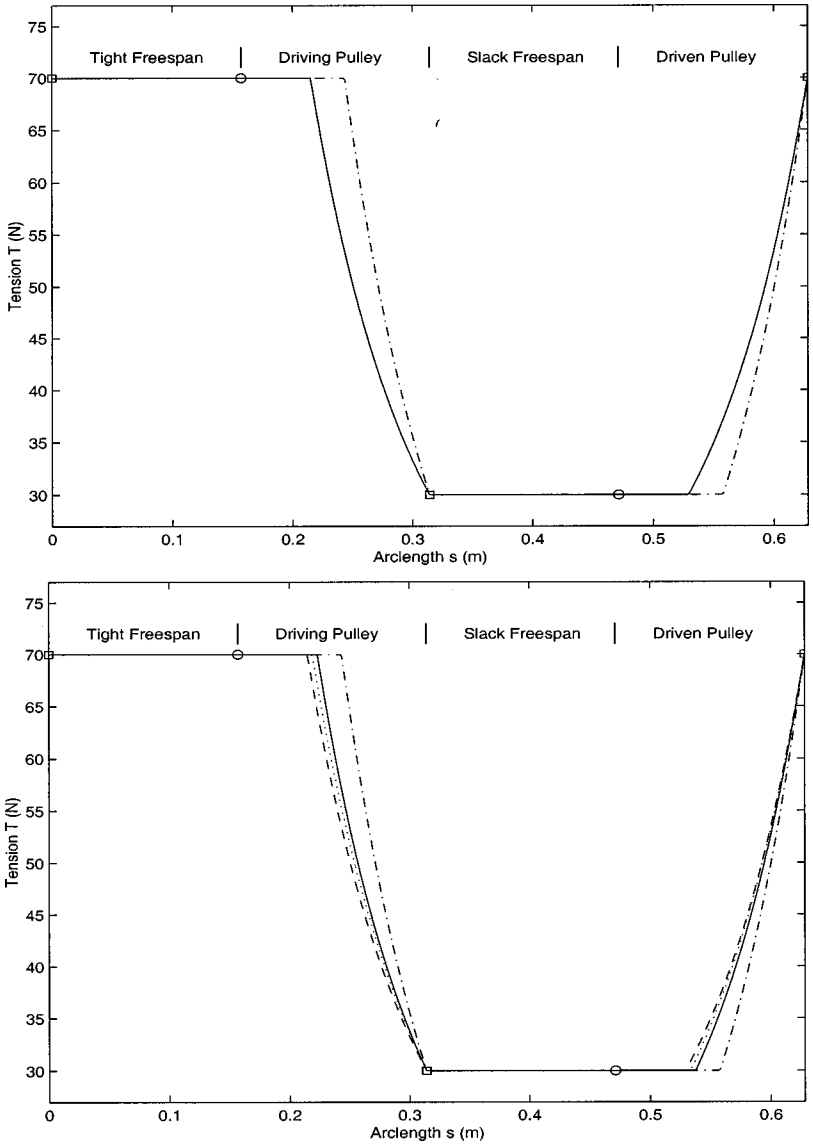

Fig. 4 Belt tension $T(s)$ as a function of arc length s for a stiff belt ($k=25$ kN, top) and a compliant belt ($k=0.2$ kN, bottom): Circles (○) indicate locations of attachment to the pulleys, and boxes (□) indicate locations of departure. Full solution (——), engineering solution (– – –), alternate solution (· · · ·), and capstan solution (—·—·—·—). The full, engineering, and alternate solutions are indistinguishable for the stiff belt case.

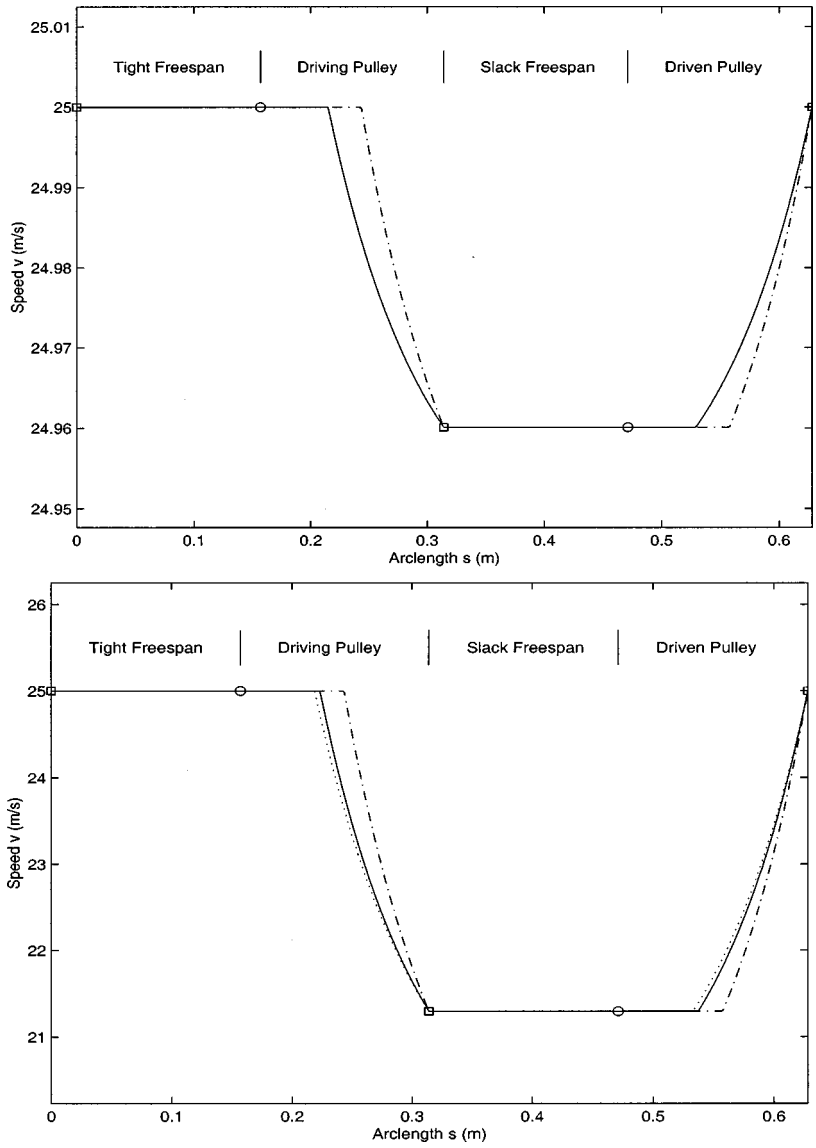

Fig. 5 Belt speed $v(s)$ as a function of arc length s for a stiff belt ($k=25$ kN, top) and a compliant belt ($k=0.2$ kN, bottom): Circles (○) indicate locations of attachment to the pulleys, and boxes (□) indicate locations of departure. Full solution (——), alternate solution (· · · ·), and capstan solution (—·—·—·—). The full and alternate solutions are indistinguishable for the stiff belt case.

The solutions for slip angle on the driven pulley, and belt tension, belt speed, and normal and frictional forces in the slip zone of the driven pulley are obtained in a similar fashion by integrating Eq. $(36)_2$,

$$\beta_2=\beta_1=\frac{1}{\mu\left(1-\dfrac{C}{B+A+1}\right)}\ln\left[\frac{B+A-\dfrac{C}{B+A+1-C}}{B-A-\dfrac{C}{B+A+1-C}}\right],$$

$$T(s)=T_{\text{init}}\left[\left(1-\frac{A}{B}-\frac{C/B}{B+A+1-C}\right)e^{\mu(1-C/(B+A+1))(s^*/r)}+\frac{C/B}{B+A+1-C}\right],$$

$$v(s)=r\omega_1\left[\left(\frac{B-A+1}{B+A+1}-\frac{1}{B+A+1-C}\right)e^{\mu(1-C/(B+A+1))(s^*/r)}+\frac{1}{B+A+1-C}\right], \tag{46}$$

$$n(s)=\frac{T_{\text{init}}}{r}\left[1-\frac{A}{B}-\left(\frac{B-A+1}{B+A+1}\right)\frac{C}{B}\right]e^{\mu(1-C/(B+A+1))(s^*/r)},$$

$$f(s)=\mu\frac{T_{\text{init}}}{r}\left[1-\frac{A}{B}-\left(\frac{B-A+1}{B+A+1}\right)\frac{C}{B}\right]e^{\mu(1-C/(B+A+1))(s^*/r)},$$

where $s^*=s-2l-\pi r-r(\pi-\beta_2)$ is the arclength from the start of the slip zone.

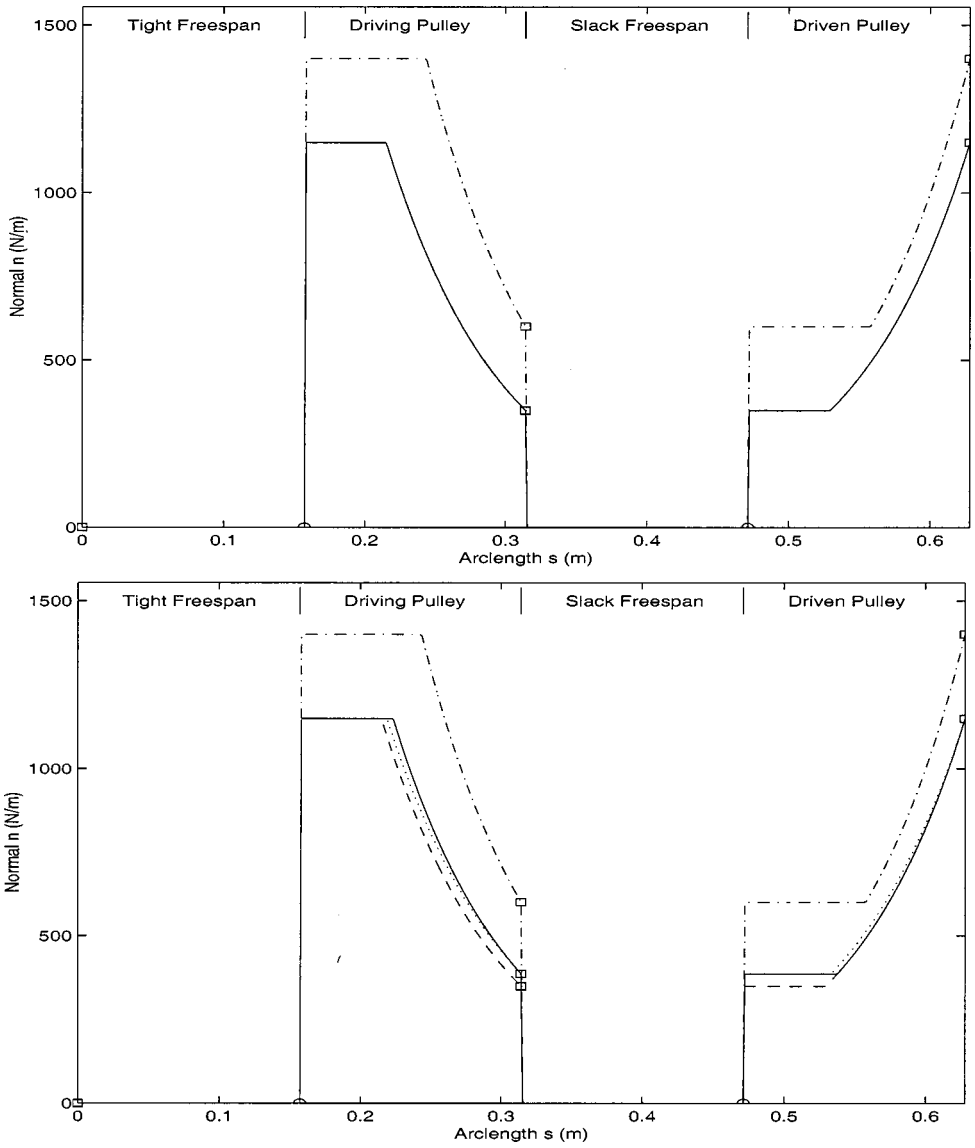

Fig. 6 Normal force per unit length $n(s)$ from the pulleys on the belt for a stiff belt ($k=25$ kN, top) and a compliant belt ($k=0.2$ kN, bottom): Full solution (——), engineering solution (– – –), alternate solution (· · · ·), and capstan solution (—·—·—·—). The full, engineering, and alternate solutions are indistinguishable for the stiff belt case.

The prediction of the maximum possible torque that can be transmitted is

$$M_{\max}=2rT_{\text{init}}\left[\frac{\gamma(B+1)-\mu\pi(B+1-C)}{B(\mu\pi-\gamma)}\right], \tag{47}$$

where γ is the root of

$$2(B+1)e^{\gamma}\gamma^2+\mu\pi[(C-3-2B)e^{\gamma}+1+C]\gamma + \mu^2\pi^2(e^{\gamma}-1)=0, \tag{48}$$

that produces the least value of $M_{\max}$.

5.3 Capstan Solution Neglecting Inertia in the Momentum Equations. The solution of Johnson [1], in which inertia is neglected in the momentum equations (i.e., Eqs. (6) and (22) are solved instead of Eqs. (3) and (22)), is recovered by setting $C=0$ with A and B finite in either the full solution of Section 5.1, the engineering solution of Section 5.2.1, or the alternate solution of Section 5.2.2; all three collapse to the same solution. (Alternatively, the solution can be obtained by setting $C/B=0$, with A/B and B^{-1} finite.) In this formulation the predictions of behavior in the two free spans are the same as those in the previous solutions, but the prediction in all zones on the pulley surfaces are altered. For instance, in the absence of inertia the momentum and friction relations in the driving pulley slip zone reduce to the capstan equation,

$$\frac{dT}{T}=-\mu d\theta, \tag{49}$$

the slip angles are given by

$$\beta_1=\beta_2=\frac{1}{\mu}\ln\left(\frac{T_t}{T_s}\right)=\frac{1}{\mu}\ln\left(\frac{B+A}{B-A}\right), \tag{50}$$

and the maximum moment $M_{\max}$ that can be transmitted is

$$M_{\max}=2rT_{\text{init}}\left(\frac{e^{\mu\pi}-1}{e^{\mu\pi}+1}\right). \tag{51}$$

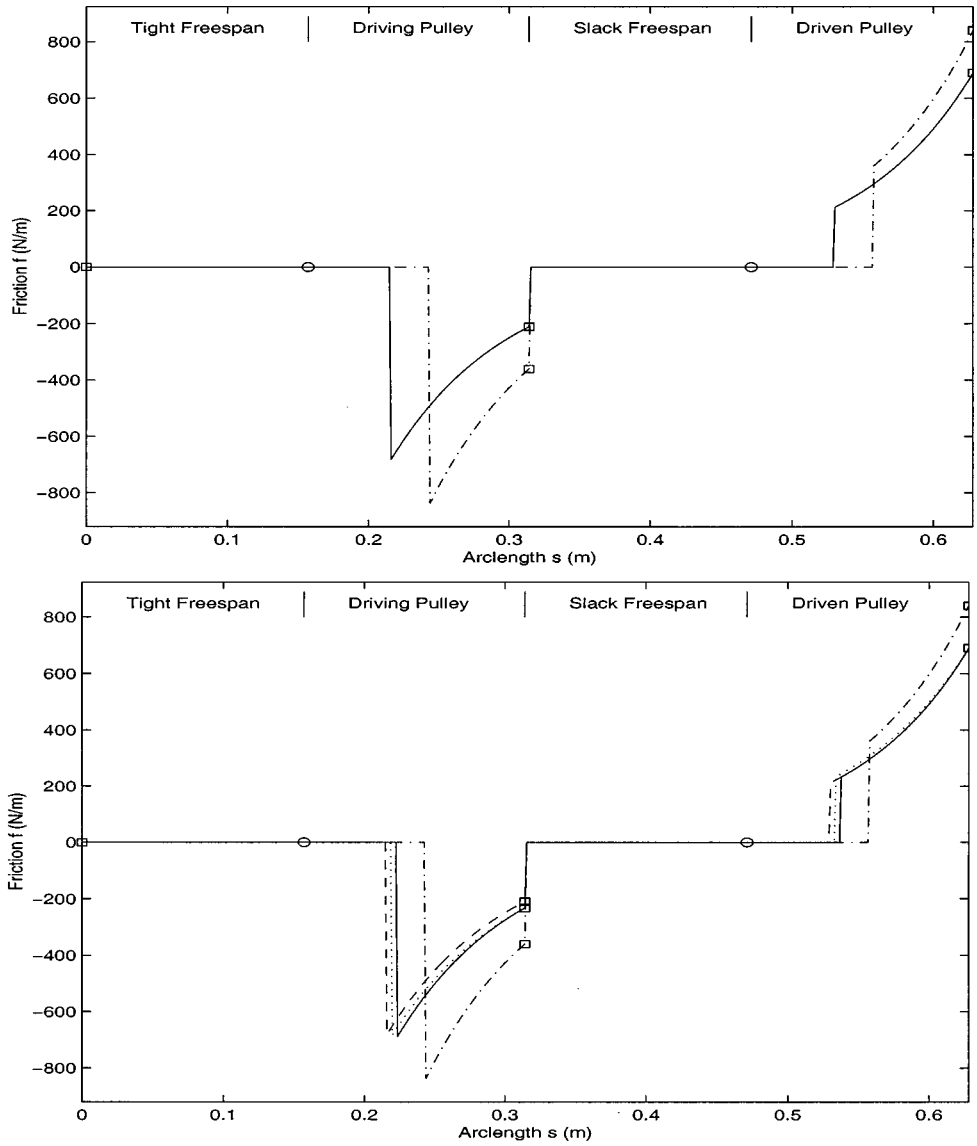

Fig. 7 Frictional force per unit length $f(s)$ from the pulleys on the belt for a stiff belt ($k=25$ kN, top) and a compliant belt ($k=0.2$ kN, bottom): Full solution (——), engineering solution (– – –), alternate solution (· · · ·), and capstan solution (—·—·—·—). The full, engineering, and alternate solutions are indistinguishable for the stiff belt case.

5.4 Comparison. We have presented four solutions to the torque transmission problem:

- our new solution (developed in Section 5.1 and referred to as the full solution), which for the first time includes the effect of stretching acceleration in the momentum equations;
- two solutions which neglect stretching acceleration in the momentum equations (contained in Sections 5.2.1 and 5.2.2, and referred to as the engineering solution and alternate solution, respectively); and
- the solution that neglects all inertia contributions in the momentum equations (contained in Section 5.3 and referred to as the capstan solution).

We first note that neither of the two solutions which include centrifugal acceleration and neglect stretching acceleration correspond to a specialization of the full solution to small $C=G\omega_1 r/k$. These solutions follow from keeping the C terms in some of the governing equations (specifically the normal projection of momentum and, in the alternate solution, the constitutive equation) but dropping the C terms from others (e.g., the tangential projection of momentum) before solving them, and hence do not represent some limit of the full solution. As noted in Section 5.3, setting $C=G\omega_1 r/k=0$ with $A=M/2rk$, $B=T_{\text{init}}/k$ finite (neglecting inertia with respect to elastic stiffness), or setting $C/B=G\omega_1 r/T_{\text{init}}=0$ with $B^{-1}=k/T_{\text{init}}$, $A/B=M/2rT_{\text{init}}$ finite (neglecting inertia with respect to initial belt tension) in the full, engineering, and alternate solutions reduces all three to the capstan solution.

To examine the differences between the predictions of the four formulations for nonzero values of C and C/B, we consider the two cases with the same initial tension $T_{\text{init}}=50$ N, pulley radius $r=0.05$ m, driving pulley angular velocity $\omega_1=500$ rad/s, belt mass flow rate $G=0.5$ kg/s, and coefficient of friction $\mu=0.6$, but with differing elastic moduli k. The modulus $k=25$ kN in the first case corresponds to a stiff belt; the value $k=0.2$ kN of the second case is much smaller, approaching that of a textile tow in a drawing process. The dimensionless combinations are $B=2\times10^{-3}$, $C=5\times10^{-4}$ for the stiff belt case ($k=25$ kN) and $B=2.5\times10^{-1}$, $C=6.25\times10^{-2}$ for the compliant belt case (k

$=0.2$ kN). In both cases we take the length L of each free span to be πr, so that the length of the total belt circuit is $2\pi r+2L=4\pi r=0.2\pi$ m (see Fig. 3).

The maximum moments $M_{\max}$ that can be transmitted in either case and the corresponding dimensionless critical value $A_{\max}$, as predicted by the four solutions, are given in Table 1. The capstan solution (47) gives the same value $M_{\max}=3.682$ Nm for both $k=25$ kN and $k=0.2$ kN since extensibility effects are decoupled from the momentum equations in this approximation; in both cases the capstan solution severely overpredicts the maximum possible moment, by 33 percent and 23 percent, respectively. When centrifugal acceleration is included in the formulation, but not stretching acceleration (the engineering and alternate solutions) the maximum moment is underpredicted. For stiff belts relative to inertia or initial tension (small values of C or C/B) the error is slight, in agreement with the common prejudice in engineering practice, but as the belt becomes relatively more compliant the error due to neglecting stretching acceleration increases: The errors are 0.11 percent and 0.14 percent for $k=25$ kN, and 7.8 percent and 2.8 percent for $k=0.2$ kN in the engineering and alternate solutions, respectively. We note that the alternate solution is worse than the engineering solution in the stiff belt case, but better than the engineering solution for the compliant belt.

Table 1 also displays the slip angles $\beta_1=\beta_2$ on the driving and driven pulleys for $M=2.0$ Nm ($A=8\times10^{-4}$ for the stiff belt case and $A=1\times10^{-1}$ for the compliant belt case), a value selected so as to be less than the maximum moment $M_{\max}$ that can be transmitted for either value of k, as predicted by all four solutions. Figures 4, 5, 6, and 7 display the four predictions of belt tension, belt speed, normal force per length, and frictional force per length as functions of arclength s for the complete circuit of the belt, for this specified subcritical moment. For the stiff belt the predictions of the engineering and alternate solutions are graphically indistinguishable from those of the full solution, whereas the capstan solution neglecting all effects of inertia significantly underpredicts the lengths of the slip zones and significantly overpredicts the strain rate of the belt and the normal and frictional forces on the belt in the slip zones. In the compliant belt case, the engineering and alternate solutions depart noticeably from the full solution as well. On the driving pulley the errors are in the opposite directions of the inertia-less capstan solution, overpredicting the slip zones and underpredicting strain rates and frictional and normal forces. On the driven pulley the errors are more complicated to describe: Both the engineering and alternate solutions overpredict the extent of the slip zone, and in this zone the alternate solution overpredicts the normal and frictional forces; the engineering solution predictions for normal and frictional forces coincide with the full solution where the zones coincide. Since the engineering solution incorrectly sets the belt speed in the no-slip zone on the driven pulley to be the surface speed of the driving pulley, it overpredicts the normal force there.

6 Discussion

The quantitative differences just observed between the solution including stretching acceleration in the momentum equations and the solutions neglecting stretching acceleration increase as the stiffness of the belt decreases and the speeds increase. The equations we have derived in this paper are also applicable to the drawing process in the manufacturing of polymer fibers and films. In these processes the fiber or film is routed through a series of rollers, each with faster surface speeds than the one before. Much if not most of the stretching (i.e., draw) can occur on the roller surfaces. In applications of the equations of this paper to fiber and film drawing, the pulleys become the rollers and the belt becomes the fiber or film. Stiffnesses are much less and speeds usually much greater than in the torque transmission problem considered here, and it will be essential to use Eqs. (3) rather than Eqs. (5) or (6).

Acknowledgments

This work was sponsored in part by the National Textile Center and the U.S. Department of Commerce under Grant E27B51, the National Science Foundation under Grant CTS-9711109, and the Air Force Office of Scientific Research, Air Force Materials Command, USAF, under Grant F49620-97-1-0003. The U.S. Government is authorized to reproduce and distribute reprints for governmental purposes notwithstanding any copyright notation thereon. The views and conclusions contained herein are those of the authors and should not be interpreted as necessarily representing the official policies or endorsements, either expressed or implied, of the U.S. Air Force Office of Scientific Research or the U.S. Government.

References

[1] Johnson, K. L., 1985, *Contact Mechanics*, Cambridge University Press, New York.
[2] Carlson, C. D., 1996, Ph.D. dissertation, The Ohio State University.
[3] Amijima, S., 1963, ''The Tension of the Belt When it is Running,'' Sci. Eng. Rev. Doshisha Univ., **4**, pp. 14–24.
[4] Amijima, S., 1962, ''Some Problems Associated With the Friction Between Belt and Pulley,'' Sci. Eng. Rev. Doshisha Univ., **3**, pp. 9–21.
[5] Rothbart, H. A., 1964, *Mechanical Design and Systems Handbook*, McGraw-Hill, New York.
[6] Fazekas, G. A. G., 1963, ''On the Lateral Creep of Flat Belts,'' ASME J. Eng. Ind., **85**, pp. 307–313.
[7] Firbank, T. C., 1970, ''Mechanics of the Belt Drive,'' Int. J. Mech. Sci., **12**, pp. 1053–1063.
[8] Amijima, S., 1962, ''Some Basic Problems About the Belts,'' Sci. Eng. Rev. Doshisha Univ., **2**, pp. 13–25.

Journal of Applied Mechanics

Brief Notes

A Brief Note is a short paper that presents a specific solution of technical interest in mechanics but which does not necessarily contain new general methods or results. A Brief Note should not exceed 1500 words *or equivalent* (a typical one-column figure or table is equivalent to 250 words; a one line equation to 30 words). Brief Notes will be subject to the usual review procedures prior to publication. After approval such Notes will be published as soon as possible. The Notes should be submitted to the Technical Editor of the JOURNAL OF APPLIED MECHANICS. Discussions on the Brief Notes should be addressed to the Editorial Department, ASME, United Engineering Center, Three Park Avenue, New York, NY 10016-5990, or to the Technical Editor of the JOURNAL OF APPLIED MECHANICS. Discussions on Brief Notes appearing in this issue will be accepted until two months after publication. Readers who need more time to prepare a Discussion should request an extension of the deadline from the Editorial Department.

Asymmetric Four-Point Crack Specimen

M. Y. He
Materials Engineering Department, University of California, Santa Barbara, CA 93106

J. W. Hutchinson
Fellow ASME, Division of Engineering and Applied Sciences, Harvard University, Cambridge, MA 02138

Accurate results for the stress intensity factors for the asymmetric four-point bend specimen with an edge crack are presented. A basic solution for an infinitely long specimen loaded by a constant shear force and a linear moment distribution provides the reference on which the finite geometry solution is based.
[S0021-8936(00)03601-1]

This note was prompted by a comparison ([1]) of existing numerical solutions ([2–4]) for the crack specimen known as the asymmetric four-point specimen shown in Fig. 1. Discrepancies among the solutions are as large as 25 percent within the parameter range of interest. Moreover, in some instances the full set of nondimensional parameters specifying the geometry (there are four) have not been reported. The specimen has distinct advantages for mixed mode testing, including the determination of mixed mode fatigue crack thresholds. Here a new fundamental reference solution is given for a infinitely long cracked specimen subject to a constant shear force and associated bending moment distribution. The small corrections needed to apply this solution to the finite four-point loading geometry are included.

By static equilibrium (the configuration in Fig. 1 is statically determinant), the shear force, Q, between the inner loading points and the bending moment, M, at the crack are related to the force, P, by (all three quantities are defined *per unit thickness*):

$$Q = P(b_2 - b_1)/(b_2 + b_1) \quad \text{and} \quad M = cQ. \tag{1}$$

Consider first the reference problem of an infinite specimen with crack of length a subject to a constant shear force Q and associated linearly varying bending moment M. In the absence of the crack, the exact solution for the cross section has a parabolic distribution of shear stress proportional to Q and a linear variation of normal stress proportional to M ([5]). By superposition of these two contributions, the solution for the intensity factors in the presence of the crack can be written exactly in the form

$$K_I^R = \frac{6cQ}{W^2}\sqrt{\pi a}F_I(a/W) \tag{2a}$$

$$K_{II}^R = \frac{Q}{W^{1/2}}\frac{(a/W)^{3/2}}{(1-a/W)^{1/2}}F_{II}(a/W) \tag{2b}$$

where, anticipating the application, we have taken $M = cQ$ at the crack. The solution (2a) is the same as that for a pure moment. It has been obtained numerically to considerable accuracy. Tada et al. [6] give

$$F_I\left(\frac{a}{W}\right) = \sqrt{\frac{2W}{\pi a}\tan\frac{\pi a}{2W}}\;\frac{0.923 + 0.199\left(1-\sin\frac{\pi a}{2W}\right)^4}{\cos\frac{\pi a}{2W}}$$

$$\text{for } 0 \leqslant \frac{a}{W} \leqslant 1 \tag{3a}$$

while Murakami [7] gives

$$F_I\left(\frac{a}{W}\right) = 1.122 - 1.121\left(\frac{a}{W}\right) + 3.740\left(\frac{a}{W}\right)^2 + 3.873\left(\frac{a}{W}\right)^3 - 19.05\left(\frac{a}{W}\right)^4 + 22.55\left(\frac{a}{W}\right)^5 \quad \text{for } \frac{a}{W} \leqslant 0.7. \tag{3b}$$

The second solution (2b) is not in the literature.

Finite element analyses of the reference problem have been carried out to obtain both F_I (as a check) and F_{II}. Our results for F_I agree with (3b) to four significant figures over the entire range

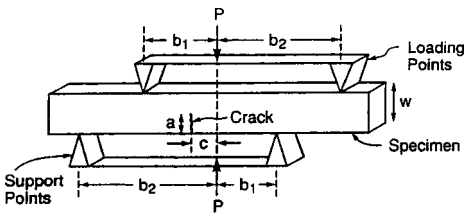

Fig. 1 Geometry of the asymmetric bending and shear specimen

Contributed by the Applied Mechanics Division of THE AMERICAN SOCIETY OF MECHANICAL ENGINEERS for publication in the ASME JOURNAL OF APPLIED MECHANICS. Manuscript received and accepted by the ASME Applied Mechanics Division, Feb. 22, 1999. Associate Technical Editor: A. Needleman.

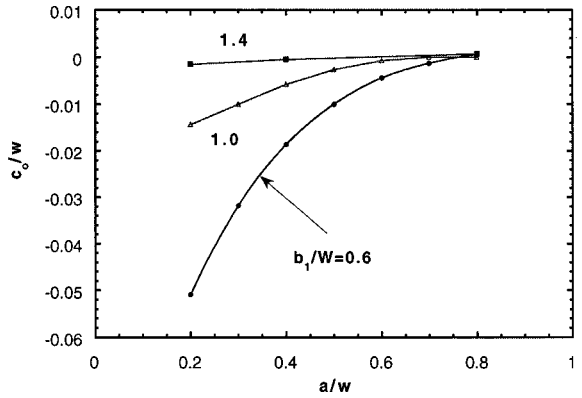

Fig. 2 Location of the crack for pure mode II at its tip ($\alpha=1$)

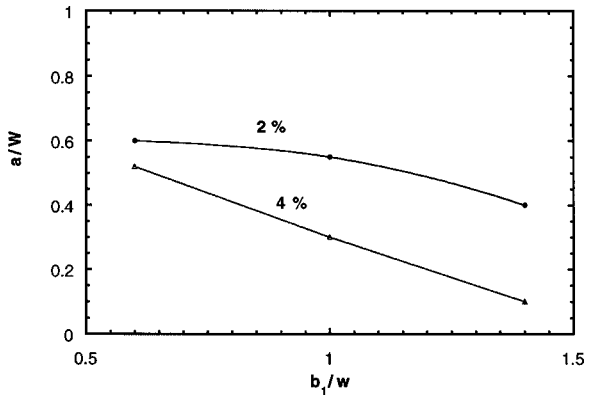

Fig. 4 Error boundaries for mode II stress intensity factor of two percent and four percent for ($\alpha=1$) for the reference solution (2). Combinations ($a/W, b_1/W$) lying above a boundary have smaller error.

of a/W indicated. Equation (3*a*) appears to be less accurate over this same range (with error less than two percent), but it can be used for $a/W>0.7$. The same finite element meshes were used to compute F_{II}. The following polynomial representation was obtained by fitting the numerical results:

$$F_{II}\left(\frac{a}{W}\right)=7.264-9.37\left(\frac{a}{W}\right)+2.74\left(\frac{a}{W}\right)^2+1.87\left(\frac{a}{W}\right)^3 -1.04\left(\frac{a}{W}\right)^4 \quad \text{for} \quad 0\leqslant\frac{a}{W}\leqslant 1. \tag{4}$$

This result is believed to be accurate to within one percent over the entire range of a/W. The results of Suresh et al. [4] determined for a specific choice of the other dimensional parameters of the finite geometry are in good agreement with (4).

Without loss of generality, the solution for the asymmetrically loaded specimen in Fig. 1 can be written as

$$K_I=\frac{6(c-c_0)Q}{W^2}\sqrt{\pi a}F_I(a/W) \tag{5a}$$

$$K_{II}=\frac{\eta Q}{W^{1/2}}\frac{(a/W)^{3/2}}{(1-a/W)^{1/2}}F_{II}(a/W) \tag{5b}$$

where, in general, c_0/W and η are functions of a/W, c/W, b_1/W, and b_2/W. The mode I stress intensity factor is not precisely zero where $M=0$, motivating the introduction of c_0. The representation (5) is chosen because it reduces to the reference solution ($c_0/W=0, \eta=1$) when the loading points are sufficiently far from the crack. The finite element results presented below indicate the reference solution is accurate to within about two percent as long as the distance of nearest loading point to the crack is greater than $1.4W$.

Figure 2 displays the dependence of c_0/W on a/W for three values of b_1/W and $\alpha\equiv(b_2-b_1)/W=1$. This was computed as the c/W at which $K_I=0$. If the moment at the crack vanishes (i.e., $c=0$), the mode I factor can be significant when the loading points are near the crack. For example, for the extreme, but not entirely unrealistic case, where $b_1/W=0.6$, $\alpha=1$, $a/W=0.2$, and $c=0$, the mode mixity, $\psi=\tan^{-1}(K_{II}/K_I)$, is 65 deg instead of 90 deg.

Variations of the mode II correction factor η with a/W for several c/W are shown in Fig. 3 for $b_1/W=1.0$ and $\alpha=1$. The error is largest for short cracks and for cracks on the order of a distance W from the closest loading point. Curves corresponding to constant values of the correction factor are plotted in Fig. 4, with $c/W=0.2$ and $\alpha=1$. If the combination ($b_1/W, a/W$) lies above the curve, the correction factor will be smaller than the corresponding η.

Finally, the effect of the parameter $\alpha=(b_2-b_1)/W$ is displayed in Fig. 5 by normalizing each of the respective stress intensity factors by the reference value from (2). These results have been computed with $b_1/W=1.4$ and $c/W=0.2$. The error in the reference values is less than roughly 2 percent when $\alpha>0.5$.

The plots in Figs. 2–5 provide guidance for either: (i) ensuring the test parameters are such that the reference solution (2) can be used with confidence, or (ii) estimating the corrections to the reference solution using (5). As long as the distance between the crack and the nearest loading point is greater than about $1.4W$

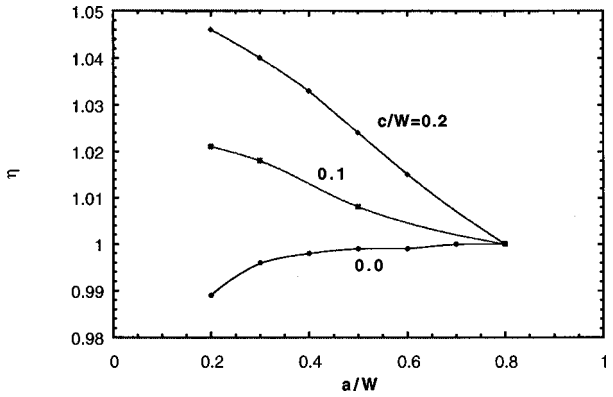

Fig. 3 Correction factor for mode II intensity factor ($\alpha=1$)

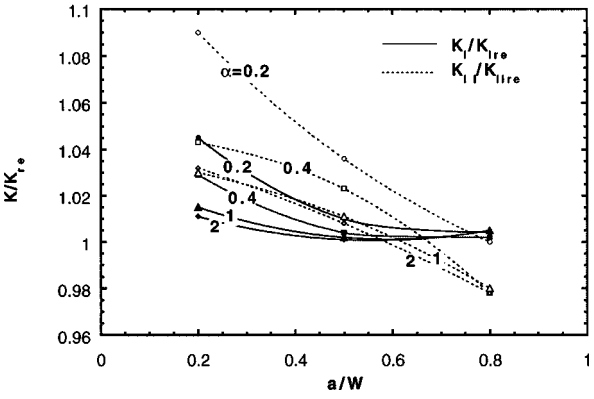

Fig. 5 Role of $\alpha=(b_2-b_1)/W$ in error of the reference solution (2) for $b_1/W=1.4$ and $c/W=0.2$

(i.e., $(b_1-c)/W>1.4$ with $b_2>b_1$) the reference solution is accurate to within a few percent. The errors in the reference solution are the smallest for deep cracks, i.e., $a/W\geqslant 0.5$.

Acknowledgment

This work was supported in part by the Multi-University Research Initiative on ''High Cycle Fatigue,'' which is funded at Harvard by AFSOR under Grant No. SA1542-22500 PG, and in part by the Division of Engineering and Applied Sciences, Harvard University.

References

[1] Campbell, J. P., 1998, private communication, University of California, Berkeley.

[2] Wang, K. J., Hsu, C. L., and Kao, H., 1977, ''Calculation of Stress Intensity Factors for Combined Mode Bend Specimens,'' *Advances in Research on the Strength and Fracture of Materials*, Vol. 4, D. M. R. Taplin, ed., ICF4, Waterloo, Canada, Pergamon Press, New York, pp. 123–133.

[3] He, M. Y., Cao, H. C., and Evans, A. G., 1990, ''Mixed-Mode Fracture: The Four-Point Shear Specimen,'' Acta Metall. Mater., **38**, pp. 839–846.

[4] Suresh, S., Shih, C. F., Morrone, A., and O'Dowd, N. P., 1990, ''Mixed-Mode Fracture Toughness of Ceramic Materials,'' J. Am. Ceram. Soc., **73**, pp. 1257–1267.

[5] Timoshenko, S. P., and Goodier, J. N., 1970, *Theory of Elasticity*, 3rd Ed. McGraw-Hill, New York.

[6] Tada, H., Paris, P. C., and Irwin, G. R., 1985, *The Stress Analysis of Cracks Handbook*, Del Research Corp., St. Louis, MO.

[7] Murakami, Y., 1987, *Stress Intensity Factors Handbook*, Pergamon Press, New York.

Large Shearing of a Prestressed Tube

M. Zidi

Université Paris 12 Val de Marne, Faculté des Sciences et Technologie, CNRS ESA 7052, Laboratoire de Mécanique Physique, 61, avenue du Général De Gaulle, 94010 Creteil Cedex, France
e-mail: zidi@univ-paris.12.fr

This study is devoted to a prestressed and hyperelastic tube representing a vascular graft subjected to combined deformations. The analysis is carried out for a neo-Hookean response augmented with unidirectional reinforcing that is characterized by a single additional constitutive parameter for strength of reinforcement. It is shown that the stress gradients can be reduced in presence of prestress. [S0021-8936(00)00101-X]

1 Introduction

Mechanical properties are of major importance when selecting a material for the fabrication of small vascular prostheses. The operation and the handing of prostheses vessel by surgeons, on the one part, the design of such grafts, on the other, induce specific loading and particularly boundary or initial conditions. Consequently, the interest in developing a theoretical model to describe the behavior of the prostheses vessel is proved ([1]). In this paper, we consider a thick-walled prestressed tube, hyperelastic, transversely isotropic, and incompressible assimilated to a vessel graft. We give an exact solution of the stress distributions when the tube is subjected to the simultaneous extension, inflation, torsion, azimuthal, and telescopic shears ([2–10]). The first theoretical results, in the case of a silicone tube, indicate that the increase of prestress minimizes the stress gradients due to the effects of the shear.

Contributed by the Applied Mechanics Division of THE AMERICAN SOCIETY OF MECHANICAL ENGINEERS for publication in the ASME JOURNAL OF APPLIED MECHANICS. Manuscript received by the ASME Applied Mechanics Division, Mar. 24, 1998; final revision, Oct. 12, 1999. Associate Technical Editor: M. M. Carroll.

2 Model Formulation

Consider a nonlinearly elastic opened tube defined by the angle ω_0 (Fig. 1). Let us suppose that the tube undergoes two successive deformations; first, including the closure of the tube which induced residual strains ([11]) and second, including inflation, extension, torsion, azimuthal and telescopic shears. The mapping is described by

$$r=r(R)\quad \theta=\left(\frac{\pi}{\omega_0}\right)\omega+\phi\alpha Z+\Theta(r)\quad z=\lambda\alpha Z+\Delta(r) \tag{1}$$

where (R,ω,Z) and (r,θ,z) are, respectively, the reference and the deformed positions of a material particle in a cylindrical system. ϕ is a twist angle per unloaded length, α and λ are stretch ratios (respectively, for the first and the second deformation), Θ is an angle which defined the azimuthal shear, and Δ is an axial displacement which defined the telescopic shear.

It follows from (1) that the physical components of the deformation gradient $\mathbf{F}$ has the following representation in a cylindrical system:

$$\mathbf{F}=\begin{bmatrix} \dot{r}(R) & 0 & 0 \\ r(R)\dot{\Theta}(r)\dot{r}(R) & \dfrac{r(R)}{R}\dfrac{\pi}{\omega_0} & r\phi\alpha \\ \dot{\Delta}(r)\dot{r}(R) & 0 & \alpha\lambda \end{bmatrix} \tag{2}$$

where the dot denotes the differentiation with respect to the argument.

Incompressibility then requires that $J\equiv\det\mathbf{F}=1$, which upon integration yields

$$r^2=r_i^2+\frac{\omega_0}{\pi\alpha\lambda}(R^2-R_i^2) \tag{3}$$

where R_i and r_i are, respectively, the inner surfaces of the tube in the free and in the loaded configurations (R_e and r_e are the outer surfaces).

The strain energy density per unit undeformed volume for an elastic material, which is locally and transversely isotropic about the $\mathbf{t}(R)$ direction, is given by

$$W=W(I_1,I_2,I_3,I_4,I_5) \tag{4}$$

where

$$I_1=Tr\mathbf{C},\quad I_2=\tfrac{1}{2}[(Tr\mathbf{C})^2-Tr\mathbf{C}^2],\quad I_3=1,$$
$$I_4=\mathbf{tCt},\quad I_5=\mathbf{tC}^2\mathbf{t} \tag{5}$$

are the principal invariants of $\mathbf{C}=\overline{\mathbf{F}}\mathbf{F}$ which is the right Cauchy-Green deformation tensor ($\overline{\mathbf{F}}$ is the transpose of $\mathbf{F}$).

The corresponding response equation for the Cauchy stress σ for transversely isotropic incompressible is (see [12])

$$\sigma=-p\mathbf{1}+2[W_1\mathbf{B}-W_2\mathbf{B}^{-1}+I_4W_4\mathbf{T}\otimes\mathbf{T}$$
$$+\mathbf{I}_4W_5(\mathbf{T}\otimes\mathbf{B}\cdot\mathbf{T}+\mathbf{T}\cdot\mathbf{B}\otimes\mathbf{T})] \tag{6}$$

where $\mathbf{B}=\mathbf{F}\overline{\mathbf{F}}$ is the left Cauchy-Green tensor, $\mathbf{1}$ the unit tensor, and p the unknown hydrostatic pressure associated with the incompressibility constraint, $W_i=(\partial W/\partial I_i)$ $(i=1,2,4,5)$ and $\mathbf{T}=(1/\sqrt{I_4})\mathbf{Ft}$.

From (6), the equilibrium equations in the absence of body forces are reduced to

$$\frac{d\sigma_{rr}}{dr}+\frac{\sigma_{rr}-\sigma_{\theta\theta}}{r}=0 \tag{7a}$$

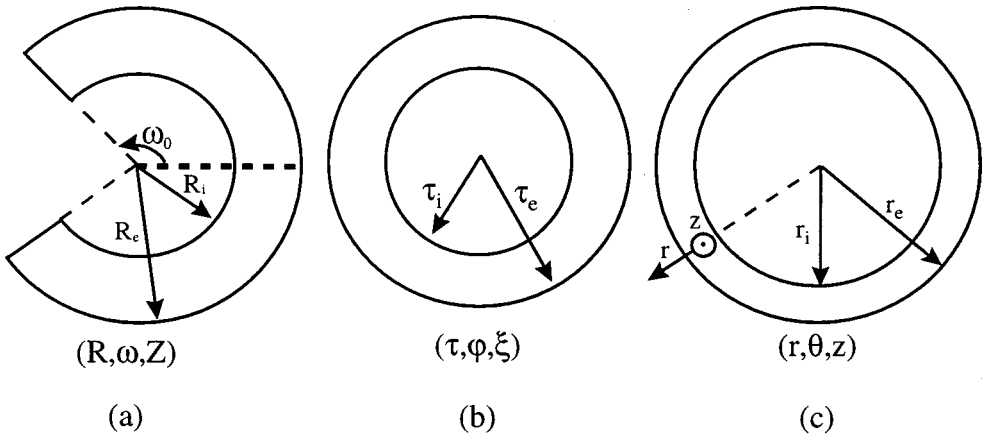

Fig. 1 Cross section of the tube in the stress-free (*a*), unloaded (*b*), and loaded configuration (*c*)

$$\frac{d\sigma_{r\theta}}{dr}+\frac{2\sigma_{r\theta}}{r}=0 \tag{7b}$$

$$\frac{d\sigma_{rz}}{dr}+\frac{\sigma_{rz}}{r}=0. \tag{7c}$$

Suppose that Θ and Δ satisfy the following boundary conditions: (a) $\Theta=\Theta_i$, $\Delta=\Delta_i$ in $r=r_i$ and (b) $\Theta=\Theta_e$, $\Delta=\Delta_e$ in $r=r_e$. Then, a simple computation by integrating (7*b*) and (7*c*) gives the expression of Θ and Δ.

Integrating (7*a*), given the boundary conditions that $\sigma_{rr}(r_i)=-p_i$ and $\sigma_{rr}(r_e)=0$, and taking $\mathbf{t}(R)=t_\omega(R)\mathbf{e}_\omega+t_Z(R)\mathbf{e}_Z$ and using (3) yields the pressure field p:

$$p(r)=p_i+2W_1\left(\frac{R\omega_0}{r\pi\alpha\lambda}\right)^2-2W_2 f(r)+\int_{r_i}^{r}\frac{\sigma_{rr}-\sigma_{\theta\theta}}{s}ds \tag{8a}$$

where

$$f(r)=\dot{\Delta}^2(r)\left[\frac{1}{(\alpha\lambda)^2}+\left(\frac{R\omega_0\phi}{\pi\lambda}\right)^2\right]+\dot{\Theta}^2(r)\left(\frac{R\omega_0}{\pi}\right)^2-2\frac{\dot{\Theta}(r)\dot{\Delta}(r)\phi\omega_0^2}{\alpha\pi}+\left(\frac{r\pi\alpha\lambda}{R\omega_0}\right)^2. \tag{8b}$$

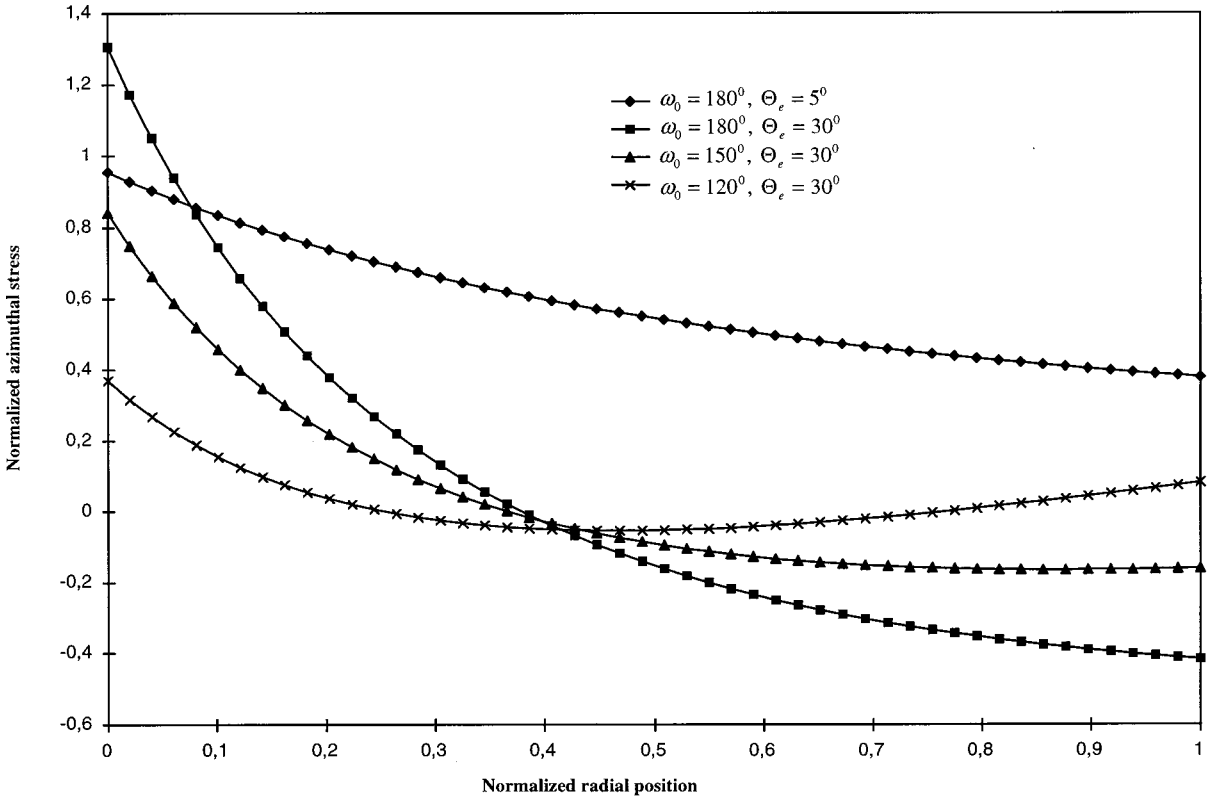

Fig. 2 Azimuthal stresses distribution inside the wall without fibers (stresses normalized by $\sigma_{r\theta}(r_e)$, $\mu=0.166$ Mpa, $p_i=0.0133$ Mpa, $\tau_i=2$ mm, $\tau_e=3$ mm)

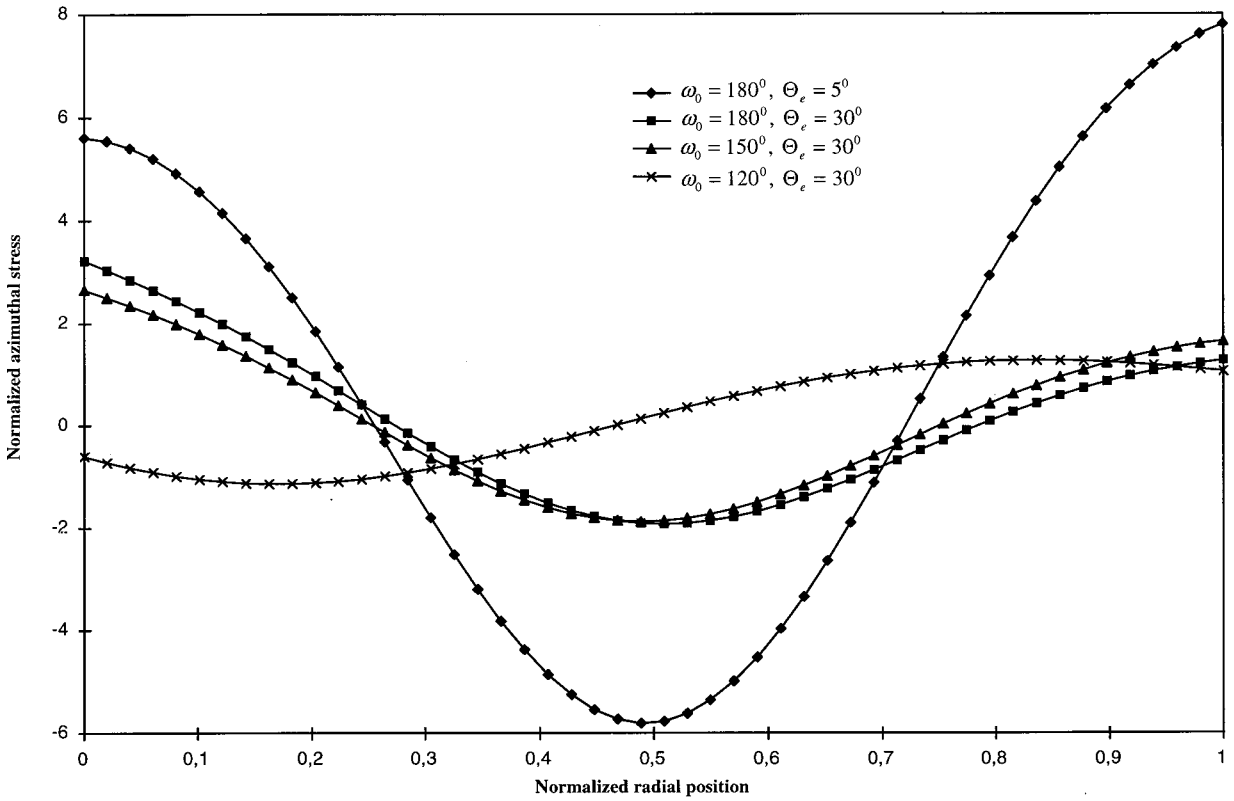

Fig. 3 Azimuthal stresses distribution inside the wall with fibers (stresses normalized by $\sigma_{r\theta}(r_e)$, $\mu = 0.166$ Mpa, $E_f = 10$ Mpa, $p_i = 0.0133$ Mpa, $\tau_i = 2$ mm, $\tau_e = 3$ mm)

The expressions of Θ, Δ, and p determine all the components of the Cauchy stress tensor σ.

3 Results

To illustrate the response of the proposed model, we use the extended Mooney Rivlin strain energy function which represents the behavior of a prosthesis ([13]) constituted of a silicone matrix and textile fibers,

$$W = W(I_1, I_4) = \frac{\mu}{2}(I_1 - 3) + \frac{E_f}{8}(I_4 - 1)^2, \tag{9}$$

where μ is the shear modulus of the isotropic matrix at infinitesimal deformations and E_f is the elastic modulus of the fibers.

The local tangent vector of the fibers is chosen here as $\mathbf{t}(R) = \cos\gamma(R)\mathbf{e}_\omega + \sin\gamma(R)\mathbf{e}_Z$ that represent a helical distribution of fibers ([1]).

From Eqs. (7*b*), (7*c*) and using (3) it easily follows that the expressions of Θ and Δ are

$$\Theta(r) = (\Theta_e - \Theta_i)\frac{\log\left[\dfrac{r}{r_i\sqrt{1 + k(r^2 - r_i^2)}}\right]}{\log\left[\dfrac{r_e}{r_i\sqrt{1 + k(r_e^2 - r_i^2)}}\right]} + \Theta_i \tag{10}$$

$$\Delta(r) = (\Delta_e - \Delta_i)\frac{\log[1 + k(r^2 - r_i^2)]}{\log[1 + k(r_e^2 - r_i^2)]} + \Delta_i \tag{11}$$

where $k = \pi\alpha\lambda/R_i^2\omega_0$.

As an illustrative result, we focus our attention only when the tube is submitted to azimuthal shear strain. Figure 2 shows the distribution of circumferential stresses generated by applied external azimuthal strain at a given pressure when taking into account the effects of such residual stresses. We show clearly that a decrease in ω_0 angle helps to distribute stresses in the loaded state when the shear is important. This result does not change qualitatively when varying the pressure p_i.

Furthermore, the particular effects of the presence of fibers have been examined with a linear distribution of fiber orientation within the data range $\gamma(R_i) = -40$ deg and $\gamma(R_e) = 40$ deg. As illustrated in Fig. 3, it is shown here that the effects of the azimuthal shear upon the distribution of the circumferential stresses within the wall become significant. When the tube is prestressed, the stresses are also distributed. Clearly these results will be able to help the design and fabrication of a small vascular prosthesis ([1]).

References

[1] How, T. V., Guidoin, R., and Young, S. K., 1992, ''Engineering Design of Vascular Prostheses,'' J. Eng. Med., **206**, Part H, pp. 61–71.

[2] Ogden, R. W., Chadwick, P., and Haddon, E. W., 1973, ''Combined Axial and Torsional Shear of a Tube of Incompressible Isotropic Elastic Material,'' Q. J. Mech. Appl. Math., **24**, pp. 23–41.

[3] Mioduchowski, A., and Haddow, J. B., 1979, ''Combined Torsional and Telescopic Shear of a Compressible Hyperelastic Tube,'' ASME J. Appl. Mech., **46**, pp. 223–226.

[4] Abeyaratne, R. C., 1981, ''Discontinuous Deformation Gradients in the Finite Twisting of an Incompressible Elastic Tube,'' J. Elast., **11**, pp. 43–80.

[5] Rajagopal, K. R., and Wineman, A. S., 1985, ''New Exact Solutions in Nonlinear Elasticity,'' Int. J. Eng. Sci., **23**, No. 2, pp. 217–234.

[6] Antman, S. S., and Heng, G. Z., 1984, ''Large Shearing Oscillations of Incompressible Nonlinearly Elastic Bodies,'' J. Elast., **14**, pp. 249–262.

[7] Simmonds, J. G., and Warne, P., 1992, ''Azimuthal Shear of Compressible or Incompressible, Nonlinearly Elastic Polar Orthotropic Tubes of Infinite Extant,'' Int. J. Non-Linear Mech., **27**, No. 3, pp. 447–467.

[8] Tao, L., Rajagopal, K. R., and Wineman, A. S., 1992, ''Circular Shearing and Torsion of Generalized Neo-Hookean Materials,'' IMA J. Appl. Math., **48**, pp. 23–37.

[9] Polignone, D. A., and Horgan, C. O., 1994, ''Pure Azimuthal Shear of

Compressible Nonlinearly Elastic Tubes,'' Q. Appl. Math., **50**, pp. 113–131.
[10] Wineman, A. S., and Waldron, W. K., Jr., 1995, ''Normal Stress Effects Induced During Circular Shear of a Compressible Nonlinear Elastic Cylinder,'' Int. J. Non-Linear Mech., **30**, No. 3, pp. 323–339.
[11] Sensening, C. B., 1965, ''Nonlinear Theory for the Deformation of Prestressed Circular Plates and Rings,'' Commun. Pure Appl. Math., **XVIII**, pp. 147–161.
[12] Spencer, A. J. M., 1984, *Continuum Theory of the Mechanics of Fibre-Reinforced Composites*, Springer-Verlag, New York.
[13] Cheref, M., Zidi, M., and Oddou, C., 1995, ''Caractérisation du Comportement Mécanique d'une Structure Polymérique: Aide à la Conception de Prothèses Vasculaires,'' Arch. Physiol. Biochem., **103**, p. C63.

Buckling of a Short Cylindrical Shell Surrounded by an Elastic Medium

S. Naili
e-mail: naili@univ-paris12.fr

C. Oddou
e-mail: oddou@univ-paris12.fr

Laboratoire de Mécanique Physique, UPRES-A CNRS 7052, Université Paris XII, Val de Marne, Faculté des Sciences et Technologie, 61, avenue du Général de Gaulle, 94010 Créteil Cedex, France

The lateral surface of a cylindrical structure, which is composed of a thin tube embedded in a large outer medium, is submitted to a uniform external pressure. The buckling pressure of such a structure, corresponding to a low flexural state of the inner tube wall, is theoretically analyzed on the basis of the asymptotic method. The theoretical results are compared with experimental ones obtained from a compression test realized on an elastic tube inserted in a foam. It is found that the Euler pressure and the associated buckling mode index strongly depend upon the rheological and geometrical parameters of both the tube and the surrounding medium. [S0021-8936(00)00201-4]

1 Formulation of the Problem and Buckling Study

A nonhomogeneous cylindrical structure composed of a thin shell inserted in a surrounding elastic medium was subjected to a state of plane strain by external pressurization and zero axial longitudinal displacement constraint. The onset of the buckling process for such a structure was analyzed. The theoretical results were compared with original experimental ones as derived from a hoop compression test which was conducted with elastic rubber tubes embedded in foamy materials.

Thus, we consider the mechanical behavior of a cylindrical nonhomogeneous structure made of an internal shell confined in a large outer medium, the whole structure being submitted to a uniform pressure p on its external lateral surface. Each solid is elastic, cylindrical—of same axis—with a circular cross section in the reference configuration. In this configuration, the mean radius of the shell is denoted as r_0. The outer radius r_∞ of the medium is assumed to be very large compared to r_0. We will denote as e_0 the thickness of the shell. The two solids have the same height which is small in comparison with r_∞. The outer lateral boundary of the medium is subjected to a uniform pressure p. We assume frictionless contact between the two tubes. Body forces and inertia effects are deemed to be negligibly small.

The work of Forrestal and Herrman [1] presents solutions for both bonded and smooth conditions at the shell-medium interface; it includes a geometrically nonlinear formulation for both the shell and the medium. Moore and Booker [2] presented the linear approximation of Forrestal and Herrman's formulation. The physical unknowns which are involved in these theoretical formulations are the buckling pressure of the shell in the first work and the hoop compression stress inside this shell in the second one.

In the present work, we use the dimensionless buckling pressure of the overall structure consisting of the shell and surrounding medium developed by Razakamiadana et al. [3] and which is given by the relation

$$\bar{p}=n^2-1+\frac{\bar{\beta}}{n^2-1}, \tag{1}$$

where the dimensionless variables are given as follows:

$$\bar{p}=\alpha p\frac{r_0^3}{D},\quad \bar{\beta}=\beta\frac{r_0^4}{d},$$

and where $D=E_1e_0^3/12(1-\nu_1^2)$ is the flexural rigidity modulus of the shell, E_1 and ν_1 being, respectively, its Young's modulus and its Poisson's ratio, while the index n characterizes the buckling mode. The parameters α and β are defined by

$$\alpha=\frac{\left[\frac{\lambda_2+2\mu_2}{\lambda_2+\mu_2}\right]\left(2\frac{e_0}{r_0}\right)}{1-\left(1-2\frac{e_0}{r_0}\right)\left[1-\frac{\mu_2}{\mu_1}\right]+\frac{\mu_2}{\lambda_1+\mu_1}},$$

$$\beta=2\frac{\mu_2}{r_0}(\lambda_2+\mu_2)\left[\frac{n^2-1}{n(\lambda_2+2\mu_2)+\mu_2}\right],$$

in which the Lame's parameters of the shell and of the medium are denoted by λ_1,μ_1 and λ_2,μ_2, respectively.

In this study, we were interested in the smallest value of the buckling pressure—the Euler pressure—, while varying the index n associated with the buckling mode; such a mode index characterizes the number of axes of symmetry in the actual configuration. Indeed, this minimal pressure is the most frequently observed experimentally while applying incremental loading to the structure. This pressure is expressed as

$$p_e=\min_{n\geq 2}\left[\frac{1}{\alpha}\left((n^2-1)\frac{D}{r_0^3}+\frac{\beta r_0}{n^2-1}\right)\right]. \tag{2}$$

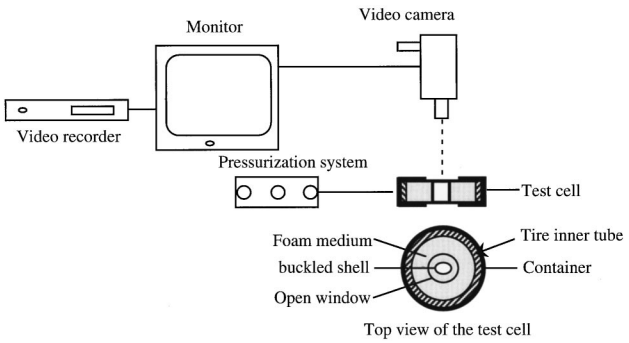

Fig. 1 Experimental apparatus for hoop compression tests. The tube inserted in the foam medium is in a buckled state with index of buckling mode equal to two.

Contributed by the Applied Mechanics Division of THE AMERICAN SOCIETY OF MECHANICAL ENGINEERS for publication in the ASME JOURNAL OF APPLIED MECHANICS. Manuscript received by the ASME Applied Mechanics Division, Feb. 12, 1999; final revision, July 22, 1999. Associate Technical Editor: S. Kyriadides.

Table 1 Experimental and theoretical results of Euler pressure normalized by E_2 and index of buckling mode n associated for various dimensionless mechanical and geometrical parameters

		Experiment				Theory	
$\overline{E}$	E_2 (kPa)	$\overline{e}$	e_0 (mm)	$p_e/E_2\times10^{-2}$	n	$p_e/E_2\times10^{-2}$	n
14.50	100	0.078	1.00	(8.69±0.80)	6	8.39	6
14.50	100	0.189	2.40	(15.34±2.19)	2	13.00	2
26.07	79	0.037	0.46	(4.21±0.40)	4	4.21	6
28.70	100	0.105	1.30	(11.00±1.00)	4	9.80	4
28.70	100	0.136	1.75	(12.89±0.92)	3	12.05	3
28.86	79	0.032	0.40	(3.98±0.33)	3	4.87	6
28.86	79	0.070	0.90	(6.13±0.63)	2	7.65	5
29.85	69	0.037	0.46	(4.66±0.78)	4	5.24	6
33.00	69	0.032	0.40	(4.21±0.21)	3	4.79	6
33.00	69	0.070	0.90	(6.10±0.31)	2	7.69	5
158.46	13	0.037	0.46	(11.76±3.69)	3	7.60	3
175.38	13	0.070	0.90	(17.69±0.10)	2	9.61	2

It is to be noted here that a classical case corresponds to the particular condition of an external incompressible fluid—i.e., $\mu_2=0$ and $\lambda_2\to\infty$—surrounding the shell, so that $\alpha=1$ and $\beta=0$ in relations (1) and (2).

2 Experimental Procedure

Hoop compression tests were performed on a cylindrical structure with a circular cross section composed by a thin rubber shell, of external radius $r_e=13$ mm which was inserted in a large foam medium of external radius $r_\infty=110$ mm. Both tubes had a height $H=30$ mm. The thin rubber shell was slightly stressed when inserted within the foam medium in order to establish a good contact between the two solids.

A steady loading was applied on the external lateral wall of the surrounding foam medium by means of a tire inner tube connected to a standard pressurization system. The plane strain of the structure was obtained by maintaining it between two circular and polished PMMA transparent plates. In order to avoid significant friction between the foam and the plates, the lower and upper faces of the foam were sprinkled with talc powder.

The applied pressure was measured by using a mercury *U*-manometer graded every 1 mm in height with a maximum reading error estimated at about 0.5 mm. When the buckling pressure is ''very low,'' the relative accuracy of the pressure measurement was estimated at about seven percent. But, in 90 percent of the cases, the measured pressure was about 50 mm Hg and the relative uncertainty of measurement was estimated, on average, to be one percent.

With this experimental setup, several tests of compression were conducted on the structure with given geometrical and mechanical characteristics. The tested structure was submitted to a gradual and slow loading so that, for each step, the system can be considered in stationary equilibrium state. The shape of the cross section of the shell remains circular before undergoing a change of shape. We monitored the evolution of shape with a CCD camera video placed on the axis of the tubes—see Fig. 1.

The thickness e_0 of the shell, in its reference configuration, was inferred from the mean value of the measurements conducted with a micrometer at various locations on the wall. The variations around the mean value were found to be in the order of two percent. The values of Young's modulus of the shell and of the medium were derived from traction and compression tests, respectively applied on samples of the constitutive materials. In the different experimental setup, four types of latex foam media with different Young's modulus and Poisson's ratio were combined with tubes made of various PCP, PCV, or latex materials having different characteristic mechanical properties as indicated in Table 1. For the deformations up to ten percent each Young's modulus was evaluated with a maximum error of five percent. Besides, these tests have shown that the Poisson's ratio of the shell was about 0.5—, i.e., the material is incompressible—whereas the Poisson's ratio for the foam media were around zero.

Next, the video images were digitized and then automatically processed using a global thresholding method so as to quantify the inner cross section area of the inserted tube and to characterize its shape. In the extreme case corresponding to a significant variation of this shape, the relative uncertainty of area measurement was estimated to be of the order of two percent. Indeed, when the structure is submitted to a gradual and slow loading, we retained as Euler pressure p_e, the one which corresponds to a clear change in the inner cross section area, as discussed later on.

For a given structure, the measurement of the buckling pressure was repeated ten times at least and the relative gap compared to the mean value varies between 1 percent and 30 percent.

3 Analysis and Discussion

We show, in columns 5 and 6 of Table 1, the experimental results obtained on 110 tests implying 12 structures of different geometry and elastic properties. The results are discussed by using the dimensionless geometrical and mechanical parameters $\overline{e}=e_0/r_0$ and $\overline{E}=E_1/E_2$ in the case of rather thin tubes and exter-

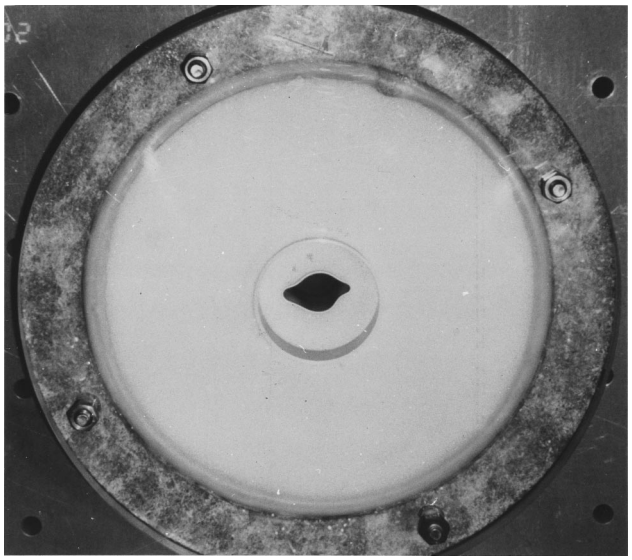

Fig. 2 Top view of the test cell giving an illustrative example of the tube inserted in the foam medium in a buckled state with index of buckling mode equal to four. Circular windows—with a radius in the order 30 mm—were cut on the top and bottom of the PPMA container for a better definition of the image during the recording.

nal foamy material softer than the rubbery one of the tube. Starting with Eq. (2), we determined the variations of the Euler pressure p_e normalized by E_2—denoted as $\overline{p_e}$—as a function of $\overline{E}$ for various values of $\overline{e}$. The associated buckling mode index n then depends on $\overline{E}$. It is worth noting that the assessment of the buckling pressure in such an experiment was based on the variation of a global geometrical parameter such as the area of the internal cross section of the inserted shell—see Fig. 2. Other more sensitive parameters, related to the changes in local shape properties could, however, be envisaged but their quantification by an image-processing system would have been more difficult to implement.

In columns 7 and 8 of Table 1, the theoretical results are compared with experimental ones. These results show that the Euler pressures, evaluated theoretically and determined experimentally, agree well accounting for the inherent scatter in experimental measurements. Moreover, the mode index n associated with $\overline{p_e}$ coincides exactly for 50 percent of the cases. Nevertheless, it is worth emphasizing that significant differences arised in the case of very thin tubes for which the mode index are rather high, the large number of lobes being more sensitive to small heterogeneities in material property and geometry. Despite this, the observed experimental results are, in general, well reproduced by our theoretical model.

References

[1] Forrestal, M. J., and Herrmann, G., 1965, ''Buckling of a Long Cylinder Shell Surrounded by an Elastic Medium,'' Int. J. Solids Struct., **1**, pp. 297–309.

[2] Moore, I. D., and Booker, J. R., 1985, ''Simplified Theory for the Behavior of Buried Flexible Cylinders Under the Influence of Uniform Hoop Compression,'' Int. J. Solids Struct., **21**, No. 9, pp. 929–941.

[3] Razakamiadana, A., Naili, S., and Oddou, C., 1997, 'Flambement d'une Coque Mince Confinée : Théorie et Expérience,' C. R. Acad. Sci., Ser. IIb: Mec., Phys., Chim., Sci. Astron., **325**, pp. 119–126.

A Numerical Tool for Periodic Heterogeneous Media: Application to Interface in Al/SiC Composites

D. Dumont
Faculté de Mathématiques et d'Informatique, 33, rue Saint-Leu, 80 039 Amiens, France
e-mail: Serge.Dumont@u-picardie.fr

F. Lebon
Laboratoire de Mécanique et Génie Civil, Université Montpellier 2, Pl. E. Bataillon, 34 095 Montpellier Cedex 5, France
e-mail: lebon@lmgc.univ-montp2.fr

A. Ould Khaoua
Departamento de Matematicas, Universidad de los Andes, Calle 19 1-11, Bogota, Columbia
e-mail: ahmed@media.uniandes.edu.co

A wavelet-Galerkin method for periodic heterogeneous media is presented. The advantages are to remove the mesh and to make adaptivity easier. Numerical results are presented. A specific study of interfaces in a Al-SiC composite is given.

[S0021-8936(00)00301-9]

Contributed by the Applied Mechanics Division of THE AMERICAN SOCIETY OF MECHANICAL ENGINEERS for publication in the ASME JOURNAL OF APPLIED MECHANICS. Manuscript received by the ASME Applied Mechanics Division, Mar. 15, 1999; final revision, Sept. 15, 1999. Associate Technical Editor: M. Ortiz.

1 Introduction

A great number of recent papers are concerned by the solution of partial differential equations by wavelet bases ([1,2]). Mainly, these works deal with one-dimensional or scalar two-dimensional problems. The solution of the elastostatics system by this kind of method is not usual ([3,4]). Boundary problems on open bounded sets are very difficult to treat ([5]). Nevertheless, periodic conditions on elementary bounded sets are natural for the use of wavelet transform. In this paper, we show how to use such a technique and we give applications to interfaces in Al-SiC composite. In the first section we give the notations and the necessary mathematical background. In the second section we present the mechanical problem: the homogenization of periodic heterogeneous media. The third section is concerned with the algorithm: a wavelet-Galerkin method using Daubechies wavelets ([6]). The determination of the macroscopic coefficients is treated in the fourth section. Applications and numerical results are described in the fifth section. Concluding remarks are given.

2 Notations and Mathematical Background

In this section, we present the notations used in the following of the paper. The sets of kinematically and statically admissible fields are denoted H, L, and S. Let

$$L=(L^2(Y))^3 \quad \text{and} \quad H=(H_p^1(Y))^2$$

$$S=\{v\in L^2_{loc}(Y), v(x_1+k_1,x_2+k_2)=v(x_1,x_2)\text{a.e.},k_1,k_2\in\mathbb{K}\} \tag{1}$$

$$H_p^1(Y)=\{v\in S,\ v_{,i}\in L^2(Y),\ i=1,2\}.$$

$u_{,i}$ denotes the ith partial derivative of the function u. We denote C the fourth-order elasticity tensor, e the strain tensor, and σ the stress tensor. In the following $Y=]0,1[^2$. To construct a wavelet basis of H, we use the compactly supported wavelets introduced by I. Daubechies [6] which is a basis of $L^2(\mathbb{R})$. These wavelets are periodized in order to obtain bases of S. By tensorial and cartesian products wavelet bases of H are obtained ([7]). We denote Ψ^l, $l=1, 2, 3$, and Ψ^0 the wavelets and the scale functions (six degrees-of-freedom for each point), $N^j=2^j-1$ and $\Lambda^j=[0,N^j]^2$.

Let V_j be the subspace of dimension 2^{2j+1} of H generated by this wavelet at approximation level j. An element of $V_{j\,\max}$ is thus written as

$$u(x_1,x_2)=(u_1(x_1,x_2),u_2(x_1,x_2))$$

$$u_d=\sum_{\kappa\in\Lambda_{j_0}} u^{d0}_{j_0\kappa}\Psi^0_{j_0\kappa}+\sum_{l=1}^{l=3}\sum_{j=j_0}^{j=j\,\max}\sum_{\kappa\in\Lambda_j} u^{dl}_{j\kappa}\Psi^l_{j\kappa}. \tag{2}$$

j_0 is a given integer, $d=1$ or 2 and $\kappa=(k_1,k_2)$.

3 The Mechanical Problem

We consider a multiphase isotropic elastic composite (Fig. 1) and we intend to study the behavior of this heterogeneous media. We introduce the notion of equivalent material, i.e., we mean that under the same loadings, this equivalent material has globally the same response. In former papers ([8,9]) bounds for the bulk and shear moduli of a two-phase composite have been given. Without going into further detail, these bounds depend on the shear and bulk moduli of the two phases and on the volumic fraction of the two phases in the composite. In the same way, the theory of periodic homogenization ([10]) focuses on an idealized composite

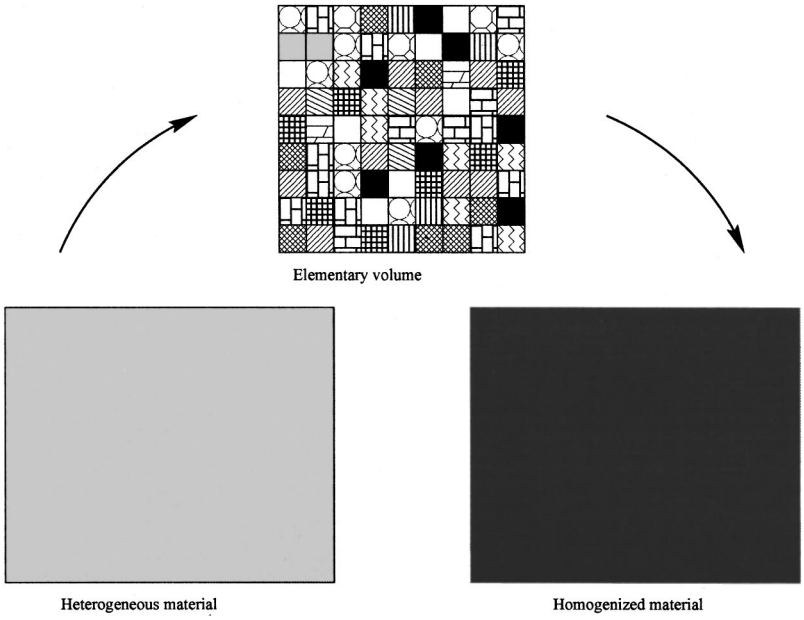

Fig. 1 An example of a composite and its representative volume

consisting of the juxtaposition of identical heterogeneities and classically, we need to solve an elastostatics problem on a representative volume Y (Problem P):

Problem. P

$E \in L$ be given, find $u \in H$ such that $a(u,v)=l(v)\ \forall v \in H$

$$\text{with } a(u,v)=\int_Y \sigma(u):e(v)dy=\int_Y C(y)e(u):e(v)dy$$

$$\text{and } l(v)=-\int_Y CE:D(v)dy$$

Because of the nonuniqueness of the solution of problem (P) (defined within a translation), problem (P) is replaced by problem (P_ε) (''viscous'' problem):

Problem. P_ε

$E \in L$ be given, find $u \in H$ such that $a_\varepsilon(u,v)=l(v)\ \forall v \in H$

$$\text{with } a_\varepsilon(u,v)=\int_Y \sigma(u):e(v)dy+\varepsilon\int_Y uvdy$$

It can be shown that the solution of this problem converges toward the solution of problem (P) with average equal to zero ([4]).

Remarks.

(i) The problem (P) is solved classically by a finite element method or by fast Fourier transform ([11]). We have chosen to introduce wavelet methods in order to eliminate the notion of mesh and to eliminate Gibbs phenomena.

(ii) If the discretization of problem (P) in a orthonormal wave-

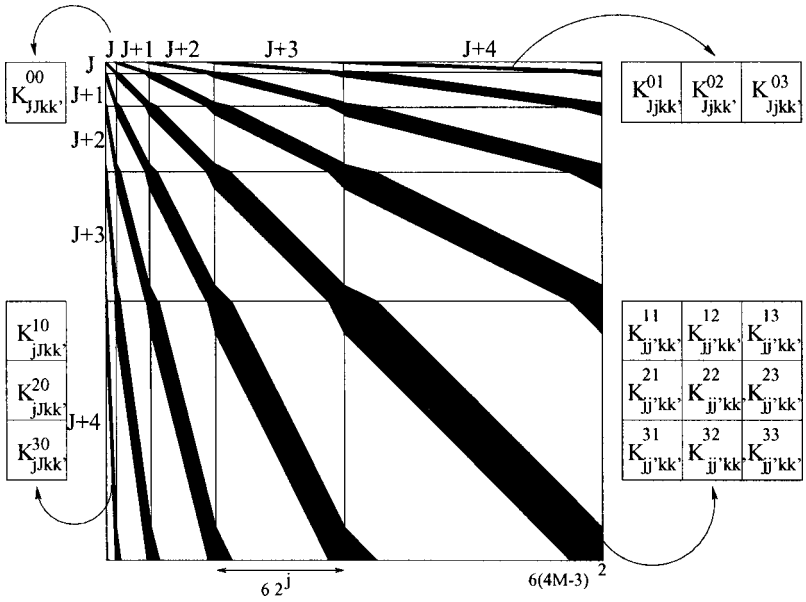

Fig. 2 Wavelet element matrix ($j_0=J$, $j_{max}=J+4$)

let basis leads to the system $KU=B$, then the discretization of problem (P_ε) leads to $(K+\varepsilon Id)U=B$, where Id is the identity matrix.

(iii) The tensor C could be given by the image (pixels) of the microstructure.

4 Wavelet-Galerkin Method

The variational problem (P_ε) is discretized by a Galerkin method. We have introduced a wavelet basis because of their localization and adaptivity properties. The projection of the plane elasticity operator into the wavelet basis ([7]) is given by a stiffness matrix K where the ''elementary matrix'' of order 2 is

$$K^{ll'}_{jj'\kappa\kappa'} = \begin{bmatrix} F_{1111}+F_{1321}+F_{3112}+F_{3322} & F_{1221}+F_{1311}+F_{3222}+F_{3312} \\ F_{1212}+F_{2322}+F_{3111}+F_{3321} & F_{2222}+F_{2312}+F_{3221}+F_{3311} \end{bmatrix} \tag{3}$$

where

$$F_{pq\alpha\beta}=\int_Y \mathbb{C}_{pq}\Psi^l_{j\kappa,\alpha}\Psi^{l'}_{j'\kappa',\beta}\,dx_1dx_2.$$

We have chosen to decompose the tensor C on a wavelet basis at level J noted θ. In the numerical applications, Haar wavelet is used with its compact support equal to the square $[l_1/2^j,(l_1+1)/2^j]\times[l_2/2^j,(l_2+1)/2^j]$. This wavelet is constant on this support which is a pixel of the image representation. Thus, the wavelet coefficient θ_{jl} is equal to the value of the tensor C on this pixel. Due to the form of the wavelets (Cartesian and tensorial products of one dimensional wavelets) the computation of the coefficients of the matrix K leads to the determination of elementary terms which are integral of products of three one-dimensional wavelets and their derivatives:

$$\int_0^1 \theta_{Jr}\frac{d^m\Psi_{js}}{dx^m}\frac{d^n\Psi_{jt}}{dx^n}, \quad m,n=0,1. \tag{4}$$

These terms are obtained by the determination of eigenvectors of a low-order matrix ([7,12]). The right-hand side of the problem corresponding to the term $l(v)$ in problem (P_ε) is computed by a similar technique ([4,5]). Classically, the matrix K is a sparse matrix (Fig. 2). Because of the form of the wavelets bases, it seems natural to solve the linear system which is a discretized version of problem (P_ε) by multigrid techniques ([13,14]). Nevertheless, we have chosen to use a conjugate gradient method.

5 Determination of the Macroscopic Coefficients

The determination of the elastic macroscopic coefficients corresponds to the computation of the macroscopic stress tensor Σ:

$$\Sigma=\int_Y (CE+Ce(u))dx_1dx_2. \tag{5}$$

The computation of these terms is in the same way as the matrix and the right-hand side [4].

6 Numerical Results

We present the example of a three-phase fiber-matrix composite (Fig. 3): SiC for the fiber, Al for the matrix and an interface. The Lamé coefficients associated to the interface are $\lambda\,\eta^\alpha$ and $\mu\,\eta^\beta$ where $\eta\gamma$ is the thickness of the interface. α and β are real positive parameters and γ is a given function with a sufficient regularity. We have shown in former papers ([15–17]) that when η tends to zero, i.e., the thickness and the rigidity parameters tend to zero, we obtain an elastostatic limit problem with an interface law. This interface law keeps in memory the mechanical and geometrical properties of the layer. The interface law is given in

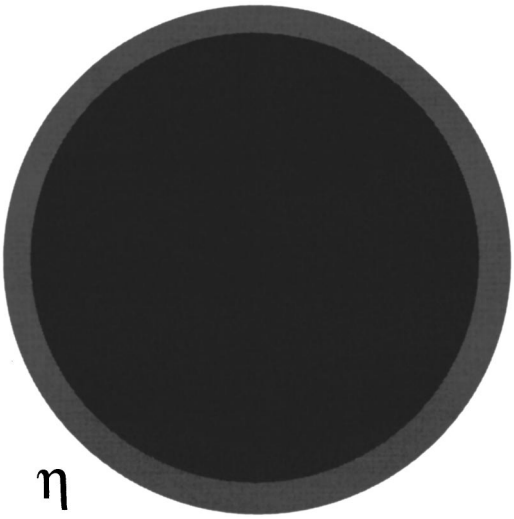

Fig. 3 Al-SiC composite with an interfacial zone (thickness η)

Table 1 Interface laws

$\mu/\epsilon\to 0$	$u_N=0\ \ \sigma_T=0$	$\sigma_N=\frac{\overline{\lambda}}{\gamma}u_N\ \ \sigma_T=0$	$\sigma_n=0$
$\mu/\epsilon\to\overline{\mu}$	$u_N=0\quad \sigma_T=\frac{\overline{\mu}}{\gamma}u_T$	$\sigma_N=\left(\frac{\overline{\mu}}{\gamma}+2\frac{\overline{\lambda}}{\gamma}\right)u_N$	$\sigma_N=2\frac{\overline{\lambda}}{\gamma}u_N$
		$\sigma_T=\frac{\overline{\mu}}{\gamma}u_T$	$\sigma_T=\frac{\overline{\mu}}{\gamma}u_T$
$\mu/\epsilon\to\infty$	$u=0$ $\lambda/\epsilon\to\infty$	$u=0$ $\lambda/\epsilon\to\overline{\lambda}$	$u=0$ $\lambda/\epsilon\to 0$

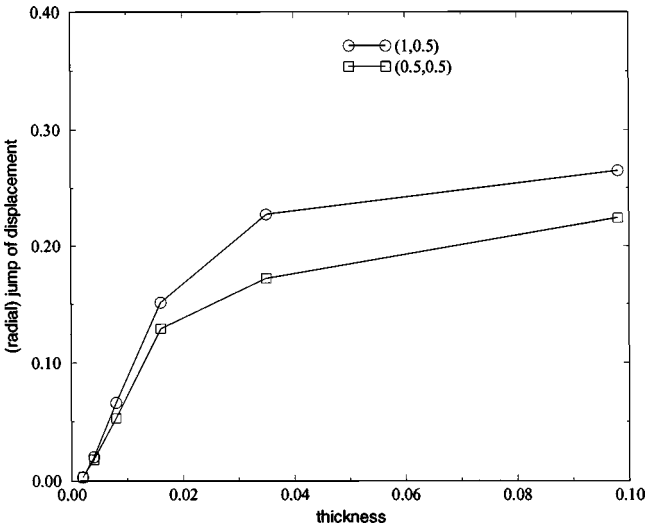

Fig. 4 Jump of displacement for different values of α and β ($M=3$)

Table 1 with respect to the value of the parameters α and β. α and β determine how the thickness and the rigidity tend to zero. It is necessary to quantify the limit, in other words we seek an interval in which the initial problem could be approximated by the limit problem for which the solution is more easy to obtain. On the other hand, it is very important to quantify the influence

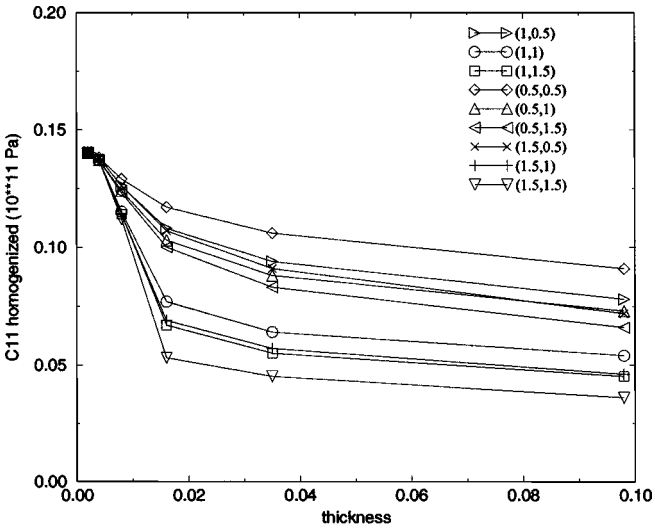

Fig. 5 Homogenized coefficient for different values of α and β ($M=3$)

of the interface on the macroscopic coefficients, i.e., on the elastic behavior of a structure. Due to the shape and the thickness of the interface this problem is very difficult to treat by classical techniques.

We present, in Fig. 4, a study of the convergence of the jump of displacement in the interface for the case $\gamma=1$, for two values of α and β. λ and μ are chosen as Aluminum coefficients. In this case the jump is equal to zero in the interface law. We have found that for values of η smaller than 0.4 p.c. of the structure the interface law could be considered as valid. Note that the displacement in the interface has the form ([16]) $u(r,\theta)\simeq ru(\theta)+u_0$. Figure 5 shows the influence of the thickness parameter on the first component of the homogenized elasticity tensor for different values of α and β. For small values of the thickness (η smaller than 0.2 p.c. of the structure) it is convenient to neglect the interface. Note that for values of the thickness larger than 0.02, the coefficient depends linearly on the thickness.

7 Concluding Remarks

In this paper, we have shown a robust tool to compute the overall response of a composite. In particular, our method is able to compute the influence of an interface even at a very small level. In the future, we want to investigate more complex materials such random materials ([18]) or other kind of interfaces ([19,20]).

References

[1] Charton, P., and Perrier, V., 1996, ''A Pseudo-Wavelet Scheme for the Two Dimensional Navier-Stokes Equation,'' Comp. Appl. Math., **15**, pp. 139–160.

[2] Lazaar, S., Ponenti, P. J., Liandrat, J., and Tchamitchian, P., 1994, ''Wavelet Algorithms for Numerical Resolution of Partial Differentiable Equations,'' Comput. Methods Appl. Mech. Eng., **116**, pp. 309–314.

[3] Dumont, S., 1996, ''Ondelettes, Homogénéisation Périodique et Elasticité,'' Ph.D. thesis, Université Montpellier 2.

[4] Dumont, S., and Lebon, F., 1996, ''Wavelet-Galerkin Method for Heterogeneous Media,'' Comput. Struct., **61**, pp. 55–65.

[5] Dumont, S., and Lebon, F., 1999, ''Wavelet-Galerkin Method for Plane Elasticity,'' Comp. Appl. Math., **18**, pp. 127–142.

[6] Daubechies, I., 1992, ''Orthonormal Bases of Compactly Supported Wavelets,'' Commun. Pure Appl. Math., **41**, pp. 909–998.

[7] Dumont, S., and Lebon, F., 1996, ''Representation of Plane Elastostatics Operators in Daubechies Wavelets,'' Comput. Struct., **60**, pp. 561–569.

[8] Hashin, Z., and Strickman, S., 1963, ''A Variational Approach to the Theory of the Elastic Behavior of Multiphase Materials,'' J. Mech. Phys. Solids, **11**, pp. 127–140.

[9] Hill, R., 1964, ''Theory of Mechanical Properties of Fiber-Strenghened Materials,'' J. Mech. Phys. Solids, **12**, pp. 199–212.

[10] Bensoussan, A., Lions, J. L., and Papanicolaou, G., 1978, *Asymptotic Analysis for Periodic Structures*, 1st Ed., North-Holland, Amsterdam.

[11] Dumontet, H., 1983, ''Homogénéisation par Développement en Séries de Fourier,'' C. R. Acad. Sci. Paris, **296**, pp. 1625–1628.

[12] Beylkin, G., 1992, ''On the Representation of Operators in Bases of Compactly Supported Wavelets,'' SIAM (Soc. Ind. Appl. Math.) J. Numer. Anal., **29**, pp. 1716–1740.

[13] Hackbusch, W., 1985, *Multigrid Method and Applications*, Springer-Verlag, New York.

[14] Lebon, F., 1995, ''Two-Grid Method for Regularized Frictional Elastostatics Problems,'' Eng. Comput., **12**, pp. 657–664.

[15] Ould Khaoua, A., 1995, ''Etude Théorique et Numérique de Problèmes de Couches Minces,'' Ph.D. thesis, Université Montpellier 2.

[16] Ould Khaoua, A., Lebon, F., Licht, C., and Michaille, G., 1996, ''Thin Layers in Elasticity: A Theoretical and Numerical Study,'' *Proceedings of the 1996 ESDA Conference*, Vol. 4, ASME, New York, pp. 171–178.

[17] Lebon, F., Ould Khaoua, A., and Licht, C., 1997, ''Numerical Study of Soft Adhesively Bonded Joints in Finite Elasticity,'' Comp. Mech., **21**, pp. 134–140.

[18] Garboczi, E. J., and Bentz, D. P., 1991, ''Digital Simulation of Interfacial Packing in Concrete,'' J. Mater. Res., **6**, pp. 196–201.

[19] Hervé, E., and Zaoui, A., 1995, ''Elastic Behavior of Multiply Coated Fibre-Reinforced Composites,'' Int. J. Eng. Sci., **33**, pp. 1419–1433.

[20] Lagache, M., Agbossou, A., Pastor, J., and Muller, D., 1994, ''Role of Interphase on the Elastic Behavior of Composite Materials: Theoretical and Experimental Analysis,'' J. Compos. Mater., **28**, pp. 1140–1157.

On the Original Publication of the General Canonical Functional of Linear Elasticity

C. A. Felippa

Mem. ASME, Department of Aerospace Engineering and Center for Aerospace Structures, University of Colorado, Boulder, CO 80309-0429

The general canonical functional of linear elastostatics is associated with the names of Hu and Washizu, who published it independently in 1955. This note discusses how that functional, in a generalized four-field form, had been derived by B. M. Fraeijs de Veubeke in a 1951 technical report. This report presents five of the seven canonical functionals of elasticity. In addition to the general functional, it exhibits what is likely the first derivation of the strain-displacement dual of the Hellinger-Reissner functional. The tour of five variational principles takes only a relatively small portion of the report: 8 pages out of 56. The bulk is devoted to the use of energy methods for analysis of wing structures. The title, technology focus, and limited dissemination may account for the subsequent neglect of this original contribution to variational mechanics. [S0021-8936(00)00401-3]

Introduction

The three-field canonical functional of linear elastostatics, herein abbreviated to C3FLE, is identified as the Hu-Washizu functional in the mechanics literature. In this functional the three interior fields, displacements, stresses, and strains, are independently varied. The attribution is supported by two independent publications that appeared concurrently, in Mar. 1955 ([1,2]). A four-field generalization, in which surface tractions are independently varied, will be called C4FLE.

An expository article (actually a book chapter) by Fraeijs de Veubeke [3] is often cited as one of the early classics in the finite element literature. That article contains the first enunciation of the ''limitation principle,'' which has since served as guide in the construction of mixed elements. His exposition of variational

Contributed by the Applied Mechanics Division of THE AMERICAN SOCIETY OF MECHANICAL ENGINEERS for publication in the ASME JOURNAL OF APPLIED MECHANICS. Manuscript received by the ASME Applied Mechanics Division, Apr. 22, 1999; final revision, Oct. 12, 1999. Associate Technical Editor: M. Ortiz.

methods starts from the C4FLE functional, which he calls ''the general variational principle.'' However, it does not reference Hu and Washizu as its source but an earlier technical report, written in French ([4]). This appears as the third reference in the 1965 article.

A subsequent journal paper on variational principles, [5], is slightly more explicit. It begins: ''There is a functional that generates all the equations of linear elasticity theory in the form of variational derivatives and natural boundary conditions. Its original construction [12] followed the method proposed by Friedrichs . . . '' The reference number points to that report.

These references motivated the writer to investigate whether de Veubeke had indeed constructed that functional in the 1951 report. That would confer him priority over Hu and Washizu, although of course these two papers were more influential in subsequent work. The writer was able to procure an archived copy thanks to Profs. Beckers and Geradin of the University of Liège, where Fraeijs de Veubeke was a professor of aeronautical engineering from the early 1950s until his untimely death in 1977.

Construction of the C4FLE Functional

As discussed below, in the 1951 report Fraeijs de Veubeke constructs not simply the canonical three-field principle, but the four-field generalization C4FLE. Consequently his priority is established unless an earlier publication can be found. The functional, however, appears as an intermediate result on the road from the total potential energy (TPE) to the total complementary energy (TCE) principle. The path also traverses a pair of two-field functionals, one being a generalization of the Hellinger-Reissner (HR) functional published the previous year by Reissner [6]. The full sequence can be sketched as

$$\text{TPE}\rightarrow\text{C4FLE}\rightarrow\text{Strain-displacement dual of HR}\rightarrow\text{HR}\rightarrow\text{TCE}. \tag{1}$$

The report does not call special attention to C4FLE, as well as to the strain-displacement functional that appears there for the first time. The bulk of the material is indeed devoted to the study of energy-based approximation methods for the analysis of monocoque wing structures, rather than to the derivation of new functionals. Its title, technology focus, and target audience (structural engineers) are likely responsible for subsequent neglect. This is reinforced by its limited dissemination and the fact that the material was apparently not submitted to an archival journal.

Fraeijs de Veubeke uses the full-component notational form popularized by Timoshenko and others, which was then common in continuum mechanics. For historical accuracy this will be followed below until Eq. (10), at which point it is changed to modern indicial notation for compactness. The equations taken from the report have been sequentially renumbered.

The report comprises three chapters. The last two, which deal with the title application, are of no concern here. Chapter I begins by summarizing the field equations of linear elastostatics for a three-dimensional body of volume V and surface S. The fields in V are displacements u, v, w, body forces X, Y, Z, infinitesimal strains $\epsilon_x, \gamma_{xy}, \ldots, \epsilon_z$ and stresses $\sigma_x, \tau_{xy}, \ldots, \sigma_z$. The surface S is divided into S_1, on which tractions $\overline{p_x}$, $\overline{p_y}$, $\overline{p_z}$ are known,and S_2, on which displacements $\overline{u}$, $\overline{v}$, $\overline{w}$ are prescribed. The direction cosines of the exterior normal to S are denoted by l, m, n.

As starting point for the variational developments (Chapter I, p. 6) Fraeijs de Veubeke exhibits the TPE principle:

$$\delta\left[\int_V W\, dV + P_V + P_S\right] = 0. \tag{2}$$

Here W is the internal energy density in terms of displacements, whose first variation is

$$\delta W = \sigma_x \delta\frac{\partial u}{\partial x} + \tau_{xy}\delta\left(\frac{\partial u}{\partial y}+\frac{\partial v}{\partial x}\right) + \cdots + \sigma_z\delta\frac{\partial w}{\partial z} \tag{3}$$

and P_V and P_S are potentials of the body (volume) forces and surface tractions, respectively,

$$P_V = \int_V (\overline{X}u + \overline{Y}v + \overline{Z}w)\,dV \tag{4}$$

$$P_S = \int_{S_1} (\overline{p_x}u + \overline{p_y}v + \overline{p_z}w)\,dS. \tag{5}$$

Fraeijs de Veubeke presents the well-known Euler equations of the TPE principle. Next (on p. 8) he recasts the internal energy density in terms of strains: $W = W(\epsilon)$ so that the variation becomes

$$\delta W = \sigma_x\delta\epsilon_x + \tau_{xy}\delta\gamma_{xy} + \cdots + \sigma_z\delta\epsilon_z\,. \tag{6}$$

Following that he states that to free (''libérer'') strains from the strain-displacement constraints and the boundary displacements from the prescribed displacement constraints, one must add to the expressions to be varied the volume term

$$\int_V\left[T_{xx}\left(\frac{\partial u'}{\partial x}-\epsilon_x\right)+T_{xy}\left(\frac{\partial u'}{\partial y}+\frac{\partial v'}{\partial x}-\gamma_{xy}\right)+\cdots\right]dV \tag{7}$$

in which $(T_{xx}, T_{xy}, \ldots)$ are Lagrange multipliers in V, as well as the surface term

$$\int_{S_2}[\alpha_x(\overline{u}-u)+\alpha_y(\overline{v}-v)+\alpha_z(\overline{w}-w)]\,dS \tag{8}$$

in which $(\alpha_x, \alpha_y, \alpha_z)$ are multipliers on S_2. The displacements in (7) are marked by a prime to emphasize that the variations of the strains have become independent of the displacement gradients.

Fraeijs de Veubeke states on p. 9 that this expanded functional is subject to 18 independent variations: three displacements, six strains, six T multipliers, and three α multipliers. He had noted earlier (on p. 8) that variations with respect to the strains in V give as Euler equations

$$T_{xx} = \frac{\partial W}{\partial\epsilon_x}, \quad T_{xy} = \frac{\partial W}{\partial\gamma_{xy}}\ \ldots \tag{9}$$

whereas variations with respect to the displacements on S_2 give as Euler equations

$$\alpha_x = lT_{xx} + mT_{xy} + nT_{xz}, \ \ldots\,. \tag{10}$$

Hence the T multipliers form a stress system whereas the α multipliers form a system of surface tractions. Fraeijs de Veubeke denotes these as σ' and p' in later publications, such as the cited 1965 article.

Except for P_V and P_S, Fraeijs de Veubeke does not define global symbols to identify his integrals. For convenience we remedy that omission by calling $U_\epsilon = \int_V W(\epsilon)dV$ and identifying Eqs. (7) and (8) by D_V and D_S, respectively, where D stands for the term ''dislocation potential'' now in vogue. We can thereby collect all the pieces into one compact expression:

$$\delta[U_\epsilon + D_V + P_V + P_S + D_S] = 0. \tag{11}$$

The expression in brackets is the C4FLE functional, which in indicial notation can be compactly presented as

$$\Pi(u_i, \sigma_{ij}, \epsilon_{ij}, t_i) = \int_V [W(\epsilon_{ij}) + \sigma_{ij}(u_{(i,j)} - \epsilon_{ij}) - f_i u_i]dV - \int_{S_1}\overline{t_i}u_i dS - \int_{S_2} t_i(\overline{u_i}-u_i)dS \tag{12}$$

in which $u_{(i,j)}$ denotes the symmetric gradient of the displacement field. The three-field standard form C3FLE is obtained by setting $t_i = \sigma_{ij}n_j$ on S_2 a priori. A variant of C3FLE involving stress derivatives, displayed for example in Gurtin [7] follows from integration by parts.

A Strain-Displacement Functional

Continuing along the path (1), Fraeijs de Veubeke replaces the multipliers in (7) and (8) by (9) and (10), respectively, and exhibits on p. 9 a two-field functional in which strains and displacements are primary variables. His full form expression is fairly long. In indicial notation it becomes

$$\Pi(u_i,\epsilon_{ij}) = \int_V \left[W(\epsilon_{ij}) + \frac{\partial W}{\partial \epsilon_{ij}}(u_{(i,j)} - \epsilon_{ij}) - f_i u_i \right] dV - \int_{S_1} \bar{t}_i u_i dS - \int_{S_2} \frac{\partial W}{\partial \epsilon_{ij}} n_j (\bar{u}_i - u_i) dS \qquad (13)$$

in which for linear elasticity $\partial W/\partial \epsilon_{ij}$ is understood to be $E_{ijkl}\epsilon_{kl}$. Now (13) is the stress-strain dual of Hellinger-Reissner (HR) but has escaped a name.

In an expository article ([8]), the writer called it ''Strain-Displacement Reissner'' following Oden and Reddy [9] who labeled it a Reissner functional when constructed as a member of a canonical set of elasticity functionals ([10]). However, in a 1995 letter to the writer, Professor Reissner indicated that he had not considered that form. This functional has had little use in mechanics until assumed-strain finite elements began appearing in the 1980s.

Again, Fraeijs de Veubeke uses Eq. (13) only as an intermediate result. He applies a Friedrichs-style Legendre transformation to it and arrives on p. 10 at a generalized form of the Hellinger-Reissner (HR) functional. He remarks that it had been published by Reissner [6] but that the rederived form is slightly more general in that it includes body forces as well as prescribed nonzero displacements.

The remainder of Chapter I (pp. 11–18) is devoted to the derivation of the TCE functional from HR, and the energy theorems of Castigliano and Menabrea. Even for this better known material Fraeijs de Veubeke displays a mastery of variational techniques unusual for the times. For example, several textbooks still thoughtlessly lift Castigliano's second theorem $u_i = \partial U(\sigma)/\partial F_i$ from trusses and frameworks to three-dimensional solids. This is incorrect because the displacement under a concentrated load is infinite. He carefully regularizes the singular energy integral before stating the theorem.

Conclusions

The 1951 report provides concrete evidence that Fraeijs de Veubeke preceded both Hu and Washizu in the publication of the C4FLE functional. Furthermore, he appears to have been the first to construct a strain-displacement dual of the HR functional. Hence it seems fair to propose

1 that the canonical functional (12) be identified as the Fraeijs de Veubeke-Hu-Washizu functional.

2 that the hitherto anonymous strain displacement functional (13) be named after Fraeijs de Veubeke. This functional was constructed independently more than 20 years later by Oden and Reddy [10].

Some historical questions remain, perhaps as curiosities for future science historians.

Fraeijs de Veubeke was a visiting professor at MIT during 1952, the year following publication of the report examined here. Washizu's publication is an MIT report dated Mar. 1955. Professor Pian (private communication) has indicated to the writer that direct or indirect influence is unlikely, since Fraeijs de Veubeke was only a summer visitor.

The writer has not seen Washizu's 1955 report. However, in an early edition of his well-known monograph ([11]) the derivation of the C4FLE functional on pp. 31–34 closely follows Fraeijs de Veubeke's, as readers may verify. The similarity of Hu's and Washizu's paper titles is also puzzling.

Fraeijs de Veubeke does not reference Hu or Washizu in any of the papers reprinted in the Memorial Volume [12]. He acknowledges Friedrichs, Courant, Hilbert, Prager, Reissner, and Pian. On the other hand, he does not explicitly claim priority for the results discussed here. Perhaps he felt that the derivation of new functionals was not the focus of the 1951 report. And indeed it was not. The tour of five variational principles takes 8 pages out of 56. In contrast, the titles of the contributions of Hu and Washizu expressly state that to be the main objective. The writer's opinion is that Fraeijs de Veubeke's personality would militate against engaging in controversy. An aristocrat by birth and gentleman by nature, he never displayed greed for priority and recognition.

Acknowledgments

The writer is indebted to Profs. M. Geradin and P. Beckers of the University of Liège for locating and providing a copy of the 1951 report, and to Profs. T. H. H. Pian and J. N. Reddy for clarifying historical points.

References

[1] Hu, H.-C., 1955, ''On Some Variational Methods on the Theory of Elasticity and the Theory of Plasticity,'' Sci. Sin., **4**, pp. 33–54.
[2] Washizu, K., 1955, ''On the Variational Principles of Elasticity and Plasticity,'' Aeroelastic and Structures Research Laboratory, Technical Report 25-18, MIT, Cambridge, MA.
[3] Fraeijs de Veubeke, B. M., 1965, ''Displacement and Equilibrium Models,'' *Stress Analysis*, O. C. Zienkiewicz and G. Hollister, eds., Wiley, London, pp. 145–197.
[4] Fraeijs de Veubeke, B. M., 1951, ''Diffusion des Inconnues Hyperstatiques dans les Voilures à Longeron Couplés,'' *Bull. Serv. Technique de L'Aéronautique No. 24*, Imprimerie Marcel Hayez, Bruxelles, 56 pp.
[5] Fraeijs de Veubeke, B. M., 1974, ''Variational Principles and the Patch Test,'' Int. J. Numer. Methods Eng., **8**, pp. 783–801.
[6] Reissner, E., 1950, ''On a Variational Theorem in Elasticity,'' J. Math. Phys., **29**, pp. 90–95.
[7] Gurtin, M. E., 1983, ''The Linear Theory of Elasticity,'' *Mechanics of Solids Vol II*, C. Truesdell, ed., Springer-Verlag, Berlin, pp. 1–296.
[8] Felippa, C. A., 1994, ''A Survey of Parametrized Variational Principles and Applications to Computational Mechanics,'' Comput. Methods Appl. Mech. Eng., **113**, pp. 109–139.
[9] Oden, J. T., and Reddy, J. N., 1982, *Variational Methods in Theoretical Mechanics*, Springer-Verlag, Berlin.
[10] Oden, J. T., and Reddy, J. N., 1974, ''On Dual Complementary Variational Principles in Mathematical Physics,'' Int. J. Eng. Sci., **12**, pp. 1–29.
[11] Washizu, K., 1968, *Variational Methods in Elasticity and Plasticity*, Pergamon Press, New York.
[12] Geradin, M., ed., 1980, *B. M. Fraeijs de Veubeke Memorial Volume of Selected Papers*, Sitthoff & Noordhoff, Alphen aan den Rijn, The Netherlands.

Logarithmic Stress Singularities Resulting From Various Boundary Conditions in Angular Corners of Plates Under Bending

G. B. Sinclair
Department of Mechanical Engineering, Carnegie Mellon University, Pittsburgh, PA 15213-3890

This note considers the occurrence of pure logarithmic singularities in angular elastic plates under bending within the context of classical theory. By paralleling the development of requirements for logarithmic singularities for plates in extension, requirements

Contributed by the Applied Mechanics Division of THE AMERICAN SOCIETY OF MECHANICAL ENGINEERS for publication in the ASME JOURNAL OF APPLIED MECHANICS. Manuscript received by the ASME Applied Mechanics Division, May 18, 1999; final revision, Oct. 19, 1999. Associate Technical Editor: J. R. Barber.

for log singularities in bending are developed, both for homogeneous boundary conditions on plate edges and for inhomogeneous. Using these singularity requirements, some 50-odd configurations with log singularities are identified, the great majority being for inhomogeneous boundary conditions.
[S0021-8936(00)00501-8]

1 Introduction

Elastic stress singularities are not of the real world. However, their presence in a stress analysis can be a real fact. Then it is essential that their participation be recognized if reasonable use is to be made of the analysis in the vicinity of the singularity. The objective of this note is to assist in achieving such recognition.

In particular, we are concerned with identifying configurations which can have pure logarithmic singularities—that is, stress resultants and attendant stresses which behave like $O(\ln r)$ as $r \to 0$. These are the weakest singularities that occur in elasticity. As a result, they can be the most difficult to detect with numerical methods. Asymptotic identification is thus especially useful in avoiding having them pass undetected.

For angular elastic plates in bending treated within classical fourth-order theory, Williams [1] identifies possible power singularities for a variety of homogeneous boundary conditions on the plate edges. No logarithmic singularities are identified in [1]. Logarithmic singularities can be found elsewhere in the literature, but these occur in concert with the far stronger singularities that attend concentrated loads. Examples may be found in Nádai [2] Article 49, and Timoshenko and Woinowsky-Krieger [3] Article 75. Pure logarithmic singularities for plates in bending within classical theory would not appear to be identified in the literature. Here, therefore, we seek to identify such singularities, and to do so when either homogeneous or inhomogeneous boundary conditions apply on plate edges.

We begin, in Section 2, with a formal statement of the class of asymptotic problems of interest. Then, in Section 3, we outline the development of requirements for pure logarithmic singularities. We close, in Section 4, with a tabulation of all the configurations found to be able to have log singularities.

2 Formulation

The angular plate region of interest is shown in Fig. 1. To describe this plate, we use cylindrical polar coordinates (r,θ,z) with origin O at the vertex of its midplane and $\theta=0$ along one of its edges. The plate has indefinite extent in the r-direction, thickness $2h$ in the z-direction, and subtends an angle ϕ at its vertex.

The displacement of primary concern is that in the z-direction, w. This displacement has associated moment resultants M_r, M_0, M_{r0}, as shown acting in a positive sense on an element in the $r\theta$-plane in Fig. 2(*a*). It also has associated shear resultants Q_r, Q_θ, as shown acting in a positive sense on an element in Fig.

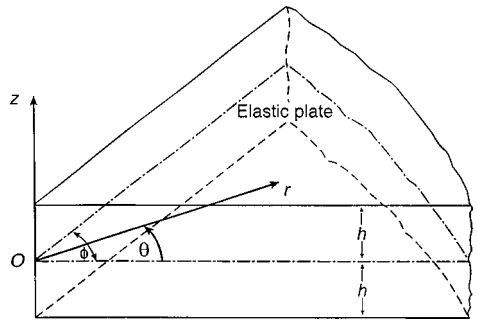

Fig. 1 Geometry and coordinates for the angular elastic plate

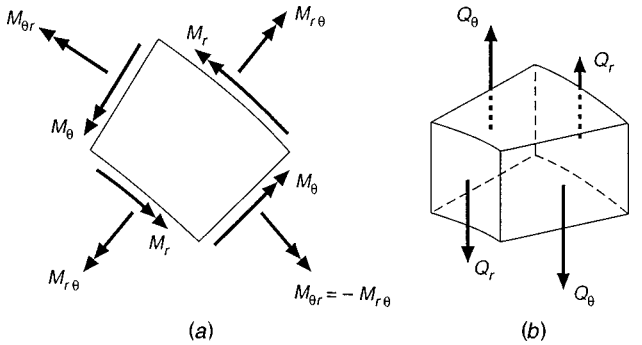

Fig. 2 Plate theory resultants: (*a*) moment resultants, (*b*) shear resultants

2(*b*). All of these field quantities are taken to be independent of z. Hence, we can confine our attention to the two-dimensional region $\Re$ where

$$\Re=\{(r,\theta)\,|\,0<r<\infty,\ 0<\theta<\phi\}.$$

With these preliminaries in place, we can formulate the class of problems for asymptotic analysis as next.

We seek the out-of-plane displacement w, together with its associated moment resultants $M_r, M_\theta, M_{r\theta}$ and shear resultants Q_r, Q_θ, as functions of r, θ throughout $\Re$ complying with the following requirements. The displacement is to satisfy the displacement equation of equilibrium in the absence of both body forces and loading on the plate faces at $z=\pm h$,

$$\nabla^4 w=0, \tag{1}$$

on $\Re$, where $\nabla^4=\nabla^2(\nabla^2)$, $\nabla^2=\partial^2/\partial r^2+r^{-1}\partial/\partial r+r^{-2}\partial^2/\partial\theta^2$. The displacement and resultants are to satisfy the resultant-displacement relations for a homogeneous and isotropic, linear elastic plate,

$$\begin{Bmatrix} M_r \\ M_\theta \end{Bmatrix} = -k\left[\begin{Bmatrix} \nu \\ 1 \end{Bmatrix}\frac{\nabla^2 w}{1-\nu}\begin{Bmatrix} + \\ - \end{Bmatrix}\frac{\partial^2 w}{\partial r^2}\right], \quad M_{r\theta}=k\frac{\partial}{\partial r}\left(\frac{1}{r}\frac{\partial w}{\partial\theta}\right), \tag{2}$$

$$Q_r=\frac{-k}{1-\nu}\frac{\partial}{\partial r}(\nabla^2 w), \quad Q_\theta=\frac{-k}{1-\nu}\frac{1}{r}\frac{\partial}{\partial\theta}(\nabla^2 w),$$

on $\Re$, where $k=4\mu h^3/3$ is the flexural stiffness of the plate while μ, ν are its shear modulus, Poisson's ratio. The displacement/resultants are to satisfy any one of the admissible sets of boundary conditions listed in Table 1 on the plate edge at $\theta=0$, as well as a further such set on $\theta=\phi$. Finally, the resultants are to comply with the following regularity-singularity requirement:

$$M=O(1), \quad Q=O(\ln r), \ \text{as} \ r\to 0, \tag{3}$$

on $\Re$, where M is any moment resultant, Q either shear resultant.

Several comments on the foregoing formulation are in order. First, regarding the boundary conditions in Table 1. In conditions I–III, M_i, V, a_i, and b are given constants $(i=1,2)$. When these constants are zero, we obtain the corresponding homogeneous boundary conditions. We distinguish these with a subscript h. Thus I_h are Kirchhoff conditions for a stress-free edge, II_h are for a simply supported edge, and III_h are for a built-in edge. Conditions IV model a plate edge which is elastically restrained by a bar: k_t is the bar's torsional stiffness, k_b its bending stiffness, and plus signs are for $\theta=\phi$, minus for $\theta=0$.[1]

Second, regarding the regularity-singularity requirement. For the usual relationships between stress resultants and stresses in plate theory, this has pure log singularities in $\tau_{rz}, \tau_{\theta z}$ while $\sigma_r, \sigma_\theta, \tau_{r\theta}$ are nonsingular.

[1]See [3], Art. 22, for a development of IV.

Table 1 Boundary conditions

Assigned Roman Numeral	Physical Description	Prescribed Quantities
I	Applied moment/shear	$M_\theta = M_1 r$
	$Q_\theta - \frac{\partial m_{r\theta}}{\partial r}$	$Q_\theta - \frac{\partial M_{r\theta}}{\partial r} = V$
II	Applied moment/displacement	$M_\theta = M_2 r$
		$w = a_1 r^3$
III	Applied displacement/rotation	$w = a_2 r^3$
		$\frac{\partial w}{\partial \theta} = b r^3$
IV	Elastically restrained	$M_\theta = \pm k_t \frac{\partial^2}{\partial r^2}\left(\frac{1}{r}\frac{\partial w}{\partial \theta}\right)$
		$Q_\theta - \frac{\partial M_{r\theta}}{\partial r} \pm k_b \frac{\partial^4 w}{\partial r^4} = 0$

Table 2 Eigenvalue equations

Boundary Conditions on $\theta = 0, \phi$	Eigenvalue Equation
I_h–I_h	$(\lambda-1)^2(\kappa^2 \sin^2 \lambda\phi - \lambda^2 \sin^2 \phi) = 0$
II_h–II_h	$\cos^2 \lambda\phi - \cos^2 \phi = 0$
III_h or IV–III_h or IV	$\sin^2 \lambda\phi - \lambda^2 \sin^2 \phi = 0$
I_h–II_h	$(\lambda-1)(\kappa \sin 2\lambda\phi + \lambda \sin 2\phi) = 0$
I_h–III_h or IV	$(\lambda-1)(\kappa^2 + 2\kappa \cos 2\lambda\phi + 1 - 4\lambda^2 \sin^2 \phi) = 0$
II_h–III_h or IV	$\sin 2\lambda\phi - \lambda \sin 2\phi = 0$

3 Analysis

As in the extensional case, requirements for logarithmic singularities under bending follow from a further development of the corresponding classical analysis for power singularities. Accordingly we next summarize the asymptotic analysis of power singularities in plates under bending.

In Williams [1], the appropriate choice of a separable biharmonic function for the displacement w leads to fields containing four constants which share a common power of r. This function has the form

$$w = r^{\lambda+1}[c_1 \sin(\lambda+1)\theta + c_2 \cos(\lambda+1)\theta + c_3 \sin(\lambda-1)\theta + c_4 \cos(\lambda-1)\theta], \tag{4}$$

where c_j $(j = 1-4)$ are the four constants, and λ is the separation-of-variables parameter. The stress resultants for this basic field follow from (2). Substituting these fields into a set of four homogeneous boundary conditions then gives

$$\mathbf{Ac} = \mathbf{0}, \tag{5}$$

where the vector $\mathbf{c} = (c_1, c_2, c_3, c_4)$, and $\mathbf{A}$ is a matrix whose elements are in general functions of λ. A nontrivial solution to (5) requires that the determinant D of $\mathbf{A}$ satisfy

$$D = 0. \tag{6}$$

This requirement generates an eigenvalue equation for λ. Determining λ satisfying (6) with $0 < \mathrm{Re}\,\lambda < 2$ then characterizes the power singularities possible in stress resultants for the particular homogeneous boundary conditions involved.

To extend the preceding to consider logarithmic singularities, we need stress resultants containing $\ln r$ terms. To this end, we differentiate the basic field of (4) with respect to λ: thus

Table 3 Configurations with $Q = O(1 \mathrm{n} r)$ as $r \to 0$

Boundary Conditions on $\theta = 0, \phi$	Configuration Specifications
I–I_h	$\phi = \pi$ or 2π, $M_1 \neq 0$ or $V \neq 0$
	$\kappa = \pm\sec\phi$, $M_1(\kappa+2)\left(\tan\frac{\phi}{2}\right)^{\pm 1} \neq \pm V(2-\kappa)$,
II–II_h	$\phi = \pi$ or 2π, $M_2 \neq 6a_1 k$
III–III_h or IV	$\phi = \pi$ or 2π, $a_2 \neq 0$ or $b \neq 0$
I–II	$\phi = (2m-1)\frac{\pi}{2}$, $24a_1 k \neq M_2(\kappa+5) - (-)^m V(\kappa+1)$ $(m = 1,2)$
	$\phi = m\pi$, $M_1 \neq (-)^m M_2$ $(m = 1,2)$
	$\kappa = -\sec 2\phi$, $(V \sin\phi - 12a_1 k)(\kappa-2) \neq M_1(\kappa+2)\cos\phi - M_2(\kappa-4)$
I–III	$\phi = \phi_\kappa$, $\kappa \neq \hat{\kappa}$, $(M_1 - 6a_2 k \cos 3\phi)(3\sin 3\phi - (\kappa+2)\sin\phi)$ $\neq (V + 2bk \cos 3\phi)(3\cos 3\phi + (\kappa-2)\cos\phi)$
I_h–III_h or IV	$\phi = \hat{\phi}_\kappa$, $\kappa = \hat{\kappa}$
I–IV	$\phi = \pi$ or 2π, $V \neq 0$
	$\phi = \pi/2$ or $3\pi/2$, $M_1 \neq 0$
	$\kappa = -\sec 2\phi$, $M_1(\kappa+2)\tan\phi \neq V(2-\kappa)$
II–III	$\phi = (2m-1)\frac{\pi}{2}$, $2M_2 \neq 3(3-\kappa)a_1 k - (-)^m(\kappa+1)bk$ $(m = 1,2)$
	$\phi = m\pi$, $a_1 \neq (-)^m a_2$ $(m = 1,2)$
II–IV	$\phi = \pi/2$ or $3\pi/2$, $M_2 \neq 6a_1 k$
III–IV	$\phi = \pi/2$ or $3\pi/2$, $a_2 \neq 0$
	$\phi = \pi$ or 2π, $b \neq 0$

$$w = r^{\lambda+1}[\ln r(\bar{c}\sin(\lambda+1)\theta + \bar{c}_2\cos(\lambda+1)\theta + \bar{c}_3\sin(\lambda-1)\theta + \bar{c}_4\cos(\lambda-1)\theta) + \theta(\bar{c}_1\cos(\lambda+1)\theta - \bar{c}_2\sin(\lambda+1)\theta + \bar{c}_3\cos(\lambda-1)\theta - \bar{c}_4\sin(\lambda-1)\theta)], \quad (7)$$

where the bars atop constants serve to indicate that they no longer need be the same as their antecedents in (4). The displacement in (7) continues to satisfy the governing biharmonic Eq. (1). Substituting (7) into (2) produces resultants containing $\ln r$ terms. Substituting (7) and these last, together with the original basic fields, into a set of four homogeneous boundary conditions gives

$$\mathbf{A}\bar{\mathbf{c}}\ln\mathbf{r} + \frac{d\mathbf{A}}{d\lambda}\bar{\mathbf{c}} + \mathbf{A}\mathbf{c} = \mathbf{0}, \quad (8)$$

where $d\mathbf{A}/d\lambda$ is formed from $\mathbf{A}$ by differentiating each element with respect to λ. General requirements for a nontrivial solution for $\bar{\mathbf{c}}$ in (8) are established in Dempsey and Sinclair [4]. From these we obtain our *requirements for pure logarithmic singularities under homogeneous boundary conditions*:

$$\lambda = 2, \quad D = 0, \quad (9a)$$

$$\frac{d^n D}{d\lambda^n} = 0 \quad \text{for} \quad n = 1, \ldots, 4 - r_A, \quad (9b)$$

$$\bar{c}_3^2 + \bar{c}_4^2 \neq 0, \quad (9c)$$

where r_A is the rank of $\mathbf{A}$ when $\lambda = 2$. Equation (9*c*) ensures that one of $\bar{c}_3$ or $\bar{c}_4$ is not zero so that the shear resultants are indeed logarithmically singular as in (3).

Turning to the inhomogeneous boundary conditions I–III of Table 1, we obtain instead of (5)

$$\mathbf{A}\mathbf{c} = \mathbf{f}, \quad (10)$$

for $\lambda = 2$, where $\mathbf{f}$ is a vector whose components involve one or more of M_i, V, a_i, and b $(i = 1,2)$. For $\mathbf{f} \neq \mathbf{0}$, we have a problem in (10) if $D = 0$ for $\lambda = 2$, unless the rank of the augmented matrix, $(\mathbf{A}') = (\mathbf{A}:\mathbf{f})$, is also reduced. If this rank reduction does not occur, we can overcome the difficulty by again supplementing the basic fields associated with (4) with the auxiliary ones stemming from (7).[2] This gives

$$\mathbf{A}\bar{\mathbf{c}}\ln\mathbf{r} + \frac{d\mathbf{A}}{d\lambda}\bar{c} + \mathbf{A}\mathbf{c} = \mathbf{f}, \quad (11)$$

for $\lambda = 2$. The system in (11) can be solved provided all the requirements in (9*b*) are *not* met. Accordingly our *requirements for pure logarithmic singularities under inhomogeneous boundary conditions* are

$$\lambda = 2, \quad D = 0, \quad r_A' \neq r_A, \quad (12a)$$

$$\frac{d^n D}{d\lambda^n} \neq 0 \quad \text{for at least one} \quad n = 1, \ldots, 4 - r_A, \quad (12b)$$

$$\bar{c}_3^2 + \bar{c}_4^2 \neq 0, \quad (12c)$$

where r_A' is the rank of $\mathbf{A}'$ when $\lambda = 2$. As with (9*c*), (12*c*) ensures (3) is complied with when $\lambda = 2$.

An additional set of requirements for logarithmic singularities under inhomogeneous boundary conditions is given in Sinclair [7] for the extensional case. These requirements arise from further auxiliary fields which result from a further differentiation with respect to λ. However, we omit these requirements here because they can never be completely satisfied for the class of problems treated. Subsequently we do note, though, the one instance of a log-squared singularity that attends partial compliance with them.

With the requirements for logarithmic singularities at hand, analysis proceeds routinely. We first derive eigenvalue equations as in (6) for all possible combinations of homogeneous boundary conditions that can be drawn from Table 1. Then we check (9) and (12). When potential new configurations with log singularities are revealed, the last requirement in either (9) or (12) requires the assembling of associated new fields. The algebra involved is straightforward but lengthy: details are furnished in Sinclair [8]. Displacements with log singularities in their companion resultants are set out ibid. All of these fields are verified directly by substituting them into the governing Eqs. (1),(2), checking the regularity-singularity requirement (3), and checking the pertinent boundary conditions. In the interests of brevity, we omit these fields here and simply provide the configurations that engender them.

4 Results

Eigenvalue equations are set out in Table 2. Therein

$$\kappa = \frac{3+\nu}{1-\nu}.$$

Except for a factor of $(\lambda-1)$ when free-edge conditions, I_h, are involved, these equations are equivalent to those derived in Williams [1]. The equivalence of built-in conditions III_h with elastically restrained conditions IV, as far as eigenvalue equations are concerned, follows from an adaptation of the argument in Sinclair [9] for boundary conditions which have terms with a different r-dependence within a single condition. This equivalence holds for any value of λ. Just for $\lambda = 2$, elastically restrained conditions are equivalent to symmetry conditions, $\partial w/\partial\theta = 0$ and $Q_\theta = 0$. We also investigate them in this role in what follows.

Configurations which have logarithmic singularities in their shear resultants as in (3) are listed in Table 3. In Table 3, ϕ_κ is such that

$$\sin^2\phi_\kappa = \frac{\kappa+1}{4\kappa}[2 \pm \sqrt{4-\kappa}]. \quad (13)$$

If in addition to (13),

$$\kappa = \frac{-\tan\phi}{\phi\cos 2\phi},$$

then $\kappa = \hat{\kappa}$, $\phi_\kappa = \hat{\phi}_\kappa$ (actual values in the physical range of $3 \leqslant \kappa \leqslant 7$ are $\hat{\kappa} = 3.27$, $\hat{\phi}_\kappa = 74.8$ deg and $\hat{\kappa} = 3.02$, $\hat{\phi}_\kappa = 265.9$ deg.). For I–II and $\phi = \hat{\phi}_\kappa$, $\kappa = \hat{\kappa}$, a log-squared singularity occurs.

There are but two geometries with logarithmic singularities under completely homogeneous conditions in Table 3. These occur for $\kappa = \hat{\kappa}$, $\phi = \hat{\phi}_\kappa$ when the boundary conditions are $I_h - III_h$ or IV. One of these geometries is a re-entrant corner ($\hat{\phi}_\kappa = 265.9$ deg) and so is not surprising, but the other is for a proud corner ($\hat{\phi}_\kappa = 74.8$ deg). Here, then, the increase in the occurrence of singularities with mixed boundary conditions is making its presence felt, as it does in the extensional case.

For inhomogeneous boundary conditions, there are a number of quite innocent looking configurations with log singularities in Table 3. For example, $I–I_h$ for $\phi = \pi$ when $M_\theta = M_1 r$: Here the moment resultant actually varies continuously along the boundary, though its derivative does not.

[2] Essentially this is the approach adopted in Dimpsey [5] to solve extensional Levy problems for certain critical wedge angles. An alternative approach for these problems is furnished in Ting [6]. The latter yields the same logarithmic fields for the critical angles, and has the added attribute of effecting a sensible evolution of stresses as the critical angles are passed through. It could be adapted to the class of problems of concern here if one sought a corresponding evolution of responses.

References

[1] Williams, M. L., 1951, ''Surface Stress Singularities Resulting From Various Boundary Conditions in Angular Corners of Plates Under Bending,'' *Proceedings of the First U.S. National Congress of Applied Mechanics*, Illinois Institute of Technology, Chicago, pp. 325–329.

[2] Nádai, A., 1925, *Die elastischen Platten*, Julius Springer Publishing, Berlin.

[3] Timoshenko, S. P., and Woinowsky-Krieger, S., 1959, *Theory of Plates and Shells*, 2nd Ed. McGraw-Hill, New York.

[4] Dempsey, J. P., and Sinclair, G. B., 1979, ''On the Stress Singularities in the Plane Elasticity of the Composite Wedge,'' J. Elast., **9**, pp. 373–391.
[5] Dempsey, J. P., 1981, ''The Wedge Subjected to Tractions: A Paradox Resolved,'' J. Elast., **11**, pp. 1–10.
[6] Ting, T. C. T., 1984, ''The Wedge Subjected to Tractions: A Paradox Re-Examined,'' J. Elast., **14**, pp. 235–247.
[7] Sinclair, G. B., 1999, ''Logarithmic Stress Singularities Resulting From Various Boundary Conditions in Angular Corners of Plates in Extension,'' ASME J. Appl. Mech., **66**, pp. 556–560.
[8] Sinclair, G. B., 1999, ''Analysis of Logarithmic Stress Singularities Resulting from Various Boundary Conditions in Angular Elastic Plates in Bending,'' Report SM 99-1, Department of Mechanical Engineering, Carnegie Mellon University, Pittsburgh, PA.
[9] Sinclair, G. B., 1980, ''On the Singular Eigenfunctions for Plane Harmonic Problems in Composite Regions,'' ASME J. Appl. Mech., **47**, pp. 87–92.

Stress and Displacement Fields for Propagating the Crack Along the Interface of Dissimilar Orthotropic Materials Under Dynamic Mode I and II Load

K. H. Lee
Department of Automotive Engineering, Sangju National University, Sangju City, Kyungbuk 742-711, Korea

General stress and displacement fields are derived as a crack steadily propagates along the interface of dissimilar orthotropic materials under a dynamic mode I and II load. They are obtained from the complex function formulation of steady plane motion problems for an orthotropic material and the complex eigenexpansion function. After the relationship between stress intensity factors and stress components for a propagating crack is defined, the stress, displacement components, and energy release rate with stress intensity factors are derived. The results are useful for both dissimilar isotropic and orthotropic and isotropic-orthotropic bimaterials, and homogeneous isotropic and orthotropic materials under subsonic crack propagation velocity.
[S0021-8936(00)00601-2]

1 Introduction

Yang et al. [1] and Deng [2] provided the asymptotic fields of the singular terms of steady-state elastodynamic bimaterial crack-tip fields and Liu et al. [3] obtained the asymptotic series representation of stress fields near the tip of a running interfacial crack in a bimaterial under steady or unsteady state conditions. However, the stress and displacement components for the interfacial propagating crack in dissimilar orthotropic media, where the elastic principal axis direction with the crack direction is orthogonal or parallel, is not clearly represented.

Therefore, the general stress and displacement fields are derived when a finite crack is steadily propagated along the interface in dissimilar orthotropic media under dynamic mode I and II loading in the paper. Lee et al. [4] derived the steady plane motion formulations for orthotropic material from the partial differential equation for an elastodynamic plane. The general stress and displacement fields are obtained from the formulation of steady plane motion which is added to the complex eigenexpansion functions and the boundary conditions. The relationship between stress intensity factors and stress components for propagating an interfacial crack is defined and the confusion of the definition for the stress intensity factors of the interface crack is clarified.

Contributed by the Applied Mechanics Division of THE AMERICAN SOCIETY OF MECHANICAL ENGINEERS for publication in the ASME JOURNAL OF APPLIED MECHANICS. Manuscript received by the ASME Applied Mechanics Division, June 23, 1999; final revision, Oct. 12, 1999. Associate Technical Editor: W. J. Drugan.

2 General Stress and Displacement Fields

When characteristic roots m_l and m_s of orthotropic material have imaginary numbers ip, iq, the complex stress for orthotropic plane motion can be represented as Eq. (1) [4],

$$\sigma_x = 2\,\mathrm{Re}\{(M_b - p^2)\phi'(z_l) + (M_b - q^2)\psi'(z_s)\}$$
$$\sigma_y = 2\,\mathrm{Re}\{(1+M_a)[\phi'(z_l) + \psi'(z_s)]\} \tag{1}$$
$$\tau_{xy} = 2\,\mathrm{Im}[\alpha_l\phi'(z_l) + \alpha_s\psi'(z_s)]\}$$

where

$$p = \sqrt{B_{12} - \sqrt{B_{12}^2 - K_{66}}}, \quad q = \sqrt{B_{12} + \sqrt{B_{12}^2 - K_{66}}}$$

$$B_{12} = \frac{1}{2}[2a_{12} + a_{66} + \rho c^2(a_{12}^2 - a_{11}a_{66} - a_{11}a_{22})]/a_{11}$$

$$K_{66} = \{a_{22} + \rho c^2[a_{12}^2 - a_{22}a_{66} - a_{11}a_{22} + \rho c^2 a_{66}(a_{11}a_{22} - a_{12}^2)]\}/a_{11}$$

$$\alpha_l = p + a_{22}\frac{\rho c^2}{p} - p\rho c^2 a_{11} - \frac{(\rho c^2)^2}{p}(a_{11}a_{22} - a_{12}^2)$$

$$\alpha_s = q + a_{22}\frac{\rho c^2}{q} - q\rho c^2 a_{11} - \frac{(\rho c^2)^2}{q}(a_{11}a_{22} - a_{12}^2)$$

$$M_a = \rho c^2(a_{12} - a_{11}), \quad M_b = \rho c^2(a_{12} - a_{22}).$$

$a_{ij}(i,j = 1,2,3,\ldots,6)$ are displacement constants, which are the $a_{i3} = a_{j3} = 0$ for plane stress and are transformed into the $b_{ij} = a_{ij} - a_{i3}a_{j3}/a_{33}$ for plane strain [5]. The ρ and c are, respectively, density and crack propagation velocity. And the characteristic roots m_l, m_s of orthotropic materials, which depend on the physical properties and the crack propagation, are either imaginary when $\sqrt{K_{66}} < B_{12}$; $K_{66} > 0$ or complex when $\sqrt{K_{66}} > |B_{12}|$; $K_{66} > 0$ [4]. Most orthotropic materials have imaginary number roots. The complex displacement for orthotropic plane motion can be represented as Eq. (2) [4],

$$u_x = 2\,\mathrm{Re}[p_l\phi(z_l) + p_s\psi(z_s)]$$
$$u_y = 2\,\mathrm{Im}[q_l\phi(z_l) + q_s\psi(z_s)] \tag{2}$$

where

$$p_l = a_{11}(M_b - p^2) + a_{12}(M_a + 1)$$

$$p_s = a_{11}(M_b - q^2) + a_{12}(M_a + 1)$$

$$q_l = [a_{12}(M_b - p^2) + a_{22}(M_a + 1)]/p$$

$$q_s = [a_{12}(M_b - q^2) + a_{22}(M_a + 1)]/q.$$

Analytical complex functions $\phi'(z_l)$ and $\psi'(z_s)$ can be represented as such a power series in

$$\phi'(z_l) = az_l^{\lambda_n} + b\overline{z_l^{\lambda_n}}, \quad \psi'(z_s) = cz_s^{\lambda n} + d\overline{z_s^{\lambda_n}} \tag{3}$$

where a, b, c, and d are complex constants and λ_n is an eigenvalue. They are to be determined from boundary conditions. From the traction-free crack ($\theta=\pm\pi$) and the traction and displacement continuous condition across interface ($\theta=0$), the following equations can be obtained:

$$e^{i2\pi\lambda_n}[S]_1\begin{bmatrix}a_1\\c_1\end{bmatrix}=[T]_1\overline{\begin{bmatrix}b_1\\d_1\end{bmatrix}} \tag{4}$$

$$e^{-i2\pi\lambda_n}[S]_2\begin{bmatrix}a_2\\c_2\end{bmatrix}=[T]_2\overline{\begin{bmatrix}b_2\\d_2\end{bmatrix}} \tag{5}$$

$$[S]_1\begin{bmatrix}a_1\\c_1\end{bmatrix}-[T]_1\overline{\begin{bmatrix}b_1\\d_1\end{bmatrix}}=[S]_2\begin{bmatrix}a_2\\c_2\end{bmatrix}-[T]_2\overline{\begin{bmatrix}b_2\\d_2\end{bmatrix}} \tag{6}$$

$$[U]_1\begin{bmatrix}a_1\\c_1\end{bmatrix}-[V]_1\overline{\begin{bmatrix}b_1\\d_1\end{bmatrix}}=[U]_2\begin{bmatrix}a_2\\c_2\end{bmatrix}-[V]_2\overline{\begin{bmatrix}b_2\\d_2\end{bmatrix}} \tag{7}$$

where

$$S_k=\begin{bmatrix}(1+M_a) & (1+M_a)\\ \alpha_l & \alpha_s\end{bmatrix},\quad T_k=\begin{bmatrix}-(1+M_a) & -(1+M_a)\\ \alpha_l & \alpha_s\end{bmatrix}$$

$$U_k=\begin{bmatrix}-p_l & -p_s\\ q_l & q_s\end{bmatrix},\quad V_k=\begin{bmatrix}p_l & p_s\\ q_l & q_s\end{bmatrix}.$$

Matrices L_k, L_k^*, H_k, and H_k^* input as follows:

$$L_k=U_kS_k^{-1},\quad L_k^*=V_kT_k^{-1}$$
$$H=L_1-L_2^*,\quad H^*=L_1^*-L_2. \tag{8}$$

Substituting Eq. (8) into Eqs. (4)–(7), the characteristic equation can be derived for eigenvalue λ_n,

$$\begin{bmatrix}\lambda_2 & 0\\ 0 & \lambda_1\end{bmatrix}(e^{i2\pi\lambda_n})^2-\begin{bmatrix}\lambda_1+\lambda_2 & 0\\ 0 & \lambda_1+\lambda_2\end{bmatrix}(e^{i2\pi\lambda_n})+\begin{bmatrix}\lambda_1 & 0\\ 0 & \lambda_2\end{bmatrix}=0 \tag{9}$$

where

$$\lambda_1=h_{11}+\sqrt{h_{12}h_{21}},\quad \lambda_2=h_{11}-\sqrt{h_{12}h_{21}}$$

$$h_{11}=(l_{11})_1-(l_{11})_2,\quad h_{12}=(l_{12})_1+(l_{12})_2$$

$$h_{21}=(l_{21})_1+(l_{21})_2$$

$$(l_{11})_k=\left\{\frac{p_s\alpha_l-p_l\alpha_s}{D}\right\}_k=\left\{\frac{q_s-q_l}{\alpha_s-\alpha_l}\right\}_k$$

$$(l_{12})_k=\left\{\frac{(1+M_\alpha)(p_l-p_s)}{D}\right\}_k,\quad (l_{21})_k=\left\{\frac{\alpha_sq_l-\alpha_lq_s}{D}\right\}_k$$

$$D_k=[(1+M_a)(\alpha_s-\alpha_l)]_k.$$

When $D_k=0$, the crack propagation velocity c becomes the Rayleigh speed. From Eq. (9), eigenvalue λ_n can be determined as Eq. (10).

$$\lambda_n=\begin{cases}n\ \ (=0,1,2,3,\dots)\\ \dfrac{2n-1}{2}\pm i\varepsilon\ \ (n=0,1,2,3,\dots)\end{cases} \tag{10}$$

$$\varepsilon=\frac{1}{2\pi}\ln\frac{1-\beta}{1+\beta},\quad \beta=\frac{h_{11}}{\sqrt{h_{12}h_{21}}}$$

Therefore the two cases, oscillatory and nonoscillatory fields, must be considered.

2.1 Oscillatory Stress and Displacement Fields. The λ_n is a complex eigenvalue in this case. Therefore, in substituting the complex eigenvalue $\lambda_n=(2n-1)/2+i\varepsilon$ in Eq. (10) into Eqs. (4)–(7), complex constants a_k, b_k, c_k, and d_k may be obtained as

$$a_k=\left[\frac{\alpha_s-(1+M_a)\eta}{D}\right]_k e^{\pi\varepsilon(-1)^{k+1}}\zeta$$

$$b_k=\left[\frac{\alpha_s+(1+M_a)\eta}{D}\right]_k e^{\pi\varepsilon(-1)^{k}}\overline{\zeta}$$

$$c_k=\left[\frac{-\alpha_l+(1+M_a)\eta}{D}\right]_k e^{\pi\varepsilon(-1)^{k+1}}\zeta$$

$$d_k=-\left[\frac{\alpha_l+(1+M_a)\eta}{D}\right]_k e^{\pi\varepsilon(-1)^{k}}\overline{\zeta} \tag{11}$$

where $\eta=(h_{21}/h_{12})^{1/2}$ and ζ is a complex constant related to stress intensity factors. Substituting Eq. (11) into Eq. (3), $\phi'_{n1}(z_l)$ and $\psi'_{n1}(z_s)$ for material 1 are written as

$$\phi'_{n1}(z_l)=\frac{z_l^{(2n-1)/2}}{D_1}\{[\alpha_s-(1+M_a)\eta]e^{\varepsilon\pi}\zeta_nz_l^{i\varepsilon}+[\alpha_s+(1+M_a)\eta]e^{-\varepsilon\pi}\overline{\zeta_nz_s^{-i\varepsilon}}\}$$

$$\psi'_{n1}(z_s)=\frac{z_s^{(2n-1)/2}}{D_1}\{[-\alpha_l+(1+M_a)\eta]e^{\varepsilon\pi}\zeta_nz_l^{i\varepsilon}-[\alpha_s+(1+M_a)\eta]e^{-\varepsilon\pi}\overline{\zeta_nz_s^{-i\varepsilon}}\}. \tag{12}$$

Stress intensity factors can be defined as Eq. (13) when the crack is propagated along the interface in dissimilar media.

$$K_{\mathrm{I}}+iK_{\mathrm{II}}=\lim_{r\to0}\sqrt{2\pi r}r^{-i\varepsilon}\left(\sigma_y+i\frac{1}{\eta}\tau_{xy}\right)_{\theta=0}. \tag{13}$$

In substituting Eq. (12) into Eq. (1) and substituting Eq. (1) into Eq. (13), the complex constants related to stress intensity factors are obtained as Eq. (14),

$$K_n^0=2\sqrt{2\pi}(e^{\varepsilon\pi}+e^{-\varepsilon\pi})\zeta_n^0$$
$$K_n^*=2\sqrt{2\pi}(e^{\varepsilon\pi}+e^{-\varepsilon\pi})\zeta_n^*, \tag{14}$$

where ζ_n^0 and ζ_n^* are real parts of complex constant ζ_n. When $n=0$ in Eq. (14), K_n^0 and K_n^* are stress intensity factors K_{I} and K_{II}. In substituting Eq. (14) into Eq. (12) and substituting Eq. (12) into Eq. (1), stress fields for propagating the crack along the interface in dissimilar orthotropic material can be obtained. Oscillatory stress fields with odd power series ($n=1,3,5,\dots$) for material 1 (the material above the interface) can be represented as

$$\sigma_{xn}=\sum_{n=\text{odd}}^{\infty}\frac{K_n^0}{2\sqrt{2\pi}D\,\cosh(\varepsilon\pi)}\Bigg[(M_b-p^2)\Bigg\{e^{\varepsilon(\pi-\theta_l)}\overline{A}\,\cos\Big(\varepsilon\,\ln r_l+\frac{n-2}{2}\theta_l\Big)+e^{-\varepsilon(\pi-\theta_l)}A\,\cos\Big(\varepsilon\,\ln r_l-\frac{n-2}{2}\theta_1\Big)\Bigg\}r_l^{(n-2)/2}$$
$$-(M_b-q^2)\Bigg\{e^{\varepsilon(\pi-\theta_s)}\overline{B}\,\cos\Big(\varepsilon\,\ln r_s+\frac{n-2}{2}\theta_s\Big)+e^{-\varepsilon(\pi-\theta_s)}B\,\cos\Big(\varepsilon\,\ln r_s-\frac{n-2}{2}\theta_s\Big)\Bigg\}r_s^{(n-2)/2}\Bigg]$$
$$+\sum_{n=\text{odd}}^{\infty}\frac{K_n^*}{2\sqrt{2\pi}D\,\cosh(\varepsilon\pi)}\Bigg[-(M_b-p^2)\Bigg\{e^{\varepsilon(\pi-\theta_l)}\overline{A}\,\sin\Big(\varepsilon\,\ln r_l+\frac{n-2}{2}\theta_l\Big)+e^{-\varepsilon(\pi-\theta_l)}A\,\sin\Big(\varepsilon\,\ln r_l-\frac{n-2}{2}\theta_l\Big)\Bigg\}r_l^{(n-2)/2}$$
$$+(M_b-q^2)\Bigg\{e^{\varepsilon(\pi-\theta_s)}\overline{B}\,\sin\Big(\varepsilon\,\ln r_s+\frac{n-2}{2}\theta_s\Big)+e^{-\varepsilon(\pi-\theta_s)}B\,\sin\Big(\varepsilon\,\ln r_s-\frac{n-2}{2}\theta_s\Big)\Bigg\}r_s^{(n-2)/2}\Bigg] \tag{15}$$

$$\sigma_{yn}=\sum_{n=\text{odd}}^{\infty}\frac{K_n^0}{2\sqrt{2\pi}D\,\cosh(\varepsilon\pi)}\Bigg[(1+M_a)\Bigg\{e^{\varepsilon(\pi-\theta_l)}\overline{A}\,\cos\Big(\varepsilon\,\ln r_l+\frac{n-2}{2}\theta_l\Big)+e^{-\varepsilon(\pi-\theta_l)}A\,\cos\Big(\varepsilon\,\ln r_l-\frac{n-2}{2}\theta_l\Big)\Bigg\}r_l^{(n-2)/2}$$
$$-(1+M_a)\Bigg\{e^{\varepsilon(\pi-\theta_s)}\overline{B}\,\cos\Big(\varepsilon\,\ln r_s+\frac{n-2}{2}\theta_s\Big)+e^{-\varepsilon(\pi-\theta_s)}B\,\cos\Big(\varepsilon\,\ln r_s-\frac{n-2}{2}\theta_s\Big)\Bigg\}r_s^{(n-2)/2}\Bigg]$$
$$+\sum_{n=\text{odd}}^{\infty}\frac{K_n^*}{2\sqrt{2\pi}D\,\cosh(\varepsilon\pi)}\Bigg[-(1+M_a)\Bigg\{e^{\varepsilon(\pi-\theta_l)}\overline{A}\,\sin\Big(\varepsilon\,\ln r_l+\frac{n-2}{2}\theta_l\Big)+e^{-\varepsilon(\pi-\theta_l)}A\,\sin\Big(\varepsilon\,\ln r_l-\frac{n-2}{2}\theta_l\Big)\Bigg\}r_l^{(n-2)/2}$$
$$+(1+M_a)\Bigg\{e^{\varepsilon(\pi-\theta_s)}\overline{B}\,\sin\Big(\varepsilon\,\ln r_s+\frac{n-2}{2}\theta_s\Big)+e^{-\varepsilon(\pi-\theta_s)}B\,\sin\Big(\varepsilon\,\ln r_s-\frac{n-2}{2}\theta_s\Big)\Bigg\}r_s^{(n-2)/2}\Bigg] \tag{16}$$

$$\tau_{xyn}=\sum_{n=\text{odd}}^{\infty}\frac{K_n^0}{2\sqrt{2\pi}D\,\cosh(\varepsilon\pi)}\Bigg[\alpha_l\Bigg\{e^{\varepsilon(\pi-\theta_l)}\overline{A}\,\sin\Big(\varepsilon\,\ln r_l+\frac{n-2}{2}\theta_l\Big)-e^{-\varepsilon(\pi-\theta_l)}A\,\sin\Big(\varepsilon\,\ln r_l-\frac{n-2}{2}\theta_l\Big)\Bigg\}r_l^{(n-2)/2}$$
$$+\alpha_s\Bigg\{-e^{\varepsilon(\pi-\theta_s)}\overline{B}\,\sin\Big(\varepsilon\,\ln r_s+\frac{n-2}{2}\theta_s\Big)+e^{-\varepsilon(\pi-\theta_s)}B\,\sin\Big(\varepsilon\,\ln r_s-\frac{n-2}{2}\theta_s\Big)\Bigg\}r_s^{(n-2)/2}\Bigg]$$
$$+\sum_{n=\text{odd}}^{\infty}\frac{K_n^*}{2\sqrt{2\pi}D\,\cosh(\varepsilon\pi)}\Bigg[\alpha_l\Bigg\{e^{\varepsilon(\pi-\theta_l)}\overline{A}\,\cos\Big(\varepsilon\,\ln r_l+\frac{n-2}{2}\theta_l\Big)-e^{-\varepsilon(\pi-\theta_l)}A\,\cos\Big(\varepsilon\,\ln r_l-\frac{n-2}{2}\theta_l\Big)\Bigg\}r_l^{(n-2)/2}$$
$$+\alpha_s\Bigg\{-e^{\varepsilon(\pi-\theta_s)}\overline{B}\,\cos\Big(\varepsilon\,\ln r_s+\frac{n-2}{2}\theta_s\Big)+e^{-\varepsilon(\pi-\theta_s)}B\,\cos\Big(\varepsilon\,\ln r_s-\frac{n-2}{2}\theta_s\Big)\Bigg\}r_s^{(n-2)/2}\Bigg] \tag{17}$$

where

$$A=\alpha_s+(1+M_a)\,\eta,\quad \overline{A}=\alpha_s-(1+M_a)\,\eta,\quad B=\alpha_l+(1+M_a)\,\eta,\quad \overline{B}=\alpha_l-(1+M_a)\,\eta.$$

By substituting Eq. (11) into Eq. (3) integrated with z and substituting Eq. (3) into Eq. (2), oscillatory displacement fields can be obtained. Oscillatory displacement fields with odd power series ($n=1,3,5,\ldots$) for material 1 can be represented as

$$u_{xn}=\sum_{n=\text{odd}}^{\infty}\frac{K_n^0}{\sqrt{2\pi}(n^2+4\varepsilon^2)D\,\cosh\varepsilon\pi}\Bigg\{e^{\varepsilon(\pi-\theta_l)}p_l\overline{A}\Big[n\,\cos\Big(\varepsilon\,\ln r_l+\frac{n}{2}\theta_l\Big)+2\varepsilon\,\sin\Big(\varepsilon\,\ln r_l+\frac{n}{2}\theta_l\Big)\Big]r_l^{n/2}$$
$$+e^{-\varepsilon(\pi-\theta_l)}p_lA\Big[n\,\cos\Big(\varepsilon\,\ln r_l-\frac{n}{2}\theta_l\Big)+2\varepsilon\,\sin\Big(\varepsilon\,\ln r_l-\frac{n}{2}\theta_l\Big)\Big]r_l^{n/2}-e^{\varepsilon(\pi-\theta_s)}p_s\overline{B}\Big[n\,\cos\Big(\varepsilon\,\ln r_s+\frac{n}{2}\theta_s\Big)$$
$$+2\varepsilon\,\sin\Big(\varepsilon\,\ln r_s+\frac{n}{2}\theta_s\Big)\Big]r_s^{n/2}-e^{-\varepsilon(\pi-\theta_s)}p_sB\Big[n\,\cos\Big(\varepsilon\,\ln r_s-\frac{n}{2}\theta_s\Big)+2\varepsilon\,\sin\Big(\varepsilon\,\ln r_s-\frac{n}{2}\theta_s\Big)\Big]r_s^{n/2}\Bigg\}$$
$$+\sum_{n=\text{odd}}^{\infty}\frac{K_n^*}{\sqrt{2\pi}(n^2+4\varepsilon^2)D\,\cosh\varepsilon\pi}\Bigg\{-e^{\varepsilon(\pi-\theta_l)}p_l\overline{A}\Big[n\,\sin\Big(\varepsilon\,\ln r_l+\frac{n}{2}\theta_l\Big)-2\varepsilon\,\cos\Big(\varepsilon\,\ln r_l+\frac{n}{2}\theta_l\Big)\Big]r_l^{n/2}$$
$$-e^{-\varepsilon(\pi-\theta_l)}p_lA\Big[n\,\sin\Big(\varepsilon\,\ln r_l-\frac{n}{2}\theta_l\Big)-2\varepsilon\,\cos\Big(\varepsilon\,\ln r_l-\frac{n}{2}\theta_l\Big)\Big]r_l^{n/2}+e^{\varepsilon(\pi-\theta_s)}p_s\overline{B}\Big[n\,\sin\Big(\varepsilon\,\ln r_s+\frac{n}{2}\theta_s\Big)$$
$$-2\varepsilon\,\cos\Big(\varepsilon\,\ln r_s+\frac{n}{2}\theta_s\Big)\Big]r_s^{n/2}+e^{-\varepsilon(\pi-\theta_s)}p_sB\Big[n\,\sin\Big(\varepsilon\,\ln r_s-\frac{n}{2}\theta_s\Big)-2\varepsilon\,\cos\Big(\varepsilon\,\ln r_s-\frac{n}{2}\theta_s\Big)\Big]r_s^{n/2}\Bigg\} \tag{18}$$

$$u_{yn}=\sum_{n=\text{odd}}^{\infty}\frac{K_n^0}{\sqrt{2\pi}(n^2+4\varepsilon^2)D\cosh\varepsilon\pi}\Bigg\{e^{\varepsilon(\pi-\theta_l)}q_l\overline{A}\Big[n\sin\Big(\varepsilon\ln r_l+\frac{n}{2}\theta_l\Big)-2\varepsilon\cos\Big(\varepsilon\ln r_l+\frac{n}{2}\theta_l\Big)\Big]r_l^{n/2}$$
$$-e^{-\varepsilon(\pi-\theta_l)}q_lA\Big[n\sin\Big(\varepsilon\ln r_l-\frac{n}{2}\theta_l\Big)-2\varepsilon\cos\Big(\varepsilon\ln r_l-\frac{n}{2}\theta_l\Big)\Big]r_l^{n/2}-e^{\varepsilon(\pi-\theta_s)}q_s\overline{B}\Big[n\sin\Big(\varepsilon\ln r_s+\frac{n}{2}\theta_s\Big)$$
$$-2\varepsilon\cos\Big(\varepsilon\ln r_s+\frac{n}{2}\theta_s\Big)\Big]r_s^{n/2}+e^{-\varepsilon(\pi-\theta_s)}q_sB\Big[n\sin\Big(\varepsilon\ln r_s-\frac{n}{2}\theta_s\Big)-2\varepsilon\cos\Big(\varepsilon\ln r_s-\frac{n}{2}\theta_s\Big)\Big]r_s^{n/2}\Bigg\}$$
$$+\sum_{n=\text{odd}}^{\infty}\frac{K_n^*}{\sqrt{2\pi}(n^2+4\varepsilon^2)D\cosh\varepsilon\pi}\Bigg\{e^{\varepsilon(\pi-\theta_l)}q_l\overline{A}\Big[n\cos\Big(\varepsilon\ln r_l+\frac{n}{2}\theta_l\Big)+2\varepsilon\sin\Big(\varepsilon\ln r_l+\frac{n}{2}\theta_l\Big)\Big]r_l^{n/2}$$
$$-e^{-\varepsilon(\pi-\theta_l)}q_lA\Big[n\cos\Big(\varepsilon\ln r_l-\frac{n}{2}\theta_l\Big)+2\varepsilon\sin\Big(\varepsilon\ln r_l-\frac{n}{2}\theta_l\Big)\Big]r_l^{n/2}-e^{\varepsilon(\pi-\theta_s)}q_s\overline{B}\Big[n\cos\Big(\varepsilon\ln r_s+\frac{n}{2}\theta_s\Big)$$
$$+2\varepsilon\sin\Big(\varepsilon\ln r_s+\frac{n}{2}\theta_s\Big)\Big]r_s^{n/2}+e^{-\varepsilon(\pi-\theta_s)}q_sB\Big[n\cos\Big(\varepsilon\ln r_s-\frac{n}{2}\theta_s\Big)+2\varepsilon\sin\Big(\varepsilon\ln r_s-\frac{n}{2}\theta_s\Big)\Big]r_s^{n/2}\Bigg\} \tag{19}$$

where $n>0$. For material 2, which is the material below the interface, parameters $\varepsilon\pi$ and $-\varepsilon\pi$ in oscillatory stress and displacement fields are changed to $-\varepsilon\pi$, $\varepsilon\pi$. When n is 1, Eqs. (15)–(19) are stress and displacement fields around the propagating interfacial crack tip. Thus, K_1^0 and K_1^* are stress intensity factors K_{I} and K_{II}.

2.2 Nonoscillatory Stress and Displacement Fields. The λ_n is a positive integer eigenvalue in this case. Nonoscillatory stress fields with the even power series ($n=2,4,6,\ldots$) for material 1 can be presented as

$$\sigma_{xn}=\sum_{n=\text{even}}^{\infty}\frac{K_n^0}{\sqrt{2\pi}}\frac{1}{1+w_s}\frac{(1+M_a)}{D}\Bigg\{(M_b-q^2)r_s^{(n-2)/2}\times\cos\frac{n-2}{2}\theta_s-(M_b-p^2)r_l^{(n-2)/2}\cos\frac{n-2}{2}\theta_l\Bigg\}$$
$$+\sum_{n=\text{even}}^{\infty}\frac{K_n^*}{\sqrt{2\pi}}\frac{1}{1+w_l}\frac{1}{D}\Bigg\{\alpha_l(M_b-q^2)r_s^{(n-2)/2}\times\sin\frac{n-2}{2}\theta_s-\alpha_s(M_b-p^2)r_l^{(n-2)/2}\sin\frac{n-2}{2}\theta_l\Bigg\} \tag{20}$$

$$\sigma_{yn}=\sum_{n=\text{even}}^{\infty}\frac{K_n^0}{\sqrt{2\pi}}\frac{1}{1+w_s}\frac{(1+M_a)^2}{D}\Bigg\{r_s^{(n-2)/2}\cos\frac{n-2}{2}\theta_s-r_l^{(n-2)/2}\cos\frac{n-2}{2}\theta_l\Bigg\}+\sum_{n=\text{even}}^{\infty}\frac{K_n^*}{\sqrt{2\pi}}\frac{1}{1+w_l}\frac{(1+M_a)}{D}$$
$$\times\Bigg\{\alpha_lr_s^{(n-2)/2}\sin\frac{n-2}{2}\theta_s-\alpha_sr_l^{(n-2)/2}\sin\frac{n-2}{2}\theta_l\Bigg\} \tag{21}$$

$$\tau_{xyn}=\sum_{n=\text{even}}^{\infty}\frac{K_n^0}{\sqrt{2\pi}}\frac{1}{1+w_s}\frac{(1+M_a)}{D}\Bigg\{\alpha_sr_s^{(n-2)/2}\sin\frac{n-2}{2}\theta_s-\alpha_lr_l^{(n-2)/2}\sin\frac{n-2}{2}\theta_l\Bigg\}+\sum_{n=\text{even}}^{\infty}\frac{K_n^*}{\sqrt{2\pi}}\frac{1}{1+w_l}\frac{\alpha_l\alpha_s}{D}$$
$$\times\Bigg\{-r_s^{(n-2)/2}\cos\frac{n-2}{2}\theta_s+r_l^{(n-2)/2}\cos\frac{n-2}{2}\theta_l\Bigg\} \tag{22}$$

where $n>0$, $w_s=(l_{12})_1/(l_{12})_2$, and $w_l=(l_{21})_1/(l_{21})_2$.

Nonoscillatory displacement fields with even power series ($n=2,4,6,\ldots$) for material 1 can be represented as

$$u_{xn}=\sum_{n=\text{even}}^{\infty}\frac{K_n^0}{\sqrt{2\pi}}\frac{2}{1+w_s}\frac{(1+M_a)}{Dn}\Bigg\{p_sr_s^{n/2}\cos\frac{n}{2}\theta_s-p_lr_l^{n/2}\cos\frac{n}{2}\theta_l\Bigg\}$$
$$+\sum_{n=\text{even}}^{\infty}\frac{K_n^*}{\sqrt{2\pi}}\frac{2}{1+w_l}\frac{1}{Dn}\Bigg\{\alpha_lp_sr_s^{n/2}\sin\frac{n}{2}\theta_s-\alpha_sp_lr_l^{n/2}\sin\frac{n}{2}\theta_l\Bigg\} \tag{23}$$

$$u_{yn}=\sum_{n=\text{even}}^{\infty}\frac{K_n^0}{\sqrt{2\pi}}\frac{2}{1+w_s}\frac{(1+M_a)}{Dn}\times\Bigg\{q_sr_s^{n/2}\sin\frac{n}{2}\theta_s-q_lr_l^{n/2}\sin\frac{n}{2}\theta_l\Bigg\}+\sum_{n=\text{even}}^{\infty}\frac{K_n^*}{\sqrt{2\pi}}\frac{2}{1+w_l}\frac{1}{Dn}$$
$$\times\Bigg\{-\alpha_lq_sr_s^{n/2}\cos\frac{n}{2}\theta_s+\alpha_sq_lr_l^{n/2}\cos\frac{n}{2}\theta_l\Bigg\}. \tag{24}$$

For material 2, which is the material below the interface, parameters w_s and w_l are changed to w_s^{-1} and w_l^{-1}. Therefore, general stress and displacement fields for propagating the interface crack can be represented as

$$\sigma_n(r,\theta)=\sum_{n=1}^{\infty}[\sigma_{xn}\ \ \sigma_{yn}\ \ \tau_{xyn}]^T$$
$$u_n(r,\theta)=\sum_{n=1}^{\infty}[u_{xn}\ \ u_{yn}]^T. \tag{25}$$

2.3 Stress and Displacement Fields at the Interfacial Propagating Crack Tip. When n is 1, the general fields become the propagating crack-tip fields. Stress and displacement components σ_x, u_x at the interfacial propagating crack tip for material 1 are expressed as

$$\sigma_x=\frac{K_{\mathrm{I}}}{2\sqrt{2\pi}rD\cosh\varepsilon\pi}\left\{(M_b-p^2)f_l(\theta)\left[e^{\varepsilon(\pi-\theta_l)}\overline{A}\cos\left(\varepsilon\ln r_l-\frac{\theta_l}{2}\right)+e^{-\varepsilon(\pi-\theta_l)}A\cos\left(\varepsilon\ln r_l+\frac{\theta_l}{2}\right)\right]\right.$$
$$\left.-(M_b-q^2)f_s(\theta)\left[e^{\varepsilon(\pi-\theta_s)}\overline{B}\cos\left(\varepsilon\ln r_s-\frac{\theta_s}{2}\right)+e^{-\varepsilon(\pi-\theta_s)}B\cos\left(\varepsilon\ln r_s+\frac{\theta_s}{2}\right)\right]\right\}$$
$$+\frac{K_{\mathrm{II}}}{2\sqrt{2\pi}rD\cosh\varepsilon\pi}\left\{-(M_b-p^2)f_l(\theta)\left[e^{\varepsilon(\pi-\theta_l)}\overline{A}\sin\left(\varepsilon\ln r_l-\frac{\theta_l}{2}\right)+e^{-\varepsilon(\pi-\theta_l)}A\sin\left(\varepsilon\ln r_l+\frac{\theta_l}{2}\right)\right]\right.$$
$$\left.+(M_b-q^2)f_s(\theta)\left[e^{\varepsilon(\pi-\theta_s)}\overline{B}\sin\left(\varepsilon\ln r_s-\frac{\theta_s}{2}\right)+e^{-\varepsilon(\pi-\theta_s)}B\sin\left(\varepsilon\ln r_s+\frac{\theta_s}{2}\right)\right]\right\} \tag{26}$$

$$u_x=\frac{K_{\mathrm{I}}}{2D(1+4\varepsilon^2)\cosh\varepsilon\pi}\sqrt{\frac{2r}{\pi}}\left\{e^{\varepsilon(\pi-\theta_l)}p_l\overline{A}\left[\cos\left(\varepsilon\ln r_l+\frac{\theta_l}{2}\right)+2\varepsilon\sin\left(\varepsilon\ln r_l+\frac{\theta_l}{2}\right)\right]\frac{1}{f_l(\theta)}\right.$$
$$+e^{-\varepsilon(\pi-\theta_l)}p_lA\left[\cos\left(\varepsilon\ln r_l-\frac{\theta_l}{2}\right)+2\varepsilon\sin\left(\varepsilon\ln r_l-\frac{\theta_l}{2}\right)\right]\frac{1}{f_l(\theta)}-e^{\varepsilon(\pi-\theta_s)}p_s\overline{B}\left[\cos\left(\varepsilon\ln r_s+\frac{\theta_s}{2}\right)+2\varepsilon\sin\left(\varepsilon\ln r_s+\frac{\theta_s}{2}\right)\right]\frac{1}{f_s(\theta)}$$
$$\left.-e^{-\varepsilon(\pi-\theta_s)}p_sB\left[\cos\left(\varepsilon\ln r_s-\frac{\theta_s}{2}\right)+2\varepsilon\sin\left(\varepsilon\ln r_s-\frac{\theta_s}{2}\right)\right]\frac{1}{f_s(\theta)}\right\}$$
$$+\frac{K_{\mathrm{II}}}{2D(1+4\varepsilon^2)\cosh\varepsilon\pi}\sqrt{\frac{2r}{\pi}}\left\{-e^{\varepsilon(\pi-\theta_l)}p_l\overline{A}\left[\sin\left(\varepsilon\ln r_l+\frac{\theta_l}{2}\right)-2\varepsilon\cos\left(\varepsilon\ln r_l+\frac{\theta_l}{2}\right)\right]\frac{1}{f_l(\theta)}\right.$$
$$-e^{-\varepsilon(\pi-\theta_l)}p_lA\left[\sin\left(\varepsilon\ln r_l-\frac{\theta_l}{2}\right)-2\varepsilon\cos\left(\varepsilon\ln r_l-\frac{\theta_l}{2}\right)\right]\frac{1}{f_l}(\theta)+e^{\varepsilon(\pi-\theta_s)}p_s\overline{B}\left[\sin\left(\varepsilon\ln r_s+\frac{\theta_s}{2}\right)-2\varepsilon\cos\left(\varepsilon\ln r_s+\frac{\theta_s}{2}\right)\right]\frac{1}{f_s(\theta)}$$
$$\left.+e^{-\varepsilon(\pi-\theta_s)}p_sB\left[\sin\left(\varepsilon\ln r_s-\frac{\theta_s}{2}\right)-2\varepsilon\cos\left(\varepsilon\ln r_s-\frac{\theta_s}{2}\right)\right]\frac{1}{f_s(\theta)}\right\} \tag{27}$$

where

$$r_l=r\sqrt{\cos^2\theta+p^2\sin^2\theta},\quad r_s=r\sqrt{\cos^2\theta+q^2\sin^2\theta}$$
$$f_l(\theta)=[\cos^2\theta+p^2\sin^2\theta]^{-(1/4)},$$
$$f_s(\theta)=[\cos^2\theta+q^2\sin^2\theta]^{-(1/4)}$$
$$\theta_j=\tan^{-1}(Z_j\tan\theta),\quad j=l,s,\quad Z_l=p,\quad Z_s=q.$$

The displacements between the crack surfaces are given by

$$\delta(r)=\delta_2+i\eta\delta_1=\sqrt{\frac{2r}{\pi}}\frac{H_{21}(K_{\mathrm{I}}+iK_{\mathrm{II}})r^{i\varepsilon}}{(1+2i\varepsilon)\cosh(\varepsilon\pi)} \tag{28}$$

and the energy release rate is given by

$$G=\frac{(K_{\mathrm{I}}^2+K_{\mathrm{II}}^2)H_{21}}{4\cosh^2(\varepsilon\pi)}. \tag{29}$$

As the stress σ_x is taken to be discontinuous and strain ε_x to be continuous across the line $y=0$, the relation between $(\sigma_x)_1$ and $(\sigma_x)_2$ is the same as

$$(\sigma_x)_2=\frac{(a_{11})_1(\sigma_x)_1+[(a_{12})_1-(a_{12})_2]\sigma_y}{(a_{11})_2}. \tag{30}$$

From Eq. (13), the stress intensity factors for propagating the crack along the interface in the infinite plate are obtained as

$$K_{\mathrm{I}}+iK_{\mathrm{II}}=\sqrt{\pi a}(1+2i\varepsilon)(2a)^{-i\varepsilon}\left(\sigma_y^{\infty}+i\frac{1}{\eta}\tau_{xy}^{\infty}\right) \tag{31}$$

where σ_y^{∞} and τ_{xy}^{∞} are the applied normal and shear stresses at infinity. Since Eq. (31) contains the term $(2a)^{-i\varepsilon}$, the ambiguity of the dependence on the measuring unit of the crack length for the value of the stress intensity factor occurs. If $(r)^{-i\varepsilon}$ is replaced with $(r/l)^{-i\varepsilon}$ in Eq. (13), where $l=2a$ (crack length), the stress intensity factors become the following equation, which does not contain the ambiguity of the dependence on the measuring unit of the crack length:

$$K_{\mathrm{I}}+iK_{\mathrm{II}}=\sqrt{\pi a}(1+2i\varepsilon)\left(\sigma_y^{\infty}+i\frac{1}{\eta}\tau_{xy}^{\infty}\right). \tag{32}$$

When stress intensity factors are the same as in Eq. (32), the term $\varepsilon\ln r_k$ $(k=l,s)$ in Eqs. (15)–(19) and (26)–(27) is replaced by $\varepsilon\ln(r_k/2a)$.

3 Conclusions

General stress, displacement fields, and energy release rate are explicitly presented for the interfacial propagating crack in dissimilar orthotropic materials.

When the orthotropic materials have characteristic roots $m_l\approx i$ and $m_s\approx i$ in the stationary crack state, the fields are the same as the Deng [2] results for the propagating interfacial crack in isotropic bimaterials. When the mechanical properties of dissimilar orthotropic materials are the same, the stress, displacement fields, and energy release rate are the same as those of homogeneous orthotropic material [4]. When the interface crack propagation velocity is zero, the fields of the interfacial propagating crack are identical to those of the interfacial stationary crack. The results are useful for both dissimilar isotropic-isotropic and isotropic-orthotropic and orthotropic-orthotropic bimaterials under subsonic crack propagation velocity lower than the two Rayleigh wave velocities and homogeneous isotropic and orthotropic materials under subsonic crack propagation velocity.

Table 1 The comparison of dissimilar isotropic and orthotropic stress component $\sigma_x\sqrt{K_I}$ under plane stress ($c/C_{s1}=0.5$)

θ (deg)	Iso-Iso.Mat	Ort-Ort.Mat	θ (deg)	Iso-Iso.Mat	Ort-Ort.Mat
0^+	.634439	.6344413	0^-	1.503408	1.503400
10	.7468052	.7468115	−10	1.302192	1.302208
20	.8190195	.8190226	−20	1.064251	1.064264
30	.8481339	.8481356	−30	.8146014	.8146035
40	.8359575	.8359596	−40	.5795064	.5794959
50	.7908002	.7907966	−50	.382161	.3821618
60	.7287843	.7287816	−60	.2386282	.2386150
70	.6730161	.6730131	−70	.1543843	.1543860
80	.6487839	.6487848	−80	.1229814	.1229963
90	.6748663	.6748638	−90	.1271673	.1271672
100	.7547211	.7547229	−100	.1428393	.1428359
110	.8735087	.8735143	−110	.1447629	.1447555
120	1.00348	1.003481	−120	.1124064	.1124141
130	1.114235	1.114237	−130	.0342066	.0341946
140	1.181642	1.181642	−140	−.0908023	−.0908047
150	1.191849	1.191844	−150	−.2536999	−.2537051
160	1.14096	1.140951	−160	−.4382891	−.4383058
170	1.032682	1.032665	−170	−.6245366	−.6245342
180	.8758961	.8758781	−180	−.7919333	−.7919445

Appendix

- Properties of isotropic-isotropic bimaterial:

$$C_{s2}/C_{s1}=2,\ \ \nu_1=0.3,\ \ \nu_2=0.2,\ \ \rho_1=\rho_2,\ \ r=0.01.$$

- Properties of orthotropic-orthotropic bimaterial:

$$C_{s2}/C_{s1}=2,\ \ \nu_{LT1}=0.3,\ \ \nu_{LT2}=0.2,\ \ \rho_1=\rho_2,\ \ r=0.01$$

$$E_{L1}:E_{T1}:G_{LT1}=2.6000001:2.6:1,\ \ C_{sk}=(\sqrt{G_{LT}/\rho})_k$$

$$E_{L2}:E_{T2}:G_{LT2}=9.600001:9.6:4,\ \ \overline{K_I}=K_I/\sqrt{2\pi r}$$

$$\alpha_1=\alpha_2=90\ \text{deg}.$$

E_L, E_T, G_{LT}, and $\nu_{LT}(-\varepsilon_T/\varepsilon_L)$ are elastic constants and Poisson's ratio, L and T are, respectively, the fiber direction and the transverse direction to the fiber, while α is the angle of the fiber direction with respect to the crack direction. The above orthotropic materials are almost like the isotropic ones ($m_l\approx i$ and $m_s\approx i$ in $c/C_{s1}=0$). As shown in Table 1, when the orthotropic materials have isotropic characteristics, the fields derived in this study are the same as the Deng's ([2]) results of the interfacial propagating crack in isotropic bimaterials.

Acknowledgment

This research was supported by research funds from the Korea Science and Engineering Foundation under Grant No. 971-1003-017-2.

References

[1] Yang, W., Suo, Z., and Shih, C. F., 1991, ''Mechanics of Dynamic Debonding,'' Proc. R. Soc. London, Ser. A, **433**, pp. 679–697.
[2] Deng, X., 1993, ''General Crack-Tip Fields for Stationary and Steadily Growing Interface Cracks in Anisotropic Bimaterials,'' J. Appl. Mech., **60**, pp. 183–189.
[3] Liu, C., Lambros, J., and Rosakis, A. J., 1993, ''Highly Transient Elastodynamic Crack Growth in a Bimaterial Interface: Higher Order Asymptotic Analysis and Optical Experiments,'' J. Mech. Phys. Solids, **41**, No. 12, pp. 1887–1954.
[4] Lee, K. H., Hawong, J. S., and Choi, S. H., 1996, ''Dynamic Stress Intensity Factors K_I, K_{II}, and Dynamic Crack Propagation Characteristics of Orthotropic Material,'' Eng. Fract. Mech., **53**, No. 1, pp. 119–140.
[5] Lekhnitskii, S. G., 1963, *Theory of Elasticity of an Anisotropic Elastic Body*, Holden-Day, San Francisco.